Anion Coordination and Gelation Study of Small Molecule based Self-assembled Systems: Recognition, Sensing and Water Remediation

A Dissertation

Submitted in the partial fulfillment for the degree of

Doctor of Philosophy

OIYAO APPUN PEGU

(Roll No. 216122024)

Thesis Supervisor: Prof. Gopal Das

Department of Chemistry

Indian Institute of Technology Guwahati

India-781039

Anion Coordination and Gelation Study of Small Molecule based Self-assembled Systems: Recognition, Sensing and Water Remediation

A Dissertation

Submitted in the partial fulfillment for the degree of

Doctor of Philosophy

Oiyao Appun Pegu

(Roll No. 216122024)

Thesis Supervisor: Prof. Gopal Das

Department of Chemistry

Indian Institute of Technology Guwahati

India-781039

Dedicated to my Late Father
Umananda Pegu (Babu)

INDIAN INSTITUTE OF TECHNOLOGY GUWAHATI

Department of Chemistry

STATEMENT

I do hereby declare that the matter embodied in this thesis is the result of investigations carried out by me in the Department of Chemistry, Indian Institute of Technology Guwahati, India, under the guidance of Prof. Gopal Das, Department of Chemistry, Indian Institute of Technology Guwahati, India.

In keeping with the general practice of reporting scientific observations, due acknowledgements have been made wherever this work is based on the findings of other investigators.

2nd March, 2026

IIT Guwahati

Oiyao Appun Pegu

INDIAN INSTITUTE OF TECHNOLOGY GUWAHATI

Department of Chemistry

CERTIFICATE

This is to certify that Mr. Oiyao Appun Pegu has been working under my supervision since July, 2021 as a regular registered Ph.D. student. His thesis, entitled **"Anion Coordination and Gelation Study of Small Molecule based Self-assembled Systems: Recognition, Sensing and Water Remediation"**, is an authentic record of the results obtained from the research work carried out under my supervision in the Department of Chemistry, Indian Institute of Technology Guwahati, Assam, India. I am forwarding his thesis to submit for the award of degree of Doctor of Philosophy, from this institute. I hereby certify that he has fulfilled all the requirements, according to the rules of this institute regarding the investigations embodied in his thesis, and this work has not been submitted elsewhere for a degree.

Prof. Gopal Das
(Thesis Supervisor)
Professor
Department of Chemistry
IIT Guwahati
Assam - 781039, India

ACKNOWLEDGEMENT

"Science is the greatest equalising force in the world"- Professor Omar M. Yaghi, with this quote, at the very outset, I would like to express my sincere appreciation to my supervisor Prof. Gopal Das, for allowing me to work under his leadership, and giving me the freedom to innovate. His constant support, motivation, and wisdom have played an instrumental role in my entire PhD journey. I will always deeply respect and value his sincerity towards work, professionalism, and kindness, and look forward to his guidance in my future journeys as well.

Coming to next, I would like to extend my sincere gratitude to my doctoral committee members, Prof. Sandip Paul, Prof. A.S. Achalkumar, and Prof. Shyam Prosad Biswas for their sincere evaluation of my research work, valuable suggestions, and feedbacks, that really helped me in improving my thesis work. I am thankful to all the HODs during my PhD tenure, Prof. Gopal Das, Prof. Aditya Narayan Panda, and Prof. Biplab Mondal, for their constant support throughout my research journey. Moreover, I would like to thank staff members, Dr. Babual Das, Dr. Kula Kamal Senapati, Mr. Imdadul Islam, Mr. Diganta Kumar Hira, Mr. Aniruddha Gogoi, Mr. Michael Deka, Mr. Shyamal Kumar Mondal, Ms. Sayanee Mukherjee, Mrs. Abhilasha M. Baruah, Mrs. Lipika Nath, for their support in my PhD journey. I sincerely acknowledge the instrument facilities of our department as well as CIF of our institute for providing the necessary instrument facilities during my PhD tenure. Moreover, I would like to thank UGC for the fellowship, which played crucial role in ensuring my smooths research journey.

I am highly grateful to all my seniors and lab mates, Dr. Asesh, Dr. Debojit, Dr. Megha, Dr. Sagnik, Dr. Debolina, Pampi, Rubi, Neha, Suleha, Bikram, Sanjana, Jumi, Akash, Sudip, Protyakshi, Maharshi, for their valuable supports during my research journey. I would also like to extend my sincere gratitude to Mr. Amarjit Pandey (Chemical Engineering Department, IIT Guwahati) and Dr. Raktim Gogoi (Chemistry Department, IIT Guwahati), for their unconditional help during my PhD tenure.

Failures are part and parcel of research and life; and sports teach us how to handle failure in the most beautiful way. So, I would like to thank all my badminton playing partners, especially,

Rubi, Nishan, Rantu, Manas, Sreeram, Jyoti Prakash, Tejaswini, and Prof. Charudatt Y Kadolkar for making my journey inside IITG campus both beautiful and memorable.

Now coming to the special mention part, in this roller-coaster journey of extreme highs and lows, I would like to mention that, I was blessed to have my best friend, Rubi Moral. Her constant support, and motivation forced me to dream big in my life. She being constant cheerer of my PhD journey, helped me immensely by giving emotional support throughout my research journey. We exchanged knowledge, ideas, and thoughts whether the topic was on science, philosophy, or humanities, whenever needed, in the most unselfish way for our mutual growth. So, I am thankful to her for all the positivity, strength, care, and constant motivation during my research tenure.

And, finally, I am forever grateful to the most important and amazing people of my life, my late father Umananda Pegu (Babu), my mother, Ms. Nirumai Pegu, for being the pillar of my journey. Your sacrifices, and hardships have always taught me to be humble and sincere. The reason I am being able to write this thesis is only because of your unwavering supports, and love. As I am completing my PhD journey with this thesis, I know you are the happiest person to see me achieve this milestone from wherever you are, Babu. I would like to thank my elder brother Mr. Pankaj Appun Pegu for pouring his constant support, and love, as a brother, and also as a teacher throughout my life and educational journey. I have always looked up to you whenever I am in trouble, and you have always motivated and advised me the best way possible. I am grateful to my sister Ms. Oikaneng Pegu for being always there for our family in both good and bad times. Lastly, I would like to thank my sister-in-law Ms. Suniya Doley for her unconditional love, and support throughout my PhD journey.

I bow down to the almighty in gratitude for the journey of life and hope his blessings continues……...!

Oiyao Appun

The synopsis report entitled **"Anion Coordination and Gelation Study of Small Molecule based Self-assembled Systems: Recognition, Sensing and Water Remediation"** has been divided into six chapters, which comprises the experimental outcomes of research work conducted throughout research tenure.

Chapter 1: Introduction and Literature Survey

Within the domain of supramolecular chemistry, supramolecular self-assembly is a nature inspired process, in which the spontaneous self-association of components leads to entities with higher order complexity with the help of various intermolecular interactions hydrogen bonding interaction, van der Waals interaction, coulomb interaction, hydrophobic interaction, π–π stacking, and so on.[1-6] The supramolecular self-assembled systems are often dynamic and reversible in nature, which makes them useful in constructing soft functional materials with fascinating properties.[7-14] Small molecule based supramolecular self-assembled systems are becoming very important for different application purposes, primarily due to their ease of synthesis, and high structural tunability. As the molecular level control of the properties of bulk material can often be accomplished to derive desired functionality, so such systems can frequently be designed and modulated for different purposes including recognition, sensing, construction of soft materials like supramolecular gel, etc.

Anion recognition is an integral part of supramolecular chemistry, and its birth can be traced back to the late 1960s when Shriver and Biallas worked on chelating Lewis acids; and ammonium containing cryptand like receptors designed for halide anions by Park and Simmons. However, the field of anion recognition truly blossomed in the past few decades only, with the emergence of its diverse range of applicability, including sensing, anion transport, recognition of molecules, anion extraction, crystal engineering etc. [1] Proper designing of receptors is a very critical step in this prospect of anion recognition, as anions are difficult to capture due to several reason such as its low charge to radius ratio, pH sensitivity, highly solvated in nature, etc. [2] Despite of all those challenges researchers have been making substantial progress in the field of anion recognition, with improved design rationale of the receptor molecules in recent times. Receptor molecules have been designed to selectively capture one of the most hydrophilic anions, such as SO_4^{2-}, and PO_4^{3-}, subsequently demonstrating their highly efficient extraction. [3,4] Researchers have also been able to demonstrated how the concept of anion recognition can be used for the development of molecular switches. [5-7] Moreover, recently the concept has also been utilised for the development of smart functional materials such as actuators, conductive materials, highly adhesive materials, stimuli responsive materials etc. [8-11]

Within the realm of supramolecular self-assembly, supramolecular gel is an another most prominent field of research, which is based on the principle of supramolecular hierarchical self-assembly. [12] Supramolecular gels are soft functional materials, derived from low molecular weight gelator (LMWG) molecules. The macroscopic level properties and performance of such soft materials can be well regulated through molecular level engineering of the LMWG molecules. [13] . To achieve gelation the LMWGs are often decorated with hydrogen bond forming units, π-π- stacking promoting units, van der Waals interaction promoting unit, hydrophobic unit etc. [14] However, gelation occurs only when there is a proper balance of all those non-covalent interactions. For the same reason appropriate rationale designing of LMWGs are very critical for the successful gelation. Moreover, use of proper solvent medium also plays a very critical role in this regard. Such soft materials can often be employed for myriads of applications such as in stimuli responsive materials development, water remediation, soft electronics, drug delivery, catalysis, etc. [15] Supramolecular gel responsive towards pH, toxic analytes, heating, light etc. are often developed by the researchers. [16] Such materials have also been used for water remediation applications including heavy metal removal, oil-spill remediation, dye adsorption from water etc. [17] Moreover, supramolecular gels are increasing becoming helpful for crystallisation for API (Active Pharmaceutical Ingredient), and catalysis purposes. [18,19]

This thesis primarily focuses on the development of small molecule based self-assembled systems for anion coordination, and supramolecular gelation purposes. The reason for choosing small molecule-based systems lies on its, ease of synthesis, high structural tunability, and economic viability. Within the subject of anion coordination chemistry, this thesis explores anion recognition (in both solid and solution state), crystal engineering, and toxic anion sensing. Anion recognition properties can be well regulated by modulating structure of the designed receptor molecules, and various non-covalent interactions involved in such anion recognition process can be visualised using crystal engineering (in the solid state), NMR technique (in solution phase), UV-vis or fluorescence spectroscopy (in solution phase). Selectivity in such anion recognition process is very important, especially in aqueous medium. With proper design rationale of the receptor molecules, selectivity can be achieved and additionally incorporation of signalling unit in such systems further allows visualisation of the recognition process via fluorescence spectroscopy as well as through naked eyes. Moreover, the concept of supramolecular self-assembly and anion recognition has further been expanded towards recognition guided sensing of toxic anion like cyanide (CN^-) in drinking water. The concept of anion recognition can also be applied in supramolecular gel systems for the development of anion responsive gel systems which have been demonstrated in the subsequent chapter of this thesis. In the same chapter, supramolecular gel system has been utilised for the sequestration of Ag^+ ion into its nanoparticles. The concept could further be applied for the

generation of a conductive hybrid gel nanocomposite as well. In the subsequent chapter, a phase selective organogelator (PSOG) molecule capable of selectively forming gel in presence of diesel and kerosene oil among a vast range of studied other solvent and oil systems has been developed. The PSOG can be utilised for oil spill recovery from water. Moreover, the idea of selective oil gelation has further been applied for the cost-effective visual detection of kerosene adulteration in petrol. Finally, the last chapter presents, how the phase transformation of a hierarchical nano-fibrillar assembly of a supramolecular gel can be well regulated to yield single crystals with well-defined crystal habits via controlled heating.

Chapter 2: Experimental methods and characterization

In this chapter, a detailed and comprehensive report of the various materials used in the synthesis is documented. The chapter outlines the design and preparation strategies employed, along with specifications of analytical instruments used in all the characterization processes.

Chapter 3A: Evaluating the Terminal Substituent Directed Differential Anion Recognition Aptitude of Bis-urea Receptors (*J. Mol. Struct., 2023, 1294, 136427*)

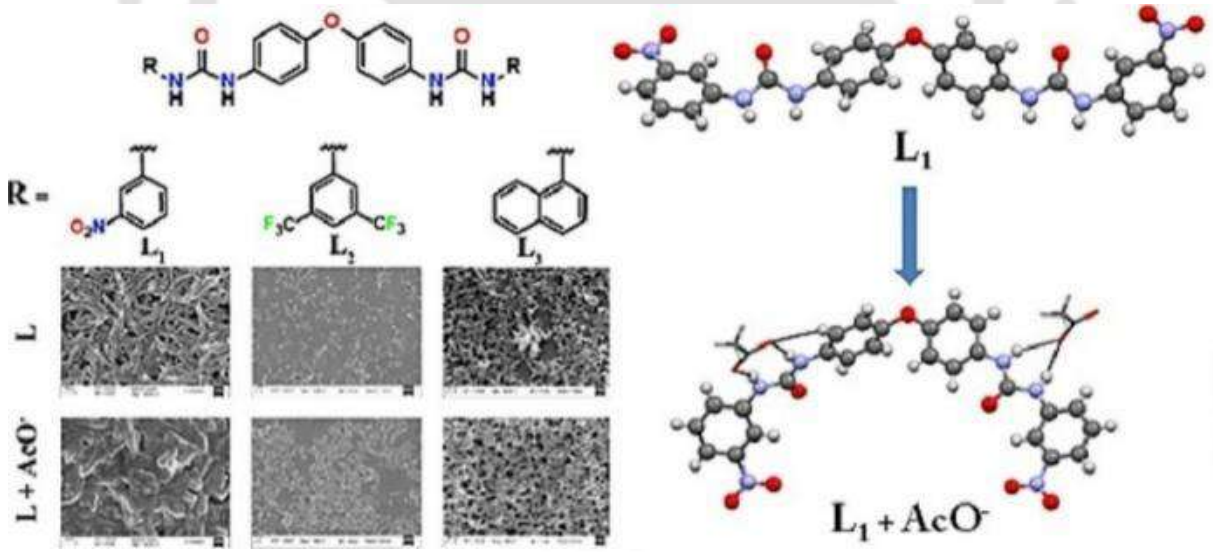

Figure 1. Pictorial depiction of significant results of the research work included in Chapter 3A.

In this chapter, anion recognition aptitude of three bis-urea receptors (L_1–L_3) was evaluated in both solid as well as in solution phase. The terminal substituents of all the three receptors were varied with different substituents, viz. electron deficient/π-acidic, -NO_2 (in L_1), -CF_3 (in L_2), and electron rich-hydrophobic naphthyl (in L_3), to investigate the effect of those terminal substituents on the anion recognition abilities of the designed receptor molecules. Among all the three receptor molecules, only receptor, L_1 could successfully be crystallised with acetate anion, where the solid-

state recognition process involves 1:2 host-guest interaction. Frequent co-crystallisation of strong hydrogen bond acceptor DMSO with L_2 having strong hydrogen bond donor sites, might be the reason why we could not crystallize L_2 with any anion. In the case of L_3, the reason for unsuccessful crystallisation with the anions could be attributed to the presence of more hydrophobic as well as electron rich naphthyl group in the terminal positions, which made the urea hydrogen less acidic as compared to that of L_1 and L_2. Subsequently, solution phase acetate recognition study was conducted for all the three receptor molecules by employing ^{1}H NMR titration experiment. Unlike in solid state, solution phase study revealed 1:1 host guest interaction, and binding discrepancy in the solution phase could be attributed to the loose orientation of the receptor in the solution phase as compared to that of the more organised solid state. ^{1}H NMR titration experiment revealed, highest acetate binding constant value for L_2 (40.38 M^{-1}), followed by L_1 (23.47 M^{-1}), and L_3 (11.65 M^{-1}). Along with this, morphological changes in presence of acetate anion were also investigated using FESEM. To establish the surface characteristics associated with our receptors as well as anion complex on the basis of various non- covalent interactions Hirshfeld surface (HS) analysis was performed as well.

Chapter 3B: Anion-Mediated Cyclisation of Urea-based Receptors: Recognition of Anion-Water-Cluster and Anions with Varied Dimensionality

[Cryst. Growth Des. 2023, 23 (11), 8370–8380]

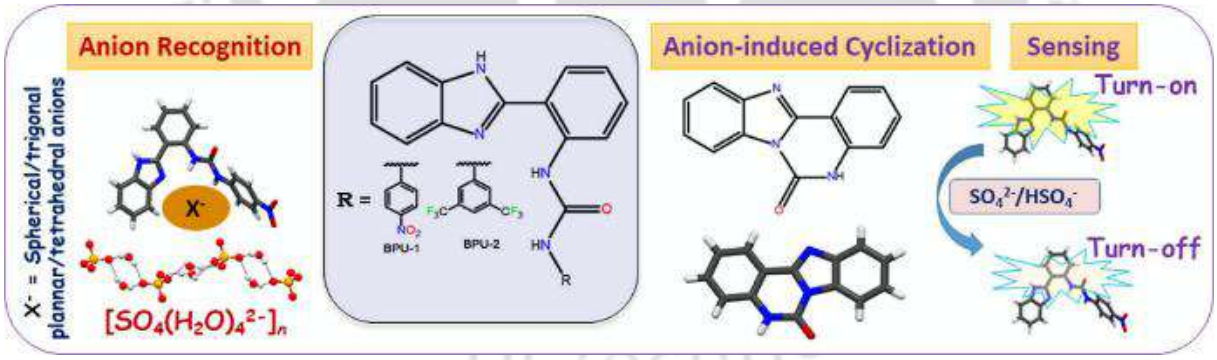

Figure 2. Representing some of the important portions of the research work presented in the Chapter 3B.

This chapter follows in line with the previous chapter, with the improved designed rationale of the receptor molecules. In this chapter, instead of bis-urea, mono-urea based receptors, namely, BPU-1 and BPU-2, having only π-acidic terminal substituents such as $–NO_2$ (in BPU-1), and $–CF_3$ (in BPU-2) in the terminal positions, were employed for anion recognition study purposes. Moreover, strategically, benzimidazole unit was also appended in both the receptor molecules, which served dual purposes: a) facilitated anion recognition by acting as a hydrogen bond donor site, and b) being a fluorophore, it enabled visualization of anion recognition using fluorescence spectroscopic

technique. The two flexible unsymmetrical arms of BPU-1 and BPU-2 allowed recognition of anions with varied geometries including spherical (halide anions), trigonal planar (such as NO_3^- anion), and tetrahedral (such as SO_4^{2-} anion) anions. Cyclic sulfate-water-cluster, $[SO_4(H_2O)_4^{2-}]_n$ could be entrapped by BPU-1, which resulted in two different cyclic arrangements such as $R_4^4(8)$ and $R_4^4(12)$ in the solid state. The SO_4^{2-} anion entrapment process involved total of 12 hydrogen bonding interactions. Furthermore, the presence of fluorophoric benzimidazole unit allowed the study of anion-sensing behavior of both receptors in the aqueous medium using fluorescence spectroscopy. As a result, it was evident that, BPU-1 could selectively sense SO_4^{2-}/HSO_4^- among other biologically relevant anions in water. However, in the presence of the most basic F^-/HO^- anions, cyclisation of both the receptor molecules took place yielding benzimidazo[1,2-c]quinazolin-6-ones.

Chapter 4A: Micellar Medium Assisted Recognition Guided Ultrafast Sensing of Cyanide in Water via Fluorogenic Nano-probes (*J. Mater. Chem. C, 2024,12, 6519-6527*)

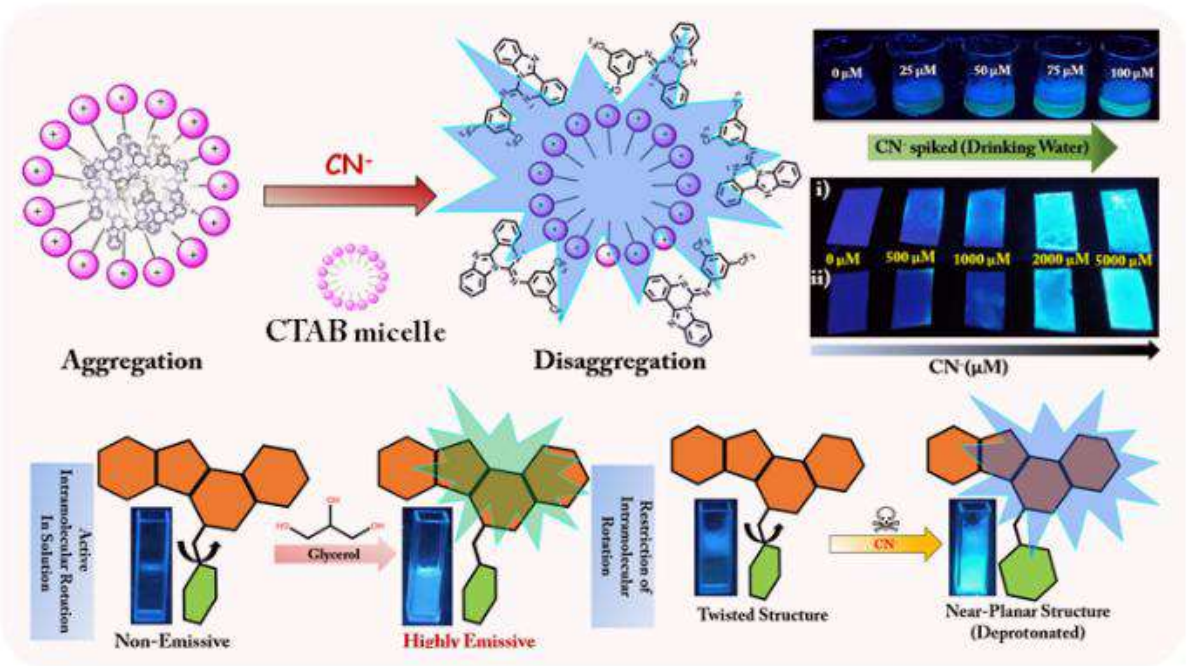

Figure 3. Pictorial depiction of the key findings of the research work included in chapter 4A.

In this chapter the scope of the study was broadened entirely towards solution state anion recognition in terms of anion sensing by using supramolecular self-assembled system like micelle as compared to that of the earlier studies, where solid-state anion recognition was the prime focus. In this prospect, we developed two pre-twisted TICT (twisted intramolecular charge transfer) active benzimidazoquinazoline based fluorogenic probes namely, Benz-d-CF_3 and Benz-m-CF_3 to

study their anion sensing ability in water. The probes were strategically appended with a single -NH unit as an anion recognition site. Anion sensing study through fluorescence spectroscopy experiment revealed that, among both the probes only Benz-d-CF_3 could selectively sense CN^- among vast range of different anions studied in water, although the sensitivity was poor. However, use of micelle system like CTAB dramatically enhanced the selectivity as well as sensitivity of both the receptors towards CN^-. Both the probes showed turn on fluorescence response towards CN^- in water containing CTAB. This observation could be attributed to the hydrophobic microenvironment provided by the CTAB micelles, and also the electrostatic interaction helped in increasing the local concentration of available CN^- for sensing. As a result, Benz-d-CF_3 could detect CN^- as low as 496.5 nM within a very few second, however, Benz-m-CF_3 showed higher detection limit of 3.73 μM. Although Benz-m-CF_3 displayed lower detection limit, the selectivity towards CN^- was much higher than that of Benz-d-CF_3, as unlike in Benz-d-CF_3, HO^- anion could not inflict much spectral changes in Benz-m-CF_3 in both UV-Vis and fluorescence spectroscopic studies. The concept of using CTAB micelle system for CN^- sensing was further expanded towards detection of CN^- in drinking water by using Benz-m-CF_3. The CN^- detection limit in drinking water was observed to be 8.85 μM. The presence of CN^- in drinking water could also be detected inside an UV-lamp (365 nm), where drinking water spiked with different concentration of CN^- could be visualised through naked eyes as well. A prototype device was further constructed for the solid-state visualisation of the presence of CN^- in drinking water by using paper strips.

Chapter 4B: Highly Selective Anion Responsive Supramolecular Gel and Sequestration of Precious Metal Salts into its Nanoparticles [*Langmuir 2024, 40 (45), 24095–24105*]

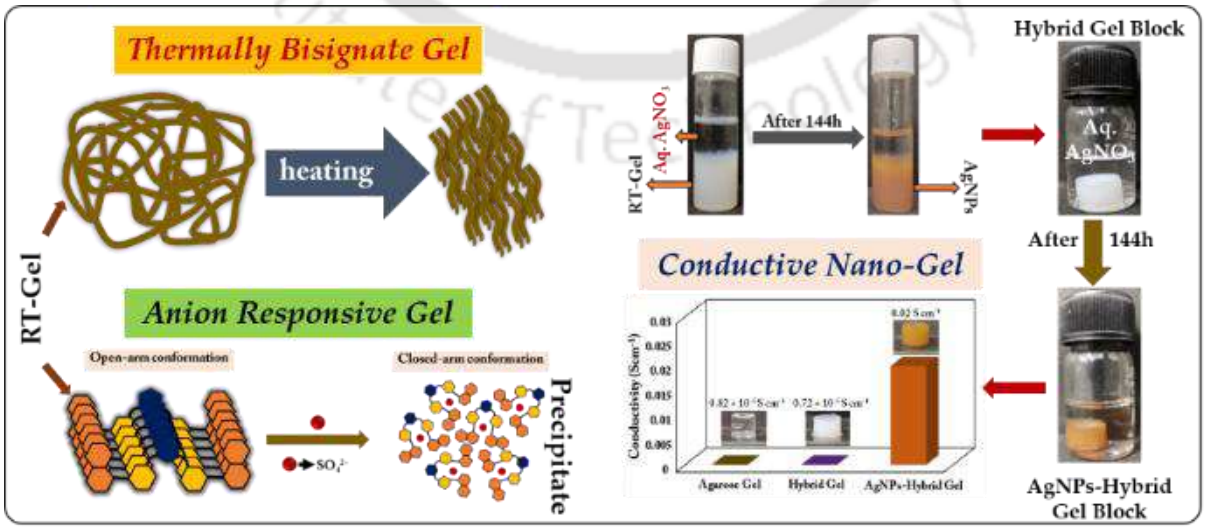

Figure 4. Representing the important findings of the research work included in chapter 4B.

In line with the previous chapter, in this chapter our focus was to develop another kind of self-assembled system like supramolecular gel. The reason being the intention of expanding the idea of anion recognition study towards real-world applications. Soft materials like supramolecular gel systems further enabled us to explore more diverse application such as sensing, water remediation, and different materials applications. In this chapter the gelation ability of two urea based dipodal ligands namely, PY-NAP and PY-CF_3 was extensively investigated, followed by the behavioural study of the resulting gel and finally explored its different applications. The ligands were rationally designed by incorporating hydrogen bond forming units like amide and urea moieties; and to further enable π-π-stacking interaction, a naphthyl unit was incorporated in the positions of PY-NAP. Gelation study revealed that, between these two ligands, only Py-NAP could form gel in a mix solvent system of DMSO and H_2O (3:2), named as RT-Gel. This result indicated the important role played by the terminal substituents on the gelation process. The resulting gel, RT-Gel, displayed high thermal stability, and thermally bisignate behaviour, which was established through rheology experiment. Moreover, RT-Gel was observed to be selectively responsive towards SO_4^{2-} anion, among a vast range of studied different anions. RT-Gel was further employed for water remediation application, where RT-Gel was employed for the sequestration of Ag^+ from water followed by spontaneous in situ reduction of the sequestrated Ag^+ to its nanoparticles. The uptake efficiency was observed to be as high as 90%. Furthermore, the idea was expanded towards developing conductive nanostructured gel nanocomposite, by using a hybrid gel composed of PY-NAP and agarose, thus holding significant implications for industrial and environmental applications. This study reverberated the concept of waste-to-wealth generation by using self-assembled system like supramolecular gel.

Chapter 5: Highly Selective Oil Gelation via PSOG: Recovery of Oil spill and Detection of Fuel-Adulteration *(Chem. Eng. J., 2025, 169128)*

Figure 5. Pictorial depiction of the significant findings of the research work included in chapter 5.

This chapter entirely focuses on the development of phase-selective organogelators (PSOGs) for water remediation application, in terms of oil spill recovery from water. A PSOG named, THD was developed, which could form gel selectively in the presence of diesel (D-THD-G) and kerosene (K-THD-G) in a phase-selective manner among a wide range of studied different oils and organic solvents. Such derived gels were observed to be thermo-reversible as well as thixotropic in nature. THD could be applied for oil spill recovery from water, where the % recovery of diesel oil was observed to be as high as ~83.33 %. The concept of highly selective oil gelation was further applied for fuel adulteration detection, where kerosene adulteration in petrol could be detected visually, without the need of any sophisticated instrumentation. The concept might also be useful in targeting some specific oil sample from a complex mixture of different oil samples, which might be useful in detecting different fuel adulteration in a cost-effective manner as well, in the near future.

Chapter 6: Regulating the Phase Transformation of a Kinetically Trapped Supramolecular Gel via Controlled Heating (*Manuscript submitted)*

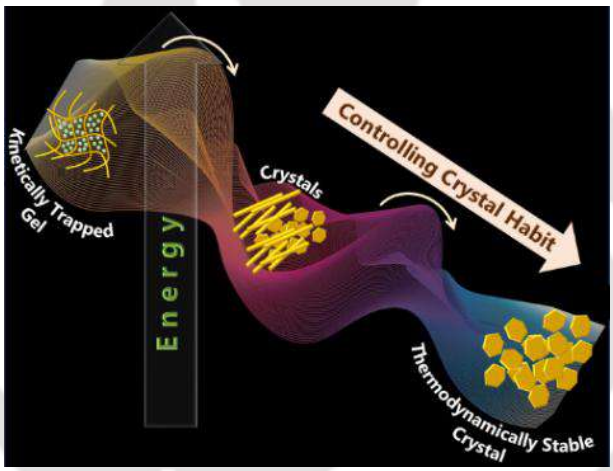

Figure 6. Pictorial representation of the research work included in chapter 6.

In this final chapter our prime focus was to control the phase transformation of a kinetically trapped gel system. A very simple amide based LMWG, named Py-M was developed as a simplistic supramolecular model, which formed metastable or kinetically trapped gel in mix solvent system of DMSO and H_2O in different ratios such as, 1:1, 2:3, 3:2, and 4:1. The phase transformation of such formed gel system to crystal could be well directed by controlled heating. When the derived gel samples were heated inside a test tube, different structural transformations were evident at different temperatures. Such transformation proceeds through complex multistep phase transition pathway starting from a nanofibrilar structure to contiguous fibrous structure, and finally leading to single crystals with varied crystal habits. However, when the gel sample smeared on a glass plate was heated at 100 °C, it resulted in a series of structural transformations, and finally leading

to a state of global minima in the form of a well-defined hexagonally shaped crystal habit. So in this particular chapter we have demonstrated that, the hierarchical self-assembly of a kinetically trapped gel could be well orchestrated to yield crystals of well-defined crystal habits, and which holds great significance especially in field like pharmaceutical industries, fine chemistry, and different materials applications.

Conclusions

In summary this particular thesis focusses on developing small molecule based self-assembled systems for anion coordination and gelation application purposes. High structural tunability of such small molecular systems allow modulation of anion recognition behavior in both solid as well as in solution phases. The anion recognition chemistry has further been utilized in developing probe for highly selective as well as sensitive sensing of toxic anions in water. Subsequently, such small molecular systems were utilized for developing supramolecular gel systems for different applications such as stimuli responsive material, water remediation applications, fuel-adulteration detection, and controlled growth of single crystals. In my future research journey, I would like carry forward the ideas unfolded in this thesis to real-world application by adopting superior design rationale of the small molecule based self-assembled systems.

References

[1] X. Wu, A. M. Gilchrist, and P. A. Gale, *Chem*, 2020, **6**, 1296-1309.

[2] P. D. Beer, and P. A. Gale, *Angew. Chem. Int. Ed.*, 2001, **40**, 486-516.

[3] S.-Q. Chen, S.-N. Yu, W. Zhao, L. Liang, Y. Gong, L. Yuan, J. Tang, X.-J. Yang, and B. Wu, *Inorg. Chem. Front.*, 2022, **9**, 6091-6101.

[4] Z.-Yu Sun, S.-Q. Chen, L. Liang, W. Zhao, X.-J. Yang, and B. Wu, *Chem. Commun.*, 2023, **59**, 12923-12926.

[5] H. Li, L. Kou, L. Liang, B. Li, W. Zhao, X.-J. Yang, and B. Wu, *Chem. Sci.*, 2022, **13**, 4915-4921.

[6] E. Lee, H. Ju, I.-H. Park, J. H. Jung, M. Ikeda, S. Kuwahara, Y. Habata, and S. S. Lee, *J. Am. Chem. Soc.*, 2018, **140** (30), 9669-9677.

[7] F. C. Parks, Y. Liu, S. Debnath, S. R. Stutsman, K. Raghavachari, and A. H. Flood, *J. Am. Chem. Soc.*, 2018, **140** (50), 17711–17723.

[8] C. A. Offiler, C. D. Jonesa, and J. W. Steed, *Chem. Commun.*, 2017, **53**, 2024-2027.

[9] Y. Gao, J. Zhao, Z. Huang, T. K. Ronson, F. Zhao, Y. Wang, B. Li, C. Feng, Y. Yu, Y. Cheng, D. Yang, X.-J. Yang, and B. Wu, *Angew. Chem. Int. Ed.*, 2022, **61**, e202201793.

[10] S. Ha, J. Lee, K. -s Kim, E. J. Choi, P. Nhem, and C. Song, *Chem. Mater.*, 2019, **31** (15), 5735-5741.

[11] S. Mommer, and S. J. Wezenberg, *ACS Appl. Mater. Interfaces*, 2022, **14** (38), 43711-43718.

[12] S. Kimura, K. Adachi, Y. Ishii, T. Komiyama, T. Saito, N. Nakayama, M. Yokoya, H. Takaya, S. Yagai, S. Kawai, T. Uchihashi, and M. Yamanaka, *Nat. Commun.*, 2025, **16**, 3758.

[13] P. R. A. Chivers, and D. K. Smith, *Nat Rev Mater*, 2019, **4**, 463-478.

[14] N. M. Sangeetha, and U. Maitra, Chem. Soc. Rev., 2005, 34, 821-836.

[15] D. K. Smith, *Soft Matter*, 2024, **20**, 10-70.

[16] S. Panja, and D. J. Adams, *Chem. Soc. Rev.*, 2021, **50**, 5165-5200.

[17] B. O. Okesola, and D. K. Smith, *Chem. Soc. Rev.*, 2016, **45**, 4226-4251.

[18] J. Buendía, E. Matesanz, D. K. Smith, and L. Sánchez, *CrystEngComm*, 2015, **17**, 8146-8152.

[19] W. Fang, Y. Zhang, J. Wu, C. Liu, H. Zhu, and T. Tu, *Chem. Asian J.*, 2018, **13**, 712-729.

CONTENTS

Chapter 3B: Anion-Mediated Cyclisation of Urea-based Receptors: Recognition of Anion-Water-Cluster and Anions with Varied Dimensionality

Chapter 4A: Micellar Medium Assisted Recognition Guided Ultrafast Sensing of Cyanide in Water via Fluorogenic Nano-probes

Chapter 6: Regulating the Phase Transformation of a Kinetically Trapped Supramolecular Gel via Controlled Heating

Chapter 1

Introduction

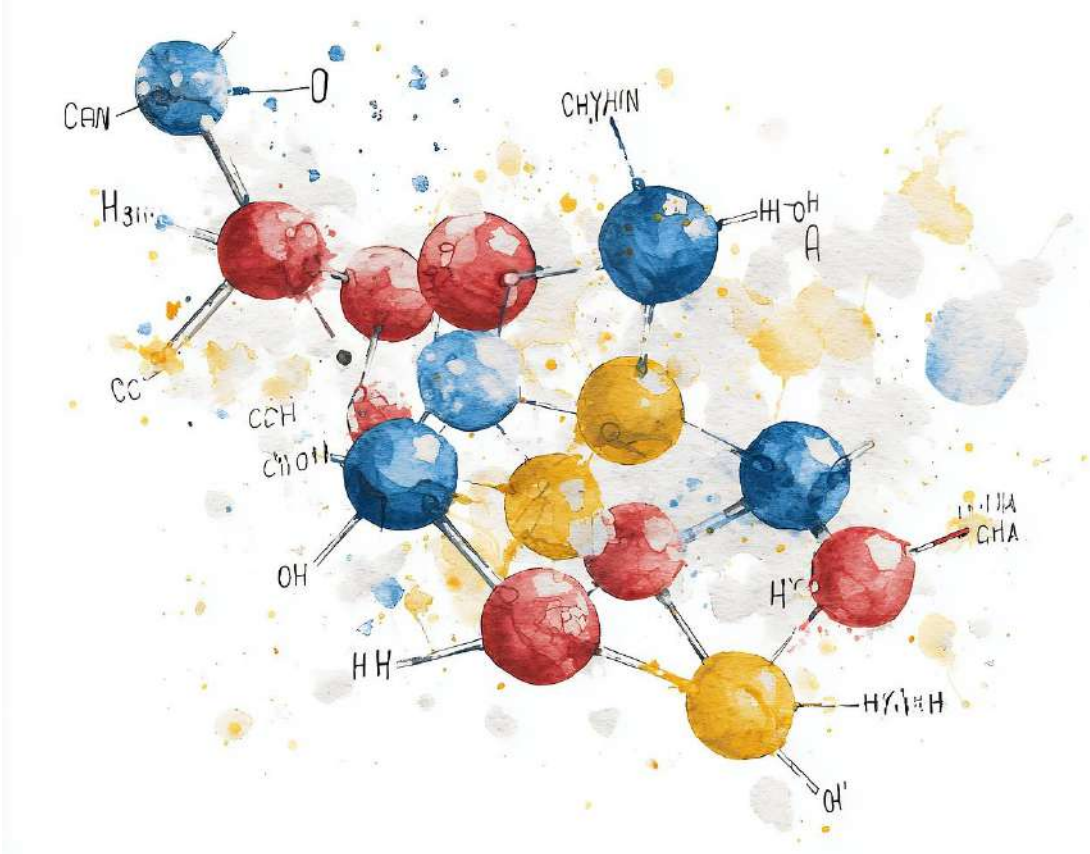

CHAPTER 1

1.1. Supramolecular Self-Assembly: An Introduction

Supramolecular self-assembly is a nature enthused process where spontaneous association of several discrete components such as macroscopic particles, molecules, colloids, or polymers leads to highly organized intricate functional structures or patterns with the help of various non-covalent interactions involving π-π stacking, hydrogen bonding, electrostatic interaction, van der Waals interaction, and host-guest interaction. (Scheme 1.1) [1.1-1.6]

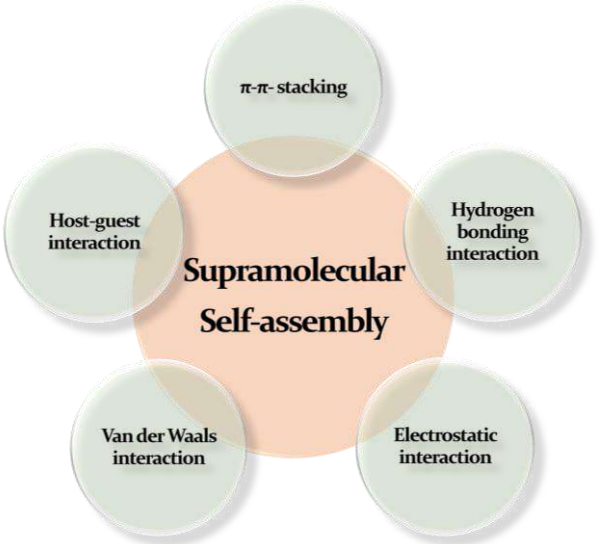

Scheme 1.1: Depicting different types of non-covalent interactions involved in supramolecular self-assembly.

Nature meticulously orchestrates different assemblies with impeccable precisions to accomplish diverse functions in the most efficient way possible, [1.7, 1.8] and which has always spurred the chemists to mimic such assemblies in artificial systems. Scientists have always aspired to exploit the nature's self-assembly process to fabricate artificial self-assembled architectures with tailored properties for different materials applications. Some significant functionalities associated with those systems comprise stimuli-responsiveness, recognition, self-healing, catalysis, transport etc. In 2002, Whitesides and Grzybowski specified two major types of self-assembly: 1) static, and 2) dynamic. [1.3] Static self-assembly refers to those systems which are at global or local equilibrium, and do not dissipate energy, and majority of the ongoing research on self-assembly falls into static type of assembly only. In dynamic assembly, the system needs to dissipates energy for the assembly to take place, and this kind of assembly is mostly apparent in complex biological

processes. The primary focus of this thesis is the designing of small molecule based self-assembled systems for different applications involving:

- anion recognition and sensing of toxic anion.
- supramolecular gel system for water remediation application.
- controlling the hierarchical-self-assembly of supramolecular gel system.

1.2. Anion Recognition

Anion recognition chemistry finds its genesis in late 1960s, when synthesis and coordination chemistry of crown ether was reported by Pedersen, and cation coordination chemistry of the cryptands was first accounted by Lehn. [1.9] However, the branch of anion recognition chemistry blossomed only after 1990s, with the emergence of its diverse potential real-world applicability in very important fields like sensing and extraction of anionic pollutants, anion transport, crystal engineering, self-assembly, recognition of anionic molecules etc. (Scheme 1.2) [1.10] The incessant growth of this particular field of research can be accredited to widespread presence of anions in nature and the important role played by them in various environmental as well as biological processes. [1.11-1.13]

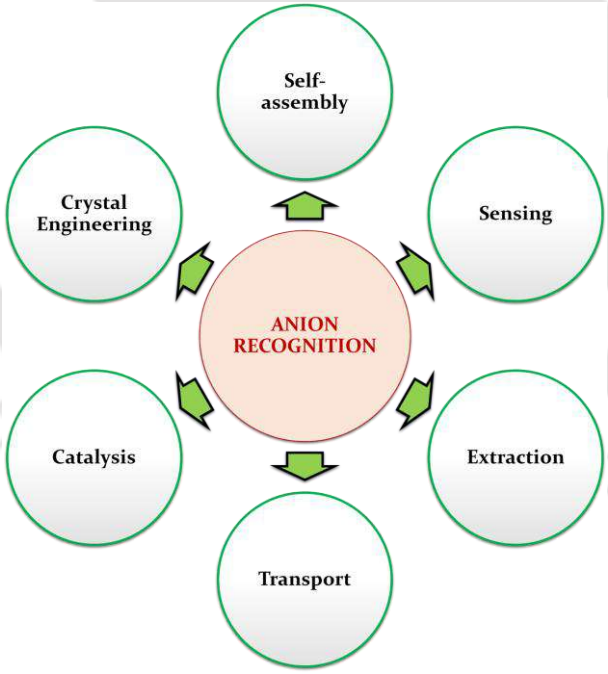

Scheme 1.2: Depicting the different applications of anion recognition.

For the efficient entrapment of the targeted anions, proficient designing of the receptor molecules is a must. However, the efficient designing of receptor molecules for the anion recognition is not devoid of some serious problems, which include:

- **Anions are known to be larger in sizes** when compared with the isoelectronic cations; thus, they possess lower charge to radius ratio. Therefore, the electrostatic binding forces are less effective for the anions in comparison to that of small cations.
- **Anions possess varied geometries**, which inflicts a great challenge towards the designing of host molecules which can be complementary to the incoming guest. So, higher degree of receptor designing may be required for the successful recognition of the anions. (Figure 1.1)
- **pH sensitivity of the anions** is another challenge in receptor designing, as at lower pH the anions may get protonated. Therefore, the designed receptor molecules should be operational within the pH window of the targeted anion.
- **High hydration enthalpy of anions** as well as its solvation in different solvents greatly impacts the anion binding selectivity as well as strength during the recognition process. So, the designed receptor molecules must be capable of competing with the solvent molecules where the anion recognition study is performed.
- **Hydrophobicity of the anions** also plays critical role in the receptor designing process, where the receptors encompassing hydrophobic binding sites favors recognition of hydrophobic anions. [1.9]

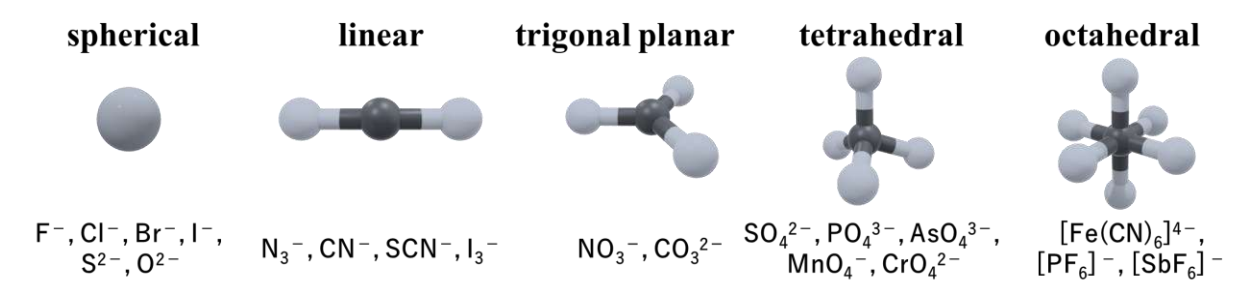

Figure 1.1: Depicting anions of varied geometries.

The supramolecular chemists strategically develop various artificial receptors appended with diverse receptor units for the successful recognition of anions, which includes, hydrogen bonding forming unit, electron deficient aromatic ring system (for facilitating anion-π-interaction), cationic receptor (for enabling electrostatic interaction), and receptors having hydrophobic binding sites that enables recognition of hydrophobic anions. [1.14] Moreover, the nature of the anion recognition process also depends upon factors such as flexibility of the spacer, whether the receptor is dipodal or tripodal (dimension) and also the functionalities of the receptor. [1.15] This thesis focuses on designing of small molecule based self-assembled systems for the recognition of anions primarily via hydrogen bonding interaction. Receptor of this kind generally comprises anion binding units such as amide, sulfonamide, urea, thiourea, squaramide, etc., which are capable of

recognizing anions with directional hydrogen bonding interactions. The receptors containing the amide, and sulfonamide units recognize anions through one-directional hydrogen bonding interaction, whereas, the urea, thiourea and squaramide unit containing receptors are capable of recognizing anions via two-directional hydrogen bonds. (Figure 1.2)

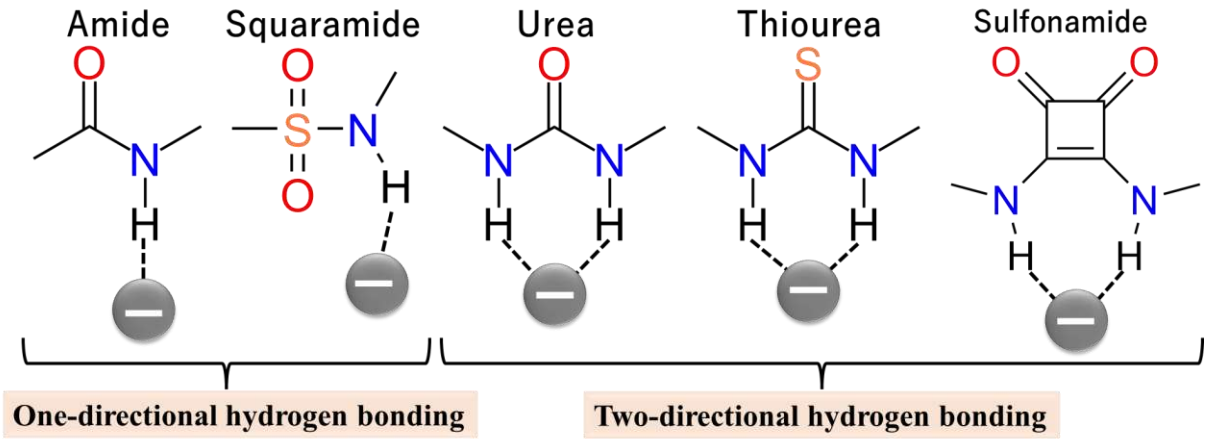

Figure 1.2: Different mode of anion recognition via different receptor units with the help of hydrogen bonding interactions.

For optical sensing purposes, anion binding sites are often covalently linked with signaling units such as fluorophore moieties/ dye molecules, and both the connected units need to be part of the same π-conjugate system. Such sensors often allow visualization of the target toxic anions present in a medium via spectroscopic method as well as through naked eyes. Amongst different methods, fluorescence spectroscopic method is considered to be advantageous, as they enable sensitive, and fast detection of the target analyte. [1.16] Such sensing generally proceeds through two different ways, either "*turn on*" or "*turn off*" response of fluorescence emission when the target anion is present. (Scheme 1.3) It is considered to be very challenging to detect anions in water through hydrogen bonding, especially, those having critical role in the nature, because of their very high hydration energies, so, the sensitivity of such sensing process is often very low. [1.17,1.18] Moreover, it is also very challenging to design a probe which is highly selective towards a certain anion. Since the real-world conditions are harsher than the controlled lab environment, so, to realize real-world applicability of such probes, proficient design rationale needs to be adopted, addressing all those mentioned challenges.

Based on all those discussions, in this section of thesis, the motivation is to design receptor/ probes for the:

- recognition of anions in both solid and solution phase.
- recognition guided sensing of toxic anion in water.

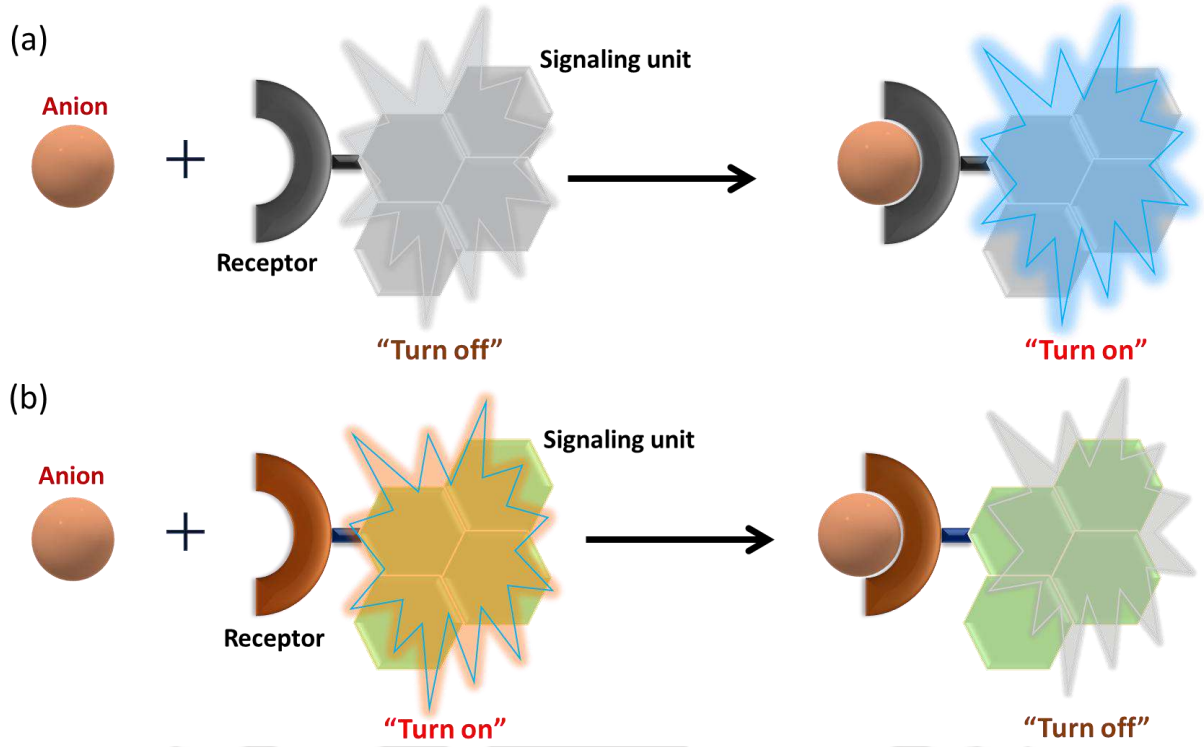

Scheme 1.3: Depicting (a) "turn on", (b) "turn off" fluorescence response of a fluorogenic probe towards anion.

1.2.1. Anion Recognition in Solid and Solution Phase

Wu et al., in 2022 demonstrated extraction of sulfate anions (SO_4^{2-}) from water using the concept of anion recognition, where they observed that, the order of sulfate binding affinities of the designed receptor molecules matches quite very well with their sulfate extraction efficiency. [1.19] In this report Wu group reported a set of three tripodal hexaurea receptors, namely, L^1, L^2, and L^3 with varying terminal substituents, where the receptors are respectively substituted with 4-nitrophenyl, 4-methylphenyl, and hexyl-chain. ^{1}H NMR titration experiment showed highest SO_4^{2-} binding affinity of L^1, followed by L^2, and L^3. The result clearly showed that, the SO_4^{2-} binding aptitude was regulated by the nature of the terminal substituents of the receptors. The nitro-group present in L^1 being a strong electron withdrawing unit, makes the urea unit more acidic ultimately leading to strong SO_4^{2-} binding. However, in the other two receptors the terminal substituents were not electron withdrawing at all, which was reflected in their less SO_4^{2-} binding affinities. Based on this result, Wu et al., further performed the SO_4^{2-} extraction from an aqueous phase to an organic phase using liquid–liquid extraction (LLE) method. ^{1}H NMR and ion chromatography (IC) experiment results revealed that, the efficiency of the SO_4^{2-} extraction was highest for L^1, followed by L^2, and L^3. SO_4^{2-} extraction selectivity experiments in presence of other competing anions such as Br^-, I^-, NO_3^-, HCO_3^-, and $H_2PO_4^-$ also revealed that, L^1 showed the strongest selectivity towards SO_4^{2-} followed by L^2, and L^3. Moreover, Wu et al. showed the reversibility of the extraction process by using acid. This study showed that, the anion recognition

process could be modulated by using proper terminal substituents, and the idea could further be advanced towards removal or extraction of toxic anions from water. (Figure 1.3)

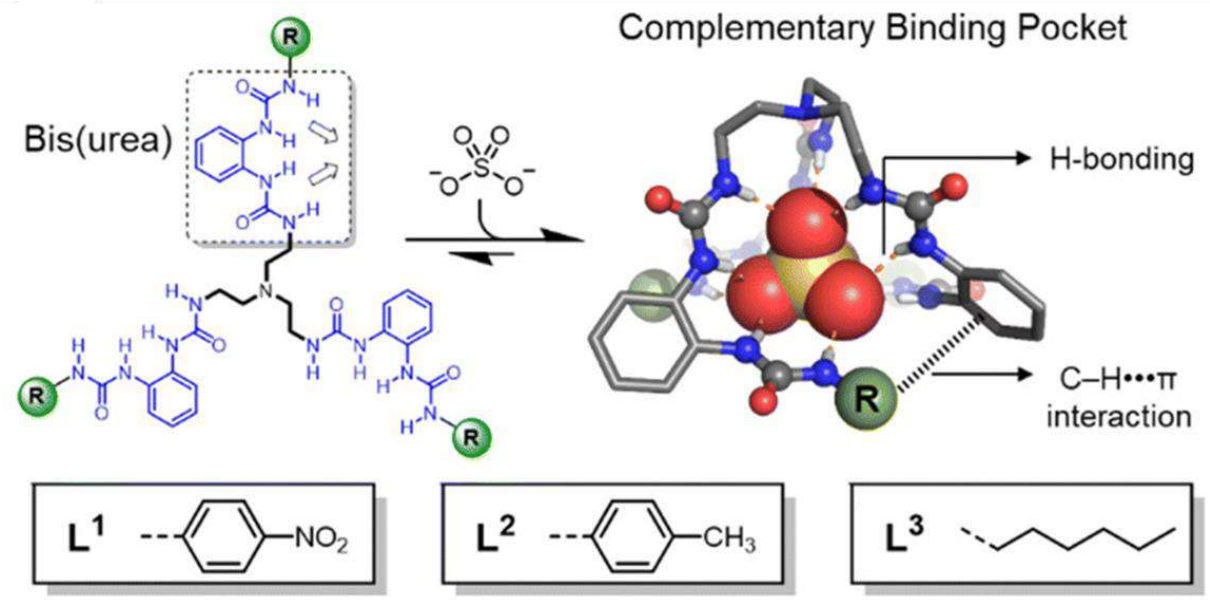

Figure 1.3: Depicting chemical structure of the receptors L^1, L^2, L^3 and their sulfate anion binding pockets. *(adapted from [1.19])*

In 2023, Wu et al., reported a tripodal hexaurea receptor, named L to demonstrate recognition guided pH dependent extraction of phosphate PO_4^{3-} anion from a very highly basic aqueous medium by using LLE method. [1.20] The PO_4^{3-} binding by the receptor L was initially verified via crystal structure analysis, and as a result Wu et al. observed that, L could encapsulate and stabilize PO_4^{3-} anion via 12 hydrogen bonding interactions involving N–H···O^- hydrogen bonds. Moreover, the competitive ^1H NMR titration experiment showed that, the PO_4^{3-} anion binding affinity of L ($K_a = 3.8 \times 10^6\ M^{-1}$) was greater than that of the SO_4^{2-} anion ($K_a = 9.9 \times 10^4\ M^{-1}$). Subsequently, Wu et al. studied the PO_4^{3-} anion extraction by using PO_4^{3-} solution at different pH, and consequently, they observed that, the PO_4^{3-} extraction efficiency of L exceeds 80% at pH > 11 as determined by NMR and IC experiments. They further observed that, at highly basic solution (pH = 13.2), the PO_4^{3-} extraction to the organic phase efficiency exceeds 90%, and during such a process the receptor L did not undergo deprotonation. The extraction process was observed to be receptor concentration dependent, where, with increase in the receptor concentration the extraction efficiency also increased. Such very high PO_4^{3-} anion extraction was solely driven by the hydrogen bonding interaction as Wu et al. observed. Furthermore, Wu et al. demonstrated that, 93% of the extracted PO_4^{3-} anion could be released by using dilute HCl solution. (Figure 1.4)

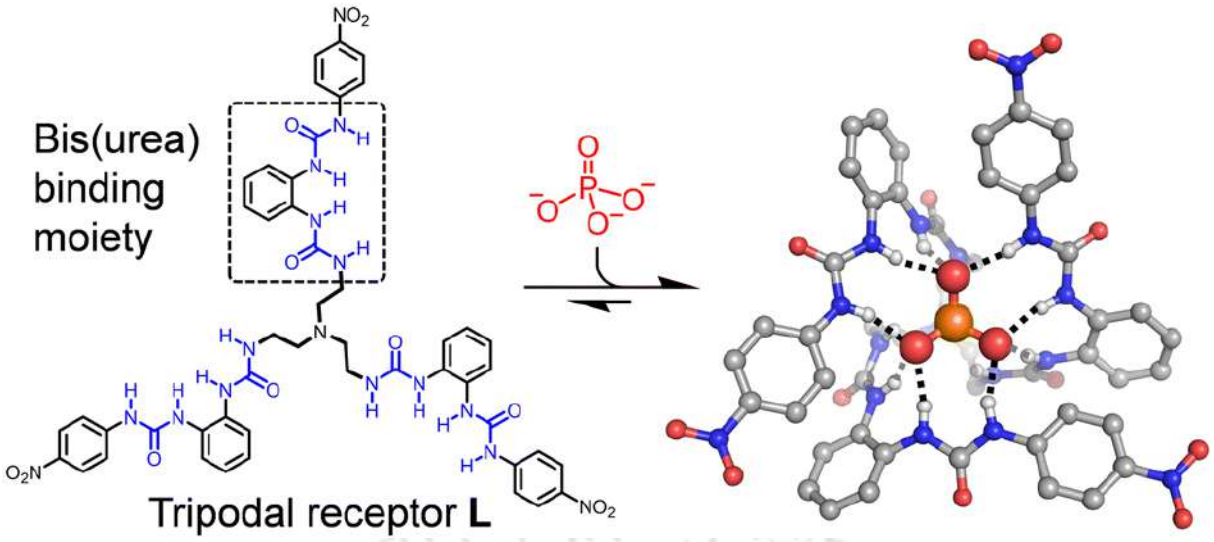

Figure 1.4: Depicting chemical structure of the receptors L and crystal structure of its PO_4^{3-} binding complex. *(adapted from [1.20])*

Pluth et al. in 2018 demonstrated how the receptors could be rationally well-engineered to modulate their hydrosulfide (HS^-) anion recognition capabilities. [1.21] They synthesized a series of tris(2-aminoethyl) amine (tren) based amide containing tripodal receptor molecules namely, baTren, $3CF_3$-baTren, $4CF_3$-baTren, $3CH_3$-baTren, $4CH_3$-baTren, and 2F-baTren by varying the position as well as the groups of the terminal substituents for their study. Initial HS^- binding study through ^1H NMR spectroscopic experiment in CD_2Cl_2 revealed involvement of both N-H, and aromatic C-H units of unsubstituted baTren in the HS^- binding with the help of hydrogen bonding interactions, involving 1:1 host-guest interaction. The binding constant value of baTren towards HS^- was $149 \pm 8\ M^{-1}$ in 1:1 host-guest binding mode. In a subsequent study, Pluth et al. observed that, the HS^- binding affinity of $3CF_3$-baTren and $4CF_3$-baTren drastically increased as compared to that of the unsubstituted baTren, with a greater binding affinity for $4CF_3$-baTren ($3500 \pm 300\ M^{-1}$), which they ascribed to the presence of electron withdrawing group, $-CF_3$ along with its positions. However, for both $3CH_3$-baTren, and $4CH_3$-baTren, the HS^- binding affinities were almost equivalent to that of the unsubstituted baTren, which reflected that, the modest electron donating effect of the $-CH_3$ unit could not affect the HS^- binding affinity of baTren regardless of their positions. Furthermore, Pluth et al. noted that, with proper designing of the receptors, the anion binding could be prevented. They observed, -N-H units of 2F-baTren did not bind HS^-, instead they formed intramolecular hydrogen bonding with the F atoms, present in the ortho positions of the phenyl rings. In a subsequent study, Pluth et al. demonstrated the reversibility of the HS^- binding by treating $3CF_3$-baTren with excess $Zn(OAc)_2$ (6 equivalent). (Figure 1.5)

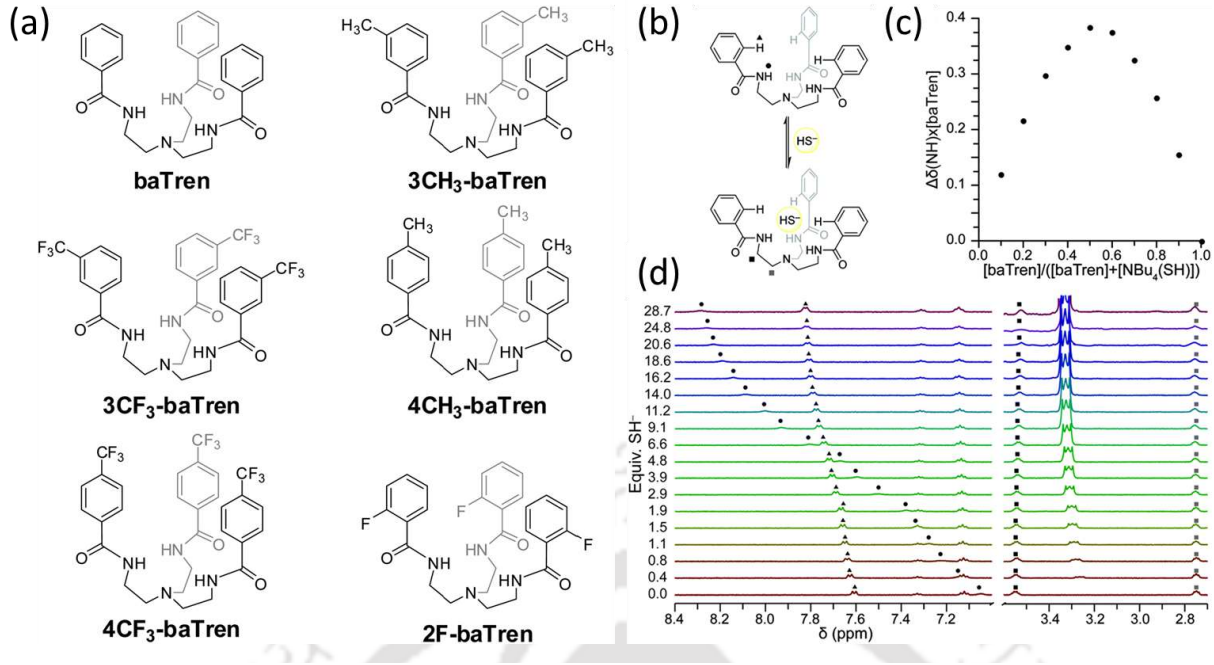

Figure 1.5: (a) Depicting chemical structure of the receptors used in this study with their names below each structure. (b) Depiction of host-guest equilibrium of HS^- in baTren, (c) Job plot for HS^- recognition by baTren in anhydrous CD_2Cl_2. (d) ^1H NMR titration experiment of baTren with $NBu_4(SH)$ in anhydrous CD_2Cl_2. *(adapted from [1.21])*

1.2.2. Recognition Guided Sensing of Toxic Anion

In 2020, Sayahi et al. developed an AIEgen, named N,N′-(pyridine-2,6-diyl)bis(2-(2,4-dichlorophenoxy)acetamide) (1) for highly sensitive "on–off" optical sensing of cyanide (CN^-) in 100% aqueous medium. [1.22] Spectral changes in both UV-Vis and fluorescence measurements, were evident upon gradual addition of CN^- into the aqueous solution of 1. With the gradual addition of CN^-, in UV-Vis study, the absorbance peak at 330 nm decreased, and in fluorescence measurement, blue-shifted emission spectra from 389 nm to 359 nm with concomitant quenching was apparent. None of the other studied competing anions as well as common cations could interfere the CN^- recognition process. Sayahi et al. also observed that, the naked eye visualization of the CN^- sensing was possible even in the presence of competing ions under UV-lamp of 365 nm. Job's plot revealed 1:1 host guest binding stoichiometry, and the limit of CN^- detection was reported as 8.2 nM. 1 was effective in solid state and the sensing process was reversible with sequential addition of CN^- and aqueous HCL, so Sayahi et al. were able to constructed a portable kit for CN^- sensing as well. Moreover, the probe could also be employed for the detection of CN^- in different seed extracts. Mechanistic investigation of the sensing phenomena revealed that, initially, 1 remained as a rigid planar structure with the help of intramolecular hydrogen bonding, and also due to the supramolecular self-assembly formation in water. However, upon addition of CN^- the intramolecular hydrogen bonding depleted and 1 became non-planar, thus resulting in its

disaggregation and "turn-off" fluorescence response. Eventually, the free -NH units formed intermolecular hydrogen bond with its neighboring amine -NH units, which resulted in larger aggregates, as was evident from TEM, SEM and DLS studies. Overall, this highly sensitive and selective sensing process involved the concept of anion recognition in a very effective way. (Figure 1.6)

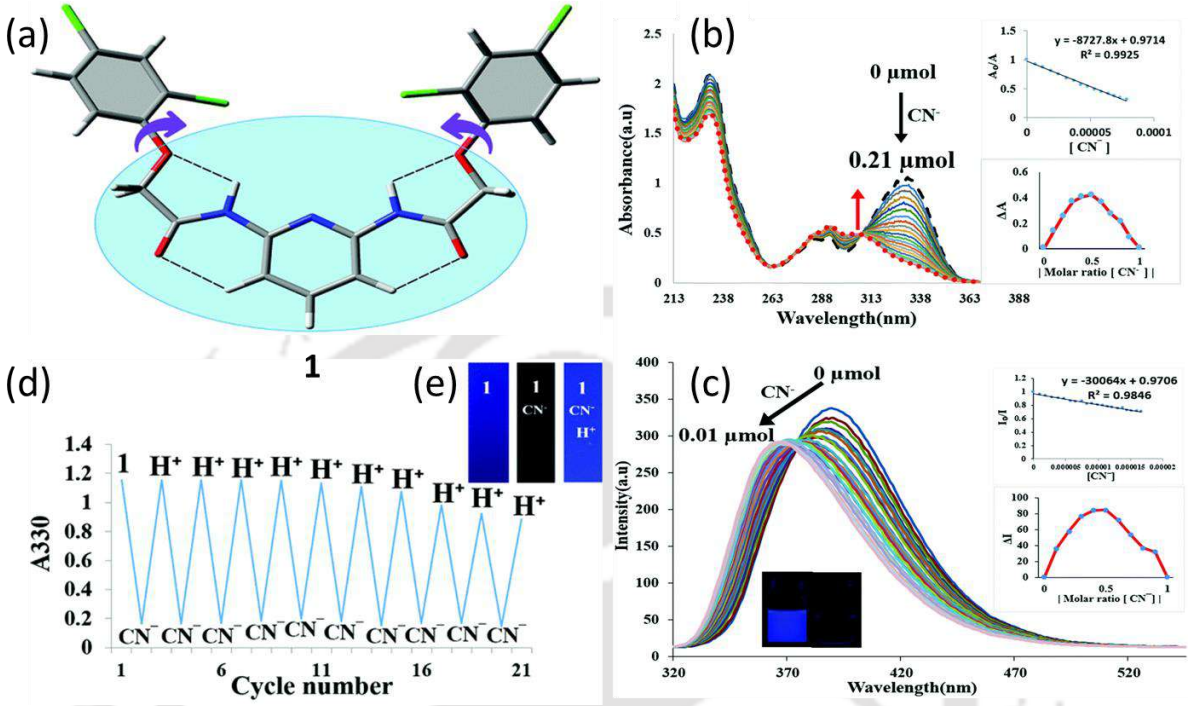

Figure 1.6: (a) Depicting chemical structure of 1 along with its intramolecular hydrogen bonding interactions. (b) Representing alteration of UV-Vis absorbance spectra of 1 with the incremental addition of CN^- anion (Top inset: changes in absorbance with increasing CN^- anion concentration, Bottom inset: Job plot of CN^- anion binding by 1). (c) Representing changes in the fluorescence emission of 1 with the incremental addition of CN^- anion (Top inset: changes in emission intensity with increasing CN^- anion concentration, (Bottom inset: Job plot of CN^- anion binding by 1). (d) Changes in the UV-Vis absorbance spectra upon sequential addition of CN^- anion and HCl. (e) Photograph of test strips under 365 nm UV light upon dipping in solution of CN^- anion and HCl. *(adapted from [1.22])*

Two years back, in 2023, Dey et al., reported two tetrazole-based fluorescent probes containing signaling units such as naphthalene (P1), and anthracene (P2) moieties, to demonstrate enhanced selectivity as well as sensitivity of CN^- sensing in the presence of amphoteric surfactants S1 (contains single alkyl chain), and S2 (contained double alkyl chains). [1.23] Both P1, and P2 could detect CN^- in a polar aprotic solvent like THF, but such sensing was at the very cost of interference from some of the other basic anions. In aqueous medium although the selectivity was good, but it suffered from poor sensitivity. However, upon using hydroxyethyl-appended amphoteric surfactants S1, and S2, both selectivity as well as the sensitivity of the CN^- sensing in water improved drastically. In fluorescence spectroscopic study, upon addition of CN^- into the aqueous solution containing P1, and P2 along with S1 and S2, fluorescence emission quenching was

evident, however such quenching was prominent in P2 because of the larger hydrophobic unit presence in it. Moreover, the degree of quenching of both P1, and P2 was observed to be greater when S2 was present, as compared to that of the S1, which could be ascribed to vesicular structure formed by S2, whereas S1 formed micelle. Vesicular structure being more rigid in structure, and having greater hydrophobic domain allowed effective charge pairing interaction with CN^-. Mechanistic investigation through ^1H NMR, FT-IR, theoretical calculations etc. revealed that, CN^- participated in hydrogen bonding interaction with the tetrazole -NH unit, which resulted in the alteration of the electronics of the tetrazole unit and thereby leading to alteration of the charge transfer characteristics of the overall molecules. (Figure 1.7)

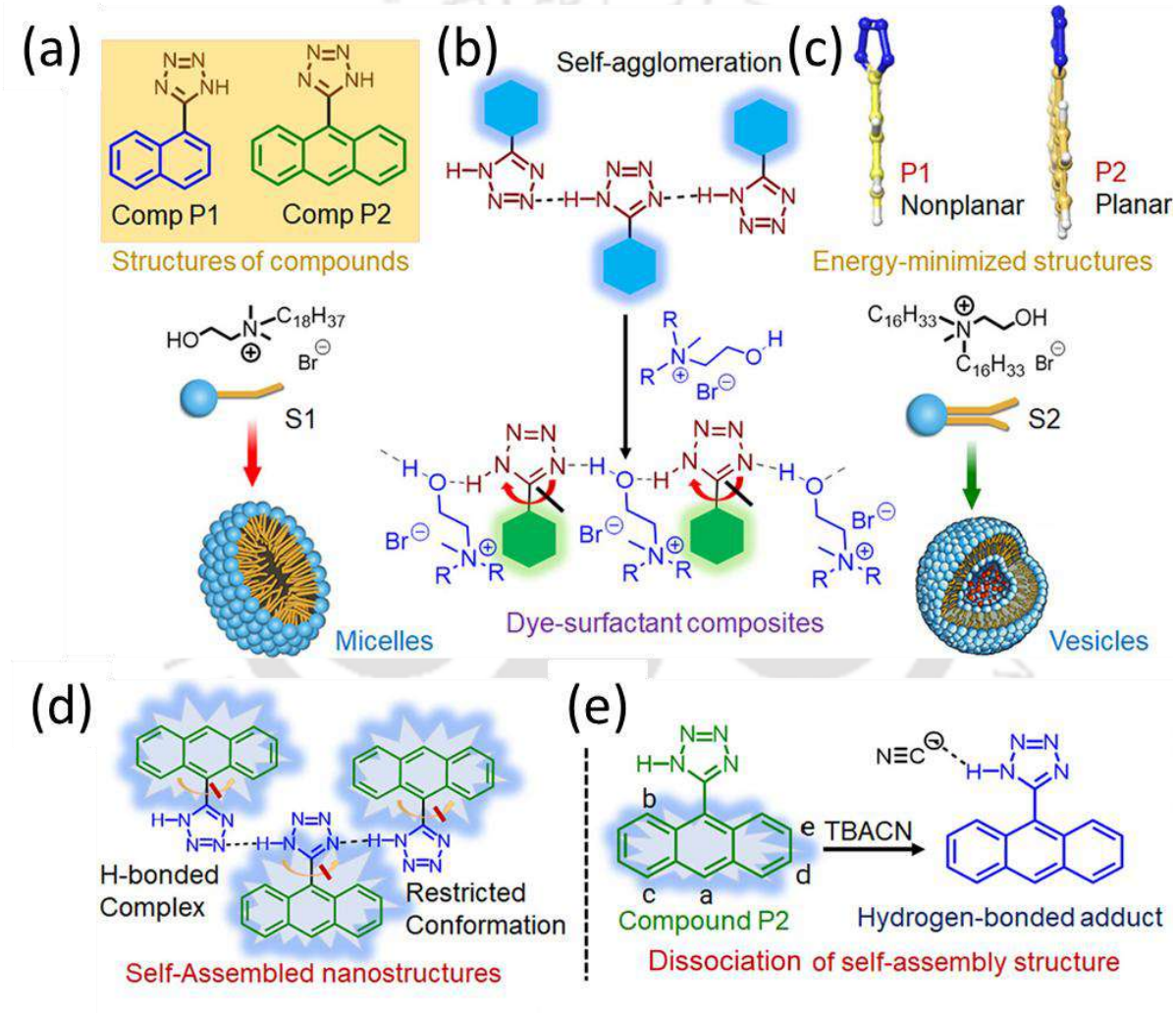

Figure 1.7: (a) Depicting chemical structures of the fluorescent probes P1, and P2. (b) Schematic representation of different dye-surfactant co-assembly formation. (c) Depicting structures of P1, and P2 in their energy minimized forms. (d, e) Representing interaction of CN^- with P2. *(adapted from [1.23])*

Similarly, very recently, two ESIPT-based fluorescent probes namely, 1, and 2, were reported for colorimetric as well as fluorometric sensing of CN^- in an aqueous medium. [1.24] 1 showed superior response towards CN^- with spectral shift towards red region, with concomitant enhanced

emission. The initially present colorless solution became yellow when CN^- was added into the aqueous solution of 1. On the contrary, 2 was poorly responsive towards CN^-, where spectral shift towards blue region was evident along with emission quenching. The red-shifting of the emission spectra of 1 could be ascribed to the charge transfer process facilitated within the molecule by the hydrogen bonding interaction with CN^-. For 1, and 2, the limit of CN^- detection was 0.24 and 0.58 μM respectively, as stated by Dey et al. Different spectroscopic studies showed involvement of arylhydrazone -NH, and phenolic -OH units in hydrogen bonding interaction with CN^-. From Job's plot, 1:1 host guest interaction was evident. Dey et al., further demonstrated that, this CN^- sensing was effective in different water samples as well, which included tap water, pond water and sea water, showing very high recovery percentages. Moreover, this sensing could also be extended towards on-site detection of CN^- via chemically modified paper strips. (Figure 1.8)

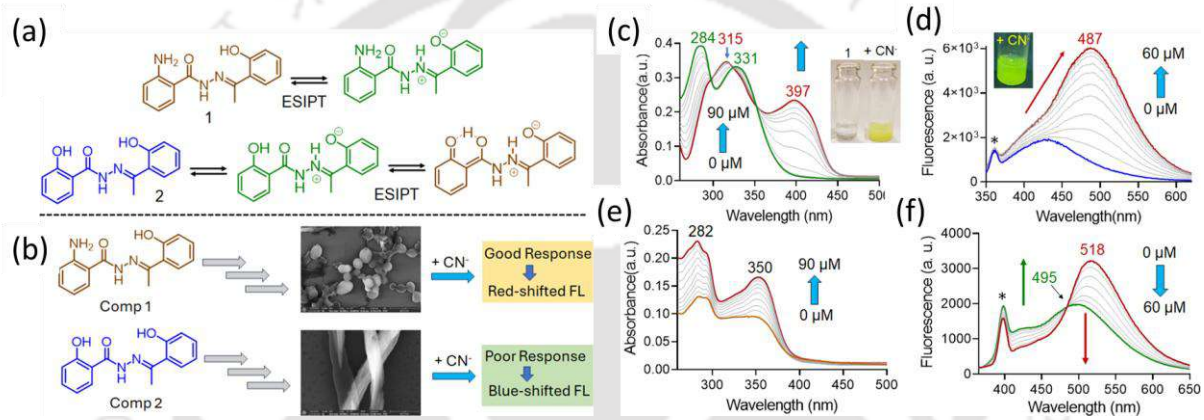

Figure 1.8: (a) Depicting chemical structures of the probes 1, and 2, along with their keto-enol tautomerism. (b) Representation of differential response of 1, and 2 with CN^- ion based on their substituents (inset: corresponding FESEM images). UV-Vis titration study of (c) 1, (d) 2 with the incremental addition of CN^- ion. Fluorescence titration experiment of (d) 1, (f) 2 with the incremental addition of CN^- ion. *(adapted from [1.24])*

1.3. Supramolecular Gel

Supramolecular gels are often defined as soft colloidal functional materials resulting from the hierarchical self-assembly of low molecular weight gelator (LMWG) molecules, which transpires into long anisotropic entangled fibrillar network structures with the help of various non-covalent interactions such as hydrogen bonding, π-π interaction, van der Waals forces, hydrophobic interaction, metal coordination etc., in an appropriate medium, and within its three-dimensional network solvent molecules are entrapped. [1.25-1.27] Such gel systems allow nanoscale engineering of the self-assembly behavior, thereby enabling translation of molecular level information to the materials performance. [1.28] Supramolecular gel derived from LMWGs can be mainly prepared in two ways:

I. **by heating the LMWG** in an appropriate solvent followed by cooling the isotropic supersaturated solution to room temperature.

II. **by adding anti-solvent** to the solution of the LMWG.

However, in both the mentioned methods, sometimes crystallization and precipitation occur depending upon the nature of the aggregation. Highly ordered aggregation results in crystallization, whereas, random aggregation leads to precipitation, and gelation is an outcome of the intermediate of the two mentioned aggregation processes. (Scheme 1.4)

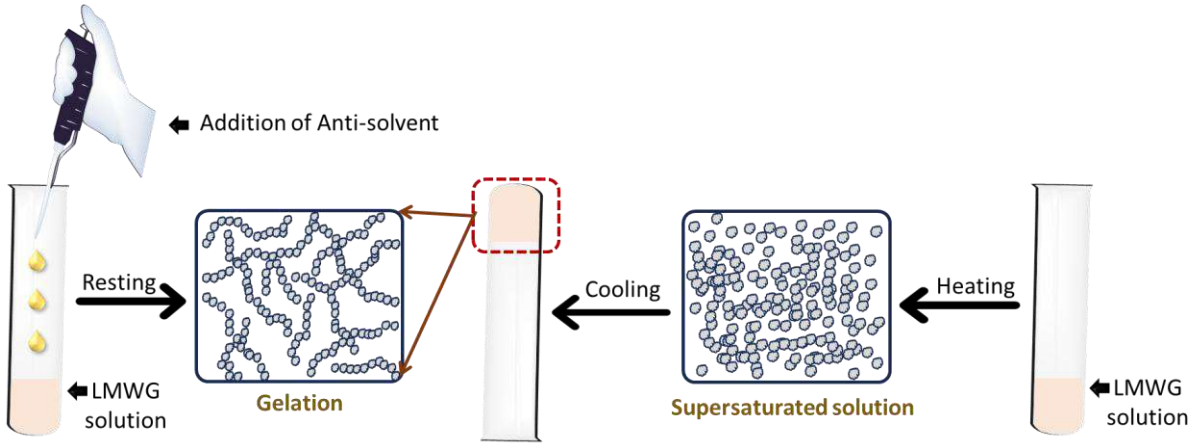

Scheme 1.4: Depicting two mostly employed procedures for supramolecular gel formation using a LMWG molecule.

Depending uopn the medium of preparation, supramolecular gel derived from LMWGs can be classified into four major types:

I. **Organogels**, are prepared in an organic solvent.

II. **Hydrogels**, are prepared in water.

III. **Organohydrogels**, are prepared in a mixture of water and organic solvents.

IV. **Aero/xerogels**, are dried gels. (Scheme 1.5)

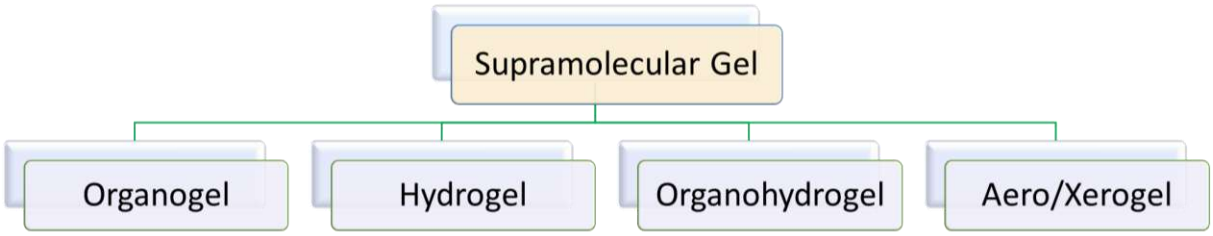

Scheme 1.5: Classification of supramolecular gel based on medium of preparation.

Supramolecular gels are very useful functional soft materials mostly because of their high structural and functional tunability, and which makes them advantageous in many prospects as compared to that of polymeric gel systems. However, to make a meaningful progressive innovation

with this soft material, molecular level and nanoscopic understanding of the supramolecular gel formation process is very critical. The detailed mechanistic insights of the supramolecular gel formation process are somewhat elusive and still developing. The generally accepted mechanism of supramolecular gel formation proceeds through following three steps:

I. One dimensional self-assembly of LMWG molecules to form supramolecular polymer.
II. Formation of mesoscopic fibers via hierarchical self-assembly of the supramolecular fibers.
III. Interweaving of these mesoscopic fibers to form three-dimensional network structure, where the solvent molecules are entrapped and immobilized. (Scheme 1.6)

However, with rapid advancement of the field along with the emergence of powerful analytical tools, detailed dynamic visualization of the supramolecular gel formation process has become possible. As a result, new mechanistic insights to the gelation mechanism are also evolving with time. Very recently, in 2025, with the help of high-speed atomic force microscopy, Yamanaka et al., demonstrated that, there exists a lag phase just before the formation of supramolecular mesoscopic fibers in the gelation process of their studied urea based gelator molecule. [1.29] In that lag phase nucleation process occurs, and where, they observed existence of, octameric or tetrameric nucleus of the gelator molecule. Accumulation of those octameric or tetrameric nucleus results in the formation of bundled fibers, and ultimately, leading to supramolecular gel formation.

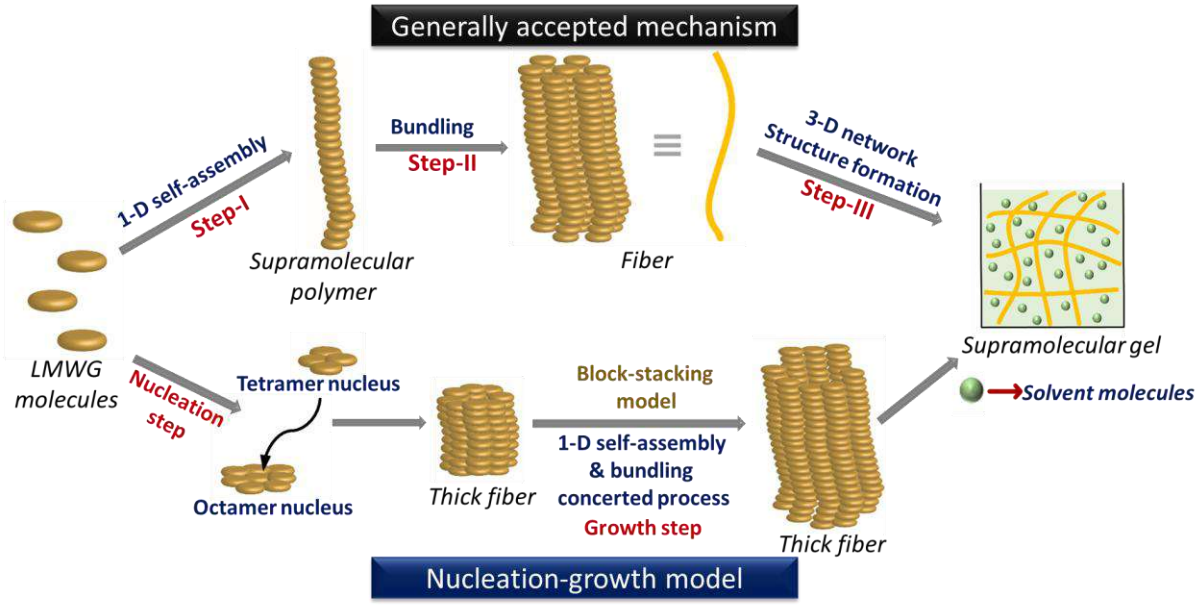

Scheme 1.6: Schematic diagram of generally accepted mechanism of supramolecular gel formation (above) and nucleation growth model of the supramolecular gel formation mechanism (below) *(adapted from [1.29])*

The formation of a supramolecular gel is primarily driven by weak non-covalent interactions, and they often exist in a kinetically trapped state. Therefore, the self-assembly of such gel systems can often be regulated with the help of external stimuli such as temperature, pH, light, ultrasound etc. As a result, when exposed to different external stimuli, alteration of both physical and chemical properties of such gel systems occurs. [1.30,1.31] Apart from this supramolecular gel also finds of myriads of applications in different fields which comprises, catalysis, water remediation, nanoelectronics, sensing, drug delivery etc. as represented in Scheme 1.7. [1.32-1.37]

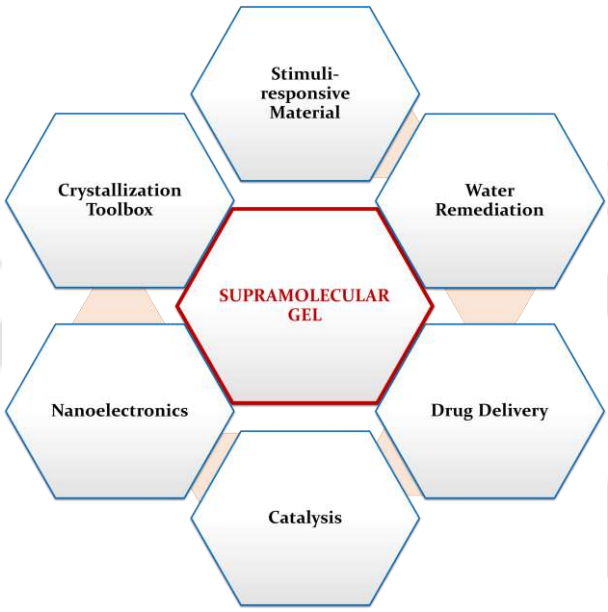

Scheme 1.7: Depicting the different applications of supramolecular gel.

In this section of thesis, the primary focus is as follows:

I. supramolecular gel as stimuli responsive material
II. supramolecular gel for environmental remediation application
III. phase transformation study of supramolecular gel

1.3.1. Supramolecular Gel as Stimuli Responsive Material

In 2020, Singh et al., developed a tripodal acylhydrazone based organogelator, named L1 for the recognition of CN^- anion in a highly selective manner in both gel and solution states. [1.38] They observed that, the gel derived from L1 collapsed into precipitate upon addition of CN^- anion, which was accompanied by colour change from white in the gel state to yellow in the precipitate form. However, the other studied anions could not inflict such changes to the studied gel system. Mechanistic investigation through ^1H NMR and IR spectroscopy revealed that, CN^- anion caused deprotonation of the -NH unit of the acylhydrazide unit, leading to accumulation of negative charge species and thus disrupting the existing fibrillar network of the gel system to give precipitate. This observation of gel to precipitate was further supported by rheology experiment,

where, Singh et al. observed crossover point between the storage modulus (G') and loss modulus (G") in presence of CN^- anion. Overall, this study presented detection of toxic analytes through naked eyes in a cost-effective manner by employing a simple supramolecular gel system. (Figure 1.9)

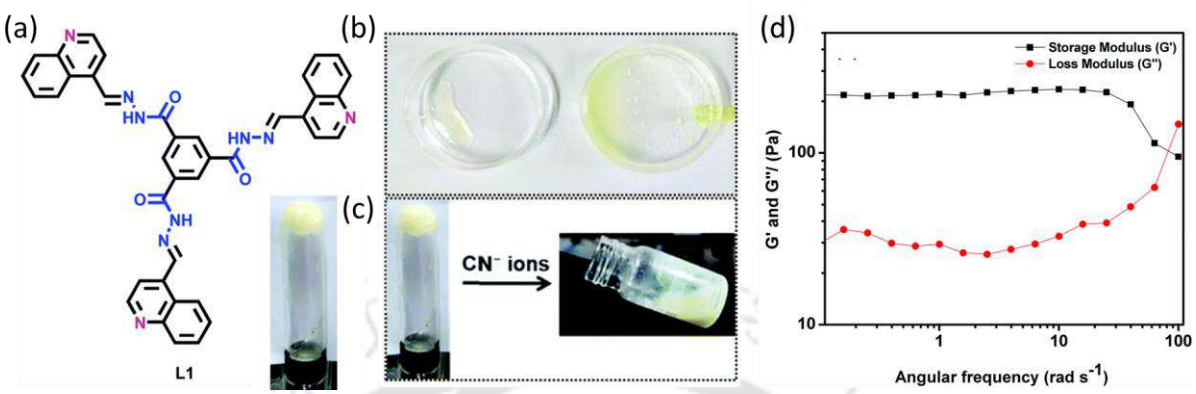

Figure 1.9: (a) Depicting chemical structures of the gelator L1 along with its gel derived in a mix solvent system of DMSO: H_2O (1:1). (b, c) Representing the collapse of the organogel with concomitant color change from white to yellow in presence of CN^- ion. (d) Rheology experiment of the organogel in presence of CN^- ion. *(adapted from [1.38])*

Adams et al. showed, how the thermal annealing could be useful for tunning material properties of a multicomponent gel systems in their report in 2019. [1.39] For this work, they developed two gelator molecules, 1, and 2, capable of individually forming gel in a mix solvent system of DMSO and H_2O (3:7). Both the gels possessed two distinctly different melting temperatures (65°C and 80°C for the gel formed from 1, and 2 respectively). Thermal annealing of the mentioned gel systems led to enhancement of the storage modulus, which could be ascribed to the microstructural change of fiber distribution from spherulitic to a more uniform domain. Subsequently, Adams et al. performed the similar annealing experiment for the two-component gel system derived from mixing 1, and 2, named as (1+2) gel. Upon heating sequential melting of the individual gel systems at their respective melting points were observed through temperature dependent rheology measurements, and as a result, after annealing two times enhancement in the magnitude of stiffness was evident from frequency dependent rheology measurement. Moreover, strain sweep experiment revealed existence of two types of networks as a result of annealing. The heating and cooling cycle resulted in self-sorting, and thus resulting in different microstructure which was absent in the initial gel state. Such microstructural transformation was solely due to annealing, and not because of time. Adams et al. further showed that, in that (1+2) gel system, selective melting of the gel of 1 could also be achieved by heating (1+2) gel to 65°C, and subsequently upon cooling the increase of the moduli was evident, which supported the initial independent network formation along with self-sorted network formation as a consequence of annealing. (Figure 1.10)

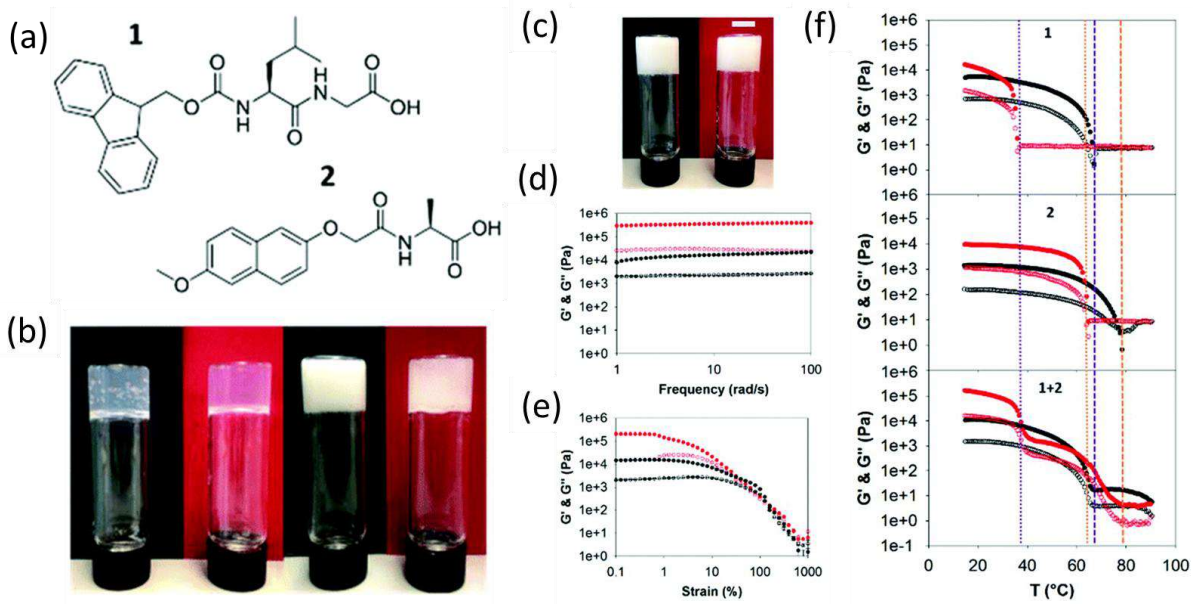

Figure 1.10: (a) Depicting chemical structures of the gelators 1, and 2. (b) (from left to right) Photograph showing gel of 1 before and after annealing, and gel of 2 before and after annealing. (c) Photograph representing (1+2) gel before and after annealing. (d) Frequency sweep rheology experiment of (1+2) gel (black: before annealing, red: after annealing). (e) Strain sweep rheology experiment of (1+2) gel (black: before annealing, red: after annealing). (f) Comparative study of the rheology measurement data of the gel derived from 1, 2 and (1 + 2) upon heating and cooling (1 °C min^{-1}). *(adapted from [1.39])*

1.3.2. Supramolecular Gel for Water Remediation Application

In 2016, Smith et al. demonstrated selective extraction of precious metal salts such as gold/silver salts from model waste by using a hydrogel derived from a LMWG based on 1,3:2,4-dibenzylidenesorbitol (DBS), named as DBS-$CONHNH_2$. [1.40] Uptake study of the individual metal salts from the aqueous solution placed on the top of the gel by using ICP-MS or UV spectroscopy revealed maximum uptake capacity of 2000 mg g^{-1} (metal: gelator) for gold and 900 mg g^{-1} for silver. Smith et al. observed that, such uptake was accompanied by spontaneous metal nanoparticle formation inside the gel matrix in the absence of any external reducing agents. The similar uptake experiment was further performed for model waste containing a mixture of different metal ions such as Ni^{2+}, Cu^{2+}, Zn^{2+}, Fe^{2+}, Pt^{2+}, Pd^{2+}, Au^{3+}, and Ag^{+} by using the derived from DBS-$CONHNH_2$. As a result, the gel showed best extraction ability towards the metal ions having the highest reduction potential, such as Au^{3+}, Ag^{+}, Pd^{2+}, and Pt^{2+}, which was evident from ICP-MS experiment. Moreover, Smith et al. prepared a hybrid gel by using DBS-$CONHNH_2$ and agarose polymer, and successfully demonstrated its Au^{3+}, and Ag^{+} ion uptake ability and spontaneous nanoparticle formation inside the hybrid gel matrix. Such nanoparticle containing hybrid gels showed higher conductance values than that of the gel doped with carbon nanotubes. Smith et al.

further utilized the idea for electrode surface modification as well as enhancing electrocatalysis. This study upholds the idea of generating wealth from waste. (Figure 1.11)

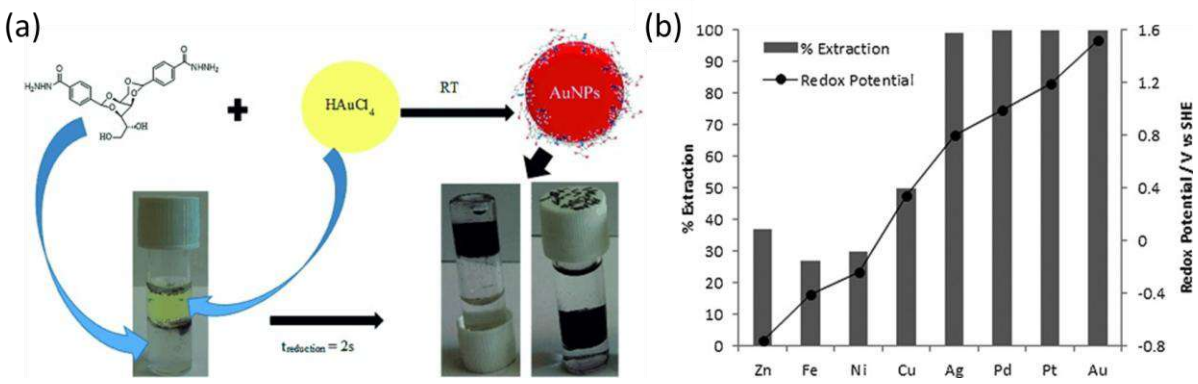

Figure 1.11: (a) Depicting chemical structure of the gelator DBS-CONHNH$_2$ along with the photographs of gold salt adsorption by the gel and concomitant spontaneous reduction of gold salt into its nanoparticles inside the gel matrix. (b) Representing % metal ion extraction from a mixture of different metal ions in water along with the redox potentials of the metal ions. *(adapted from [1.40])*

Oil spill recovery and detection of fuel oil contamination could be accomplished by using an imine based gelator molecule (OG-1), as demonstrated by Nandi et al. in 2019. [1.41] THF solution of OG-1 was applied on the diesel oil phase of an oil-water biphasic mixture, resulting in instant gelation of the diesel oil within 60 s in a phase selective manner without interfering the aqueous phase. Such phase selective oil gelling ability of OG-1 remained intake even in presence of different salts, acids or bases in the aqueous phase. Mechanistic investigation of such oil gelation through FTIR, and PXRD study revealed involvement of strong hydrogen bonding interaction involving -NH and -C=O units, π-π stacking interaction involving the aromatic anthracene moiety, and van der Waals interaction involving the long alkyl chain, in the such gel formation process. The recovered OG-1 gelator after the vacuum distillation of the oil gel could be reused for further studies. Nandi et al. observed diesel oil recovery percentage as high as 87%. In a subsequent study, Nandi et al., demonstrated detection of kerosene contamination in both diesel and petrol oil by employing fluorescence spectroscopic method. In this particular study, they purposefully adulterated both diesel and petrol oil with kerosene oil and used OG-1 to form gel in those adulterated solutions. Subsequently, the emission spectra of such formed gels were recorded and compared with the previously recorded emission spectra of the gel derived from pure kerosene, diesel and petrol oil to detect contamination. (Figure 1.12)

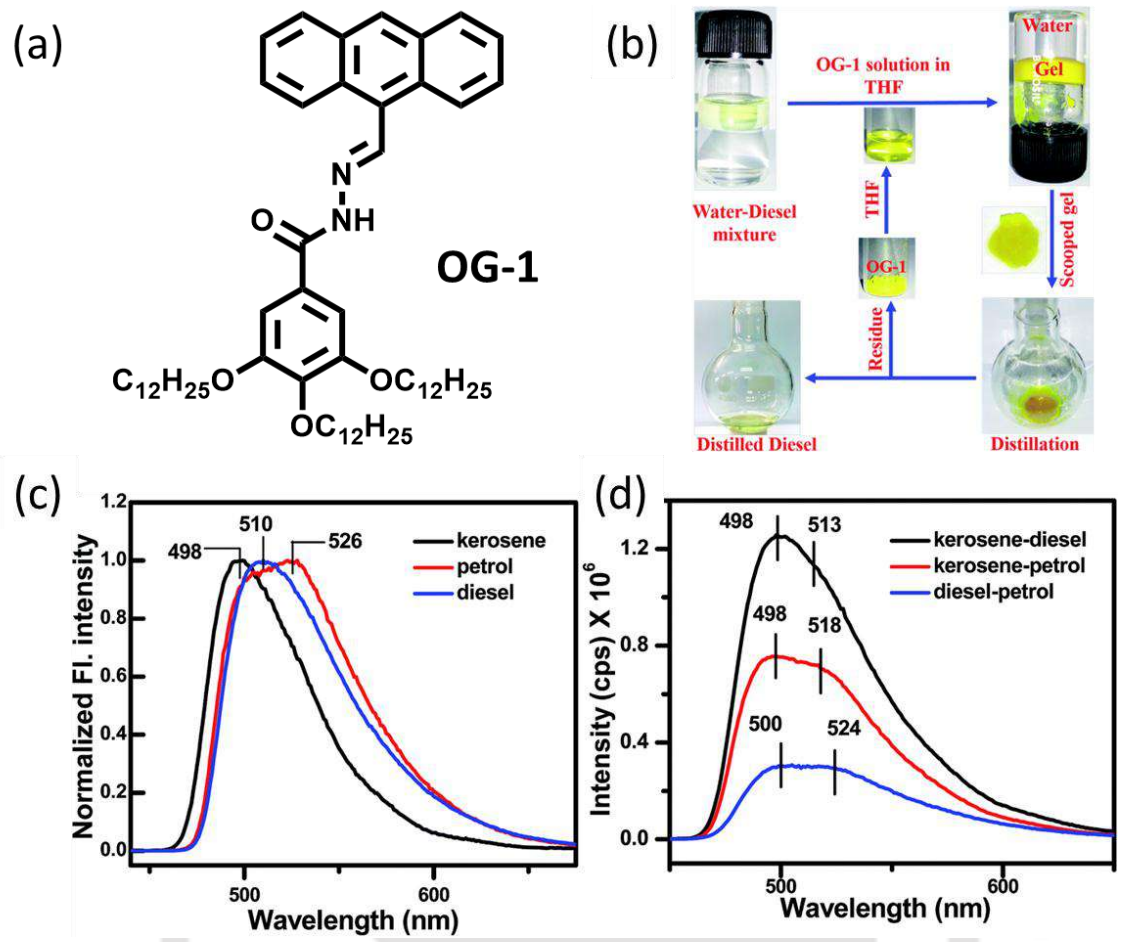

Figure 1.12: (a) Depicting chemical structure of the gelator OG-1. (b) Schematic depiction of diesel oil gelation and recovery from a biphasic mixture of water and diesel oil. (c, d) Representation of the oil contamination detection using fluorescence spectroscopy. *(adapted from [1.41])*

1.3.3. Phase Transformation Study of Supramolecular Gel

In 2016, Gazit et al. studied spontaneous phase transformation of a supramolecular gel into single crystals by adopting a minimal supramolecular polymer model, Fmoc-DOPA. [1.42] Initial macroscopic view of the self-assemble of Fmoc-DOPA was examined by diluting Fmoc-DOPA ethanol stock solution into water, which unveiled three observable changes: change in turbidity, development of gel like viscoelastic characteristics, and finally, spontaneous formation of crystals inside the gel matrix. Cryogenic TEM (cryo-TEM) study enabled visualization of detailed view of the different assembly formation during such a phase transformation. Cryo-TEM study revealed, initial formation of spherical self-assembly, and within four hours the diameter of the spheres became smaller, along with the emergence of tangled fibers as a result of weak gel formation. Within few days, along with the fibrils and the spheres, tubes and helical ribbons also started appearing, and this time the diameter of the spheres became even more smaller than the previous one. Subsequently, after 1.5 months, along with tubes and helical ribbons, macroscopically observable crystals were appeared. Circular dichroism (CD) spectroscopy study showed that, with

increase in time the band at 30 nm intensifies, which was ascribed to the increase in the population of tubes and helical ribbons as facilitated by π-π stacking of the Fmoc moieties. In FTIR spectroscopic study, the band at 1689 cm^{-1} intensified with increase in time, thus inferring formation of more numbers of well-organized assemblies of Fmoc-DOPA. Further studies including ^{1}H NMR, and ssNMR experiments supported the earlier observed microscopic transformations. Crystal structure analysis revealed the hydrogen bonding and aromatic interactions to be the stabilizing force of the crystal structure of Fmoc-DOPA. (Figure 1.13)

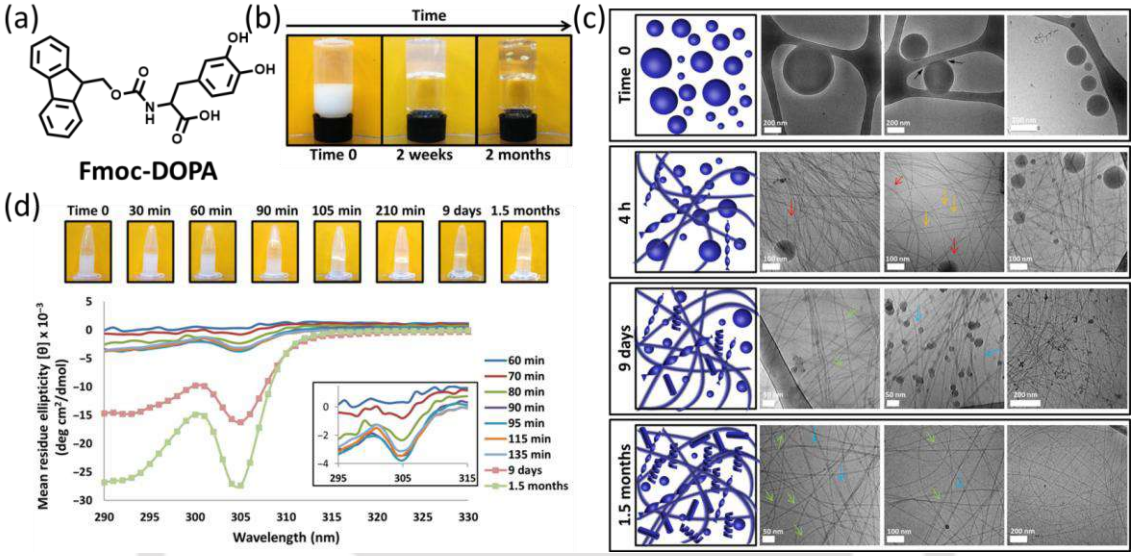

Figure 1.13: (a) Depicting chemical structure of the gelator Fmoc-DOPA. (b) Macroscopically observable changes of Fmoc-DOPA with time from turbid solution to gel and finally to crystals inside gel (from left to right). (c) Cryo-TEM analysis showing different assembly formation of Fmoc-DOPA at different time frames. (d) Vial inversion assay depicting gelation of Fmoc-DOPA with time, and their corresponding time dependent CD spectra. *(adapted from [1.42])*

Very recently, Nanda et al., demonstrated pathway complexity involved in the self-assembly behavior of a naphthalimide-(NMI)-conjugated dipeptide (N2) molecule with varying ratio of water in a mix solvent system of DMSO and water. [1.43] Depending upon the percentage of water, the system could adopt two distinctly different transformation pathways. At lower water percentages (at least 40%), the self-assembly was directed towards metastable gel formation, whereas the self-assembly proceeded towards the formation of crystalline precipitate at higher water percentages (at 60% and above). Different spectroscopic and microscopic study of the metastable gel formation revealed initial formation of tiny particles, followed by formation of helical nano fibers, which gradually entangled to form 3-D fiber gel network. Nanda et al. were further able to demonstrate the tunability of the helicity just by varying the achiral solvent composition, where they observed that, right-handed helical nanofibers formed at lower water percentages, whereas at higher water percentages the helicity was inverted to left-handed helical

fibers. Moreover, the temperature dependent study revealed thermoresversibility of the self-assembly process while retaining the helical memory. (Figure 1.14)

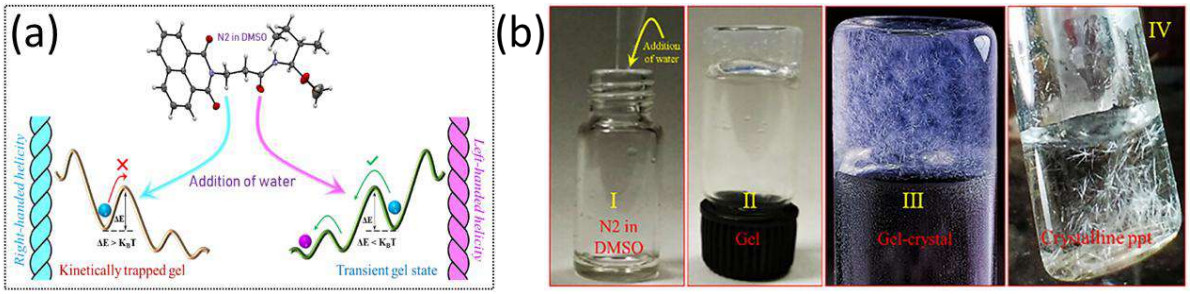

Figure 1.14: (a) Depicting solvent composition directed differential self-assembly in N2 (in a mix solvent system od DMSO and water). (b) Photograph depicting gel preparation, gel formation, gel-crystal formation, and crystalline precipitate formation (from left to right). *(adapted from [1.43])*

1.4. Summary of Literature Review and Research Gaps

This comprehensive review highlights and summarizes the use of small molecule based self-assembled systems for anion coordination and supramolecular gelation purposes. Within the domain of anion coordination, this review highlights its potential application in areas like anion recognition and toxic anion sensing. And, within the realm of supramolecular gel, the review demonstrates development of stimuli-responsive materials, material for water remediation, and controlled phase transformation of supramolecular gel systems. Small molecule-based systems are finding an importance place in the development of functional materials due to their high structural tunability, easy synthesis method, and economic viability. Due to their high structural tunability, researchers have been able to design small molecule-based systems capable of targeting some specific anions in a highly selective manner. The idea of selective anion recognition has further been advanced towards selective extraction of the desired anions from water. Moreover, the structures of the receptors can often be modulated in such a way that, the recognition chemistry can also be applied for the sensing of toxic anions such as CN^- in water. Such structural modulation primarily involves incorporation of a recognition site such as hydrogen bond forming unit, and a signaling unit, such as fluorophore moiety. Anions are known to exist mostly in their hydrated forms in nature, so sometimes the sensitivity as well as selectivity of their recognition/sensing is not effective. In such cases, some other self-assembly forming systems are co-assembled with receptor/probe for improving the selectivity and sensitivity of the sensing performance. The chemical structures of such small molecules can further be modulated for the designing of LMWGs, which forms supramolecular gel given the appropriate medium. Such soft materials can be used as stimuli responsive materials, which responses towards stimuli such as heat, anion, pH, light etc. The response generally involves gel to sol, gel to gel, and gel to precipitate

transformations in presence of that stimulus. Moreover, the design rational of the LMWGs can also be modulated for oil gelation purposes, which can further be extended towards oil spill recovery from water, and detection of oil contamination. For such oil spill recovery from water, the designed LMWGs need to be phase selective in nature, so that, it selectively forms gel in the oil phase only without disturbing the aquatic life. Supramolecular gels are often observed to be remained in a metastable state, which eventually transforms into its global minima. Such transformation sometimes occurs spontaneously, and in many cases, it happens only in presence of external stimuli. However, self-assembly of such systems can also be well-directed by adjusting the combinations of the medium as well. It is important to understand the pathway complexities associated with such transformations, so that, the macroscopic materials performance can be controlled at the very microscopic level. Despite of all those commendable progresses being made in all the mentioned fields by employing small molecule-based systems, their real-world application is still very far away from reality. This can be attributed to factors such as improper understanding of structure-function relationship, and selectivity related issues, as the real-world systems are harsher than that of the controlled lab environment. With proper design rationale of the molecules, the shortcomings in its functionalities in the macroscopic level can be addressed. By proper structural tuning of a small molecule-based systems in its molecular level, many important applications such as recognition, sensing, gelation etc. can be achieved. Considering all those factors, this thesis demonstrates and establishes how the structural tunability of the small molecule-based systems can be exploited to accomplish wide range of applications having potential real-world applicability. The applications involve recognition of anions in both solid as well as in solution phase by receptors, recognition guided highly selective and sensitive detection of toxic anions in water by fluorogenic probes, sequestration of heavy and precious metal ions by supramolecular gel, oil-spill remediation by a phase selective organogelator (PSOG), fuel adulteration detection by PSOG, and controlling of crystal habit during phase transformation of a supramolecular gel.

1.5. Objectives of the Thesis

This thesis aims to address some of the important real-world problems with the help of small molecule based self-assembled systems. Such systems have been rationally synthesized and designed for effective materials performance. So, this thesis has primarily been divided into two parts:

- Designing of small molecule based self-assembled systems for anion coordination.
- Designing of small molecule based self-assembled systems for supramolecular gelation.

This thesis entirely focuses on designing of small molecule based self-assembled systems for different material applications, since, such systems are high tunable, easy to synthesis, and economically viable. Within the ambit of anion coordination, this thesis explores the development of receptors for anion recognition in both solid as well as in solution phase. The structures of the receptors can be modulated to control the anion binding propensities in both solid as well as in solution phase. Such studies might be helpful for designing receptors for extracting anions, as well as in its transport. Moreover, this thesis also demonstrates the potential use of recognition chemistry for the detection of toxic anion like CN^- in water in a very highly selective manner. The detection can be achieved in different natural water bodies. Subsequently, LMWGs has also been developed by rationally tunning the structures of the small molecular systems. The supramolecular gel derived from those LMWGs have been employed as stimuli responsive materials, that responses towards certain anions, and heating. The gel could also be employed for the sequestration of precious metal salts from water, along with concomitant spontaneous in situ reduction of the metal salts to its nanoparticles inside the gel matrix. This particular study upholds the concept of waste to wealth generation, which is very important for the sustainable growth of a nation. Furthermore, PSOG has also been designed for oil spill remediation from water. The same PSOG can also be utilized for visual cost-effective detection of fuel adulteration as well. Such very simple fuel adulteration detection method might be beneficial especially for the developing nations, where such a problem is predominant. And finally, controlled phase transformation of a kinetically trapped supramolecular gel to single crystals has been established, where the crystal habit of the resulting single crystals can be controlled. This study might be very beneficial, especially for the pharmaceutical industries, where, controlling of crystal habit is very important. Overall, this thesis demonstrates how the proper design rationale and molecular level engineering of small molecular systems can offer a platform to develop innovative materials for different materials application with potential real-world applicability. The overall objective of this thesis is depicted in a flow chart in Scheme 1.8.

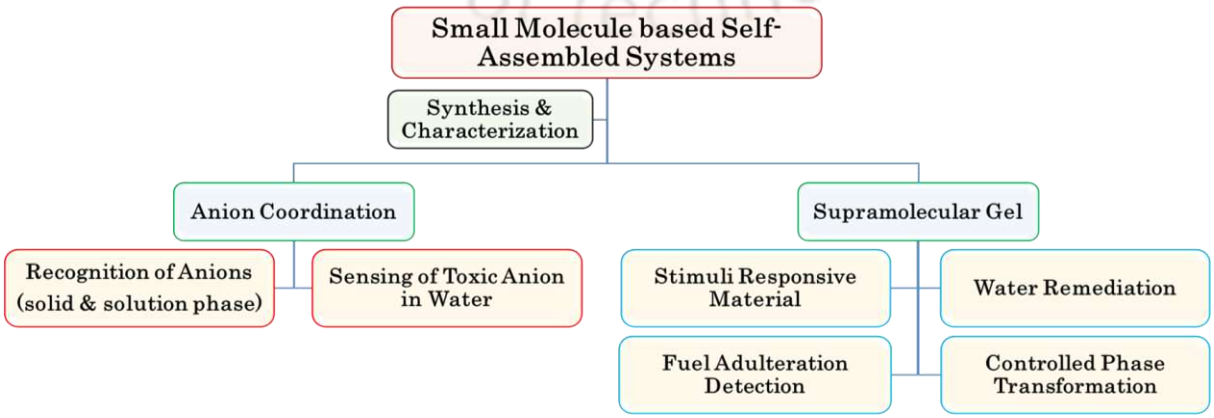

Scheme 1.8: Thesis objectives.

References

[1.1] J-M. Lehn, Supramolecular Chemistry-Scope and Perspectives Molecules-Supramolecules-Molecular Devices, Nobel lecture, December 8,1987.

[1.2] Y. Zhou, and D. Yan, *Chem. Commun.*, 2009, 1172-1188.

[1.3] G. M. Whitesides, and B. A. Grzybowski, *Science*, 2002, **295**, 2418-2421.

[1.4] Supramolecular Chemistry Concepts and Perspectives, ed. J. M. Lehn, 1995.

[1.5] H. Ringsdorf, and J. Simon, *Nature*, 1994, **371**, 284.

[1.6] B. A. Grzybowski, C. E. Wilmer, J. Kim, K. P. Browne, and K. J. M. Bishop, *Soft Matter*, 2009, **5**, 1110-1128.

[1.7] A. C. Mendes, E. T. Baran, R. L. Reis, and H. S. Azevedo, *Rev.: Nanomed. Nanobiotechnol.*, 2013, **5**, 582-612.

[1.8] S. Datta, H. Itabashi, T. Saito, and S. Yagai, Nat. *Chem.*, 2025, 17, 477-492.

[1.9] P. D. Beer, and P. A. Gale, *Angew. Chem. Int. Ed.*, 2001, **40**, 486-516.

[1.10] X. Wu, A. M. Gilchrist, and P. A. Gale, *Chem*, 2020, **6**, 1296-1309.

[1.11] P. Molina, F. Zapata, and A. Caballero, *Chem. Rev.*, 2017, **117**, 9907-9972.

[1.12] U. Manna, B. Portis, T. K. Egboluche, M. Nafis, and M. A. Hossain, *Front. Chem.*, 2021, **8**, 575701.

[1.13] D. Markovich, *Physiol. Rev.*, 2001, **81**, 1499-1533.

[1.14] N. Busschaert, C. Caltagirone, W. V. Rossom, and P. A. *Gale, Chem. Rev.*, 2015, **115**, 15, 8038-8155.

[1.15] S. Kundu, T. K. Egboluche, and Md. A. Hossain, *Acc. Chem. Res.*, 2023, **56**, 1320−1329.

[1.16] C. Zhou, J. Ma, and D. W. Sun, *Trends Food Sci.*, 2023, **134**, 232-246

[1.17] Y. Wu, C. Zhang, S. Fang, D. Zhu, Y. Chen, C. Ge, H. Tang, and H. Li, *Angew. Chem., Int. Ed.*, 2022, **61**, e202209078.

[1.18] K. I. Assaf, and W. M. Nau, *Org. Biomol. Chem.*, 2023, **21**, 6636-6651.

[1.19] S.-Q. Chen, S.-N. Yu, W. Zhao, L. Liang, Y. Gong, L. Yuan, J. Tang, X.-J. Yang, and B. Wu, *Inorg. Chem. Front.*, 2022, **9**, 6091-6101.

[1.20] Z.-Y. Sun, S.-Q. Chen, L. Liang, W. Zhao, X.-J. Yang, and B. Wu, *Chem. Commun.*, 2023, **59**, 12923-2926.

[1.21] N. Lau, L. N. Zakharov, and M. D. Pluth, *Chem. Commun.*, 2018, **54**, 2337-2340.

[1.22] R. Nazarian, H. R. Darabi, K. Aghapoor, R. Firouzi, and H. Sayahi, *Chem. Commun.*, 2020, **56**, 8992-8995.

[1.23] R. S. Fernandes, J. Kumari, D. Sriram, and N. Dey, *ACS Appl. Bio Mater.*, 2023, **6** (10), 4158-4167.

[1.24] A. Pal, O. Sarkar, N. R. Pramanik, and N. Dey, *Ind. Eng. Chem. Res.*, 2024, **63** (19), 8489-8496.

[1.25] P. Slavík, D. W. Kurka, and D. K. Smith, *Chem. Sci.*, 2018, **9**, 8673– 8681.

[1.26] E. R. Draper, and D. J. Adams, *Chem.*, 2017, **3**, 390-410.

[1.27] N. M. Sangeetha, and U. Maitra, *Chem. Soc. Rev.*, 2005, **34**, 821-836.

[1.28] P. R. A. Chivers, and D. K. Smith, *Nat. Rev. Mater.*, 2019, **4**, 463-478.

[1.29] S. Kimura, K. Adachi, Y. Ishii, T. Komiyama, T. Saito, N. Nakayama, M. Yokoya, H. Takaya, S. Yagai, S. Kawai, T. Uchihashi, and M. Yamanaka, *Nat. Commun.* 2025, **16**, 3758.

[1.30] S. Panja, and D. J. Adams, *Chem. Soc. Rev.*, 2021, **50**, 5165-5200.

[1.31] C. D. Jones, and J. W. Steed, *Chem. Soc. Rev.*, 2016, **45**, 6546-6596.

[1.32] P. Slavík, D. W. Kurka, and D. K. Smith, *Chem. Sci.*, 2018, **9**, 8673-8681.

[1.33] S. Mondal, P. Bairi, S. Das, and A. K. Nandi, *J. Mater. Chem. A*, 2019, **7**, 381-392.

[1.34] H.-L. Yang, X.-W. Sun, Y.-M. Zhang, Z.-H. Wang, W. Zhu, Y.-Q. Fan, T.-B. Wei, H. Yao and Q. Lin, *Soft*

Matter, 2019, **15**, 9547-9552.

[1.35] A. R. Hirst, B. Escuder, J. F. Miravet, and D. K. Smith, *Angew. Chem. Int. Ed.*, 2008, **47**, 8002-8018.

[1.36] S. Panja, A. Panjab, and K. Ghosh, *Mater. Chem. Front.*, 2021, **5**, 584-602.

[1.37] C. C. Piras, C. S. Mahon, and D. K. Smith, *Chem. Eur. J.*, 2020, **26**, 8452 – 8457.

[1.38] S. Sharma, M. Kumari, and N. Singh, *Soft Matter*, 2020, **16**, 6532-6538.

[1.39] A. M. Fuentes-Caparrós, F. de P. Gómez-Franco, B. Dietrich, C. Wilson, C. Brasnett, A. Seddon, and D. J. Adams, *Nanoscale*, 2019, **11**, 3275-3280.

[1.40] B. O. Okesola, S. K. Suravaram, A. Parkin, and D. K. Smith, *Angew. Chem. Int. Ed.*, 2016, **55**, 183-187.

[1.41] S. Mondal, P. Bairi, S. Das, and A. K. Nandi, *J. Mater. Chem. A*, 2019, **7**, 381-392.

[1.42] G. Fichman, T. Guterman, J. Damron, L. Adler-Abramovich, J. Schmidt, E. Kesselman, L. J. W. Shimon, A. Ramamoorthy, Y. Talmon, and E. Gazit, *Sci. Adv.*, 2016, **2**, e1500827.

[1.43] S. Kuila, S. Misra, T. Singha, A. Ghosh, P. Singh, R. Saha, D. Ganguly, P. Brandão, B. Satpati, and J. Nanda, *Small*, 2025, **21**, 2501718.

Chapter 2

Experimental & Characterization Details

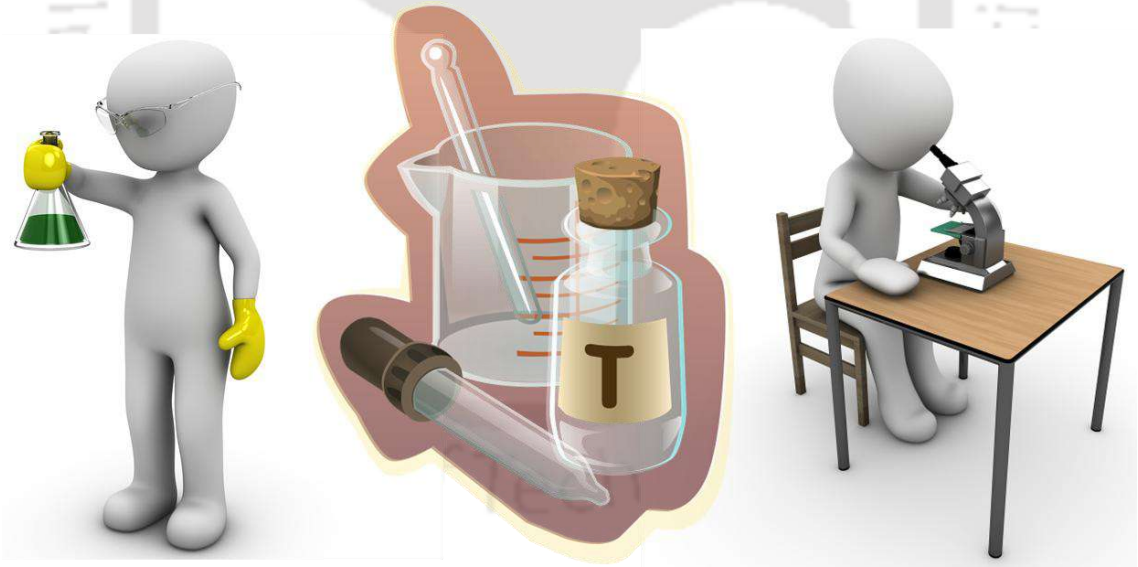

CHAPTER 2

2. Experimental Details and Characterizations

This chapter provides a comprehensive thorough description of various materials and methods employed for the synthesis and characterisation of the studied receptors/probes/gelator molecules. Moreover, it covers specifications of the various analytical tools, techniques, experimental setups, and different methods employed during all the studies in a detailed manner.

2.1. General Information on Materials and Methods

All reagents and solvents were obtained from commercial sources and used as received without further purification. Solvents for synthesis and crystallization experiments were purchased from purchased from Sigma-Aldrich Chemical Co., and used as received without further purification. ^{1}H NMR spectra were recorded on 400, 500 and 600 MHz instrument, and chemical shifts were recorded in parts per million (ppm) on the scale using tetramethylsilane [$Si(CH_3)_4$] or a residual solvent peak as a reference. The following abbreviations are used to describe spin multiplicities in ^{1}H NMR spectra: s =singlet; d = doublet; t = triplet; q= quartet, m = multiplet. The binding stoichiometry and the binding constants were determined through proton NMR (600 MHz) titrations of the receptors with the tetrabutylammonium salts, in DMSO-d_6 at 298K. The preliminary concentrations of the hosts and the guests were, $[ligand]_0$ = 50 mM, and $[anion]_0$ = 500 mM respectively. All the titrations were performed by 11-16 measurements at room temperature, and the peak of DMSO-d_6 (at 2.5 ppm) was used for an internal reference. BindFit v0.5 program was used for the determination of binding stoichiometry as well as binding constant values from ^{1}H NMR titration experiments. The mass spectra (ESI-MS) of all the synthesized compounds were recorded in methanol/acetonitrile using Agilent Q-ToF mass spectrometer. IR spectra of all of the four receptors and the complex were recorded on PerkinElmer FT-IR spectrometer as KBr disks in the range 4000-450 cm^{-1}. In some cases, FTIR-ATR instrument was also employed to recorded the IR spectra. The absorption measurements were recorded on a PerkinElmer Lamda-25 UV-Vis spectrophotometer using 10 mm path-length quartz cuvettes in the wavelength range of 300-700 nm and the fluorescence spectra were recorded on a HoribaFluoromax-4 Spectrofluorometer using 10 mm path length quartz cuvettes.

2.2. Synthetic Procedure and Characterization of all the Compounds

2.2.1. Synthesis and Characterization of L_1 [*1,1'-(oxybis(4,1-phenylene))bis(3-(3-nitrophenyl)urea)*], L_2 [*1,1'-(oxybis(4,1-phenylene))bis(3-(3,5-bis(trifluoromethyl)phenyl)urea)*], and L_3 [*1,1'-(oxybis(4,1-phenylene))bis(3-(naphthalen-1-yl)urea)*]

Each of these neutral bis-urea receptors have been synthesized by adding 4,4′-Diaminodiphenyl Ether (0.200 g, 0.998 mmol) in 10 mL of acetonitrile in a dropwise manner to a solution of 3-nitophenyl isocyanate (0.328 g, 1.998 mmol, for L_1), 3,5-Bis (trifluoromethyl) phenyl isocyanate (0.508 g, 1.991 mmol, for L_2) and 1-Naphthyl isocyanate (0.338 g, 1.998 mmol, for L_3). After vigorous stirring for 24 h, for L_1, a yellow precipitate was obtained and for other receptors, L_2 and L_3 white precipitate was obtained and all the precipitates were filtered off and washed several times with acetonitrile and then dried in a vacuum. These compounds were characterised by different characterisation methods and also recrystallization is done for all of the compounds from either DMSO or DMF solution. (Scheme 2.1)

L_1: ^{1}H NMR (500 MHz, DMSO-d_6) δ(ppm): 9.17 (s, 2H), 8.80 (s, 2H), 8.56 (s, 2H), 7.82 (d, J = 8.1 Hz, 2H), 7.72 (d, J = 8.1 Hz, 2H), 7.56 (t, 2H), 7.48 (d, J = 8.7 Hz, 4H), 6.97 (d, J = 8.7 Hz, 4H).; ^{13}C NMR (126 MHz, DMSO) δ(ppm): 153.01, 152.62, 148.64, 141.61, 135.11, 130.51, 124.76, 120.95, 119.29, 116.67, 112.59; FT-IR (υ, cm^{-1}): 3375 cm^{-1} Vs (urea N-H), 1678 cm^{-1} Vs (urea C=O), 1501 cm^{-1} Vs (NO_2-asymmetric), 1343 cm^{-1} Vs (NO_2-symmetric), 3114 cm^{-1} Vs (aromatic C-H). MS: calculated mass 528.1393, obtained ESI mass m/z 528.0587. (Figure A2.1-A2.4)

L_2: ^{1}H NMR (500 MHz, DMSO-d_6) δ(ppm): 9.35 (s, 2H), 8.95 (s, 2H), 8.14 (s, 4H), 7.63 (s, 2H), 7.48 (d, J = 8.8 Hz, 4H), 6.97 (d, J = 8.8 Hz, 4H). ^{13}C NMR (151 MHz, DMSO) δ(ppm): 153.02, 152.76, 142.42, 134.88, 131.50, 131.28, 131.07, 130.85, 126.51, 124.71, 122.90, 121.32, 121.09, 119.27, 118.43, 114.71. FT-IR (υ, cm^{-1}): broad band at 3318 cm^{-1} Vs (urea N−H), 1562cm^{-1} Vs (C=C),1655 cm^{-1} Vs (urea C=O), 3108 cm^{-1}Vs (aromatic C-H). MS: calculated mass 710.1187, obtained MALDI mass m/z 733.502 (L_1 + Na^+). (Figure A2.5-A2.8)

L_3: ^{1}H NMR (400 MHz, DMSO-d_6) δ(ppm): 9.04 (s, 2H), 8.74 (s, 2H), 8.14 (d, J = 8.3 Hz, 2H), 8.03 (d, J = 7.5 Hz, 2H), 7.94 (d, J = 7.9 Hz, 2H), 7.66 – 7.46 (m, 12H), 6.99 (d, J = 6.9 Hz, 4H); ^{13}C NMR (126 MHz, DMSO) δ(ppm): 153.53, 152.36, 135.69, 134.79, 134.21, 128.90, 126.45, 126.38, 126.36, 126.18, 123.42, 121.80, 120.37, 119.36, 117.92;

FT-IR (υ, cm^{-1}): broad band at 3280 cm^{-1} Vs (urea N−H), 1555 cm^{-1} Vs (C=C), 1637 cm^{-1} Vs (urea C=O), 3051 cm^{-1}Vs (aromatic C-H). (Figure A2.9-A2.11)

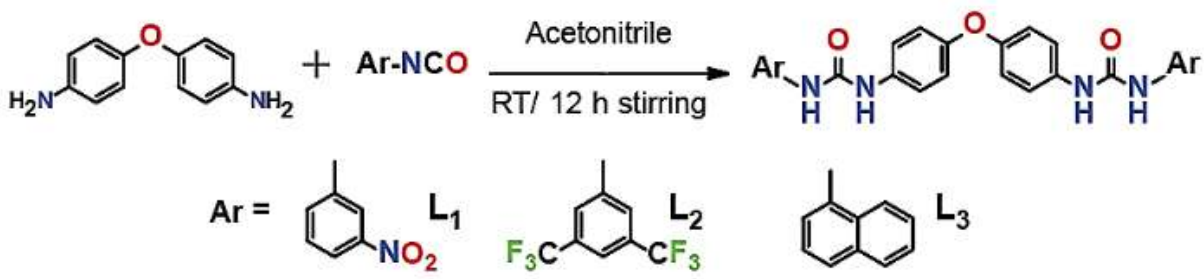

Scheme 2.1: Synthetic scheme of receptors L_1, L_2, and L_3.

2.2.2 Synthesis and Characterization of Acetate Complex of L_1 (L_1A)

$[(n\text{-}TBA)_2\{(L_1)(OCOCH_3)_2\}]$ (L_1A): Complex L_1A was obtained by adding an excess of tetrabutylammonium acetate [*n*-TBA(CH_3COO)] (15 eqv.) into a 6 mL DMSO/DMF solution of L_1 (100 mg, 0.189 mmol). After the addition of *n*-TBA(CH_3COO), the solution was stirred for about 15 min and kept it in an undisturbed place for crystallisation through slow evaporation. After 25 days of slow evaporation, yellow colour block shaped crystals suitable for single crystal XRD analysis were obtained.

Complex L_1A: ^{1}H NMR (600 MHz, DMSO-d_6) δ(ppm): 11.04 (s, 2H), 10.59 (s, 2H), 8.64 (s, 2H), 7.82 (d, J = 8.1 Hz, 2H), 7.77 (d, J = 8.1 Hz, 2H), 7.54 (t, J = 9.1 Hz, 6H), 6.93 (d, J = 8.8 Hz, 4H), 3.17 (t, J = 8.4 Hz, 8H, TBA-CH_2), 1.81 (s, 3H, Acetate-CH_3), 1.6-1.55 (m, 8H, TBA-CH_2), 1.35-1.29 (m, 8H, TBA-CH_2), 0.94 (t, J = 7.3 Hz, 12H, TBA-CH_3). ^{13}C NMR (151 MHz, DMSO) δ(ppm): 176.80, 153.68 (×2C, carbonyl-C), 152.17 (×2C, Ar-C), 148.61 (×2C, Ar-C), 142.69 (×2C, Ar-C), 136.07 (×2C, Ar-C), 130.28 (×2C, Ar-C), 124.60 (×2C, Ar-C), 120.51 (×4C, Ar-C), 119.08 (×4C, Ar-C), 115.95 (×2C, Ar-C), 112.29 (×2C, Ar-C), 58.00 (×4C, TBA-N+CH_2), 25.37 (×1C, acetate-C), 23.53 (×4C, TBA-CH_2), 19.68 (×4C, TBA-CH_2), 13.97 (×4C, TBA-CH_3). (Figure A2.12-A2.14)

2.2.3. Synthesis and Characterization of BPU-1 [*1-(2-(1H-benzo[d]imidazol-2-yl)phenyl)-3-(4-nitrophenyl)urea*], BPU-2 [*1-(2-(1H-benzo[d]imidazol-2-yl)phenyl)-3-(3,5-bis(trifluoromethyl)phenyl)urea*] , and BP-Cyc [*benzo[4,5]imidazo[1,2-c]quinazolin-6(5H)-one*]

BPU-1: 2-(1H-Benzimidazol-2-yl)aniline (500 mg, 2.39 mmol, 1 equiv.) was placed in a 50 mL round-bottomed flask and dissolved in dichloromethane (DCM) (15 mL). A

solution of 4-Nitrophenyl isocyanate (392.1 mg, 2.39 mmol, 1 equiv.) was added into the flask in dropwise manner. The reaction was stirred at room temperature for 12 hours. The precipitates were separated by filtration and washed with DCM (30 mL) and diethyl ether (30 mL). The obtained yellow powder was further dried over vacuum dried and isolated as compound BPU-1. Yield, 90%. ^{1}H NMR (600 MHz, DMSO-d_6) δ (ppm): 13.11 (s, 1H), 12.30 (s, 1H), 10.48 (s, 1H), 8.39 (d, J = 8.4 Hz, 1H), 8.22 (d, J = 9.0 Hz, 2H), 8.08 (d, J = 7.8 Hz, 1H), 7.83 (d, J = 9.0 Hz, 3H), 7.59 (d, J = 6.4 Hz, 1H), 7.48 (t, J = 7.8 Hz, 1H), 7.30 (s, 2H), 7.22 (t, J = 7.5 Hz, 1H). ^{13}C NMR (151 MHz, DMSO) δ(ppm): 152.71, 151.30, 147.23, 142.69, 141.60, 139.07, 134.13, 130.85, 127.86, 125.50 (×2C, Ar-C), 123.79, 122.53 (×2C, Ar-C), 121.07, 119.37, 118.56 (×2C, Ar-C), 116.13, 111.93. FT-IR spectra (KBr pellet used): 3287 cm^{-1} vs (urea N–H), 3067 cm^{-1} vs (aromatic C–H), 1730 cm^{-1} vs (urea C═O), 1533 cm^{-1} vs (NO_2-asymmetric), 1298 cm^{-1} vs (NO_2-symmetric). ESI-MS (positive mode, m/z): calculated for $C_{20}H_{15}N_5O_3$: 373.1175. Found: 374.1255 [M + H]$^{+}$. m.p.: 213˚C. (Figure A2.15-A2.18)

BPU-2: 2-(1H-Benzimidazol-2-yl) aniline (500 mg, 2.39 mmol, 1 equiv.) was placed in a 50 mL round-bottomed flask and dissolved in DCM (15 mL). A solution of 3,5-Bis(trifluoromethyl)phenyl Isocyanate (610 mg, 2.39 mmol, 1 equiv.) was added into the flask in dropwise manner. The reaction was stirred at room temperature for 12 hours. The precipitates were separated by filtration and washed with DCM (30 mL) and diethyl ether (30 mL). The obtained white powder was further dried over vacuum dried and isolated as compound BPU-2. Yield, 85%. ^{1}H NMR (600 MHz, DMSO-d_6) δ(ppm): 13.13 (s, 1H), 12.44 (s, 1H), 10.42 (s, 1H), 8.43 (d, J = 8.4 Hz, 1H), 8.29 (s, 2H), 8.09 (d, J = 9.2 Hz, 1H), 7.85 (d, J = 7.4 Hz, 1H), 7.67 (s, 1H), 7.59 (d, J = 8.0 Hz, 1H), 7.48 (t, J = 8.5 Hz, 1H), 7.33 – 7.27 (m, 2H), 7.22 (t, J = 7.6 Hz, 1H). ^{13}C NMR (151 MHz, DMSO) δ(ppm): 152.98, 151.36, 142.62, 139.13, 134.08, 131.45, 131.24, 131.02, 130.88, 130.81, 127.79, 124.77, 123.82, 122.96, 122.56, 122.47, 120.86, 119.40, 118.84, 115.89, 114.96, 111.92. FT-IR spectra (KBr pellet used): 3258 cm^{-1} vs (urea N–H), 3082 cm^{-1} vs (aromatic C–H), 1686 cm^{-1} vs (urea C═O), 1124 cm^{-1} vs (C-F). ESI-MS (positive mode, m/z): calculated for $C_{22}H_{14}F_6N_4O$: 464.1072. Found: 465.1144 [M + H]$^{+}$. m.p.: 233˚C. (Scheme 2.2, Figure A2.19-A2.22)

BP-Cyc: BPU-1 (100 mg, 0.27 mmol, 1 equiv.)/BPU-2 (100mg, 0.22 mmol, 1 equiv.) was placed in a 50 mL round-bottom flask and dissolved in acetonitrile (ACN). Excess of TBAF/TBAOH (~ 10 equiv.) was added into the flask in dropwise manner and the reaction mixture was stirred for 8 hours at room temperature for BPU-1, and refluxed for 8 hours in the

case of BPU-2. Cold water was poured into the reaction mixture while stirring, which yielded white precipitate. The precipitates were separated by filtration and washed with ACN (30 mL) and diethyl ether (30 mL). The obtained white powder was further dried over vacuum dried and isolated as compound BP-Cyc. Yield, 80-85%. ^{1}H NMR (600 MHz, DMSO-d_6) δ(ppm): 11.95 (s, 1H), 8.37 (d, J = 7.8 Hz, 1H), 8.33 (d, J = 7.9 Hz, 1H), 7.87 (d, J = 7.9 Hz, 1H), 7.67 (t, J = 7.7 Hz, 1H), 7.50 (t, J = 8.2 Hz, 1H), 7.46 (t, J = 7.1 Hz, 1H), 7.42 (d, J = 8.2 Hz, 1H), 7.39 (t, J = 7.9 Hz, 1H). ^{13}C NMR (151 MHz, DMSO) δ (ppm): 148.20, 146.92, 144.00, 137.74, 132.76, 131.12, 125.48, 124.91, 124.12, 123.83, 119.60, 116.44, 115.24, 112.28. FT-IR spectra (KBr pellet used): 3424 cm^{-1} vs (urea N–H), 3180 cm^{-1} vs (aromatic C–H), 1710 cm^{-1} vs (urea C═O). ESI-MS (positive mode, m/z): calculated for $C_{14}H_9N_3O$: 235.0746. Found: 236.0824 $[M + H]^+$. (Scheme 2.2, Figure A2.23-A2.26)

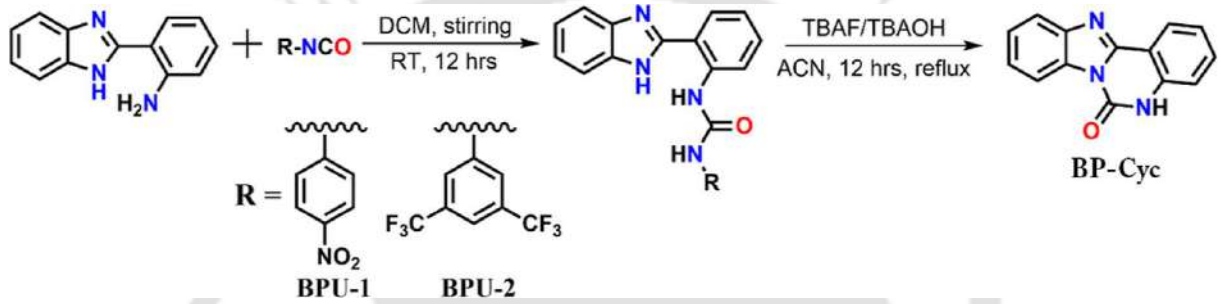

Scheme 2.2: Synthetic scheme of receptors BPU-1, BPU-2, and BP-Cyc.

2.2.4. Synthesis and Characterization of Anionic Complexes of BPU-1, and BPU-2

[BPU-1 (n-TBA) Cl] (1a): Complex 1a was prepared by adding an excess of tetrabutylammonium chloride 15 equiv. into a 10 mL DMF and DMSO solution of BPU-1 (100 mg, 0.267 mmol) in a small glass vial. After the addition of the chloride salts, the resulting solutions were stirred for about 30 minutes and were left open to the atmosphere for slow evaporation at room temperature. Yellow coloured block shaped crystals of 1a suitable for single crystal X-ray analysis was obtained within 10 days. Yield: 70%. ^{1}H NMR (600 MHz, DMSO-d_6) δ(ppm): 13.25 (s, 1H, NH_c), 12.32 (s, 1H, NH_b), 10.52 (s, 1H, NH_a), 8.39 (d, 1H, Ar-H), 8.22 (d, 2H, Ar-H), 8.13 (d, 1H, Ar-H), 7.84 (d, 3H, Ar-H), 7.61 (d, 1H, Ar-H), 7.48 (t, 1H, Ar-H), 7.29 (t, 2H, Ar-H), 7.22 (t, 1H, Ar-H), 3.16 (t, 8H, TBA-CH_2), 1.56 (m, 8H, TBA-CH_2), 1.31 (m, 8H, TBA-CH_2), 0.93 (t,12H, TBA-CH_3). FT-IR spectra (KBr pellet): 2960 cm^{-1} vs (N–H), 2873 cm^{-1} vs (C–H), 1698 cm^{-1} vs (C═O), 1485 cm^{-1} vs (NO_2-asymmetric), 1215 cm^{-1} vs (NO_2-symmetric). (Figure A2.27, A2.28)

[BPU-1 (n-TBA) Br] (1b): Complex 1b was prepared by adding an excess (15 equiv.) of tetrabutylammonium bromide to a solution of BPU-1 (100 mg, 0.267 mmol) in 10 ml of DMSO.

After the addition of excess tetrabutylammonium bromide salt (15 equiv.) under stirring conditions, the clear solution was allowed to slowly evaporate at room temperature. After 18–20 days, colorless needle shaped crystals of complex 1(b) were obtained. Yield 60–65%. ^{1}H NMR (600 MHz, DMSO-d_6) δ(ppm): 13.12 (s, 1H, NH_c), 12.31 (s, 1H, NH_b), 10.49 (s, 1H, NH_a), 8.39 (d, 1H, Ar-H), 8.22 (d, 2H, Ar-H), 8.09 (d, 1H, Ar-H), 7.83 (d, 3H, Ar-H), 7.64 (d, 1H, Ar-H), 7.49 (t, 1H, Ar-H), 7.31 (t, 2H, Ar-H), 7.23 (t, 1H, Ar-H), 3.16 (t, 8H, TBA-CH_2), 1.56 (m, 8H, TBA-CH_2), 1.31 (m, 8H, TBA-CH_2), 0.94 (t, 12H, TBA-CH_3). FT-IR spectra (KBr pellet): 2962 cm^{-1} vs (N–H), 2873 cm^{-1} vs (C–H), 1697 cm^{-1} vs (C═O), 1486 cm^{-1} vs (NO_2-asymmetric), 1212 cm^{-1} vs (NO_2-symmetric). (Figure A2.29, A2.30)

[BPU-1 (n-TBA) I] (1c): Complex 1c was obtained as suitable crystals for X-ray diffraction analysis via slow evaporation of a 10 mL DMSO/DMF (1:1) solution of BPU-1 (100 mg, 0.267 mmol) and an excess of tetrabutylammonium iodide (15 equiv.). After the addition of the iodide salt, the solution was stirred for about 10 min at room temperature. Finally, the resulting colorless crystals were isolated by filtration and dried at room temperature. Colourless needle shaped crystals of 1c suitable for single crystal X-ray analysis was obtained within20 days. Yield: 60%. ^{1}H NMR (600 MHz, DMSO-d_6) δ 13.12 (s, 1H, NH_c), 12.31 (s, 1H, NH_b), 10.49 (s, 1H, NH_a), 8.39 (d, 1H, Ar-H), 8.23 (d, 2H, Ar-H), 8.09 (d, 1H, Ar-H), 7.84 (d, 3H, Ar-H), 7.65 (d, 1H, Ar-H), 7.49 (t, 1H, Ar-H), 7.30 (t, 2H, Ar-H), 7.23 (t, 1H, Ar-H), 3.16 (t, 8H, TBA-CH_2), 1.56 (m, 8H, TBA-CH_2), 1.31 (m, 8H, TBA-CH_2), 0.94 (t, 12H, TBA-CH_3). FT-IR spectra (KBr pellet): 3181 cm^{-1} vs (N–H), 2961 cm^{-1} vs (C–H), 1697 cm^{-1} vs (C═O), 1485 cm^{-1} vs (NO_2-asymmetric), 1300 cm^{-1} vs (NO_2-symmetric). (Figure A2.31, A2.32)

[{BPU-1(n-TBA)(NO_3)] (1d): Complex 1d was attained by introducing an excess amount of tetrabutylammonium nitrate (15 equiv.) into a 10 mL THF solution of BPU-1 (100 mg, 0.267 mmol) in a small test tube. After the addition of the above salt, the resulting solution was further stirred for about 10 min at room temperature and left exposed to air for a spontaneous slow evaporation. Yellow coloured block shaped crystals of 1d suitable for single crystal X-ray analysis was obtained within 25 days. Yield: 70-75%. ^{1}H NMR (600 MHz, DMSO-d_6) δ(ppm): 13.13 (s, 1H, NH_c), 12.32 (s, 1H, NH_b), 10.50 (s, 1H, NH_a), 8.40 (d, 1H, Ar-H), 8.23 (d, 2H, Ar-H), 8.09 (d, 1H, Ar-H), 7.83 (d, 3H, Ar-H), 7.60 (d, 1H, Ar-H), 7.49 (t, 1H, Ar-H), 7.3 (t, 2H, Ar-H), 7.23 (t, 1H, Ar-H). FT-IR spectra (KBr pellet): sharp band at 2960 cm^{-1} vs (N–H), 2874 cm^{-1} vs (C–H), 1702 cm^{-1} vs (C═O), 1488 cm^{-1} vs (NO_2-asymmetric), 1327 cm^{-1} vs (NO_2-symmetric), 1327 cm^{-1} vs (NO_3). (Figure A2.33, A2.34)

[(BPU-1-H)$^{+}$(n-TBA)$^{+}$(H_2O)$_4$(SO_4)$^{2-}$] (1e): Hydrated complex 1e was prepared by adding an excess (15 equiv.) of tetrabutylammonium bisulfate to a solution of BPU-1 (100 mg, 0.267 mmol) in a 10 ml solvent mixture of DMSO and acetonitrile (1:1). After the addition of excess tetrabutylammonium bisulfate salt (15 equiv.) under stirring conditions, the clear yellow color solution was allowed to slowly evaporate at room temperature. Yellow coloured block shaped crystals of 1e suitable for single crystal X-ray analysis was obtained within 15 days. Yield: 75-80%. ^{1}H NMR (600 MHz, DMSO-d_6) δ(ppm): 8.12 (d, 1H, Ar-H), 8.06 (d, 1H, Ar-H), 7.99 (d, 1H, Ar-H), 7.93 (m, 1H, Ar-H), 7.79 (d, 2H, Ar-H), 7.47 (m, 2H, Ar-H), 7.33 (t, 1H, Ar-H), 7.11 (m, 1H, Ar-H), 6.78 (s, 1H, Ar-H), 6.62 (m, 1H, Ar-H). FT-IR spectra (KBr pellet): sharp band at 2962 cm^{-1} vs (N–H), 2875 cm^{-1} vs (C–H), 1382 cm^{-1} vs (S=O), 1650 cm^{-1} vs (C═O), 1486 cm^{-1} vs (NO_2-asymmetric), 1324 cm^{-1} vs (NO_2-symmetric). (Figure A2.35, A2.36)

[BPU-2 (n-TBA) Cl] (2a): Complex 2a was obtained as suitable crystals for X-ray diffraction analysis via slow evaporation of a 10 mL DMSO/DMF (1:1) solution of BPU-2 (100 mg, 0.215 mmol) and an excess of tetrabutylammonium chloride (15 equiv.). After the addition of the iodide salt, the solution was stirred for about 10 min at room temperature. Finally, the resulting colorless crystals were isolated and dried at room temperature. Colourless block shaped crystals of 2a suitable for single crystal X-ray analysis was obtained within 7 days. Yield: 70-75%. ^{1}H NMR (600 MHz, Chloroform-*d*) δ(ppm): 13.18 (s, 1H, NH_c), 12.46 (s, 1H, NH_b), 10.45 (s, 1H, NH_a), 8.43 (d, 1H, Ar-H), 8.30 (s, 2H, Ar-H), 8.11 (d,1H, Ar-H), 7.80 (s, 1H, Ar-H), 7.67 (s, 1H, Ar-H), 7.62 (s, 1H, Ar-H), 7.47 (t, 1H, Ar-H), 7.30 (m, 2H, Ar-H), 7.22 (t, 1H, Ar-H), 3.16 (t, 8H, TBA-CH_2), 1.57 (m, 8H, TBA-CH_2), 1.30 (m, 8H, TBA-CH_2), 0.93 (t, 12H, TBA-CH_3). FT-IR spectra (KBr pellet used): 2958 cm^{-1} vs (urea N–H), 2875 cm^{-1} vs (aromatic C–H), 1701 cm^{-1} vs (urea C═O), 1280 cm^{-1} vs (C-F). (Figure A2.37, A2.38)

[BPU-2 (n-TBA) Br] (2b): Complex 2b was prepared by charging an excess (10 equiv.) of tetrabutylammonium bromide into a 10 mL DMSO/DMF (1:1) solution of BPU-2 (100 mg, 0.215 mmol). After the salt was added, the colorless solution was stirred for about 10 min at room temperature. Finally, the resulting solution was kept open to the atmosphere in a test tube and allowed to evaporate slowly at room temperature. Colourless needle shaped crystals of 2b suitable for X-ray analysis were obtained within 15 days. Yield: 65-70%. ^{1}H NMR (600 MHz, DMSO-d_6) δ(ppm): 13.12 (s, 1H, NH_c), 12.45 (s, 1H, $_{NHb}$), 10.42 (s, 1H, NH_a), 8.43 (d, 1H, Ar-H), 8.29 (d, 2H, Ar-H), 8.10 (d, 1H, Ar-H), 7.81 (s, 1H, Ar-H), 7.67 (s, 1H, Ar-H), 7.62 (s, 1H, Ar-H), 7.48 (t, 1H, Ar-H), 7.30 (m, 2H, Ar-H), 7.22 (t, 1H, Ar-H), 3.16 (t, 8H, TBA-CH_2), 1.56 (m, 8H, TBA-CH_2), 1.31 (m, 8H, TBA-CH_2), 0.93 (t, 12H, TBA-CH_3). FT-IR spectra (KBr

pellet used): 3137 cm^{-1} vs (urea N–H), 2963 cm^{-1} vs (aromatic C–H), 1701 cm^{-1} vs (urea C═O), 1273 cm^{-1} vs (C-F). (Figure A2.39, A2.40)

2.2.5. Synthesis and Characterization of Benz-d-CF_3 *[(E)-N-(3,5-bis(trifluoromethyl)phenyl)benzo[4,5]imidazo[1,2-c]quinazolin-6(5H)-imine*] and Benz-m-CF_3 [*(E)-N-(3-(trifluoromethyl)phenyl)benzo[4,5]imidazo[1,2-c]quinazolin-6(5H)-imine*]

Benz-d-CF_3: 2-(1H-Benzimidazol-2-yl)aniline (200 mg, 0.955 mmol, 1 equiv.) was placed in a 50 mL round-bottomed flask and dissolved in acetonitrile (ACN) (10 mL). A solution of Bis-(Trifluoromethyl)phenyl Isothiocyanate (259.2 mg, 0.955 mmol, 1 equiv.) was added into the flask in dropwise manner. The reaction was refluxed at 80˚C for 48 hours. The precipitates were separated by filtration and washed with ACN (30 mL) and diethyl ether (30 mL). The obtained white crystalline product was further vacuum dried and isolated as compound Benz-d-CF_3. It was further crystallized in 1:1 solvent mixture of DMSO and ACN, and suitable single crystal was isolated for SC-XRD analysis. Calculated yield: 85%. ^{1}H NMR [600 MHz, DMSO-d_6, δ (ppm)]: δ 10.67 (s, 1H), 8.64 (d, J = 8.1 Hz, 1H), 8.30 (d, J = 6.9 Hz, 1H), 7.86 (d, J = 8.0 Hz, 1H), 7.80 (s, 2H), 7.77 (s, 1H), 7.58 (t, J = 7.0 Hz, 1H), 7.49 (t, J = 7.6 Hz, 1H), 7.45 (d, J = 8.2 Hz, 1H), 7.41 (t, J = 7.2 Hz, 1H), 7.31 (t, J = 7.5 Hz, 1H). ^{13}C NMR [151 MHz, DMSO-d_6, δ (ppm)]: 149.93, 147.08, 144.39, 140.68, 137.53, 132.63 (×2C, Ar-C), 132.01, 131.80, 131.54, 125.29, 124.94, 124.76, 123.83 (×2C, -/CF3), 123.33, 123.14, 119.37, 117.03, 116.29, 116.07, 112.10. ESI-MS (positive mode, m/z) calculated for $C_{22}H_{12}F_6N_4$: 446.0966, found: 447.1042 [M + H^+]. (Scheme 2.3, Figure A2.41-A2.44)

Benz-m-CF_3: Benz-m-CF3 was synthesized with similar procedure as to that of Benz-d-CF3, where, 2-(1H-Benzimidazol-2-yl)aniline (200 mg, 0.955 mmol, 1 equiv.) was placed in a 50 mL round-bottomed flask and dissolved in acetonitrile (ACN) (10 mL). A solution of 3-(Trifluoromethyl)phenyl Isothioyanate (194.2 mg, 0.955 mmol, 1 equiv.) was added into the flask in dropwise manner. The reaction was refluxed at 80˚C for 48 hours. The precipitates were separated by filtration and washed with ACN (30 mL) and diethyl ether (30 mL). The obtained white powder product was further vacuum dried and isolated as compound Benz-d-CF_3. It was further crystallized in 1:1 solvent mixture of DMSO and ACN, and suitable single crystal was isolated for SC-XRD analysis. Calculated yield: 80%. ^{1}H NMR [600 MHz, DMSO-d_6, δ (ppm)]: δ 10.48 (s, 1H), 8.65 (d, J = 8.1 Hz, 1H), 8.28 (d, J = 7.7 Hz, 1H), 7.86 (d, J = 7.9 Hz, 1H), 7.64 (t, J = 7.6 Hz, 1H), 7.55 (t, 1H), 7.50 (d, J = 8.6 Hz, 1H), 7.47 (t, J = 7.0 Hz, 2H), 7.42 (m, J = 15.2, 7.5 Hz, 3H), 7.27 (t, J = 7.4 Hz, 1H). ^{13}C NMR [151 MHz, DMSO-d_6, δ (ppm)]: 148.26, 147.11, 144.39, 139.76, 137.72, 132.53 (×2C, Ar-C), 131.62, 131.04, 126.86, 125.83, 125.17,

124.73, 123.77, 123.06, 119.75, 119.55, 119.34, 117.00, 116.33, 111.94. ESI-MS (positive mode, m/z) calculated for $C_{21}H_{13}F_3N_4$: 378.1092, found: 379.1154 [M + H^+]. (Scheme 2.3, Figure A2.45-A2.48)

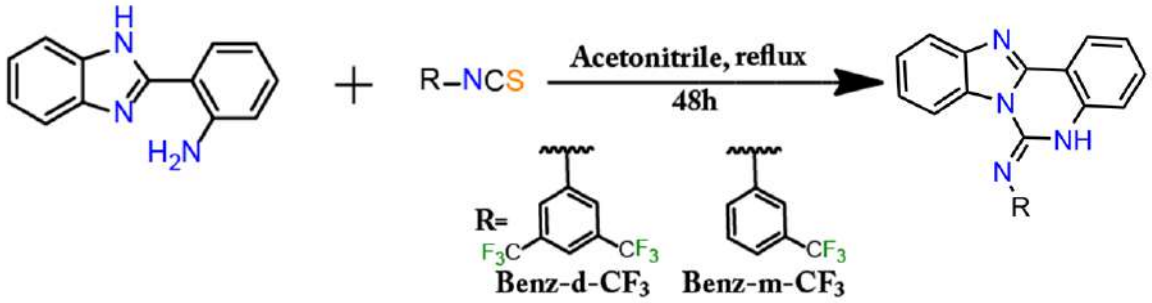

Scheme 2.3: Synthetic scheme of Benz-d-CF_3, and Benz-m-CF_3.

2.2.6. Synthesis and Characterization of PY-NAP [*N^2,N^6-bis(3-(3-(naphthalen-1-yl)ureido)phenyl)pyridine-2,6-dicarboxamide*], PY-CF_3 [*N^2,N^6-bis(3-(3-(3,5-bis(trifluoromethyl)phenyl)ureido)phenyl)pyridine-2,6-dicarboxamide*] , PY-NO_2 [*N^2,N^6-bis(3-nitrophenyl)pyridine-2,6-dicarboxamide*], and PY-NH_2 [*N^2,N^6-bis(3-aminophenyl)pyridine-2,6-dicarboxamide*]

PY-NAP: PY-NH_2 (100 mg, 0.287 mmol, 1 equiv.) was placed in a 25 mL round-bottomed flask and dissolved in acetonitrile (ACN) (10 mL). A solution of 1-Naphthyl isocyanate (97.4 mg, 0.575 mmol, 2 equiv.) was added into the flask in dropwise manner. The reaction was refluxed at 80˚C for 24 hours. The gelatinous precipitates were collected through filtration and washed with ACN for several times. The obtained white powder product was further vacuum dried and isolated as compound PY-NAP. It was further crystallized in DMSO solvent, and suitable single crystal was grown within 25 days and was analysed through SC-XRD. Calculated yield: 83%. ^{1}H NMR [600 MHz, DMSO-*d_6*, δ(ppm)]: 11.07 (s, 2H), 9.25 (s, 2H), 8.79 (s, 2H), 8.44 (d, J = 7.7 Hz, 2H), 8.35 – 8.32 (t, 1H), 8.18 (s, 2H), 8.15 (d, J = 8.4 Hz, 2H), 8.07 (d, J = 7.3 Hz, 2H), 7.94 (d, J = 8.0 Hz, 2H), 7.64 (d, J = 8.2 Hz, 2H), 7.60 (t, J = 7.1 Hz, 2H), 7.56 (t, J = 7.1 Hz, 2H), 7.49 (m, J = 7.8, 4.3 Hz, 4H), 7.46 (d, J = 8.5 Hz, 2H), 7.38 (t, J = 8.0 Hz, 2H). ^{13}C NMR [151 MHz, DMSO-*d_6*, δ(ppm)]: 162.27(×2C), 153.32(×2C), 149.44(×2C), 140.69(×2C), 140.45(×1C), 139.01(×2C), 134.74(×2C), 134.19(×2C), 129.63(×2C), 128.95(×2C), 126.40(×2C), 126.38(×2C), 126.26(×2C), 126.22(×2C), 125.90(×2C), 123.38(×2C), 121.71(×2C), 117.63(×2C), 115.47(×2C), 114.69(×2C), 111.33(×2C). ESI-MS (positive mode, m/z) calculated for: 685.2438, found: 686.2540 [M + H^+]. FTIR: 3276 cm^{-1} ($NH_{urea/amide}$), 1690 cm^{-1} (urea C=O), 1630 cm^{-1} (amide C=O). (Scheme 2.4, Figure A2.49-A2.52)

PY-CF_3: PY-NH_2 (100 mg, 0.287 mmol, 1 equiv.) was placed in a 25 mL round-bottomed flask, and dissolved in acetonitrile (ACN) (10 mL). A solution of 1-Naphthyl isocyanate (146.88 mg, 0.575 mmol, 2 equiv.) was added into the flask in dropwise manner. The reaction was refluxed at 80˚C for 24 hours. The precipitates were collected through filtration, and washed with ACN for several times. The obtained white powder product was further vacuum dried, and isolated as compound PY-CF_3. It was further crystallized in DMSO solvent, and suitable single crystal was grown within 3-4 days and was analysed through SC-XRD. Calculated yield: 80%. ^{1}H NMR [600 MHz, DMSO-d_6, δ (ppm)]: 11.09 (s, 2H), 9.37 (s, 2H), 9.17 (s, 2H), 8.43 (d, J = 7.7 Hz, 2H), 8.33 (t, J = 7.7 Hz, 1H), 8.22 (s, 2H), 8.15 (s, 4H), 7.63 (s, 2H), 7.58 (d, J = 7.9 Hz, 2H), 7.37 (t, J = 7.9 Hz, 2H), 7.32 (d, J = 8.0 Hz, 2H). ^{13}C NMR [151 MHz, DMSO-d_6, δ(ppm)]: 162.27(×2C), 152.85(×2C), 149.40(×2C), 142.27(×2C), 140.45(×1C), 139.93(×2C), 138.99(×2C), 131.26(×2C), 131.05(×2C), 130.83(×2C), 129.49(×2C), 125.90(×2C), 124.68(×2C), 122.88(×2C), 118.40(×2C), 116.00(×2C), 115.42(×2C), 114.85(×2C), 112.08(×2C). ESI-MS (positive mode, m/z) calculated for: 857.1620, found: 858.1699 [M + H^+]. FTIR: 3300 cm^{-1} ($NH_{urea/amide}$), 1690 cm^{-1} (urea C=O), 1640 cm^{-1} (amide C=O), 1125 cm^{-1} (C-F). (Scheme 2.4, Figure A2.53-A2.56)

Synthesis of PY-NO_2: PY-NO_2 was synthesized using a previously reported procedure. [2.1] Pyridine-2,6-dicarboxylic acid chloride (2.45 mmol) was added in portions to a solution of nitroamine or to the respective nitroaminophenol (4.90 mmol) and triethylamine (5 mmol) in DMF (25 mL). The mixture was heated for 12 h at 60 °C. The cooled reaction mixture was diluted with water. The resulting solid was filtered off and washed properly with water several times, which gives a white-colored solid product on drying. The obtained product was used for synthesis without further purification. (Scheme 2.4)

Synthesis of PY-NH_2: To a suspension of PY-NO_2 (1 g) in ethanol (50 mL) was added Pd/C (10%, w/w, 0.05 g), followed by the dropwise addition of hydrazine monohydrate (5 mL). The reaction mixture was refluxed and stirred magnetically at 74 °C for 12 h. After the substrate was consumed entirely, the catalyst was removed by filtration through a Whatman filter paper, and the solvent was kept for slow evaporation, which resulted in a crystalline precipitate. The precipitate was collected and washed several times with water until the smell of hydrazine monohydrate went away to get a fluffy crystalline product. The remaining residue in the Whatman filter paper was washed with DMF, and the filtrate was collected in an ice-cold water, which resulted in a white precipitate. The precipitate was washed several times with water and dried to get a white powdery product. Calculated yield: 65%. ^{1}H NMR [600 MHz, DMSO-d_6,

δ(ppm)]: 10.82 (s, 2H), 8.37 (d, *J* = 7.5 Hz, 2H), 8.29–8.26 (m, 1H), 7.21 (t, *J* = 2.0 Hz, 2H), 7.06 (t, *J* = 7.9 Hz, 2H), 6.99 (d, *J* = 8.8 Hz, 2H), 6.40 (d, *J* = 7.9 Hz, 2H), 5.21 (s, 4H). ^{13}C NMR [151 MHz, DMSO-d_6, δ(ppm)]: 161.92(×2C), 149.64(×2C), 149.56(×2C), 140.27(×1C), 139.08(×2C), 129.42(×2C), 125.57(×2C), 110.91(×2C), 109.62(×2C), 107.31(×2C). (Scheme 2.4, Figure A2.57-A2.58)

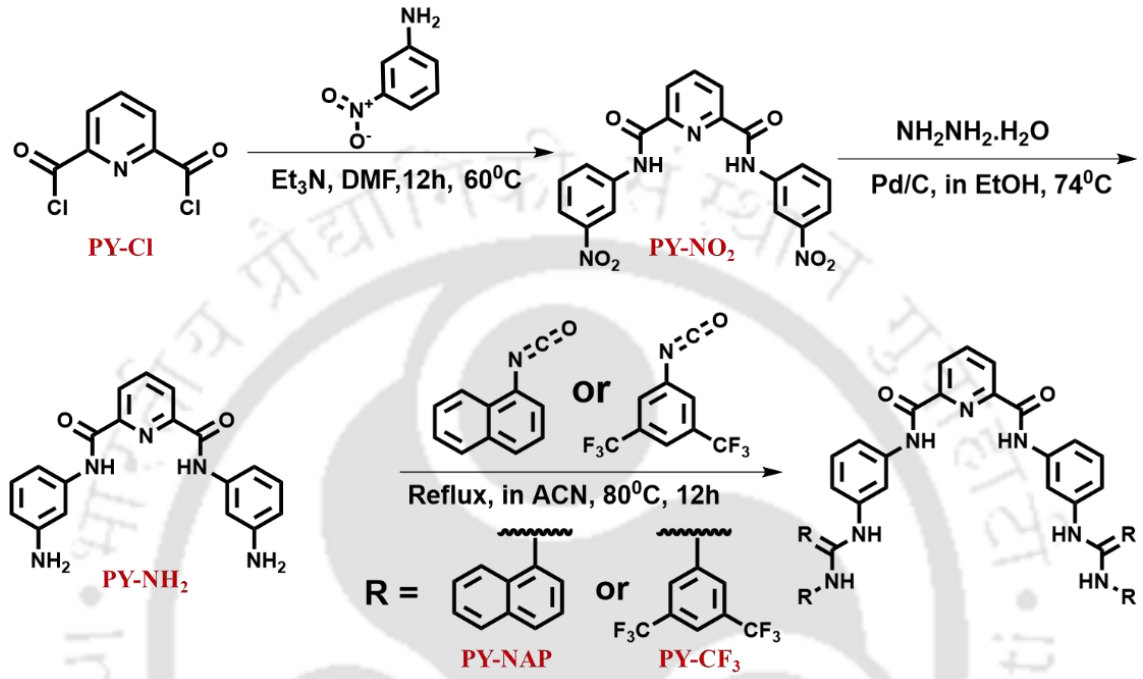

Scheme 2.4: Synthetic scheme of PY-NAP, and PY-CF_3.

2.2.7. Synthesis and Characterization of THD [*N′¹,N′³,N′⁵-tris((E)-(2-(dodecyloxy)naphthalen-1-yl)methylene)benzene-1,3,5-tricarbohydrazide*], and THX [*N′¹,N′³,N′⁵-tris((E)-(2-(hexyloxy)naphthalen-1-yl)methylene)benzene-1,3,5-tricarbohydrazide*]

THD: TAH (50mg, 0.198mmol, 1equiv.) was placed in a 250 mL round bottom flask and dispersed in 10ml of ethanol followed by the addition of NAP-D (202.5mg, 0.594mmol, 3equiv.) into it. Then 100µL of AcOH (acetic acid) was added into the above reaction mixture and refluxed it for 24h. The light-yellow colour precipitate was collected through filtration and washed with ethanol several times. The obtained yellow powder product was further vacuum dried and isolated as compound THD. Calculated yield: 75-80%. 1H NMR [600 MHz, DMSO-d6, δ(ppm)]: 12.28 (s, 1H), 9.45 (d, J = 8.7 Hz, 1H), 9.24 (s, 1H), 8.77 (s, 1H), 8.04 (d, J = 8.9 Hz, 1H), 7.92 (d, J = 7.7 Hz, 1H), 7.66 – 7.57 (m, 1H), 7.51 (d, J = 9.2 Hz, 1H), 7.47 – 7.40 (m, 1H), 4.24 (t, J = 6.3 Hz, 2H), 1.85 – 1.76 (m, 2H), 1.47 (dt, J = 14.3, 9.0 Hz, 2H), 1.31 (dt, J = 13.6, 5.7 Hz, 2H), 1.25 – 1.10 (m, 14H), 0.77 (t, J = 7.0 Hz, 3H). 13C NMR [151 MHz, DMSO-d6, δ(ppm)]: 162.67, 157.94, 146.73, 134.78, 133.31, 131.36, 130.40, 129.28, 128.94, 128.49,

126.41, 124.54, 115.11, 115.01, 69.75, 31.71, 29.47, 29.44, 29.39, 29.34, 29.24, 29.20, 29.14, 25.90, 22.51, 14.35. ESI-MS (positive mode, m/z) calculated for 1218.7861, found: 1219.7847 [M + H^+]. FTIR: -NH (3197 cm^{-1}), C-H (2924 cm^{-1}, asymmetric), C-H (2855 cm^{-1}, symmetric), -C=O (1676 cm^{-1}). (Scheme 2.5, Figure A2.59-A2.62)

THX: TAH (50mg, 0.198mmol, 1equiv.) was placed in a 250mL round bottom flask and dispersed in 10ml of ethanol followed by the addition of NAP-H (180mg, 0.702mmol, 3.5equiv.) into it. Then 100µL of AcOH (acetic acid) was added into the above reaction mixture and refluxed it for 24h. The yellow colour precipitate was collected through filtration and washed with ethanol several times. The obtained yellow powder product was further vacuum dried and isolated as compound THD. Calculated yield: 75-80%. ^{1}H NMR [600 MHz, DMSO-d_6, δ(ppm)]: 12.29 (s, 1H), 9.46 (d, J = 8.7 Hz, 1H), 9.23 (s, 1H), 8.75 (s, 1H), 8.05 (d, J = 9.0 Hz, 1H), 7.93 (d, J = 7.6 Hz, 1H), 7.65 – 7.59 (m, 1H), 7.52 (d, J = 9.2 Hz, 1H), 7.48 – 7.43 (m, 1H), 4.25 (t, J = 6.4 Hz, 2H), 1.82 (dt, J = 13.6, 6.5 Hz, 2H), 1.48 (p, J = 7.4 Hz, 2H), 1.34 – 1.27 (m, 4H), 0.83 (t, J = 6.8 Hz, 3H). ^{13}C NMR [151 MHz, DMSO-d_6, δ(ppm)]: 162.75, 157.97, 146.72, 134.84, 133.34, 131.34, 130.41, 129.27, 128.96, 128.55, 126.38, 124.57, 115.06 (×2C), 69.79, 31.44, 29.37, 25.54, 22.52, 14.31. ESI-MS (positive mode, *m/z*) calculated for 966.5044, found: 967.5120 [M + H^+]. FTIR: -NH (3198 cm^{-1}), C-H (2929 cm^{-1}, asymmetric), C-H (2865 cm^{-1}, symmetric), -C=O (1653 cm^{-1}). (Scheme 2.5, Figure A2.63-A2.66)

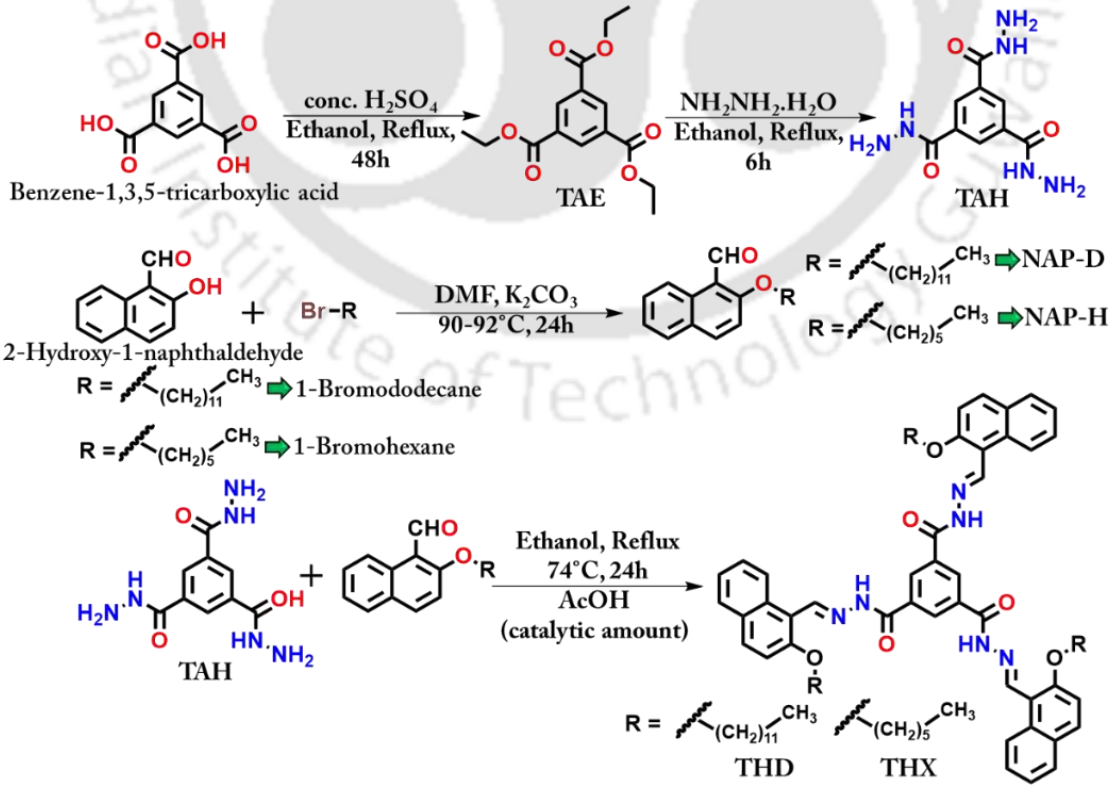

Scheme 2.5: Synthetic scheme of THD, and THX.

2.2.8. Synthesis and Characterization of Py-M [*tetramethyl 5,5'-((pyridine-2,6-dicarbonyl)bis(azanediyl))diisophthalate*], and Py-H [*N^2,N^6-bis(3,5-di(hydrazinecarbonyl)phenyl)pyridine-2,6-dicarboxamide*]

Py-M: Dimethyl 5-aminoisophthalate (DAI) (205 mg, 0.98 mmol, 2 equiv.) was placed in a 50 mL round-bottomed flask and dissolved in acetonitrile (ACN) (20 mL). Then an excess amount of triethylamine (400 µL) was added to the mentioned solution and stirred for a few minutes. 2,6-Pyridinedicarbonyl dichloride (PDC) (100 mg, 0.490 mmol, 1 equiv.) was carefully added into the flask, and the reaction mixture was refluxed at 80℃ for 12 hours. The precipitates were separated by filtration and washed with ACN (30 mL). The obtained white fluffy product was further vacuum-dried and isolated as compound Py-M. Calculated yield: 75-80%. ^{1}H NMR (600 MHz, DMSO-d_6) δ(ppm): 11.38 (s, 2H), 8.89 (s, 4H), 8.44 (d, J = 7.7 Hz, 2H), 8.35 (t, J = 7.6 Hz, 1H), 8.30 (s, 2H), 3.95 (s, 12H). (Figure S1) ^{13}C NMR (151 MHz, DMSO-d_6) δ(ppm): 165.76 (× 4C), 162.64 (× 2C), 148.81 (× 2C), 140.67 (× 1C), 139.69 (× 2C), 131.25 (× 4C), 126.30 (× 2C), 125.67 (× 4C), 125.49 (× 2C), 53.11 (× 4C). (Figure S2) FTIR-ATR: ν = 3545 cm^{-1} (-N-H), 3256 cm^{-1} (-N-H), 3123 cm^{-1} (Aromatic-C-H), 2962 cm^{-1} (aliphatic-C-H), 1723 cm^{-1} (-C=O). (Figure S3) ESI-MS (positive mode, m/z) calculated for $C_{27}H_{23}N_3O_{10}$: 549.1383, found: 550.1429 [M + H$^+$]. (Scheme 2.6, Figure A2.67-A2.70)

Py-H: Py-M (50 mg, 0.090 mmol) was placed in a 50 mL round-bottomed flask and dispersed in Dimethylformamide (DMF) (20 mL). Then excess amount of hydrazine hydrate (5 mL) was added to the mentioned solution and refluxed at 60℃ for 12 hours. The precipitates were separated by filtration and washed with DMF (50 mL) followed by distilled water (30 mL). The obtained white powder product was further vacuum dried and isolated as compound Py-H Calculated yield: 75-80%. ^{1}H NMR (400 MHz, DMSO-d_6) δ(ppm): 11.29 (s, 2H), 9.78 (s, 4H), 8.50 (s, 4H), 8.46 (d, J = 7.8 Hz, 2H), 8.38 – 8.32 (m, 1H), 8.04 (s, 2H), 4.59 (s, 8H). (Figure S5) ^{13}C NMR (151 MHz, DMSO-d_6) δ(ppm): 165.91 (× 4C), 162.52 (× 2C), 149.11 (× 2C), 140.65 (× 1C), 138.86 (× 2C), 134.77 (× 4C), 126.23 (× 2C), 123.06 (× 4C), 121.55 (× 2C). (Figure S6) FTIR-ATR: ν = 3217 cm^{-1} (-NH_2), 3032 cm^{-1} (-N-H), 1676 cm^{-1} (-C=O). (Figure S7) ESI-MS (positive mode, m/z) calculated for $C_{27}H_{23}N_3O_{10}$: 549.1833, found: 550.1864 [M + H$^+$]. (Scheme 2.6, Figure A2.71-A2.74)

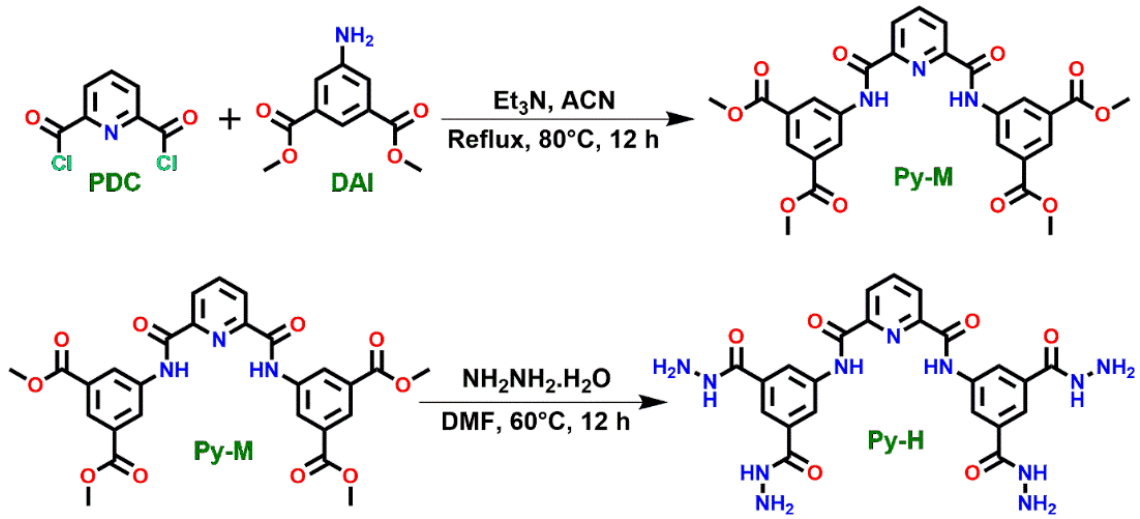

Scheme 2.5: Synthetic scheme of Py-M, and Py-H.

2.3. Crystallographic Refinement Details

Single crystals of proper size were chosen for all the crystals and, were dipped into silicon oil prior to mounting into a glass fibre tube. Supernova (a single source at an offset) Eos diffractometer with Mo Kα radiation (λ = 0.71073 Å) source, connected with a CCD region detector was used to collect the X-ray intensity data and with the help of APEX 4 all the data refinement and cell reduction were done. [2.2] Using a narrow-frame algorithm and XPREP, [2.3] the frames were combined with the Bruker SAINT software kit, and data were corrected for absorption effects using the multi-scan process (SADABS). [2.4] Using direct methods in XT, version 2014/15, all of the structures were solved and after that, refinement was done using the full-matrix least-squares technique in the SHELXL-2016 and 2018 software packages on F^2. [2.5] The positions of the hydrogen atoms were fixed. MERCURY 4.2.0 for Windows was used for the sack of creating structural drawings. [2.6] The hydrogen atoms were found on a separate Fourier map and refined where it was most advantageous. For all non-hydrogen atoms Anisotropic refinement was employed. All the details of the refinement parameters of crystallographic data collection, and the detailed data on hydrogen bonding distances and bond angles are furnished in the annextures of the respective chapters. Moreover, all the alerts wherever applicable have been explained in the annextures of the respective chapters. All the crystallographic data have been submitted to CCDC. The CCDC number assigned to the receptor anion complexes, $[(n\text{-}TBA)_2\{(L_1)(OCOCH_3)_2\}]$ (L_1A), [BPU-1 (n-TBA) Cl] (1a), [BPU-1 (n-TBA) Br] (1b), [BPU-1 (n-TBA) I] (1c), [{BPU-1(n-TBA) (NO_3)] (1d), $[(BPU\text{-}1\text{-}H)^+(n\text{-}TBA)^+(H_2O)_4(SO_4)^{2-}]$ (1e), [BPU-2 (n-TBA) Cl] (2a), [BPU-2 (n-TBA) Br] (2b), and PY-NAP.Sulfate are 2214037, 2249703, 2267434, 2267435, 2249708, 2249710, 2249713, 2267436, and 2376908 respectively. Moreover, the CCDC numbers assigned to the crystal structure of the

molecules L_1, L_2.DMSO, L_3, BPU-1.DMF, BPU-2, Benz-d-CF_3.DMSO, Benz-d-CF_3.H_2O, Benz-m-CF_3, [Benz-m-CF_3].[Benz-m-CF_3]$^-$.TBA^+, PY-NAP.DMSO, PY-CF_3.DMSO, and Py-M. DMSO are 2214012, 2241252, 2241257, 2249705, 2249712, 2331451, 2331449, 2331458, 2331466, 2376906, 2376907, and 2506038 respectively.

2.4. Quantitative Anion Binding Study

^{1}H-NMR titration experiment was conducted for receptor L_1-L_3 (50 mM each) with the incremental addition of TBA(OAc) (500 mM) in DMSO-*d*6 solvent. The plot of chemical shift (δ) of NH_a and NH_b protons *vs.* Equivalent total ($[G]_0/[H]_0$) added, fitted to 1:1 binding model of BindFit v0.5 program [here 'H' represents Host and 'G' represents Guest (TBA(OAc))], and subsequently the binding constant values were evaluated. Similarly, ^{1}H NMR titration experiment was conducted for all the complexes 1a, 1b, 1c, 1d, 1e, 2a, and 2b. For the complexes 1a, 1b, 1d, 2a and 2b, the peaks corresponding to NH_a, NH_b, and NH_c were observed to be downfield shifted, although the chemical shift values were not very high, with an average downfield shift value of Δδ = 0.31 ppm ($\Delta\delta NH_a$ = 0.26 ppm, $\Delta\delta NH_b$ = 0.12 ppm, and $\Delta\delta NH_c$ = 0.57 ppm), Δδ = 0.17 ppm ($\Delta\delta NH_a$ = 0.14 ppm, $\Delta\delta NH_b$ = 0.11 ppm, and ΔδNHc = 0.27 ppm), Δδ = 0.10 ppm ($\Delta\delta NH_a$ = 0.12 ppm, $\Delta\delta NH_b$ = 0.10 ppm, and $\Delta\delta NH_c$ = 0.09 ppm), Δδ = 0.39 ppm ($\Delta\delta NH_a$ = 0.45 ppm, $\Delta\delta NH_b$ = 0.13 ppm, and $\Delta\delta NH_c$ = 0.58 ppm) and Δδ = 0.20 ppm ($\Delta\delta NH_a$ = 0.22 ppm, $\Delta\delta NH_b$ = 0.12 ppm, and $\Delta\delta NH_c$ = 0.27 ppm) respectively. The NMR titration data for all the aforementioned complexes were best fit into 1:1 stoichiometry giving binding constant values (Ka)s of 7.04 M^{-1}, 0.92 M^{-1}, 0.53 M^{-1}, 7.31 M^{-1} and 1.32 M^{-1} respectively for the complexes 1a, 1b, 1d, 2a and 2b (obtained by using BindFit v0.5). However, the non-shifting of the NH_a, NH_b, and NH_c peaks in complex 1c did not allow us to find the binding constant value for the same. A quite fascinating peak shifting of NH_a, NH_b, and NH_c was observed in the case of complex 1e. All three peaks were observed to be associated with a unique peak shifting, where, the incremental addition of $(TBA)_2SO_4$ solution results in severe broadening, and ultimately, the disappearance of the NH_c peak which might be due to hydrogen bond- induced rapid dynamic effect or deprotonation; whereas the peak corresponding to Nha undergoes downfield shifting with a chemical shift value of $\Delta\delta NH_a$ = 1.58 ppm indicating strong hydrogen bonding interaction involving the same. Interestingly, the peak corresponding to NH_b undergoes upfield shifting with severe peak broadening ultimately leading to peak vanishing; at some point in time both the peaks corresponding to NH_a and NH_c were observed to converge and then diverge from each other. The upfield shifting with concomitant broadening and vanishing of NH_b peak can be attributed to the deprotonation of NH_b proton caused by the progressive addition of SO_4^{2-} anion, which resulted in the accumulation ofnegative charges thus leading to

upfield shifting of NH_b proton. However, due to severe peak broadening of the peaks especially the peak corresponding to the NH_c proton, we could not determine the binding constant value for 1e through NMR titration.

2.5. Hirshfeld Surface (HS) Analysis

HS analysis was performed using CrystalExplorer software. The crystallographic information files (CIFs) were used in the CrystalExplorer software to generate 3D Hirshfeld surface, which could be broken down into two-dimensional fingerprint plots (2D FPs), that helped in understanding the role played by all the non-covalent interactions inside a crystalline molecule through "contact contribution". [2.7, 2.8]

2.6. UV-Vis and Fluorescence Spectroscopic Studies in Solution

Stock solutions of all the anions (using n-Tetrabutylammonium salts of the corresponding anions) and antibiotics (each 50×10^{-3} mol L^{-1}) were prepared in DMSO. Stock solutions of L_1-L_3, BPU-1, BPU-2, Benz-d-CF_3, Benz-m-CF_3, PY-NAP, THD, and THX (each 5×10^{-3} mol L^{-1}) were prepared in DMSO and then diluted to 10×10^{-6} mol L^{-1} for various spectral studies by placing only 4.0 µL of stock solution into an aqueous medium to a final volume of 2.0 mL. In the fluorescence/UV-Vis sensing experiment, the test samples were prepared by placing the appropriate amounts of the stock solutions of the respective analytes into 2.0 mL of probe solution (containing 10×10^{-6} $molL^{-1}$ of probe and 0.2% DMSO). For fluorescence titration experiments of L_3, BPU-1, Benz-d-CF_3, Benz-m-CF_3, 5×10^{-3} $molL^{-1}$, stock solution of different analytes was prepared in DMSO, then it was gradually added into a 2.0 mL of probe solution (containing 10×10^{-6} $molL^{-1}$ of probe and 0.2% DMSO) using a micropipette in a quartz optical cell with 1.0 cm path lengths. Competitive/selectivity experiments were conducted through fluorescence spectroscopy, by recording fluorescence spectra of the probe-analyte ensemble in presence and absence of competitive analytes (10 equiv.). For the UV-vis and fluorescence spectroscopic study of THD in kerosene and diesel oil, from the 5 mM stock solution of THD (prepared in DMSO), 4µL was added to 2 mL of diesel and kerosene oil taken in a cuvette, and after proper mixing, the spectra were recorded.

2.7. Estimation of Apparent Binding Constant

Benesi-Hildebrand plot (concentration Vs $(I_{max}-I_{min})/(I-I_{min})$) was employed for the determination of binding constant of BPU-1 with SO_4^{2-}/HSO_4^-.

2.8. Detection Limit (LOD) Determination

The detection limits for BPU-1, Benz-d-CF_3 and Benz-m-CF_3, with different analytes were calculated on the basis of the fluorescence titration experiments. The fluorescence emission spectrum of all the probes was measured 10 times, and the standard deviation of blank measurement was also attained from that experiment. To gain the slope, the fluorescence emission intensity plot was plotted as a concentration of the respective analytes. The detection limit was calculated using the following equation:

$$\text{Detection limit} = 3\sigma/k \quad \cdots\cdots\cdots\cdots\cdots\cdots\cdots\cdots\cdots\cdots\cdots\cdots \quad (1)$$

Where σ is the standard deviation of blank measurement, and k is the slope achieved from the plot of fluorescence emission intensity vs [analyte].

2.9. Field Emission Scanning Electron Microscope (FESEM) Study

Microscopic morphological studies were conducted by using instruments like Gemini 300-FESEM (Zeiss) and Sigma 300-FESEM (Zeiss). For the experiment, stock solution of L_1, L_2, L_3, Benz-d-CF_3, and Benz-m-CF_3, as well as all of those three ligands with the studied analytes (wherever applicable) were separately drop casted on Al-foil covered cover slip. The drop casted sample was dried, followed by gold coating prior to analysis. However, for the xerogel samples, derived from the gels formed by PY-NAP, the dried gel samples were placed on the surface of a carbon tape followed by gold coating prior to analysis. For the aggregation study of THD and THX in THF-H_2O binary solvent system, firstly, from a 5 mM stock solution of THD and THX (prepared in DMSO), 10 μL solution was added to different vials containing different percentages of water (here we have strategically taken 0% H_2O, 30% H_2O, 70% H_2O, and 100% H_2O) and mixed properly at room temperature by using a vortex. Then, drop-casting was performed by placing 20 μL of each mentioned solutions on the surface of an aluminium foil wrapped in a small glass plate separately. Subsequently, the drop-casted samples were properly kept inside a vacuum desiccator at room temperature for 48 h, followed by heating at 50°C for 12 h for drying purposes. The xerogels of both D-THD-G and K-THD-G were prepared by drying a very small portion of the respective gels in a vacuum desiccator for two weeks, followed by heating at 80°C for 12 h, and the resulting dried xerogel samples were then taken for the analysis. For xerogel derived from Py-M-G, a small amount of gel sample was smeared on a small glass surface and kept for vacuum drying inside a desiccator for 24 h at room temperature. After 24 h, the sample was subjected to heating at 80°C for 12 h. For the crystal morphology, the smeared gel was subjected to heating at 100°C immediately, without prior vacuum drying.

2.10. Dynamic Light Scattering (DLS) Studies

The particle size of the nano-aggregates of both the probes namely, Benz-d-CF_3 and Benz-m-CF_3 were measured by dynamic light scattering (DLS) experiments on a Malvern Zetasizer Nano ZS instrument equipped with a 4.0 mW He-Ne laser operating at a wavelength of 633 nm. All the measurements were done at room temperature (25°C). The DLS measurements were carried out with optically clear solutions of Benz-d-CF_3 and Benz-m-CF_3 (10 μM) in aqueous CTAB (3 mM) solution. Before taking the measurements, the solutions were equilibrated for 30 minutes. The change in particle size upon interaction with 10 equivalents of CN^- was determined through DLS measurement, carried out with an optically clear solution in aqueous CTAB (3 mM). Before taking the measurements, the solutions were equilibrated for 30 minutes.

2.11. Theoretical Investigation (DFT Study)

Calculated the electrostatic potential map using DFT, B3LYP/6-31+G(d) method basis set for both the receptors BPU-1, and BPU-2 to identify the most probable anion binding sites (using water as a solvent in the CPCM model). The structures of Benz-d-CF_3, [Benz-d-CF_3]$^-$, Benz-m-CF_3, and [Benz-m-CF_3]$^-$ were energy optimised in water using the B3LYP/6-31 G level of theory employing CPCM model.

2.12. Preparation of RT-Gel, and H-Gel

10 mg of PY-NAP was placed in a glass vial, and was dissolved in DMSO (600 μL) followed by rapid addition of water (400 μL), and the resulting white turbid solution was kept at room temperature for 5 min (referred to as RT-Gel in this article)., which resulted into a white coloured gel as confirmed by inverting the glass vial. Heating the RT-Gel at 100°C for 20 min. resulted in a mechanically more rigid gel, which has been termed as H-Gel. Additionally, both PY-CF_3, and PY-NH_2 were also studied for gelation in similar conditions, which yielded no gelation property as depicted below.

2.13. Field Emission Transmission Electron Microscope (TEM) Analysis

FETEM (JEOL, Model :2100F) instrument was used for FETEM study. Spherical micelle formation of 3 mM aqueous CTAB solution was visualised via TEM, which was carried out by drop casting it on carbon-coated copper grids (400 meshes) and drying them in vacuum. AgNPs formation was visualised via FETEM, where stock solution of AgNPs-RT-Gel composite, prepared in MeOH (with the help of a small portion of DMSO) was drop casted on carbon-coated copper grids (400 meshes) and dried them in vacuum.

2.14. Preparation of Hybrid Gel

The hybrid gel was prepared by mixing PY-NAP with agarose powder. To do this both PY-NAP, and agarose (20 mg each) were dissolved in DMSO (1200 µL) followed by rapid addition of water (800 µL), and the resulting white turbid solution was heated at 100°C for 1 min. which eventual turns into a white coloured gel as confirmed by inverting the glass vial.

2.15. Uptake of Ag^+ onto PY-NAP-G/ Hybrid Gel and In Situ Formation of Nanoparticles

An aqueous solution of $AgNO_3$ (290 mM, 1500 µL) was added on top of both RT-Gel, and H-Gel (prepared by rapid addition of water, 800 µl into a 20 mg/2 mL PY-NAP solution in DMSO), and allowed to diffuse into the gel network for 144 h. The supernatants were collected in certain time intervals such as 36 h, 72 h, 108 h, and 144 h, and analysed the same through Atomic Absorption Spectroscopy (AAS) to monitor the metal ion uptake. The same experiment was repeated for the hybrid gel block as well, where the hybrid gel block was suspended inside an aqueous solution of $AgNO_3$ (290 mM, 5 mL) and kept it for 144 h, and the supernatant collected after 144 h was analysed through AAS.

The Ag^+ ion loading after 144 h in different gels were quantified by using the following equation [2.9]:

$$L_{144h} = \frac{([C]_i - [C]_f)V}{W_g}$$

Where, L_{144h} is the amount of Ag^+ ion loaded into the gel network of RT-Gel/H-Gel (in mg/g), $[C]_i$ and $[C]_f$ are the initial and the final concentration of Ag^+ ion in aqueous solution (in mg/L) respectively, V is the volume of Ag^+ ion in aqueous solution (in L), and W_g is the weight of the gelator used (in g).

The AgNPs formation can be visualised by the colour change of the gel network from white colour to yellow (in RT-Gel), and dark brown (in H -Gel) with time as the Ag^+ ion uptake proceeds, which are characteristics of the reduction of metals into metal NPs which are capped inside the gel fibers. It was further conformed via UV-vis spectroscopic measurement where characteristic surface plasmon resonance (SPR) band of formed AgNPs was observed at ~ 460 nm (in DMSO solvent medium), which is a characteristic of the existence of spherical silver nanoparticles.

2.16. Measurement of the Conductance of the AgNPs-Hybrid-Gel

Conductivity measurement of AgNPs-Hybrid-Gel, was performed using 2450 Source Meter, and compared it with the conductivities of the agarose gel, and the hybrid gel. The gels were

prepared in a cylindrical mould with length (l) = 0.7 cm, and diameter (d) = 1.3 cm. The cylindrical gels were placed in between two uniformly cut copper meshes, and connected to the 2450 Source Meter through copper wires at both the ends as shown in Figure S28b. From the current (I) Vs Voltage (V) plot obtained from this, conductance was calculated, and conductivity was calculated by multiplying conductance with the cell constant value.

2.17. Details of Rheology Experiment

A Thermo Scientific Rheometer (HAAKE MARS iQ Air) equipped with a 35 mm parallel plate arrangement was employed to perform rheology experiments of all the gel samples. Linear viscoelastic regions of the gel samples were determined by measuring the storage modulus (G′), and the loss modulus (G″) as a function of the stress amplitude. The transitions of gel to sol for both the mentioned gels were monitored over different shear strains with a fixed frequency at 1 Hz. For the gel samples, RT-Gel, and H-Gel, As the storage modulus (G′) starts to decrease after a 1% shear strain, so shear strain of 0.1% was decided to measure the frequency-dependent rheological behaviors of the gels. The storage moduli (G′) and loss moduli (G″) were monitored as functions of frequency sweep for both gels at room temperature, and it was observed that G′ values were always above G″ over the entire range of frequencies tested, thus inferring the true gel nature of RT-Gel and H-Gel. In the case of D-THD-G and K-THD-G derived from THD in diesel and kerosene, respectively, G′ started decreasing after 1 % sheer strain, so a sheer strain of 0.15 % was decided to measure the frequency-dependent rheology experiments of the gel samples. Subsequently, G′ values were observed to be always above G″ over the entire range of frequencies tested, thus inferring their true gel nature. Rheological study was performed for the quantification of the thixotropic behaviour of both D-THD-G and K-THD-G by applying and releasing a certain % strain cyclically. At first, both the gels were placed at a constant strain of 0.15 %, where G′ is higher than G″, inferring the presence of gel form. Subsequently, when the % strain is increased to 50 % and held for 25 s. resulted in a complete reversal of the G′ and G″, where the latter was higher than that of the former, indicating complete transformation of the gel to sol form. Upon releasing the % strain to 0.15 % and holding on for 50 s. resulted in higher G′ than G″ inferring restoration of the gel form. The said experiment was continued up to two cycles, and in each cycle, the restoration of the gel form was evident.

2.18. Preparation of Gel (D-THD-G, and K-THD-G)

500 µL of diesel and kerosene oils were taken in three separate vials, and 5mg of **THD** powder sample was added to each vial, followed by heating at 70°C, which resulted in a semi-transparent solution for both. Upon resting the resulting solutions for 5min. formation of gels, namely, **D-**

THD-G (derived from diesel), and **K-THD-G** (derived from kerosene) was observed. The formation of the gels was first confirmed through an inverted tube experiment, followed by rheology experiments. However, **THX** could not induce gelation in any of the studied oil samples as well as in different organic solvents.

2.19. Gel Preparation Method of Py-M-G

Py-M (5 mg) was dispersed in DMSO (200 µL) solvent inside a glass vial via sonication, and the mixture was subjected to heating until a clear solution appeared. Afterwards, water (300 µL) was added rapidly to the mentioned hot solution.

2.20. Crystallization Method for Py-M-G (prepared inside a test tube)

The test tube containing Py-M-G was placed inside an oil bath placed over a heating plate, and the temperature was set at 150 °C. The temperature slowly rises and was further monitored using a thermometer to maintain the accuracy of our observation. As soon as the temperature reaches ~120 °C, the gel separates from the solvent phase, which is attributable to the water vaporisation. The separated gel was placed again inside the solvent and kept heating. As the temperature reached ~150 °C, the gel completely converted into a sol. Upon slow cooling inside the oil bath (at the rate of ~1.5 °C/min) for 4-5 h, crystallisation was observed (resulting crystals were of varied shapes and sizes).

2.21. Crystallization Method for Py-M-G (smeared on a glass plate)

A small portion of Py-M-G was placed on a glass plate and uniformly smeared using a spatula. Then the smeared gel was placed inside an oven and heated at 100 °C for 30 min, which resulted in hexagonal-shaped single crystals.

2.22. Powder X-ray Diffraction (PXRD) Study

PXRD (Rigaku, Model: Smartlab) instrument was employed for all the PXRD analysis. To prepare the PXRD sample for the xerogels of both D-THD-G and K-THD-G, a very small portion of the respective gels were placed inside a vacuum desiccator for two weeks, followed by heating at 80°C for 12 h, and the resulting dried xerogel samples were then taken for the analysis. For the xerogel sample of Py-M-G, the gel was subjected to solvent exchange with methanol for 12 h (performed three times), followed by vacuum drying inside a desiccator for 24 h. Then the dried sample was further heated at 80°C for 12 h. For the crystal samples, the collected crystals were vacuum-dried for 24 h.

2.23. Differential Scanning Calorimetry (DSC) Experimental Details

DSC thermogram of wet Py-M-G (5mg) was obtained using a Mettler Toledo DSC-1 instrument with a heating rate of 5 °C min^{-1}.

2.24. Phase Selective Oil Gelation

10 mg of THD powder was added to the 1mL of oil samples (diesel and kerosene) placed over an aqueous medium (1mL), followed by heating at 70°C. Upon resting the heated solution for 5min. Gelation was observed as confirmed from the inverted tube experiment, where the gel was observed to be capable of upholding the aqueous part against gravity.

2.25. Procedure for Fuel Adulteration Detection via Gelation Method

Petrol oil was adulterated with different percentages of kerosene oil ranging from 0% to 80% while keeping the total volume as 500µL. Then 10mg of THD powder was added to each petrol adulterated solution, followed by sonication and heating (at 70°C) until a transparent solution was observed. Upon resting each heated solution, gelation was observed in different time frames in those adulterated solutions where the percentage of kerosene oil was 40% or above. For the 40%, 50%, 60%, 70%, and 80% kerosene adulterated solutions, the time taken for gelation was 48 h, 24 h, 12 h, 12 h, and 6 h, respectively. However, for the 40% adulterated solution, the gel formed after 48h was observed to be weak in nature.

References

[2.1] E. W. Wysiecka, J. Chojnacki, *Supramol. Chem.*, 2012, **24**, (9), 684-695.

[2.2] Apex 4, Bruker AXS Inc., 2016.

[2.3] XPREP, SMART SAINT, Siemens Analytical X-ray Instruments Inc., 1995. Software.

[2.4] G. M. Sheldrick, SADABS, Program for Area Detector Adsorption Correction; Institute for Inorganic Chemistry, University of G¨ottingen, 1996.

[2.5] G.M. Sheldrick, *Acta Crystallogr. Sect. C Struct. Chem.*, 2015, **71**, 3-8.

[2.6] C. F. Macrae, I. Sovago, S. J. Cottrell, P. T. A. Galek, P. McCabe, E. Pidcock, M. Platings, G. P. Shields, J.S. Stevens, M. Towler, and P.A. Wood, *J. Appl. Crystallogr*, 2020, **53**, 226-235.

[2.6] C. F. Macrae, I. Sovago, S. J. Cottrell, P. T. A. Galek, P. McCabe, E. Pidcock, M. Platings, G. P. Shields, J.S. Stevens, M. Towler, and P.A. Wood, *J. Appl. Crystallogr*, 2020, **53**, 226-235.

[2.7] J. J. McKinnon, A. S. Mitchell, and M. A. Spackman, *Chem. Eur. J.*, 1998, **4** (11), 2136-2141.

[2.8] T. E. Clark, M. Makha, A. N. Sobolev, and C. L. Raston, *Cryst. Growth Des.*, 2008, **8** (3), 890-896.

[2.9] B. O. Okesola, S. K. Suravaram, A. Parkin, D. K. Smith, *Angew. Chem. Int. Ed.*, 2016, **55** (1), 183-187

Annexure 2

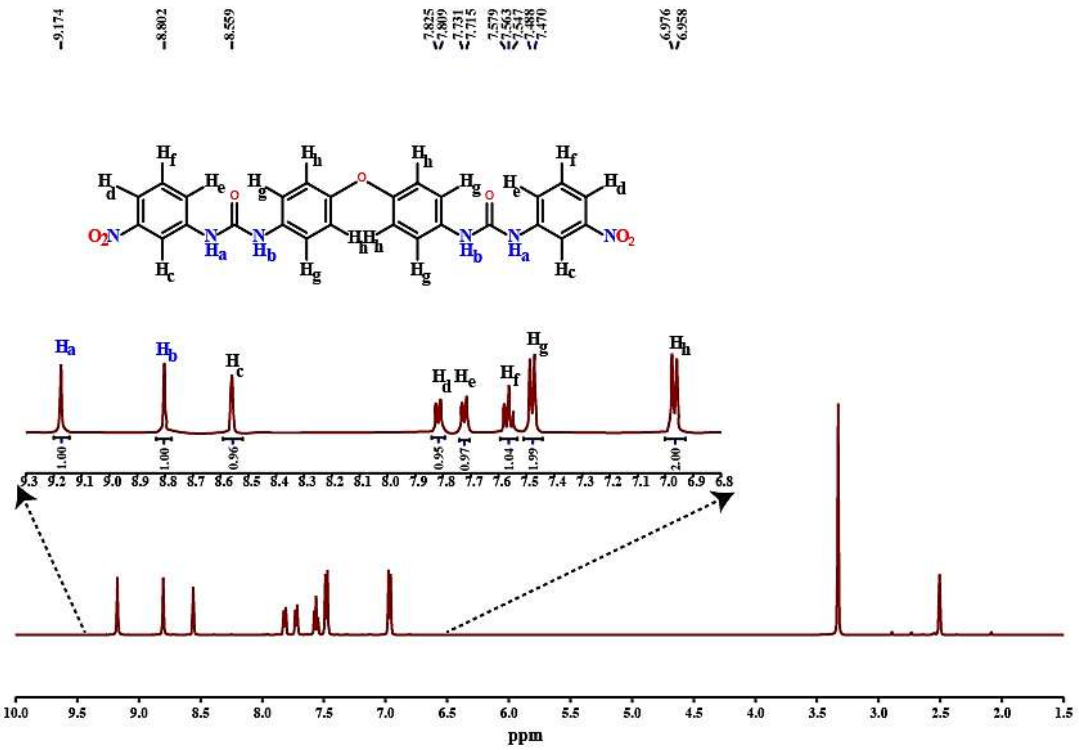

Figure A2.1: ^{1}H NMR spectrum of receptor L_1 at 25°C and interpretation of all the hydrogen atoms of the receptor.

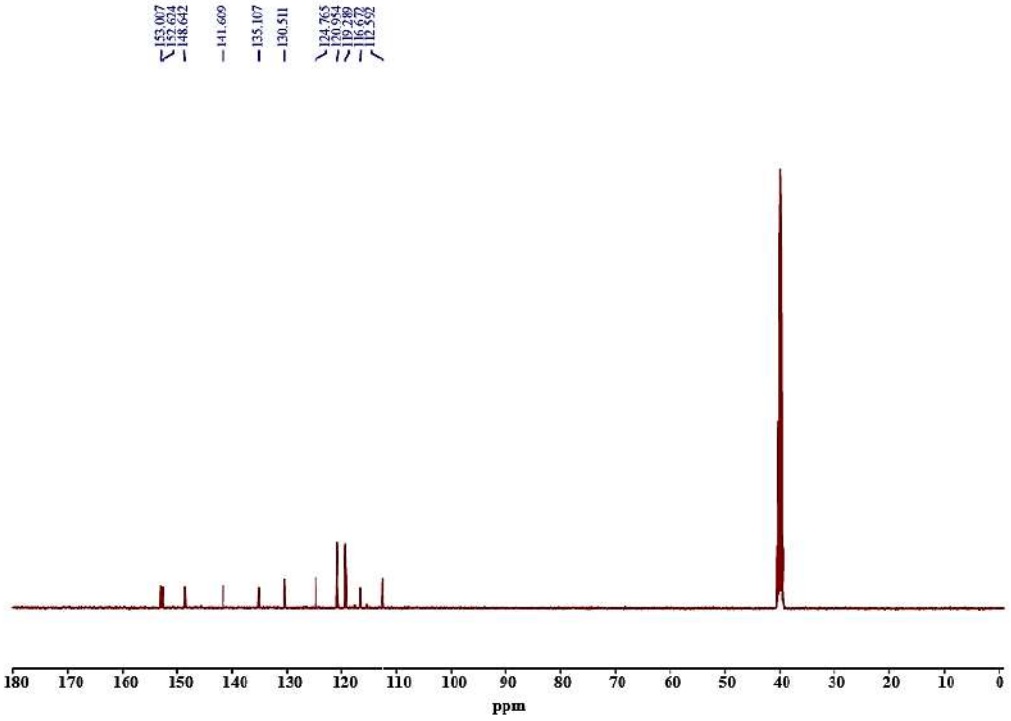

Figure A2.2: ^{13}C NMR spectrum of receptor L_1 at 25°C in DMSO-d_6.

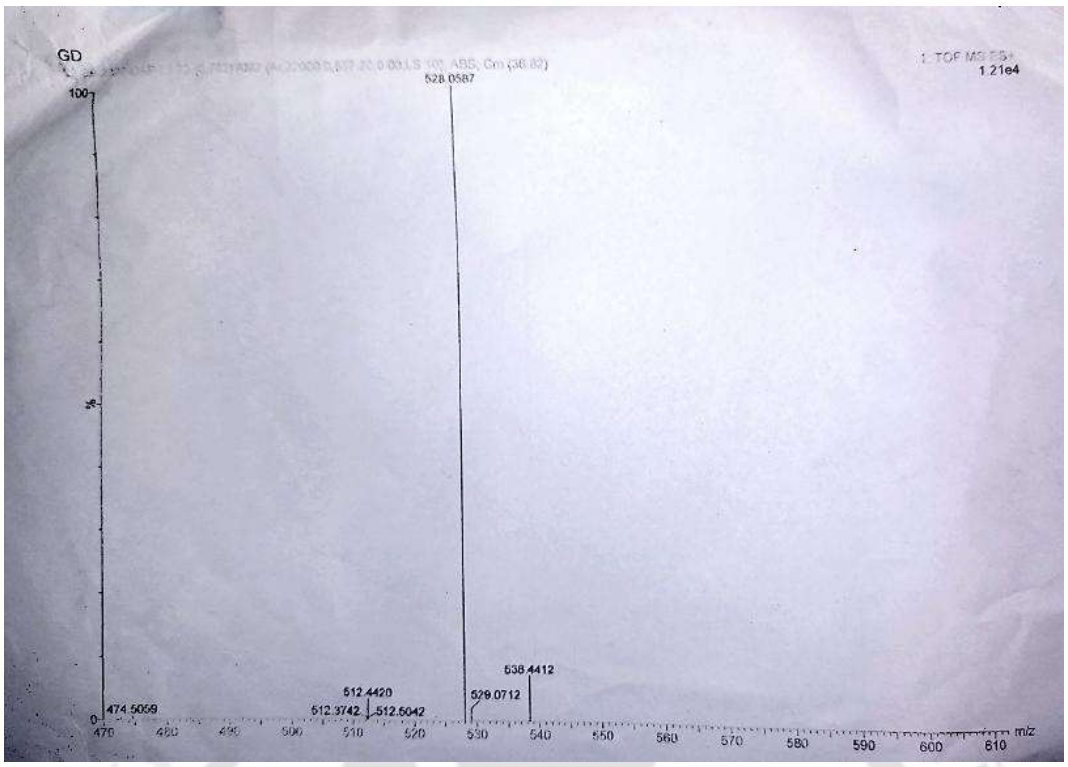

Figure A2.3: ESI-Mass spectrum of receptor L_1.

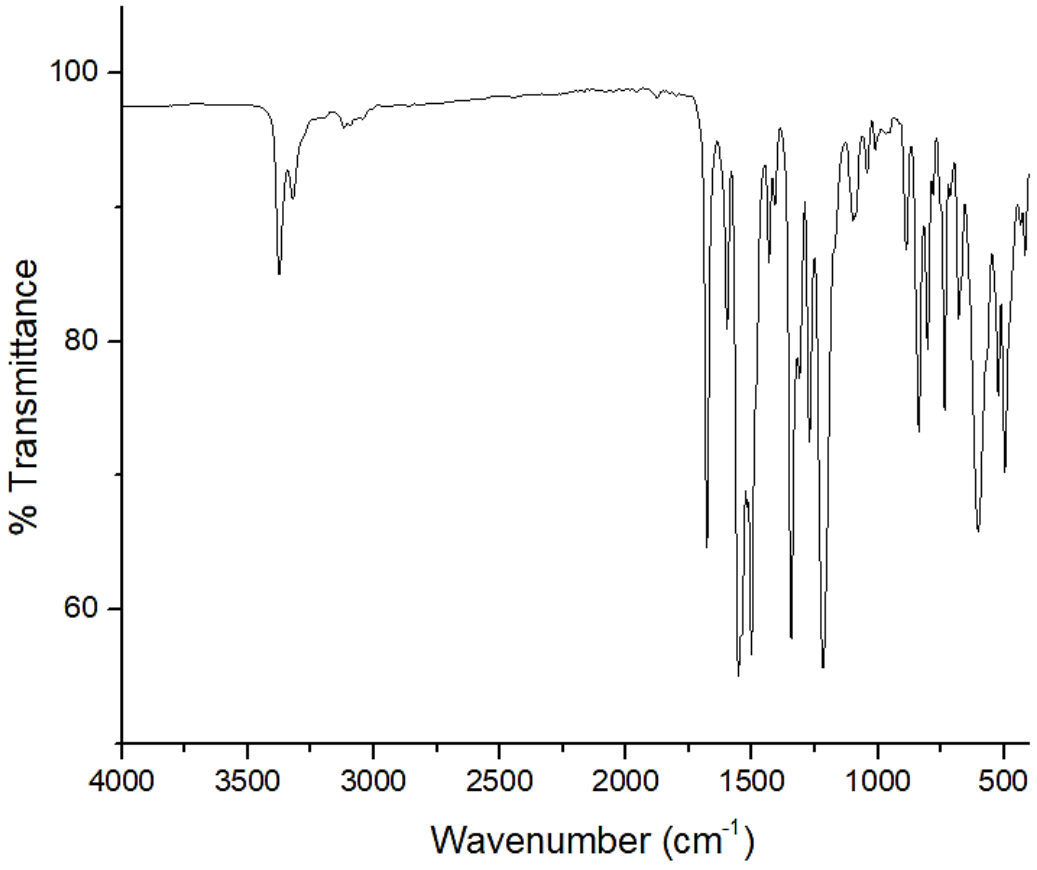

Figure A2.4: FT-IR spectrum of receptor L_1 recorded in KBr pellet at 25°C.

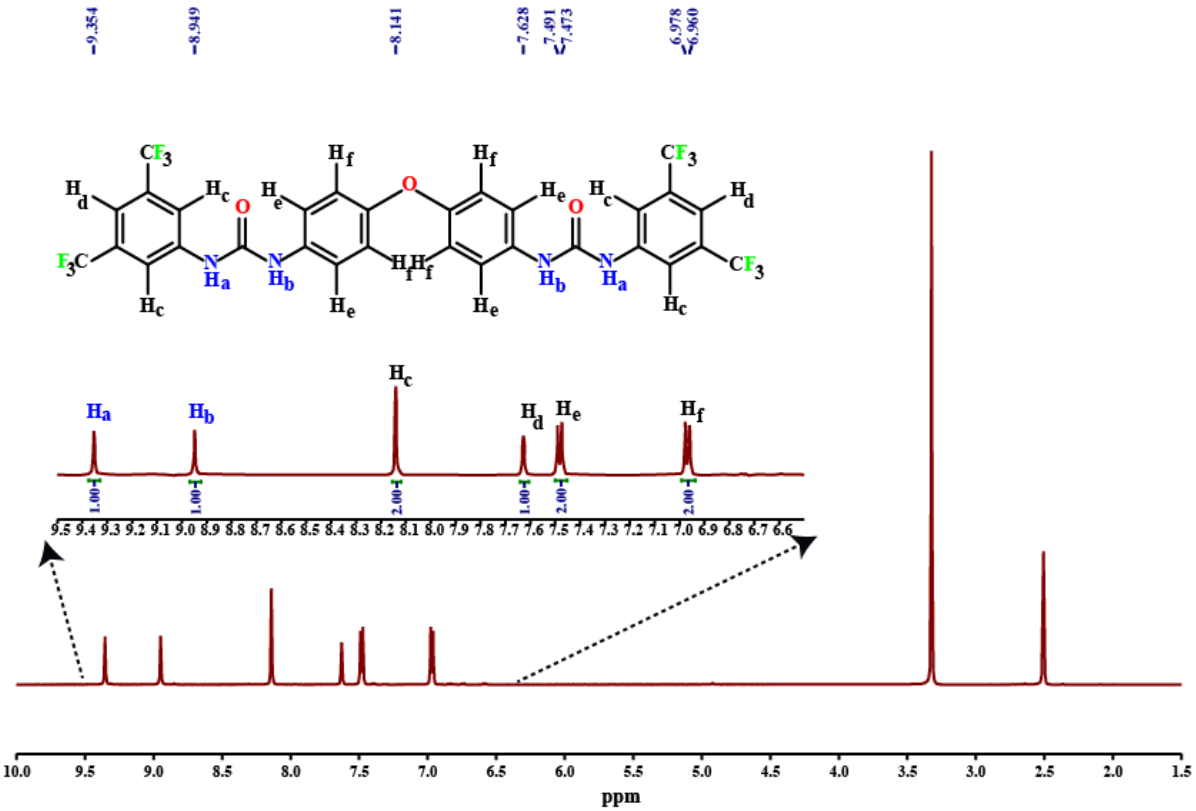

Figure A2.5: ^{1}H NMR spectrum of receptor L_2 at 25°C in DMSO-d_6 and interpretation of all the hydrogen atoms of the receptor.

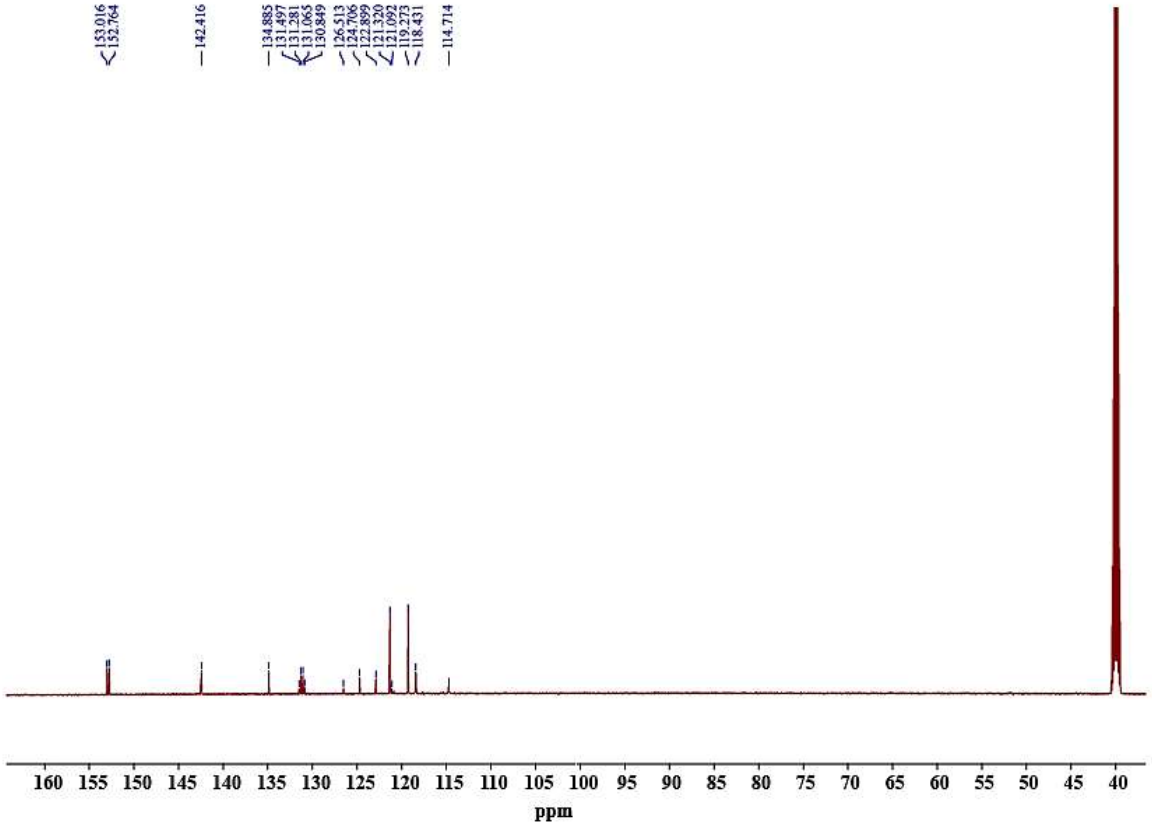

Figure A2.6: ^{13}C NMR spectrum of receptor L_2 at 25°C in DMSO-d_6.

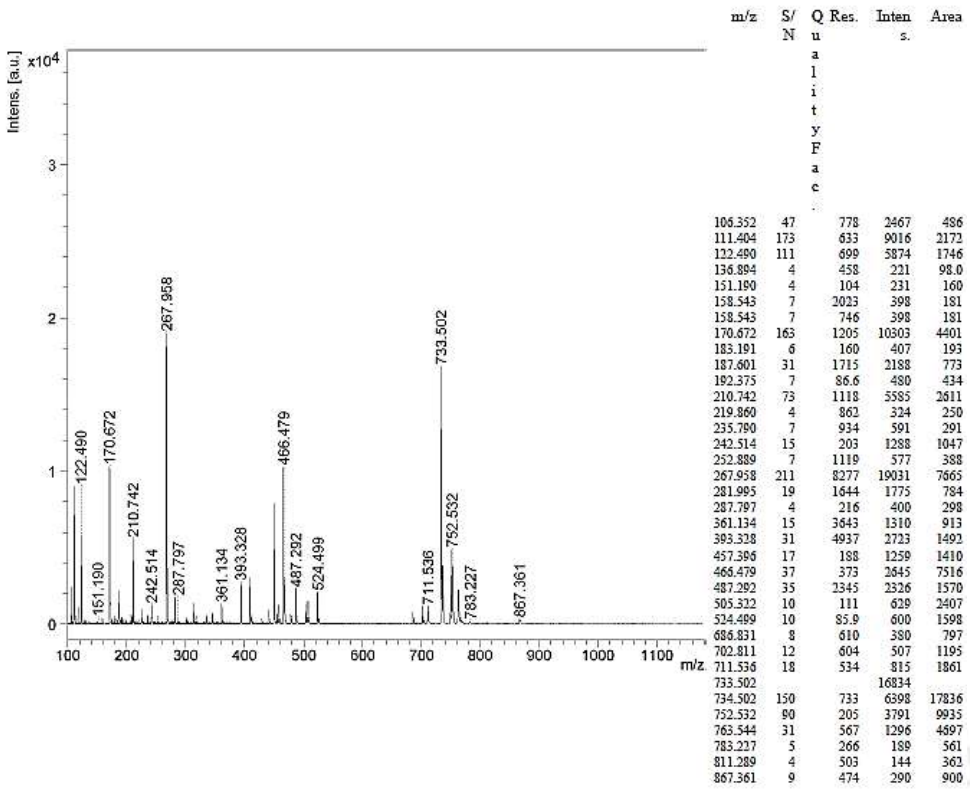

m/z	S/N	Quality Fac.	Res.	Intens.	Area
106.352	47		778	2467	486
111.404	173		633	9016	2172
122.490	111		699	5874	1746
136.894	4		458	221	98.0
151.190	4		104	231	160
158.543	7		2023	398	181
158.543	7		746	398	181
170.672	163		1205	10303	4401
183.191	6		160	407	193
187.601	31		1715	2188	773
192.375	7		86.6	480	434
210.742	73		1118	5585	2611
219.860	4		862	324	250
235.790	7		934	591	291
242.514	15		203	1288	1047
252.889	7		1119	577	388
267.958	211		8277	19031	7665
281.995	19		1644	1775	784
287.797	4		216	400	298
361.134	15		3643	1310	913
393.328	31		4937	2723	1492
457.396	17		188	1259	1410
466.479	37		373	2645	7516
487.292	35		2345	2326	1570
505.322	10		111	629	2407
524.499	10		85.9	600	1598
686.831	8		610	380	797
702.811	12		604	507	1195
711.536	18		534	815	1861
733.502				16834	
734.502	150		733	6398	17836
752.532	90		205	3791	9935
763.544	31		567	1296	4697
783.227	5		266	189	561
811.289	4		503	144	362
867.361	9		474	290	900

Figure A2.7: MALDI-mass spectrum of receptor L_2.

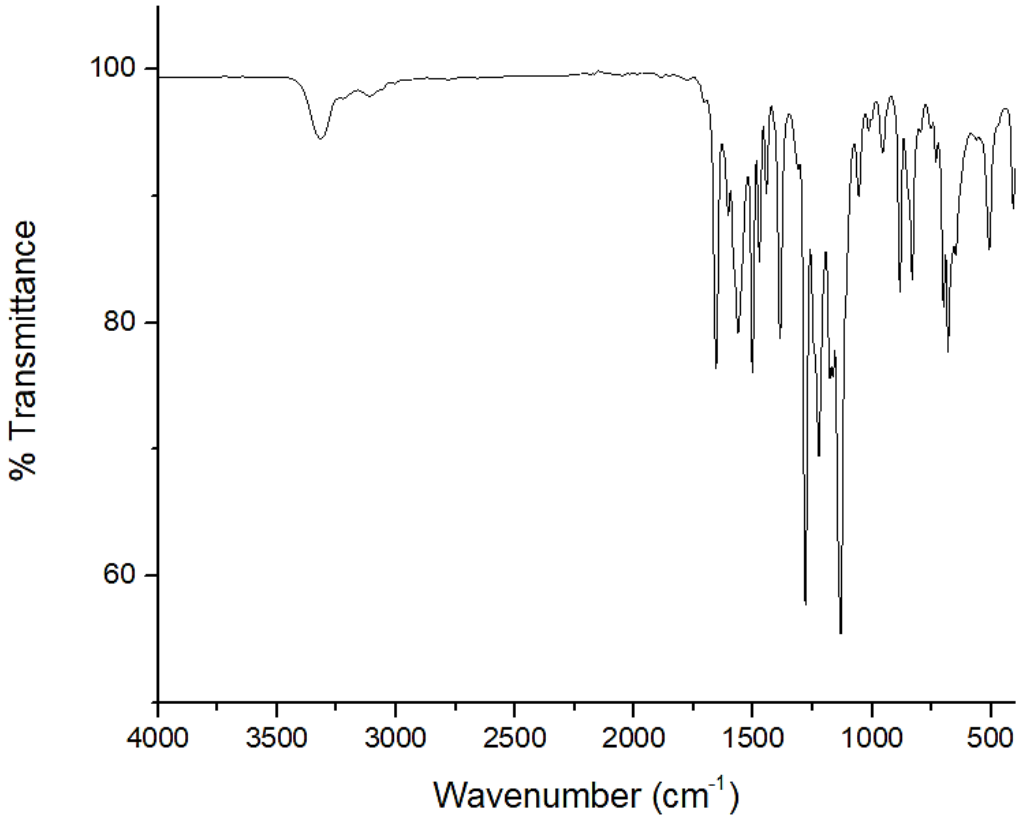

Figure A2.8: FT-IR spectrum of receptor L_2 recorded in KBr pellet at 25°C.

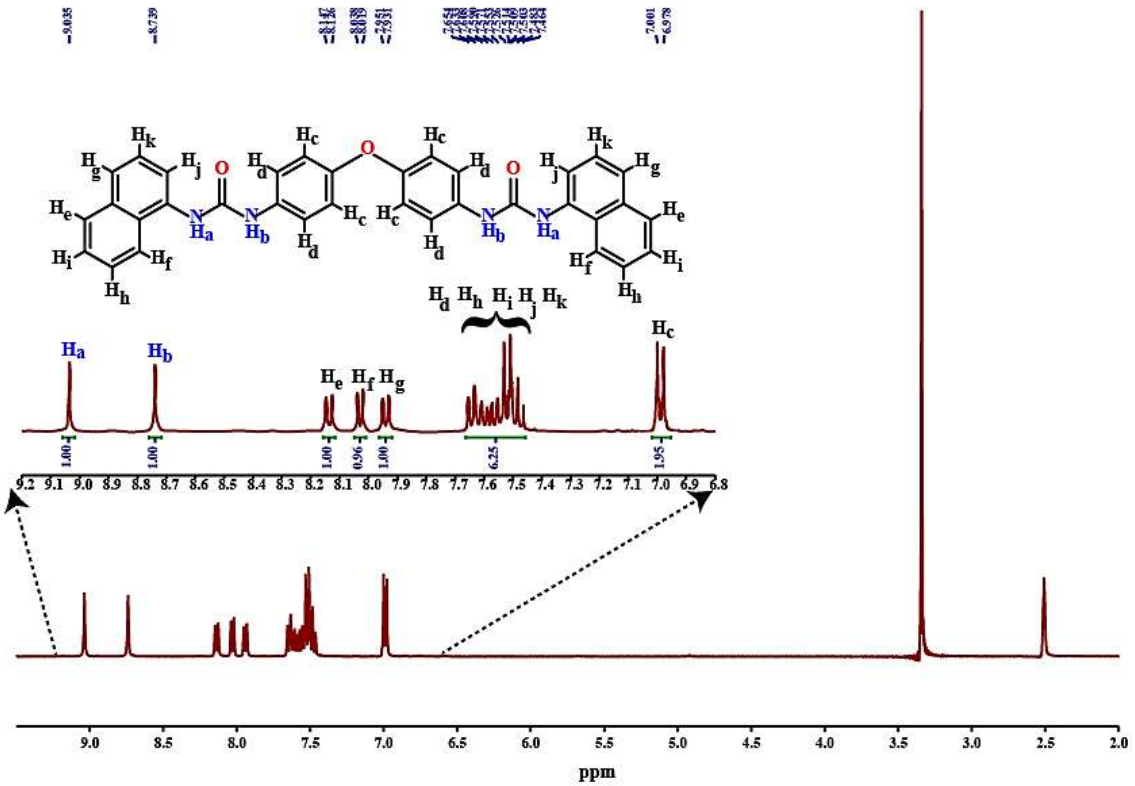

Figure A2.9: ^{1}H NMR spectrum of receptor L_3 at 25°C in DMSO-d_6 and interpretation of all the hydrogen atoms of the receptor.

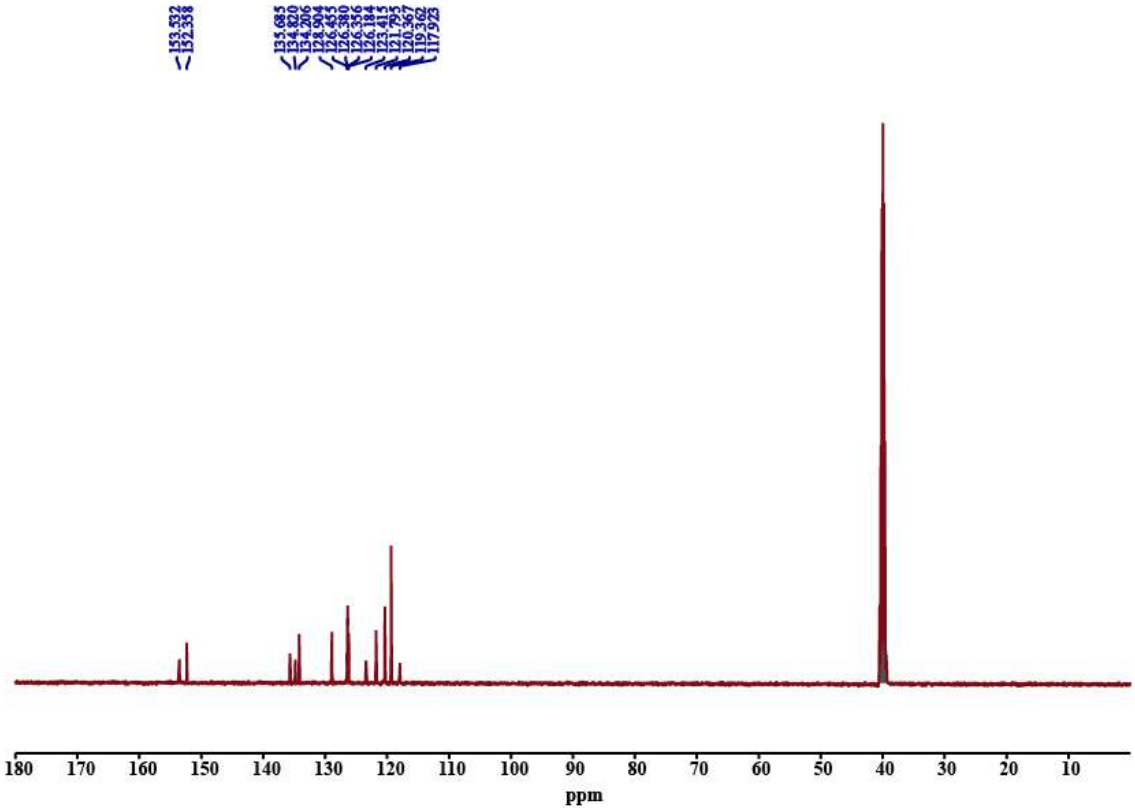

Figure A2.10: ^{13}C NMR spectrum of receptor L_3 at 25°C in DMS0-d_6.

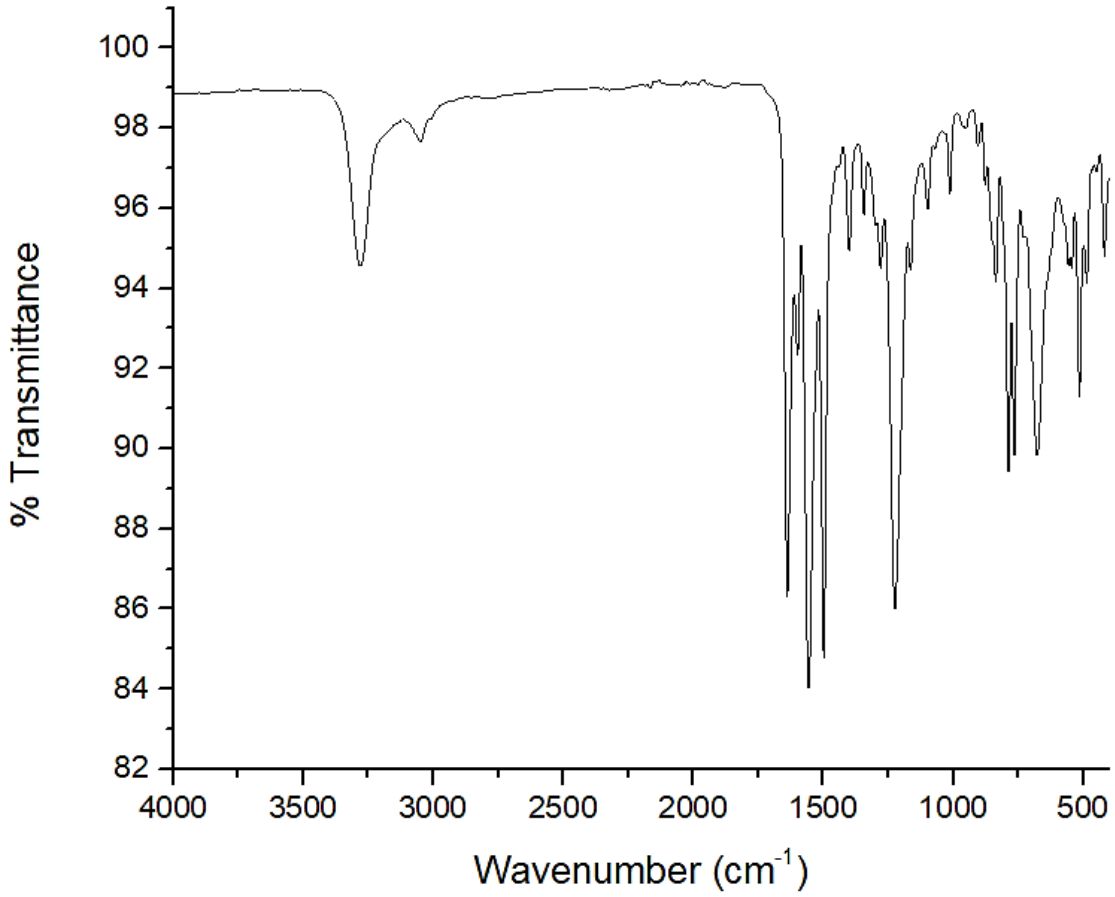

Figure A2.11: FT-IR spectrum of receptor L_3 recorded in KBr pellet at 25°C.

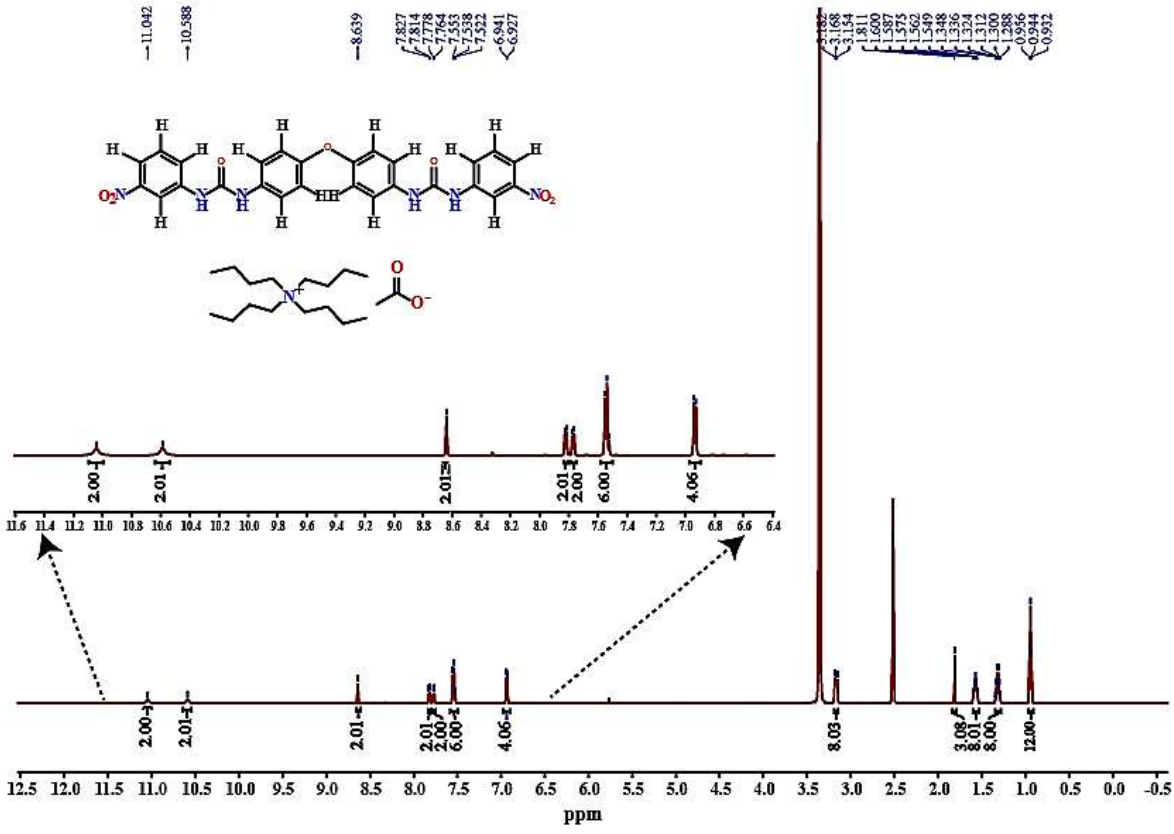

Figure A2.12: 1H NMR spectrum of the complex, complex L_1A at 25°C in DMSO-d_6.

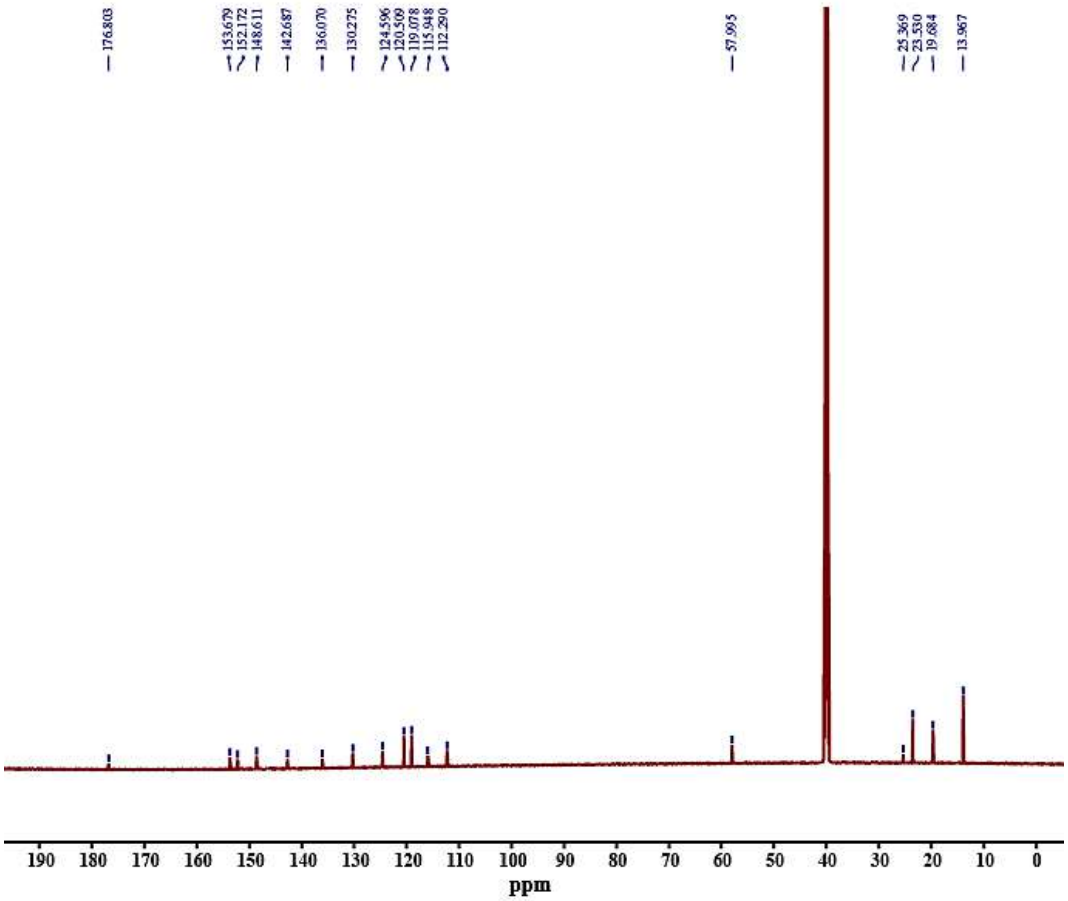

Figure A2.13: ^{13}C NMR spectrum of the complex L_1A at 25°C in DMSO-d_6.

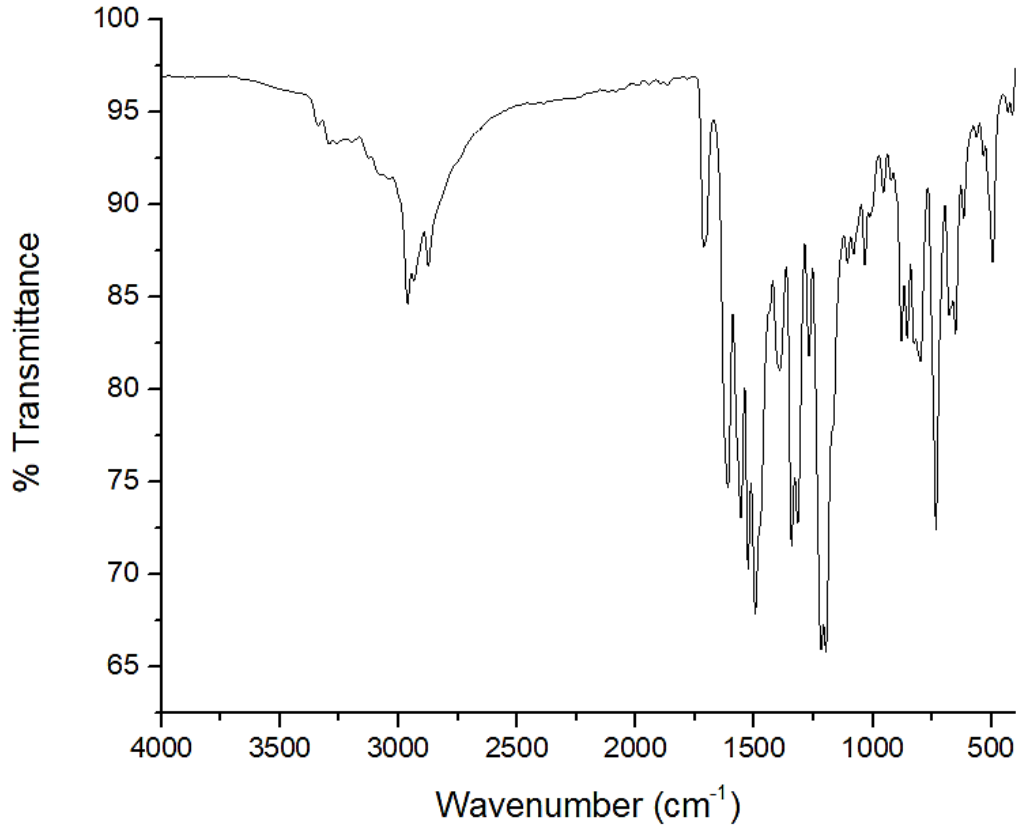

Figure A2.14: FT-IR spectrum of the complex L_1A recorded in KBr pellet at 25°C.

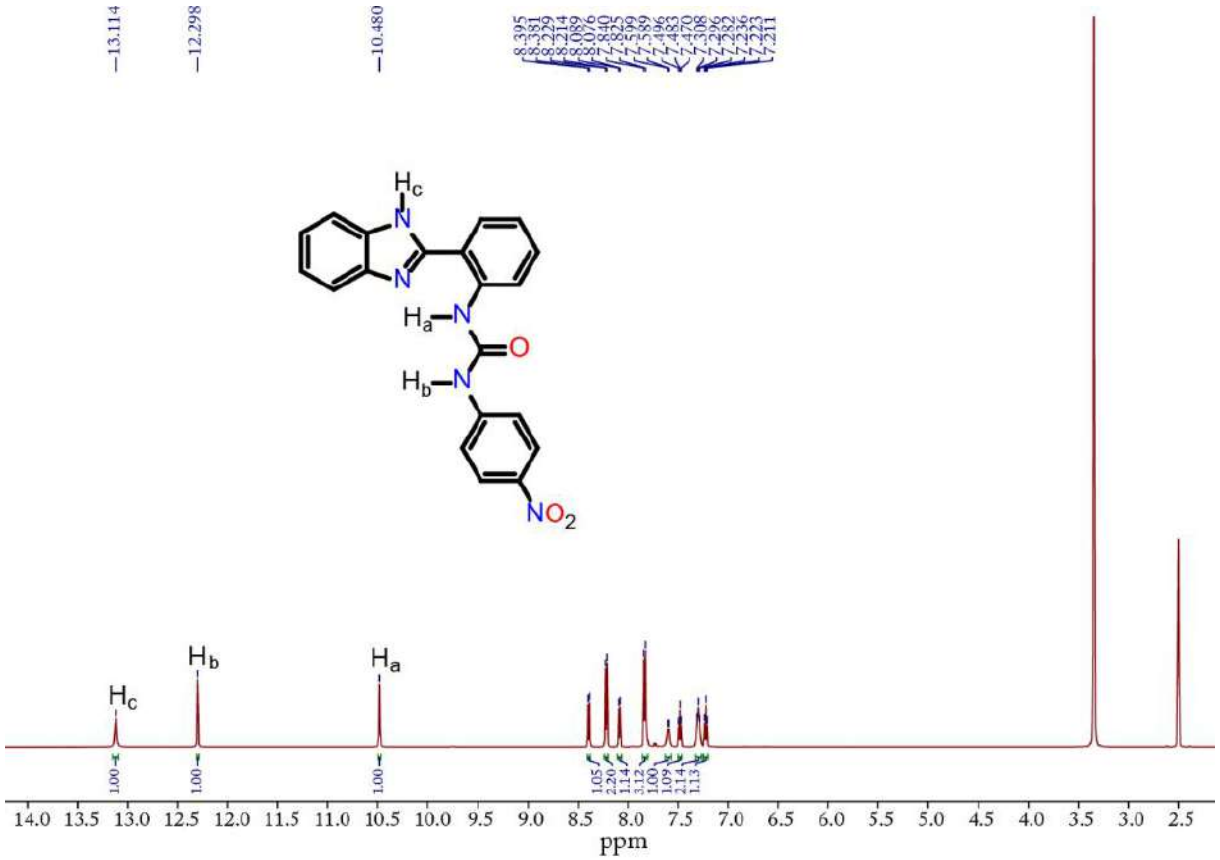

Figure A2.15: ^{1}H NMR of BPU-1.

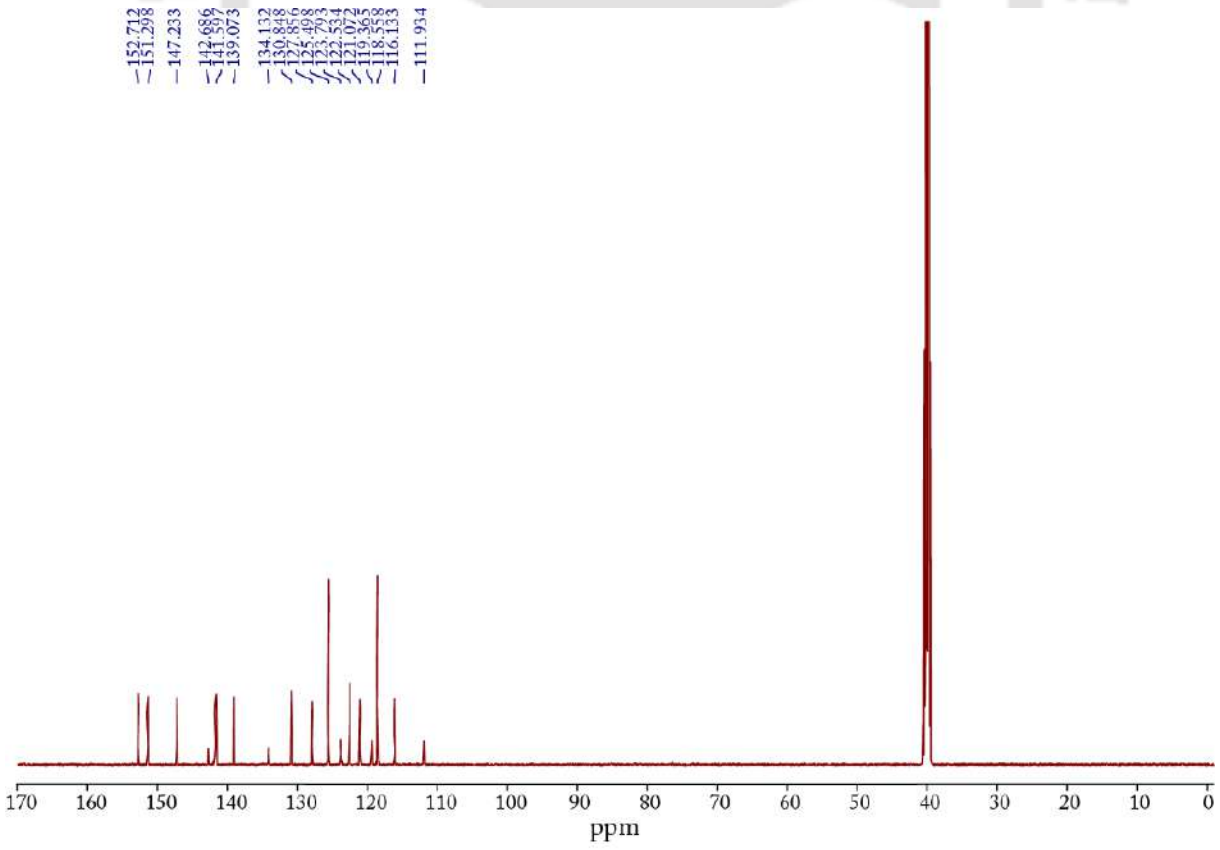

Figure A2.16: ^{13}C NMR of BPU-1.

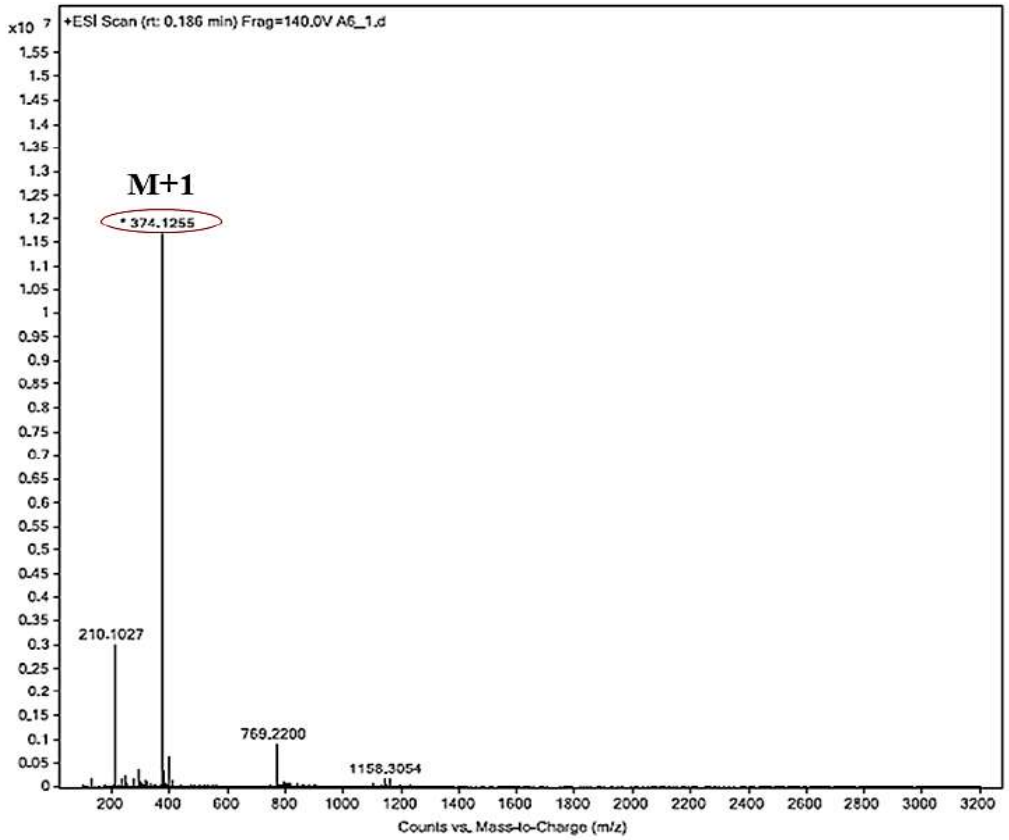

Figure A2.17: Mass spectrum of BPU-1.

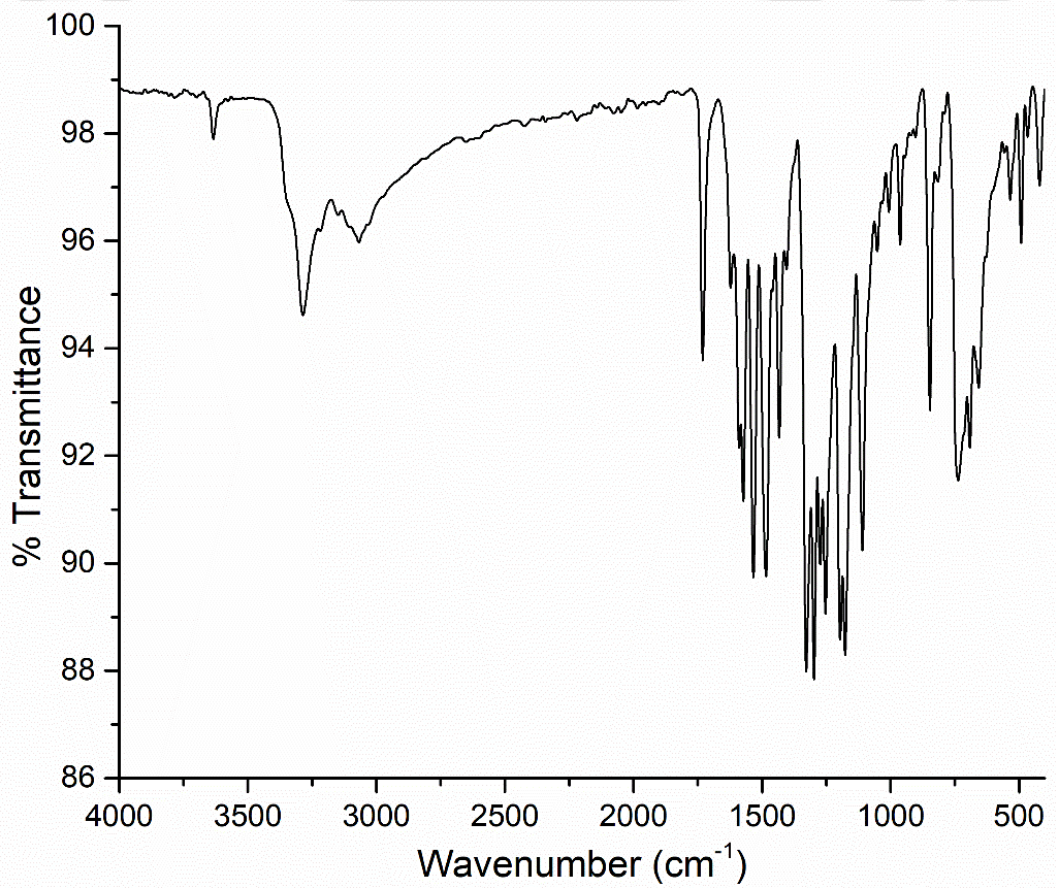

Figure A2.18: FT-IR spectrum of BPU-1.

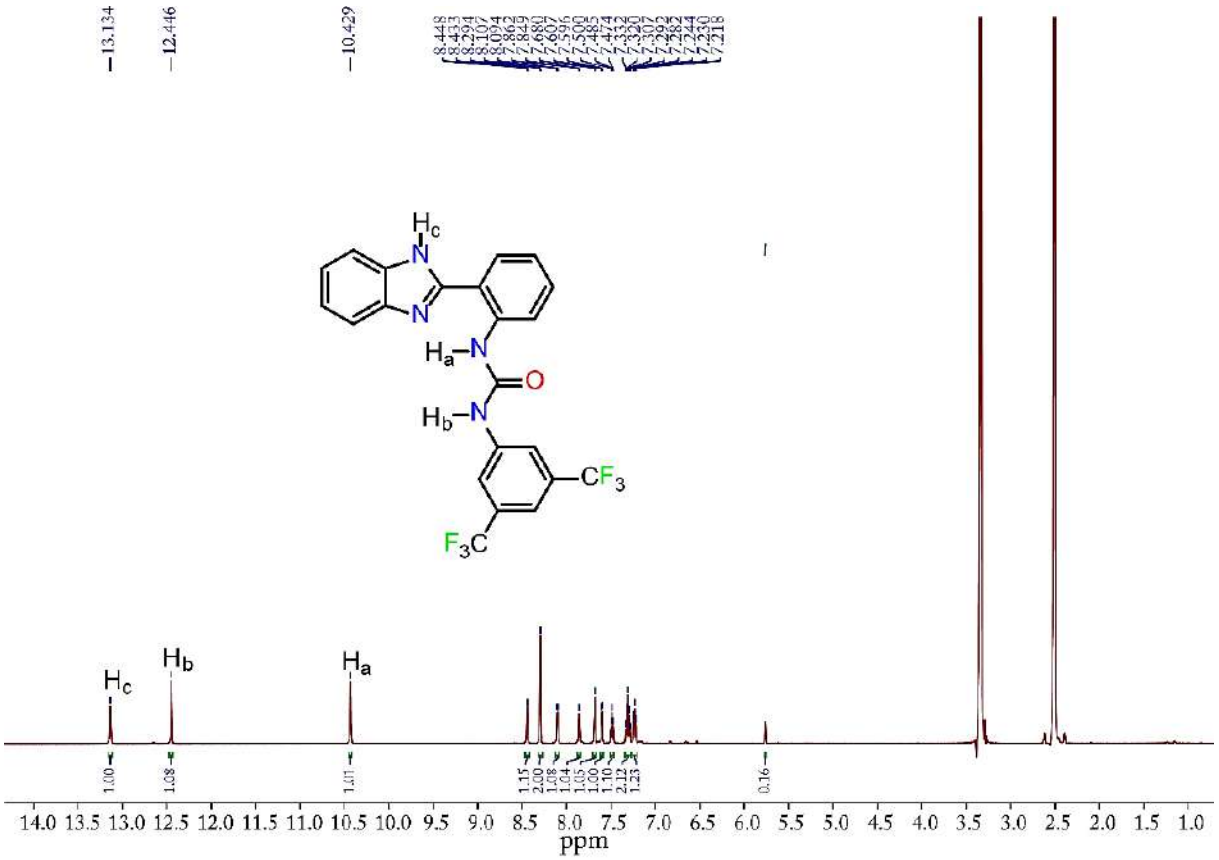

Figure A2.19: ^{1}H NMR of BPU-2.

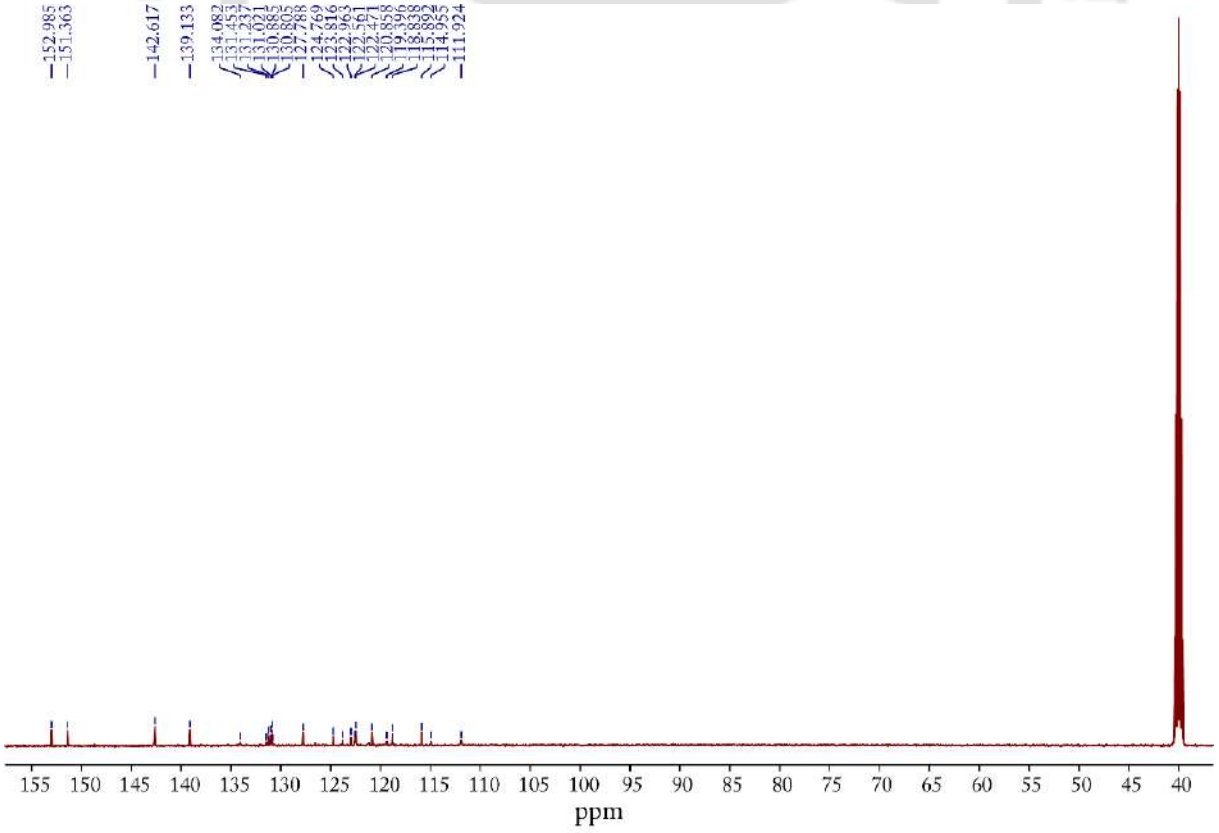

Figure A2.20: ^{13}C NMR of BPU-2.

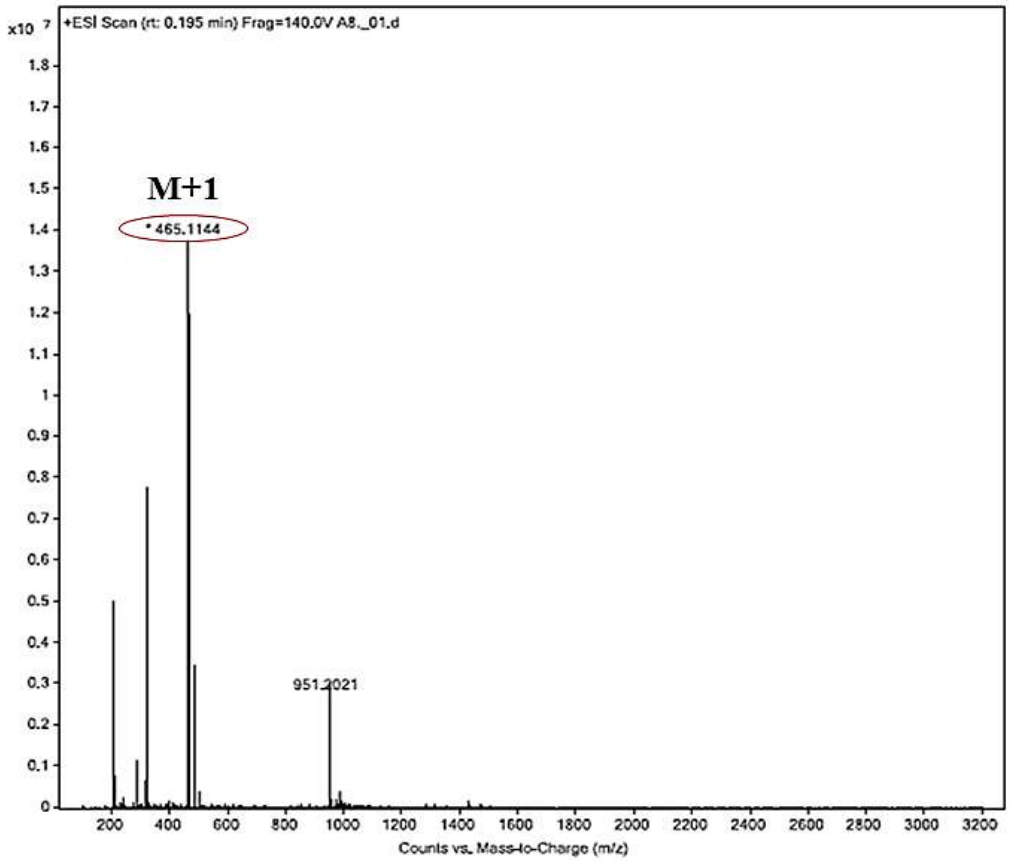

Figure A2.21: Mass spectrum of BPU-2.

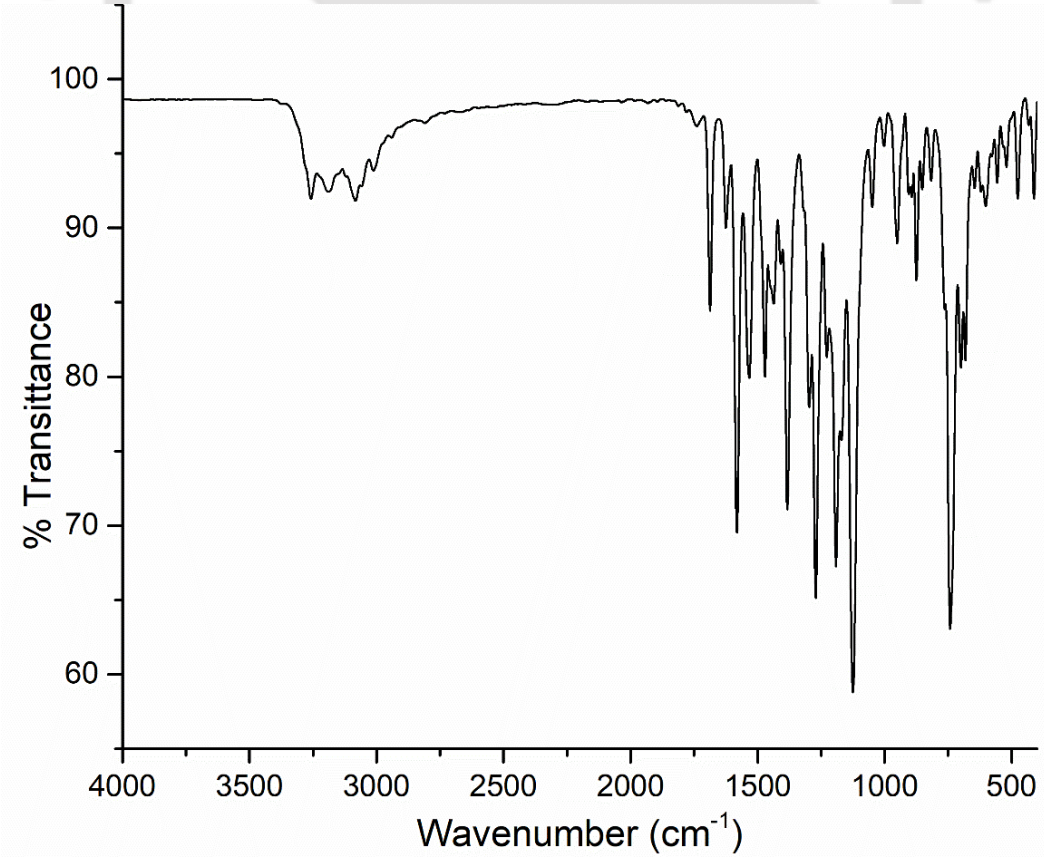

Figure A2.22: FT-IR spectrum of BPU-2.

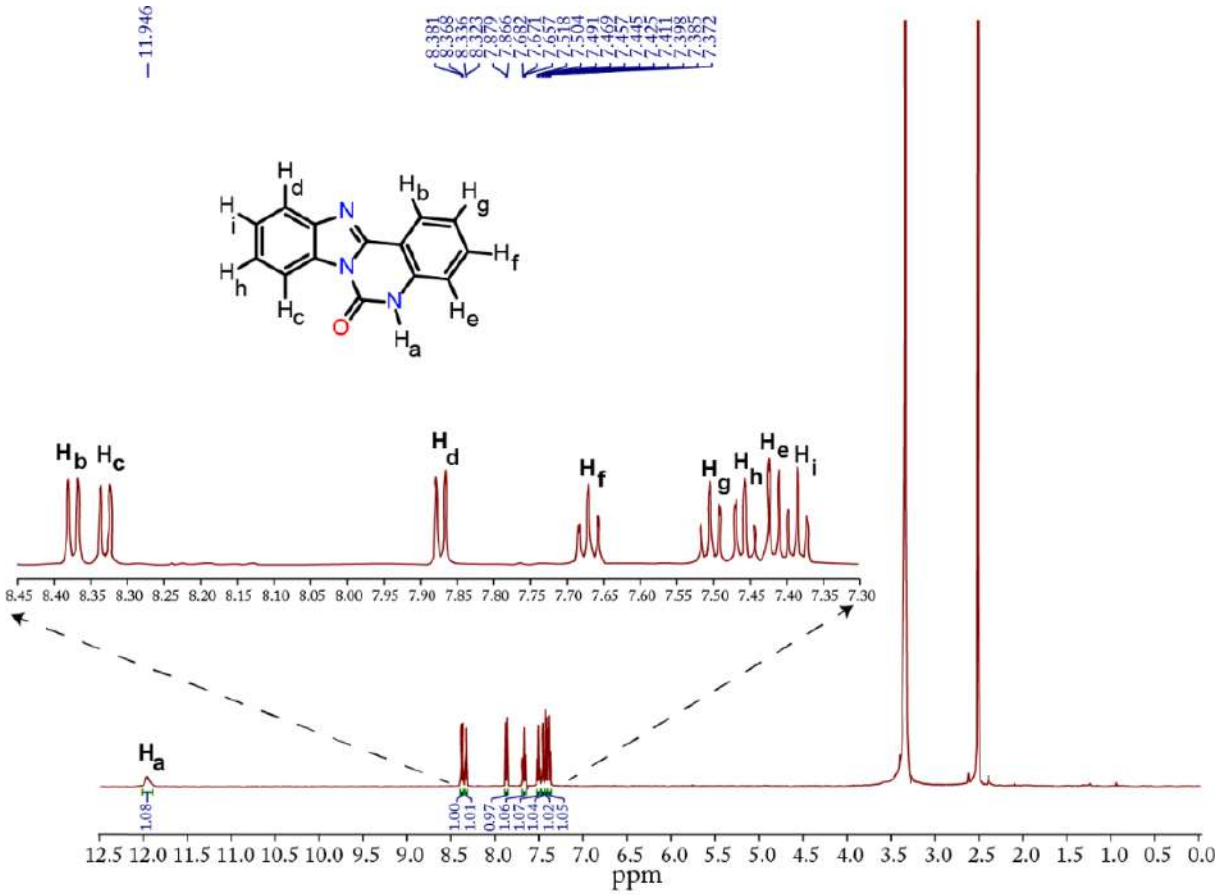

Figure A2.23: ^{1}H NMR of BP-Cyc.

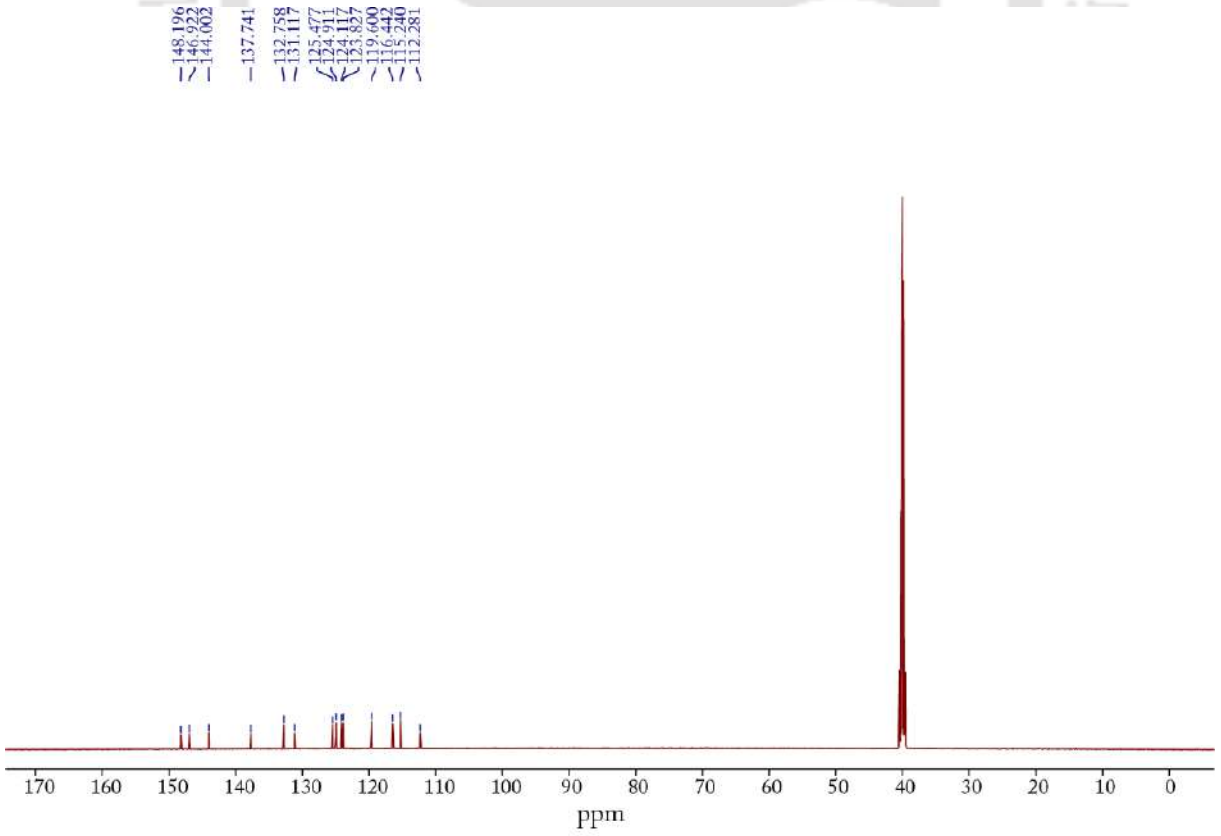

Figure A2.24: ^{13}C NMR of BP-Cyc.

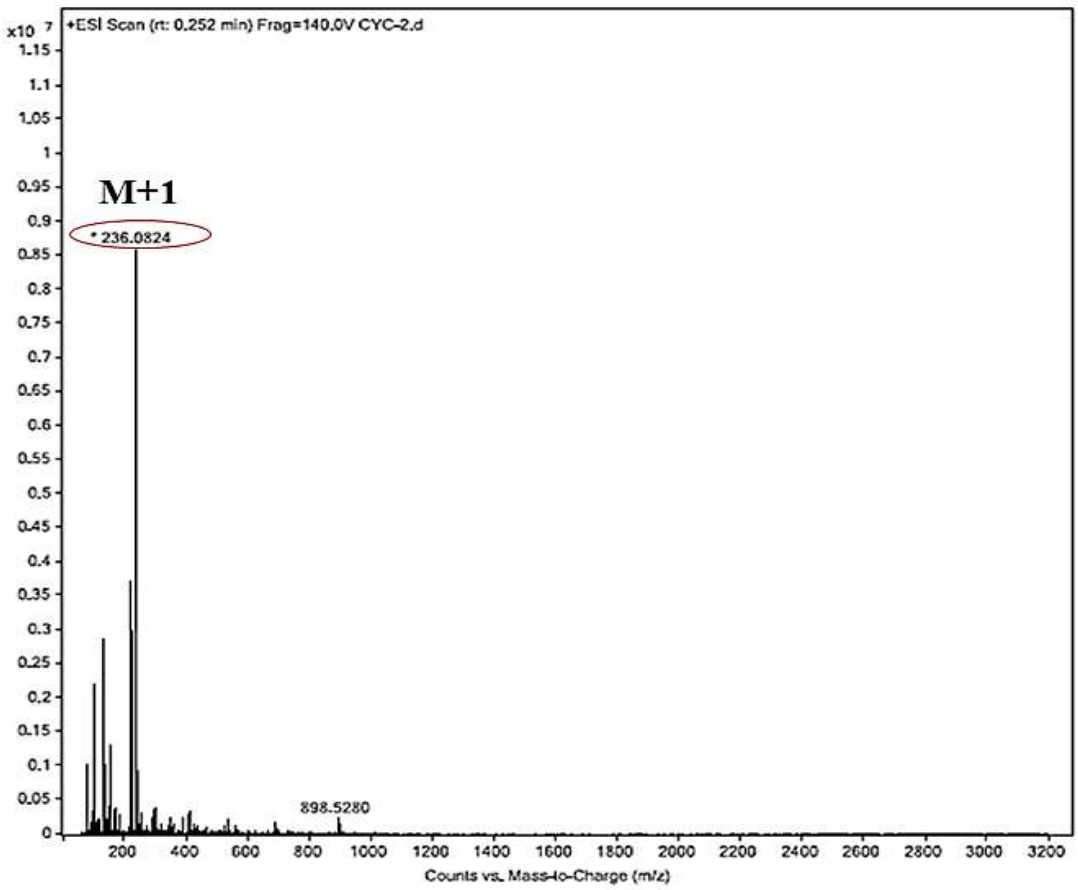

Figure A2.25: Mass spectrum of BP-Cyc.

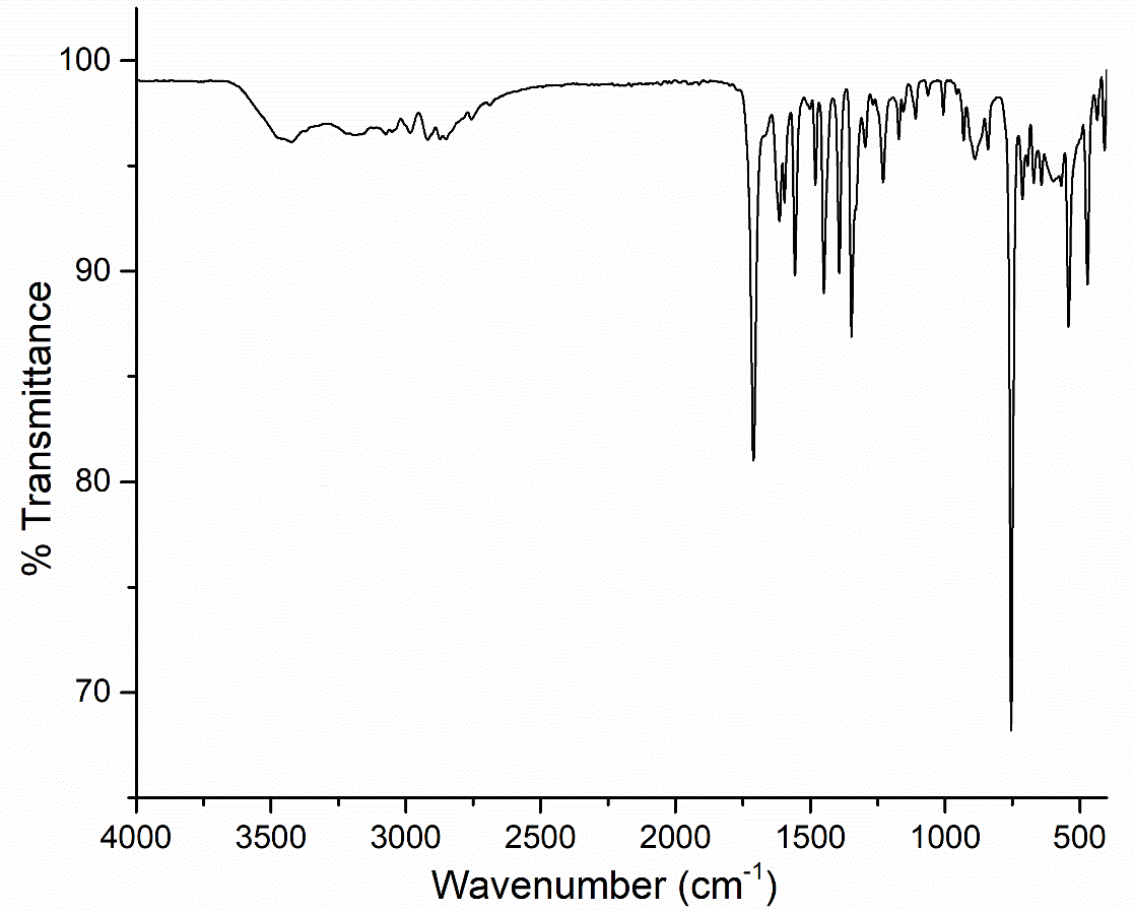

Figure A2.26: FT-IR spectrum of BP-Cyc.

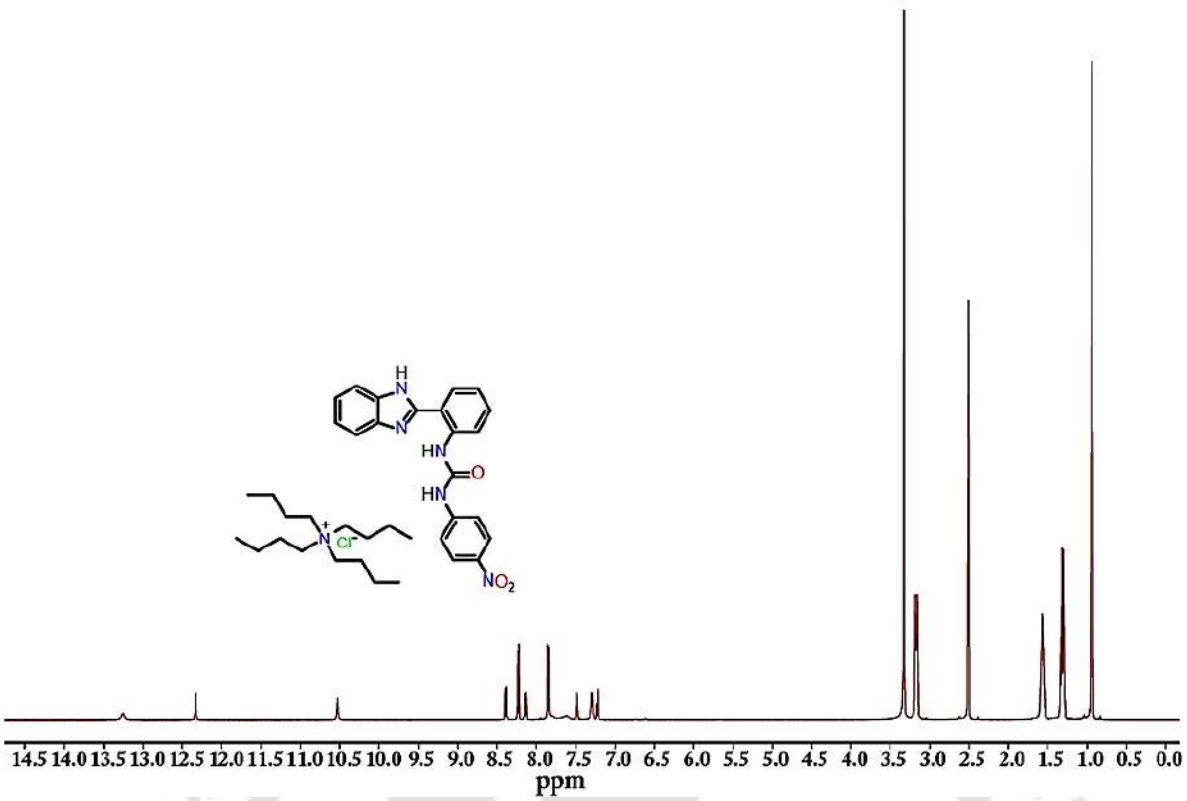

Figure A2.27: ^{1}H NMR of complex 1a.

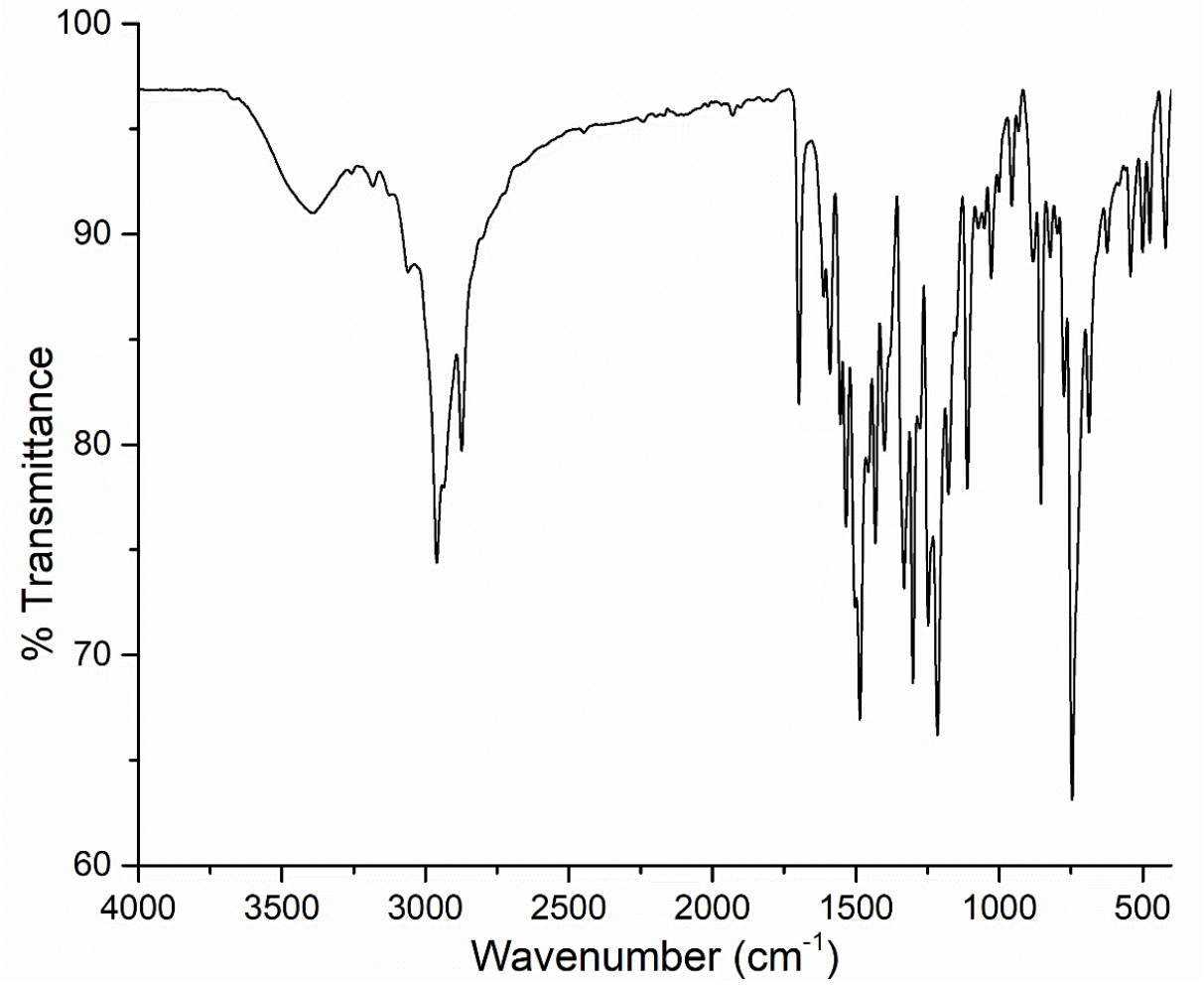

Figure A2.28: FT-IR spectra of complex 1a.

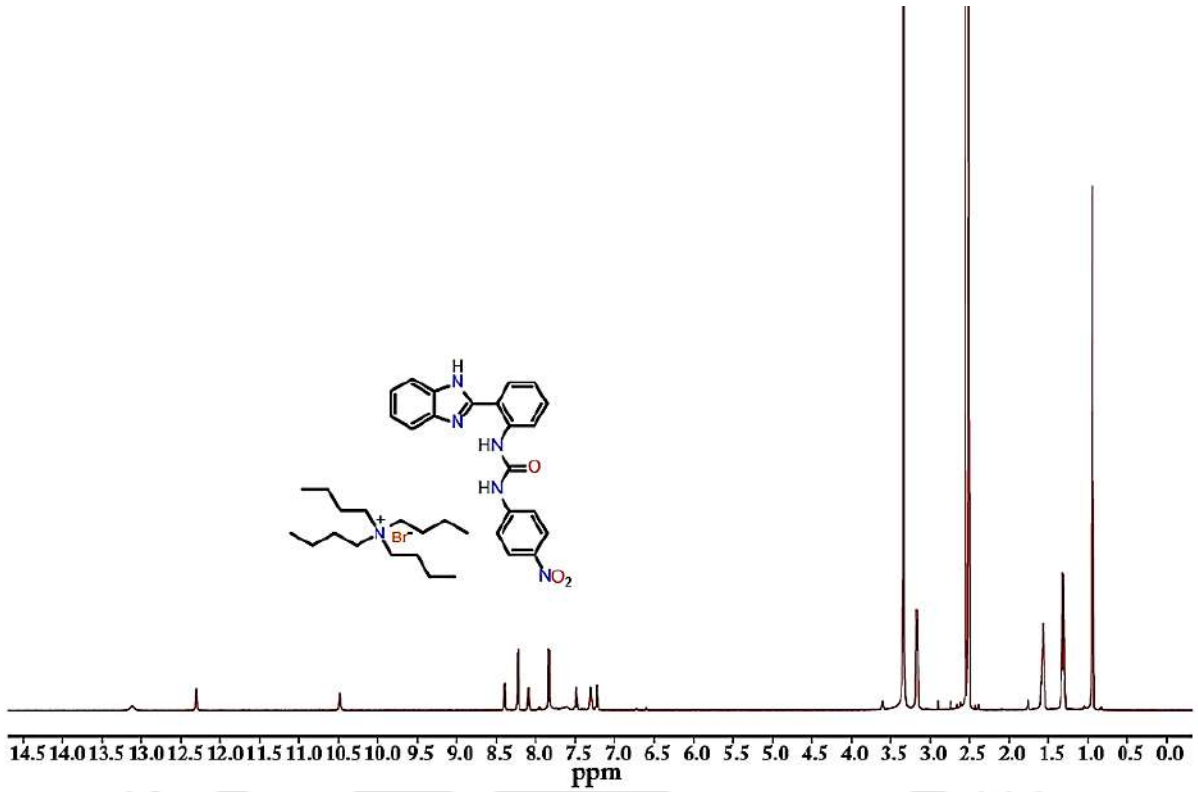

Figure A2.29: ^{1}H NMR of complex 1b.

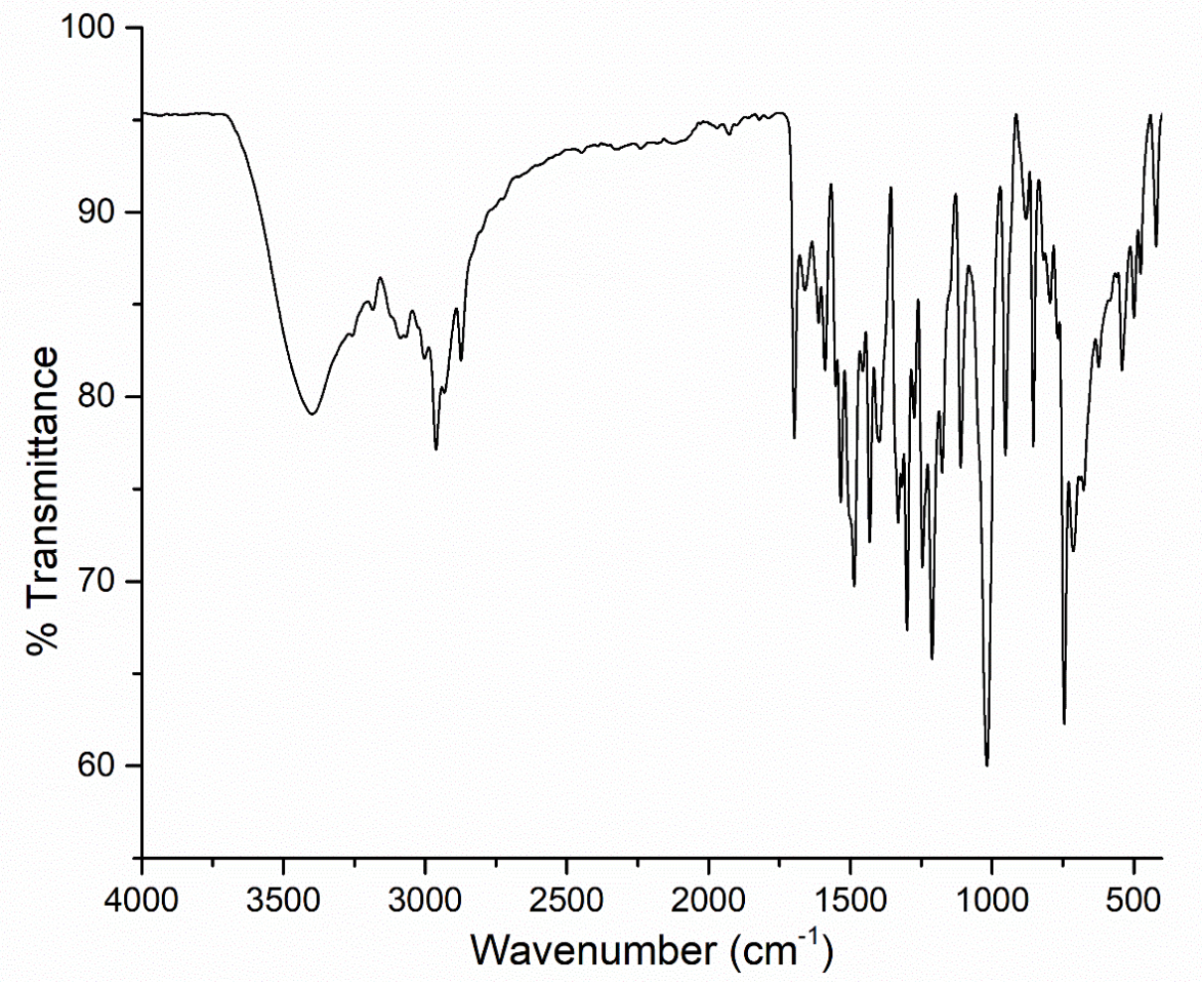

Figure A2.30: FT-IR spectra of complex 1b.

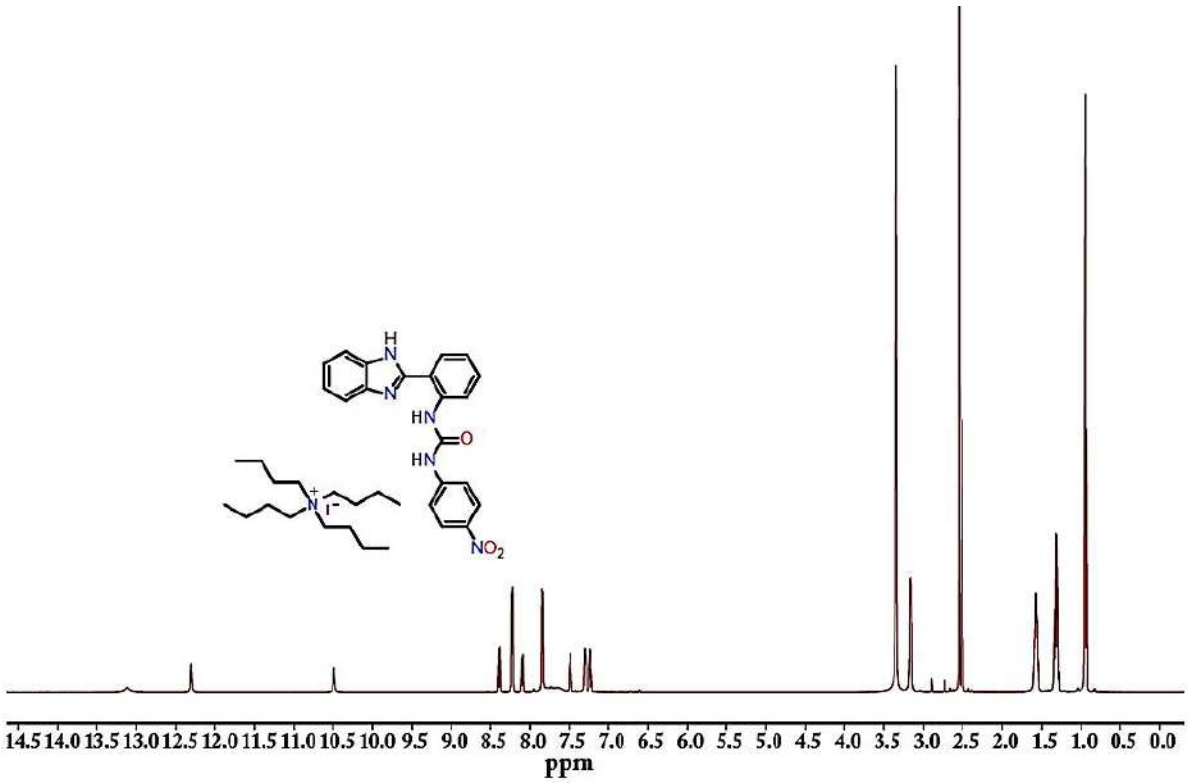

Figure A2.31: ^{1}H NMR of complex 1c.

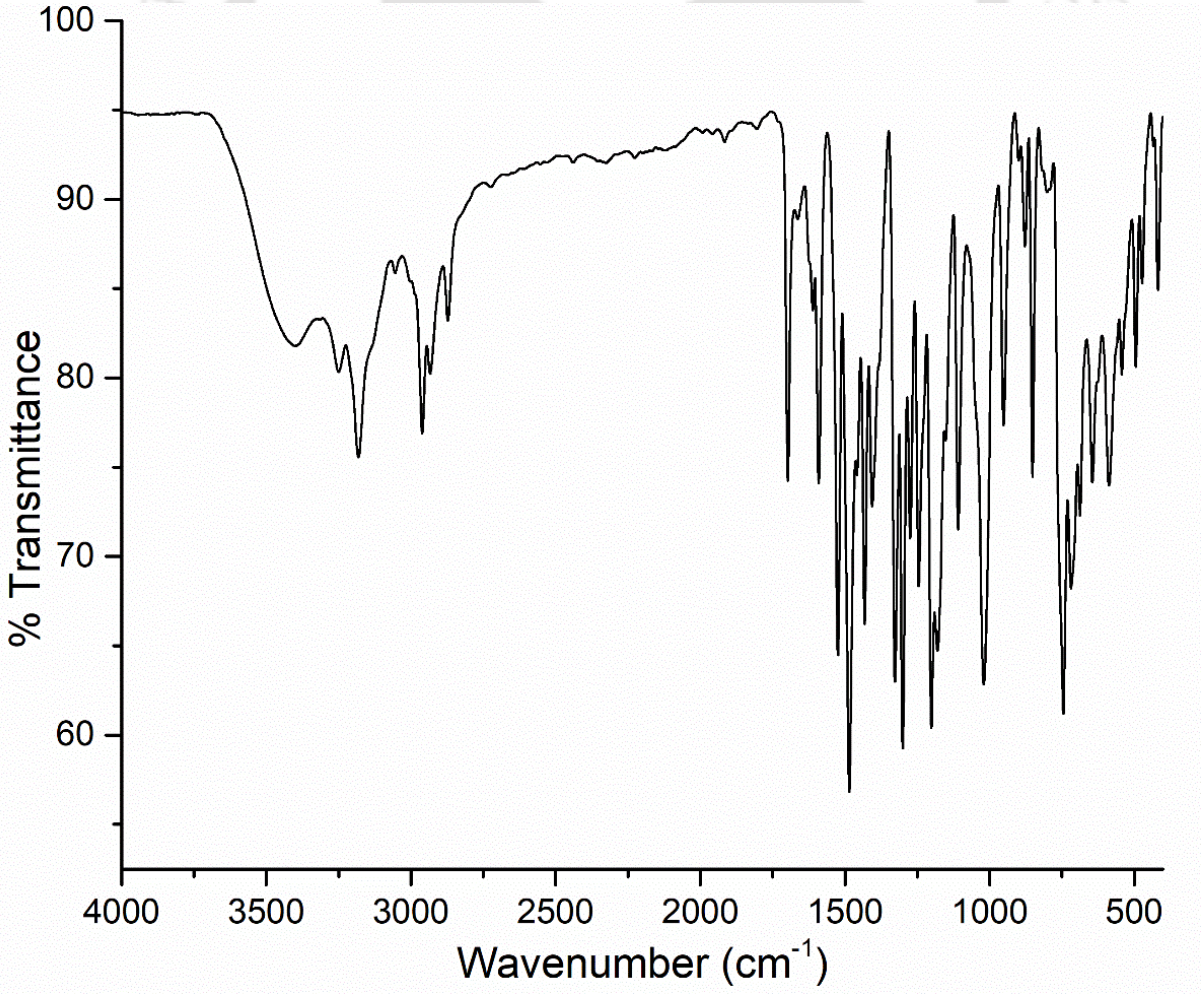

Figure A2.32: FT-IR spectra of complex 1c.

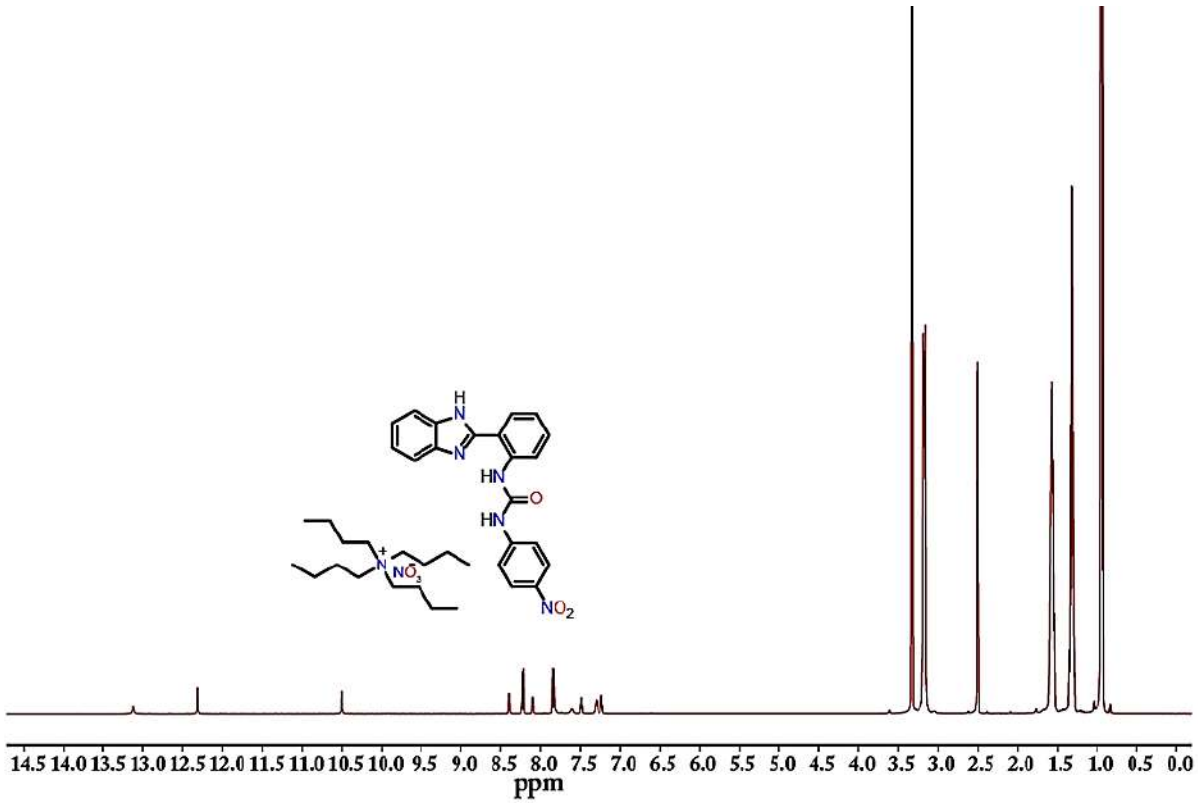

Figure A2.33: ^{1}H NMR of complex 1d.

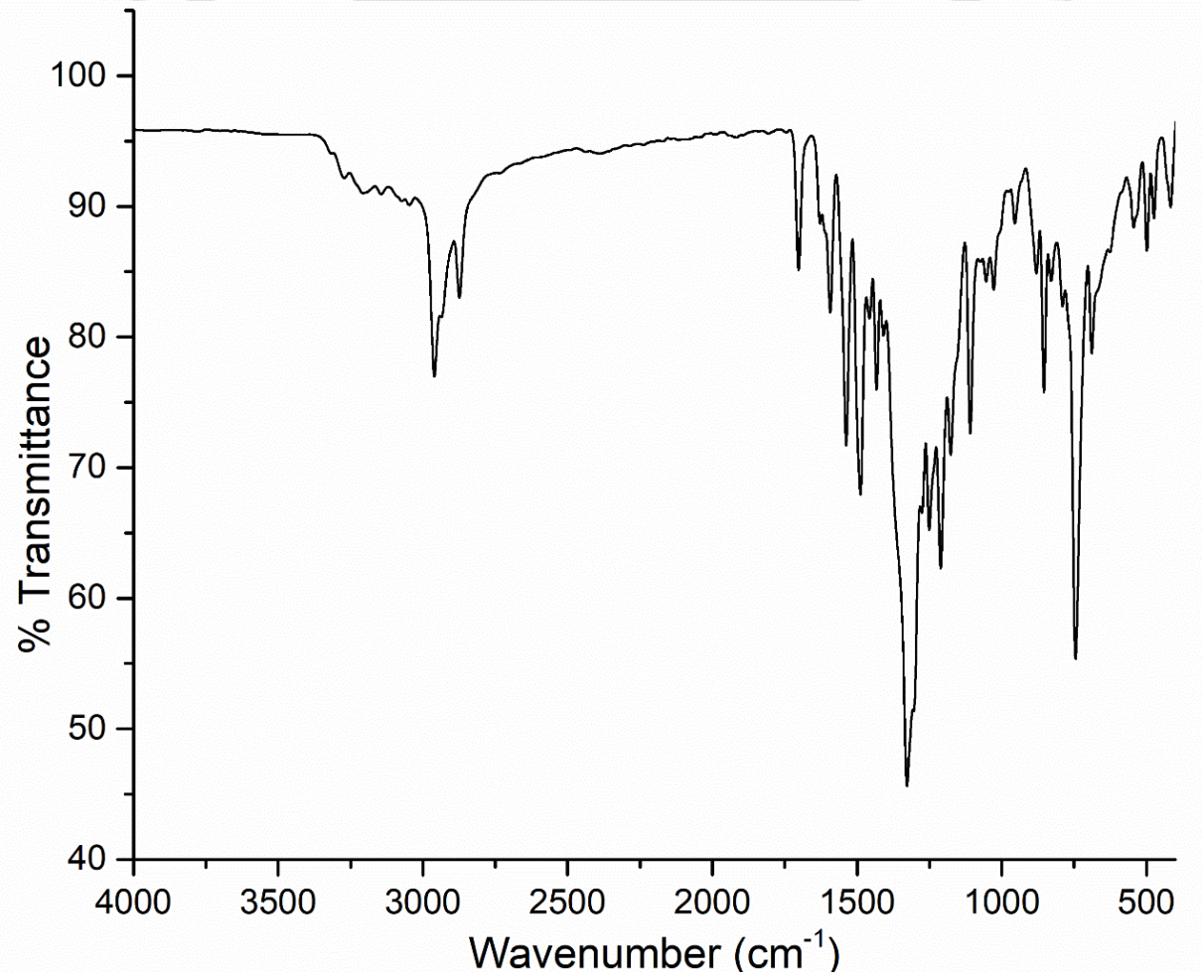

Figure A2.34: FT-IR spectra of complex 1d.

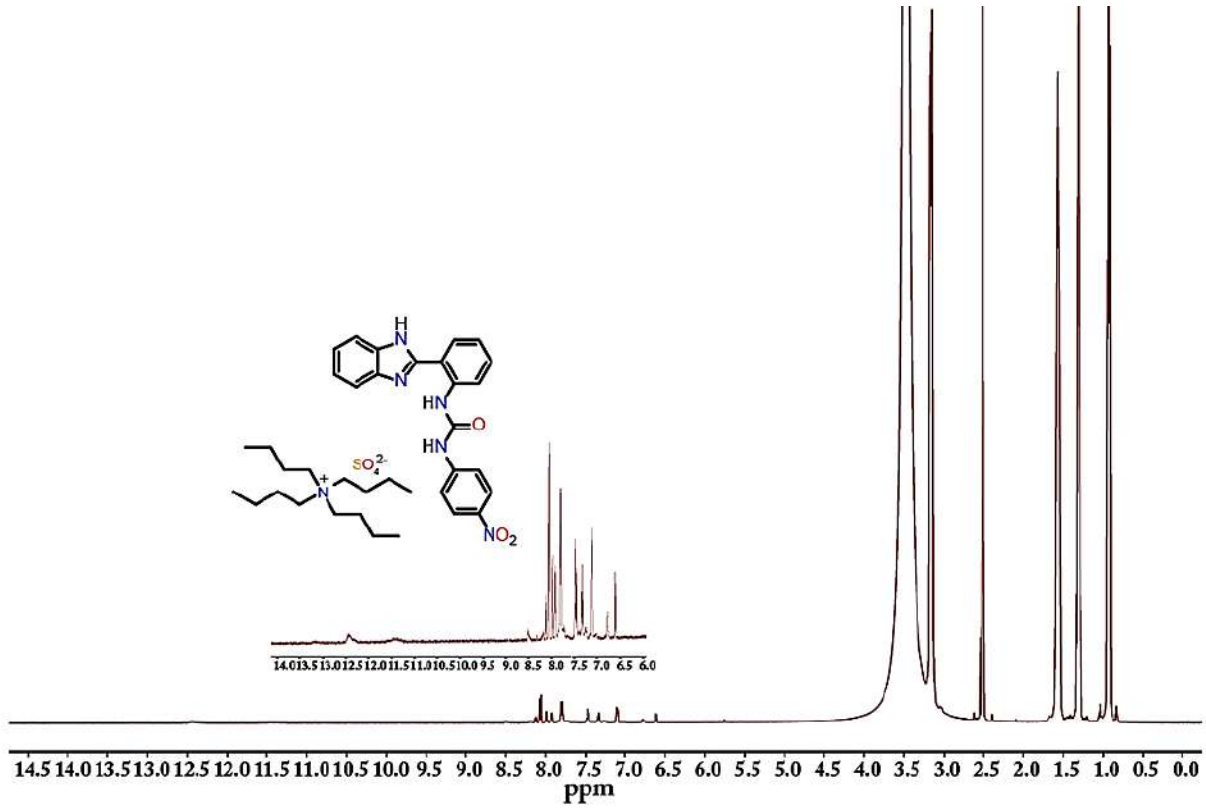

Figure A2.35: ^{1}H NMR of complex 1e.

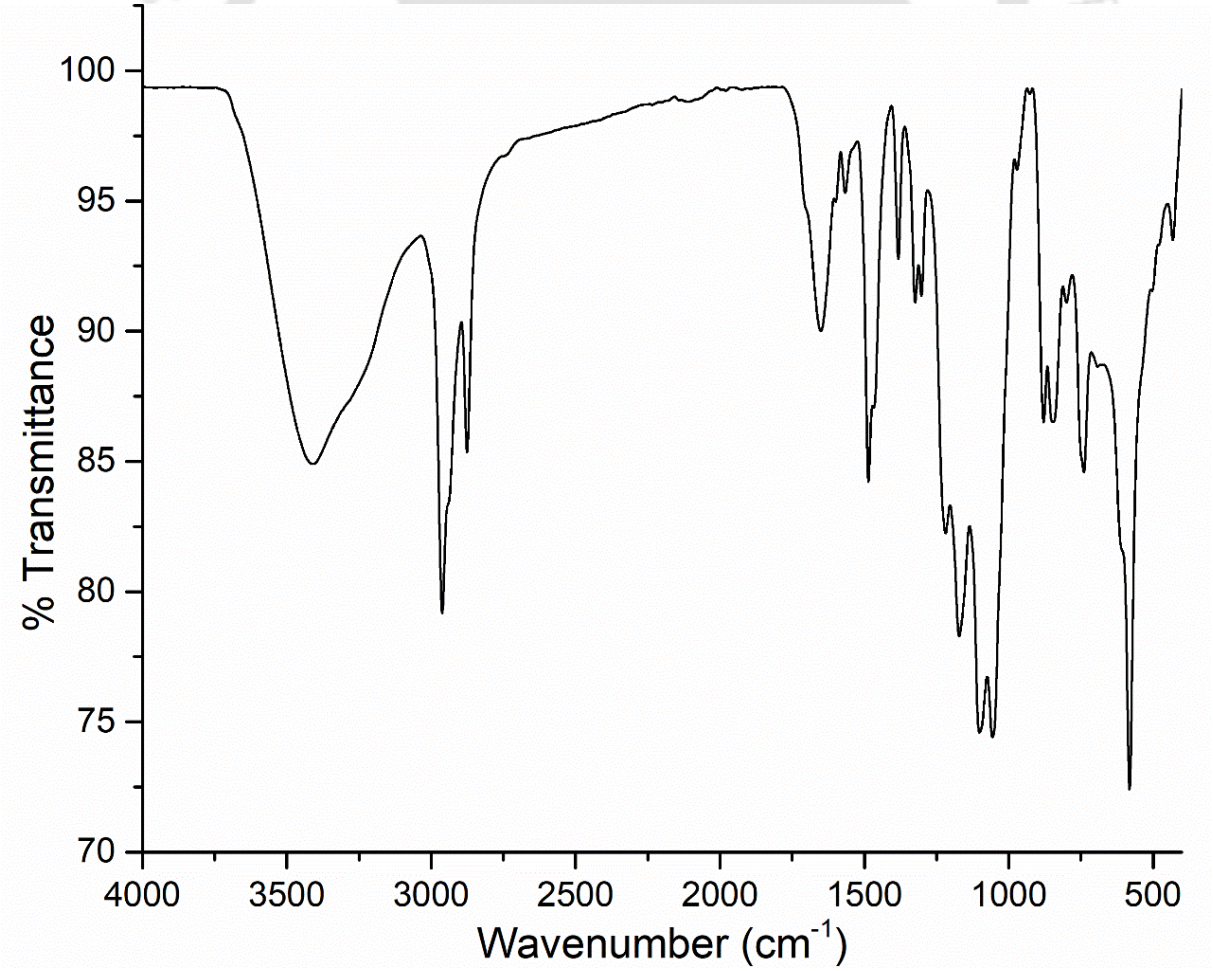

Figure A2.36: FT-IR spectra of complex 1e.

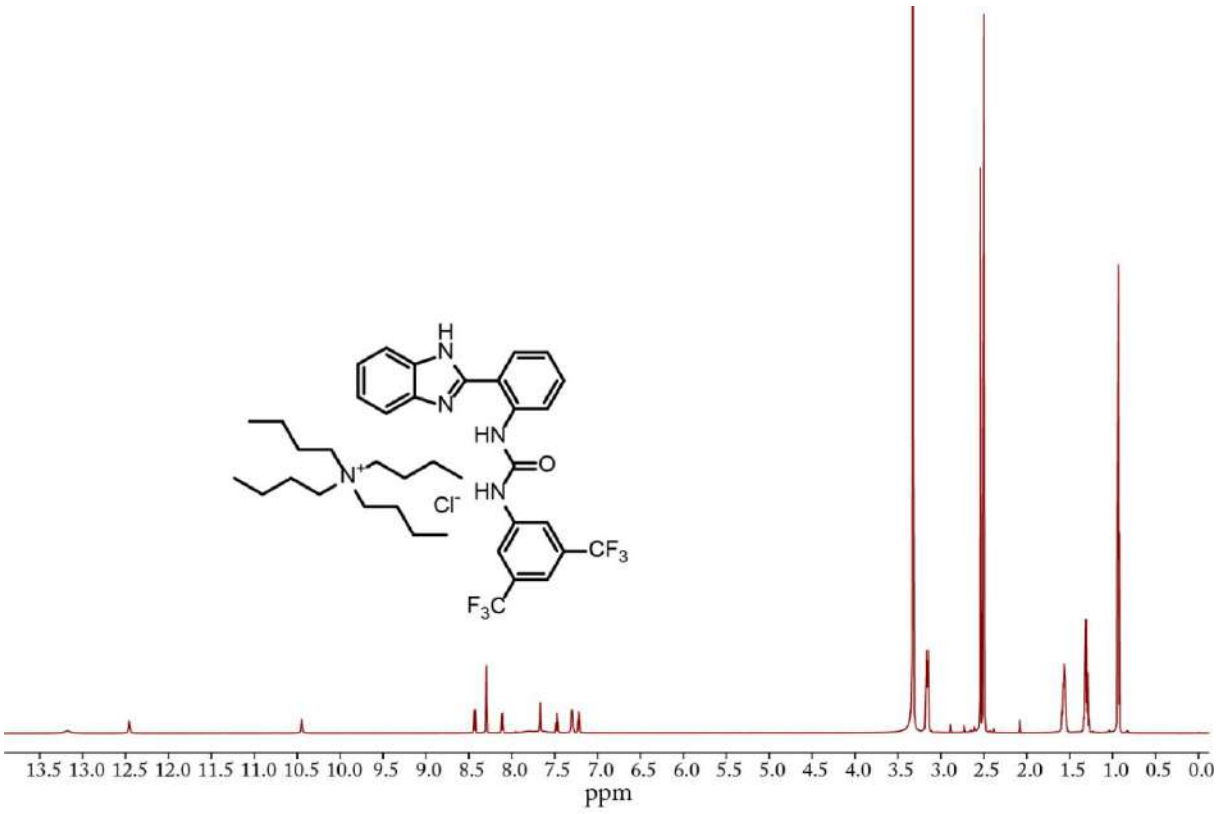

Figure A2.37: ^{1}H NMR of complex 2a.

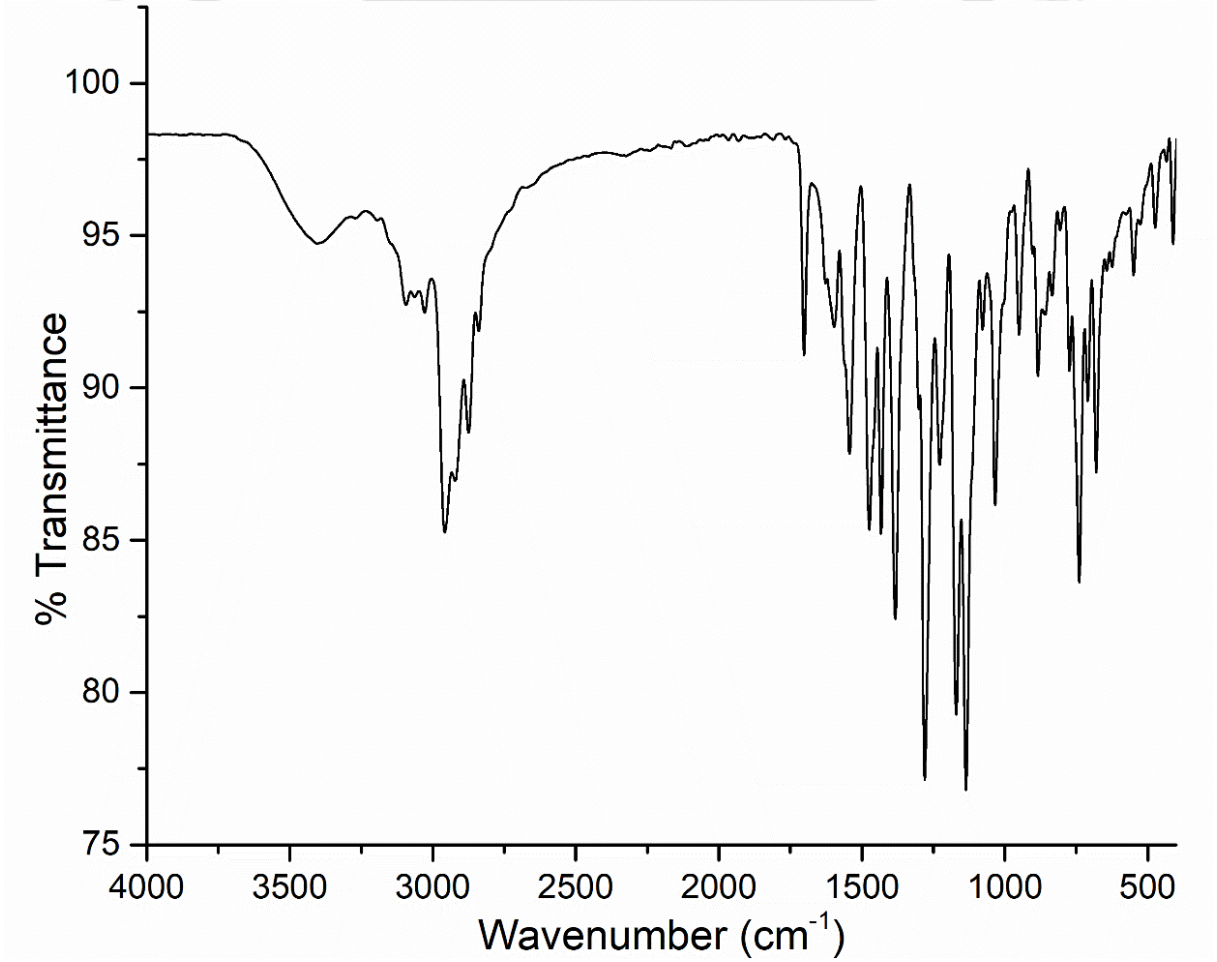

Figure A2.38: FT-IR spectra of complex 2a.

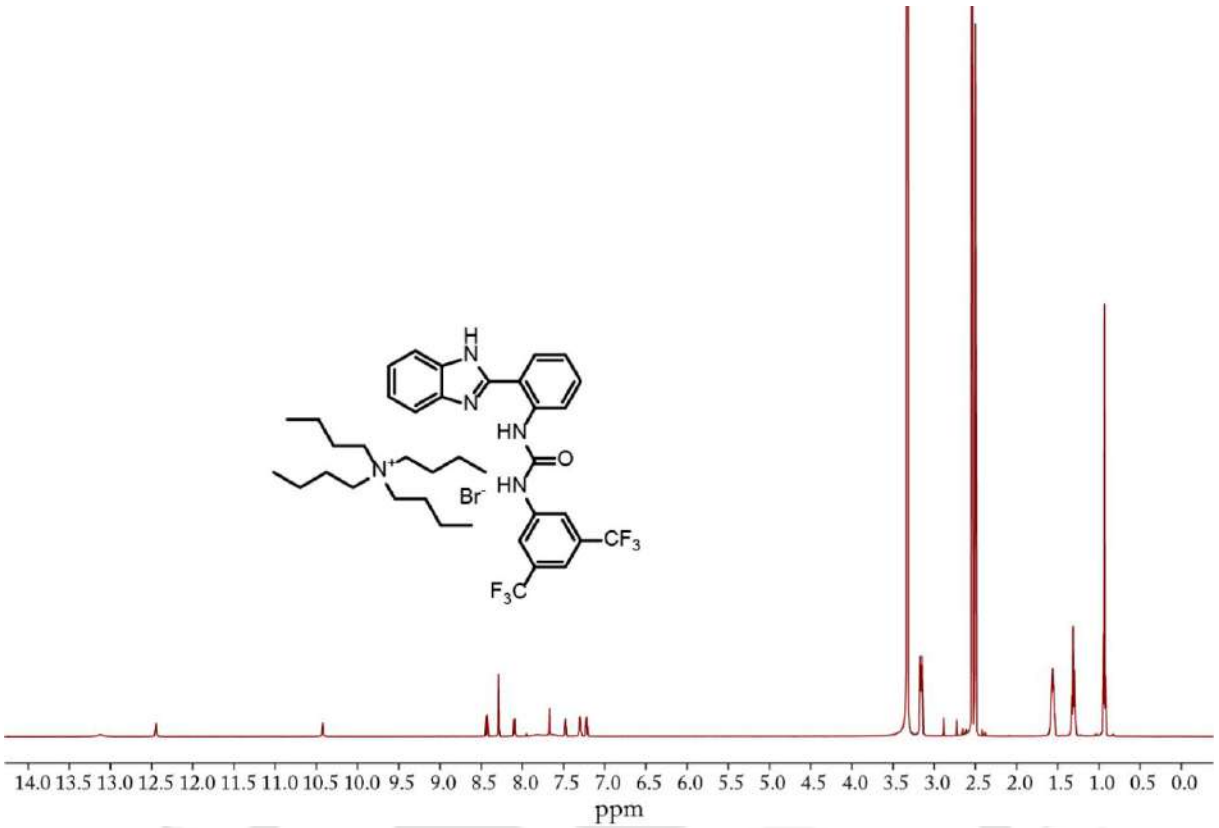

Figure A2.39: ^{1}H NMR of complex 2b.

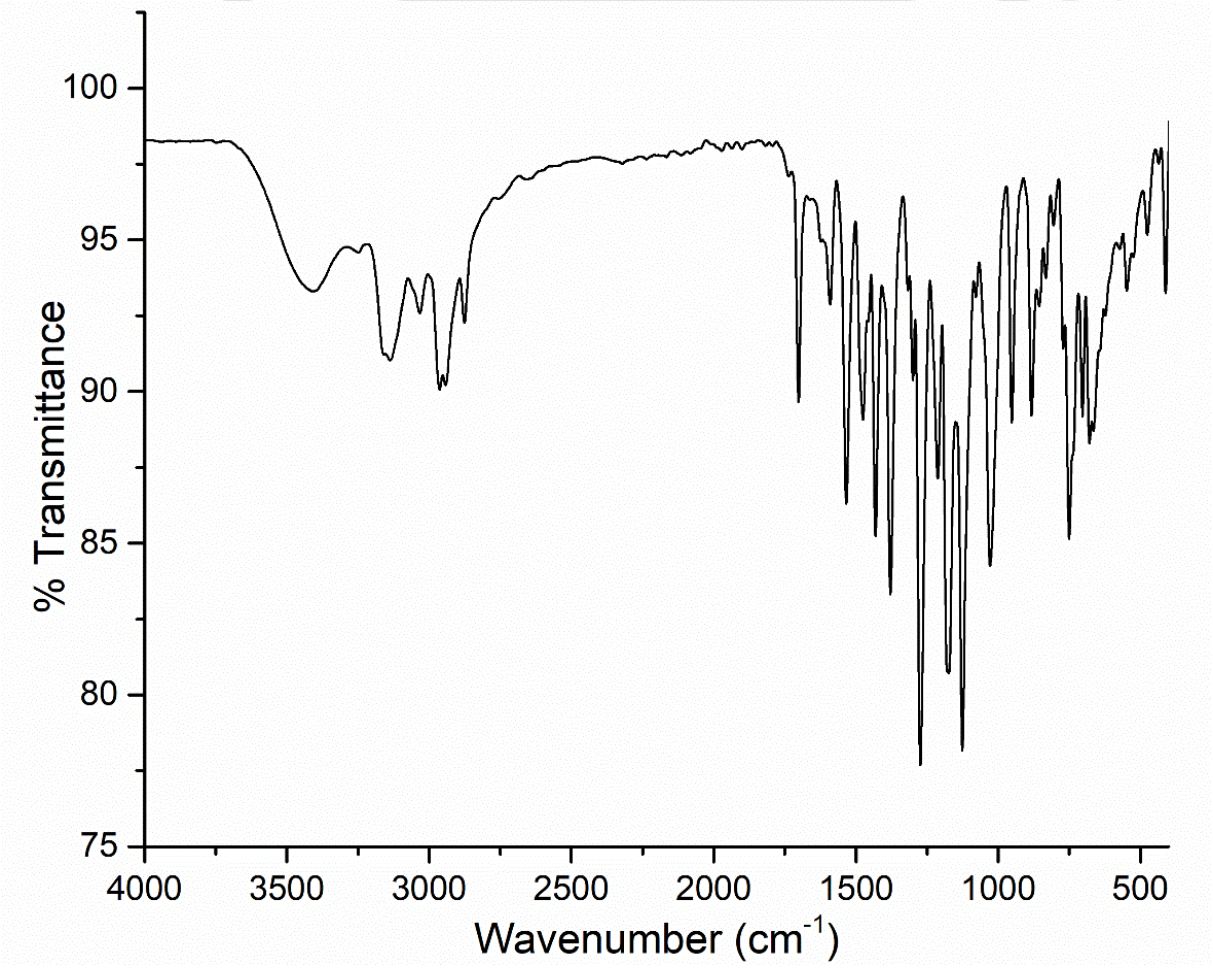

Figure A2.40: FT-IR spectra of complex 2b.

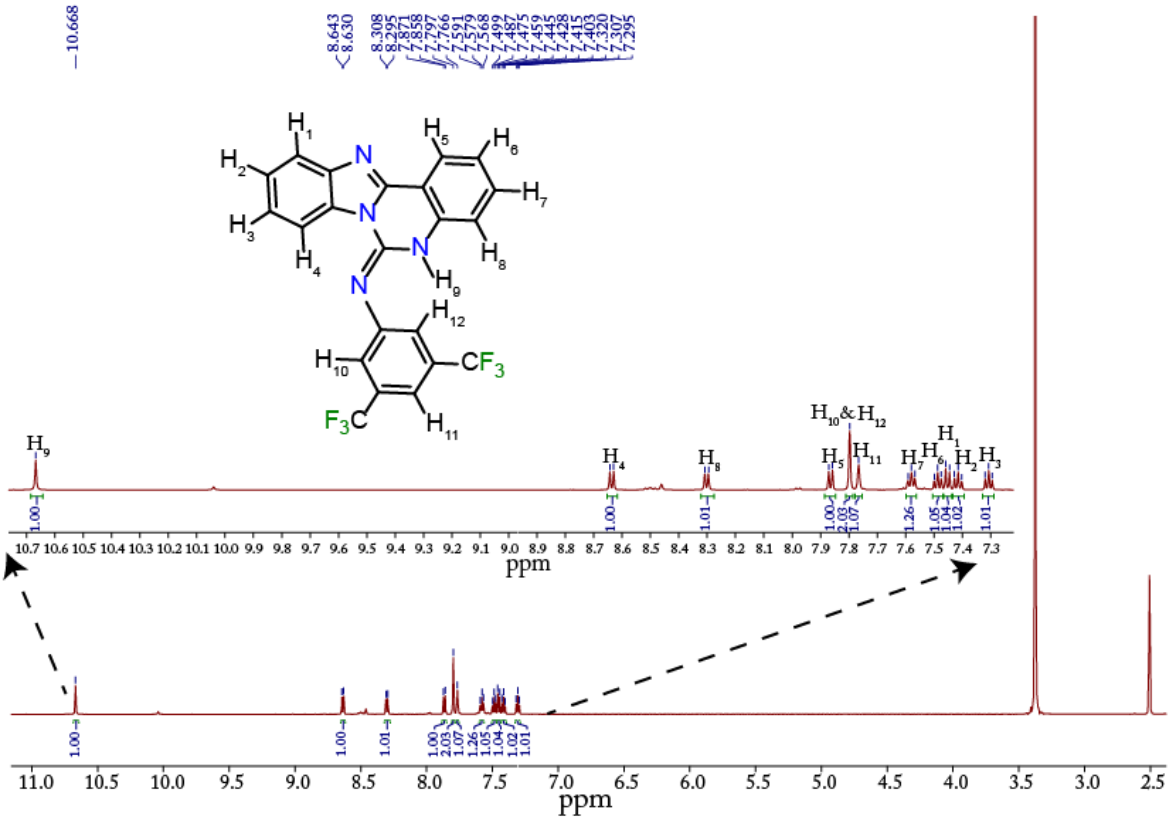

Figure A2.41: ^{1}H NMR spectrum of Benz-d-CF_3 in DMSO-d_6.

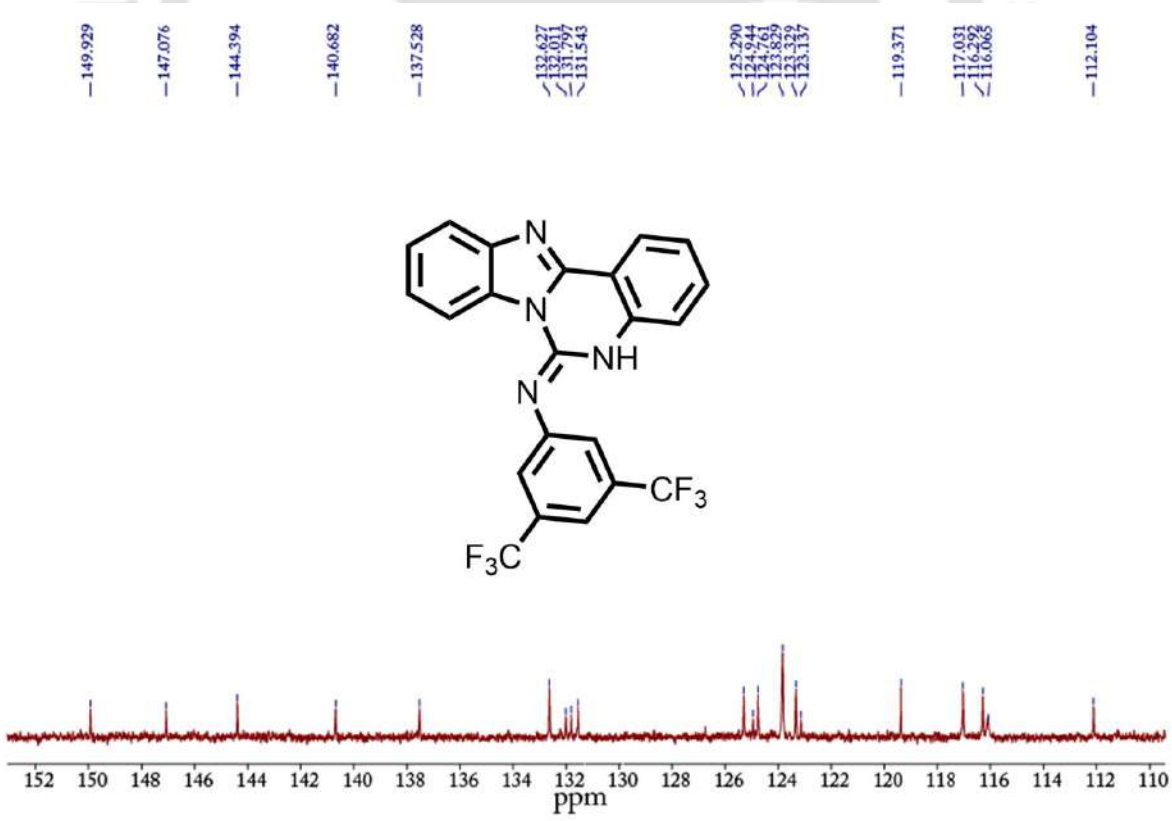

Figure A2.42: ^{13}C NMR spectrum of Benz-d-CF_3 in DMSO-d_6.

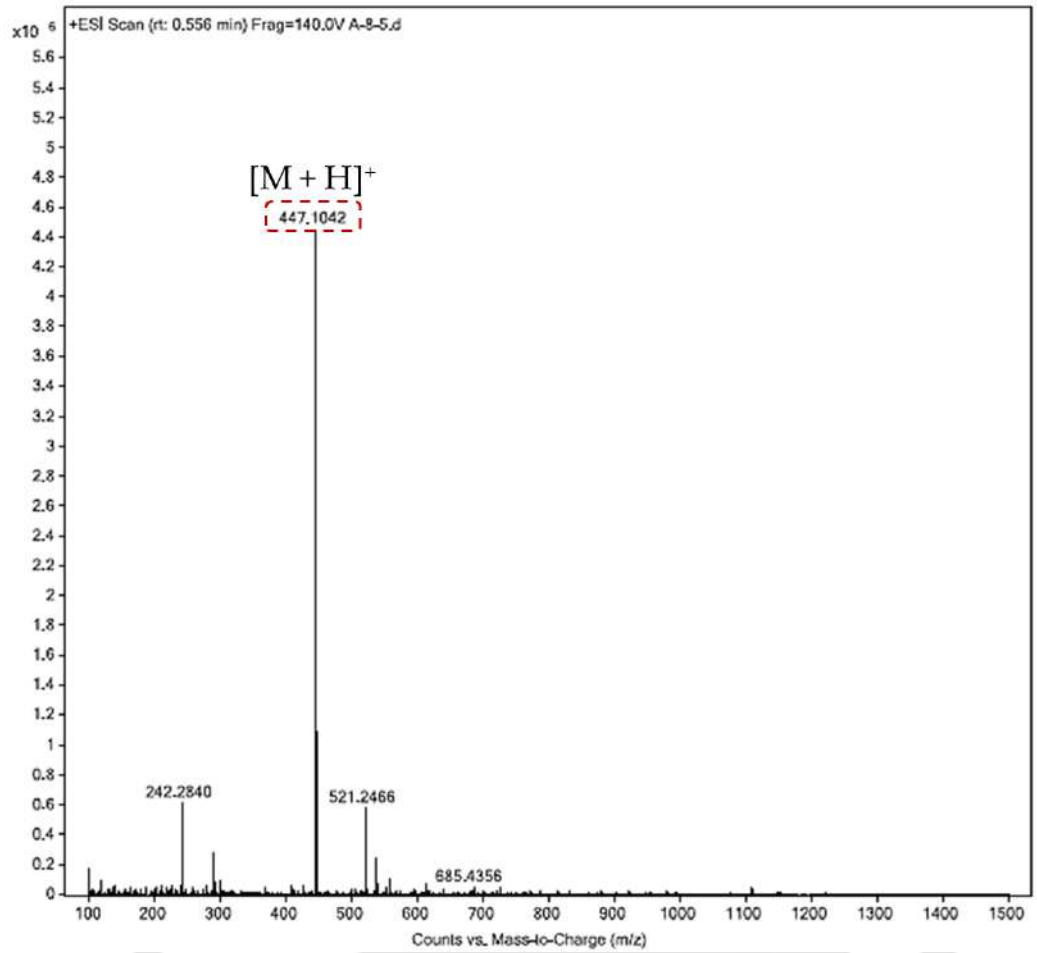

Figure A2.43: HRMS of Benz-d-CF_3.

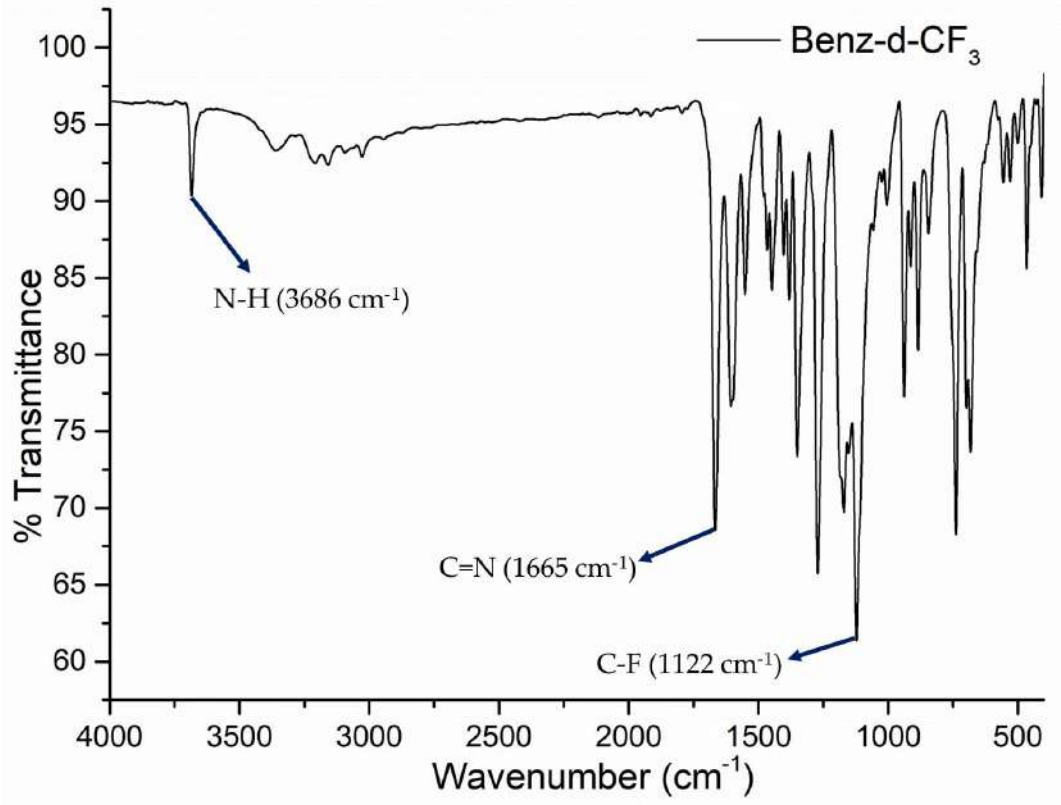

Figure A2.44: FTIR spectra of Benz-d-CF_3.

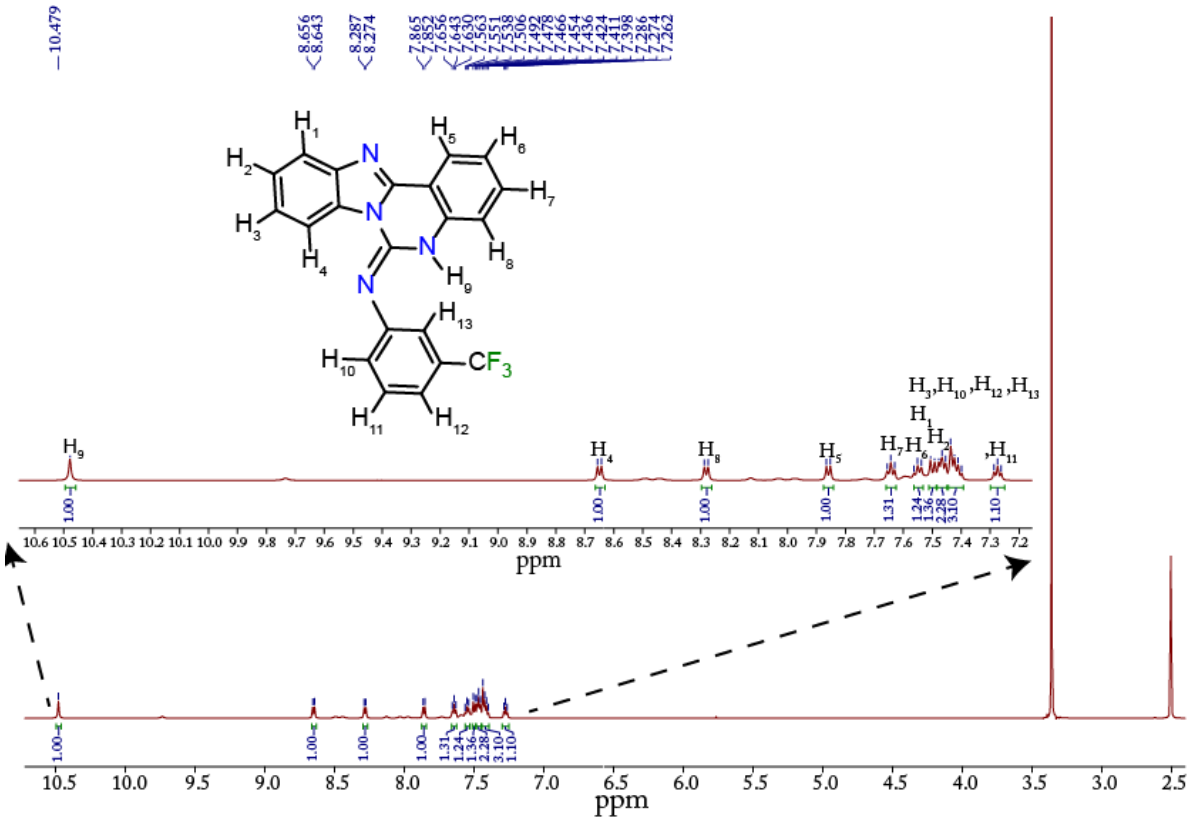

Figure A2.45: ^{1}H NMR spectrum of Benz-m-CF_3 in DMSO-d_6.

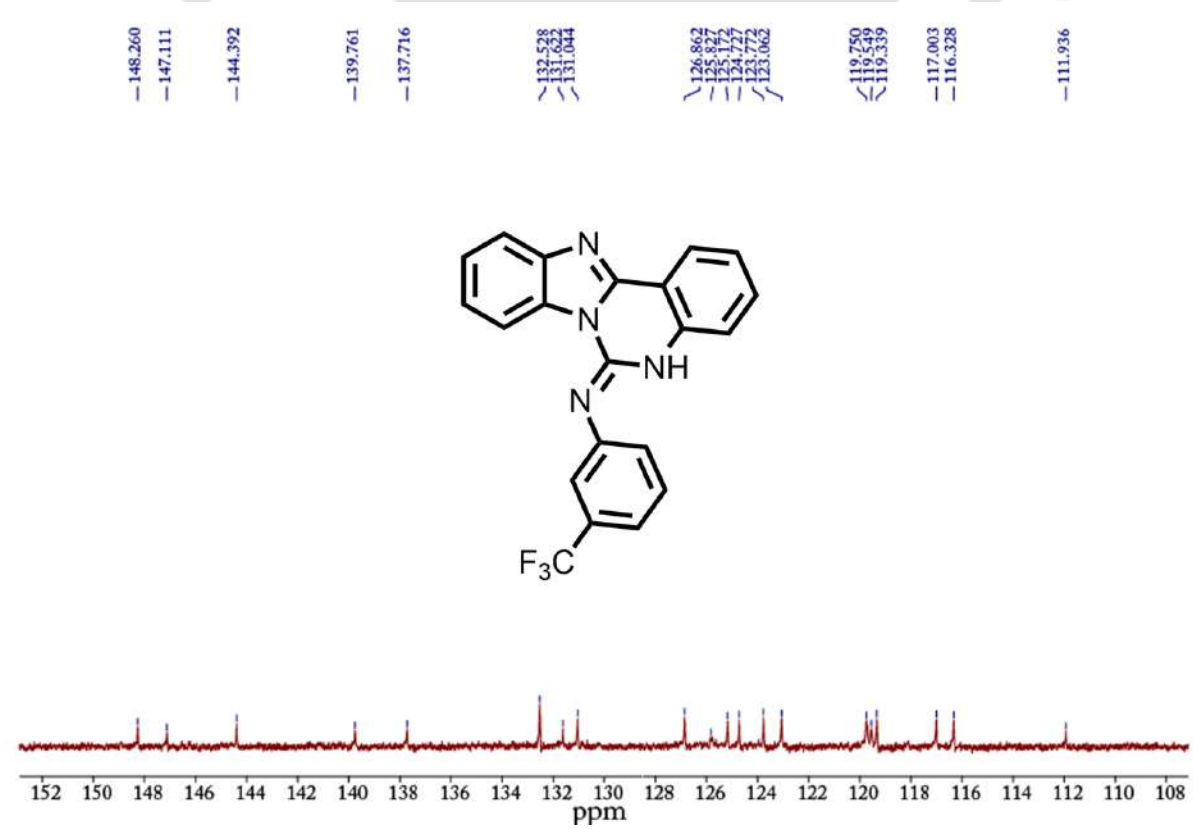

Figure A2.46: ^{13}C NMR spectrum of Benz-m-CF_3 in DMSO-d_6.

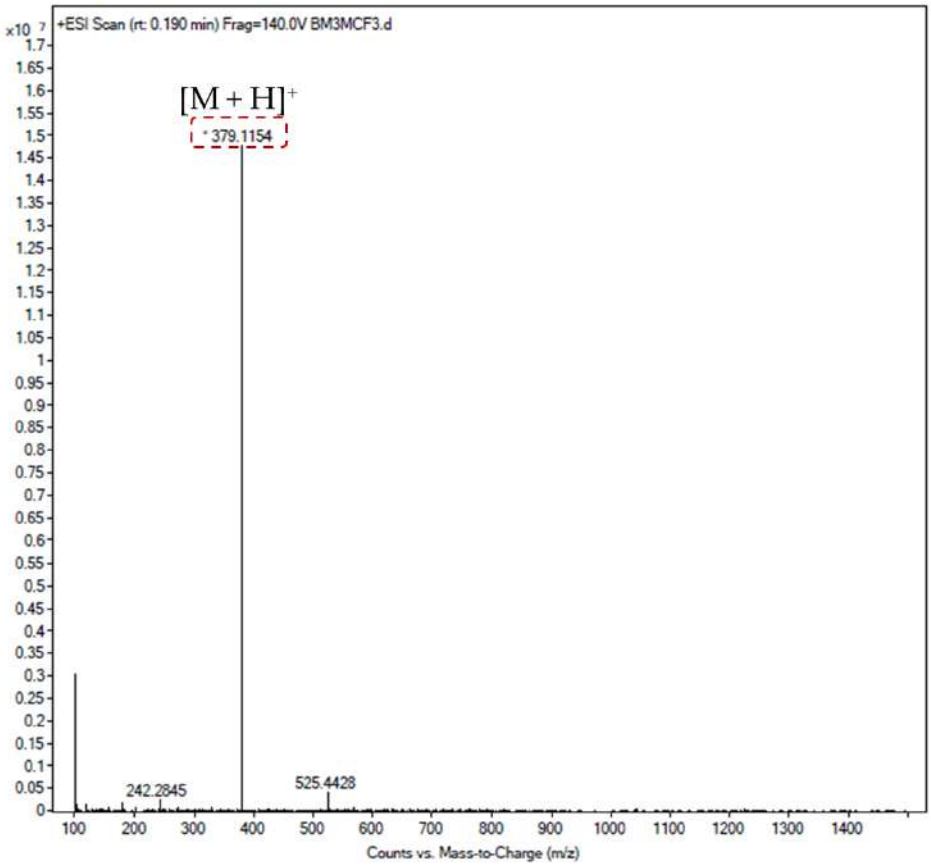

Figure A2.47: HRMS of Benz-m-CF_3.

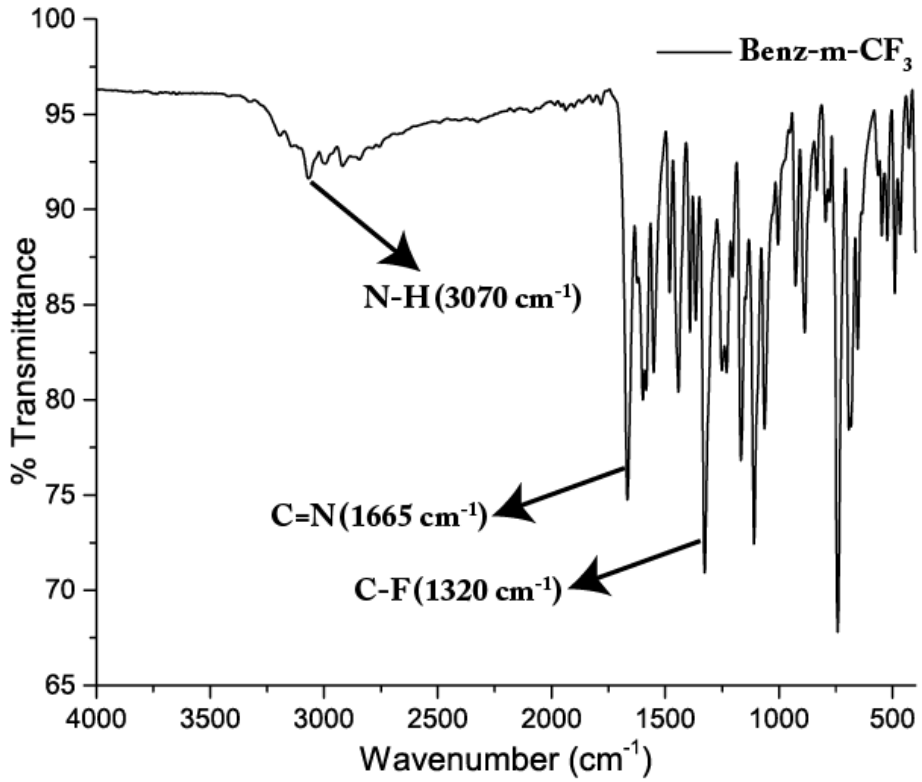

Figure A2.48: FTIR spectra of Benz-m-CF_3.

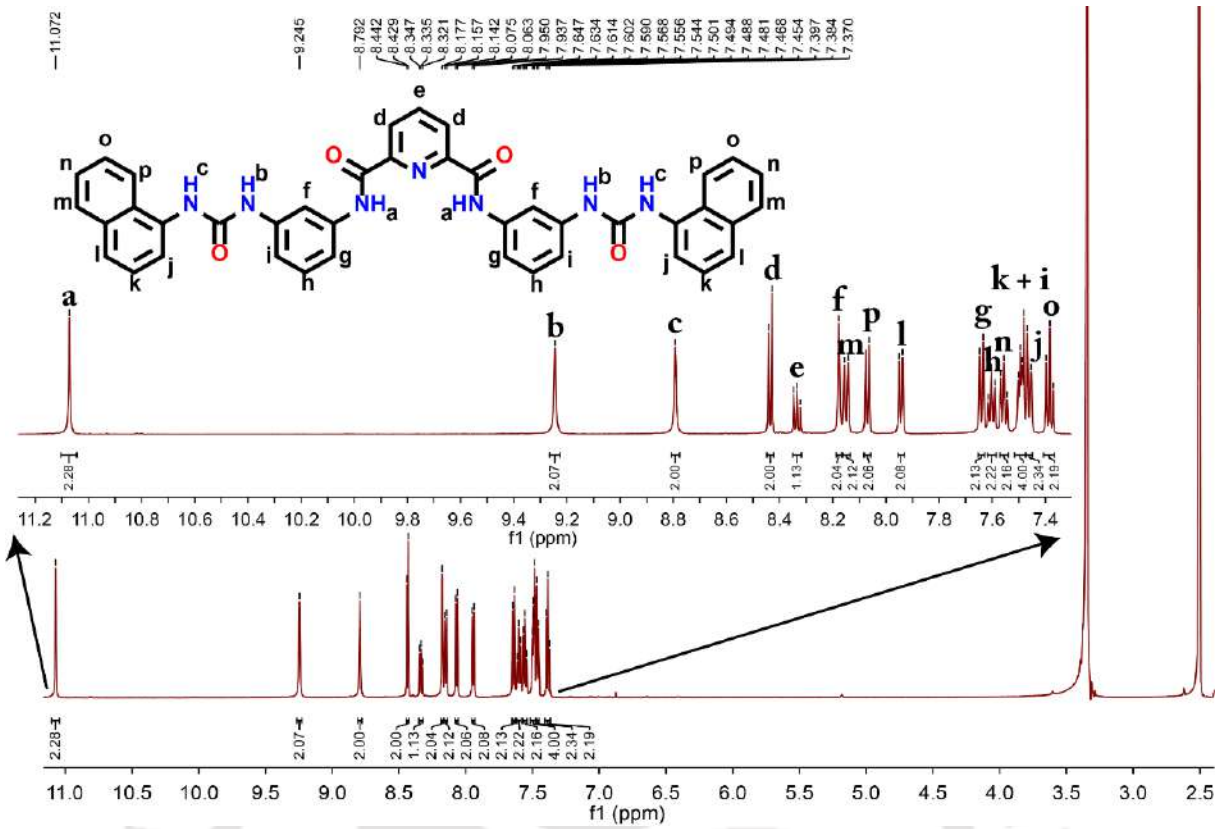

Figure A2.49: ^{1}H NMR spectrum of PY-NAP in DMSO-d_6.

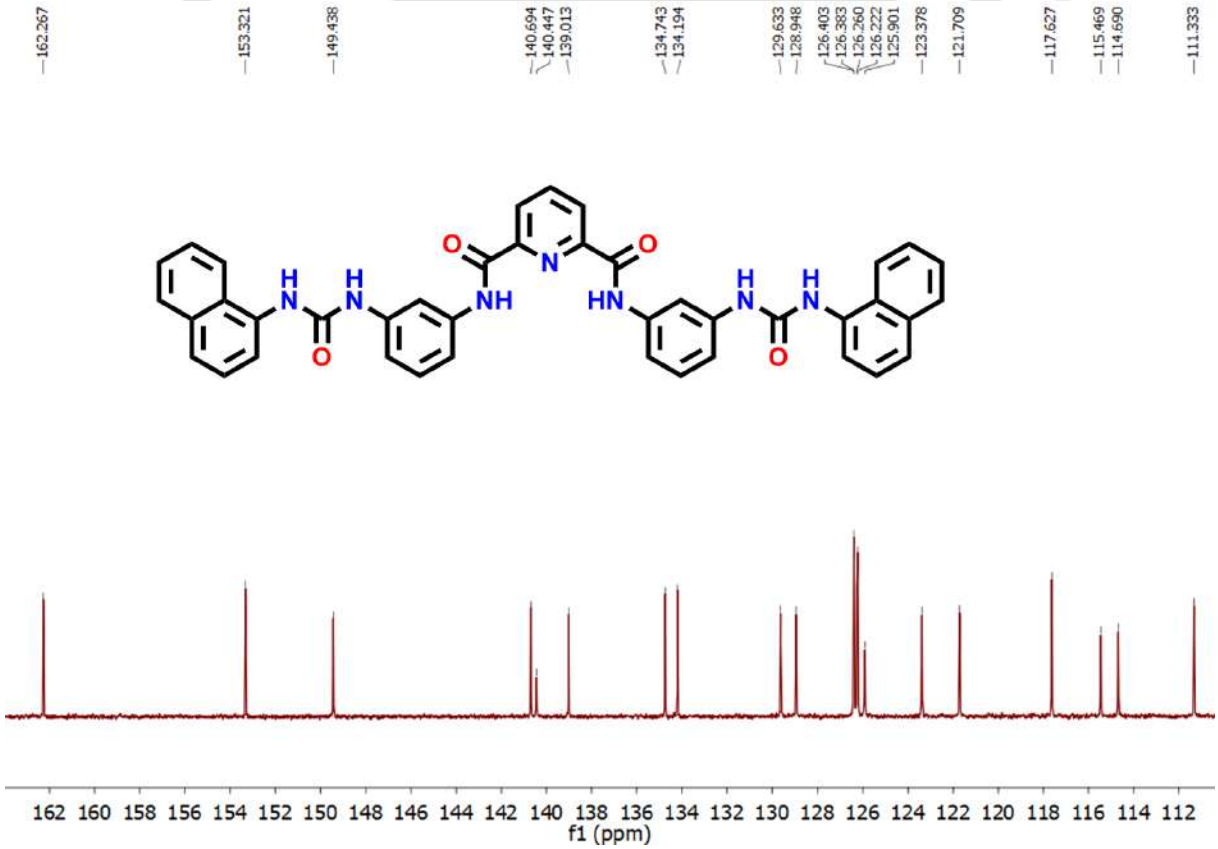

Figure A2.50: ^{13}C NMR spectrum of PY-NAP in DMSO-d_6.

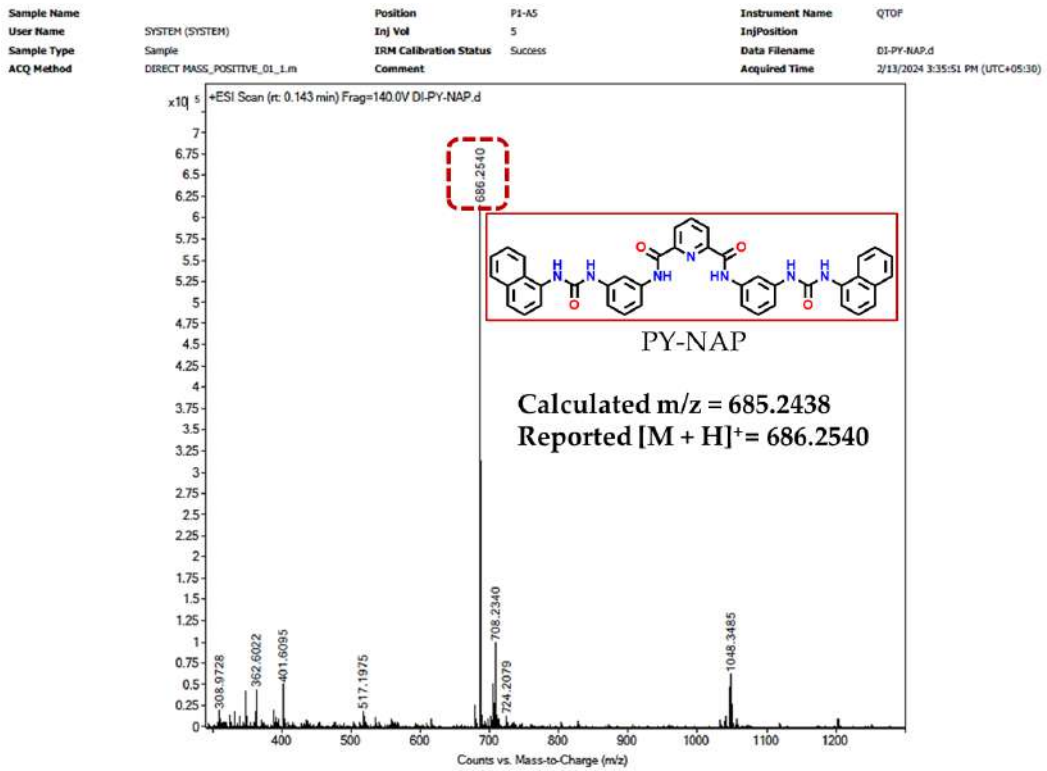

Figure A2.51: HRMS of PY-NAP.

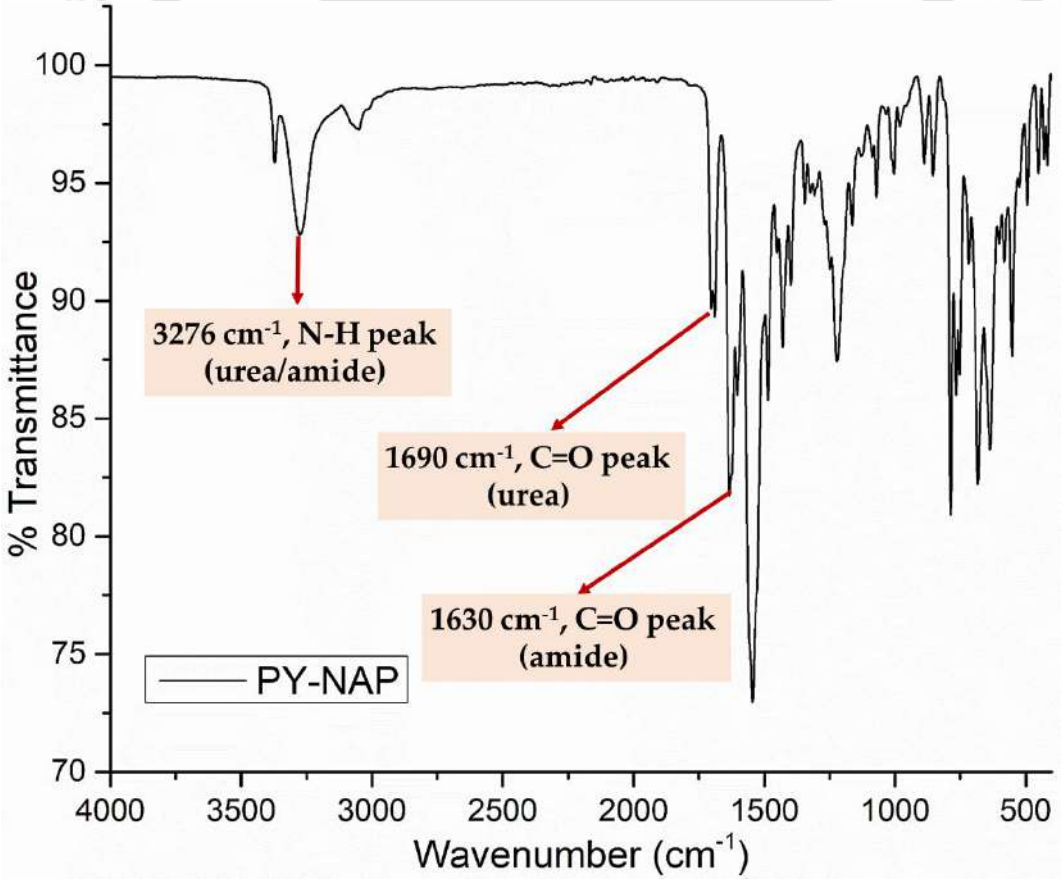

Figure A2.52: FTIR spectrum of PY-NAP.

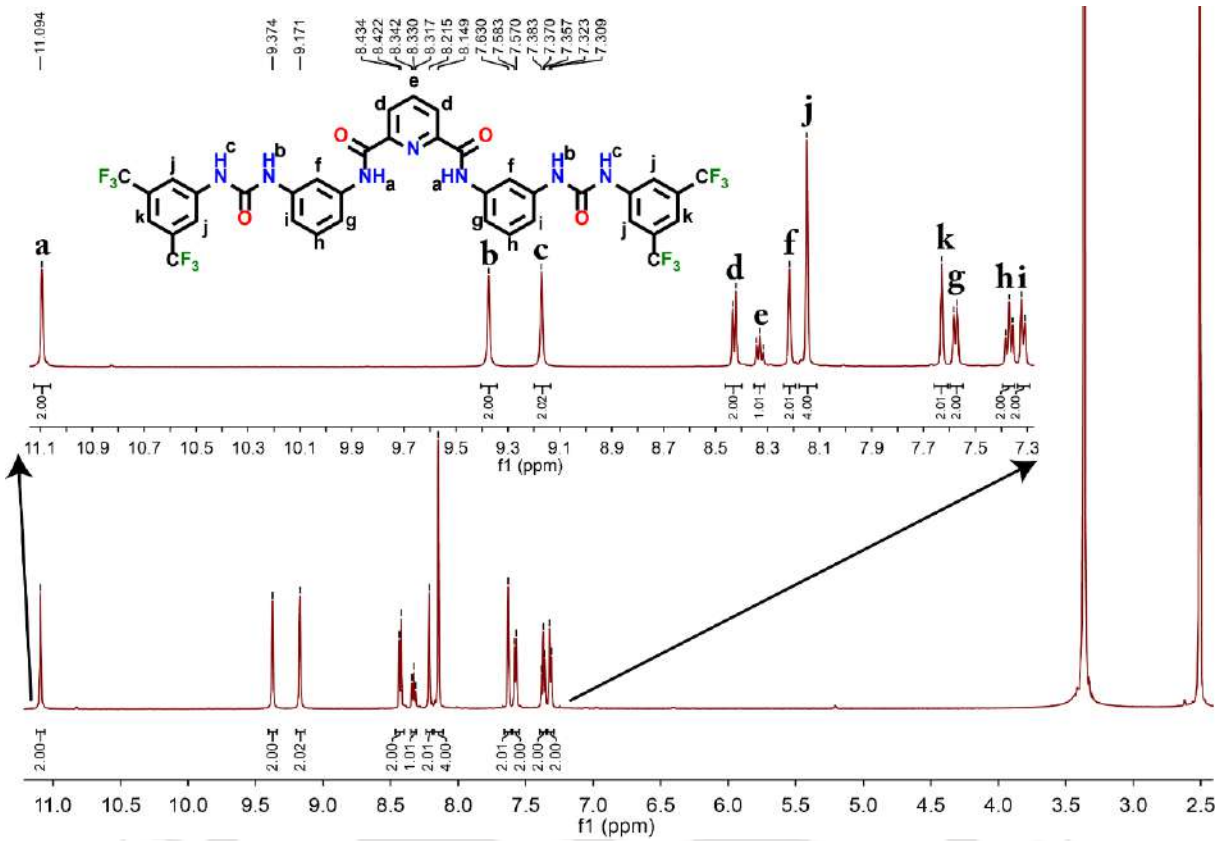

Figure A2.53: ^{1}H NMR spectrum of PY-CF_3 in DMSO-d_6.

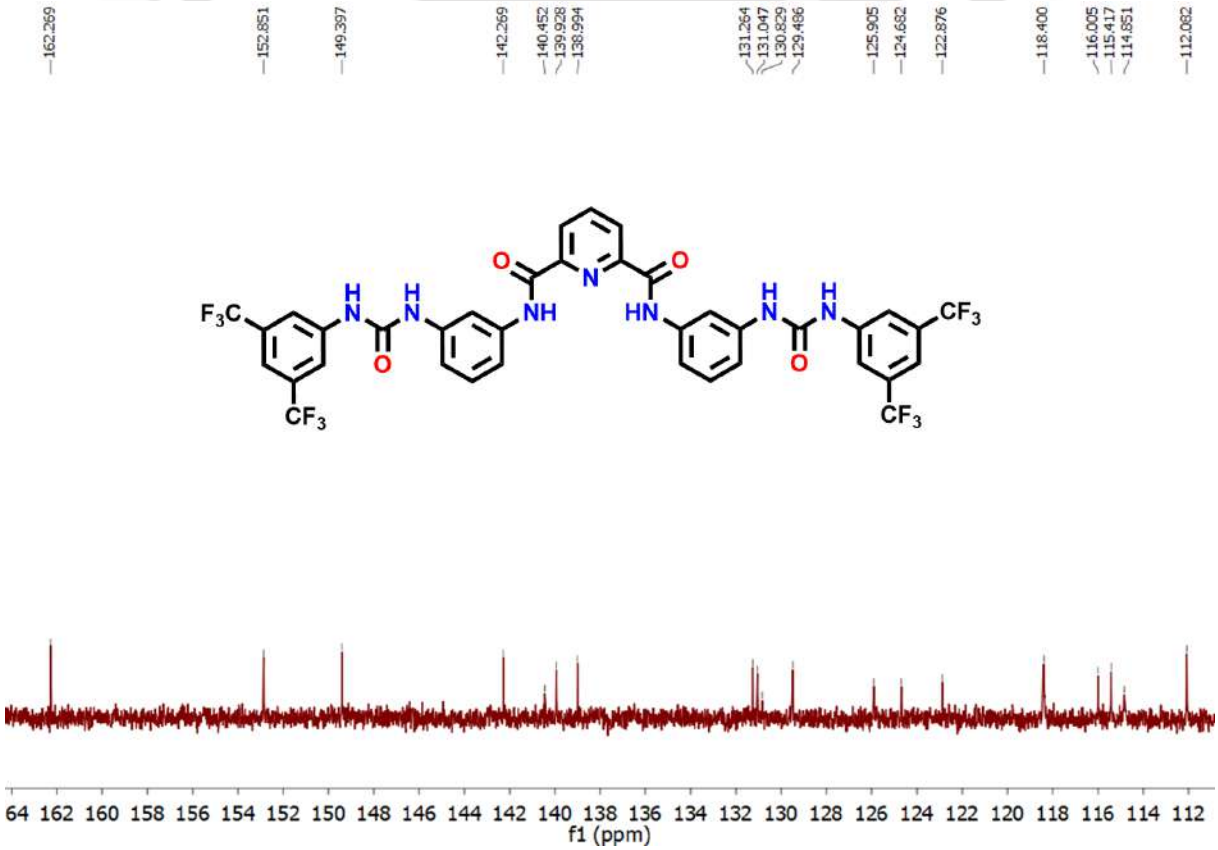

Figure A2.54: ^{13}C NMR spectrum of PY-CF_3 in DMSO-d_6.

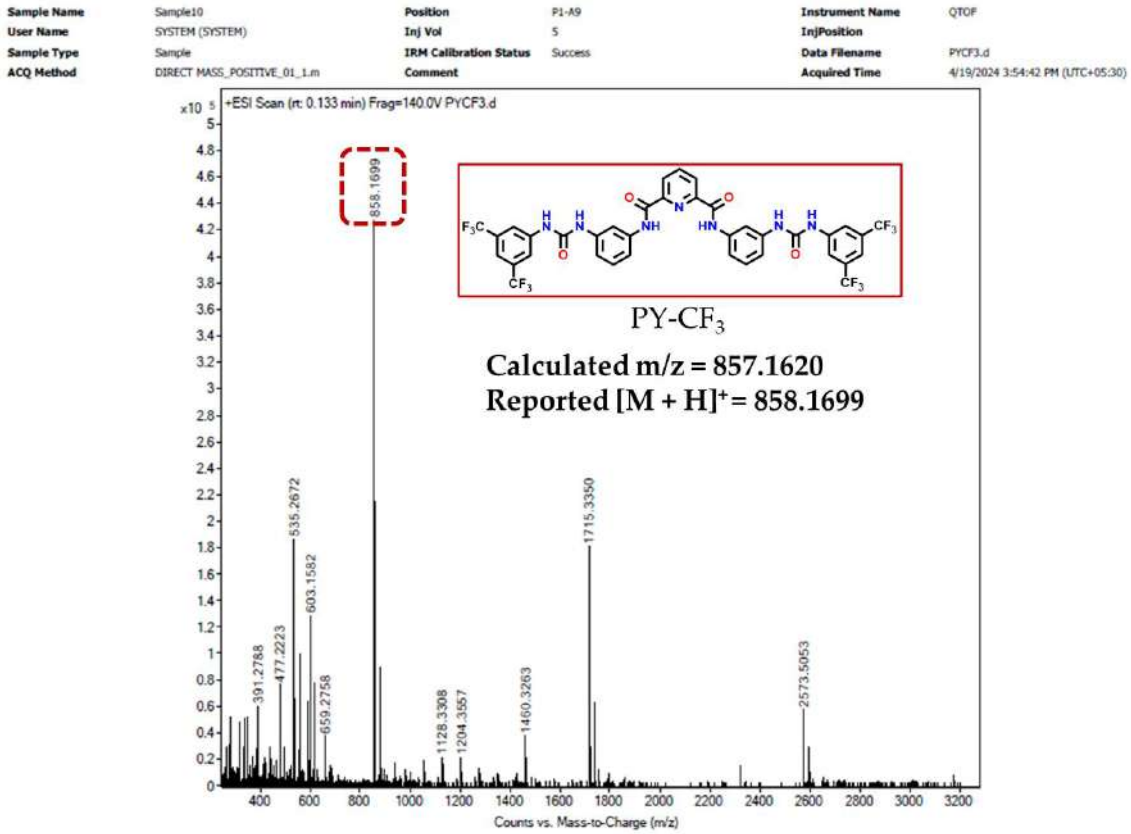

Figure A2.55: HRMS of PY-CF_3.

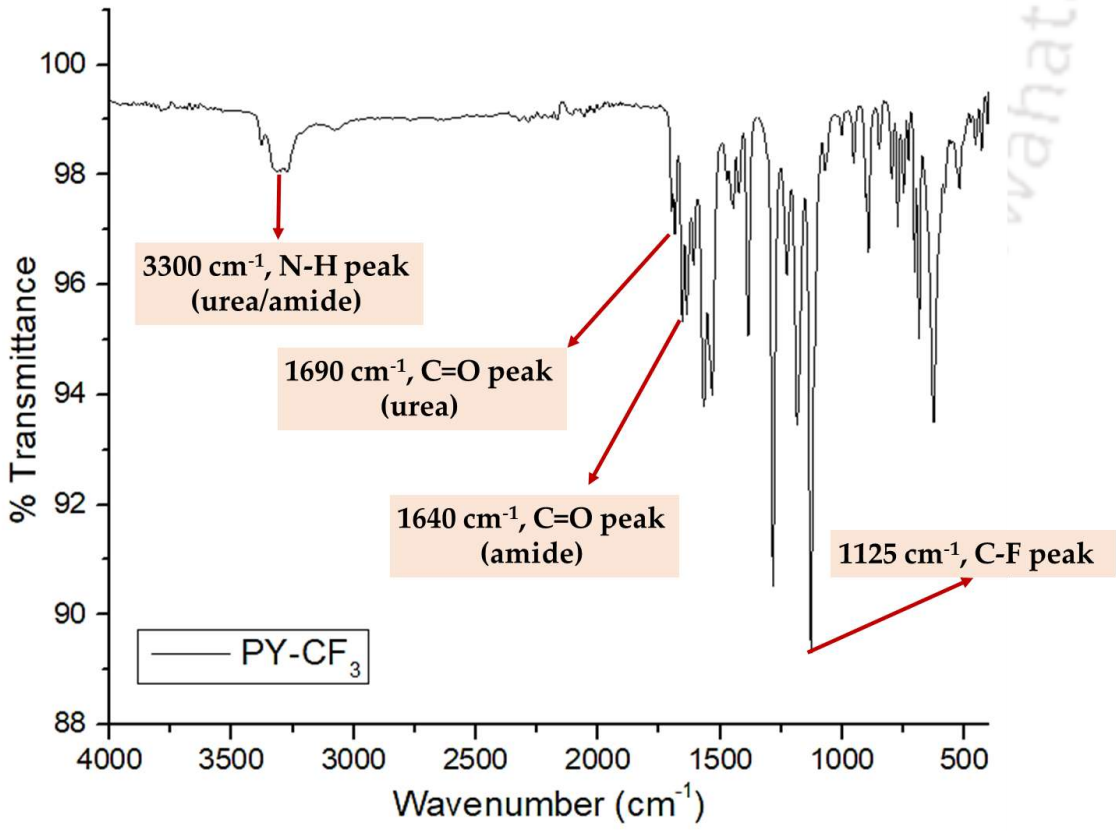

Figure A2.56: FTIR spectrum of. PY-CF_3.

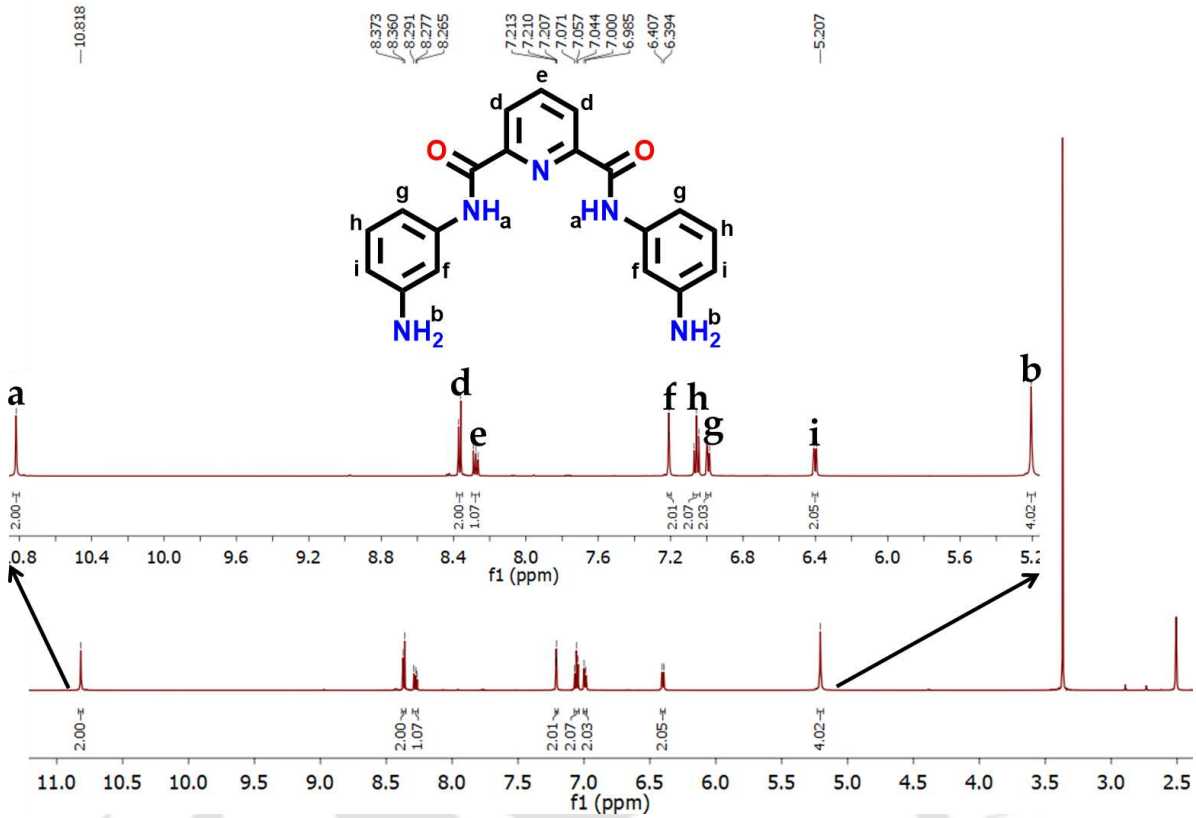

Figure A2.57: ^{1}H NMR spectrum of PY-NH_2 in DMSO-d_6.

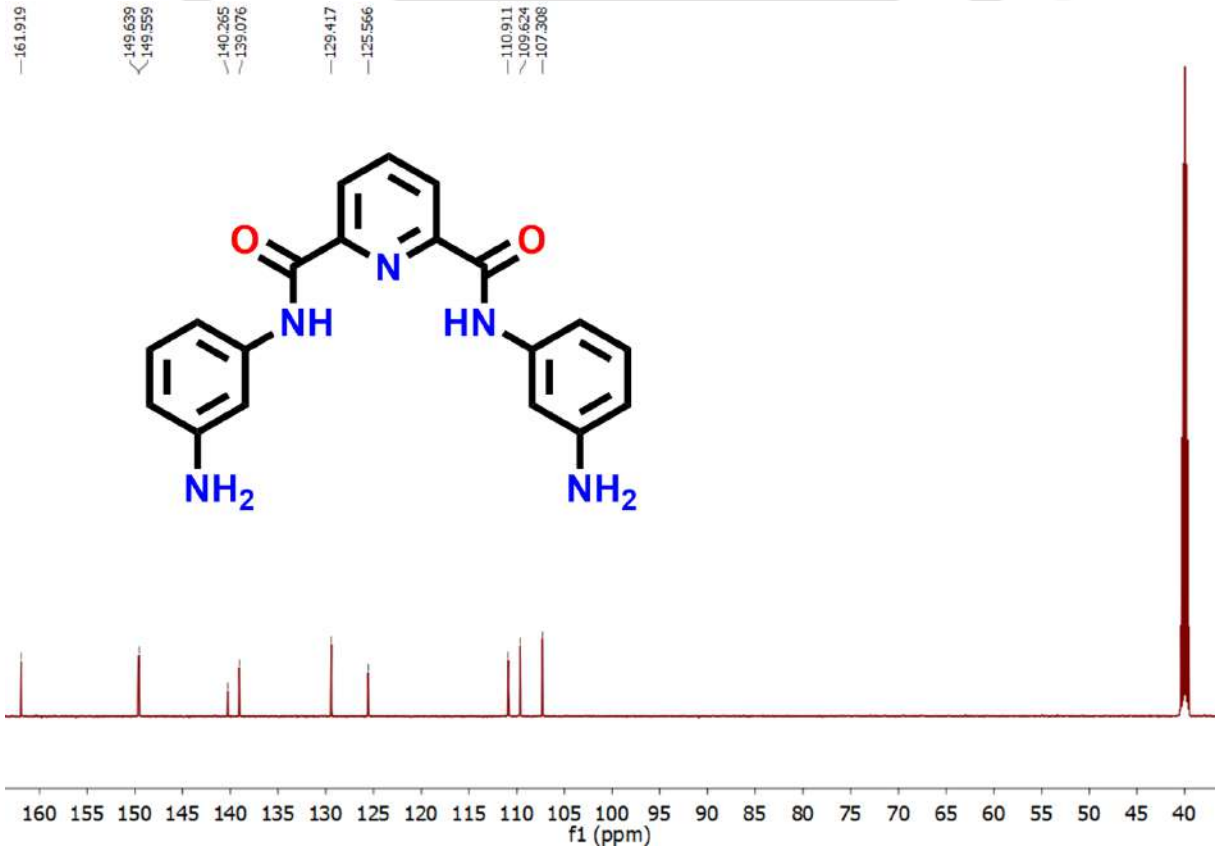

Figure A2.58: ^{13}C NMR spectrum of PY-NH_2 in DMSO-d_6.

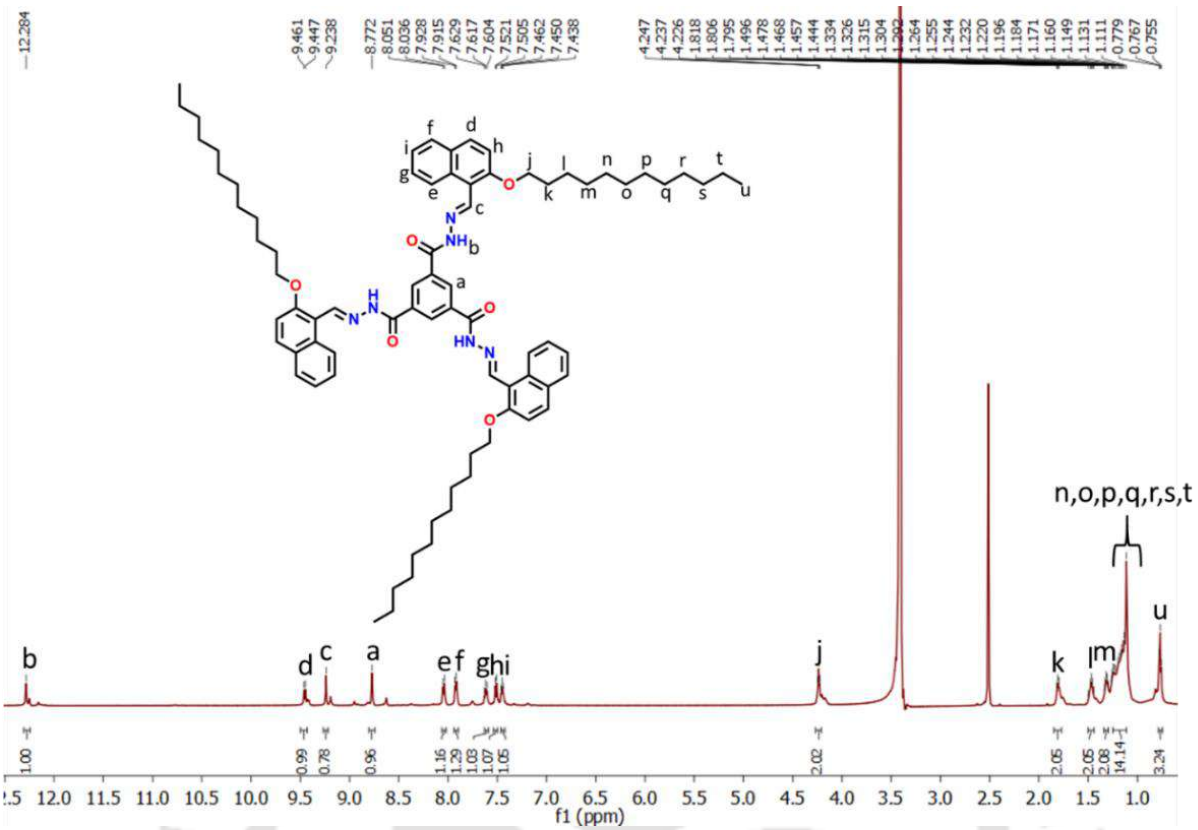

Figure A2.59: ^{1}H NMR spectra of THD in DMSO-d_6.

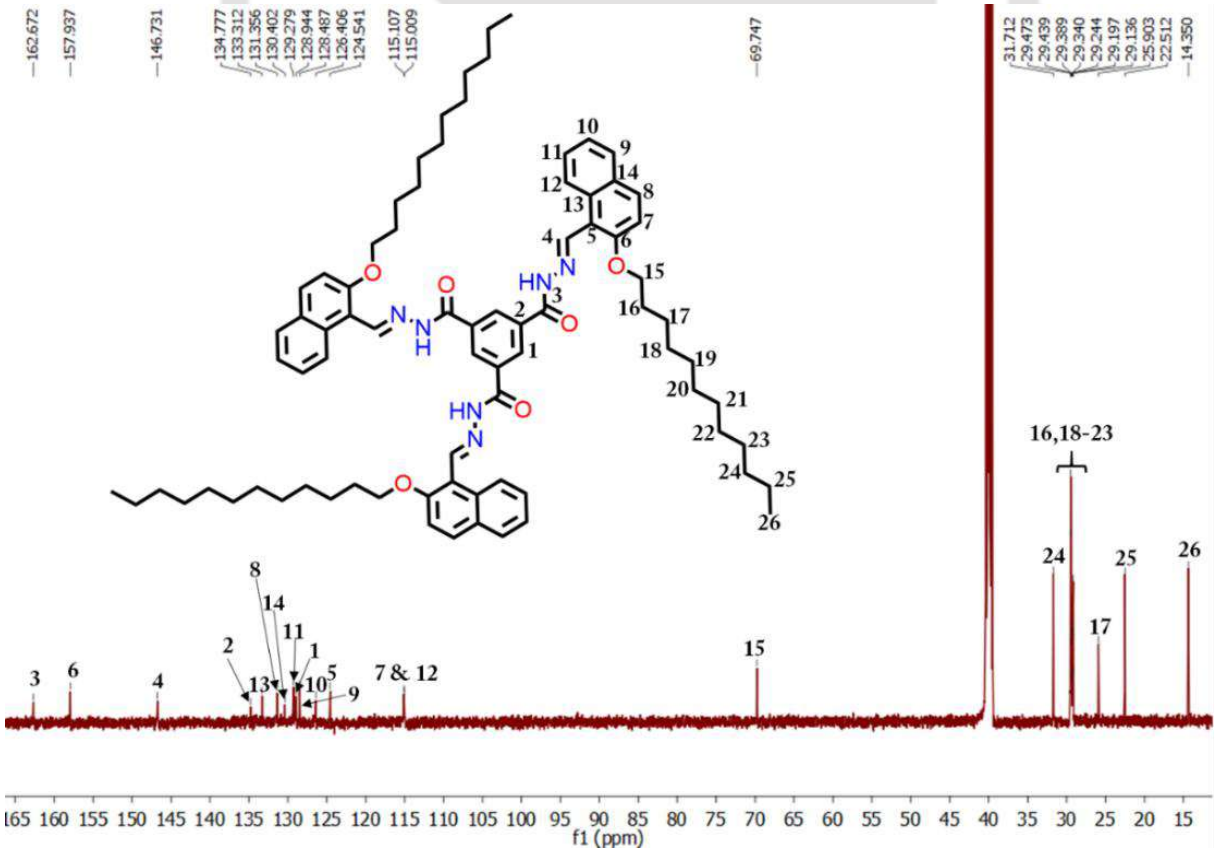

Figure A2.60: ^{13}C NMR spectra of PY-NAP in DMSO-d_6.

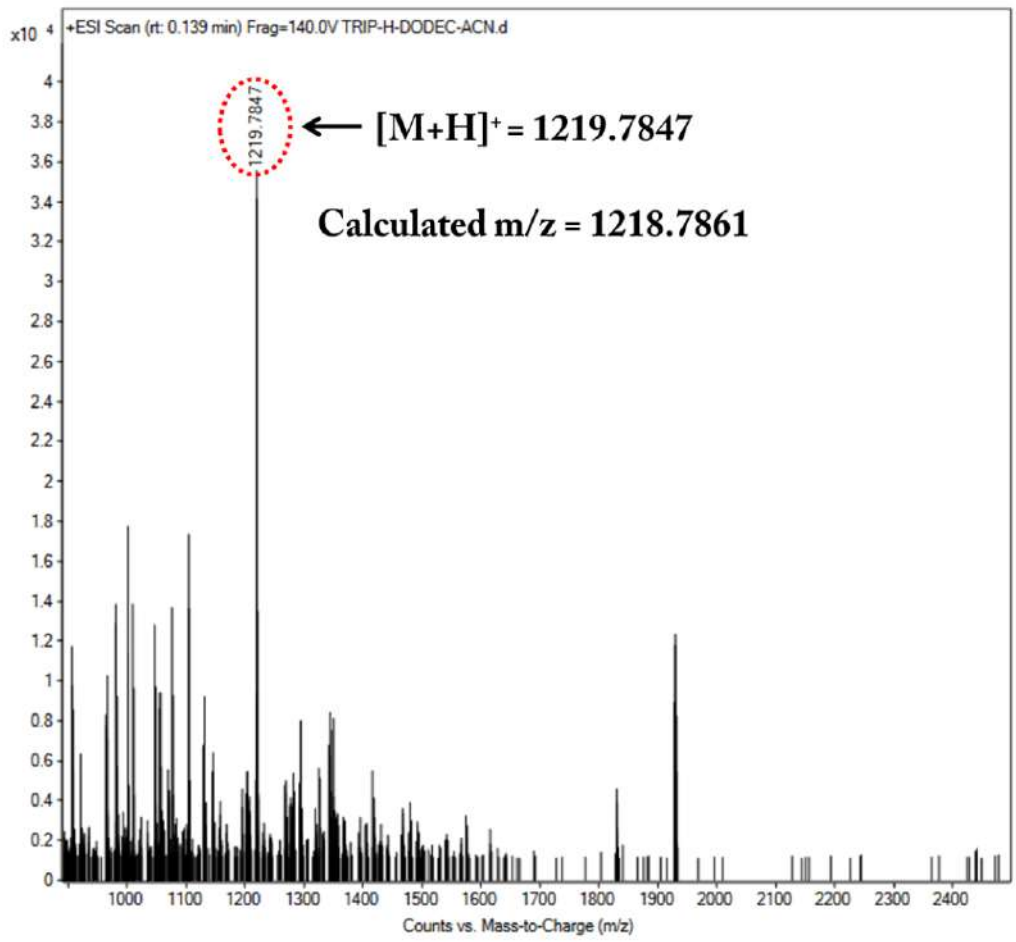

Figure A2.61: HRMS of THD.

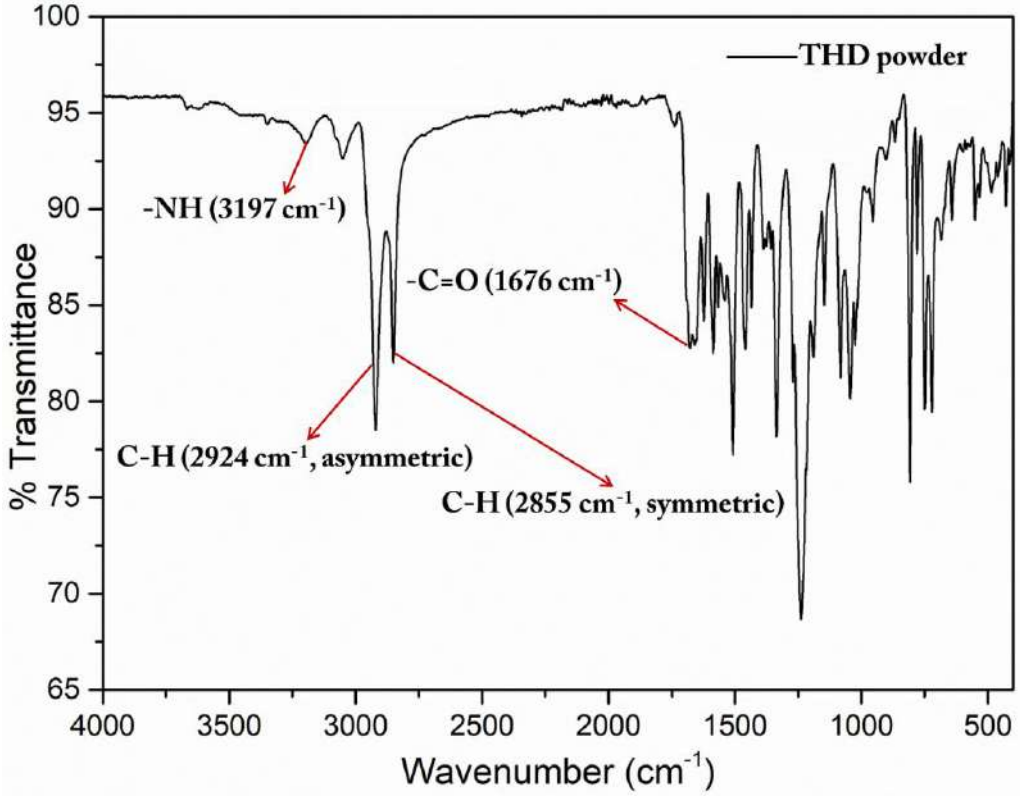

Figure A2.62: FTIR spectra of THD.

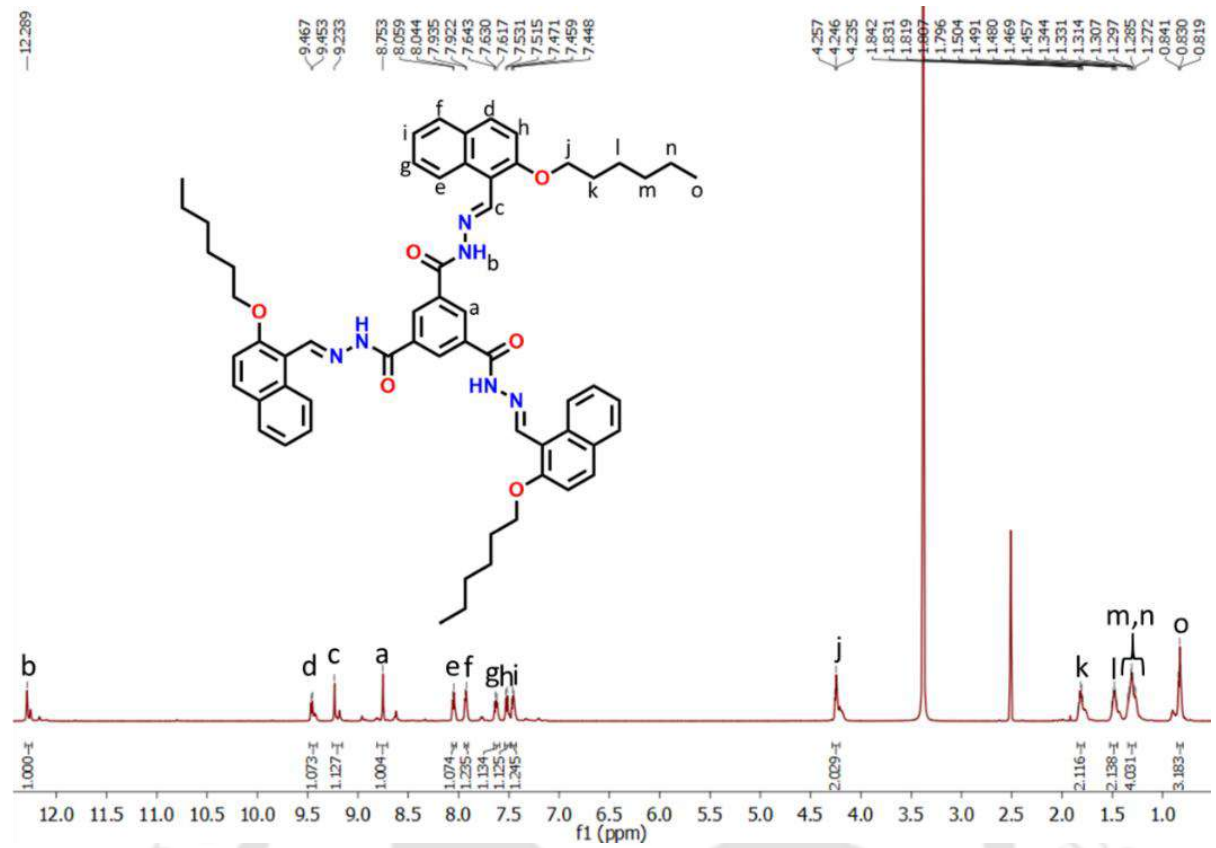

Figure A2.63: ^{1}H NMR spectra of THX in DMSO-d_6.

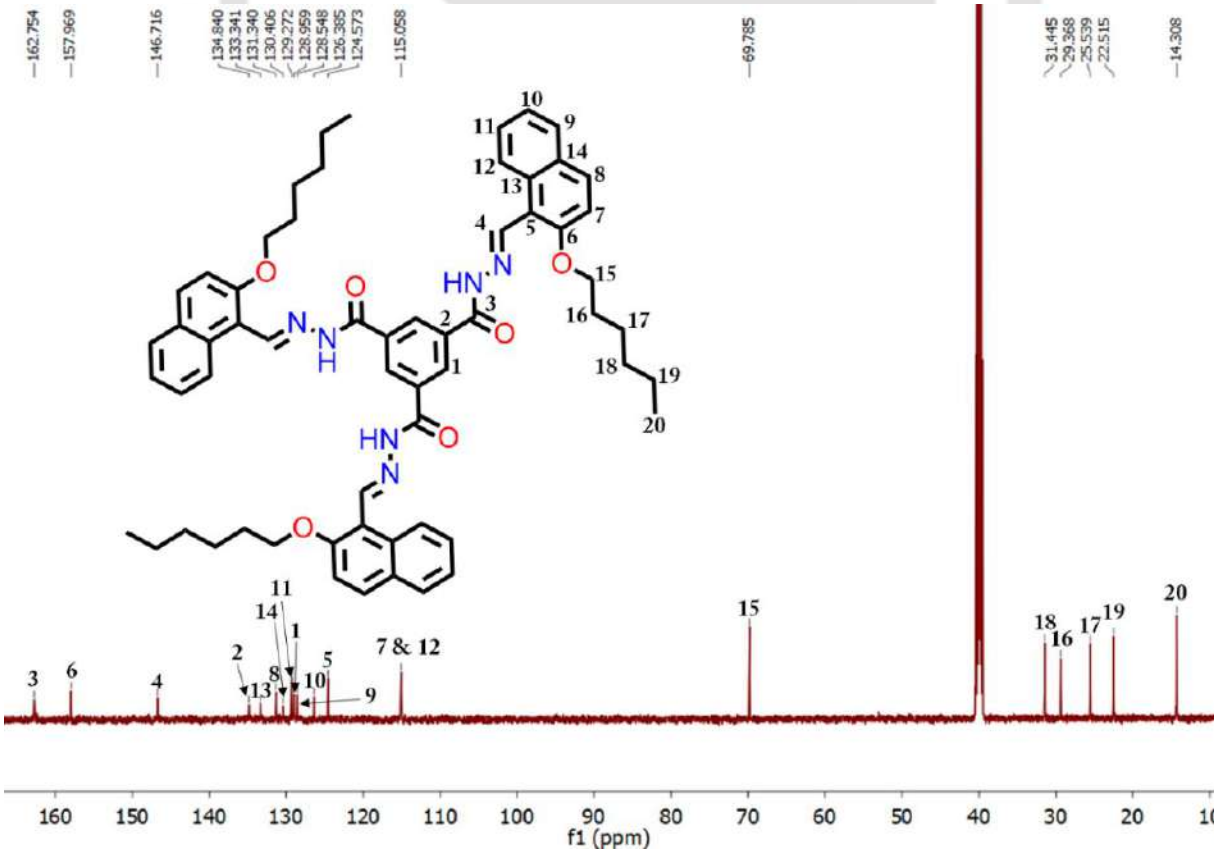

Figure A2.64: ^{13}C NMR spectra of THX in DMSO-d_6.

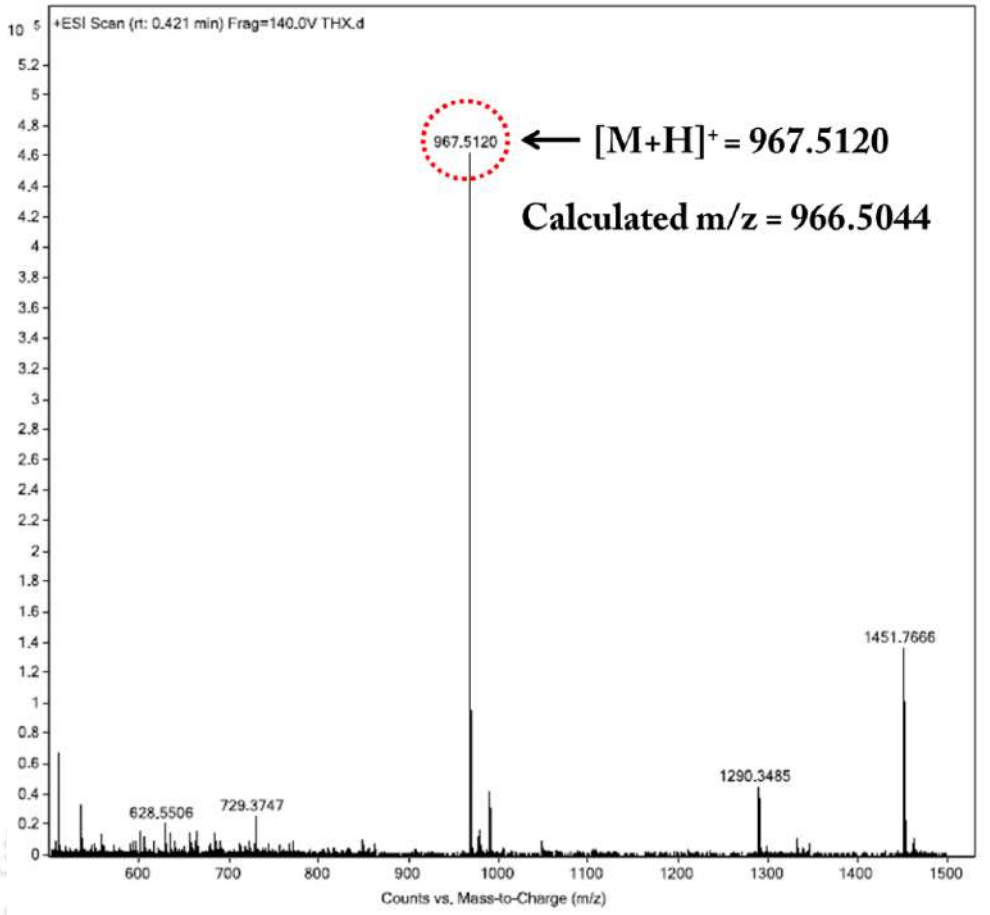

Figure A2.65: HRMS of THX.

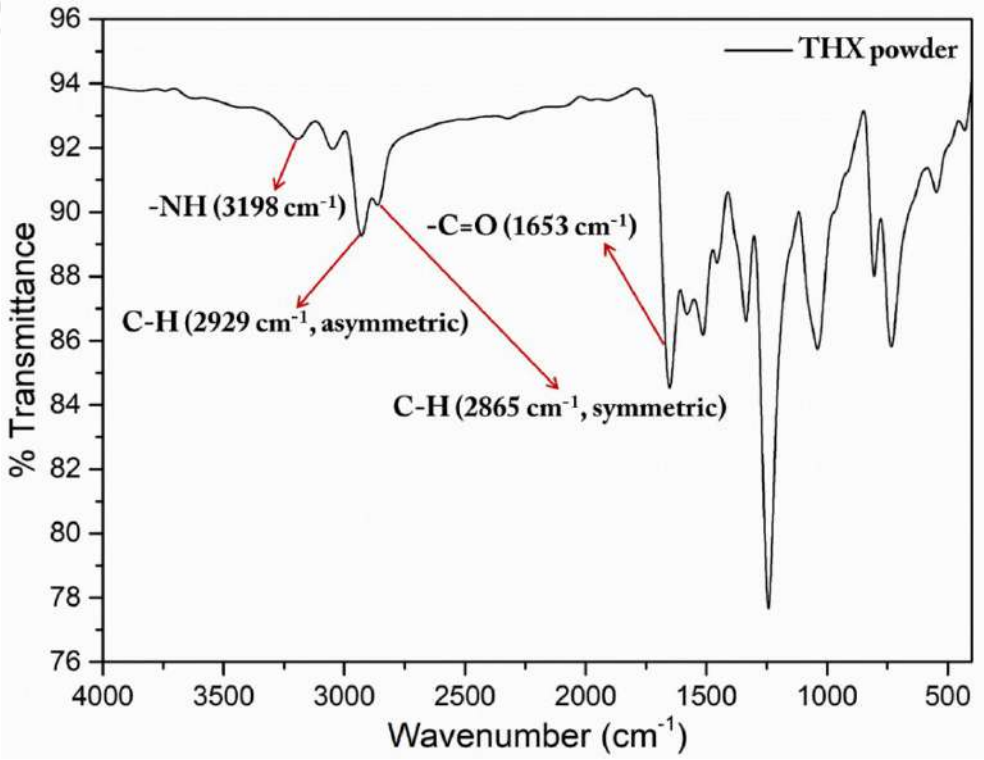

Figure A2.66: FTIR spectra of THX.

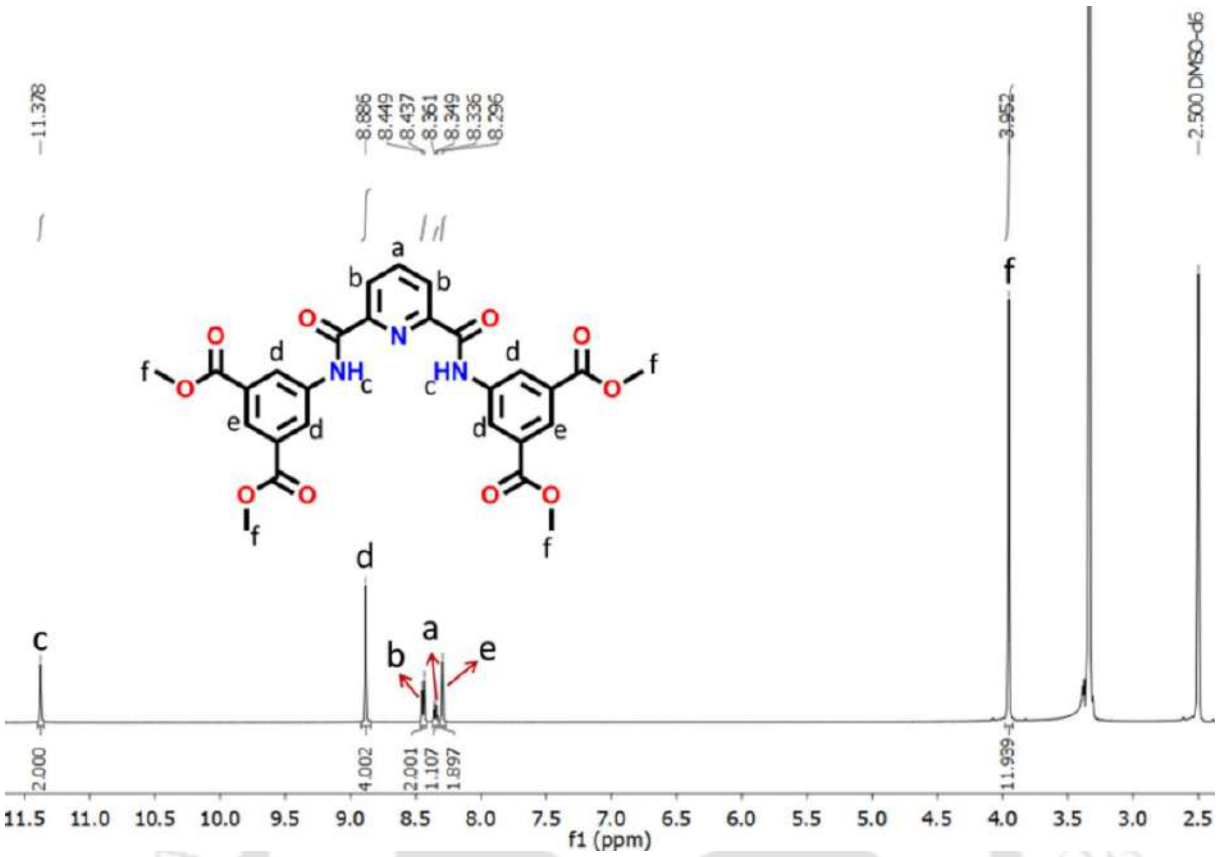

Figure A2.67: [1]H NMR spectra of Py-M.

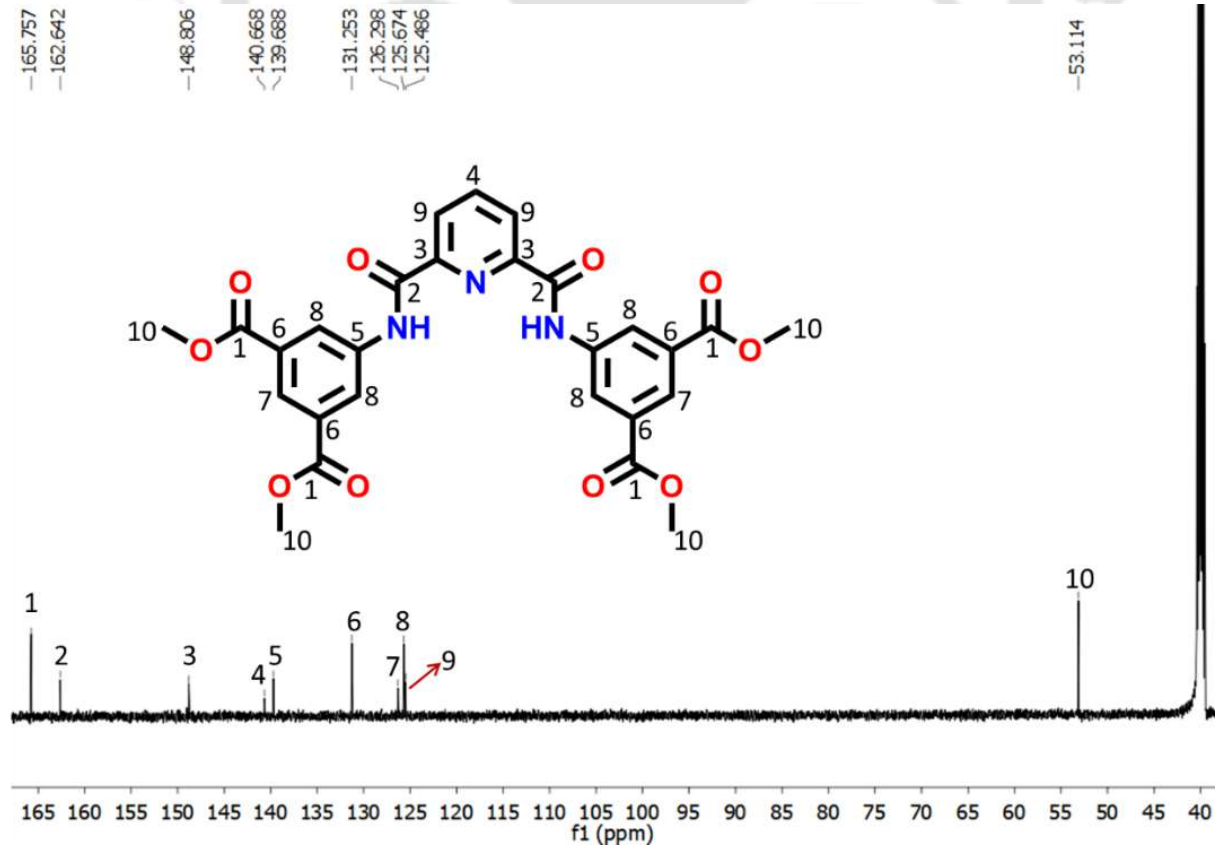

Figure A2.68: [13]C NMR spectra of Py-M.

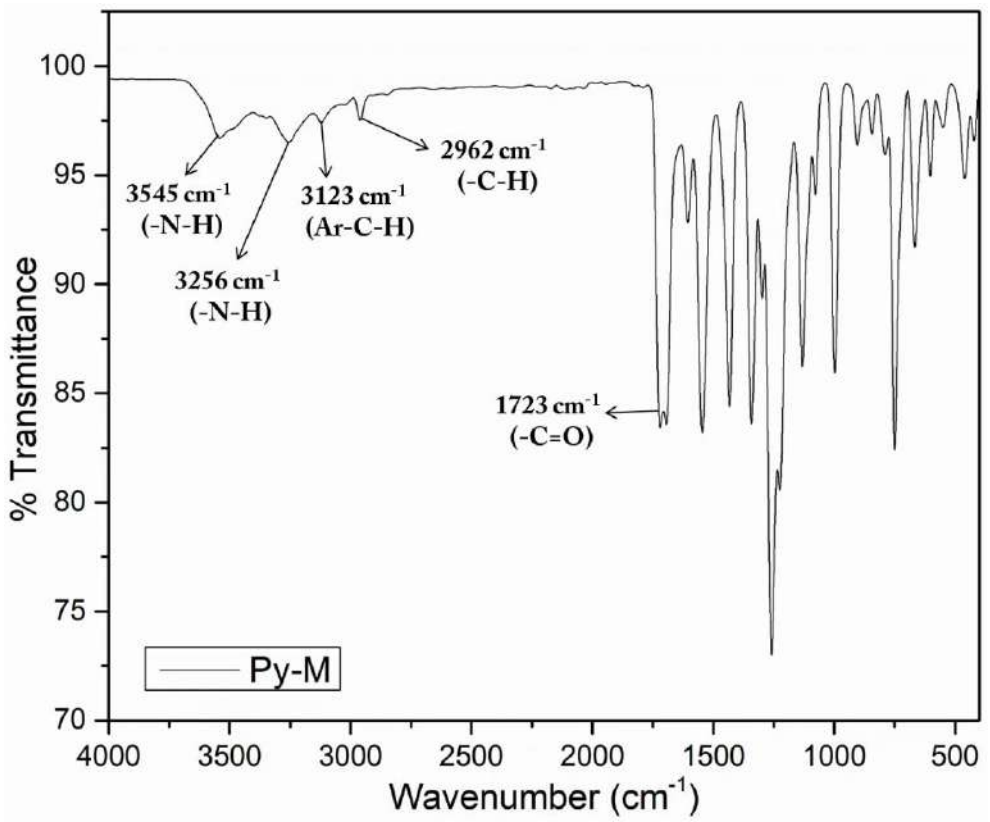

Figure A2.69: FTIR-ATR spectra of Py-M.

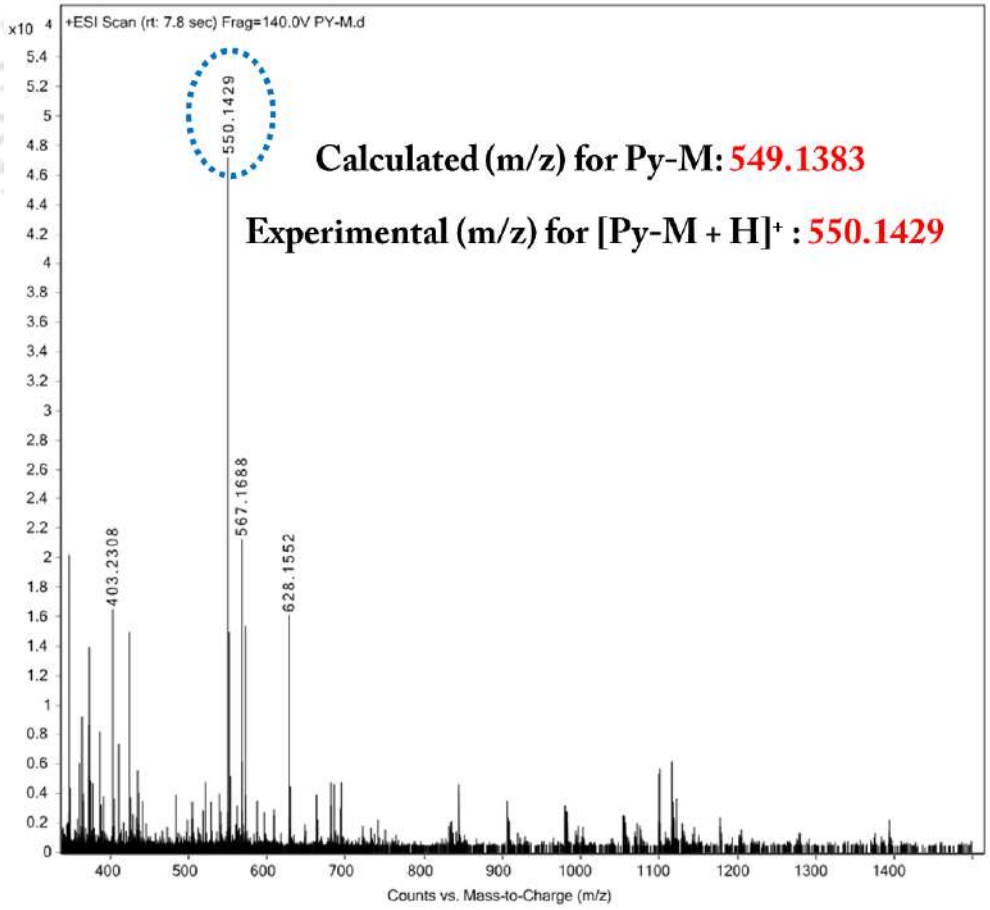

Figure A2.70: HRMS of Py-M.

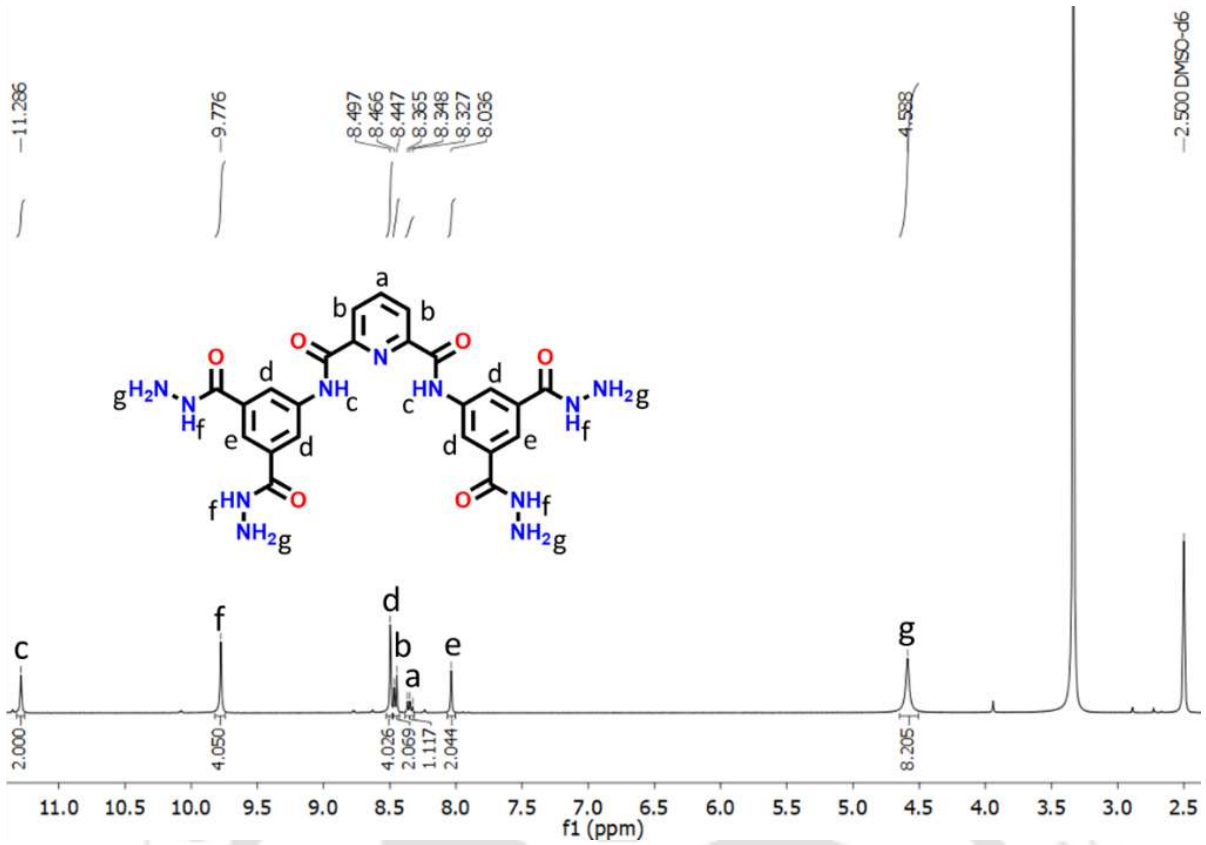

Figure A2.71: [1]H NMR spectra of Py-H.

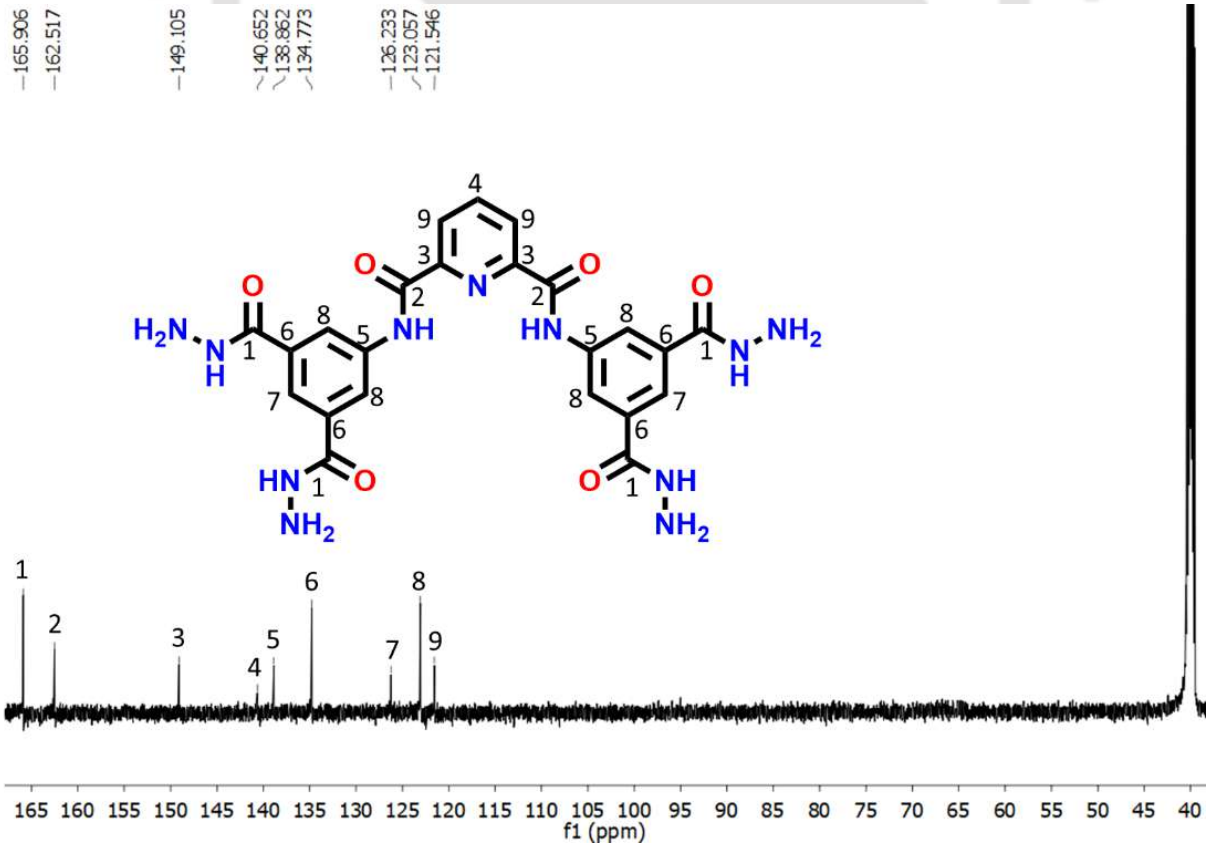

Figure A2.72: [13]C NMR spectra of Py-H.

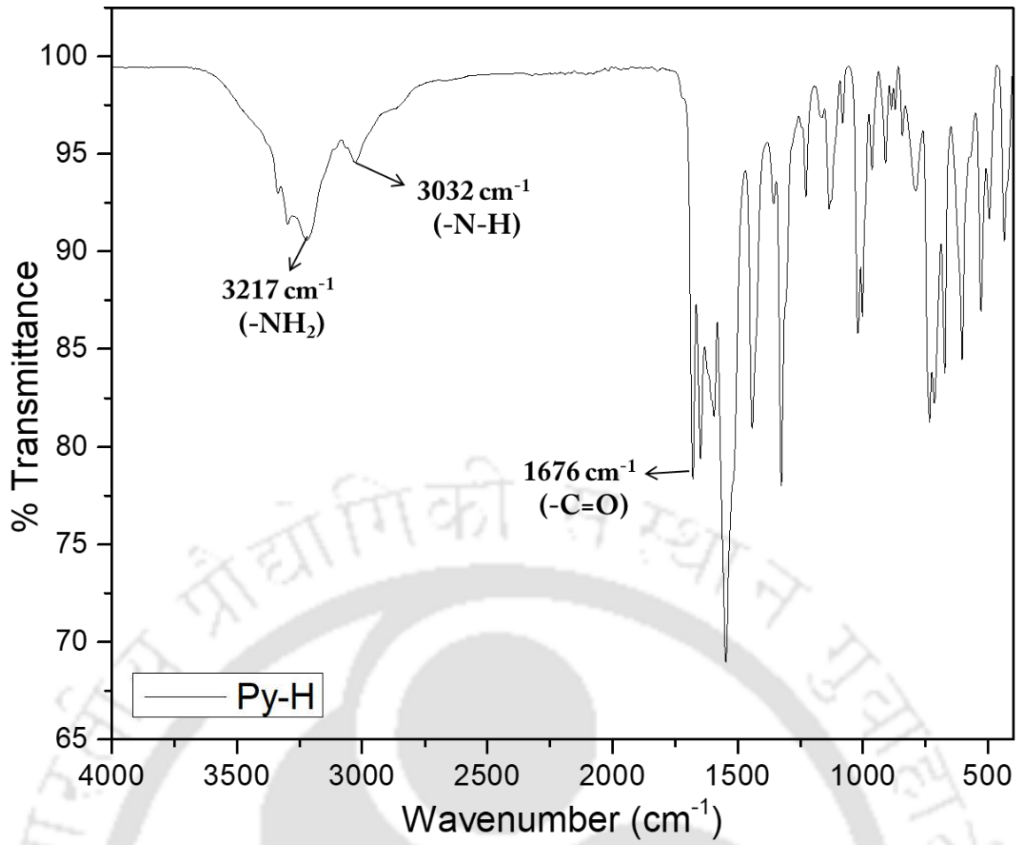

Figure A2.73: FTIR-ATR spectra of Py-H.

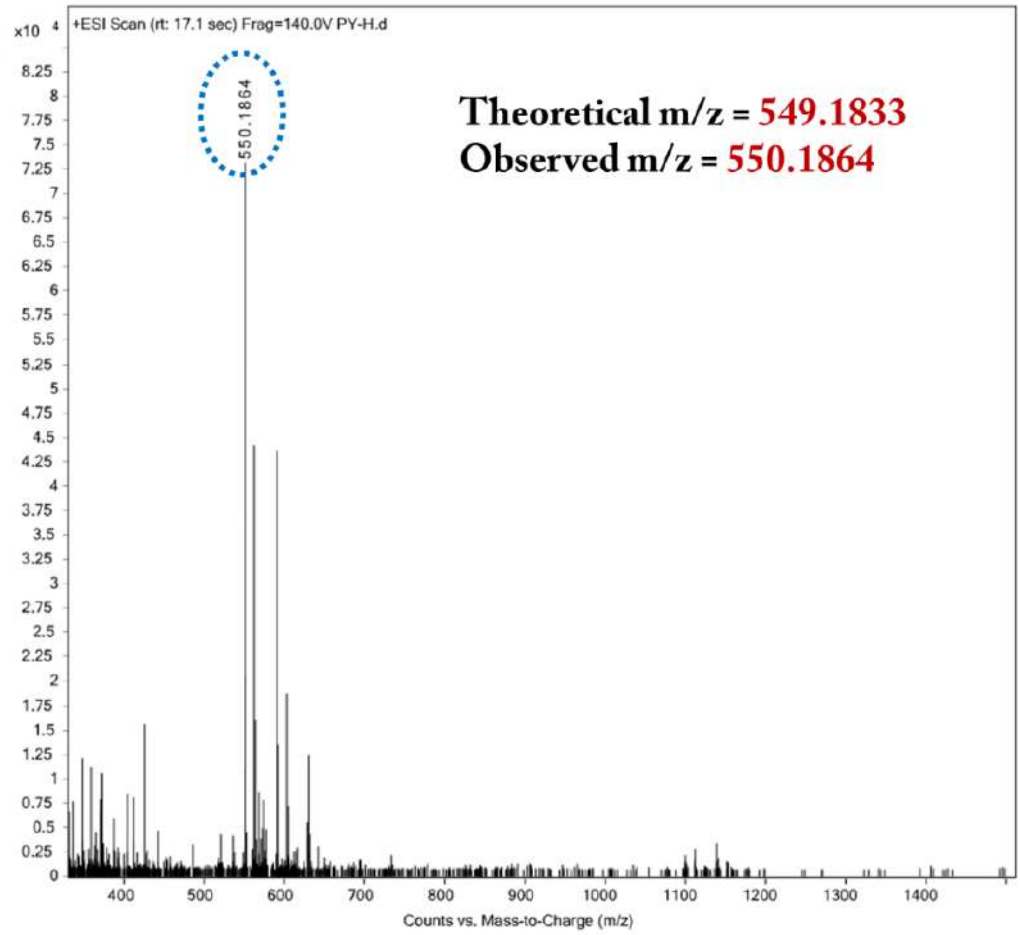

Figure A2.74: HRMS of Py-H.

Chapter 3A

Evaluating the Terminal Substituent Directed Differential Anion Recognition Aptitude of Bis-urea Receptors

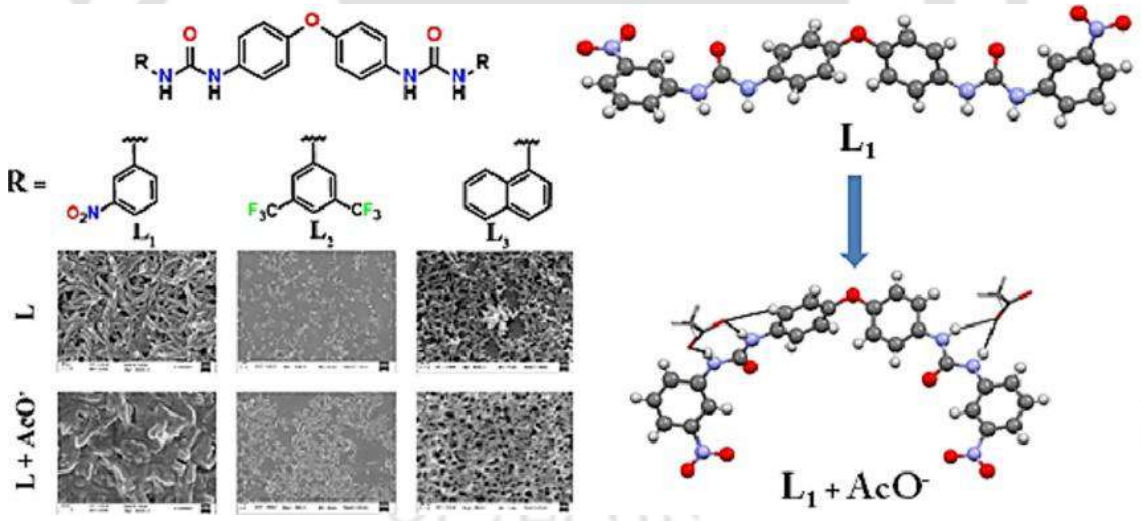

CHAPTER 3A

3A.1. Background and Focus of the Chapter

Anion receptor chemistry deals with the design as well as the synthesis of molecules that can bind or sense anions with high selectivity. [3A.1] To date plethora of selective receptors or sensors have been reported [3A.2-3A.3] demonstrating their applications in various fields, which include sensing, self-assembly, extraction, anion transport, crystal engineering, catalysis, etc. [3A.4] Among various anions acetate plays a significant role in our biological system, which confers numerous metabolic functions such as the production of energy, and synthesis of lipid and protein acetylation in our body. [3A.5] In a similar way, halide anions also play vital role in many biological processes including dental health, transportation, signal transduction, tissue development, production of hormones etc. [3A.6-3A.8] Receptor designing process plays a key role in the efficient binding of those anions through various non-covalent interactions. In this regard, small molecule-based receptor systems have gained lots of attention owing to their high structural tunability, and ease of synthesis, which ultimately enables easy regulation of their anion binding aptitude in both solid as well as in solution phases.

A large number of acyclic urea/thiourea-based anion receptors capable of recognising halide/oxyanions with different functional groups (electron withdrawing/donating) have been reported so far to understand their anion recognising ability through hydrogen bonding interactions. [3A.9] Tripodal urea/thiourea based anion receptors are common in the literature, because of its ability to form flexible as well as pre-organised cavity via molecular capsule formation with complementarity. On the contrary, dipodal urea/thiourea-based anion recognition within the self-assembled architecture of the receptors is not common in the literature, because of its greater rigidity and lesser binding sites.

In our continuing effort to understand the effect of substituents of the receptor in anion coordination as well as self-assembly, both in solution and solid state [3A.10-3A.16] herein we have reported a set of three dipodal bis-urea receptors (L_1-L_3), with varying electronic properties. L_1-L_3 are functionalized with nitro phenyl, 3,5-bis(trifluoromethyl)phenyl, and naphthyl groups respectively. Only with receptor L_1, the acetate anion was successfully crystallised among all the other free receptors (L_2 and L_3), where the acetate anion is efficiently trapped inside the self-assembled architecture of L_1 through various non-covalent interactions majorly hydrogen bonding interaction, which has been established through Single Crystal X-ray Diffraction (SC-XRD)

analysis. This solid-state result inspired us to conduct an acetate recognition study for all three receptors in both solid as well as in solution phases, which has been executed through various analytical techniques including ^{1}H NMR, SC-XRD, Hirshfeld Surface (HS) analysis, FESEM study, etc. Overall, this study demonstrates the regulation of anion binding aptitude of the bis-urea receptors (L_1-L_3) just by varying the terminal substituents attached to it. This study might be beneficial for the rationale designing of receptor molecules to target some specific anions for different applications such as anion transport, extraction of toxic anions, selective sensing of toxic anions etc.

3A.2. Objective of the Chapter

Three bis-urea receptors (L_1-L_3) with varying terminal substituents (viz. electron deficient/π-acidic, -NO_2, -CF_3, and electron rich-hydrophobic naphthyl) with different electronic properties have been designed to investigated the effect of those terminal substituents on their anion recognition potential in both solid as well as in solution phases. Moreover, the anion binding discrepancies of the receptor molecules in both solid and solution phases has also been addressed in this particular study.

3A.3. Results and Discussion

3A.3.1. Design Aspect and Structural Analysis of Free Receptors

4 4′-diaminodiphenyl ether-based three bis-urea receptors namely, L_1-L_3 have been purposefully synthesized in quantitative yield to study their anion recognition aptitude in both solid as well as solution phase on varying the terminal groups. All of the aforementioned receptors have been synthesised with a good yield by reacting 4,4′-diaminodiphenyl ether with different isocyanates in acetonitrile medium at room temperature. The receptors L_1 and L_3 have been successfully recrystallized from DMSO/DMF (1:1) whereas, L_2 has been recrystallized from DMSO and the solid-state study through SC-XRD has been executed for all the single crystals isolated for the corresponding receptors. Receptor L_1 and L_2 both contain electron-withdrawing terminal groups NO_2 and CF_3 respectively, while on the other hand, L_3 contains electron rich naphthyl group, thereby comparison has been made on their anion binding aptitude based on their different electronic properties in both solid-state as well in solution phase.

3A.3.2. Single Crystal X-ray Structural Analysis

Structure of the Free Receptors L_1, L_2 and L_3

SC-XRD study of the receptor L_1 reveals that, the bis-urea units orient themselves about in the same direction creating a dihedral angle of 31.89° in one arm and 35.13° in the other arm with the central phenyl ring. (Figure A3A.5a,b) In one arm both the NH units are on the same plane while in the other arm, the urea NHs are slightly out of the plane. The receptor molecule forms a layered architecture through self-assembly among themselves as facilitated by various weak noncovalent interactions such as C-H_{phenyl}···O_{nitro} (2.533-2.623 Å), N-H_{urea}···O_{nitro} (2.411-2.702 Å), N-H_{urea}···$O_{carbonyl}$ (2.342-2.658 Å), CH_{phenyl}···π (2.749-2.837 Å) and π···π (3.297-3.364 Å) interactions. (Figure 3A.1a; Figure A3A.4b; Figure A3A.8a,d) L_2 is prone to crystallisation in DMSO. Frequent co-crystallisation of DMSO with L_2 was consistent in each and every crystallisation attempt that we made. (Figure 3A.1b; Figure A3A.6a, b) Crystal structure analysis reveals that the urea units in both arms are oriented in syn fashion with twisted arms, as was observed in the case of receptor L_1. The oxygen atom (O4) of DMSO is forming bifurcated hydrogen bonds with the urea NHs (H3N and H4N) of the L_2 receptor with an average hydrogen bonding distance of 2.017 Å. Two nearby L_2 receptors are interconnected by π···π (3.381 Å) interaction as well as two rare trifurcated hydrogen bonding interactions, where the oxygen atom (O6) of DMSO forms three hydrogen bonds with two phenyl hydrogens, O6···H3, O6···H21(2.524 Å, 2.584 Å) and one urea hydrogen atom O6···H2N (2.525 Å). (Figure A3A.8b,e) On the other hand, two remote L_2 receptors are also interconnected by another DMSO molecule, where the O4 of DMSO forms bifurcated hydrogen bonds with two urea hydrogen atoms O4···H3N, O4···H4N (2.005 Å, 2.029 Å) in one end and in the other end, one methyl hydrogen (H31B) of the same DMSO molecule forms hydrogen bonding with the oxygen atom (O3) of the urea C=O. The oxygen atom (O5) of the disordered DMSO forms a hydrogen bond with one urea NH (O5···H1N) in one arm of the receptor L_2 in each molecule. (Figure 3A.1b) As mentioned earlier, DMSO always co-crystallises with the receptor, which is prominent even in the presence of different anions (using tetrabutylammonium salts). This observation can be attributed to the presence of strong hydrogen bond donor sites (urea NHs) as induced by the presence of strong electron-withdrawing group trifluoromethyl group and also the ability of DMSO to act as a strong hydrogen bond acceptor site, which leads to strong donor-acceptor assembly as evident from SC-XRD data. Single crystal XRD analysis of L_3 reveals that the ligand forms a regular 1D self-assembled architecture as facilitated by various noncovalent interactions including hydrogen bonding and π···π interactions. (Figure A3A.7a,b; Figure A3A.8c,f) The two arms of the receptor take a twisted

conformation as observed in the case of L_1 and L_2. DMSO, but here the urea hydrogen atoms in both the arms orient opposite to each other unlike in the case of L_1 and L_2. DMSO, which can be attributed to the presence of a comparatively bulky naphthyl group. (Figure 3A.1c) It is interesting to note that, both the bis-urea units in L_3 are equally involved in uniform hydrogen bonding interactions as assisted by the presence of naphthyl groups (hydrophobic interactions) in the terminal positions, which is missing in the case of the other two receptors. The oxygen (O2) atom acts as a hydrogen bond acceptor site, and forms hydrogen bond with the urea hydrogen atoms O2···H1N, O2···H2N (2.057 Å, 2.112 Å). These hydrogen bonding interactions accompanied by π···π interactions (3.313 Å) facilitate a regular self-assembled 1D framework of L_3. (Crystallographic details have been furnished in Table A3A.1-Table A3A.34)

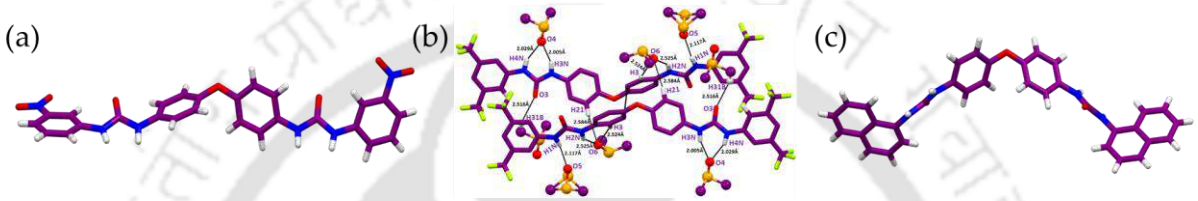

Figure 3A.1: SC-XRD view of (a) receptor L_1, (b) hydrogen bonding and π···π interactions between DMSO and L_2, (c) receptor L_3.

Acetate Complex [(n-TBA)$_2${(L_1)($OCOCH_3$)$_2$}]

Suitable block-shaped single crystals of L_1 with TBA(OAc), were successfully isolated from slow evaporation of DMSO: DMF (1:1) solution of L_1 in the presence of excess n-tetrabutylammonium acetate (n-TBA$OCOCH_3$). Single crystal XRD reveals a 1:2 host-guest interaction between the acetate anion and the receptor L_1 in the solid state. The bis-urea units in the two arms of the L_1 receptor are projected in anti-fashion unlike in L_1 (where it was syn orientation), hence facilitating the binding of the acetate anion unhindered. (Figure A3A.2, Figure A3A.3, Figure A3A.4a) It is quite interesting to note that, both the arms of a single L_1 receptor undergo different numbers of hydrogen bonding interactions with the acetate anion. (Figure 3A.2b,c) The total number of hydrogen bonding interactions in both arms to stabilise two equivalents of acetate anion remains the same, where two L_1 receptors stabilise the acetate anion through a total of five hydrogen bonding interactions in each arm. (Figure 3A.2a) One arm is capable of acting as three hydrogen bond donor sites, out of which two are from the urea protons and the other is a central phenyl ring hydrogen atom; while the other arm is capable of donating two urea hydrogen atoms, such unsymmetrical anion binding is quite unusual, which can be visualised through the nonplanarity of the central phenyl ring with the urea NHs in the respective arms, creating a dihedral angle of 9.88°, unlike the other arm, where the dihedral angle becomes zero indicating planarity of the urea

NHs and the central phenyl ring. (Figure A3A.5c) It has been observed that L_1 self assembles to trap two equivalents of acetate anion, enclosed by two counter n-TBA cations each. (Figure 3A.2a) In the dimeric assembly of the receptors, each acetate anion shows five non-covalent interactions with the receptors, which include four strong urea N-H_{urea}···OAc (average H-bonding distance is 2.033 Å) and one aromatic C-H_{phenyl}···OAc (with ahydrogen bonding distance of 2.645 Å) hydrogen bonding interactions. The acetate-surrounded host system gets extra stability through some additional weaker C-$H_{n\text{-}TBA}$···O_{urea} (2.593-2.630 Å), C-H_{phenyl}···O_{nitro} (2.650 Å) and C-$H_{n\text{-}TBA}$···O_{nitro} (2.541-2.657 Å) interactions. It has been observed that, in the presence of acetate anion, the self-assembled architecture gets disturbed, which was present earlier among the free receptors as assisted by various non-covalent interactions. For example, the non-covalent interactions like N-H_{urea}···O_{nitro}, N-H_{urea}···$O_{carbonyl}$, CH_{phenyl}···π and π···π are absent in the L_1-acetate complex. The alteration of various non-covalent interactions is also reflected in the dnorm surface of Hirshfeld Surface Analyses. (all the hydrogen bonding distances have been furnished in Table A3A.2)

On comparing FT-IR data of the complex [(n-TBA)$_2${(L_1) ($OCOCH_3$)$_2$}] with the free receptor as well as TBA(OAc), it was observed that the sharp characteristic peak for N-H at 3375 cm^{-1} as well as the shoulder peak at 3321 cm^{-1} becomes very broad indicating strong hydrogen bonding interactions. (Figure A3A.1) These all observations are in parallel with the solid-state data obtained from SC-XRD.

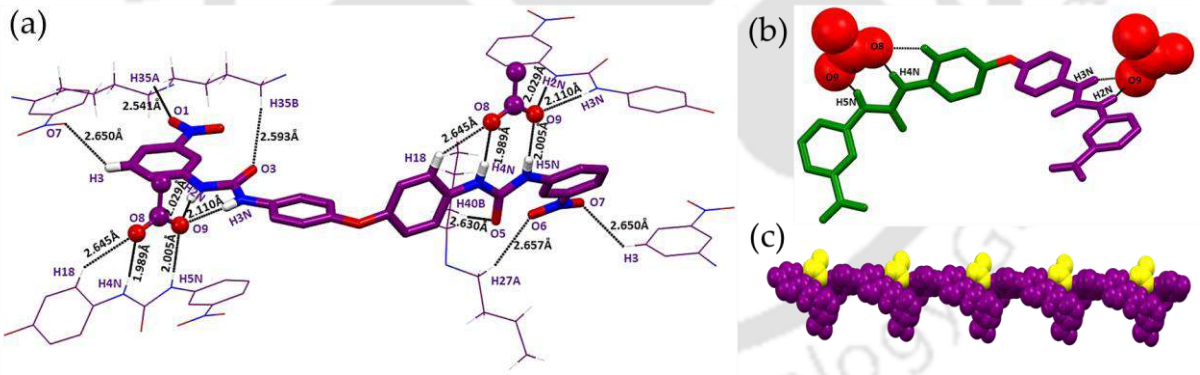

Figure 3A.2: (a) Showing total H-bonding interactions around the receptor L_1 with acetate and n-TBA. (b) Unsymmetrical binding of the acetate anion in both the arms by receptor L_1. (c) Spacefill view of 1-D polymeric chain arrangement of the L_1-acetate complex (Dashed line in all the cases indicate hydrogen bonding interactions).

Among all of the three receptors (L_1-L_3), only with L_1, successful crystallisation with acetate anion was achieved. The receptor L_1 contains NO_2 group as a terminal substituent, which helps in enhancing the acidity of the bis-urea units, thereby, increasing the chance of anion recognition

through hydrogen bonding interactions. It has been observed that receptor L_1 pre-organises itself in such a way as to facilitate the approach of acetate anion and thus facilitate the recognition of the same through hydrogen bonding interactions, which can be visualized through changes in the dihedral angle between the bis-urea units and the central phenyl ring, where the initial dihedral angle between them was observed to be 31.89°/35.13° (Figure A3A.5a,b), which gradually changes to 0°/9.88° (Figure A3A.5c) on binding the acetate anion. It has been observed that, DMSO frequently co-crystallises with L_2, and the addition of any anion led to the same result. This can be attributed to very strong as well as stable host-guest interaction between L_2 and DMSO; where L_2 contains a strong hydrogen bond donor site and DMSO acts as a strong hydrogen bond acceptor site. Such DMSO-solvated crystals are very important in the designing of 'urea-based drug-DMSO solvate'. [3A.17] In the case of L_3 also we could not crystallise any anions, which can be attributed to the presence of more hydrophobic as well as electron-rich naphthyl group in the terminal positions, which makes the urea hydrogen less acidic as compared to that of L_1 and L_2 and also the presence of naphthyl group helps in further strengthening of the self-assembled network through hydrophobic interactions. One important observation while trying to crystallise L_3 in different solvents was that we often got gel-like material in some of the solvents. Although the gelation study is out of the scope of this article, this sort of result might be very important for the understanding of gelation at the molecular level through crystal engineering. [3A.18] (Crystallographic details have been furnished in Table A3A.1-Table A3A.34)

3A.3.3. Hirshfeld Surface Analyses

Hirshfeld surface (HS) analysis is performed to establish the surface characteristics associated with a molecule on the basis of various noncovalent interactions such as strong N-H···A (anion), weaker interactions like C-H···Cl^-/Br^- , C-H···O, C-H···π etc. [3A.19] In addition to this, it also helps in visualising structural alterations in linear isomeric ligands, caused by anion complexation. HS provides us a platform to visualise various interactions either strong or weak as indicated by colour intensities; high-intensity colour signifies strong interaction and weak interaction is represented by low-intensity colour. The two-dimensional fingerprint plots (2D FPs) of Hirshfeld surface analyses give information about "contact contribution", which primarily helps in understanding the role played by all the non-covalent interactions as well as its nature in a specific crystalline molecule and quantitatively establishes it. [3A.20] The C-H and O-H contact contributions in the free receptor L_1 and its acetate complex have been shown in Table 3A.1.

Table 3A.1. Contact contributions (%) from the d_{norm} surface area of dipodal segments in free receptors and in the anion complex

Contacts	L_1	L_1 +TBA(OAc)	L_2+DMSO	L_3
C···H	23.6	14.2	9.1	33.1
O···H	28	26	14	13.8
H···H	29.9	50.8	25.5	43.1

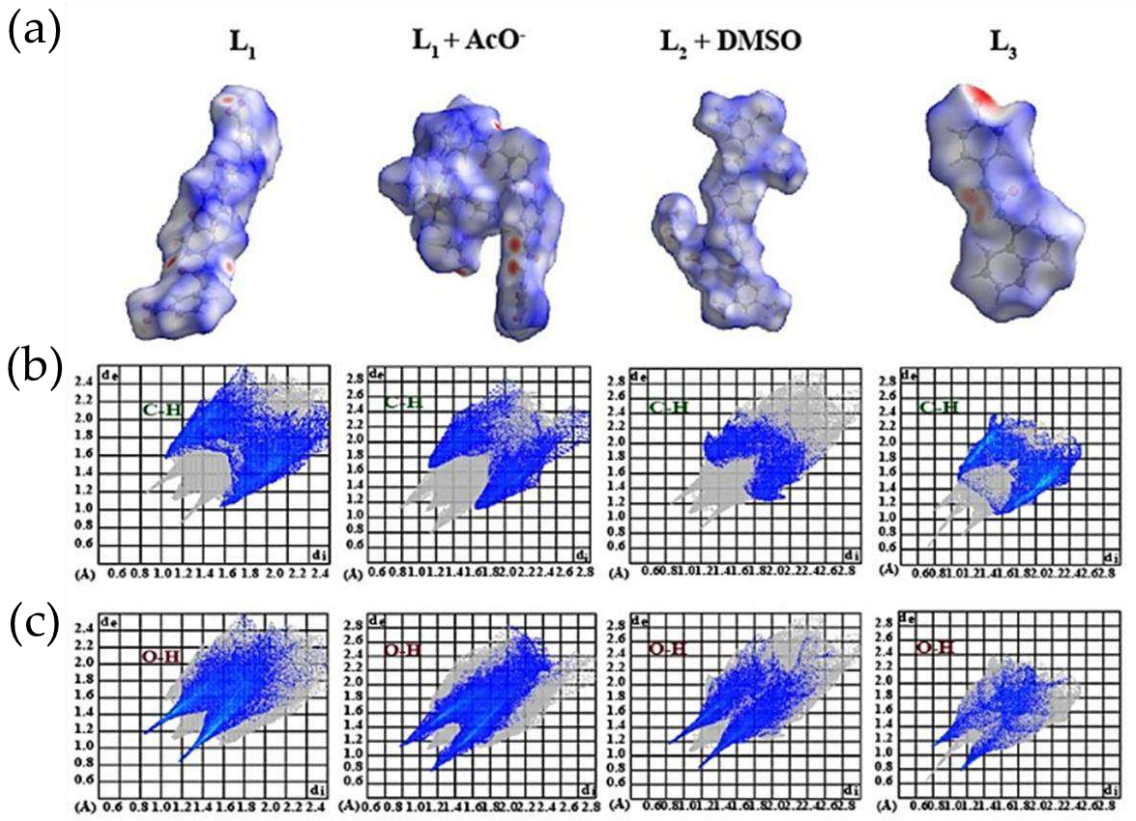

Figure 3A.3: Hirshfeld surface analysis displaying (a) the d_{norm} surfaces of L_1, L_1 + AcO^-, L_2 + DMSO and L_3; (b) corresponding 2D FPs with the C···H interactions highlighted in colour involved in C-H···π or C-H···O contacts; and (c) corresponding 2D FPs with the O-H interactions including N-H···O or C-H···O marked in colour.

The bright red spots observed on the dnorm surfaces iindicatethe strong N-H···O interactions involving N-Hurea and the faded reddish spots are indicative of other important interactions such as C-H···O and C-H···π interactions. The contact contributions of both C-H (14.2%) as well as O-H (26%) are observed to be lower in the case of the L_1-acetate complex than that of the free receptor L_1 (C-H = 23.6%, O-H = 28%), which indicates the alteration of various non-covalent interactions such as C-H···π, C-H···O, N-H···O or C-H···O in presence of the acetate anion. Most significant changes have been observed for C-H contact contributions, which go down

significantly in the complex as compared to that of the free receptor, which indicates disruption of the self-assembled solid- state architecture of the free receptor as facilitated by various C-H contacts in the presence of the acetate anion. Also, the high O-H contact contribution in the complex can be ascribed to the interaction of the acetate anion with the receptor L_1. Hence, all of these HSs results mapped with dnorm surface and 2D FPs for the receptor L_1 and its acetate complex strongly corroborate with the solid state results obtained from the SC-XRD study. (Figure 3A.3a-c)

3A.3.4. Anion Binding in Solution

^{1}H NMR Study in the Presence of Halide Anions

^{1}H NMR analysis of free L_1 receptor shows chemical shift values of, δ-NH_a = 9.18 ppm; δ-NH_b = 8.81 ppm. After the addition of fluoride anion (as tetrabutylammonium salt) the corresponding peaks for both NH_a and NH_b vanishes. While adding chloride and bromide anion as their TBA salts to the DMSO-d_6 solution of the free receptor L_1, a significant downfield shift of the peaks for both NH_a and NH_b has been observed. An average downfield shift of $\Delta\delta$ = 0.99 ppm (for chloride, $\Delta\delta$-NH_a = 1.07 ppm, $\Delta\delta$-NH_b = 0.93 ppm) and $\Delta\delta$ = 0.79 ppm (for bromide, $\Delta\delta$-NH_a = 0.86 ppm, $\Delta\delta$-NH_b = 0.72 ppm) have been observed for chloride and bromide respectively. (Figure A3A.12) In the case of iodide, the chemical shift values remain almost the same, the average chemical shift value observed is $\Delta\delta$ = 0.02 ppm (for iodide, $\Delta\delta$-NH_a = 0.02 ppm, $\Delta\delta$-NH_b = 0.01 ppm). In the receptor L_2, the observed chemical shift values are, δ-NH_a = 9.35 ppm; δ-NH_b = 8.94 ppm. For chloride, the average downfield shift of $\Delta\delta$ = 0.71 ppm (for chloride, $\Delta\delta$-NH_a = 0.88 ppm, $\Delta\delta$-NH_b = 0.54 ppm), and for bromide average downfield shift of $\Delta\delta$ = 0.81 ppm (for bromide, $\Delta\delta$-NH_a = 1.01 ppm, $\Delta\delta$-NH_b = 0.61 ppm) have been observed. (Figure A3A.13) On adding fluoride anion, the two NH peaks vanish. Upon addition of iodide, a very slight downfield shift of the peaks has been observed with an average downfield shift of $\Delta\delta$ = 0.01 ppm (for iodide, $\Delta\delta$-NH_a = 0.02 ppm, $\Delta\delta$-NH_b = 0.01 ppm). In the case of the free receptor L_3, the initial chemical shift values for the urea protons are, δ-NH_a = 9.03 ppm; δ-NH_b = 8.73 ppm. In the presence of fluoride anion (as its tetrabutylammonium salt), both the NH peaks go away. In the presence of chloride and bromide, average downfield shift of $\Delta\delta$ = 1.10 ppm (for chloride, $\Delta\delta$-NH_a = 1.43 ppm, $\Delta\delta$-NH_b = 0.78 ppm) and $\Delta\delta$ = 0.90 ppm (for bromide, $\Delta\delta$-NH_a = 1.23 ppm, $\Delta\delta$-NH_b = 0.58 ppm) have been observed respectively. For iodide anion, the chemical shift values are very less as compared to the other halide anions, the observed average downfield shift value in the presence of iodide anion is $\Delta\delta$ = 0.05 ppm (for iodide, $\Delta\delta$-NH_a = 0.09 ppm, $\Delta\delta$-NH_b = 0.01 ppm). (Figure A3A.14)

For all three receptors, the NH peaks vanish in the presence of fluoride anion, which can be attributed to the deprotonation of the same. In the presence of iodide, very slight downfield shift has been observed; this result can be attributed to the lower charge density, higher polarizability, and lower basicity of iodide as compared to the other remaining halides. In both L_1 and L_3, the same chemical shift trend has been observed, where the highest chemical shift value has been observed for Cl^- followed by Br^- and I^-. In the case of L_2, a slight change in this trend has been noted, where slightly higher chemical shifting has been observed for Br- as compared to Cl^-, which is not unusual. Hence, the above results corroborate well with the electronic properties of the respective receptors.

^{1}H NMR Study in the Presence of Acetate Anion

In the presence of acetate anion all the free receptors (L_1-L_3), significant downfield shift of the peaks for the urea protons (NH_a and NH_b) have been observed which has been depicted in. (Figure 3A.4)

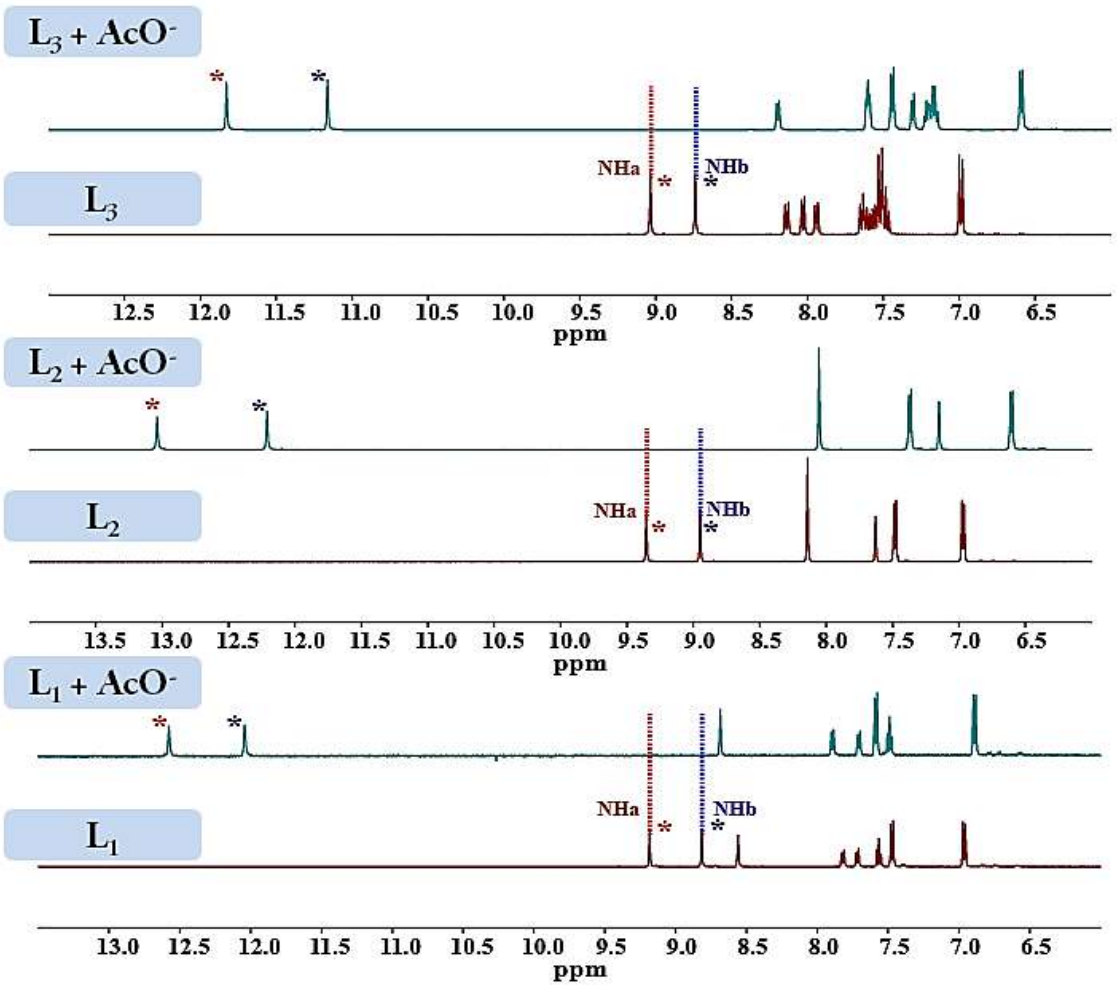

Figure 3A.4: Expanded and stacked ^{1}H NMR spectra of L_1, L_2 and L_3 upon addition of TBA(OAc) in DMSO-d_6.

Upon addition of TBA(OAc) to the DMSO-d_6 solution of free receptor L_1-L_3, an average downfield shift of $\Delta\delta$ = 3.31 ppm (for L_1, $\Delta\delta$-NH_a = 3.39 ppm, $\Delta\delta$-NH_b = 3.22 ppm), $\Delta\delta$ = 3.47 ppm (For L_2, $\Delta\delta$-NH_a = 3.68 ppm, $\Delta\delta$-NH_b = 3.26 ppm) and $\Delta\delta$ = 2.60 ppm (For L_3, $\Delta\delta$-NH_a = 2.79 ppm, $\Delta\delta$-NH_b = 2.42 ppm) have been observed respectively. Such huge downfield shifting of the peaks for the urea protons can be attributed to the strong hydrogen bonding interactions between the bis-urea units of the respective receptors with the acetate anion. Receptor L_2, containing the most electronegative substituent in its terminal positions shows the highest downfield shifting of the N-H_{urea} peaks followed by the receptors L_1 and L_3. Hence, these chemical shift values strongly agree with the electronic properties of the respective receptors.

Quantitative ^{1}H NMR experiments in DMSO-d_6 have been performed for all three ligands (L_1-L_3) using tetrabutylammonium salt of acetate (n-$TBAOCOCH_3$). Upon addition of quantitative amounts of n-$TBAOCOCH_3$ to the DMSO-d_6 solution of all the three receptors, the most significant changes have been observed for urea NH, which indicates that the primary interaction site for the acetate anion is the N-H_{urea} protons of the respective receptors. Quantitative titration of L_1 with acetate anion has been performed by adding aliquots of DMSO-d_6 solution of n-$TBAOCOCH_3$ salts to the DMSO-d_6 solution of L_1; upon gradual addition of n-$TBAOCOCH_3$ salt led to an average downfield shift of $\Delta\delta$ = 0.50 ppm ($\Delta\delta$-NH_a = 0.52 ppm and $\Delta\delta$-NH_b = 0.49 ppm) followed by broadening of NH peaks, indicating rapid and strong hydrogen bonding interaction between the receptor and the acetate anion.

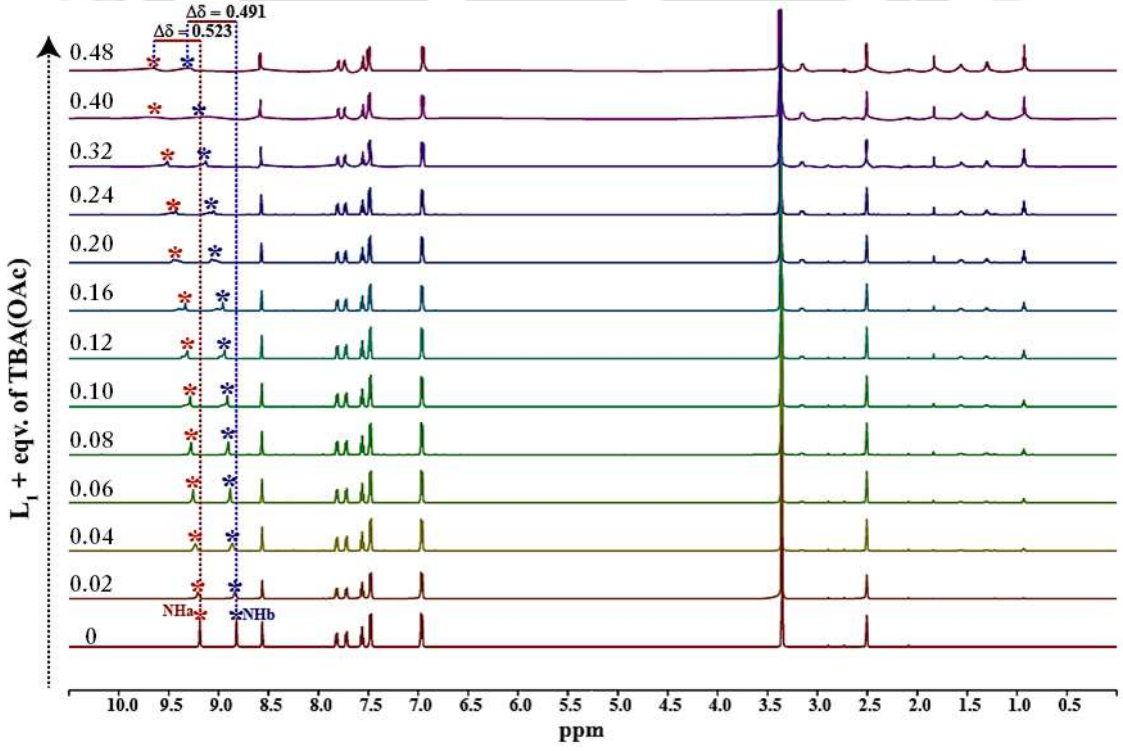

Figure 3A.5: Expanded ^{1}H NMR spectra of L_1 upon titration with TBA(OAc) in DMSO-d_6.

Similarly, for the other two receptors, L_2 and L_3, average downfield shift of $\Delta\delta$ = 0.859 ppm ($\Delta\delta$-NH_a = 0.90 ppm and $\Delta\delta$-NH_b = 0.81 ppm) and $\Delta\delta$ = 1.23 ppm ($\Delta\delta$-NH_a = 1.30 ppm and $\Delta\delta$-NH_b = 1.16 ppm) have been observed. (Figure 3A.5-3A.7) From the above NMR titration data, it is clear that the average downfield shift values for NH_a is more than that of NH_b in all three receptors, which means NH_a undergoes strong hydrogen bonding interaction than that of NH_b in the presence of acetate anion. NMR titration data was best fit into 1:1 host-guest binding stoichiometry in all of the three receptors using the BindFit model. Such binding discrepancy in the solution phase is not uncommon in literature, which can be attributed to the loose orientation of the receptor in the solution phase as compared to that of the solid state, where the receptor is more organized.

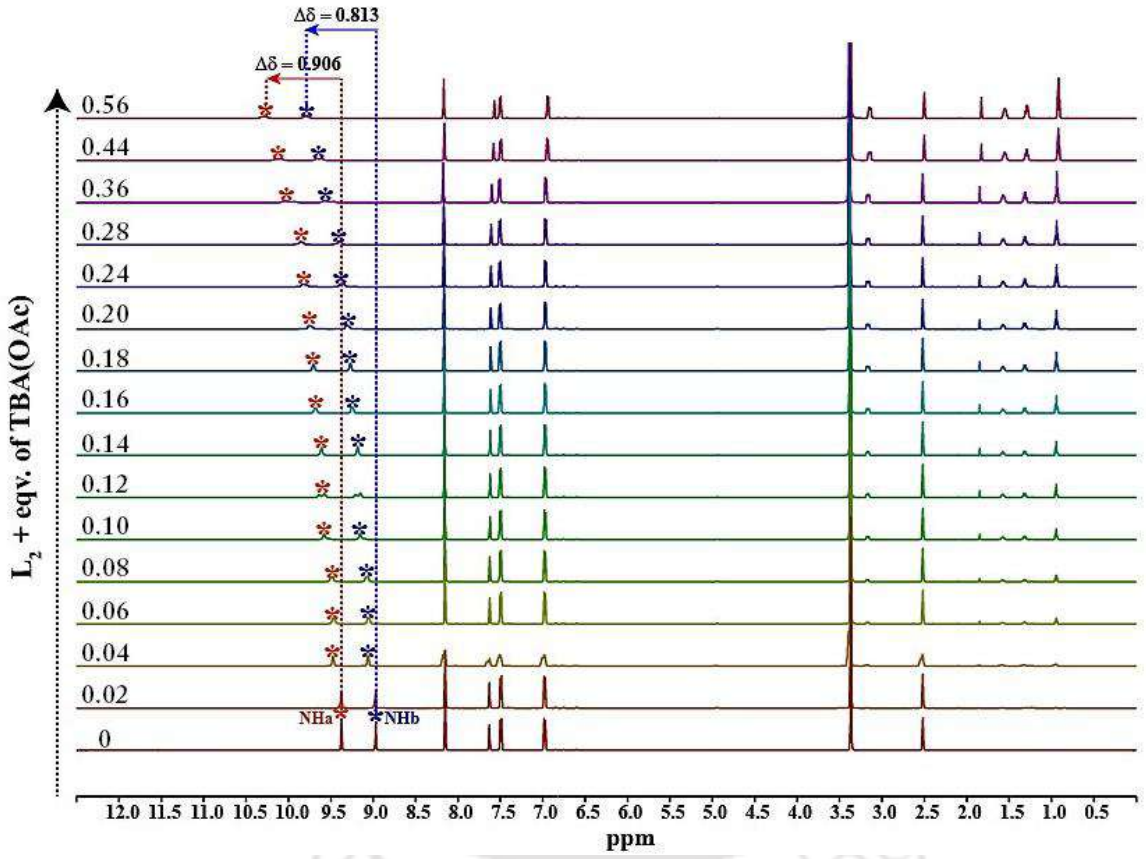

Figure 3A.6: Expanded ^{1}H NMR spectra of L_2 upon titration with TBA(OAc) in DMSO-d_6.

For L_2-AcO^- a very high binding constant value (K = 40.38 M^{-1}) was observed followed by L_1-AcO^- and L_3-AcO^- where the binding constant values are 23.47 M^{-1} and K = 11.65 M^{-1} respectively, which indicates that because of the presence of more electron withdrawing CF_3 substituent, the urea NHs are more acidic in L_2 receptor hence it undergoes stronger hydrogen bonding interaction with the acetate anion as compared to that of the L_1 and L_3 where the terminal substituents are lesser electron withdrawing group nitro and electron rich napthyl group respectively (Figure A3A.9-11; Table 3A.2).

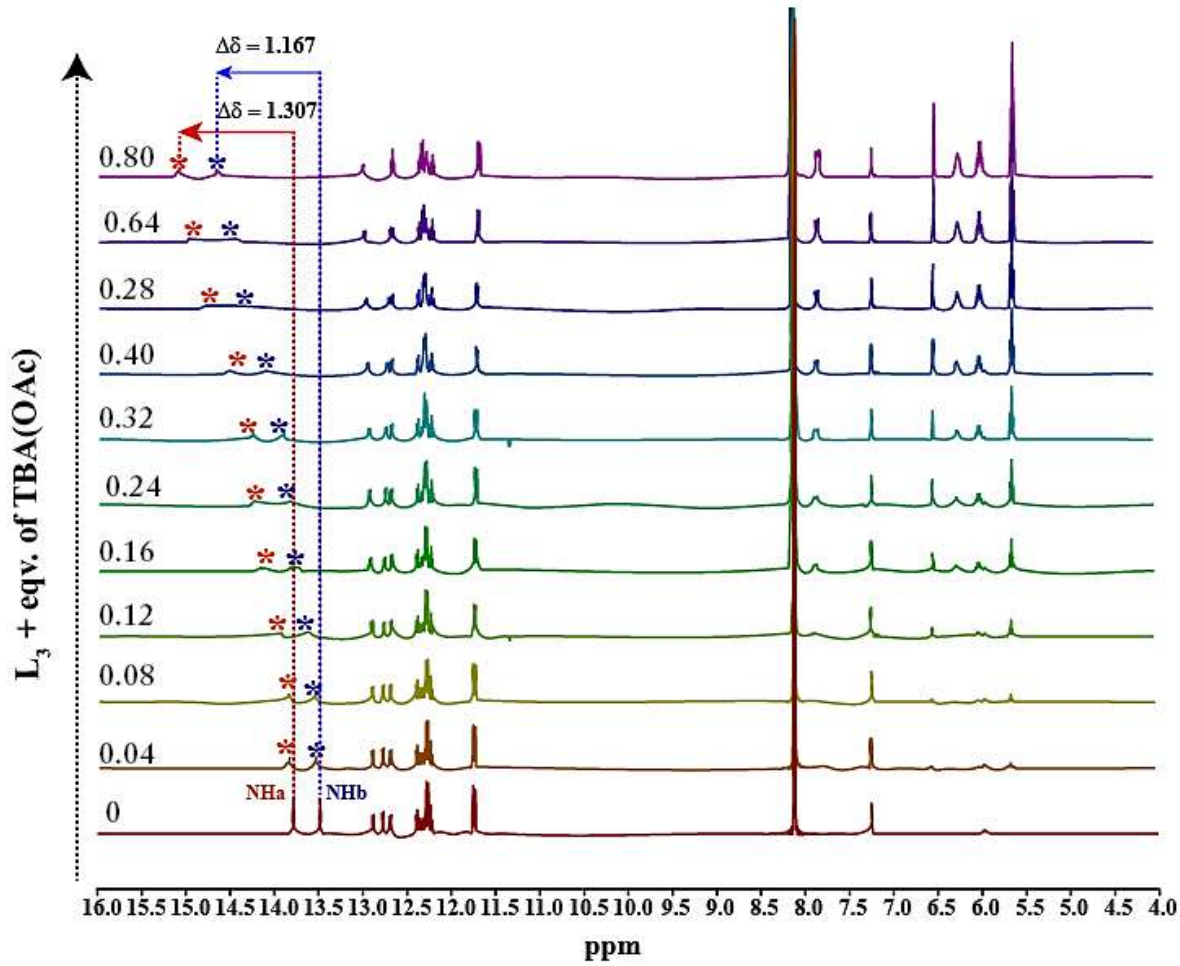

Figure 3A.7: Expanded ^{1}H NMR spectra of L_3 upon titration with TBA(OAc) in DMSO-d_6.

Table 3A.2. Binding constant values obtained from ^{1}H NMR titration for acetate anion (CH_3COO^-).

Host	Binding Stoichiometry	Binding Constant, K (M^{-1})
L_1	1:1	23.47
L_2	1:1	40.38
L_3	1:1	11.65

3A.3.5. Self-aggregation Studies of the Receptors

SC-XRD results have shown us the self-assembled architecture of the free receptor as induced by various intermolecular non-covalent interactions viz. C-H_{phenyl}···O_{nitro}, N-H_{urea}···O_{nitro}, N-H_{urea}···$O_{carbonyl}$, C-H_{phenyl}···π and π···π interactions among the free receptors as well in the acetate complex. This motivated us to conduct morphological study of the free receptor as well as its acetate complex. To do an extensive study of the same we performed FESEM study in an aqueous medium with a stock solution of L_1, L_2, and L_3 in DMSO (1 mM each) as well as all of those three

ligands with TBA(OAc) (1 mM each) (1:1). Very fine rod-shaped architectures have been observed for the free receptor L_1 alone, which disintegrates completely in the presence of the acetate anion. (Figure 3A.8a,d) In the case of L_2, very distinct blocked-shaped morphologies have been observed; while in the presence of acetate anion deterioration of those fine morphologies occurs. (Figure 3A.8b,e) For L_3, rice grain-like morphology was observed, however in the presence of the acetate anion a honeycomb-like morphology was observed. (Figure 3A.8c,f) Most remarkable morphological changes have been observed for L_1 as compared to the other two receptors L_2 and L_3. The reason for such morphological changes can be attributed to the interference of the acetate anion in the self-assembled architecture of the free receptor causing the breakdown of some of the aforementioned weak noncovalent interactions.

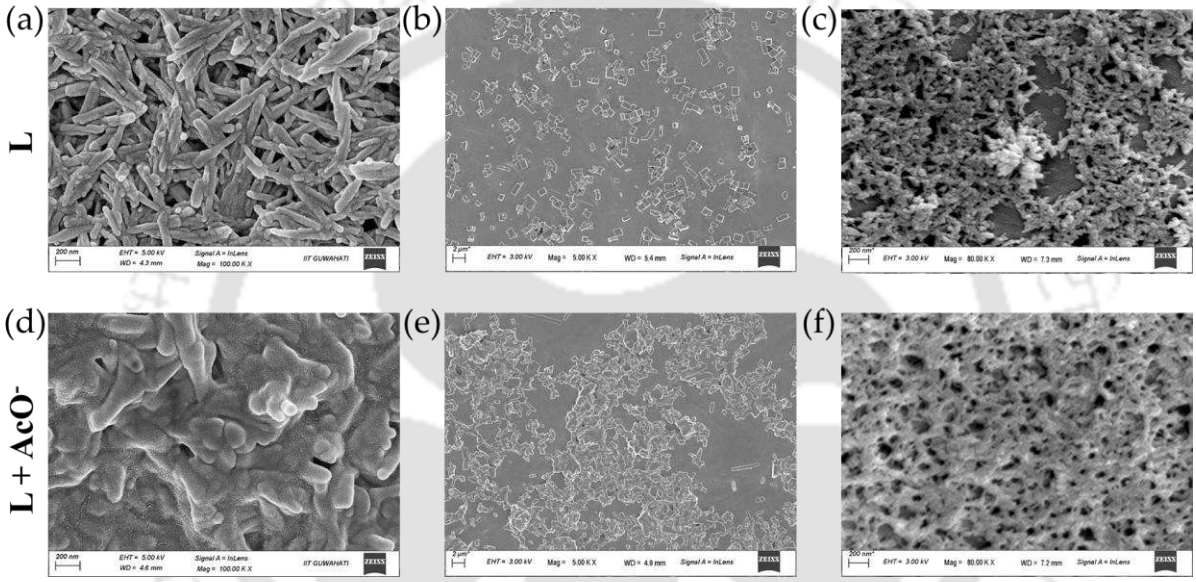

Figure 3A.8: FESEM image of (a) rod like free receptor L_1, (b) distinct blocked shaped morphology of L_2 (c) rice grain like morphology of L_3, (d) L_1 in presence of AcO^- (e) L_2 in presence of AcO^-, and (f) L_3 in presence of AcO^-.

3A.4. Conclusions

In summary, we have successfully designed a series of three bis-urea anion receptors (L_1-L_3) with varying electronic properties at the bis-urea receptor site. Only with receptor L_1, successful crystallisation with acetate anion was achieved among all of the other three receptors. Frequent co-crystallisation of strong hydrogen bond acceptor DMSO with L_2 having strong hydrogen bond donor sites, might be the reason why we could not crystallize L_2 with any anion. In the case of L_3, the reason for unsuccessful crystallisation with the anions can be attributed to the presence of more hydrophobic as well as electron rich naphthyl group in the terminal positions, which makes the urea hydrogen less acidic as compared to that of L_1 and L_2. This solid-state result encouraged us to do solution phase study of all of these three receptors in presence of acetate anion, which has

been executed through ^{1}H NMR. Along with this, morphological changes in presence of acetate anion have also been investigated using FESEM. We have also performed Hirshfeld surface (HS) analysis to establish the surface characteristics associated with our receptors as well as anion complex on the basis of various noncovalent interactions. This particular study shows how the anion recognition aptitude of the receptors can be modulated or tuned via minute structural modification of the receptor molecules.

References

[3A.1] L. Chen, S. N. Berry, X. Wu, E. N.W. Howe, and P.A. Gale, *Chem*, 2020, **6**, 61–141.

[3A.2] M. J. Langton, C. J. Serpell, and P. D. Beer, *Angew. Chem. Int. Ed.*, 2016, **55**, 1974–1987.

[3A.3] N. Busschaert, C. Caltagirone, W.V. Rossom, and P.A. Gale, *Chem. Rev.*, 2015, **115**, 8038–8155.

[3A.4] X. Wu, A.M. Gilchrist, and P.A. Gale, *Chem*, 2020, **6**, 1296–1309.

[3A.5] S. Bose, V. Ramesh, and J. W. Locasale, *Trends Cell Biol.*, 2019, **29** (9), 695-703.

[3A.6] S. Ayoob, and A. K. Gupta, *Crit. Rev. Environ. Sci. Technol.*, 2006, **36**, 433.

[3A.7] A. S. McCall, C. F. Cummings, G. Bhave, R. Vanacore, A. Page-McCaw, and B. G. Hudson, *Cell*, 2014, **15**, 1380.

[3A.8] U. Manna, S. Kayal, B. Nayak, and G. Das, *Dalton Trans.*, 2017, **46**, 11956-11969.

[3A.9] V.S. Bryantsev, and B. P. Hay, *Org. Lett.*, 2005, **7** (22), 5031-5034.

[3A.10] B. Nayak, S. Halder, and G. Das, *Cryst. Growth Des.*, 2019, **19** (4), 2298–2307.

[3A.11] A. Das, B. Nayak, and G. Das, *CrystEngComm*, 2020, **22**, 2197–2207.

[3A.12] U. Manna, and G. Das, *J. Mol. Struct.*, 2020, **1202**, 127289.

[3A.13] U. Manna, and G. Das, *CrystEngComm*, 2017, **19**, 5622–5634.

[3A.14] B. Nayak, U. Manna, and G. Das, *ChemistrySelect*, 2018, **3** (12), 3548–3554.

[3A.15] U. Manna, A. Das, and G. Das, *Cryst. Growth Des.*, 2018, **18** (11), 6801–6815.

[3A.16] B. Nayak, S. Halder, S. De, and G. Das, *CrystEngComm*, 2019, **21**, 7172–7181.

[3A.17] C. Li, J. Zhong, B. Liu, T. Yang, B. Lv, and Y. Luo, *ACS Omega*, 2021, **6** (8), 5532–5547.

[3A.18] H. Goyal, S. Pachisia, and R. Gupta, *Cryst. Growth Des.*, 2020, **20** (9), 6117–6128.

[3A.19] J.J. McKinnon, A.S. Mitchell, and M.A. Spackman, *Chem. Eur. J.*, 1998, **4** (11), 2136-2141.

[3A.20] T.E. Clark, M. Makha, A.N. Sobolev, and C.L. Raston, *Cryst. Growth Des.*, 2008, **8** (3), 890-896.

Annexure 3A

Table A3A.1: Crystallographic parameters and refinement data of the free receptors and the anionic complex.

Parameters	**L_1**	**L_1**+AcO^-	**L_2**+DMSO	**L_3**
formula	C_{26} H_{20} N_6 O_7	C_{44} H_{59} N_7 O_9	C_{36} H_{34} F_{12} N_4 O_6 S_3	C_{34} H_{26} N_4 O_3
fw	528.48	829.98	942.85	538.59
cryst syst	monoclinic	triclinic	triclinic	orthorhombic
space group	P 21	P 1	P-1	P c c n
a (Å)	13.1109 (7)	8.753 (3)	9.796 (5)	50.331 (6)
b (Å)	4.9682 (2)	10.534 (4)	10.393 (5)	4.5754 (6)
c (Å)	18.9365 (9)	13.332 (5)	23.958 (12)	11.2896 (14)
α (deg)	90	110.124 (10)	98.900 (15)	90
β (deg)	108.162 (2)	93.196 (10)	95.568 (14)	90
γ (deg)	90	98.877 (10)	111.834 (13)	90
V ($Å^3$)	1172.03 (10)	1132.5 (7)	2205.0 (19)	2599.8(6)
Z	2	1	2	4
DC (g cm-3)	1.497	1.217	1.420	1.376
μ (Mo Kα) (mm−1)	0.112	0.086	0.265	0.090
F (000)	548.0	444.0	964.0	1128.0
T (K)	296 K	296 K	297 K	296 K
θmax (deg)	27.973	24.998	19.808	24.997
total no. of rflns	52306	32116	35013	58593
no. of indep rflns	5650	7882	3957	2304
no. of obsd rflns	3648	6907	2986	1767
no.of params refined	353	547	565	187
R1, I > 2σ(I)	0.0481(3648)	0.0419 (6907)	0.1147 (2986)	0.1109 (1765)
wR2, I > 2σ(I)	0.1499(5650)	0.1301 (7882)	0.3342 (3957)	0.3689 (2302)
GOF (F^2)	0.677	0.743	1.030	1.167
CCDC no.	2214012	2214037	2241252	2241257

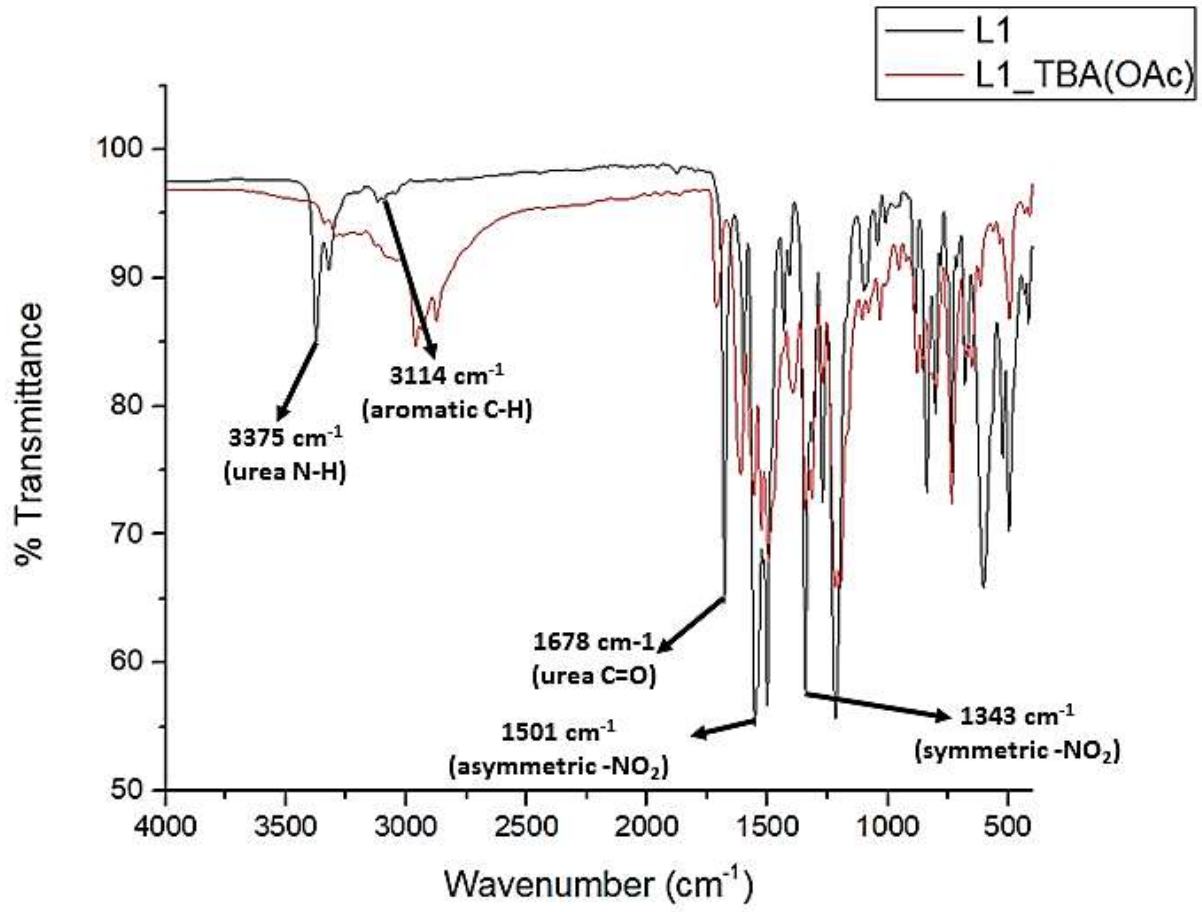

Figure A3A.1: Combined FT-IR spectrum of the complex L_1 and L_1 + TBA(OAc) recorded in KBr pellet at 25°C.

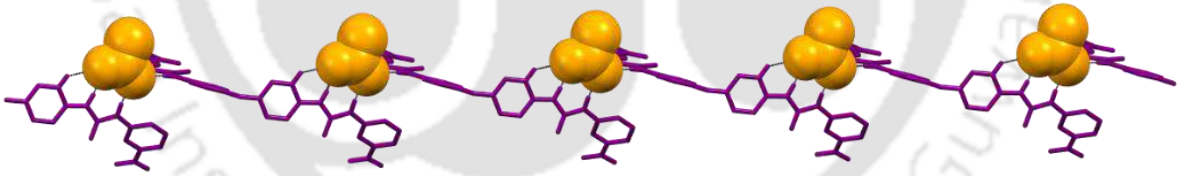

Figure A3A.2: Symmetry equivalent view of the L_1. acetate complex.

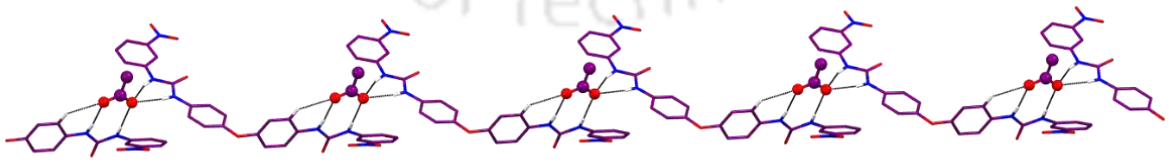

Figure A3A.3: 1-D polymeric chain arrangement of the L_1.acetate complex.

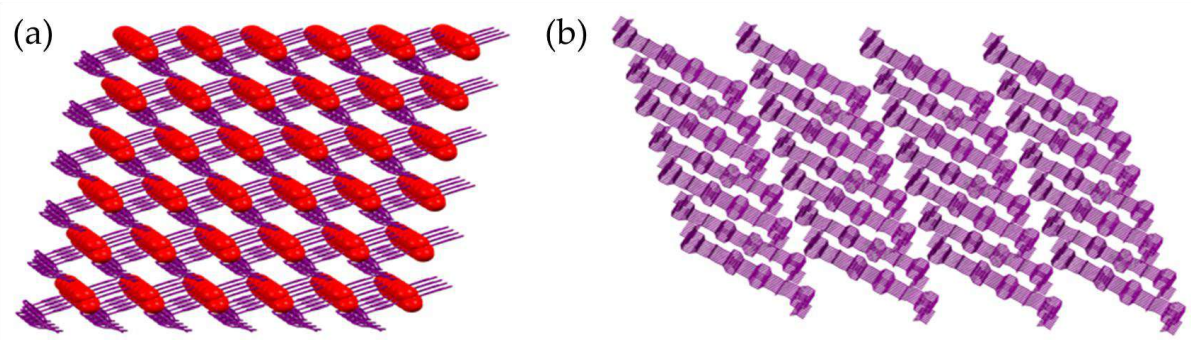

Figure A3A.4: Parallel packing of (a) L_1 + AcO^- and (b) free receptor L_1.

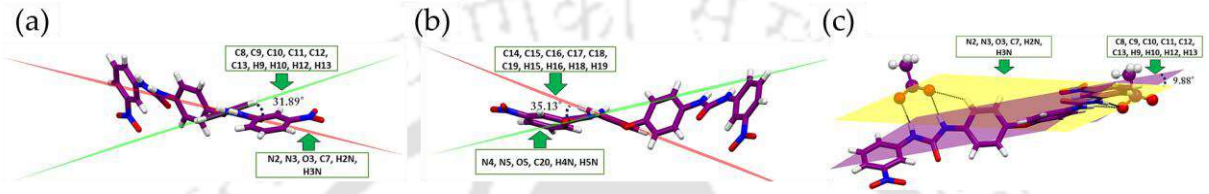

Figure A3A.5: Dihedral angle between the central phenyl ring and the receptor site (urea NH) in the two arms of the free receptor L_1, (a) & (b) before acetate binding. (c) Change in the dihedral angles after acetate binding. (the atoms through which the planes are passing by have been depicted in the rectengular box near each plane)

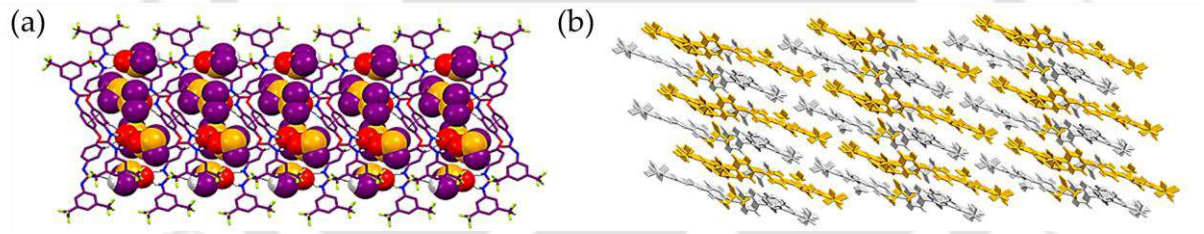

Figure A3A.6: (a) DMSO assisted 1D self-assembled polymeric arrangement of L_2.DMSO. (b) Symmetry operation view of L_2.DMSO.

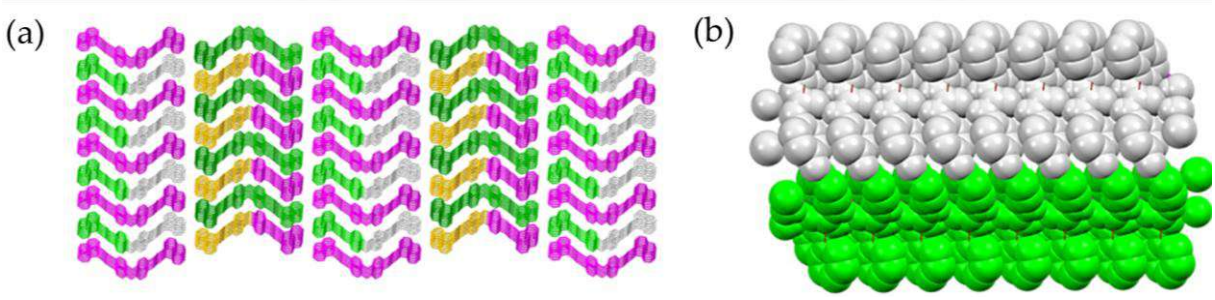

Figure A3A.7: Symmetry operation view of (a) parallelly packed self-assembled architecture of L_3. (b) Self-assembled architecture of L_3 in space fill model.

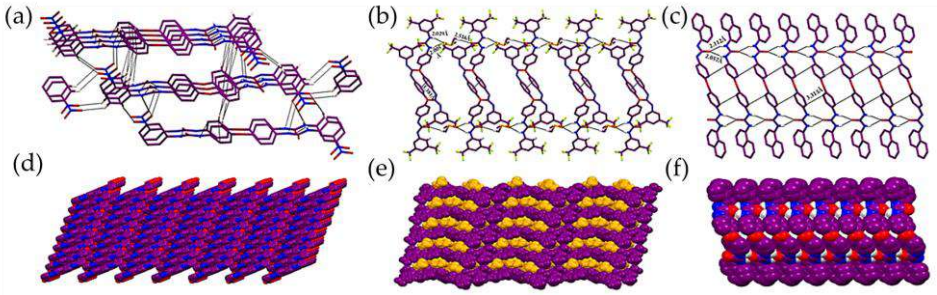

Figure A3A.8: SC-XRD view of (a) ligand-ligand interactions of the free receptor L_1, (b) hydrogen bonding and π···π interactions between DMSO and L_2, (c) 1D uniformly layered self-assembled architecture of L_3 as facilitated by hydrogen bonding interaction and π···π stacking interaction, (d) space fill packing view of L_1, (e) space-fill view of L_2.DMSO packing, (f) space-fill view of L_3 packing.

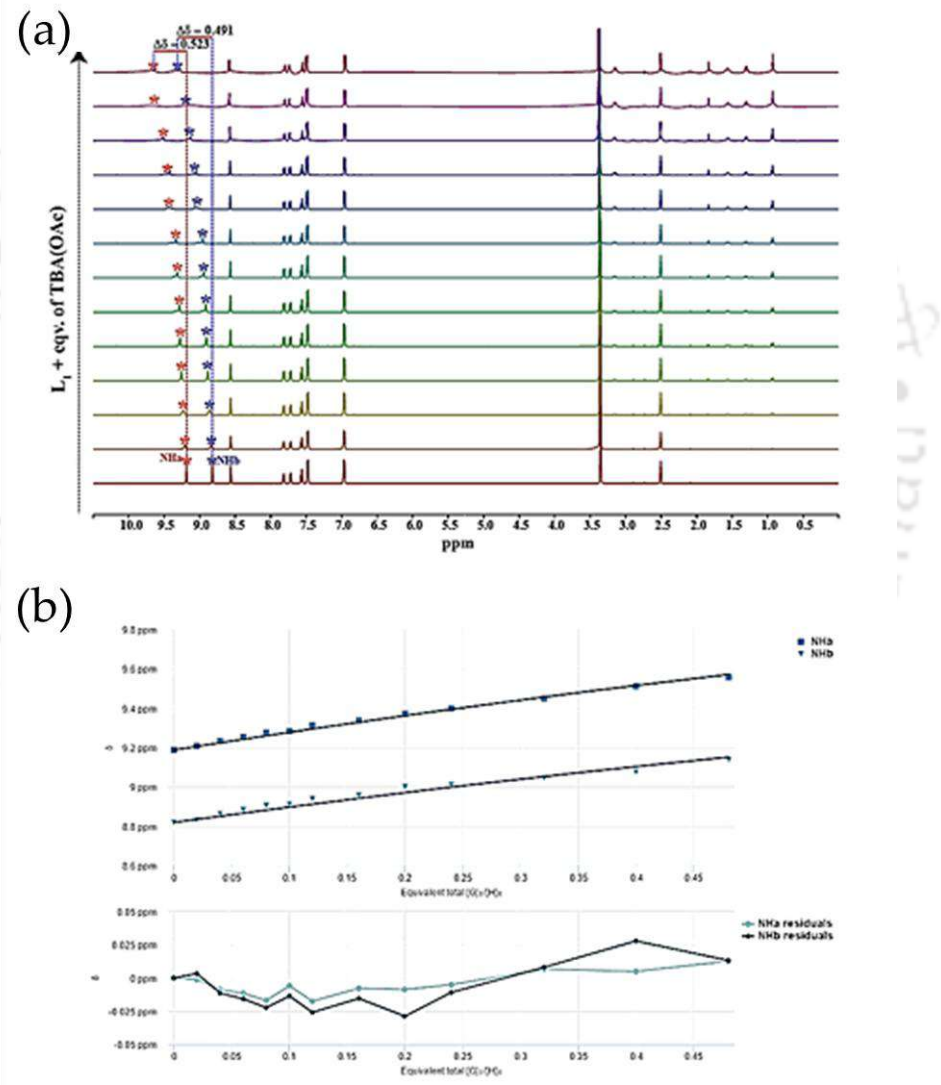

Figure A3A.9: (a) ^{1}H-NMR titration spectra for receptor L_1 (50 mM) with the incremental addition of TBA(OAc) (500 Mm) in DMSO-d_6 solvent. The amounts of added TBA(OAc) are shown on the spectra. (b) The plot of chemical shift (δ) of NH_a and NH_b protons vs. Equivalent total ($[G]_0/[H]_0$) added, fitted to 1:1 binding model of BindFit v0.5 program. Here 'H' represents Host and 'G' represents Guest (TBA(OAc)). (http://app.supramolecular.org/bindfit/view/4e2a7893-9b1b-4abd-8469-d8f20d4d54eb)

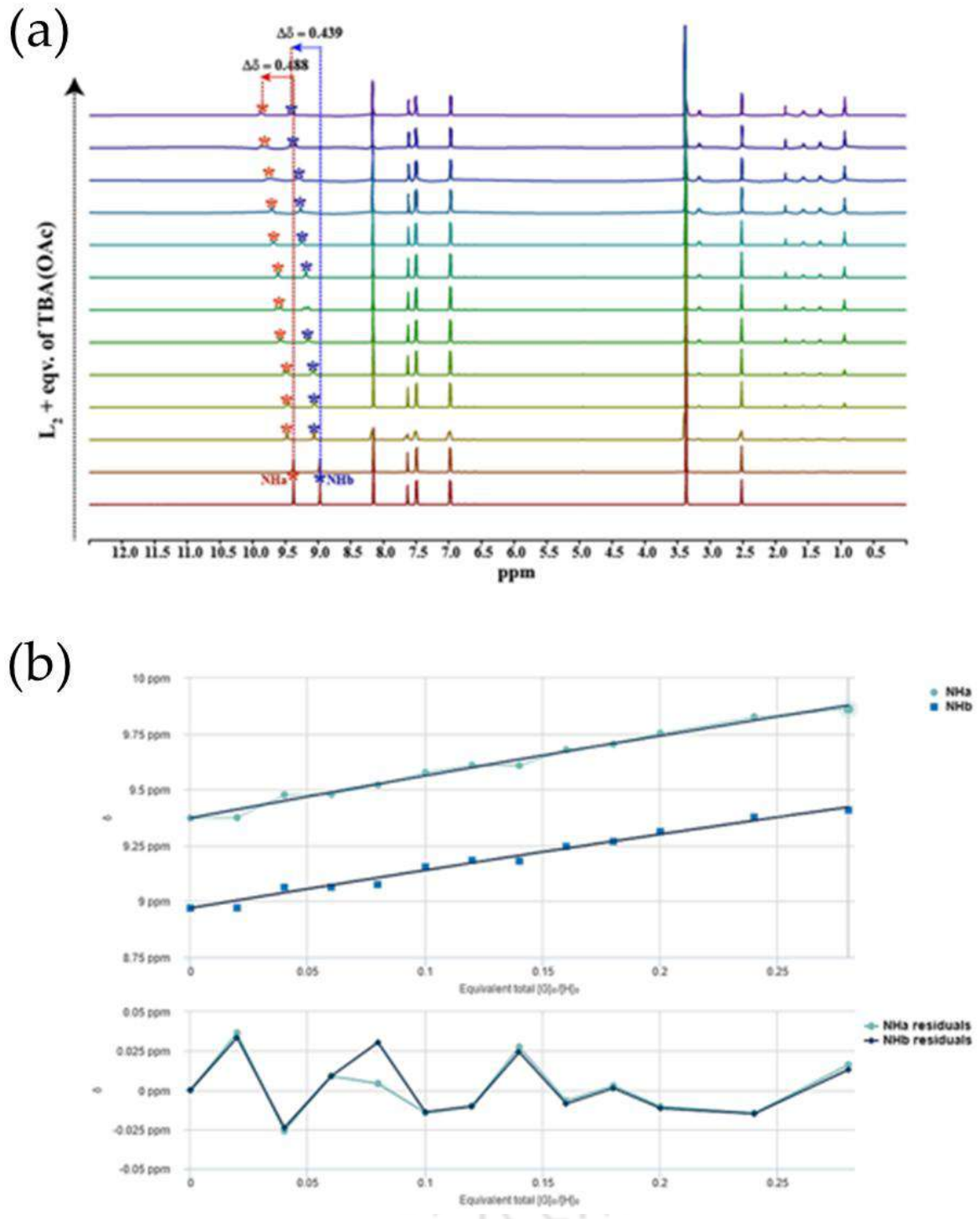

Figure A3A.10: (a) ^{1}H-NMR titration spectra for receptor L_2 (50 mM) with the incremental addition of TBA(OAc) (500 mM) in DMSO-d_6 solvent. The amounts of added TBA(OAc) are shown on the spectra. (b) The plot of chemical shift (δ) of NH_a and NH_b protons vs. Equivalent total ($[G]_0/[H]_0$) added, fitted to 1:1 binding model of BindFit v0.5 program. Here 'H' represents Host and 'G' represents Guest (TBA(OAc)). (http://app.supramolecular.org/bindfit/view/0409340a-04d8-4bc8-8208-3a216dd0a707)

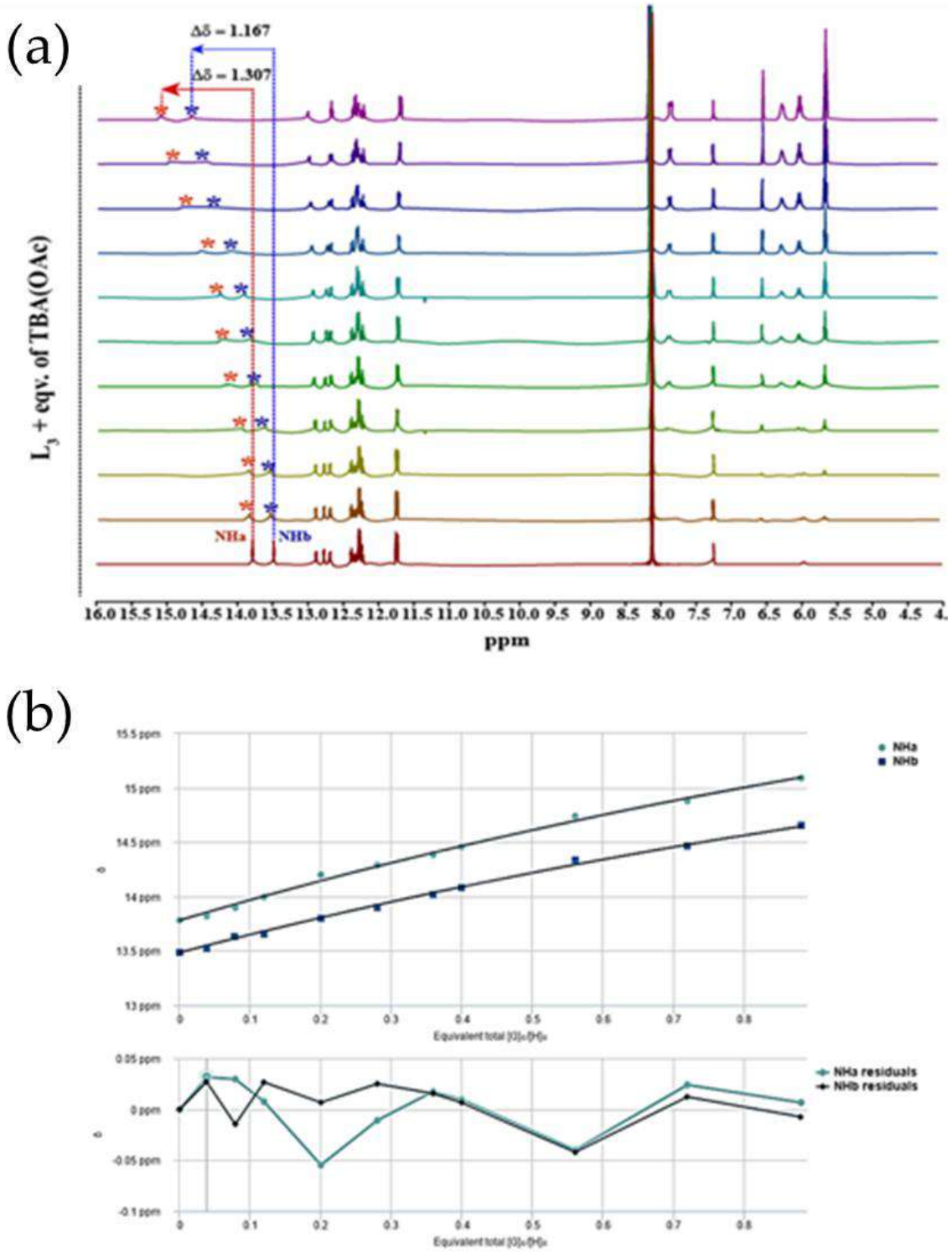

Figure A3A.11: (a) ^{1}H-NMR titration spectra for receptor L_3 (50 mM) with the incremental addition of TBA(OAc) (500 mM) in DMSO-d_6 solvent. The amounts of added TBA(OAc) are shown on the spectra. (b) The plot of chemical shift (δ) of NH_a and NH_b protons vs. Equivalent total ($[G]_0/[H]_0$) added, fitted to 1:1 binding model of BindFit v0.5 program. Here 'H' represents Host and 'G' represents Guest (TBA(OAc)). (http://app.supramolecular.org/bindfit/view/6e5fff58-be22-43a2-9b3b-c099fead90f3)

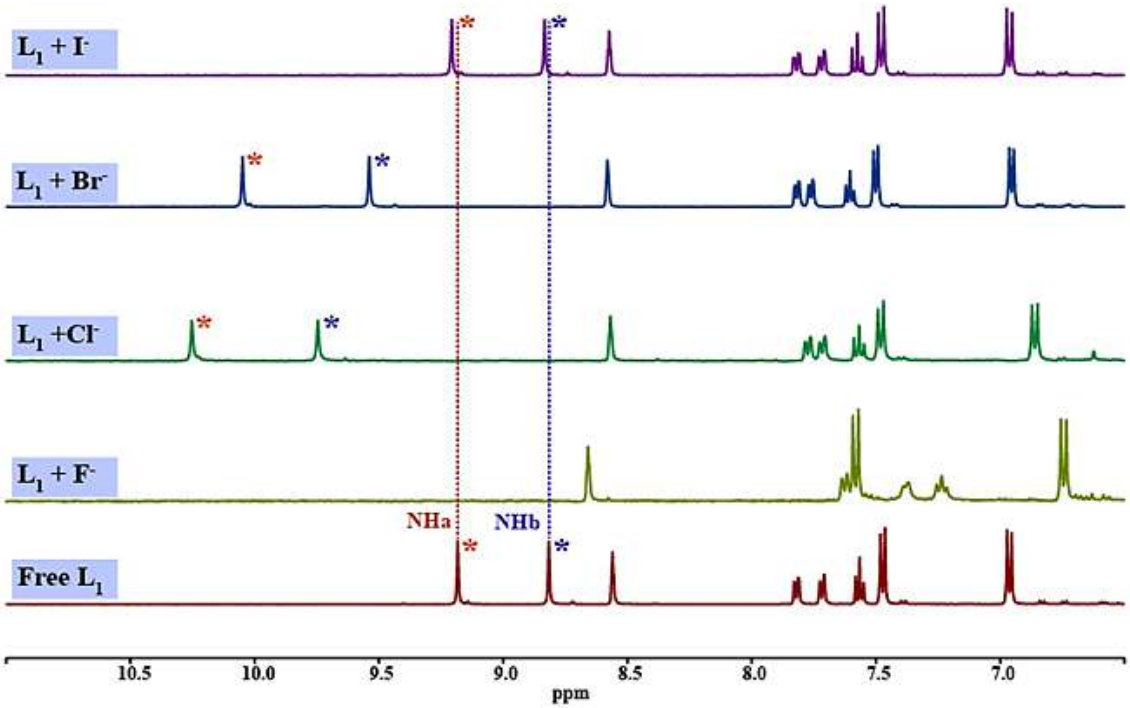

Figure A3A.12: Expanded comparative stacked ^{1}H NMR spectra of the bis-urea receptors L_1, in DMSO-d_6 at 25°C in the presence of different halides as their TBA salts and the observable downfield shifting of the NH_a and NH_b peaks for L_1.

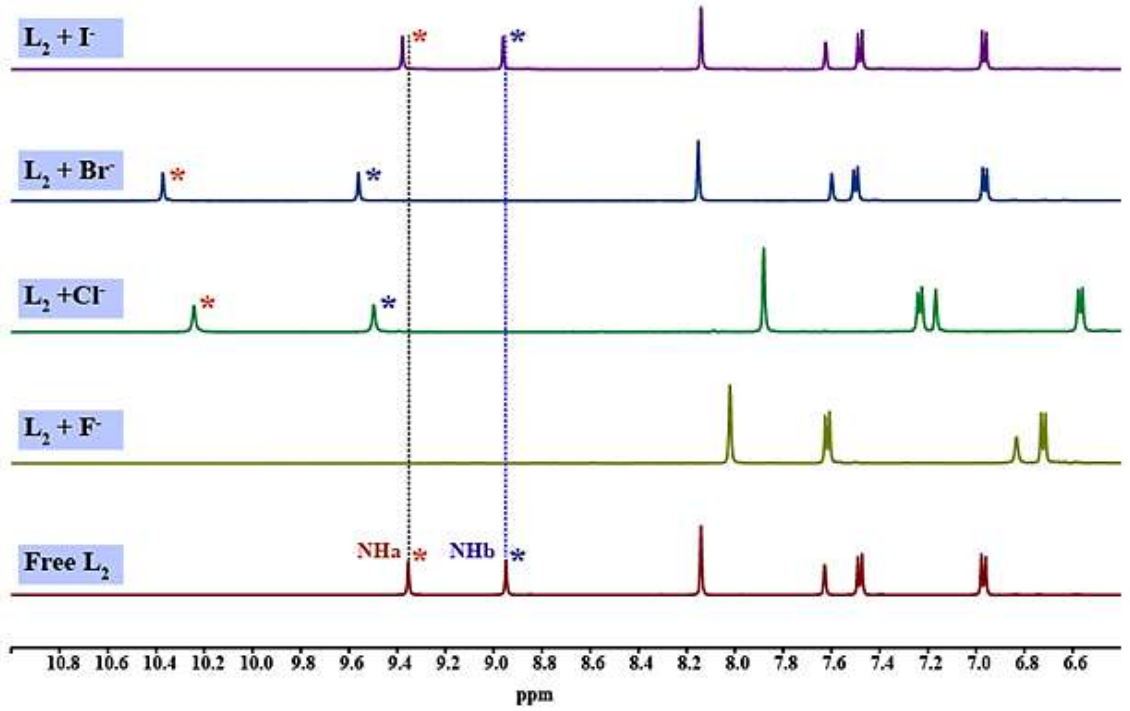

Figure A3A.13: Expanded comparative stacked ^{1}H NMR spectra of the bis-urea receptors L_2 in DMSO-d_6 at 25°C in the presence of different halides as their TBA salts and the observable downfield shifting of the NH_a and NH_b peaks for L_2.

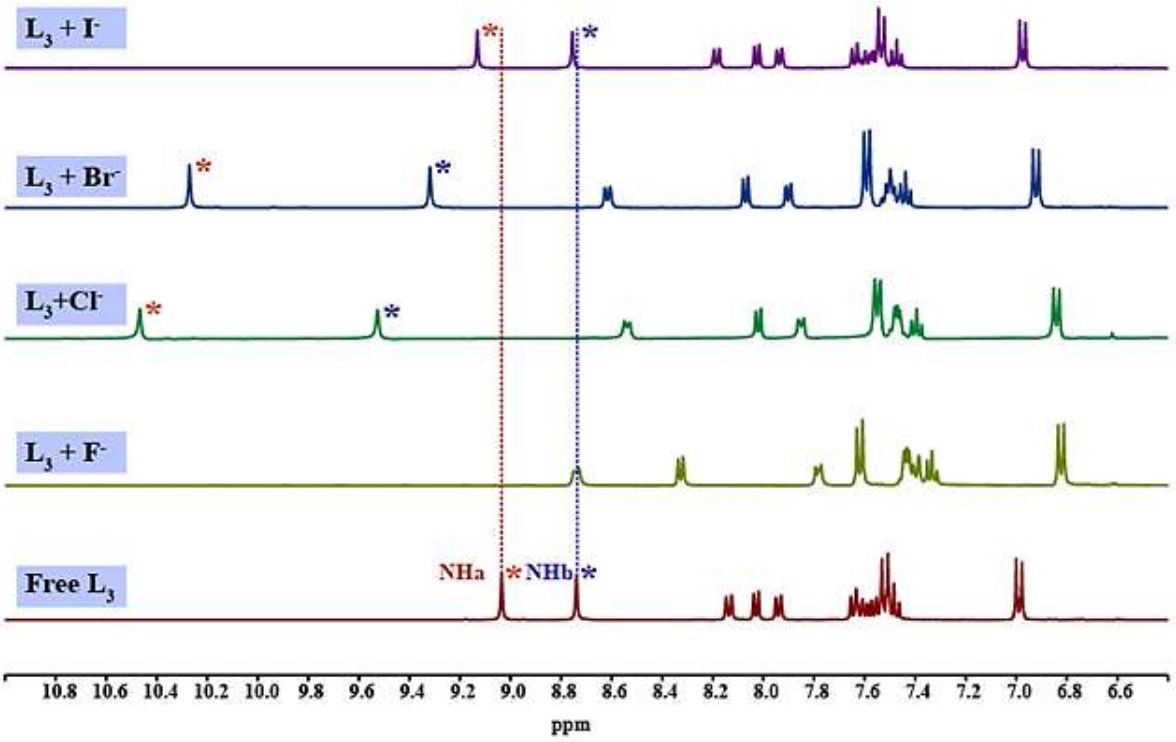

Figure A3A.14: Expanded comparative stacked ^{1}H NMR spectra of the bis-urea receptors L_3 in DMSO-d_6 at 25°C in the presence of different halides as their TBA salts and the observable downfield shifting of the NH_a and NH_b peaks for L_3.

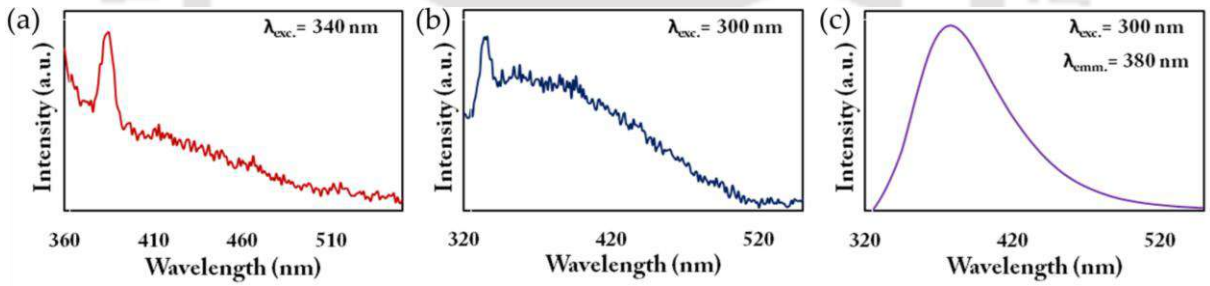

Figure A3A.15: Emission spectrum of (a) L_1, (b) L_2 and (c) L_3 in aqueous medium.

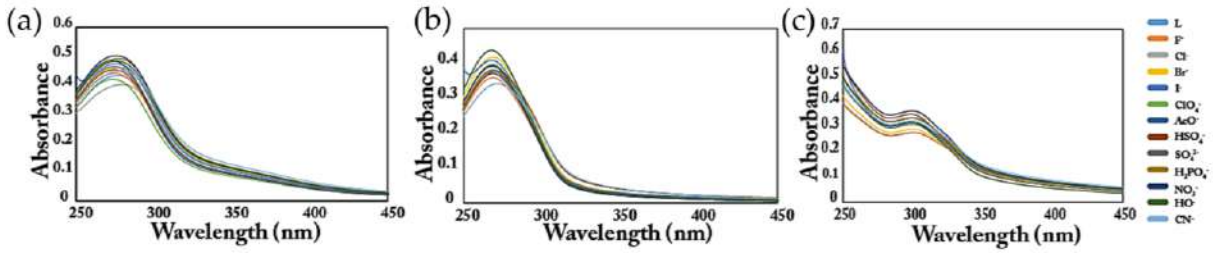

Figure A3A.16: UV-Vis spectrum of (a) L_1, (b) L_2 and (c) L_3 in presence of different anions in aqueous medium.

Table A3A.2: Hydrogen bonding distances (Å) and Bond angles (°) in the neutral receptor and the anionic complex.

Ligand/Complex	D–H···A	d(D···H)/Å	d(H···A)/Å	d(D···A)/Å	<D–H···A/°	Symmetry codes
$L_1 + AcO^-$	N2-H2N···O9	0.86	2.03	2.858 (4)	162	x, y, 1+z
	N3-H3N···O9	0.86	2.11	2.918 (4)	156	x, y, 1 + z
	N4-H4N···O8	0.86	1.99	2.842 (5)	171	-1+x, y, z
	N5-H5N···O9	0.86	2.00	2.798 (4)	153	-1+x, y, z
	C6-H6···O3	0.93	2.30	2.884 (5)	121	x, y, z
	C13-H13···O3	0.93	2.34	2.928 (6)	121	x, y, z
	C16-H16···O5	0.93	2.32	2.907 (5)	121	x, y, z
	C22-H22···O5	0.93	2.43	2.911 (5)	112	x, y, z
	C35-H35A···O1	0.97	2.54	3.196 (6)	125	-1+x, y, z
	C35-H35B···O3	0.97	2.59	3.554 (5)	171	x, y, z
L_1	N2-H2N···O3	0.86	2.13	2.921 (5)	152	x, -1+y, z
	N3H3N···O6	0.86	2.41	3.086 (5)	135	-x, -3/2+y, 1-z
	N4-H4N···O5	0.86	2.34	3.178 (5)	164	x, -1 + y, z
	N5-H5N···O2	0.86	2.41	3.077 (6)	135	1-x, -1/2+y, 1-z
	C6-H6···O3	0.93	2.34	2.814 (5)	111	x, y, z
	C13-H13···O3	0.93	2.40	2.867 (5)	111	x, y, z
	C18-H18···O5	0.93	2.54	2.979 (6)	109	x, y, z
	C22-H22···O1	0.93	2.53	3.448 (6)	168	1-x, -1/2+y, 1-z
	C23-H23···O1	0.93	2.55	3.227 (5)	130	-1 + x, y, 1 + z
	C26-H26···O5	0.93	2.41	2.931 (5)	115	x, y, z
L_2 + DMSO	N1-H1N···O5	0.86	2.11	2.906 (13)	153	2-x, 1-y, 1-z
	N2-H2N···O6	0.86	2.54	3.28 (2)	145	2-x, 1-y, 1-z
	N3-H3N···O4	0.86	2.01	2.821 (13)	158	1+x, y, z
	N4-H4N···O4	0.86	2.03	2.842 (13)	156	1+x, y, z
	C3-H3···O6	0.93	2.51	3.34 (2)	148	2-x, 1-y, 1-z
	C5-H5···O1	0.93	2.43	2.921 (12)	113	x, y, z
	C13-H13···O1	0.93	2.39	2.901 (12)	115	x, y, z
	C20-H20···O3	0.93	2.34	2.891 (12)	118	x, y, z
	C21-H21···O6	0.93	2.59	3.509 (19)	173	-1+x, y, z
	C31-H31B···O3	0.96	2.54	3.37 (2)	144	x, y, z
L_3	N1-H1N···O2	0.86	2.06	2.834 (6)	150	x, -1+y, z
	N2-H2N···O2	0.86	2.11	2.893 (6)	151	x, -1+y, z
	C5-H5···O2	0.93	2.52	2.908 (6)	106	x, y, z

Table A3A.3: Final Coordinates and Equivalent Isotropic Displacement Parameters of the non-Hydrogen atoms For **L_1**

Atom	x	y	z	U(eq) [Ang^2]
O1	0.83442	0.93717	0.08548	0.0777
O2	0.80109	1.07939	0.18275	0.0629
O3	0.52514	0.90425	0.25779	0.0534
O4	0.28790	1.25382	0.48591	0.0702
O5	0.00839	1.33296	0.70930	0.0540
O6	-0.26984	1.66113	0.77999	0.0620
O7	-0.31612	1.57048	0.87682	0.0782
N1	0.78536	0.92424	0.13072	0.0490
N2	0.51692	0.47252	0.21667	0.0456
N3	0.43475	0.59063	0.30187	0.0470
N4	0.07048	0.93333	0.68101	0.0548
N5	0.00343	0.95841	0.77718	0.0590
N6	-0.26077	1.53132	0.83620	0.0501
C1	0.70203	0.71971	0.12035	0.0378
C2	0.67740	0.55894	0.05841	0.0449

C3	0.59948	0.36793	0.05074	0.0490
C4	0.54687	0.34039	0.10302	0.0437
C5	0.57209	0.50879	0.16497	0.0371
C6	0.65196	0.69837	0.17461	0.0384
C7	0.49500	0.67565	0.25895	0.0390
C8	0.40040	0.75624	0.35088	0.0391
C9	0.30361	0.69547	0.36242	0.0452
C10	0.26629	0.85318	0.40899	0.0510
C11	0.32537	1.07313	0.44384	0.0462
C12	0.42232	1.12898	0.43436	0.0466
C13	0.46005	0.97124	0.38789	0.0424
C14	0.23209	1.15875	0.53199	0.0477
C15	0.27062	0.95375	0.58173	0.0592
C16	0.21652	0.88586	0.63111	0.0551
C17	0.12464	1.02134	0.63064	0.0417
C18	0.08688	1.22306	0.58035	0.0500
C19	0.14109	1.29244	0.53086	0.0514

C20	0.02592	1.09639	0.72053	0.0427
C21	-0.05042	1.05075	0.82495	0.0404
C22	-0.03352	0.91358	0.89143	0.0452
C23	-0.09080	0.97817	0.93875	0.0495
C24	-0.16563	1.17900	0.92145	0.0464
C25	-0.17966	1.31861	0.85611	0.0416
C26	-0.12346	1.26032	0.80777	0.0408

U(eq) = 1/3 of the trace of the orthogonalized U Tensor

Table A3A.4: Hydrogen Atom Positions and Isotropic Displacement Parameters For **L_1**

Atom	x	y	z	U(iso) [Ang^2]
H2	0.71240	0.57903	0.02290	0.0539
H2N	0.49536	0.31287	0.22235	0.0547
H3	0.58172	0.25479	0.00957	0.0589
H3N	0.41628	0.42388	0.29890	0.0563
H4	0.49433	0.20891	0.09695	0.0524
H4N	0.06571	0.76260	0.68679	0.0658
H5N	0.02558	0.79460	0.78369	0.0708

H6	0.67169	0.80881	0.21633	0.0461
H9	0.26379	0.54801	0.33870	0.0542
H10	0.20156	0.81174	0.41693	0.0612
H12	0.46294	1.27351	0.45926	0.0560
H13	0.52601	1.01011	0.38150	0.0508
H15	0.33255	0.86155	0.58217	0.0711
H16	0.24234	0.74735	0.66502	0.0661
H18	0.02450	1.31430	0.57931	0.0600
H19	0.11524	1.43056	0.49682	0.0617
H22	0.01716	0.77630	0.90413	0.0542
H23	-0.07844	0.88400	0.98308	0.0594
H24	-0.20583	1.22035	0.95270	0.0557
H26	-0.13428	1.35961	0.76442	0.0489

==========

The Temperature Factor has the Form of Exp(-T) Where

T = 8*(Pi**2)*U*(Sin(Theta)/Lambda)**2 for Isotropic Atoms

Table A3A.5: (An)isotropic Displacement Parameters For L_1

Atom	U(1,1) or U	U(2,2)	U(3,3)	U(2,3)	U(1,3)	U(1,2)

O1	0.0824	0.0847	0.0918	-0.0073	0.0644	-0.0265
O2	0.0642	0.0658	0.0601	-0.0099	0.0215	-0.0277
O3	0.0833	0.0302	0.0658	0.0002	0.0511	-0.0079
O4	0.1055	0.0457	0.0897	0.0054	0.0745	0.0036
O5	0.0712	0.0407	0.0620	0.0056	0.0381	0.0081
O6	0.0675	0.0561	0.0597	0.0036	0.0159	0.0209
O7	0.0700	0.0993	0.0771	0.0015	0.0399	0.0388
N1	0.0424	0.0499	0.0572	0.0084	0.0190	-0.0031
N2	0.0640	0.0288	0.0556	-0.0004	0.0356	-0.0102
N3	0.0674	0.0391	0.0464	-0.0047	0.0351	-0.0155
N4	0.0803	0.0411	0.0606	0.0101	0.0473	0.0127
N5	0.0838	0.0499	0.0633	0.0219	0.0519	0.0339
N6	0.0472	0.0527	0.0485	-0.0068	0.0120	0.0129
C1	0.0395	0.0362	0.0419	0.0079	0.0186	-0.0003
C2	0.0493	0.0492	0.0409	0.0017	0.0207	0.0031
C3	0.0548	0.0520	0.0427	-0.0093	0.0188	-0.0023

C4	0.0492	0.0375	0.0474	-0.0051	0.0194	-0.0074
C5	0.0439	0.0323	0.0403	0.0016	0.0204	0.0010
C6	0.0443	0.0345	0.0389	-0.0009	0.0164	-0.0044
C7	0.0476	0.0347	0.0395	0.0022	0.0204	-0.0044
C8	0.0468	0.0406	0.0333	0.0058	0.0177	-0.0021
C9	0.0514	0.0500	0.0387	0.0013	0.0206	-0.0112
C10	0.0518	0.0559	0.0550	0.0113	0.0307	-0.0010
C11	0.0617	0.0414	0.0440	0.0056	0.0288	0.0043
C12	0.0591	0.0426	0.0418	0.0007	0.0208	-0.0055
C13	0.0467	0.0461	0.0396	0.0009	0.0211	-0.0078
C14	0.0626	0.0434	0.0479	-0.0031	0.0329	-0.0012
C15	0.0589	0.0630	0.0670	0.0093	0.0357	0.0202
C16	0.0686	0.0558	0.0497	0.0128	0.0313	0.0216
C17	0.0543	0.0421	0.0351	0.0023	0.0233	0.0044
C18	0.0517	0.0510	0.0539	0.0086	0.0259	0.0114
C19	0.0644	0.0470	0.0491	0.0114	0.0267	0.0044
C20	0.0490	0.0433	0.0425	0.0065	0.0241	0.0082

C21	0.0432	0.0428	0.0418	0.0019	0.0225	0.0076
C22	0.0474	0.0463	0.0454	0.0038	0.0196	0.0118
C23	0.0584	0.0572	0.0383	0.0041	0.0229	0.0077
C24	0.0474	0.0580	0.0390	-0.0038	0.0209	0.0046
C25	0.0385	0.0429	0.0440	-0.0048	0.0137	0.0060
C26	0.0461	0.0416	0.0380	0	0.0180	0.0047

==========

The Temperature Factor has the Form of Exp(-T) Where
T = 8*(Pi**2)*U*(Sin(Theta)/Lambda)**2 for Isotropic Atoms
T = 2*(Pi**2)*Sumij(h(i)*h(j)*U(i,j)*Astar(i)*Astar(j)), for Anisotropic Atoms. Astar(i) are Reciprocal Axial Lengths and h(i) are the Reflection Indices.

Table A3A.6: Bond Distances (Angstrom) For **L1**

O1	-N1	1.2228(1)	C8	-C13	1.3792(1)
O2	-N1	1.2169(1)	C8	-C9	1.3863(1)
O3	-C7	1.2050(1)	C9	-C10	1.3784(1)
O4	-C11	1.3878(1)	C10	-C11	1.3825(1)
O4	-C14	1.3848(1)	C11	-C12	1.3665(1)
O5	-C20	1.2037(1)	C12	-C13	1.3801(1)
O6	-N6	1.2183(1)	C14	-C19	1.3598(1)

O7	-N6	1.2265(1)	C14	-C15	1.3723(1)
N1	-C1	1.4598(1)	C15	-C16	1.3802(1)
N2	-C5	1.3984(1)	C16	-C17	1.3776(1)
N2	-C7	1.3731(1)	C17	-C18	1.3648(1)
N3	-C7	1.3652(1)	C18	-C19	1.3847(1)
N3	-C8	1.4148(1)	C21	-C22	1.3872(1)
N4	-C17	1.4239(1)	C21	-C26	1.3830(1)
N4	-C20	1.3529(1)	C22	-C23	1.3746(1)
N5	-C20	1.3801(1)	C23	-C24	1.3657(1)
N5	-C21	1.3876(1)	C24	-C25	1.3799(1)
N6	-C25	1.4628(1)	C25	-C26	1.3730(1)
C1	-C2	1.3718(1)	C2	-H2	0.9300
C1	-C6	1.3851(1)	C3	-H3	0.9300
C2	-C3	1.3685(1)	C4	-H4	0.9300
N2	-H2N	0.8600	C6	-H6	0.9300
N3	-H3N	0.8600	C9	-H9	0.9300
C3	-C4	1.3785(1)	C10	-H10	0.9300

N4	-H4N	0.8600	C12	-H12	0.9300
C4	-C5	1.3941(1)	C13	-H13	0.9300
C5	-C6	1.3776(1)	C15	-H15	0.9300
N5	-H5N	0.8600	C16	-H16	0.9300
C18	-H18	0.9300	C23	-H23	0.9300
C19	-H19	0.9300	C24	-H24	0.9300
C22	-H22	0.9300	C26	-H26	0.9300

Table A3A.7: Bond Angles (Degrees) For **L_1**

C11	-O4	-C14	119.48(1)	C1	-C6	-C5	118.07(1)
O1	-N1	-O2	122.72(1)	O3	-C7	-N2	123.56(1)
O1	-N1	-C1	118.51(1)	O3	-C7	-N3	123.81(1)
O2	-N1	-C1	118.74(1)	N2	-C7	-N3	112.64(1)
C5	-N2	-C7	124.15(1)	N3	-C8	-C9	118.09(1)
C7	-N3	-C8	124.91(1)	N3	-C8	-C13	122.52(1)
C17	-N4	-C20	125.32(1)	C9	-C8	-C13	119.38(1)
C20	-N5	-C21	128.16(1)	C8	-C9	-C10	120.13(1)
O6	-N6	-O7	123.26(1)	C9	-C10	-C11	119.80(1)
O6	-N6	-C25	118.21(1)	C10	-C11	-C12	120.24(1)

O7	-N6	-C25	118.53(1)	O4	-C11	-C10	122.65(1)
N1	-C1	-C2	119.16(1)	O4	-C11	-C12	117.02(1)
N1	-C1	-C6	117.47(1)	C11	-C12	-C13	120.10(1)
C2	-C1	-C6	123.37(1)	C8	-C13	-C12	120.30(1)
C1	-C2	-C3	117.61(1)	O4	-C14	-C19	117.18(1)
C5	-N2	-H2N	118.00	C15	-C14	-C19	120.45(1)
C7	-N2	-H2N	118.00	O4	-C14	-C15	122.13(1)
C2	-C3	-C4	121.12(1)	C14	-C15	-C16	119.31(1)
C7	-N3	-H3N	118.00	C15	-C16	-C17	120.62(1)
C8	-N3	-H3N	118.00	N4	-C17	-C18	123.01(1)
C20	-N4	-H4N	117.00	C16	-C17	-C18	119.31(1)
C3	-C4	-C5	120.28(1)	N4	-C17	-C16	117.60(1)
C17	-N4	-H4N	117.00	C17	-C18	-C19	120.27(1)
N2	-C5	-C6	122.21(1)	C14	-C19	-C18	120.04(1)
N2	-C5	-C4	118.23(1)	O5	-C20	-N4	125.35(1)
C20	-N5	-H5N	116.00	O5	-C20	-N5	123.17(1)
C4	-C5	-C6	119.53(1)	N4	-C20	-N5	111.48(1)

C21	-N5	-H5N	116.00	N5	-C21	-C22	117.35(1)
N5	-C21	-C26	123.46(1)	C11	-C12	-H12	120.00
C22	-C21	-C26	119.10(1)	C13	-C12	-H12	120.00
C21	-C22	-C23	120.78(1)	C8	-C13	-H13	120.00
C22	-C23	-C24	120.78(1)	C12	-C13	-H13	120.00
C23	-C24	-C25	117.87(1)	C14	-C15	-H15	120.00
N6	-C25	-C24	118.51(1)	C16	-C15	-H15	120.00
C24	-C25	-C26	122.85(1)	C15	-C16	-H16	120.00
N6	-C25	-C26	118.60(1)	C17	-C16	-H16	120.00
C21	-C26	-C25	118.57(1)	C17	-C18	-H18	120.00
C1	-C2	-H2	121.00	C19	-C18	-H18	120.00
C3	-C2	-H2	121.00	C14	-C19	-H19	120.00
C2	-C3	-H3	119.00	C18	-C19	-H19	120.00
C4	-C3	-H3	119.00	C21	-C22	-H22	120.00
C3	-C4	-H4	120.00	C23	-C22	-H22	120.00
C5	-C4	-H4	120.00	C22	-C23	-H23	120.00
C1	-C6	-H6	121.00	C24	-C23	-H23	120.00
C5	-C6	-H6	121.00	C23	-C24	-H24	121.00

C8	-C9	-H9	120.00	C25	-C24	-H24	121.00
C10	-C9	-H9	120.00	C21	-C26	-H26	121.00
C9	-C10	-H10	120.00	C25	-C26	-H26	121.00
C11	-C10	-H10	120.00				

Table A3A.8: Torsion Angles (Degrees) For **L1**

C14	-O4	-C11	-C12	-143.62(1)
C11	-O4	-C14	-C19	-135.04(1)
C11	-O4	-C14	-C15	50.57(1)
C14	-O4	-C11	-C10	39.96(1)
O1	-N1	-C1	-C6	176.26(1)
O2	-N1	-C1	-C6	-5.75(1)
O2	-N1	-C1	-C2	174.49(1)
O1	-N1	-C1	-C2	-3.51(1)
C7	-N2	-C5	-C6	32.52(1)
C5	-N2	-C7	-O3	-3.15(1)
C5	-N2	-C7	-N3	176.37(1)
C7	-N2	-C5	-C4	-149.51(1)
C8	-N3	-C7	-O3	-0.55(1)

C7	-N3	-C8	-C13	-31.98(1)
C8	-N3	-C7	-N2	179.93(1)
C7	-N3	-C8	-C9	148.94(1)
C20	-N4	-C17	-C18	-43.78(1)
C20	-N4	-C17	-C16	139.37(1)
C17	-N4	-C20	-N5	-165.02(1)
C17	-N4	-C20	-O5	14.22(1)
C20	-N5	-C21	-C22	-159.26(1)
C21	-N5	-C20	-O5	6.82(1)
C20	-N5	-C21	-C26	24.41(1)
C21	-N5	-C20	-N4	-173.93(1)
O7	-N6	-C25	-C24	-2.81(1)
O6	-N6	-C25	-C26	-5.13(1)
O6	-N6	-C25	-C24	177.10(1)
O7	-N6	-C25	-C26	174.97(1)
C2	-C1	-C6	-C5	-1.17(1)
N1	-C1	-C2	-C3	179.50(1)
C6	-C1	-C2	-C3	-0.25(1)

N1	-C1	-C6	-C5	179.08(1)
C1	-C2	-C3	-C4	0.72(1)
C2	-C3	-C4	-C5	0.25(1)
C3	-C4	-C5	-C6	-1.70(1)
C3	-C4	-C5	-N2	-179.73(1)
N2	-C5	-C6	-C1	-179.94(1)
C4	-C5	-C6	-C1	2.11(1)
C9	-C8	-C13	-C12	-1.81(1)
C13	-C8	-C9	-C10	1.68(1)
N3	-C8	-C13	-C12	179.12(1)
N3	-C8	-C9	-C10	-179.21(1)
C8	-C9	-C10	-C11	0.36(1)
C9	-C10	-C11	-O4	173.99(1)
C9	-C10	-C11	-C12	-2.32(1)
O4	-C11	-C12	-C13	-174.31(1)
C10	-C11	-C12	-C13	2.21(1)
C11	-C12	-C13	-C8	-0.13(1)

C15	-C14	-C19	-C18	0.32(1)
O4	-C14	-C19	-C18	-174.16(1)
C19	-C14	-C15	-C16	-0.52(1)
O4	-C14	-C15	-C16	173.69(1)
C14	-C15	-C16	-C17	0.13(1)
C15	-C16	-C17	-C18	0.46(1)
C15	-C16	-C17	-N4	177.44(1)
N4	-C17	-C18	-C19	-177.47(1)
C16	-C17	-C18	-C19	-0.66(1)
C17	-C18	-C19	-C14	0.28(1)
N5	-C21	-C22	-C23	-174.41(1)
C26	-C21	-C22	-C23	2.09(1)
N5	-C21	-C26	-C25	173.90(1)
C22	-C21	-C26	-C25	-2.37(1)
C21	-C22	-C23	-C24	-0.04(1)
C22	-C23	-C24	-C25	-1.63(1)
C23	-C24	-C25	-N6	179.00(1)
C23	-C24	-C25	-C26	1.32(1)

N6	-C25	-C26	-C21	-176.98(1)
C24	-C25	-C26	-C21	0.69(1)

Table A3A.9: Contact Distances(Angstrom) For **L_1**

O1	.C2	2.7155(1)	O6	.C22_d	3.3985(2)
O1	.C23_a	3.2283(2)	O6	.C21_d	3.3497(2)
O1	.C24_a	3.3304(2)	O7	.C24	2.7112(1)
O1	.C21_b	3.4041(2)	O7	.O3_g	3.2149(2)
O2	.N5_c	3.0786(2)	N1	.C3_d	3.2850(2)
O2	.O5_b	2.9552(2)	O1	.H2	2.4400
O2	.C6	2.6911(1)	O1	.H22_c	2.5300
O2	.N4_c	3.1424(2)	O1	.H23_a	2.5500
O2	.C2_d	3.3868(2)	O1	.H24_a	2.7800
O2	.C3_d	3.3424(2)	O2	.H6	2.4000
O2	.C20_b	3.4157(2)	O2	.H4N_c	2.7000
O3	.C5	2.8290(2)	O2	.H5N_c	2.4100
O3	.O7_e	3.2149(2)	N2	.O3_i	2.9217(2)
O3	.N2_d	2.9217(2)	O3	.H6	2.3400
O3	.C13	2.8669(2)	O3	.H2N_d	2.1400

O3	.C6	2.8151(2)	N3	.O6_j	3.0889(2)
O3	.C8	2.8497(2)	N3	.C12_i	3.4403(2)
O4	.C10_d	3.2881(2)	O3	.H13	2.4000
O4	.C9_d	3.2598(2)	N3	.C13_i	3.4490(2)
O5	.C18	2.9810(2)	O4	.H15	2.6100
O5	.O2_c	2.9552(2)	O4	.H12	2.5000
O5	.C17	2.8903(2)	O4	.H10	2.6200
O5	.C26	2.9335(2)	N4	.O5_i	3.1809(2)
O5	.C21	2.8999(2)	N4	.O2_b	3.1424(2)
O5	.N4_d	3.1809(2)	O4	.H19	2.5000
O6	.C8_g	3.2363(2)	O5	.H5N_d	2.6600
O6	.N3_f	3.0889(2)	O5	.H18	2.5400
O6	.C26	2.7011(1)	O5	.H4N_d	2.3500
N5	.O2_b	3.0786(2)	N4	.H16	2.5400
O5	.H26	2.4100	N4	.H5N	2.3100
O6	.H26	2.4100	C4	.C1	2.7169(1)
O6	.H3N_f	2.4200	C4	.C6_i	3.5701(2)

N6	.C23_d	3.3119(2)	C5	.O3	2.8290(2)
N6	.C22_d	3.4111(2)	N5	.H26	2.6500
O7	.H24	2.4300	N5	.H22	2.5200
O7	.H4_f	2.6300	C5	.C2	2.7888(1)
O7	.H2N_f	2.7800	N5	.H4N	2.3300
O7	.H2_h	2.6700	N6	.H24	2.6000
C1	.C3_d	3.5793(2)	C6	.O2	2.6911(1)
C1	.C4	2.7169(1)	C6	.C7	2.9744(2)
N1	.H2	2.6100	N6	.H26	2.5900
N1	.H6	2.5900	C6	.C4_d	3.5701(2)
N2	.H3N	2.3500	C6	.O3	2.8151(2)
N2	.H4	2.5500	C6	.C3	2.7684(1)
C2	.C5	2.7888(1)	C7	.C13	3.0044(2)
C2	.O2_i	3.3868(2)	C7	.C6	2.9744(2)
N2	.H6	2.6300	C8	.C12_i	3.4655(2)
C2	.O1	2.7155(1)	C8	.C11	2.7612(1)
N3	.H9	2.5600	C8	.O3	2.8497(2)

C3	.C1_i	3.5793(2)	C8	.O6_e	3.2363(2)
N3	.H2N	2.3600	C9	.C11_i	3.4270(2)
C3	.O2_i	3.3424(2)	C9	.O4_i	3.2598(2)
C3	.C6	2.7684(1)	C9	.C12_i	3.2981(2)
N3	.H13	2.6300	C9	.C12	2.7559(1)
C3	.N1_i	3.2850(2)	C9	.C26_e	3.3651(2)
N4	.H18	2.6300	C10	.C15	3.2921(2)
C10	.C13	2.7551(1)	C18	.C20	3.0667(2)
C10	.C14	2.9295(2)	C18	.O5	2.9810(2)
C10	.O4_i	3.2881(2)	C19	.C16_d	3.4791(2)
C11	.C19	3.4960(2)	C19	.C11	3.4960(2)
C11	.C15	2.9755(2)	C19	.C16	2.7372(1)
C11	.C9_d	3.4270(2)	C20	.C16	3.5839(2)
C11	.C8	2.7612(1)	C20	.C26	3.0406(2)
C12	.C14	3.5405(2)	C20	.C18	3.0667(2)
C12	.C9	2.7559(1)	C20	.O2_c	3.4157(2)
C12	.C8_d	3.4655(2)	C21	.O1_c	3.4041(2)

C12	.N3_d	3.4403(2)	C21	.O6_i	3.3497(2)
C12	.C9_d	3.2981(2)	C21	.C24	2.7834(1)
C13	.C7	3.0044(2)	C21	.O5	2.8999(2)
C13	.O3	2.8669(2)	C22	.C25	2.7146(1)
C13	.C10	2.7551(1)	C22	.C25_i	3.4724(2)
C13	.N3_d	3.4490(2)	C22	.N6_i	3.4111(2)
C14	.C17	2.7534(1)	C22	.O6_i	3.3985(2)
C14	.C10	2.9295(2)	C23	.C26	2.7637(1)
C14	.C12	3.5405(2)	C23	.N6_i	3.3119(2)
C15	.C11	2.9755(2)	C23	.O1_l	3.2283(2)
C15	.C10	3.2921(2)	C24	.C21	2.7834(1)
C15	.C18	2.7486(1)	C24	.O7	2.7112(1)
C16	.C19_i	3.4791(2)	C24	.O1_l	3.3304(2)
C16	.C20	3.5839(2)	C25	.C22	2.7146(1)
C16	.C19	2.7372(1)	C25	.C22_d	3.4724(2)
C17	.O5	2.8903(2)	C26	.O6	2.7011(1)
C17	.C14	2.7534(1)	C26	.O5	2.9335(2)

C18	.C15	2.7486(1)	C26	.C23	2.7637(1)
C26	.C9_g	3.3651(2)	H2	.N1	2.6100
C26	.C20	3.0406(2)	H2	.H3	2.3100
C3	.H3_k	2.9900	H2N	.O3_i	2.1400
C4	.H2N	2.5600	H2N	.N3	2.3600
C4	.H3_k	3.0600	H2N	.C4	2.5600
C7	.H6	2.7600	H2N	.H3N	2.1000
C7	.H13	2.7800	H2N	.H4	2.4300
C8	.H12_i	3.1000	H2N	.O7_j	2.7800
C9	.H3N	2.5600	H3	.H2	2.3100
C9	.H26_e	2.8400	H3	.H4	2.3000
C11	.H9_d	3.0300	H3	.C3_o	2.9900
C11	.H15	2.8000	H3	.C4_o	3.0600
C12	.H3N_d	2.9300	H3N	.N2	2.3500
C12	.H9_d	3.1000	H3N	.C9	2.5600
C12	.H12_b	2.7500	H3N	.C12_i	2.9300
C13	.H3N_d	2.7600	H3N	.C13_i	2.7600

C13	.H12_b	2.9200	H3N	.H2N	2.1000
C14	.H10	2.7100	H3N	.H9	2.4300
C15	.H10	3.0500	H3N	.O6_j	2.4200
C16	.H4N	2.5900	H4	.N2	2.5500
C18	.H19_e	2.9800	H4	.H2N	2.4300
C20	.H26	2.8100	H4	.H3	2.3000
C20	.H18	2.8800	H4	.O7_j	2.6300
C22	.H5N	2.4700	H4N	.O5_i	2.3500
C23	.H23_m	3.0200	H4N	.N5	2.3300
C26	.H9_g	3.0000	H4N	.C16	2.5900
H2	.O1	2.4400	H4N	.H5N	2.0700
H2	.O7_n	2.6700	H4N	.H16	2.4800
H4N	.O2_b	2.7000	H13	.N3	2.6300
H5N	.O5_i	2.6600	H13	.C7	2.7800
H5N	.N4	2.3100	H13	.H12	2.3100
H5N	.C22	2.4700	H13	.H15_c	2.4800
H5N	.H4N	2.0700	H15	.O4	2.6100

H5N	.H22	2.3200	H15	.C11	2.8000
H5N	.O2_b	2.4100	H15	.H16	2.3100
H6	.O2	2.4000	H15	.H13_b	2.4800
H6	.O3	2.3400	H16	.N4	2.5400
H6	.N1	2.5900	H16	.H4N	2.4800
H6	.N2	2.6300	H16	.H15	2.3100
H6	.C7	2.7600	H18	.O5	2.5400
H9	.N3	2.5600	H18	.N4	2.6300
H9	.C11_i	3.0300	H18	.C20	2.8800
H9	.C12_i	3.1000	H18	.H19	2.3100
H9	.H3N	2.4300	H19	.O4	2.5000
H9	.H10	2.3100	H19	.H18	2.3100
H9	.C26_e	3.0000	H19	.C18_g	2.9800
H10	.O4	2.6200	H22	.N5	2.5200
H10	.C14	2.7100	H22	.H5N	2.3200
H10	.C15	3.0500	H22	.H23	2.2900
H10	.H9	2.3100	H22	.O1_b	2.5300

H12	.O4	2.5000	H23	.O1_l	2.5500
H12	.C8_d	3.1000	H23	.H22	2.2900
H12	.H13	2.3100	H23	.H24	2.3100
H12	.C12_c	2.7500	H23	.C23_p	3.0200
H12	.C13_c	2.9200	H24	.O1_l	2.7800
H13	.O3	2.4000	H24	.O7	2.4300
H24	.N6	2.6000	H26	.N5	2.6500
H24	.H23	2.3100	H26	.N6	2.5900
H26	.O5	2.4100	H26	.C20	2.8100
H26	.O6	2.4100	H26	.C9_g	2.8400

Table A3A.10: Hydrogen Bonds (Angstrom, Deg) For **L**ı

N2 -- H2N .. O3	0.8600	2.1400	2.9217(2)	152.00	1_545
N3 -- H3N .. O6	0.8600	2.4200	3.0889(2)	136.00	2_536
N4 -- H4N .. O5	0.8600	2.3500	3.1809(2)	164.00	1_545
N5 -- H5N .. O2	0.8600	2.4100	3.0786(2)	135.00	2_646
C6 -- H6 .. O3	0.9300	2.3400	2.8151(2)	111.00	.
C13 -- H13 .. O3	0.9300	2.4000	2.8669(2)	111.00	.
C18 -- H18 .. O5	0.9300	2.5400	2.9810(2)	110.00	.

C22 -- H22 .. O1	0.9300	2.5300	3.4491(2)	168.00	2_646
C23 -- H23 .. O1	0.9300	2.5500	3.2283(2)	130.00	1_456
C26 -- H26 .. O5	0.9300	2.4100	2.9335(2)	115.00	.

Translation of Symmetry Code to Equiv.Pos

a =[1654.00] =	1+x,y,-1+z
b =[2646.00] =	1-x,-1/2+y,1-z
c =[2656.00] =	1-x,1/2+y,1-z
d =[1565.00] =	x,1+y,z
e =[2546.00] =	-x,-1/2+y,1-z
f =[2566.00] =	-x,3/2+y,1-z
g =[2556.00] =	-x,1/2+y,1-z
h =[1466.00] =	-1+x,1+y,1+z
i =[1545.00] =	x,-1+y,z
j =[2536.00] =	-x,-3/2+y,1-z
k =[2655.00] =	1-x,1/2+y,-z
l =[1456.00] =	-1+x,y,1+z
m =[2557.00] =	-x,1/2+y,2-z
n =[1644.00] =	1+x,-1+y,-1+z
o =[2645.00] =	1-x,-1/2+y,-z
p =[2547.00] =	-x,-1/2+y,2-z

Table A3A.11: Final Coordinates and Equivalent Isotropic Displacement Parameters of the non-Hydrogen atoms for **L**$_{\mathbf{I}}$+TBA(OAC)

Atom	x	y	z	U(eq) [Ang^2]
O1	1.00292	0.36903	0.67563	0.1211
O2	0.81521	0.44511	0.61876	0.1117
O3	0.41283	0.60178	0.77299	0.0725

O4	-0.20648	0.89637	0.81439	0.0899
O5	-0.23866	1.10093	0.40025	0.0754
O6	0.07588	1.18156	0.15757	0.1339
O7	0.00606	1.20229	0.00810	0.1143
N1	0.88541	0.41875	0.68846	0.0812
N2	0.51377	0.60065	0.93557	0.0676
N3	0.29309	0.68263	0.92519	0.0640
N4	-0.37969	0.90469	0.40853	0.0629
N5	-0.40787	0.95264	0.25603	0.0649
N6	-0.02498	1.17209	0.08639	0.0909
C1	0.82789	0.44825	0.79367	0.0646
C2	0.90608	0.41735	0.87242	0.0792
C3	0.84987	0.44949	0.97075	0.0821
C4	0.72130	0.50821	0.98866	0.0707
C5	0.64218	0.53850	0.90835	0.0576
C6	0.69687	0.50881	0.80922	0.0594
C7	0.40663	0.62682	0.86885	0.0562

C8	0.17085	0.73528	0.88980	0.0566
C9	0.05921	0.77176	0.95923	0.0589
C10	-0.06413	0.82440	0.93240	0.0606
C11	-0.07913	0.84176	0.83487	0.0647
C12	0.02964	0.80577	0.76507	0.0858
C13	0.15438	0.75190	0.79233	0.0813
C14	-0.24007	0.89849	0.71182	0.0705
C15	-0.17843	1.00964	0.68585	0.0809
C16	-0.22030	1.01601	0.58557	0.0729
C17	-0.32609	0.90988	0.51155	0.0594
C18	-0.38651	0.79928	0.53934	0.0834
C19	-0.34462	0.79400	0.63955	0.0882
C20	-0.33283	0.99385	0.35911	0.0580
C21	-0.36842	1.01250	0.18009	0.0627
C22	-0.21833	1.07429	0.17702	0.0660
C23	-0.18785	1.11870	0.09342	0.0700
C24	-0.30164	1.10824	0.01371	0.0833

C25	-0.45012	1.04845	0.01796	0.0890
C26	-0.48541	1.00089	0.10062	0.0780
N7	0.32234	0.27222	0.45961	0.0505
O8	0.40408	0.65905	0.29239	0.0824
O9	0.40178	0.69799	0.14066	0.0725
C27	0.20595	0.35367	0.43404	0.0590
C28	0.24289	0.50737	0.49369	0.0674
C29	0.11500	0.57586	0.46739	0.0887
C30	0.15937	0.72980	0.50393	0.1018
C31	0.48922	0.33792	0.45700	0.0552
C32	0.52314	0.36177	0.35410	0.0611
C33	0.69238	0.42520	0.36125	0.0678
C34	0.72758	0.45951	0.26215	0.0824
C35	0.30319	0.26930	0.57084	0.0612
C36	0.40413	0.18759	0.61064	0.0776
C37	0.35432	0.18409	0.71756	0.1501

C38	0.43817	0.12055	0.76959	0.2280
C39	0.29082	0.12833	0.37568	0.0586
C40	0.13841	0.03622	0.37298	0.0612
C41	0.11984	-0.09454	0.27656	0.0750
C42	-0.02687	-0.19596	0.26288	0.0827
C43	0.27058	0.48423	0.13806	0.1268
C44	0.36569	0.62420	0.19510	0.0638

U(eq) = 1/3 of the trace of the orthogonalized U Tensor

Table A3A.12: Hydrogen Atom Positions and Isotropic Displacement Parameters for **L_1**+TBA(OAC)

Atom	x	y	z	U(iso) [Ang^2]
H2	0.99339	0.37640	0.85958	0.0950
H2N	0.49933	0.62594	1.00237	0.0812
H3	0.90058	0.43077	1.02580	0.0986
H3N	0.29656	0.68613	0.99070	0.0768
H4	0.68537	0.52859	1.05574	0.0849
H4N	-0.45161	0.83581	0.37236	0.0755
H5N	-0.48504	0.88471	0.23709	0.0778

H6	0.64733	0.52882	0.75443	0.0712
H9	0.06837	0.76022	1.02526	0.0707
H10	-0.13753	0.84833	0.98003	0.0727
H12	0.01989	0.81747	0.69913	0.1029
H13	0.22700	0.72702	0.74425	0.0975
H15	-0.10773	1.08168	0.73593	0.0971
H16	-0.17714	1.09143	0.56866	0.0875
H18	-0.45698	0.72654	0.48973	0.1001
H19	-0.38805	0.71914	0.65706	0.1058
H22	-0.13934	1.08558	0.23067	0.0792
H24	-0.27812	1.14084	-0.04123	0.1000
H25	-0.52869	1.03947	-0.03527	0.1068
H26	-0.58716	0.96131	0.10284	0.0936
H27A	0.19820	0.33657	0.35748	0.0708
H27B	0.10456	0.31848	0.44968	0.0708
H28A	0.25595	0.52625	0.57049	0.0808

H28B	0.34008	0.54536	0.47433	0.0808
H29A	0.08573	0.53931	0.39018	0.1064
H29B	0.02452	0.55265	0.50087	0.1064
H30A	0.20558	0.76567	0.57748	0.1527
H30B	0.06810	0.76810	0.49800	0.1527
H30C	0.23278	0.75397	0.45964	0.1527
H31A	0.51458	0.42570	0.51609	0.0662
H31B	0.55809	0.27973	0.46960	0.0662
H32A	0.49888	0.27490	0.29401	0.0733
H32B	0.45772	0.42240	0.34140	0.0733
H33A	0.75717	0.36163	0.36926	0.0814
H33B	0.71811	0.50853	0.42451	0.0814
H34A	0.69154	0.37957	0.19875	0.1236
H34B	0.83786	0.48814	0.26522	0.1236
H34C	0.67558	0.53250	0.25989	0.1236
H35A	0.19509	0.23198	0.57194	0.0735
H35B	0.32473	0.36339	0.62144	0.0735

H36A	0.51288	0.23054	0.62019	0.0931
H36B	0.39139	0.09474	0.55863	0.0931
H37A	0.35923	0.27817	0.76557	0.1802
H37B	0.24623	0.13844	0.70498	0.1802
H38A	0.44463	0.03054	0.72079	0.3420
H38B	0.38743	0.11258	0.82972	0.3420
H38C	0.54112	0.17407	0.79466	0.3420
H39A	0.29491	0.13631	0.30549	0.0703
H39B	0.37491	0.08261	0.38664	0.0703
H40A	0.13777	0.01500	0.43824	0.0734
H40B	0.05244	0.08301	0.36882	0.0734
H41A	0.12377	-0.07079	0.21249	0.0900
H41B	0.20775	-0.13877	0.28175	0.0900
H42A	-0.04259	-0.20720	0.33025	0.1240
H42B	-0.01870	-0.28287	0.21003	0.1240
H42C	-0.11341	-0.16286	0.23959	0.1240

H43A	0.33803	0.42058	0.10813	0.1902
H43B	0.19982	0.48663	0.08135	0.1902
H43C	0.21266	0.45537	0.18798	0.1902

==========

The Temperature Factor has the Form of Exp(-T) Where
T = 8*(Pi**2)*U*(Sin(Theta)/Lambda)**2 for Isotropic Atoms

Table A3A.13: (An)isotropic Displacement Parameters for **L_I**+TBA(OAC)

Atom	U(1,1) or U	U(2,2)	U(3,3)	U(2,3)	U(1,3)	U(1,2)
O1	0.0895	0.1535	0.1240	0.0342	0.0449	0.0582
O2	0.0882	0.1786	0.0624	0.0292	0.0176	0.0372
O3	0.0813	0.1010	0.0420	0.0249	0.0100	0.0376
O4	0.0973	0.1387	0.0520	0.0353	0.0145	0.0708
O5	0.0955	0.0661	0.0605	0.0203	0.0003	0.0117
O6	0.1183	0.1630	0.1219	0.0863	-0.0237	-0.0391
O7	0.1310	0.1178	0.1092	0.0702	0.0166	-0.0034
N1	0.0595	0.0940	0.0735	0.0093	0.0143	0.0120
N2	0.0738	0.0976	0.0426	0.0290	0.0098	0.0380
N3	0.0687	0.0894	0.0421	0.0251	0.0091	0.0338

N4	0.0674	0.0702	0.0530	0.0255	0.0006	0.0125
N5	0.0684	0.0741	0.0533	0.0249	0.0037	0.0131
N6	0.1112	0.0784	0.0834	0.0411	0.0019	-0.0070
C1	0.0577	0.0650	0.0643	0.0142	0.0083	0.0118
C2	0.0616	0.0826	0.0965	0.0319	0.0026	0.0251
C3	0.0800	0.0971	0.0838	0.0460	0.0024	0.0296
C4	0.0701	0.0891	0.0650	0.0397	0.0069	0.0219
C5	0.0602	0.0639	0.0529	0.0252	0.0029	0.0154
C6	0.0599	0.0639	0.0543	0.0203	0.0031	0.0146
C7	0.0600	0.0671	0.0432	0.0194	0.0032	0.0188
C8	0.0665	0.0639	0.0414	0.0178	0.0039	0.0211
C9	0.0729	0.0649	0.0394	0.0174	0.0070	0.0171
C10	0.0732	0.0653	0.0426	0.0146	0.0087	0.0214
C11	0.0763	0.0776	0.0422	0.0166	0.0050	0.0325
C12	0.1010	0.1346	0.0507	0.0486	0.0246	0.0647
C13	0.0942	0.1238	0.0512	0.0424	0.0275	0.0620

C14	0.0781	0.0917	0.0516	0.0263	0.0099	0.0420
C15	0.0774	0.1005	0.0543	0.0142	-0.0034	0.0215
C16	0.0741	0.0802	0.0618	0.0238	0.0010	0.0126
C17	0.0620	0.0708	0.0487	0.0202	0.0057	0.0248
C18	0.1118	0.0725	0.0637	0.0301	-0.0138	0.0058
C19	0.1227	0.0788	0.0705	0.0366	-0.0011	0.0213
C20	0.0619	0.0625	0.0514	0.0172	0.0074	0.0236
C21	0.0786	0.0596	0.0511	0.0180	0.0047	0.0220
C22	0.0841	0.0556	0.0597	0.0223	0.0010	0.0158
C23	0.0932	0.0545	0.0638	0.0246	0.0068	0.0112
C24	0.1259	0.0715	0.0558	0.0288	0.0022	0.0163
C25	0.1065	0.1013	0.0602	0.0326	-0.0076	0.0198
C26	0.0846	0.0864	0.0633	0.0273	-0.0020	0.0192
N7	0.0472	0.0556	0.0469	0.0146	0.0081	0.0123
O8	0.0995	0.0954	0.0501	0.0315	-0.0017	0.0025
O9	0.0887	0.0814	0.0483	0.0251	0.0070	0.0143

C27	0.0508	0.0690	0.0557	0.0184	0.0039	0.0169
C28	0.0714	0.0720	0.0616	0.0205	0.0092	0.0289
C29	0.0843	0.0971	0.1006	0.0445	0.0132	0.0417
C30	0.1495	0.0993	0.0879	0.0478	0.0394	0.0719
C31	0.0447	0.0606	0.0569	0.0180	0.0026	0.0084
C32	0.0574	0.0687	0.0551	0.0208	0.0101	0.0076
C33	0.0587	0.0748	0.0714	0.0303	0.0102	0.0060
C34	0.0811	0.0907	0.0868	0.0459	0.0239	0.0107
C35	0.0618	0.0729	0.0496	0.0200	0.0117	0.0171
C36	0.0798	0.0918	0.0715	0.0411	0.0045	0.0198
C37	0.1828	0.2039	0.1150	0.1094	0.0233	0.0609
C38	0.2841	0.2950	0.1839	0.1630	0.0403	0.0989
C39	0.0566	0.0589	0.0537	0.0106	0.0118	0.0115
C40	0.0556	0.0636	0.0616	0.0193	0.0088	0.0093
C41	0.0740	0.0629	0.0786	0.0139	0.0195	0.0075
C42	0.0836	0.0639	0.0879	0.0184	0.0069	-0.0015

C43	0.1677	0.1025	0.0876	0.0412	-0.0380	-0.0395
C44	0.0664	0.0755	0.0495	0.0230	0.0024	0.0134

The Temperature Factor has the Form of Exp(-T) Where
T = 8*(Pi**2)*U*(Sin(Theta)/Lambda)**2 for Isotropic Atoms
T = 2*(Pi**2)*Sumij(h(i)*h(j)*U(i,j)*Astar(i)*Astar(j)), for Anisotropic Atoms. Astar(i) are Reciprocal Axial Lengths and h(i) are the Reflection Indices.

Table A3A.14: Bond Distances (Angstrom) For **L**$_1$+TBA(OAC)

O1	-N1	1.2189(5)	C8	-C13	1.3724(5)
O2	-N1	1.2185(5)	C8	-C9	1.3897(5)
O3	-C7	1.2191(5)	C9	-C10	1.3708(5)
O4	-C11	1.3857(5)	C10	-C11	1.3760(5)
O4	-C14	1.3911(5)	C11	-C12	1.3724(5)
O5	-C20	1.2205(5)	C12	-C13	1.3911(5)
O6	-N6	1.2265(5)	C14	-C19	1.3558(5)
O7	-N6	1.2239(5)	C14	-C15	1.3736(5)
N1	-C1	1.4645(6)	C15	-C16	1.3932(5)
N2	-C5	1.3903(5)	C16	-C17	1.3786(5)
N2	-C7	1.3792(5)	C17	-C18	1.3794(5)

N3	-C7	1.3628(5)	C18	-C19	1.3876(5)
N3	-C8	1.4079(5)	C21	-C22	1.3826(5)
N4	-C17	1.4064(5)	C21	-C26	1.3919(5)
N4	-C20	1.3496(5)	C22	-C23	1.3731(5)
N5	-C20	1.3818(5)	C23	-C24	1.3788(5)
N5	-C21	1.3975(5)	C24	-C25	1.3672(5)
N6	-C23	1.4701(6)	C25	-C26	1.3895(5)
C1	-C2	1.3785(5)	C2	-H2	0.9300
C1	-C6	1.3880(5)	C3	-H3	0.9300
C2	-C3	1.3760(5)	C4	-H4	0.9300
N2	-H2N	0.8600	C6	-H6	0.9300
N3	-H3N	0.8600	N7	-C39	1.5150(6)
C3	-C4	1.3599(5)	N7	-C35	1.5117(6)
N4	-H4N	0.8600	N7	-C27	1.5241(6)
C4	-C5	1.3958(5)	N7	-C31	1.5245(6)
C5	-C6	1.3806(5)	C9	-H9	0.9300
N5	-H5N	0.8600	C10	-H10	0.9300
C12	-H12	0.9300	C29	-H29A	0.9700

C13	-H13	0.9300	C29	-H29B	0.9700
C15	-H15	0.9300	C30	-H30C	0.9600
C16	-H16	0.9300	C30	-H30A	0.9600
C18	-H18	0.9300	C30	-H30B	0.9600
C19	-H19	0.9300	C31	-H31B	0.9700
C22	-H22	0.9300	C31	-H31A	0.9700
C24	-H24	0.9300	C32	-H32A	0.9700
C25	-H25	0.9300	C32	-H32B	0.9700
C26	-H26	0.9300	C33	-H33A	0.9700
O8	-C44	1.2312(5)	C33	-H33B	0.9700
O9	-C44	1.2525(5)	C34	-H34B	0.9600
C27	-C28	1.5107(6)	C34	-H34C	0.9600
C28	-C29	1.5087(6)	C34	-H34A	0.9600
C29	-C30	1.5029(6)	C35	-H35A	0.9700
C31	-C32	1.5142(6)	C35	-H35B	0.9700
C32	-C33	1.5116(6)	C36	-H36A	0.9700
C33	-C34	1.5202(6)	C36	-H36B	0.9700

C35	-C36	1.5166(6)	C37	-H37A	0.9700
C36	-C37	1.5244(6)	C37	-H37B	0.9700
C37	-C38	1.3719(5)	C38	-H38B	0.9600
C39	-C40	1.5144(6)	C38	-H38A	0.9600
C40	-C41	1.5051(6)	C38	-H38C	0.9600
C41	-C42	1.4967(6)	C39	-H39B	0.9700
C27	-H27B	0.9700	C39	-H39A	0.9700
C27	-H27A	0.9700	C40	-H40B	0.9700
C28	-H28A	0.9700	C40	-H40A	0.9700
C28	-H28B	0.9700	C41	-H41B	0.9700
C41	-H41A	0.9700	C43	-C44	1.4915(6)
C42	-H42C	0.9600	C43	-H43A	0.9600
C42	-H42A	0.9600	C43	-H43B	0.9600
C42	-H42B	0.9600	C43	-H43C	0.9600

Table A3A.15: Bond Angles (Degrees) for **L1**+TBA(OAC)

C11	-O4	-C14	118.75(1)	C1	-C6	-C5	118.10(1)
O1	-N1	-O2	123.33(2)	O3	-C7	-N2	124.37(2)
O1	-N1	-C1	117.51(1)	O3	-C7	-N3	125.33(1)
O2	-N1	-C1	119.16(2)	N2	-C7	-N3	110.29(3)

C5	-N2	-C7	128.11(2)	N3	-C8	-C9	116.87(2)
C7	-N3	-C8	128.26(2)	N3	-C8	-C13	124.73(1)
C17	-N4	-C20	128.37(2)	C9	-C8	-C13	118.40(2)
C20	-N5	-C21	125.24(2)	C8	-C9	-C10	121.36(2)
O6	-N6	-O7	122.10(2)	C9	-C10	-C11	119.88(1)
O6	-N6	-C23	119.06(2)	C10	-C11	-C12	119.58(2)
O7	-N6	-C23	118.81(1)	O4	-C11	-C10	116.19(1)
N1	-C1	-C2	119.35(2)	O4	-C11	-C12	124.23(2)
N1	-C1	-C6	117.43(1)	C11	-C12	-C13	120.42(2)
C2	-C1	-C6	123.20(2)	C8	-C13	-C12	120.35(1)
C1	-C2	-C3	117.38(2)	O4	-C14	-C19	119.17(2)
C5	-N2	-H2N	116.00	C15	-C14	-C19	119.73(2)
C7	-N2	-H2N	116.00	O4	-C14	-C15	120.90(1)
C2	-C3	-C4	121.00(1)	C14	-C15	-C16	120.94(1)
C7	-N3	-H3N	116.00	C15	-C16	-C17	119.63(2)
C8	-N3	-H3N	116.00	N4	-C17	-C18	116.32(1)
C20	-N4	-H4N	116.00	C16	-C17	-C18	118.45(2)
C3	-C4	-C5	121.30(2)	N4	-C17	-C16	125.24(2)

C17	-N4	-H4N	116.00	C17	-C18	-C19	121.56(1)
N2	-C5	-C6	124.27(1)	C14	-C19	-C18	119.69(2)
N2	-C5	-C4	116.71(2)	O5	-C20	-N4	124.86(2)
C20	-N5	-H5N	117.00	O5	-C20	-N5	122.93(1)
C4	-C5	-C6	119.00(2)	N4	-C20	-N5	112.18(2)
C21	-N5	-H5N	117.00	N5	-C21	-C22	123.04(1)
N5	-C21	-C26	117.49(2)	C13	-C12	-H12	120.00
C22	-C21	-C26	119.34(2)	C12	-C13	-H13	120.00
C21	-C22	-C23	118.90(1)	C8	-C13	-H13	120.00
N6	-C23	-C24	119.24(2)	C14	-C15	-H15	120.00
C22	-C23	-C24	122.83(2)	C16	-C15	-H15	120.00
N6	-C23	-C22	117.84(1)	C15	-C16	-H16	120.00
C23	-C24	-C25	117.92(2)	C17	-C16	-H16	120.00
C24	-C25	-C26	121.00(1)	C19	-C18	-H18	119.00
C21	-C26	-C25	119.98(2)	C17	-C18	-H18	119.00
C1	-C2	-H2	121.00	C14	-C19	-H19	120.00
C3	-C2	-H2	121.00	C18	-C19	-H19	120.00
C2	-C3	-H3	119.00	C21	-C22	-H22	121.00

C4	-C3	-H3	119.00	C23	-C22	-H22	121.00
C3	-C4	-H4	119.00	C25	-C24	-H24	121.00
C5	-C4	-H4	119.00	C23	-C24	-H24	121.00
C1	-C6	-H6	121.00	C24	-C25	-H25	119.00
C5	-C6	-H6	121.00	C26	-C25	-H25	120.00
C35	-N7	-C39	111.33(2)	C25	-C26	-H26	120.00
C27	-N7	-C39	109.11(2)	C21	-C26	-H26	120.00
C27	-N7	-C31	111.45(2)	N7	-C27	-C28	115.93(2)
C27	-N7	-C35	107.79(1)	C27	-C28	-C29	111.22(2)
C31	-N7	-C35	109.45(1)	C28	-C29	-C30	113.77(2)
C31	-N7	-C39	107.73(2)	N7	-C31	-C32	115.92(1)
C10	-C9	-H9	119.00	C31	-C32	-C33	110.66(1)
C8	-C9	-H9	119.00	C32	-C33	-C34	111.89(1)
C9	-C10	-H10	120.00	N7	-C35	-C36	116.52(1)
C11	-C10	-H10	120.00	C35	-C36	-C37	108.19(2)
C11	-C12	-H12	120.00	C36	-C37	-C38	116.96(2)
N7	-C39	-C40	117.23(2)	H31A	-C31	-H31B	107.00

C39	-C40	-C41	109.20(2)	C31	-C32	-H32A	110.00
C40	-C41	-C42	115.29(2)	C31	-C32	-H32B	110.00
N7	-C27	-H27A	108.00	C33	-C32	-H32A	110.00
N7	-C27	-H27B	108.00	C33	-C32	-H32B	110.00
C28	-C27	-H27A	108.00	H32A	-C32	-H32B	108.00
C28	-C27	-H27B	108.00	C32	-C33	-H33A	109.00
H27A	-C27	-H27B	107.00	C32	-C33	-H33B	109.00
C27	-C28	-H28A	109.00	C34	-C33	-H33A	109.00
C27	-C28	-H28B	109.00	C34	-C33	-H33B	109.00
C29	-C28	-H28A	109.00	H33A	-C33	-H33B	108.00
C29	-C28	-H28B	109.00	C33	-C34	-H34A	109.00
H28A	-C28	-H28B	108.00	C33	-C34	-H34B	109.00
C28	-C29	-H29A	109.00	C33	-C34	-H34C	109.00
C28	-C29	-H29B	109.00	H34A	-C34	-H34B	109.00
C30	-C29	-H29A	109.00	H34A	-C34	-H34C	109.00
C30	-C29	-H29B	109.00	H34B	-C34	-H34C	109.00
H29A	-C29	-H29B	108.00	N7	-C35	-H35A	108.00

C29	-C30	-H30A	109.00	N7	-C35	-H35B	108.00
C29	-C30	-H30B	109.00	C36	-C35	-H35A	108.00
C29	-C30	-H30C	109.00	C36	-C35	-H35B	108.00
H30A	-C30	-H30B	109.00	H35A	-C35	-H35B	107.00
H30A	-C30	-H30C	109.00	C35	-C36	-H36A	110.00
H30B	-C30	-H30C	109.00	C35	-C36	-H36B	110.00
N7	-C31	-H31A	108.00	C37	-C36	-H36A	110.00
N7	-C31	-H31B	108.00	C37	-C36	-H36B	110.00
C32	-C31	-H31A	108.00	H36A	-C36	-H36B	108.00
C32	-C31	-H31B	108.00	C36	-C37	-H37A	108.00
C36	-C37	-H37B	108.00	C40	-C41	-H41A	108.00
C38	-C37	-H37A	108.00	C40	-C41	-H41B	108.00
C38	-C37	-H37B	108.00	C42	-C41	-H41A	108.00
H37A	-C37	-H37B	107.00	C42	-C41	-H41B	108.00
C37	-C38	-H38A	109.00	H41A	-C41	-H41B	107.00
C37	-C38	-H38B	109.00	C41	-C42	-H42A	109.00
C37	-C38	-H38C	109.00	C41	-C42	-H42B	109.00

H38A	-C38	-H38B	109.00	C41	-C42	-H42C	109.00
H38A	-C38	-H38C	109.00	H42A	-C42	-H42B	109.00
H38B	-C38	-H38C	109.00	H42A	-C42	-H42C	109.00
N7	-C39	-H39A	108.00	H42B	-C42	-H42C	109.00
N7	-C39	-H39B	108.00	O8	-C44	-O9	124.46(2)
C40	-C39	-H39A	108.00	O8	-C44	-C43	117.76(1)
C40	-C39	-H39B	108.00	O9	-C44	-C43	117.78(2)
H39A	-C39	-H39B	107.00	C44	-C43	-H43A	109.00
C39	-C40	-H40A	110.00	C44	-C43	-H43B	109.00
C39	-C40	-H40B	110.00	C44	-C43	-H43C	109.00
C41	-C40	-H40A	110.00	H43A	-C43	-H43B	109.00
C41	-C40	-H40B	110.00	H43A	-C43	-H43C	109.00
H40A	-C40	-H40B	108.00	H43B	-C43	-H43C	109.00

Table A3A.16: Torsion Angles (Degrees) for **L**$_1$+TBA(OAC)

C14	-O4	-C11	-C12	9.12(1)
C11	-O4	-C14	-C19	94.58(1)
C11	-O4	-C14	-C15	-90.61(1)
C14	-O4	-C11	-C10	-171.13(1)

O1	-N1	-C1	-C6	178.04(1)
O2	-N1	-C1	-C6	-1.65(1)
O2	-N1	-C1	-C2	179.37(1)
O1	-N1	-C1	-C2	-0.94(1)
C7	-N2	-C5	-C6	9.54(1)
C5	-N2	-C7	-O3	-2.52(1)
C5	-N2	-C7	-N3	176.75(1)
C7	-N2	-C5	-C4	-172.10(1)
C8	-N3	-C7	-O3	-7.00(1)
C7	-N3	-C8	-C13	-6.98(1)
C8	-N3	-C7	-N2	173.74(1)
C7	-N3	-C8	-C9	172.60(1)
C20	-N4	-C17	-C18	-175.40(1)
C20	-N4	-C17	-C16	5.06(1)
C17	-N4	-C20	-N5	177.71(1)
C17	-N4	-C20	-O5	-4.27(1)
C20	-N5	-C21	-C22	29.76(1)

C21	-N5	-C20	-O5	11.64(1)
C20	-N5	-C21	-C26	-154.26(1)
C21	-N5	-C20	-N4	-170.30(1)
O7	-N6	-C23	-C24	-2.06(1)
O6	-N6	-C23	-C22	-3.65(1)
O6	-N6	-C23	-C24	179.83(1)
O7	-N6	-C23	-C22	174.46(1)
N1	-C1	-C2	-C3	178.65(1)
C2	-C1	-C6	-C5	-0.43(1)
C6	-C1	-C2	-C3	-0.26(1)
N1	-C1	-C6	-C5	-179.36(1)
C1	-C2	-C3	-C4	0.61(1)
C2	-C3	-C4	-C5	-0.27(1)
C3	-C4	-C5	-C6	-0.45(1)
C3	-C4	-C5	-N2	-178.90(1)
C4	-C5	-C6	-C1	0.77(1)
N2	-C5	-C6	-C1	179.10(1)
N3	-C8	-C13	-C12	-179.59(1)

C9	-C8	-C13	-C12	0.84(1)
C13	-C8	-C9	-C10	-0.61(1)
N3	-C8	-C9	-C10	179.79(1)
C8	-C9	-C10	-C11	0.10(1)
C9	-C10	-C11	-O4	-179.60(1)
C9	-C10	-C11	-C12	0.17(1)
O4	-C11	-C12	-C13	179.81(1)
C10	-C11	-C12	-C13	0.06(1)
C11	-C12	-C13	-C8	-0.58(1)
O4	-C14	-C15	-C16	-175.58(1)
C15	-C14	-C19	-C18	1.04(1)
O4	-C14	-C19	-C18	175.90(1)
C19	-C14	-C15	-C16	-0.80(1)
C14	-C15	-C16	-C17	0.55(1)
C15	-C16	-C17	-N4	179.00(1)
C15	-C16	-C17	-C18	-0.54(1)
C16	-C17	-C18	-C19	0.80(1)

N4	-C17	-C18	-C19	-178.78(1)
C17	-C18	-C19	-C14	-1.06(1)
N5	-C21	-C22	-C23	173.86(1)
C26	-C21	-C22	-C23	-2.04(1)
C22	-C21	-C26	-C25	1.40(1)
N5	-C21	-C26	-C25	-174.73(1)
C21	-C22	-C23	-N6	-174.35(1)
C21	-C22	-C23	-C24	2.04(1)
N6	-C23	-C24	-C25	175.05(1)
C22	-C23	-C24	-C25	-1.29(1)
C23	-C24	-C25	-C26	0.58(1)
C24	-C25	-C26	-C21	-0.67(1)
C31	-N7	-C27	-C28	-47.60(1)
C35	-N7	-C27	-C28	72.53(1)
C39	-N7	-C27	-C28	-166.44(1)
C27	-N7	-C35	-C36	177.49(1)
C31	-N7	-C35	-C36	-61.14(1)
C27	-N7	-C31	-C32	-54.85(1)

C35	-N7	-C31	-C32	-174.00(1)
C39	-N7	-C31	-C32	64.81(1)
C27	-N7	-C39	-C40	-66.34(1)
C31	-N7	-C39	-C40	172.52(1)
C35	-N7	-C39	-C40	52.51(1)
C39	-N7	-C35	-C36	57.85(1)
N7	-C27	-C28	-C29	-176.35(1)
C27	-C28	-C29	-C30	-167.13(1)
N7	-C31	-C32	-C33	-179.17(1)
C31	-C32	-C33	-C34	-176.06(1)
N7	-C35	-C36	-C37	-173.65(1)
C35	-C36	-C37	-C38	-176.63(1)
N7	-C39	-C40	-C41	173.06(1)
C39	-C40	-C41	-C42	-179.67(1)

Table A3A.17: Contact Distances (Angstrom) for **L_1**+TBA(OAC)

O1	.C2	2.7061(10)	O2	.H31B	2.8200
O1	.C35_a	3.1960(12)	N2	.O9_i	2.8580(11)
O2	.C6	2.7031(10)	O3	.H35B	2.5900

O2	.C31	3.2729(12)	O3	.H28A	2.7500
O3	.C5	2.9272(11)	O3	.H19_c	2.8100
O3	.C6	2.8839(11)	O3	.H13	2.3400
O3	.C13	2.9280(11)	O3	.H6	2.3000
O3	.C8	2.9444(11)	N3	.O9_i	2.9175(11)
O4	.C24_d	3.0783(12)	O4	.H19	2.5400
O5	.C22	2.9099(11)	O4	.H10	2.4900
O5	.C17	2.9230(11)	O4	.H15	2.5800
O5	.C21	2.8624(11)	O4	.H12	2.6400
O5	.C16	2.9071(11)	O4	.H24_d	2.8200
O6	.C22	2.7118(10)	N4	.O8_j	2.8425(11)
O7	.C24	2.7369(10)	O5	.H16	2.3200
O7	.C43_g	3.3276(13)	O5	.H33A_e	2.9200
O7	.C3_h	3.2883(12)	O5	.H31B_e	2.7500
O8	.C18_c	3.3950(13)	O5	.H22	2.4300
O8	.N4_c	2.8425(11)	O5	.H40B_f	2.6300
O9	.N5_c	2.7988(11)	N5	.O9_j	2.7988(11)
O9	.N2_m	2.8580(11)	O6	.H39A_f	2.8800

O9	.N3_m	2.9175(11)	O6	.H43C_g	2.8300
O1	.H2	2.4300	O6	.H27A_f	2.6600
O1	.H16_b	2.9200	O6	.H22	2.4100
O1	.H35A_a	2.5400	O7	.H3_h	2.6500
O2	.H29B_a	2.8300	O7	.H24	2.4600
O2	.H6	2.4100	O8	.H30C	2.7400
O2	.H31A	2.8400	O8	.H4N_c	1.9900
O8	.H18_c	2.6400	N4	.H5N	2.3400
O8	.H43A	2.8000	N4	.H18	2.5000
O8	.H32B	2.8800	N4	.H16	2.6800
O8	.H43C	2.4300	C5	.O3	2.9272(11)
O8	.H5N_c	2.7800	N5	.H39B_e	2.8400
O8	.H34C	2.8800	N5	.H26	2.5400
O9	.H43B	2.4700	N5	.H4N	2.3000
O9	.H3N_m	2.1100	N5	.H22	2.6500
O9	.H43A	2.7600	C5	.C2	2.7940(11)
O9	.H5N_c	2.0000	C5	.C10_c	3.5547(13)

O9	.H2N_m	2.0300	N6	.H22	2.5800
O9	.H41B_f	2.9000	N6	.H24	2.6200
C1	.C4	2.7111(10)	C6	.C10_c	3.4408(13)
N1	.H6	2.5900	C6	.C7	3.0250(11)
C1	.C9_c	3.5751(14)	C6	.O2	2.7031(10)
N1	.H2	2.6200	C6	.O3	2.8839(11)
N2	.H3N	2.2800	C6	.C3	2.7721(11)
C2	.O1	2.7061(10)	N7	.H40B	2.7500
C2	.C5	2.7940(11)	N7	.H28B	2.7900
N2	.H4	2.5100	N7	.H32A	2.7700
C2	.C9_c	3.5190(13)	N7	.H32B	2.7800
N2	.H6	2.6600	N7	.H36A	2.8300
N3	.H13	2.6600	N7	.H36B	2.7500
C3	.O7_k	3.2883(12)	N7	.H40A	2.8500
C3	.C6	2.7721(11)	C7	.C6	3.0250(11)
N3	.H9	2.5200	N7	.H28A	2.7500
N3	.H2N	2.2900	C7	.C13	3.0370(12)
C4	.C1	2.7111(10)	C8	.O3	2.9444(11)

C8	.C11	2.7795(11)	C17	.O5	2.9230(11)
C9	.C12	2.7365(10)	C18	.C15	2.7244(10)
C9	.C2_l	3.5190(13)	C18	.O8_j	3.3950(13)
C9	.C1_l	3.5751(14)	C19	.C16	2.7625(10)
C10	.C5_l	3.5547(13)	C19	.C12	3.5592(14)
C10	.C6_l	3.4408(13)	C19	.C11	3.2400(12)
C10	.C23_d	3.4798(13)	C20	.C22	3.0068(11)
C10	.C13	2.7561(10)	C20	.C16	3.0417(12)
C11	.C19	3.2400(12)	C21	.C24	2.7895(11)
C11	.C8	2.7795(11)	C21	.O5	2.8624(11)
C11	.C15	3.2449(12)	C22	.O5	2.9099(11)
C12	.C14	2.8342(11)	C22	.C25	2.7640(10)
C12	.C9	2.7365(10)	C22	.C20	3.0068(11)
C12	.C30	3.5854(14)	C22	.O6	2.7118(10)
C12	.C19	3.5592(14)	C23	.C10_m	3.4798(13)
C12	.C15	3.4055(13)	C23	.C26	2.7286(10)
C13	.C10	2.7561(10)	C24	.O4_m	3.0783(12)
C13	.C7	3.0370(12)	C24	.O7	2.7369(10)

C13	.O3	2.9280(11)	C24	.C21	2.7895(11)
C14	.C17	2.7811(11)	C25	.C22	2.7640(10)
C14	.C12	2.8342(11)	C26	.C23	2.7286(10)
C15	.C18	2.7244(10)	C27	.C32	3.0283(11)
C15	.C12	3.4055(13)	C27	.C40	3.1077(12)
C15	.C11	3.2449(12)	C28	.C35	3.1222(12)
C16	.C19	2.7625(10)	C28	.C31	2.9629(11)
C16	.O5	2.9071(11)	C28	.C32	3.3969(13)
C16	.C20	3.0417(12)	C30	.C12	3.5854(14)
C17	.C14	2.7811(11)	C31	.C28	2.9629(11)
C31	.C36	3.0490(12)	C20	.H16	2.8100
C31	.O2	3.2729(12)	C20	.H42C_f	2.9100
C32	.C39	3.0453(12)	C21	.H32A_e	3.1000
C32	.C27	3.0283(11)	C22	.H10_m	3.0800
C32	.C28	3.3969(13)	C23	.H34A_e	3.0100
C35	.O1_1	3.1960(12)	C23	.H10_m	2.8400
C35	.C28	3.1222(12)	C24	.H34A_e	3.0800
C35	.C40	3.0155(11)	C26	.H5N	2.5200

C36	.C31	3.0490(12)	C27	.H35A	2.5800
C36	.C39	3.0500(12)	C27	.H32B	2.7100
C36	.C40	3.5424(13)	C27	.H31A	2.7500
C39	.C36	3.0500(12)	C27	.H40B	2.7700
C39	.C32	3.0453(12)	C27	.H39A	2.6000
C40	.C36	3.5424(13)	C27	.H29B	2.7600
C40	.C35	3.0155(11)	C27	.H29A	2.5700
C40	.C27	3.1077(12)	C27	.H35B	2.6100
C43	.O7_s	3.3276(13)	C28	.H30C	2.8000
C4	.H2N	2.4400	C28	.H30A	2.6400
C7	.H6	2.7900	C28	.H32B	2.8600
C7	.H13	2.7900	C28	.H35B	2.7700
C9	.H3N	2.4600	C28	.H31A	2.6900
C12	.H30A	2.9500	C29	.H27B	2.6300
C13	.H30A	2.9700	C29	.H27A	2.6800
C14	.H12	2.5500	C30	.H28A	2.8100
C15	.H12	2.9100	C30	.H12	2.8600
C18	.H4N	2.4400	C30	.H28B	2.6300

C20	.H39B_e	2.8600	C31	.H33B	2.6400
C20	.H22	2.7700	C31	.H39A	2.6500
C31	.H28B	2.6600	C36	.H40A	3.0400
C31	.H35B	2.6500	C37	.H35A	2.5600
C31	.H36A	2.7900	C37	.H35B	2.6600
C31	.H39B	2.5400	C38	.H36A	2.6900
C31	.H27A	2.8000	C38	.H25_k	3.0200
C31	.H33A	2.6900	C38	.H36B	2.7300
C32	.H27A	2.8200	C39	.H27B	2.7300
C32	.H34A	2.6500	C39	.H27A	2.5300
C32	.H39A	2.7200	C39	.H41B	2.6200
C32	.H34C	2.7600	C39	.H35A	2.7000
C32	.H28B	2.8300	C39	.H31B	2.5900
C33	.H31B	2.6400	C39	.H32A	2.7200
C33	.H31A	2.6500	C39	.H41A	2.6100
C34	.H4_m	3.1000	C39	.H36B	2.7000
C34	.H32B	2.6700	C40	.H36B	3.0500
C34	.H32A	2.7300	C40	.H42A	2.6600

C35	.H27B	2.5400	C40	.H42C	2.8300
C35	.H31B	2.6800	C40	.H35A	2.7000
C35	.H28A	2.8000	C40	.H27B	2.8600
C35	.H31A	2.5900	C41	.H39A	2.5600
C35	.H37A	2.5800	C41	.H39B	2.6600
C35	.H40A	2.7700	C42	.H40B	2.7400
C35	.H37B	2.6300	C42	.H40A	2.7500
C35	.H39B	2.7400	C44	.H3N_m	3.0600
C36	.H38A	2.6100	C44	.H4N_c	2.8200
C36	.H38C	2.7300	C44	.H41B_f	2.9600
C36	.H39B	2.7900	C44	.H2N_m	2.8900
C36	.H31B	2.7300	C44	.H5N_c	2.7000
H2	.N1	2.6200	H5N	.H26	2.3900
H2	.O1	2.4300	H5N	.H4N	2.0600
H2	.H3	2.3200	H5N	.O8_j	2.7800
H2N	.H3N	1.9900	H5N	.O9_j	2.0000
H2N	.O9_i	2.0300	H5N	.N4	2.3400
H2N	.H4	2.2600	H5N	.C26	2.5200

H2N	.N3	2.2900	H5N	.C44_j	2.7000
H2N	.C44_i	2.8900	H6	.N1	2.5900
H2N	.C4	2.4400	H6	.N2	2.6600
H3	.O7_k	2.6500	H6	.C7	2.7900
H3	.H2	2.3200	H6	.O3	2.3000
H3	.H4	2.2700	H6	.O2	2.4100
H3N	.O9_i	2.1100	H9	.N3	2.5200
H3N	.H2N	1.9900	H9	.H41A_o	2.4900
H3N	.C9	2.4600	H9	.H3N	2.2700
H3N	.C44_i	3.0600	H9	.H10	2.2900
H3N	.H9	2.2700	H10	.O4	2.4900
H3N	.N2	2.2800	H10	.C22_d	3.0800
H4	.H2N	2.2600	H10	.C23_d	2.8400
H4	.H3	2.2700	H10	.H9	2.2900
H4	.C34_n	3.1000	H12	.C30	2.8600
H4	.N2	2.5100	H12	.H13	2.3200
H4N	.N5	2.3000	H12	.C15	2.9100

H4N	.O8_j	1.9900	H12	.O4	2.6400
H4N	.H5N	2.0600	H12	.H30A	2.3500
H4N	.C18	2.4400	H12	.C14	2.5500
H4N	.C44_j	2.8200	H13	.C7	2.7900
H4N	.H18	2.2400	H13	.H12	2.3200
H13	.O3	2.3400	H25	.H38B_r	2.3100
H13	.N3	2.6600	H25	.H24	2.3000
H13	.H30A	2.4000	H25	.H26	2.3100
H15	.H16	2.3200	H25	.C38_r	3.0200
H15	.O4	2.5800	H26	.N5	2.5400
H16	.H15	2.3200	H26	.H5N	2.3900
H16	.C20	2.8100	H26	.H25	2.3100
H16	.N4	2.6800	H27A	.C32	2.8200
H16	.O1_p	2.9200	H27A	.C39	2.5300
H16	.O5	2.3200	H27A	.H28B	2.3200
H18	.N4	2.5000	H27A	.H29A	2.4000
H18	.O8_j	2.6400	H27A	.H32B	2.3600
H18	.H4N	2.2400	H27A	.H39A	2.2900

H18	.H28B_q	2.3400	H27A	.O6_s	2.6600
H18	.H19	2.3100	H27A	.C29	2.6800
H19	.H18	2.3100	H27A	.C31	2.8000
H19	.O4	2.5400	H27B	.C29	2.6300
H19	.O3_l	2.8100	H27B	.C35	2.5400
H22	.O6	2.4100	H27B	.C40	2.8600
H22	.N5	2.6500	H27B	.H28A	2.3600
H22	.O5	2.4300	H27B	.H29B	2.5400
H22	.H40B_f	2.4300	H27B	.H35A	2.2800
H22	.C20	2.7700	H27B	.H40B	2.3000
H22	.N6	2.5800	H27B	.C39	2.7300
H24	.O7	2.4600	H28A	.O3	2.7500
H24	.H25	2.3000	H28A	.C35	2.8000
H24	.O4_m	2.8200	H28A	.H27B	2.3600
H24	.N6	2.6200	H28A	.H29B	2.2800
H28A	.H30A	2.6000	H30A	.H12	2.3500
H28A	.H35B	2.2000	H30A	.H13	2.4000
H28A	.N7	2.7500	H30A	.H28A	2.6000

H28A	.C30	2.8100	H30A	.H29B	2.3900
H28B	.N7	2.7900	H30A	.C28	2.6400
H28B	.C31	2.6600	H30B	.H29B	2.2600
H28B	.C32	2.8300	H30B	.H42A_f	2.5000
H28B	.H18_c	2.3400	H30B	.H29A	2.3800
H28B	.H27A	2.3200	H30C	.O8	2.7400
H28B	.H29A	2.4200	H30C	.C28	2.8000
H28B	.H30C	2.5800	H30C	.H28B	2.5800
H28B	.C30	2.6300	H30C	.H29A	2.2700
H28B	.H32B	2.2200	H31A	.O2	2.8400
H28B	.H31A	2.2800	H31A	.C27	2.7500
H29A	.H28B	2.4200	H31A	.C28	2.6900
H29A	.H30B	2.3800	H31A	.H32B	2.3400
H29A	.H34B_q	2.5300	H31A	.H33B	2.4300
H29A	.C27	2.5700	H31A	.H35B	2.3900
H29A	.H30C	2.2700	H31A	.H28B	2.2800
H29A	.H27A	2.4000	H31A	.C33	2.6500
H29B	.O2_1	2.8300	H31A	.C35	2.5900

H29B	.C27	2.7600	H31B	.O2	2.8200
H29B	.H27B	2.5400	H31B	.O5_b	2.7500
H29B	.H28A	2.2800	H31B	.C33	2.6400
H29B	.H30A	2.3900	H31B	.C35	2.6800
H29B	.H30B	2.2600	H31B	.C39	2.5900
H30A	.C12	2.9500	H31B	.H32A	2.3500
H30A	.C13	2.9700	H31B	.H33A	2.4800
H31B	.H36A	2.2800	H33B	.H34B	2.3800
H31B	.H39B	2.3000	H33B	.H31A	2.4300
H31B	.C36	2.7300	H33B	.H32B	2.3700
H32A	.N7	2.7700	H33B	.H34C	2.3100
H32A	.C39	2.7200	H34A	.H32A	2.5100
H32A	.H31B	2.3500	H34A	.C23_b	3.0100
H32A	.H33A	2.3300	H34A	.C24_b	3.0800
H32A	.H34A	2.5100	H34A	.C32	2.6500
H32A	.H39A	2.1700	H34A	.H33A	2.3900
H32A	.C21_b	3.1000	H34B	.H29A_a	2.5300
H32A	.C34	2.7300	H34B	.H33A	2.3000

H32B	.O8	2.8800	H34B	.H33B	2.3800
H32B	.C27	2.7100	H34C	.O8	2.8800
H32B	.C28	2.8600	H34C	.C32	2.7600
H32B	.C34	2.6700	H34C	.H32B	2.5600
H32B	.H27A	2.3600	H34C	.H33B	2.3100
H32B	.H28B	2.2200	H35A	.H40A	2.3200
H32B	.H31A	2.3400	H35A	.O1_1	2.5400
H32B	.N7	2.7800	H35A	.C27	2.5800
H32B	.H34C	2.5600	H35A	.C37	2.5600
H32B	.H33B	2.3700	H35A	.C39	2.7000
H33A	.H31B	2.4800	H35A	.C40	2.7000
H33A	.H32A	2.3300	H35A	.H27B	2.2800
H33A	.H34B	2.3000	H35A	.H37B	2.3600
H33A	.O5_b	2.9200	H35A	.H36B	2.3900
H33A	.H34A	2.3900	H35B	.C31	2.6500
H33A	.C31	2.6900	H35B	.C37	2.6600
H33B	.C31	2.6400	H35B	.C28	2.7700
H35B	.H31A	2.3900	H37B	.H38B	2.1300

H35B	.H36A	2.3200	H37B	.H36B	2.3400
H35B	.H28A	2.2000	H37B	.C35	2.6300
H35B	.C27	2.6100	H37B	.H35A	2.3600
H35B	.O3	2.5900	H38A	.C36	2.6100
H35B	.H37A	2.4100	H38A	.H36B	2.5200
H36A	.C31	2.7900	H38A	.H37B	2.2600
H36A	.C38	2.6900	H38B	.H25_k	2.3100
H36A	.N7	2.8300	H38B	.H37A	2.2300
H36A	.H35B	2.3200	H38B	.H37B	2.1300
H36A	.H37A	2.3800	H38C	.C36	2.7300
H36A	.H31B	2.2800	H38C	.H36A	2.6000
H36A	.H38C	2.6000	H38C	.H37A	2.1600
H36B	.C39	2.7000	H39A	.H41A	2.3400
H36B	.C40	3.0500	H39A	.C27	2.6000
H36B	.C38	2.7300	H39A	.C32	2.7200
H36B	.H37B	2.3400	H39A	.C41	2.5600
H36B	.H38A	2.5200	H39A	.H27A	2.2900
H36B	.H35A	2.3900	H39A	.H32A	2.1700

H36B	.N7	2.7500	H39A	.H40B	2.3900
H36B	.H40A	2.5100	H39A	.O6_s	2.8800
H36B	.H39B	2.2500	H39A	.C31	2.6500
H37A	.C35	2.5800	H39B	.N5_b	2.8400
H37A	.H35B	2.4100	H39B	.H41B	2.4500
H37A	.H38B	2.2300	H39B	.C31	2.5400
H37A	.H38C	2.1600	H39B	.C35	2.7400
H37A	.H36A	2.3800	H39B	.C36	2.7900
H37B	.H38A	2.2600	H39B	.C41	2.6600
H39B	.H31B	2.3000	H41A	.H42C	2.2500
H39B	.H36B	2.2500	H41A	.H40B	2.3400
H39B	.C20_b	2.8600	H41A	.C39	2.6100
H39B	.H40A	2.3100	H41B	.C39	2.6200
H40A	.C42	2.7500	H41B	.C44_u	2.9600
H40A	.H35A	2.3200	H41B	.H39B	2.4500
H40A	.C36	3.0400	H41B	.H40A	2.3400
H40A	.H39B	2.3100	H41B	.H42A	2.3900
H40A	.H41B	2.3400	H41B	.H42B	2.2400

H40A	.H36B	2.5100	H41B	.O9_u	2.9000
H40A	.C35	2.7700	H42A	.H41B	2.3900
H40A	.N7	2.8500	H42A	.H40A	2.5200
H40A	.H42A	2.5200	H42A	.C40	2.6600
H40B	.N7	2.7500	H42A	.H30B_v	2.5000
H40B	.C27	2.7700	H42B	.H41B	2.2400
H40B	.O5_s	2.6300	H42B	.H41A	2.3700
H40B	.H22_s	2.4300	H42C	.C20_s	2.9100
H40B	.H27B	2.3000	H42C	.C40	2.8300
H40B	.C42	2.7400	H42C	.H41A	2.2500
H40B	.H41A	2.3400	H43A	.O8	2.8000
H40B	.H39A	2.3900	H43A	.O9	2.7600
H41A	.H9_t	2.4900	H43B	.O9	2.4700
H41A	.H39A	2.3400	H43C	.O6_s	2.8300
H41A	.H42B	2.3700	H43C	.O8	2.4300

Table A3A.18: Hydrogen Bonds (Angstrom, Deg) for **L**ı+TBA(OAC)

N2 -- H2N .. O9	0.8600	2.0300	2.8580(11)	162.00	1_556	
N3 -- H3N .. O9	0.8600	2.1100	2.9175(11)	156.00	1_556	
N4 -- H4N .. O8	0.8600	1.9900	2.8425(11)	171.00	1_455	

N5 -- H5N .. O9	0.8600	2.0000	2.7988(11)	153.00	1_455
C6 -- H6 .. O3	0.9300	2.3000	2.8839(11)	121.00	.
C13 -- H13 .. O3	0.9300	2.3400	2.9280(11)	121.00	.
C16 -- H16 .. O5	0.9300	2.3200	2.9071(11)	121.00	.
C22 -- H22 .. O5	0.9300	2.4300	2.9099(11)	112.00	.
C35 -- H35A .. O1	0.9700	2.5400	3.1960(12)	125.00	1_455
C35 -- H35B .. O3	0.9700	2.5900	3.5539(13)	171.00	.

Translation of Symmetry Code to Equiv.Pos

a =[1655.00] =	1+x,y,z
b =[1645.00] =	1+x,-1+y,z
c =[1655.00] =	1+x,y,z
d =[1556.00] =	x,y,1+z
e =[1465.00] =	-1+x,1+y,z
f =[1565.00] =	x,1+y,z
g =[1565.00] =	x,1+y,z
h =[1464.00] =	-1+x,1+y,-1+z
i =[1556.00] =	x,y,1+z
j =[1455.00] =	-1+x,y,z
k =[1646.00] =	1+x,-1+y,1+z
m =[1554.00] =	x,y,-1+z
o =[1566.00] =	x,1+y,1+z
p =[1465.00] =	-1+x,1+y,z
r =[1464.00] =	-1+x,1+y,-1+z
s =[1545.00] =	x,-1+y,z
t =[1544.00] =	x,-1+y,-1+z
u =[1545.00] =	x,-1+y,z

v =[1545.00] = x,-1+y,z

Table A3A.19: Final Coordinates and Equivalent Isotropic Displacement Parameters of the non-Hydrogen atoms for **L**$_2$ + DMSO

Atom	x	y	z	U(eq) [Ang^2]
*S1	0.87298	0.84043	0.37933	0.1459
*S2	0.86832	0.70021	0.34699	0.1048
S3	0.90781	0.37284	0.41082	0.2287
S4	-0.02140	0.54306	0.19274	0.1893
F1	0.97960	-0.08546	0.76925	0.2190
F2	0.89646	-0.12084	0.83940	0.3011
F3	1.02975	0.07300	5/6	0.2979
F4	0.30750	-0.13880	0.79100	0.1886
F5	0.36326	0.06880	0.82001	0.1767
F6	0.43940	-0.03670	0.87148	0.2281
F7	0.15794	0.62537	-0.00639	0.2379
F8	0.27544	0.80468	-0.03269	0.2574
F9	0.24180	0.81027	0.04998	0.2479
F10	0.73011	0.71792	-0.08009	0.2771

F11	0.87459	0.73085	-0.01534	0.3632
F12	0.83222	0.89426	-0.02801	0.2731
O1	0.44770	0.07294	0.62854	0.1177
O2	0.29594	0.26549	0.39551	0.1047
O3	0.37986	0.57638	0.17945	0.1044
N1	0.69415	0.14076	0.66573	0.1035
N2	0.63026	0.20868	0.58542	0.0942
N3	0.54554	0.49151	0.21541	0.0922
N4	0.57624	0.57955	0.13460	0.0919
C1	0.38396	0.24992	0.44129	0.0831
C00Z	0.42704	0.65996	0.07166	0.0900
C2	0.51859	0.35398	0.46664	0.1023
C3	0.59676	0.33992	0.51449	0.0973
C4	0.54440	0.22114	0.53728	0.0808
C5	0.40785	0.11480	0.51119	0.0893

O5	1.02234	0.81130	0.37318	0.1591
C6	0.32683	0.13078	0.46304	0.0879
C7	0.58001	0.13675	0.62673	0.0925
C8	0.68005	0.08215	0.71520	0.0842
C9	0.79643	0.05197	0.73644	0.0919
C10	0.79176	-0.00418	0.78517	0.0959
C11	0.67129	-0.02843	0.81369	0.0941
C12	0.55582	0.00301	0.79146	0.0871
C13	0.55809	0.05771	0.74309	0.0865
C14	0.42179	-0.02832	0.82048	0.1174
C15	0.91567	-0.04056	0.80703	0.1441
C16	0.36511	0.32770	0.35291	0.0836
C17	0.47457	0.29225	0.33079	0.0800
C18	0.53119	0.34918	0.28593	0.0795
C19	0.48261	0.44158	0.26253	0.0777
C20	0.37485	0.47961	0.28626	0.0846
C21	0.31894	0.42291	0.33194	0.0859

C22	0.49215	0.55185	0.17709	0.0831
C23	0.55522	0.63780	0.08779	0.0788
C24	0.66626	0.67181	0.05438	0.0878
C25	0.65278	0.72870	0.00719	0.0925
C26	0.52551	0.75233	-0.00828	0.1011
C27	0.41671	0.71861	0.02371	0.0966
C28	0.27595	0.74162	0.00913	0.1379
C29	0.77560	0.76955	-0.02440	0.1521
O6	1.06298	0.51130	0.40581	0.4297
C32	0.78587	0.80018	0.30921	0.1600
C33	0.76015	0.68301	0.40079	0.1387
O4	-0.18720	0.50600	0.17673	0.1770
C34	0.92035	0.26439	0.44993	0.2591
C35	0.87914	0.23673	0.34951	0.2242
C30	-0.00672	0.39175	0.17844	0.3634

C31	0.05768	0.61033	0.13966	0.2050

U(eq) = 1/3 of the trace of the orthogonalized U Tensor

Starred Atom sites have a S.O.F less than 1.0

Table A3A.20: Hydrogen Atom Positions and Isotropic Displacement Parameters for **L_2** + DMSO

Atom	x	y	z	U(iso) [Ang^2]
H00Z	0.34922	0.63600	0.09254	0.1080
H1N	0.78327	0.18323	0.65941	0.1242
H2	0.55763	0.43473	0.45149	0.1227
H2N	0.72543	0.25176	0.58888	0.1131
H3	0.68737	0.41275	0.53183	0.1168
H3N	0.62758	0.48250	0.21048	0.1107
H4N	0.65282	0.55778	0.13731	0.1102
H5	0.36999	0.03282	0.52565	0.1072
H6	0.23443	0.06032	0.44601	0.1055
H9	0.87899	0.06922	0.71809	0.1103
H11	0.66862	-0.06486	0.84684	0.1129
H13	0.47844	0.07838	0.72899	0.1037

H17	0.50922	0.23088	0.34605	0.0961
H18	0.60437	0.32502	0.27078	0.0954
H20	0.34104	0.54221	0.27160	0.1015
H21	0.24917	0.44982	0.34859	0.1031
H24	0.75187	0.65568	0.06417	0.1053
H26	0.51544	0.79082	-0.04022	0.1214
H32A	0.83914	0.85114	0.28212	0.1920
H32B	0.67803	0.76713	0.30133	0.1920
H33A	0.79600	0.66233	0.43613	0.1664
H33B	0.65264	0.64772	0.39002	0.1664
H34A	0.99082	0.22645	0.43785	0.3886
H34B	0.82449	0.18856	0.44606	0.3886
H34C	0.95326	0.31322	0.48928	0.3886
H35A	0.95958	0.20522	0.35245	0.3362
H35B	0.87596	0.27370	0.31530	0.3362

H35C	0.78652	0.15846	0.34797	0.3362
H30A	-0.10124	0.32008	0.15928	0.5451
H30B	0.06676	0.39764	0.15410	0.5451
H30C	0.02303	0.36783	0.21346	0.5451
H31A	0.03006	0.68703	0.13333	0.3075
H31B	0.16419	0.64469	0.14971	0.3075
H31C	0.02442	0.53808	0.10533	0.3075

==========

The Temperature Factor has the Form of Exp(-T) Where
T = 8*(Pi**2)*U*(Sin(Theta)/Lambda)**2 for Isotropic Atoms

Table A3A.21: (An)isotropic Displacement Parameters for **L_2** + DMSO

Atom	U(1,1) or U	U(2,2)	U(3,3)	U(2,3)	U(1,3)	U(1,2)
S1	0.1230	0.1155	0.1780	0.0149	0.0412	0.0255
S2	0.0851	0.1069	0.1245	0.0220	0.0438	0.0345

S3	0.1942	0.3317	0.2089	0.0202	0.0250	0.1740
S4	0.1577	0.2864	0.2201	0.1286	0.0976	0.1488
F1	0.1947	0.3732	0.1976	0.1136	0.0514	0.2070
F2	0.2373	0.5312	0.3530	0.3501	0.1634	0.2664
F3	0.2026	0.2430	0.3994	-0.0515	-0.1704	0.1330
F4	0.1132	0.1712	0.2147	-0.0334	0.0849	-0.0038
F5	0.1570	0.1894	0.2201	0.0457	0.1020	0.0904
F6	0.1546	0.4330	0.1401	0.1331	0.0815	0.1214
F7	0.1285	0.2589	0.3144	0.0741	-0.0390	0.0757
F8	0.2257	0.4395	0.2467	0.2307	0.0775	0.2153
F9	0.2517	0.4201	0.1715	0.0286	-0.0025	0.2654
F10	0.2348	0.3127	0.1933	0.0181	0.1371	-0.0048
F11	0.2841	0.6994	0.4122	0.4404	0.2830	0.3539
F12	0.2549	0.1772	0.3864	0.1086	0.2094	0.0265
O1	0.0759	0.1944	0.1018	0.0589	0.0287	0.0602

O2	0.0822	0.1517	0.0941	0.0590	0.0306	0.0446
O3	0.0874	0.1688	0.0948	0.0556	0.0342	0.0770
N1	0.0709	0.1508	0.1036	0.0543	0.0165	0.0489
N2	0.0803	0.1161	0.0897	0.0272	0.0088	0.0414
N3	0.0794	0.1464	0.0843	0.0515	0.0343	0.0660
N4	0.0793	0.1316	0.0934	0.0510	0.0331	0.0581
C1	0.0782	0.1129	0.0693	0.0323	0.0235	0.0422
C00Z	0.0828	0.1177	0.0778	0.0318	0.0146	0.0437
C2	0.1194	0.0996	0.0869	0.0371	0.0247	0.0332
C3	0.0987	0.1028	0.0825	0.0279	0.0126	0.0280
C4	0.0840	0.0885	0.0717	0.0163	0.0126	0.0360
C5	0.1032	0.0969	0.0814	0.0302	0.0185	0.0491
O5	0.0754	0.1994	0.1923	0.0676	0.0459	0.0262
C6	0.0730	0.0982	0.0943	0.0261	0.0231	0.0310
C7	0.0894	0.1229	0.0838	0.0346	0.0244	0.0550
C8	0.0701	0.1056	0.0801	0.0312	0.0114	0.0336
C9	0.0740	0.1254	0.0878	0.0426	0.0144	0.0440
C10	0.0673	0.1207	0.1036	0.0353	0.0048	0.0390

C11	0.0824	0.1022	0.0938	0.0306	0.0147	0.0279
C12	0.0724	0.1013	0.0823	0.0090	0.0148	0.0317
C13	0.0747	0.1082	0.0839	0.0234	0.0163	0.0422
C14	0.0996	0.1361	0.1182	0.0301	0.0378	0.0421
C15	0.1097	0.2479	0.1081	0.0730	0.0345	0.0896
C16	0.0743	0.1082	0.0714	0.0255	0.0207	0.0344
C17	0.0886	0.0840	0.0811	0.0327	0.0241	0.0406
C18	0.0725	0.0952	0.0827	0.0203	0.0193	0.0439
C19	0.0678	0.0997	0.0711	0.0224	0.0148	0.0366
C20	0.0709	0.1281	0.0768	0.0382	0.0203	0.0549
C21	0.0770	0.1228	0.0766	0.0271	0.0197	0.0562
C22	0.0703	0.1187	0.0743	0.0336	0.0218	0.0452
C23	0.0721	0.0925	0.0737	0.0266	0.0172	0.0295
C24	0.0912	0.0961	0.0889	0.0349	0.0282	0.0420
C25	0.0944	0.0909	0.0929	0.0304	0.0291	0.0296
C26	0.1207	0.1028	0.0809	0.0341	0.0229	0.0376
C27	0.0972	0.1142	0.0812	0.0219	0.0015	0.0474

C28	0.1501	0.1828	0.0965	0.0336	-0.0002	0.0862
C29	0.1702	0.2010	0.1238	0.0977	0.0706	0.0800
O6	0.0767	0.5936	0.4406	-0.3016	-0.0600	0.1176
C32	0.0990	0.2063	0.1894	0.0798	0.0324	0.0593
C33	0.1000	0.1519	0.1622	0.0506	0.0615	0.0308
O4	0.1173	0.2956	0.2376	0.1723	0.1092	0.1496
C34	0.4559	0.1122	0.2026	0.0297	0.1474	0.0832
C35	0.2219	0.2327	0.1532	-0.0223	-0.0012	0.0496
C30	0.1469	0.2142	0.7866	0.3184	0.0710	0.0531
C31	0.1449	0.2863	0.2446	0.1139	0.0868	0.1164

==========

The Temperature Factor has the Form of Exp(-T) Where
T = 8*(Pi**2)*U*(Sin(Theta)/Lambda)**2 for Isotropic Atoms
T = 2*(Pi**2)*Sumij(h(i)*h(j)*U(i,j)*Astar(i)*Astar(j)), for
Anisotropic Atoms. Astar(i) are Reciprocal Axial Lengths and
h(i) are the Reflection Indices.

Table A3A.22: Bond Distances (Angstrom) for **L_2** + DMSO

S1	-O5	1.6161(8)	N1	-C7	1.3695(7)
S1	-C32	1.7217(9)	N1	-C8	1.4097(7)
S1	-C33	1.7855(9)	N2	-C4	1.4118(7)
S2	-O5	1.5165(8)	N2	-C7	1.3531(7)
S2	-C32	1.8233(9)	N3	-C19	1.4148(7)
S2	-C33	1.7355(9)	N3	-C22	1.3560(7)
S3	-O6	1.6905(9)	N4	-C22	1.3693(7)
S3	-C34	1.6033(8)	N4	-C23	1.3871(7)
S3	-C35	1.7942(9)	N1	-H1N	0.8600
S4	-C31	1.6640(8)	C1	-C2	1.3632(7)
S4	-C30	1.6192(8)	C1	-C6	1.3634(7)
S4	-O4	1.5171(8)	C00Z	-C27	1.3933(7)
F1	-C15	1.2751(7)	C00Z	-C23	1.3884(7)
F2	-C15	1.2019(6)	N2	-H2N	0.8600
F3	-C15	1.3004(7)	C2	-C3	1.3735(7)
F4	-C14	1.3077(7)	C3	-C4	1.3701(7)

F5	-C14	1.3344(7)	N3	-H3N	0.8600
F6	-C14	1.2384(6)	C4	-C5	1.3877(7)
F7	-C28	1.2935(7)	N4	-H4N	0.8600
F8	-C28	1.2798(7)	C5	-C6	1.4028(7)
F9	-C28	1.2665(6)	C8	-C13	1.3857(7)
F10	-C29	1.3236(7)	C8	-C9	1.3638(7)
F11	-C29	1.1940(6)	C9	-C10	1.3811(7)
F12	-C29	1.2265(6)	C10	-C11	1.3826(7)
O1	-C7	1.2256(6)	C10	-C15	1.4730(8)
O2	-C1	1.3956(7)	C11	-C12	1.3717(7)
O2	-C16	1.3899(7)	C12	-C13	1.3662(7)
O3	-C22	1.2224(6)	C12	-C14	1.4975(8)
C16	-C21	1.3706(7)	C18	-H18	0.9300
C16	-C17	1.3821(7)	C20	-H20	0.9300
C17	-C18	1.3715(7)	C21	-H21	0.9300
C18	-C19	1.3850(7)	C24	-H24	0.9300
C19	-C20	1.3969(7)	C26	-H26	0.9300

C20	-C21	1.3859(7)	C32	-H32A	0.9700
C23	-C24	1.3856(7)	C32	-H32B	0.9700
C24	-C25	1.3715(7)	C33	-H33B	0.9700
C25	-C29	1.4480(7)	C33	-H33A	0.9700
C25	-C26	1.3850(7)	C34	-H34C	0.9600
C26	-C27	1.3454(7)	C34	-H34A	0.9600
C27	-C28	1.5027(8)	C34	-H34B	0.9600
C00Z	-H00Z	0.9300	C35	-H35A	0.9600
C2	-H2	0.9300	C35	-H35B	0.9600
C3	-H3	0.9300	C35	-H35C	0.9600
C5	-H5	0.9300	C30	-H30A	0.9600
C6	-H6	0.9300	C30	-H30B	0.9600
C9	-H9	0.9300	C30	-H30C	0.9600
C11	-H11	0.9300	C31	-H31A	0.9600
C13	-H13	0.9300	C31	-H31B	0.9600
C17	-H17	0.9300	C31	-H31C	0.9600

Table A3A.23: Bond Angles (Degrees) for **L_2** + DMSO

O5	-S1	-C33	100.67(3)	C19	-N3	-H3N	116.00
C32	-S1	-C33	98.55(3)	C3	-C4	-C5	118.18(3)
O5	-S1	-C32	102.56(2)	C22	-N4	-H4N	115.00
O5	-S2	-C33	107.19(3)	C23	-N4	-H4N	115.00
C32	-S2	-C33	96.62(3)	N2	-C4	-C5	121.93(3)
O5	-S2	-C32	102.13(4)	N2	-C4	-C3	119.88(2)
O6	-S3	-C35	105.73(3)	C4	-C5	-C6	120.11(3)
C34	-S3	-C35	87.56(4)	C1	-C6	-C5	119.80(2)
O6	-S3	-C34	119.69(3)	N1	-C7	-N2	112.22(3)
O4	-S4	-C30	103.86(2)	O1	-C7	-N2	124.03(1)
O4	-S4	-C31	106.40(2)	O1	-C7	-N1	123.74(3)
C30	-S4	-C31	97.80(2)	N1	-C8	-C9	116.57(2)
C1	-O2	-C16	118.60(3)	N1	-C8	-C13	123.70(2)
C7	-N1	-C8	126.46(2)	C9	-C8	-C13	119.71(3)
C4	-N2	-C7	127.46(3)	C8	-C9	-C10	120.04(2)
C19	-N3	-C22	127.86(3)	C9	-C10	-C11	120.96(2)
C22	-N4	-C23	129.08(3)	C9	-C10	-C15	119.90(2)

C8	-N1	-H1N	117.00	C11	-C10	-C15	119.14(3)
O2	-C1	-C2	121.76(3)	C10	-C11	-C12	117.81(3)
C2	-C1	-C6	120.12(2)	C13	-C12	-C14	119.53(2)
C7	-N1	-H1N	117.00	C11	-C12	-C13	122.02(2)
O2	-C1	-C6	117.95(2)	C11	-C12	-C14	118.42(3)
C23	-C00Z	-C27	119.03(1)	C8	-C13	-C12	119.45(2)
C7	-N2	-H2N	116.00	F4	-C14	-F5	98.76(4)
C4	-N2	-H2N	116.00	F4	-C14	-F6	110.48(2)
C1	-C2	-C3	120.20(3)	F6	-C14	-C12	117.10(3)
C2	-C3	-C4	121.56(2)	F5	-C14	-C12	112.60(2)
C22	-N3	-H3N	116.00	F4	-C14	-C12	111.89(3)
F5	-C14	-F6	104.25(1)	C00Z	-C27	-C26	122.37(2)
F2	-C15	-C10	119.60(2)	C00Z	-C27	-C28	116.27(1)
F2	-C15	-F3	105.20(3)	C26	-C27	-C28	121.37(3)
F1	-C15	-C10	115.92(3)	F7	-C28	-F8	103.85(3)
F3	-C15	-C10	110.63(4)	F9	-C28	-C27	115.11(2)
F1	-C15	-F3	98.03(4)	F8	-C28	-F9	106.09(4)

F1	-C15	-F2	104.87(3)	F8	-C28	-C27	114.20(2)
O2	-C16	-C17	121.37(2)	F7	-C28	-C27	113.59(4)
C17	-C16	-C21	120.40(2)	F7	-C28	-F9	102.73(3)
O2	-C16	-C21	118.20(2)	F12	-C29	-C25	117.64(1)
C16	-C17	-C18	118.82(2)	F11	-C29	-C25	119.18(3)
C17	-C18	-C19	121.95(2)	F10	-C29	-F12	96.13(2)
C18	-C19	-C20	118.69(2)	F11	-C29	-F12	107.45(3)
N3	-C19	-C18	117.46(2)	F10	-C29	-F11	101.28(2)
N3	-C19	-C20	123.85(2)	F10	-C29	-C25	111.56(3)
C19	-C20	-C21	119.19(2)	C27	-C00Z	-H00Z	120.00
C16	-C21	-C20	120.87(2)	C23	-C00Z	-H00Z	120.00
O3	-C22	-N4	123.59(2)	C1	-C2	-H2	120.00
O3	-C22	-N3	123.92(2)	C3	-C2	-H2	120.00
N3	-C22	-N4	112.47(3)	C4	-C3	-H3	119.00
N4	-C23	-C00Z	123.53(1)	C2	-C3	-H3	119.00
N4	-C23	-C24	118.21(3)	C4	-C5	-H5	120.00
C00Z	-C23	-C24	118.24(3)	C6	-C5	-H5	120.00

C23	-C24	-C25	121.49(3)	C1	-C6	-H6	120.00
C26	-C25	-C29	120.68(3)	C5	-C6	-H6	120.00
C24	-C25	-C29	119.23(3)	C8	-C9	-H9	120.00
C24	-C25	-C26	120.03(1)	C10	-C9	-H9	120.00
C25	-C26	-C27	118.84(3)	C12	-C11	-H11	121.00
C10	-C11	-H11	121.00	S3	-C34	-H34B	109.00
C12	-C13	-H13	120.00	H34A	-C34	-H34C	109.00
C8	-C13	-H13	120.00	S3	-C34	-H34C	109.00
C16	-C17	-H17	121.00	H34A	-C34	-H34B	109.00
C18	-C17	-H17	121.00	S3	-C34	-H34A	109.00
C19	-C18	-H18	119.00	H34B	-C34	-H34C	109.00
C17	-C18	-H18	119.00	S3	-C35	-H35C	109.00
C21	-C20	-H20	120.00	H35A	-C35	-H35C	109.00
C19	-C20	-H20	120.00	H35B	-C35	-H35C	109.00
C20	-C21	-H21	120.00	H35A	-C35	-H35B	109.00
C16	-C21	-H21	120.00	S3	-C35	-H35A	109.00
C23	-C24	-H24	119.00	S3	-C35	-H35B	109.00

C25	-C24	-H24	119.00	S4	-C30	-H30A	109.00
C27	-C26	-H26	121.00	S4	-C30	-H30B	109.00
C25	-C26	-H26	121.00	S4	-C30	-H30C	109.00
S2	-C32	-H32B	119.00	H30A	-C30	-H30B	109.00
S1	-C32	-H32B	119.00	H30A	-C30	-H30C	109.00
S1	-C32	-H32A	119.00	H30B	-C30	-H30C	109.00
S2	-C32	-H32A	119.00	S4	-C31	-H31A	109.00
H32A	-C32	-H32B	116.00	S4	-C31	-H31B	109.00
S1	-C33	-H33A	119.00	S4	-C31	-H31C	109.00
S1	-C33	-H33B	119.00	H31A	-C31	-H31B	109.00
S2	-C33	-H33B	119.00	H31A	-C31	-H31C	109.00
H33A	-C33	-H33B	116.00	H31B	-C31	-H31C	109.00
S2	-C33	-H33A	119.00				

Table A3A.24: Torsion Angles (Degrees) for **L₂** + DMSO

C16	-O2	-C1	-C2	41.37(1)
C16	-O2	-C1	-C6	-143.24(1)
C1	-O2	-C16	-C17	43.67(1)
C1	-O2	-C16	-C21	-138.18(1)

C8	-N1	-C7	-N2	176.96(1)
C8	-N1	-C7	-O1	-4.39(1)
C7	-N1	-C8	-C9	157.04(1)
C7	-N1	-C8	-C13	-24.48(1)
C4	-N2	-C7	-N1	176.88(1)
C4	-N2	-C7	-O1	-1.77(1)
C7	-N2	-C4	-C3	150.73(1)
C7	-N2	-C4	-C5	-30.36(1)
C19	-N3	-C22	-O3	2.61(1)
C19	-N3	-C22	-N4	-176.04(1)
C22	-N3	-C19	-C18	162.14(1)
C22	-N3	-C19	-C20	-17.57(1)
C22	-N4	-C23	-C00Z	-9.86(1)
C22	-N4	-C23	-C24	172.12(1)
C23	-N4	-C22	-N3	178.74(1)
C23	-N4	-C22	-O3	0.09(1)
O2	-C1	-C6	-C5	-176.24(1)

C2	-C1	-C6	-C5	-0.77(1)
C6	-C1	-C2	-C3	-0.56(1)
O2	-C1	-C2	-C3	174.73(1)
C27	-C00Z	-C23	-C24	-1.68(1)
C23	-C00Z	-C27	-C28	-179.17(1)
C23	-C00Z	-C27	-C26	1.25(1)
C27	-C00Z	-C23	-N4	-179.70(1)
C1	-C2	-C3	-C4	1.47(1)
C2	-C3	-C4	-N2	177.98(1)
C2	-C3	-C4	-C5	-0.98(1)
C3	-C4	-C5	-C6	-0.37(1)
N2	-C4	-C5	-C6	-179.30(1)
C4	-C5	-C6	-C1	1.24(1)
C9	-C8	-C13	-C12	-0.28(1)
N1	-C8	-C9	-C10	179.27(1)
N1	-C8	-C13	-C12	-178.72(1)
C13	-C8	-C9	-C10	0.73(1)

C8	-C9	-C10	-C15	178.21(1)
C8	-C9	-C10	-C11	-1.11(1)
C9	-C10	-C11	-C12	1.01(1)
C11	-C10	-C15	-F2	18.37(1)
C9	-C10	-C15	-F2	-160.96(1)
C11	-C10	-C15	-F3	-104.05(1)
C11	-C10	-C15	-F1	145.54(1)
C15	-C10	-C11	-C12	-178.31(1)
C9	-C10	-C15	-F3	76.63(1)
C9	-C10	-C15	-F1	-33.79(1)
C10	-C11	-C12	-C14	177.50(1)
C10	-C11	-C12	-C13	-0.57(1)
C13	-C12	-C14	-F5	-38.25(1)
C14	-C12	-C13	-C8	-177.83(1)
C13	-C12	-C14	-F4	71.94(1)
C11	-C12	-C13	-C8	0.21(1)
C11	-C12	-C14	-F6	22.81(1)

C13	-C12	-C14	-F6	-159.08(1)
C11	-C12	-C14	-F5	143.64(1)
C11	-C12	-C14	-F4	-106.17(1)
C17	-C16	-C21	-C20	3.51(1)
O2	-C16	-C21	-C20	-174.66(1)
C21	-C16	-C17	-C18	-2.83(1)
O2	-C16	-C17	-C18	175.27(1)
C16	-C17	-C18	-C19	0.44(1)
C17	-C18	-C19	-C20	1.28(1)
C17	-C18	-C19	-N3	-178.45(1)
C18	-C19	-C20	-C21	-0.64(1)
N3	-C19	-C20	-C21	179.08(1)
C19	-C20	-C21	-C16	-1.73(1)
N4	-C23	-C24	-C25	179.49(1)
C00Z	-C23	-C24	-C25	1.36(1)
C23	-C24	-C25	-C26	-0.53(1)
C23	-C24	-C25	-C29	176.62(1)

C24	-C25	-C26	-C27	0.03(1)
C29	-C25	-C26	-C27	-177.07(1)
C24	-C25	-C29	-F10	130.56(1)
C24	-C25	-C29	-F11	13.08(1)
C24	-C25	-C29	-F12	-119.79(1)
C26	-C25	-C29	-F10	-52.31(1)
C26	-C25	-C29	-F11	-169.80(1)
C26	-C25	-C29	-F12	57.34(1)
C25	-C26	-C27	-C00Z	-0.41(1)
C25	-C26	-C27	-C28	-179.97(1)
C00Z	-C27	-C28	-F7	-65.80(1)
C00Z	-C27	-C28	-F8	175.35(1)
C00Z	-C27	-C28	-F9	52.24(1)
C26	-C27	-C28	-F7	113.78(1)
C26	-C27	-C28	-F8	-5.07(1)
C26	-C27	-C28	-F9	-128.18(1)

Table A3A.25: Contact Distances(Angstrom) for $\mathbf{L_2}$ + DMSO

S2 .H1N_q 3.2000 O1 .C13 2.9003(15)

F1 .C9 2.8032(14) F2 .H11 2.5200

F2 .C11 2.7681(14) F3 .H31A_c 2.7900

F2 .F10_a 2.9603(15) O3 .C00Z 2.8748(15)

F2 .C30_b 3.3551(17) O3 .C19 2.9086(15)

F3 .C9 3.0171(15) O3 .C23 2.9207(15)

F3 .C11 3.2304(16) O3 .C31 3.3678(17)

F4 .C13 3.0096(15) O3 .C20 2.8891(15)

F4 .C11 3.2713(17) O4 .N3_t 2.8208(14)

F5 .C00Z_g 3.3612(17) O4 .C22_t 3.3483(17)

F5 .C13 2.7987(14) F4 .H35B_f 2.8000

F5 .C23_g 3.2523(17) F4 .H18_d 2.7000

F6 .C11 2.7545(14) F4 .H30A_e 2.7200

F7 .C26 3.3503(17) O4 .N4_t 2.8418(15)

F7 .C00Z 2.9504(15) F5 .H13 2.5500

F8 .C26 2.7296(14) O5 .N1_q 2.9064(15)

F9 .C00Z 2.8600(15) O6 .C3_q 3.3414(17)

F10 .C22_j 3.2347(17) F6 .H11 2.4800

F10 .C26 2.8490(15) F7 .H31C_h 2.7100

F10 .F2_i 2.9603(15) F7 .H00Z 2.8400

F11 .C24 2.7163(14) F8 .H26 2.4300

F12 .C24 3.3352(17) F9 .H00Z 2.6800

F12 .C26 2.9362(15) F10 .H26 2.6900

O1 .C32_k 3.3905(17) F11 .H24 2.4300

O1 .C5 2.9220(15) F12 .H26 2.8500

O1 .C4 2.8999(15) O1 .H5 2.4300

F1 .H9 2.5700 N1 .O5_l 2.9064(15)

O1 .C8 2.8913(15) O1 .H35C_f 2.8200

O1 .H32B_k 2.8600 N1 .H9 2.5000

O1 .H13 2.3900 N1 .H2N 2.3100

O2 .H6 2.5200 C1 .C17 2.9182(15)

O2 .H2 2.5900 C1 .C21 3.5336(18)

O2 .H21 2.5200 C1 .C4 2.7766(14)

O2 .H17 2.6100 C00Z .F9 2.8600(15)

O3	.H30B	2.8800	C00Z	.C25	2.7595(14)
O3	.H31B	2.5400	C00Z	.F7	2.9504(15)
O3	.H20	2.3300	C00Z	.F5_g	3.3612(17)
O3	.H00Z	2.2900	C00Z	.O3	2.8748(15)
N3	.O4_m	2.8208(14)	C00Z	.C22	3.0247(15)
O4	.H3N_t	2.0100	C2	.C5	2.7450(14)
O4	.H4N_t	2.0300	C2	.C17	3.1728(16)
O4	.H31A	2.6800	N2	.H3	2.5600
O4	.H31C	2.7700	C2	.C2_g	3.3667(17)
N4	.O4_m	2.8418(15)	C2	.C16	2.9033(15)
O4	.H30A	2.3800	N2	.H1N	2.3200
O5	.H32A	2.8700	N2	.H5	2.6300
O5	.H9_q	2.7600	N3	.H4N	2.3100
O5	.H33A	2.9000	C3	.O6_n	3.3414(17)
O5	.H1N_q	2.1100	N3	.H18	2.5300
O5	.H2N_q	2.8800	N3	.H20	2.6800
O5	.H6_r	2.8200	C3	.C6	2.7384(14)

O6	.H3_q	2.5200	N4	.H3N	2.3100
O6	.H2N_q	2.5400	C4	.C1	2.7766(14)
O6	.H35B	2.8900	N4	.H00Z	2.6500
O6	.H21_s	2.5900	N4	.H24	2.5300
N1	.H13	2.6600	C4	.O1	2.8999(15)
C5	.C2	2.7450(14)	C13	.C7	3.0307(15)
C5	.C7	3.0284(15)	C16	.C19	2.7708(14)
C5	.O1	2.9220(15)	C16	.C6	3.5474(18)
C5	.C5_d	3.4983(18)	C16	.C2	2.9033(15)
C6	.C16	3.5474(18)	C17	.C8_d	3.5517(18)
C6	.C3	2.7384(14)	C17	.C1	2.9182(15)
C7	.C5	3.0284(15)	C17	.C20	2.7820(14)
C7	.C13	3.0307(15)	C17	.C9_d	3.5725(18)
C8	.C17_d	3.5517(18)	C17	.C2	3.1728(16)
C8	.O1	2.8913(15)	C18	.C12_d	3.5825(18)
C8	.C11	2.7751(14)	C18	.C11_d	3.5276(18)
C9	.F3	3.0171(15)	C18	.C21	2.7376(14)

C9	.C12	2.7332(14)	C19	.C16	2.7708(14)
C9	.C17_d	3.5726(18)	C19	.O3	2.9086(15)
C9	.F1	2.8032(14)	C20	.C22	3.0454(16)
C10	.C13	2.7420(14)	C20	.C17	2.7820(14)
C11	.F6	2.7545(14)	C20	.O3	2.8891(15)
C11	.F2	2.7681(14)	C21	.C1	3.5336(18)
C11	.F4	3.2713(17)	C21	.C18	2.7376(14)
C11	.F3	3.2304(16)	C22	.F10_j	3.2347(17)
C11	.C18_d	3.5276(18)	C22	.O4_m	3.3483(17)
C11	.C8	2.7751(14)	C22	.C20	3.0454(16)
C12	.C9	2.7332(14)	C22	.C00Z	3.0247(15)
C12	.C18_d	3.5825(18)	C23	.F5_g	3.2523(17)
C13	.O1	2.9003(15)	C23	.O3	2.9207(15)
C13	.C10	2.7420(14)	C23	.C26	2.7884(14)
C13	.F5	2.7987(14)	C24	.F11	2.7163(14)
C13	.F4	3.0096(15)	C24	.C27	2.7202(14)
C24	.F12	3.3352(17)	C28	.H00Z	2.5900

C25	.C00Z	2.7595(14)	C28	.H26	2.6500
C26	.C23	2.7884(14)	C29	.H24	2.5700
C26	.F8	2.7296(14)	C29	.H26	2.6400
C26	.F12	2.9362(15)	C30	.H31C	2.4600
C26	.F7	3.3503(17)	C30	.H31B	2.7700
C26	.F10	2.8490(15)	C31	.H30B	2.3200
C27	.C24	2.7202(14)	C31	.H30A	2.9700
C30	.F2_d	3.3551(17)	C32	.H33B	2.8000
C31	.O3	3.3678(17)	C33	.H32B	2.8100
C32	.O1_g	3.3905(17)	C34	.H35A	2.4300
C1	.H17	2.7100	C34	.H35C	2.5200
C2	.H17	2.9500	C35	.H34B	2.5100
C2	.H2_g	3.0700	C35	.H34A	2.3200
C3	.H2N	2.5600	H00Z	.F9	2.6800
C7	.H5	2.8000	H00Z	.F7	2.8400
C7	.H13	2.8000	H00Z	.O3	2.2900
C9	.H1N	2.4800	H00Z	.N4	2.6500

C14	.H11	2.6200	H00Z	.C22	2.7800
C14	.H13	2.6200	H00Z	.C28	2.5900
C15	.H11	2.6300	H00Z	.H31B	2.3900
C15	.H9	2.6200	H1N	.H9	2.3100
C16	.H2	2.6700	H1N	.S2_1	3.2000
C17	.H2	2.9200	H1N	.H2N	2.0400
C18	.H3N	2.4900	H1N	.C9	2.4800
C22	.H20	2.8200	H1N	.N2	2.3200
C22	.H00Z	2.7800	H1N	.O5_1	2.1100
C24	.H4N	2.4600	H2	.H3	2.2900
H2	.C2_g	3.0700	H6	.H5	2.3300
H2	.O2	2.5900	H6	.O5_o	2.8200
H2	.C16	2.6700	H6	.O2	2.5200
H2	.C17	2.9200	H9	.H1N	2.3100
H2N	.H1N	2.0400	H9	.O5_1	2.7600
H2N	.O6_n	2.5400	H9	.C15	2.6200
H2N	.C3	2.5600	H9	.H32A_1	2.5700

H2N	.O5_1	2.8800	H9	.N1	2.5000
H2N	.H3	2.4200	H9	.F1	2.5700
H2N	.N1	2.3100	H11	.F6	2.4800
H3	.H2	2.2900	H11	.F2	2.5200
H3	.O6_n	2.5200	H11	.C14	2.6200
H3	.N2	2.5600	H11	.C15	2.6300
H3	.H2N	2.4200	H13	.N1	2.6600
H3N	.H18	2.3100	H13	.F5	2.5500
H3N	.H4N	2.0300	H13	.O1	2.3900
H3N	.C18	2.4900	H13	.C7	2.8000
H3N	.N4	2.3100	H13	.C14	2.6200
H3N	.O4_m	2.0100	H17	.C2	2.9500
H4N	.H3N	2.0300	H17	.C1	2.7100
H4N	.O4_m	2.0300	H17	.O2	2.6100
H4N	.H24	2.2800	H17	.H18	2.3000
H4N	.C24	2.4600	H18	.H3N	2.3100
H4N	.N3	2.3100	H18	.H17	2.3000

H5	.C7	2.8000	H18	.F4_d	2.7000
H5	.H6	2.3300	H18	.N3	2.5300
H5	.O1	2.4300	H20	.O3	2.3300
H5	.N2	2.6300	H20	.C22	2.8200
H20	.H21	2.3200	H31B	.H30B	2.4100
H20	.N3	2.6800	H31B	.O3	2.5400
H21	.H20	2.3200	H31B	.H00Z	2.3900
H21	.O6_p	2.5900	H31C	.H30B	2.1300
H21	.O2	2.5200	H31C	.F7_v	2.7100
H24	.H4N	2.2800	H31C	.C30	2.4600
H24	.C29	2.5700	H31C	.O4	2.7700
H24	.F11	2.4300	H32A	.H9_q	2.5700
H24	.N4	2.5300	H32A	.O5	2.8700
H26	.F12	2.8500	H32B	.C33	2.8100
H26	.C28	2.6500	H32B	.O1_g	2.8600
H26	.C29	2.6400	H33A	.O5	2.9000
H26	.F10	2.6900	H33B	.C32	2.8000

H26	.F8	2.4300	H34A	.C35	2.3200
H30A	.O4	2.3800	H34A	.H35A	2.0000
H30A	.C31	2.9700	H34B	.C35	2.5100
H30A	.F4_u	2.7200	H34B	.H35C	2.3000
H30B	.H31C	2.1300	H35A	.C34	2.4300
H30B	.H31B	2.4100	H35A	.H34A	2.0000
H30B	.C31	2.3200	H35B	.O6	2.8900
H30B	.O3	2.8800	H35B	.F4_d	2.8000
H31A	.F3_g	2.7900	H35C	.C34	2.5200
H31A	.O4	2.6800	H35C	.H34B	2.3000
H31B	.C30	2.7700	H35C	.O1_d	2.8200

Table A3A.26: Hydrogen Bonds (Angstrom, Deg) for **L**$_2$ + DMSO

N1 -- H1N .. O5	0.8600	2.1100	2.9064(15)	153.00	2_766
N2 -- H2N .. O6	0.8600	2.5400	3.2751(17)	145.00	2_766
N3 -- H3N .. O4	0.8600	2.0100	2.8208(14)	158.00	1_655
N4 -- H4N .. O4	0.8600	2.0300	2.8418(15)	156.00	1_655
C00Z -- H00Z .. O3	0.9300	2.2900	2.8748(15)	121.00	.
C3 -- H3 .. O6	0.9300	2.5200	3.3414(17)	148.00	2_766

C5 -- H5 .. O1	0.9300	2.4300	2.9220(15)	113.00	.
C13 -- H13 .. O1	0.9300	2.3900	2.9003(15)	115.00	.
C20 -- H20 .. O3	0.9300	2.3300	2.8891(15)	118.00	.
C21 -- H21 .. O6	0.9300	2.5900	3.5119(18)	173.00	1_455
C31 -- H31B .. O3	0.9600	2.5400	3.3678(17)	144.00	.

Translation of Symmetry Code to Equiv.Pos

a =[1546.00] =	x,-1+y,1+z
b =[2656.00] =	1-x,-y,1-z
c =[2666.00] =	1-x,1-y,1-z
d =[2656.00] =	1-x,-y,1-z
e =[2556.00] =	-x,-y,1-z
f =[2656.00] =	1-x,-y,1-z
g =[2666.00] =	1-x,1-y,1-z
h =[2565.00] =	-x,1-y,-z
i =[1564.00] =	x,1+y,-1+z
j =[2665.00] =	1-x,1-y,-z
k =[2666.00] =	1-x,1-y,1-z
l =[2766.00] =	2-x,1-y,1-z
m =[1655.00] =	1+x,y,z
o =[1445.00] =	-1+x,-1+y,z
p =[1455.00] =	-1+x,y,z
r =[1665.00] =	1+x,1+y,z
u =[2556.00] =	-x,-y,1-z
v =[2565.00] =	-x,1-y,-z

Table A3A.27: Final Coordinates and Equivalent Isotropic Displacement Parameters of the non-Hydrogen atoms For **L_3**

Atom	x	y	z	U(eq) [Ang^2]
O1	1/4	3/4	-0.28584	0.0665
O2	0.14281	0.77242	0.00647	0.0648
N1	0.15947	0.34270	-0.05788	0.0574
N2	0.12422	0.35094	0.06932	0.0580
C1	0.22793	0.65239	-0.22530	0.0551
C2	0.21261	0.44440	-0.27946	0.0598
C3	0.18948	0.34898	-0.22522	0.0629
C4	0.18210	0.45607	-0.11535	0.0517
C5	0.19755	0.66566	-0.06293	0.0608
C6	0.22025	0.76632	-0.11784	0.0614
C7	0.14226	0.50496	0.00638	0.0492
C8	0.10463	0.48357	0.13989	0.0488
C9	0.11189	0.67841	0.22624	0.0580
C10	0.09285	0.82509	0.29452	0.0630
C11	0.06671	0.77170	0.27740	0.0638

C12	0.05804	0.56094	0.19067	0.0523
C13	0.07752	0.42320	0.12077	0.0476
C14	0.06878	0.22358	0.03278	0.0557
C15	0.04251	0.17279	0.01904	0.0667
C16	0.02350	0.30555	0.08857	0.0751
C17	0.03123	0.49819	0.17412	0.0668

U(eq) = 1/3 of the trace of the orthogonalized U Tensor

Table A3A.28: Hydrogen Atom Positions and Isotropic Displacement Parameters For **L_3**

Atom	x	y	z	U(iso) [Ang^2]
H1N	0.15641	0.15842	-0.06412	0.0688
H2	0.21769	0.36755	-0.35228	0.0717
H2N	0.12475	0.16325	0.06603	0.0696
H3	0.17881	0.21169	-0.26299	0.0755
H5	0.19268	0.74093	0.01045	0.0730
H6	0.23040	0.91158	-0.08214	0.0737
H9	0.12983	0.71398	0.23978	0.0696
H10	0.09820	0.95922	0.35164	0.0755
H11	0.05417	0.87217	0.32212	0.0765

H14	0.08106	0.12830	-0.01514	0.0668
H15	0.03705	0.04326	-0.03959	0.0800
H16	0.00558	0.26419	0.07727	0.0901
H17	0.01853	0.58803	0.22160	0.0801

==========

The Temperature Factor has the Form of Exp(-T) Where
T = 8*(Pi**2)*U*(Sin(Theta)/Lambda)**2 for Isotropic Atoms

Table A3A.29: (An)isotropic Displacement Parameters For **L_3**

Atom	U(1,1) or U	U(2,2)	U(3,3)	U(2,3)	U(1,3)	U(1,2)
O1	0.0554	0.0882	0.0557	0	0	-0.0163
O2	0.0720	0.0382	0.0842	0.0021	0.0174	-0.0032
N1	0.0604	0.0365	0.0752	-0.0087	0.0165	-0.0071
N2	0.0609	0.0368	0.0764	0.0027	0.0174	-0.0005
C1	0.0516	0.0574	0.0563	0.0022	-0.0005	-0.0068
C2	0.0606	0.0719	0.0467	-0.0071	0.0063	-0.0069
C3	0.0647	0.0571	0.0669	-0.0117	0.0025	-0.0099

C4	0.0529	0.0401	0.0622	-0.0017	0.0025	-0.0018
C5	0.0582	0.0570	0.0673	-0.0159	0.0050	-0.0066
C6	0.0588	0.0582	0.0673	-0.0154	0.0054	-0.0103
C7	0.0501	0.0394	0.0582	0.0028	0.0032	-0.0023
C8	0.0646	0.0320	0.0499	0.0058	0.0070	0.0019
C9	0.0688	0.0497	0.0554	-0.0015	0.0003	-0.0039
C10	0.0867	0.0527	0.0494	-0.0060	0.0057	0.0011
C11	0.0799	0.0545	0.0569	0.0008	0.0146	0.0081
C12	0.0738	0.0404	0.0426	0.0099	0.0085	0.0009
C13	0.0627	0.0380	0.0422	0.0082	0.0050	0.0001
C14	0.0747	0.0474	0.0450	0.0002	0.0070	-0.0076
C15	0.0842	0.0598	0.0561	-0.0013	0.0008	-0.0169
C16	0.0643	0.0919	0.0691	0.0189	0.0015	-0.0063
C17	0.0660	0.0686	0.0657	0.0101	0.0063	0.0005

==========

The Temperature Factor has the Form of Exp(-T) Where

T = 8*(Pi**2)*U*(Sin(Theta)/Lambda)**2 for Isotropic Atoms

T = 2*(Pi**2)*Sumij(h(i)*h(j)*U(i,j)*Astar(i)*Astar(j)), for

Anisotropic Atoms. Astar(i) are Reciprocal Axial Lengths and h(i) are the Reflection Indices.

Table A3A.30: Bond Distances (Angstrom) For **L3**

O1	-C1	1.3785(2)	C11	-C12	1.4419(2)
O1	-C1_a	1.3785(2)	C12	-C17	1.3924(2)
O2	-C7	1.2241(2)	C12	-C13	1.4074(2)
N1	-C4	1.4101(2)	C13	-C14	1.4193(2)
N1	-C7	1.3518(2)	C14	-C15	1.3513(2)
N2	-C7	1.3513(2)	C15	-C16	1.3788(2)
N2	-C8	1.4055(2)	C16	-C17	1.3641(2)
C1	-C2	1.3692(2)	C2	-H2	0.9300
C1	-C6	1.3758(2)	C3	-H3	0.9300
N1	-H1N	0.8600	C5	-H5	0.9300
N2	-H2N	0.8600	C6	-H6	0.9300
C2	-C3	1.3859(2)	C9	-H9	0.9300
C3	-C4	1.3842(2)	C10	-H10	0.9300
C4	-C5	1.3691(2)	C11	-H11	0.9300
C5	-C6	1.3792(2)	C14	-H14	0.9300

C8	-C9	1.3706(2)	C15	-H15	0.9300
C8	-C13	1.4088(2)	C16	-H16	0.9300
C9	-C10	1.4011(2)	C17	-H17	0.9300
C10	-C11	1.3520(2)			

Table A3A.31: Bond Angles (Degrees) For **L_3**

C1	-O1	-C1_a	120.55(1)	C11	-C12	-C13	118.00(1)
C4	-N1	-C7	124.23(1)	C8	-C13	-C12	120.06(1)
C7	-N2	-C8	122.98(1)	C8	-C13	-C14	122.25(1)
O1	-C1	-C2	117.24(1)	C12	-C13	-C14	117.70(1)
O1	-C1	-C6	122.74(1)	C13	-C14	-C15	119.62(1)
C2	-C1	-C6	119.93(1)	C14	-C15	-C16	122.55(1)
C4	-N1	-H1N	118.00	C15	-C16	-C17	119.32(1)
C7	-N1	-H1N	118.00	C12	-C17	-C16	120.31(1)
C1	-C2	-C3	119.66(1)	C1	-C2	-H2	120.00
C7	-N2	-H2N	119.00	C3	-C2	-H2	120.00
C8	-N2	-H2N	119.00	C2	-C3	-H3	120.00
C2	-C3	-C4	120.64(1)	C4	-C3	-H3	120.00
N1	-C4	-C3	119.92(1)	C4	-C5	-H5	120.00

N1	-C4	-C5	121.17(1)	C6	-C5	-H5	120.00
C3	-C4	-C5	118.89(1)	C1	-C6	-H6	120.00
C4	-C5	-C6	120.67(1)	C5	-C6	-H6	120.00
C1	-C6	-C5	120.17(1)	C8	-C9	-H9	119.00
O2	-C7	-N2	122.42(1)	C10	-C9	-H9	119.00
N1	-C7	-N2	115.23(1)	C9	-C10	-H10	120.00
O2	-C7	-N1	122.34(1)	C11	-C10	-H10	120.00
N2	-C8	-C9	119.80(1)	C10	-C11	-H11	120.00
N2	-C8	-C13	120.53(1)	C12	-C11	-H11	120.00
C9	-C8	-C13	119.66(1)	C13	-C14	-H14	120.00
C8	-C9	-C10	121.36(1)	C15	-C14	-H14	120.00
C9	-C10	-C11	120.02(1)	C14	-C15	-H15	119.00
C10	-C11	-C12	120.83(1)	C16	-C15	-H15	119.00
C11	-C12	-C17	121.49(1)	C15	-C16	-H16	120.00
C13	-C12	-C17	120.50(1)	C17	-C16	-H16	120.00
C12	-C17	-H17	120.00	C16	-C17	-H17	120.00

Table A3A.32: Torsion Angles (Degrees) For **L_3**

C1_a	-O1	-C1	-C2	-150.73
C1_a	-O1	-C1	-C6	32.86
C7	-N1	-C4	-C3	-142.23
C7	-N1	-C4	-C5	39.71
C4	-N1	-C7	-O2	10.57
C4	-N1	-C7	-N2	-170.21
C8	-N2	-C7	-N1	-179.20
C7	-N2	-C8	-C13	123.23
C7	-N2	-C8	-C9	-55.25
C8	-N2	-C7	-O2	0.02
C2	-C1	-C6	-C5	1.83
O1	-C1	-C6	-C5	178.15
C6	-C1	-C2	-C3	-0.31
O1	-C1	-C2	-C3	-176.82
C1	-C2	-C3	-C4	-1.77
C2	-C3	-C4	-C5	2.29
C2	-C3	-C4	-N1	-175.81

C3	-C4	-C5	-C6	-0.75
N1	-C4	-C5	-C6	177.32
C4	-C5	-C6	-C1	-1.30
N2	-C8	-C9	-C10	176.97
C13	-C8	-C9	-C10	-1.53
N2	-C8	-C13	-C12	-178.94
N2	-C8	-C13	-C14	1.54
C9	-C8	-C13	-C12	-0.46
C9	-C8	-C13	-C14	-179.97
C8	-C9	-C10	-C11	1.22
C9	-C10	-C11	-C12	1.05
C10	-C11	-C12	-C13	-2.94
C10	-C11	-C12	-C17	178.35
C11	-C12	-C13	-C8	2.61
C11	-C12	-C13	-C14	-177.85
C17	-C12	-C13	-C8	-178.66
C17	-C12	-C13	-C14	0.87

C11	-C12	-C17	-C16	177.66
C13	-C12	-C17	-C16	-1.02
C8	-C13	-C14	-C15	179.53
C12	-C13	-C14	-C15	0.00
C13	-C14	-C15	-C16	-0.77
C14	-C15	-C16	-C17	0.64
C15	-C16	-C17	-C12	0.27

Table A3A.33: Contact Distances(Angstrom) For **L_3**

O2	.C5	2.9056(4)	C2	.C5	2.7523(4)
O2	.C7_b	3.3518(4)	C2	.C1_a	3.5685(5)
O2	.C8	2.7765(4)	C3	.C6_c	3.3130(4)
O2	.C9	2.9602(4)	C3	.C6	2.7413(4)
O2	.N1_b	2.8352(4)	C4	.O2	2.8103(4)
O2	.N2_b	2.8958(4)	C4	.C1	2.7691(4)
O2	.C4	2.8103(4)	C5	.C2	2.7523(4)
O1	.H2	2.5000	C5	.O2	2.9056(4)
O1	.H6	2.6100	C5	.C7	2.9828(4)
O1	.H2_a	2.5000	C6	.C1_a	2.9002(4)

O1	.H6_a	2.6100	C6	.C3	2.7413(4)
N1	.O2_c	2.8352(4)	C6	.C6_a	2.9981(4)
O2	.H1N_b	2.0500	C6	.C3_b	3.3130(4)
O2	.H5	2.5100	C7	.C5	2.9828(4)
O2	.H9	2.7300	C7	.O2_c	3.3518(4)
O2	.H2N_b	2.1200	C7	.C13	3.5251(5)
N2	.O2_c	2.8958(4)	C7	.C10_d	3.5369(5)
N2	.C14	2.8802(4)	C7	.C9	3.0211(4)
N1	.H5	2.5900	C8	.C11	2.7910(4)
N1	.H2N	2.3800	C8	.C10_c	3.5321(5)
N1	.H3	2.5800	C8	.O2	2.7765(4)
C1	.C6_a	2.9002(4)	C9	.C7	3.0211(4)
C1	.C4	2.7691(4)	C9	.C12	2.7921(4)
C1	.C2_a	3.5685(5)	C9	.O2	2.9602(4)
N2	.H1N	2.3800	C10	.C13	2.7973(4)
N2	.H9	2.5600	C10	.C7_e	3.5369(5)
N2	.H14	2.5800	C10	.C13_b	3.4543(5)

N2	.H10_d	2.9200	C10	.C8_b	3.5321(5)
C11	.C8	2.7910(4)	C7	.H9	2.8700
C11	.C13_b	3.5083(5)	C7	.H10_d	2.8300
C11	.C14_b	3.4514(5)	C7	.H5	2.7600
C12	.C15	2.7422(4)	C8	.H14	2.6700
C12	.C15_b	3.4932(5)	C9	.H2N_b	2.9300
C12	.C14_b	3.5583(5)	C9	.H2N	3.0400
C12	.C9	2.7921(4)	C10	.H14_f	3.0500
C13	.C11_c	3.5083(5)	C11	.H15_f	2.9300
C13	.C7	3.5251(5)	C11	.H14_f	3.0600
C13	.C10	2.7973(4)	C11	.H17	2.6400
C13	.C16	2.7954(4)	C13	.H2N	2.7300
C13	.C10_c	3.4543(5)	C14	.H10_d	2.9100
C14	.C11_c	3.4514(5)	C14	.H2N	2.8600
C14	.N2	2.8802(4)	C16	.H16_g	3.0900
C14	.C17	2.7744(4)	C17	.H11	2.6600
C14	.C12_c	3.5583(5)	H1N	.O2_c	2.0500

C15	.C12	2.7422(4)	H1N	.N2	2.3800
C15	.C12_c	3.4932(5)	H1N	.C3	2.6200
C15	.C17_c	3.5937(5)	H1N	.C5_c	3.0600
C16	.C13	2.7954(4)	H1N	.H2N	2.1700
C16	.C16_g	3.5721(5)	H1N	.H3	2.5200
C17	.C15_b	3.5937(5)	H2	.O1	2.5000
C17	.C14	2.7744(4)	H2	.H3	2.3100
C1	.H6_a	2.6600	H2N	.O2_c	2.1200
C2	.H5_d	2.9500	H2N	.N1	2.3800
C3	.H1N	2.6200	H2N	.C9_c	2.9300
C5	.H1N_b	3.0600	H2N	.C9	3.0400
C6	.H6_a	2.6400	H2N	.C13	2.7300
H2N	.C14	2.8600	H10	.C7_e	2.8300
H2N	.H1N	2.1700	H10	.C14_e	2.9100
H2N	.H14	2.3900	H10	.H14_e	2.5600
H3	.N1	2.5800	H11	.C17	2.6600
H3	.H1N	2.5200	H11	.H10	2.2800

H3	.H2	2.3100	H11	.H17	2.4900
H5	.O2	2.5100	H14	.N2	2.5800
H5	.N1	2.5900	H14	.C8	2.6700
H5	.C7	2.7600	H14	.H2N	2.3900
H5	.H6	2.3000	H14	.H15	2.2700
H5	.C2_e	2.9500	H14	.C10_h	3.0500
H6	.O1	2.6100	H14	.C11_h	3.0600
H6	.H5	2.3000	H14	.H10_d	2.5600
H6	.C1_a	2.6600	H15	.H14	2.2700
H6	.C6_a	2.6400	H15	.H16	2.3000
H6	.H6_a	2.4700	H15	.C11_h	2.9300
H9	.O2	2.7300	H16	.H15	2.3000
H9	.N2	2.5600	H16	.H17	2.3000
H9	.C7	2.8700	H16	.C16_g	3.0900
H9	.H10	2.3200	H17	.C11	2.6400
H10	.H9	2.3200	H17	.H11	2.4900
H10	.H11	2.2800	H17	.H16	2.3000

H10 .N2_e 2.9200

Table A3A.34: Hydrogen Bonds (Angstrom, Deg) For **L3**

N1 -- H1N .. O2	0.8600	2.0500	2.8352(4)	151.00	1_545
N2 -- H2N .. O2	0.8600	2.1200	2.8958(4)	151.00	1_545
C5 -- H5 .. O2	0.9300	2.5100	2.9056(4)	106.00	.

Translation of Symmetry Code to Equiv.Pos

a =[2565.00] =	1/2-x,3/2-y,z
b =[1565.00] =	x,1+y,z
c =[1545.00] =	x,-1+y,z
d =[8564.00] =	x,3/2-y,-1/2+z
e =[8565.00] =	x,3/2-y,1/2+z
f =[8555.00] =	x,1/2-y,1/2+z
g =[5565.00] =	-x,1-y,-z
h =[8554.00] =	x,1/2-y,-1/2+z

Chapter 3B

Anion-Mediated Cyclisation of Urea-based Receptors: Recognition of Anion-Water-Cluster and Anions with Varied Dimensionality

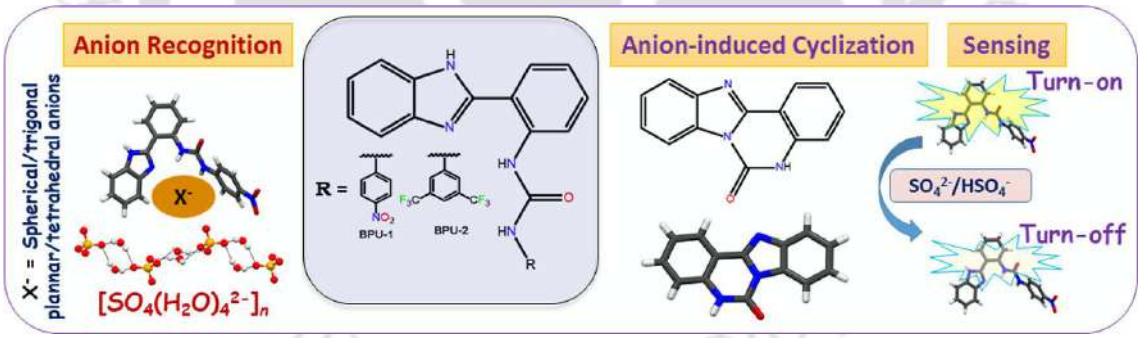

CHAPTER 3B

3B.1. Background and Focus of the Chapter

The field of anion recognition chemistry has made enormous progress with a varied range of synthetic receptors owing to its vital role in the environment as well as in biology. This particular field possesses enormous potential in terms of addressing the world's most persistent problems related to ecological contamination such as sequestration and extraction of toxic anions from industrial or radioactive waste. [3B.1] Among various inorganic anions, halides and oxoanions play a vital role in both human health and environment, [3B.2] and most of them exist in their hydrated forms naturally, which necessitates entrapment of hydrated anions to get insights into the structural complexities associated with such anion water clusters. [3B.3-3B.11] The nitrate anion (NO_3^-) with its typical trigonal-planar geometry, having high hydration energy (ΔG_{hyd} = −300 kJ/mol) along with large ionic radii (1.79 Å) and low basicity (pK_a = −1.44), makes it reluctant toward hydrogen-bonding interactions, which complicate the designing of neutral molecular receptors with appropriately matched complementary recognition motifs for selective and effective NO_3^- anion recognition. [3B.12, 3B.13] As evident from the Hofmeister series, sulfate is a strong kosmotropic molecule, [3B.14] and because of the strong intramolecular Coulomb repulsion of the two excess charges, the isolated sulfate dianion is found to be unstable, [3B.15-3B.17] whereas it is stabilized in the condensed phase by solvation in solution or counterions in solid. Unlike spherical anions such as the halides, the tetrahedral sulfate anion (SO_4^{2-}) is one of the most hydrophilic anions in nature, with a very high free energy of hydration (ΔG_{hyd} = −1080 kJ mol^{-1}), and it is highly sensitive toward pH (mostly present as HSO_4^- when pH < 1) as well; [3B.18-3B.21] all of those factors complicate the designing of sulfate-binding receptors. The sulfate anion (SO_4^{2-}) is known as an end metabolite of cysteine and methionine. Expression of some of the key functions in the physiological system such as biosynthesis and detoxification is associated with the proper maintenance of SO_4^{2-} anion concentration. [3B.22] Thus, maintaining sulfate concentration at a precise level is of great significance for biology, environments, and industrial productions, and to do the same, it is very important to design receptors capable of recognizing the SO_4^{2-} anion with high selectivity, most importantly in aqueous medium.

Despite all such challenges associated with anion recognition, inspired by the nature's anion recognition process such as encapsulation of sulfate anion by sulfate-binding protein of

Salmonella typhimurium, [3B.23, 3B.24] a plethora of receptors with multiple hydrogen-bonding sites have been reported till date. Johnson et al. have designed a ditopic 3,5-bis((2-iodophenyl)ethynyl)pyridinium receptor recently, which could recognize halide anions. [3B.25] Both cyclic as well as acyclic receptors have been designed by many groups for NO_3^- recognition. [3B.26, 3B.27] Very recently, Wang et al. have reported a calix[4]pyrrole strapped benzenebistriazole bis-cycle that displays strong sulfate-binding affinity of $>10^6$ M^{-1} in an aqueous medium. [3B.28] Urea-based and squaramide-based ion pair receptors have also been designed for selective SO_4^{2-} anion recognition recently by many groups. [3B.29-3B.31] Cage-type receptors have also been developed for SO_4^{2-} binding by Kubik and his group, [3B.32] whereas, on the other hand, Kataev et al. have reported an amide-based fluorescent receptor that can sense SO_4^{2-} in aqueous solution. [3B.33] There is always some lacuna associated with the designing of effective receptors for the anions, such as complex synthesis, inability to operate in aqueous medium, and poor selectivity, which confines the real-life applicability of most of the receptors designed until now.

Previously, our group has already explored numerous receptors ranging from monopodal to tripodal receptors for both solid- as well as solution-phase anion recognition study, [3B.34-3B.38] and most of our studies were limited to organic solvent medium only; less exploration was done toward selective anion recognition in aqueous medium. So keeping that in mind, in our continuous endeavor toward anion recognition chemistry, herein, we have designed a set of two unsymmetrical dipodal monourea receptors BPU-1 and BPU-2 having pi-acidic terminal substituents, containing the benzimidazole moiety as a signaling unit as well as a hydrogen donor/acceptor site, to investigate their anion recognition behavior in both solid states as well as in solution phase and also to perform fluorimetric sensing study of both the receptors in the presence of various anions in 100% aqueous medium.

Urea-based receptors are generally used for anion recognition purposes. Using the same method for the synthesis of heterocyclic compounds is scarce in the literature. A very important class of heterocycles such as imidazo[l,2-c]quinazolin-6-ones is well-known for its enriched biological profiles. [3B.39] However, many groups have already reported numerous synthetic routes for the synthesis of heterocycles like benzimidazo[1,2-c] quinazolin-6-ones; [3B.40-3B.43] nonetheless, most of the reported procedures suffer from some serious limitations such as the use of metals, multistep synthesis, and complex synthetic routes, etc. So, it is very important to address all those issues and to minimize the complexities associated with the synthesis of such heterocycles. Herein, we have reported for the first time a simple anion-induced cyclization method for the

synthesis of benzimidazo[1,2-c]quinazolin-6-ones, which prohibits the use of any metals and simplifies the overall synthesis process. (Scheme 2.2 of Chapter 2)

3B.2. Objective of the Chapter

Two unsymmetrical dipodal monourea based receptors, namely, BPU-1 and BPU-2 with varying π-acidic terminal electron-withdrawing substituents (–NO_2 and –CF_3) have been developed to study their anion recognition behavior in both solid as well as in solution phases. Receptors are designed with an arm having a flexible urea unit, and the other arm contains a semirigid fluorophoric benzimidazole unit. The studied anions include anions of varied geometries such as spherical, trigonal planar, and tetrahedral. As both the receptors are appended with fluorophoric units, so, their anion-sensing behavior has been investigated in an aqueous medium through fluorescence spectroscopy. Moreover, anion-induced intramolecular cyclization of both receptors in the presence of F^-/HO^- to yield benzimidazo[1,2-c]quinazolin-6-ones has also been thoroughly investigated in this particular work.

3B.3. Results and Discussion

3B.3.1. Design Aspects of the Receptors

Two unsymmetrical dipodal monourea anion receptors BPU-1 and BPU-2, with varying pi-acidic terminal substituents, encompassing electron-withdrawing groups (–NO_2 and –CF_3) and additionally, incorporating the benzimidazole moiety as a signaling unit as well as hydrogen-bond donor/acceptor site, have been designed to investigate their propensity toward recognition of anions of varied geometries (e.g., tetrahedral, trigonal planar, and spherical) in both solid as well as in solution phases. As evident from the calculated electrostatic potential map [DFT, B3LYP/6-31+G(d), solvent: water, using the CPCM model], the blue regions are majorly located on the NH_{urea} (urea hydrogen) and NH_{benz} (benzimidazole hydrogen), indicating strong positive electrostatic potential in those regions, signifying them as the most probable anion recognition sites, (Figure A3B.1a,b) which is quite evident from the single-crystal X-ray diffraction (SC-XRD) results as well. We intentionally made the arm containing the primary anion-binding site, that is, the urea-containing arm, flexible and the benzimidazole part semirigid so that our probe could preorganize its flexible arm, if required the semirigid arm as well, to accommodate anions with varied geometries. One of the reasons behind incorporating the benzimidazole fluorophore unit is to make our receptors BPU-1 and BPU-2 viable for the fluorimetric anion-sensing study in the solution phase. Both the aforementioned receptors undergo different conformational adaptations to accommodate anions of varied geometries inside their self-assembled cavities.

BPU-1 could undergo structural manifestation in such a way as to entrap all the spherical halide anions (except F^- anion), tetrahedral SO_4^{2-}, and trigonal planar NO_3^- anions, whereas BPU-2 could accommodate spherical anions such as Cl^- and Br^- quite efficiently. Interestingly, both the receptors undergo intramolecular cyclization in the presence of F^-/HO^- anions; such anion-induced cyclization to give benzimidazo[1,2-c]quinazolin-6-ones (BP-Cyc) is rare in the literature.

3B.3.2. Single-Crystal X-ray Structural Analysis

Structural Analysis of DMF-Solvated Receptor BPU-1 and Free Receptor BPU-2

SC-XRD structural analysis of BPU-1.DMF reveals that two BPU-1 receptors self-assemble to form two types of dimeric self-assembled structures with the help of strong intermolecular hydrogen-bonding interactions. (Figure 3B.1a,b, Table A3B.2.2, Table A3B.3) The urea oxygen atom undergoes bifurcated hydrogen-bonding interactions with its neighboring benzimidazole hydrogen atom ($N–H_{benz}\cdots O=C_{urea}$ = 2.11 Å) and the phenyl ring hydrogen atom ($C–H_{phenyl}\cdots O=C_{urea}$ = 2.72 Å) with an average hydrogen-bonding distance of 2.42 Å, thus facilitating the formation of self-assembled dimeric arrangement with pseudo capsular cavity. (Figure 3B.1b) Hydrogen-bonding interaction between the oxygen atom of the $–NO_2$ group and the hydrogen atom of the phenyl spacer ($C–H_{pheny}\cdots O–N=O$ = 2.64 Å) as well as π···π interaction between the two nitro-phenyl groups (distance between the two centroids of the nitro-phenyl rings is 3.75 Å) facilitates the formation of pseudocylindrical dimeric assembly. (Figure 3B.1b) The self-assembled structure in the BPU-1 receptor forms a layered polymeric chain architecture, and two such layers are interconnected via dimethylformamide (DMF) molecules through hydrogen bonding, involving $N–H_{urea}\cdots O=C_{DMF}$ and $C–H_{DMF}\cdots\pi$ (involving the methyl hydrogen atom of DMF and terminal nitro-phenyl ring) interactions with distances of 2.08 and 2.84 Å, respectively. (Figure 3B.1e) In the case of the receptor BPU-2 as well, two types of dimeric self-assembly have been observed, where one of the assembly processes involves hydrogen-bonding interactions between the hydrogen atom of the benzimidazole ring and oxygen atom of urea ($N–H_{benz}\cdots O=C_{urea}$ = 1.92 Å) forming a pseudo capsular cavity with a diameter of ~3.73 Å, (Figure 3B.1c,f) whereas the other assembly is facilitated by hydrogen-bonding interaction involving the nitrogen atom of the benzimidazole ring and one of the urea hydrogen ($N–H_{urea}\cdots N_{benz}$ = 2.05 Å) atoms. Self-assembled dimeric receptors are very important since this type of assemblies can form cage-like structures that can be effectively utilized for guest encapsulation within its cavity as recently reported by Jana and his group. [3B.44] Four BPU-2 receptor molecules having different orientations in space are interconnected through

hydrogen-bonding interactions and extend themselves in a repeating pattern to give a helical structure viewed down the crystallographic c-axis. (Figure 3B.1d, Table A3B.2.2)

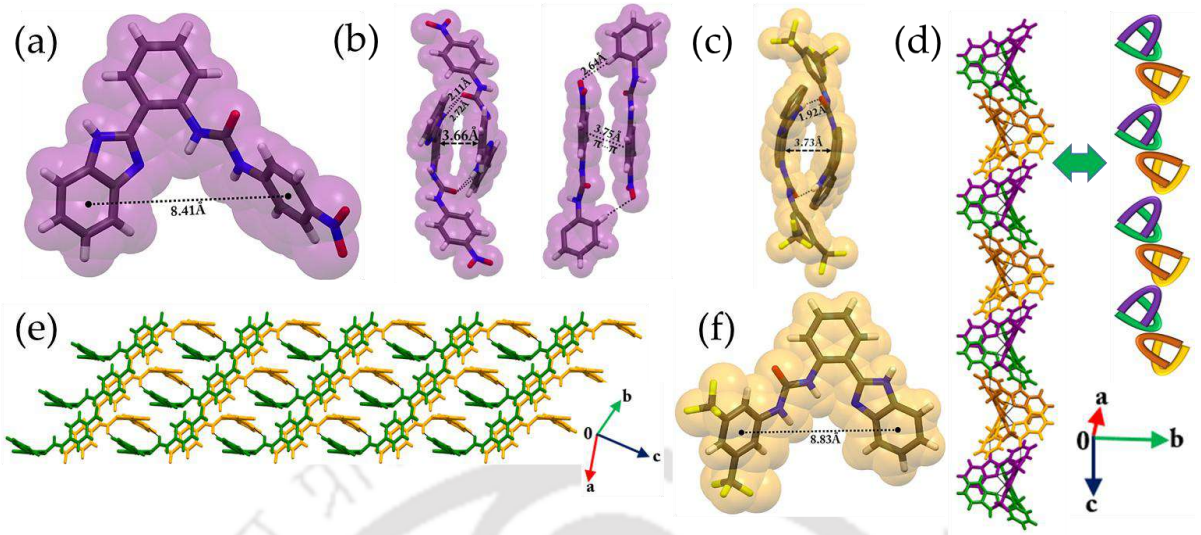

Figure 3B.1: (a) Crystal structure of BPU-1.DMF displays the distance between the centroids of the two terminal phenyl rings (DMF omitted for clarity). (b) Pseudocapsular/cylindrical cavity formed by the BPU-1 receptor. (c) Pseudocapsular cavity formed by the BPU-2 receptor. (d) Helical structure formed by the BPU-2 receptor. (e) 3D packing of the BPU-1 receptor. (f) Crystal structure of BPU-2 showing the distance between the centroids of the terminal phenyl rings.

Comparative Structural Analysis of the Halide Complexes of the Receptor BPU-1, [BPU-1 (n-TBA) Cl] (1a), [BPU-1 (n-TBA) Br] (1b), and [BPU-1 (n-TBA) I] (1c)

Receptor BPU-1 could undergo structural manifestation in such a way as to facilitate the approach of spherical halide anions with varied sizes toward its biding sites, thus leading to solid-state recognition of all the halides except F^- anions (where cyclization of BPU-1 takes place), through hydrogen-bonding interactions involving $N–H_{urea}\cdots X^-$, $N–H_{benz}\cdots X^-$, $CH_{phenyl}\cdots X^-$, and $C–H_{TBA}\cdots X^-$ (where, $X^- = Cl^-$, Br^-, and I^-), which is evident from SC-XRD study, (Figure A3B.13a-c; Table A3B.2.1; Table A3B.3) also supported by Fourier transform infrared (FT-IR) analysis, where the peaks for NH_{urea} change appreciably (from 3287 cm^{-1} for the free receptor BPU-1 to 2960, 2962, and 3181 cm^{-1} in the complexes 1a, 1b, and 1c, respectively). (Figure A2.18, Figure A2.28, Figure A2.30, and Figure A2.32 of Chapter 2) In all three complexes, the coordination number (C.N.) is observed to be the same (C.N. = 4), with average hydrogen-bonding distances of 2.57, 2.73, and 3.055 Å for complexes 1a, 1b, and 1c, respectively. (Figure 3B.2a-f) It is quite fascinating to note that as the size of the halide anions increases, the dihedral angle between the two arms as well as the twisting pattern of the receptor molecule also changes. (Figure 3B.3d-f) In complexes 1a and 1b, one-fold twisting was observed

between the two arms with an increase in the dihedral angle (angle between the plane passing through the benzimidazole ring and the urea hydrogen atom that is participating in hydrogen-bonding interaction with the halides) from 28.67° to 32.8° for Cl^- and Br^-, respectively. On the contrary, for complex 1c, two-fold twisting was observed with dihedral angles of 19.64° (angle between the plane passing through the benzimidazole ring and the urea hydrogen atom that is participating in hydrogen-bonding interaction with the halides) and 17.94° (angle between the plane passing through the benzimidazole ring and the terminal phenyl ring). In addition, while measuring the distance between the two centroids of the terminal phenyl rings for all the three halide complexes, it was observed that, for Cl^- and Br^-, the distance remains almost the same (which was measured to be 8.79 and 8.80 Å for complexes 1a and 1b, respectively), whereas in the case of complex 1c, the distance increases significantly by ~0.27 Å (distance was calculated to be 9.07 Å), which indicates the increase in the cavity size of BPU-1 to accommodate the largest halide anion. (Figure 3B.3a-c) The high flexibility of the monourea arm allowed many-fold structural changes such as changes in the hydrogen-bonding distance, twisting pattern, dihedral angle, and cavity sizes of the receptor BPU-1, thus allowing it to recognize different spherical halide anions. While analyzing the ^{1}H NMR spectra of the complexes 1a, 1b, and 1c (in DMSO-d_6), no observable spectral changes occurred, indicating lesser binding of NH_{urea} in the solution phase; broadening of the NH_{benz} peaks was quite prevalent in all the three complexes with concomitant downfield shifting of the same in the case of complex 1a ($\Delta\delta NH_{benz}$ = 0.13 ppm), indicating rapid hydrogen-bonding interactions. (Figure A3B.6,7,9; Table A3B.1; Figure A2.15, Figure A2.27, Figure A2.29, and Figure A2.31 of Chapter 2)

The packing arrangement of these complexes while viewed along the crystallographic b-axis reveals that for complexes 1a and 1b, the packing arrangements are quite similar, where they form Cl^-/Br^- embedded parallel sheet-like layered architecture, each layer separated by layers of n-TBA cations, whereas in the case of 1c, the packing pattern is quite different; here also layered architecture is prevalent although the BPU-1 receptor forms I^- mediated layered helical architecture, each layer separated by layers of TBA cations. (Figure 3B.2f)

Comparative Structural Analysis of the Halide Complexes of the Receptor BPU-2, [BPU-2 (n-TBA) Cl] (2a) and [BPU-2 (n-TBA) Br] (2b)

SC-XRD structural analysis of complexes 2a and 2b reveals the involvement of very similar kinds of hydrogen-bonding interactions to recognize Cl^- and Br^- anions, as observed earlier in the case of 1a and 1b. In both complexes, the receptor molecule BPU-2 entraps Cl^-/Br^- through H-bonding interactions with C.N. = 6 for 2a, whereas C.N. = 4 was observed for 2b involving N–

$H_{urea}\cdots X^-$, $N–H_{benz}\cdots X^-$, $C–H_{phenyl}\cdots X^-$, and $C–H_{TBA}\cdots X^-$ with average H-bonding distances of 2.67 and 2.77 Å for 2a and 2b, respectively. (Figure 3B.4a,e; Figure A3B.13d,e; Table A3B.2.2; Table A3B.3)

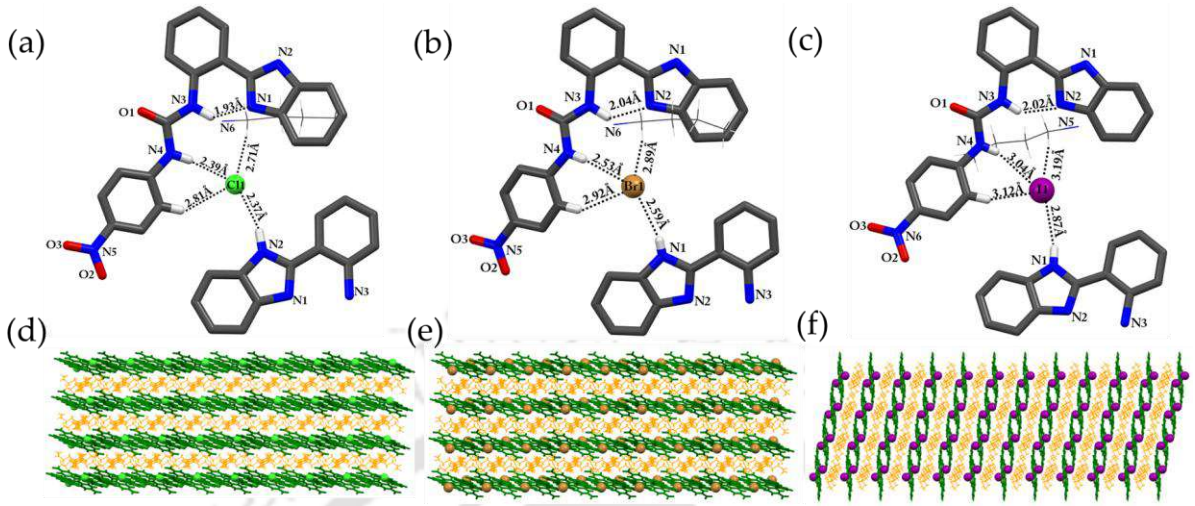

Figure 3B.2: Hydrogen-bonding interactions of (a) complex 1a, (b) complex 1b, and (c) complex 1c (noninteracting hydrogen atoms and half of the molecular structure have been omitted for clarity). Packing arrangement of (d) complex 1a, (e) complex 1b, and (f) complex 1c (viewed along crystallographic b-axis).

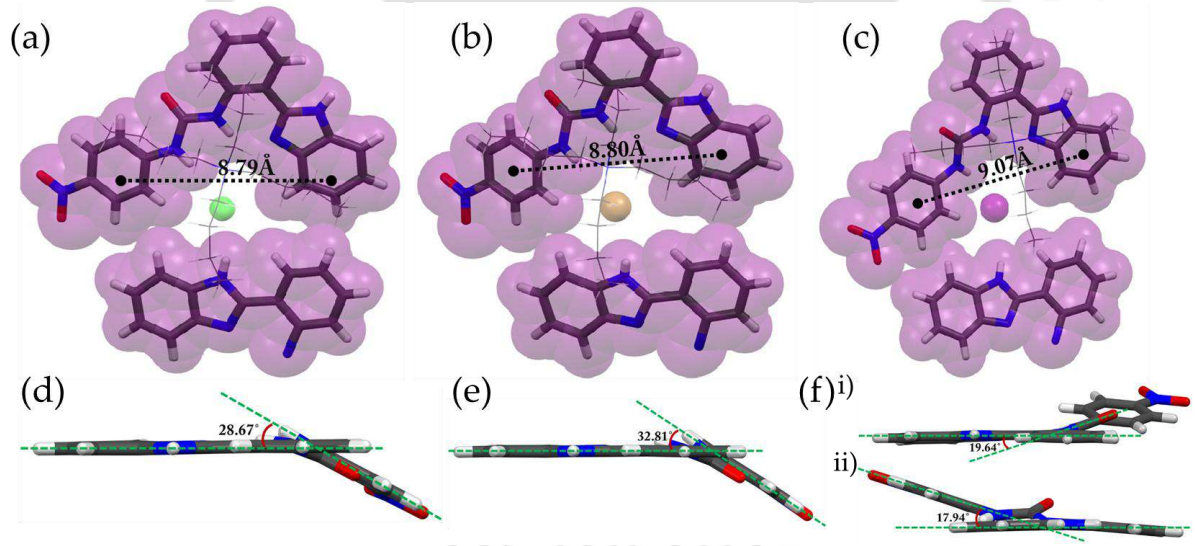

Figure 3B.3: Displaying the cavity size of (a) complex 1a, (b) complex 1b, and (c) complex 1c. Depicting the dihedral angle between the two arms of (d) complex 1a and (e) complex 1b. (f) Showing the dihedral angle between (i) the two arms and (ii) the benzimidazole plane and the plane passing through the urea hydrogen atom of complex 1c.

The involvement of $N–H_{urea}$ in the recognition process is also quite evident from FT-IR data analysis where the characteristic peak corresponding to $N–H_{urea}$ changes appreciably from 3258 cm^{-1} for the free receptor BPU-2 to 2958 and 3137 cm^{-1} in the complexes 2a and 2b,

respectively. (see Figure A2.22, Figure A2.38, and Figure A2.40 of Chapter 2) The distance between the two centroids of the terminal phenyl rings has been measured, which was found to be 8.96 Å for both 2a and 2b. (Figure 3B.4b,f) The dihedral angle between the two arms (angle between the plane passing through the benzimidazole ring and the terminal phenyl ring) of both 2a and 2b was observed to be equal, which is ~43°. (Figure 3B.4g) It is quite interesting to note the changes in the C.N. while moving from 2a to 2b indicate the important role played by the size of the anions in the number of hydrogen-bonding interactions to encapsulate the same. As evident from all of these observations, receptor BPU-2 could also undergo structural manifestation to coordinate Cl^- and Br^- quite efficiently as observed earlier in the case of halide complexes of BPU-1. Unfortunately, we could not isolate single crystals of BPU-2 with the iodide anion despite several attempts being made. The possible reason might be because of the structural rigidity as inflicted by the $–CF_3$ phenyl group, which does not allow many fold twisting in BPU-2 as was observed earlier in the case of BPU-1, to accommodate a large spherical I^- anion. The packing arrangements were quite similar in both complexes (while viewed along the crystallographic b-axis), where the halide anions are embedded within the self-assembled architecture of the receptors. (Figure 3B.4c,d) On analyzing the ^1H NMR of both the complexes, no appreciable shifting of the peaks was observed, while slight broadening of the N–H_{benz} peak was prevalent in all the two complexes, thus indicating hydrogen-bonding interactions involving the same. (Figure A3B.11,12; Table A3B.1; see Figure A2.19, Figure A2.37, and Figure A2.39 of Chapter 2)

Structural Analysis of Nitrate Complex [{BPU-1(n-TBA)(NO_3)] (1d)

Complex 1d crystallizes in a monoclinic P21/c space group. Unlike as observed earlier in the case of the halide complexes, both the urea hydrogen atoms of BPU-1 are observed to be involved in hydrogen-bonding interaction with the NO_3^- anion with an average hydrogen-bonding distance of 2.25 Å (O5···H3N = 2.52 Å and O5···H4N = 1.98 Å), while one of the urea hydrogen atoms (H–N3) undergoes intramolecular hydrogen-bonding interaction as well, with its neighboring nitrogen atom (N2) of the benzimidazole ring (N2···H–N3 = 1.87 Å, as depicted in Figure 3B.5b). The NO_3^- anion is encapsulated via a total of 13 noncovalent interactions involving both classical and nonclassical hydrogen-bonding interactions with an average hydrogen-bonding distance of 2.43 Å, suggesting very tight encapsulation of the NO_3^- anion by the BPU-1 receptor, which is quite evident from SC-XRD analysis, (Figure 3B.5b,e; Table A3B.2.1; Table A3B.3) and supported by the FT-IR analysis of the isolated complex 1d, where

the peaks representing the NH_{urea} change appreciably (from 3287 cm^{-1} for the free receptor BPU-1 to 2960 cm^{-1} in complex 1d). (Figure A2.18, and Figure A2.34 of Chapter 2)

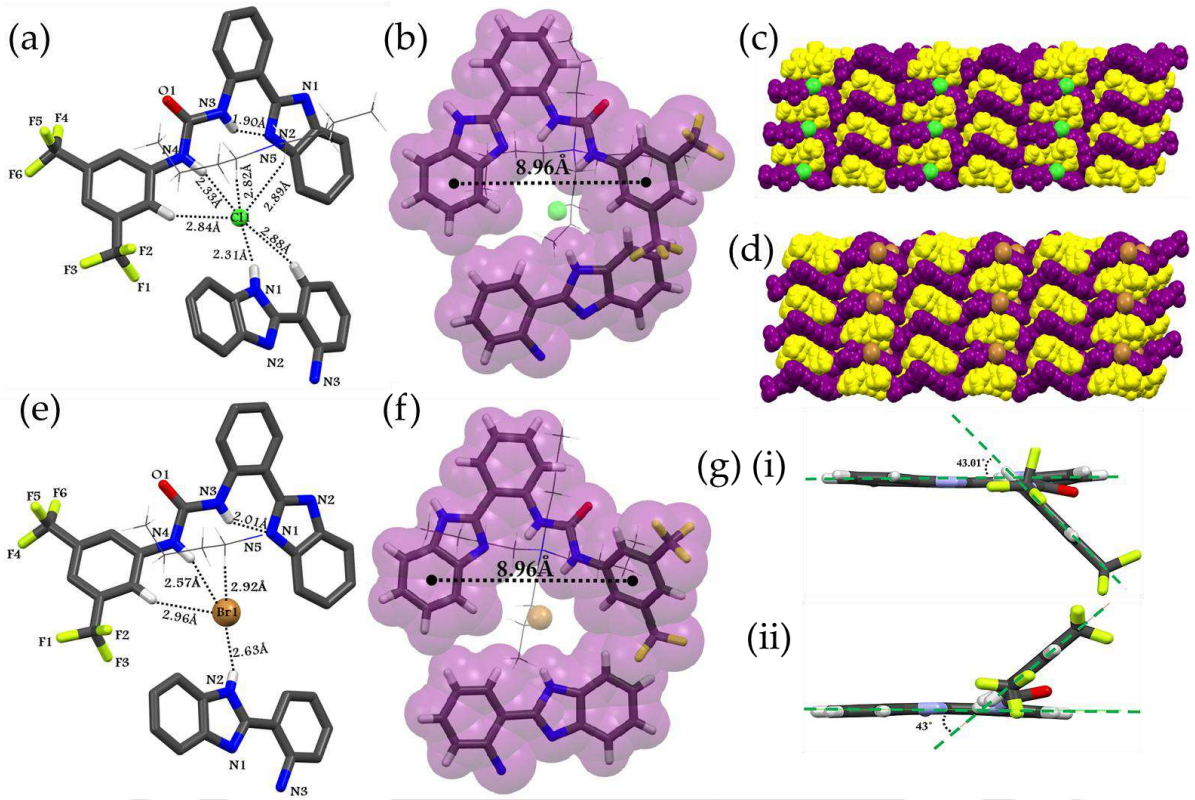

Figure 3B.4: Depiction of hydrogen-bonding interactions in (a) complex 2a and (e) complex 2b. Encapsulation as well as cavity sizes of (b) complex 2a and (f) complex 2b. Packing pattern of (c) complex 2a and (d) complex 2b (viewed along the crystallographic b-axis). (g) Dihedral angle between the two arms of (i) complex 2a and (ii) complex 2b

What is more interesting in this whole encapsulation process of the NO_3^- anion is the major role played by the nonclassical hydrogen-bonding interactions, where 9 out of 13 hydrogen-bonding interactions are coming from nonclassical hydrogen-bonding interactions (involving five C–$H_{TBA}\cdots O_{Nitrate}$ and four C–$H_{Phenyl}\cdots O_{Nitrate}$). Receptor BPU-1 adopts layered architecture as assisted by the NO_3^- anion, and two such layers are interconnected via n-TBA cations through a vast number of noncovalent interactions involving C–$H_{TBA}\cdots$O, C–$H_{TBA}\cdots\pi$, and C–$H_{TBA}\cdots$N and are separated by a distance of ~8.79 Å (distance between the two planes passing through the nitrogen atom of the NO_3^- anion in each layer). (Figure 3B.5g) ^{1}H NMR analysis of the crystal of complex 1d reveals a very small chemical shift for both NH_a, NH_b ($\Delta\delta$ = 0.015–0.016 ppm), and NH_{benz} ($\Delta\delta$ = 0.01 ppm) suggesting negligible binding of NO_3^- in solution phase. (Figure A3B.8, Table A3B.1; Figure A2.33 of Chapter 2)

Structural Analysis of Hydrated Sulfate Complex $[(BPU\text{-}1\text{-}H)^+(n\text{-}TBA)^+(H_2O)_4(SO_4)^{2-}]$ (1e)

Proton-coupled sulfate (SO_4^{2-}) anion recognition inside the cation-sealed pseudocapsular cavity of BPU-1 (BPU-1-H^+), TBA cation, and water molecules through 12 hydrogen-bonding interactions (involving four C–H_{phenyl}···O, four HO–H_{water}···O, two N–H_{urea}···O, one C–H_{TBA}···O, and one N–H_{benz}···O) has been reported. (Figure 3B.5a,c,d, Figure A3B.14a, Table A3B.2.1, Table A3B.3) It is fascinating to note that the intramolecular hydrogen-bonding interaction existed earlier in the case of all the halide complexes of the receptor BPU-1 (N1···H–N3, N2···H–N3, and N2···HN3 for complex 1a, 1b, and 1c, respectively, as depicted in Figure 3B.2) vanishes in complex 1e, and also the flexible arm containing the urea unit turns inside out to accommodate the large tetrahedral SO_4^{2-} anion. (Figure 3B.5f) The semirigid arm also rotates to a certain angle to facilitate the tetrahedral anion recognition, which can be visualized through changes in the dihedral angle between the spacer phenyl ring and the benzimidazole ring from 22.21° (for BPU-1.DMF) to 35.82° (for BPU-1.SO_4^{2-}). (Figure A3B.14b,c) The average hydrogen-bonding distance was observed to be 2.22 Å, suggesting strong sulfate binding by BPU-1. Each SO_4^{2-} anion is surrounded by four receptor molecules, and each of them interacts differently with the SO_4^{2-} anion, where one of the receptors act as three hydrogen-bond donor site (involving two N–H_{urea}···O and one C–H_{phenyl}···O), other two receptors involve its aryl hydrogen atoms (two C–H_{phenyl}···O), and the remaining one receptor contributes two hydrogen-bonding interactions (one C–H_{phenyl}···O and one N–H_{benz}···O). Out of those four receptors, two are interconnected via π···π interactions involving spacer phenyl rings (the distance between the centroids of the two spacer phenyl rings is found to be ~3.82 Å), and the remaining two are also interconnected via π···π interactions but involving two benzimidazole rings (distance between the centroids of the two benzimidazole rings is found to be ~3.64 Å). (Figure 3B.5a,d) The sulfate anion forms two types of cyclic "sulfate-water-sulfate" cluster, where one is an eight-membered ring with $R_4^4(8)$ arrangement, involving hydrogen-bonding interaction between the oxygen atom (O6) of sulfate and hydrogen atoms (H9A and H9B) of the water molecule (H9A···O6 = 2.11 Å, H9B···O6 = 1.98 Å) and the other one is 12-membered ring encompassing oxygen atoms (O4 and O5) of the sulfate anion and hydrogen atoms (H8A and H8B) of the water molecule (O4···H8A = 2.45 Å and O5···H8B = 2.15 Å) with $R_4^4(12)$ arrangement, arranged in alternate fashion. (Figure 3B.5h) Each sulfate anion is surrounded by four water molecules through four hydrogen-bonding interactions with an average hydrogen bonding distance of 2.17 Å, thus facilitating the formation of one-dimensional $[SO_4(H_2O)_4^{2-}]_n$ clusters. (Figure 3B.5h) It is very important to understand various structural intricacies associated with such sulfate-water-clusters since this can be used as a tool for sulfate separation, which has already been

demonstrated by many groups in recent years. [3B.45, 3B.46] Thus, the high flexibility of one arm and the semiflexibility of the other give rise to a perfect combination to facilitate efficient SO_4^{2-} binding.

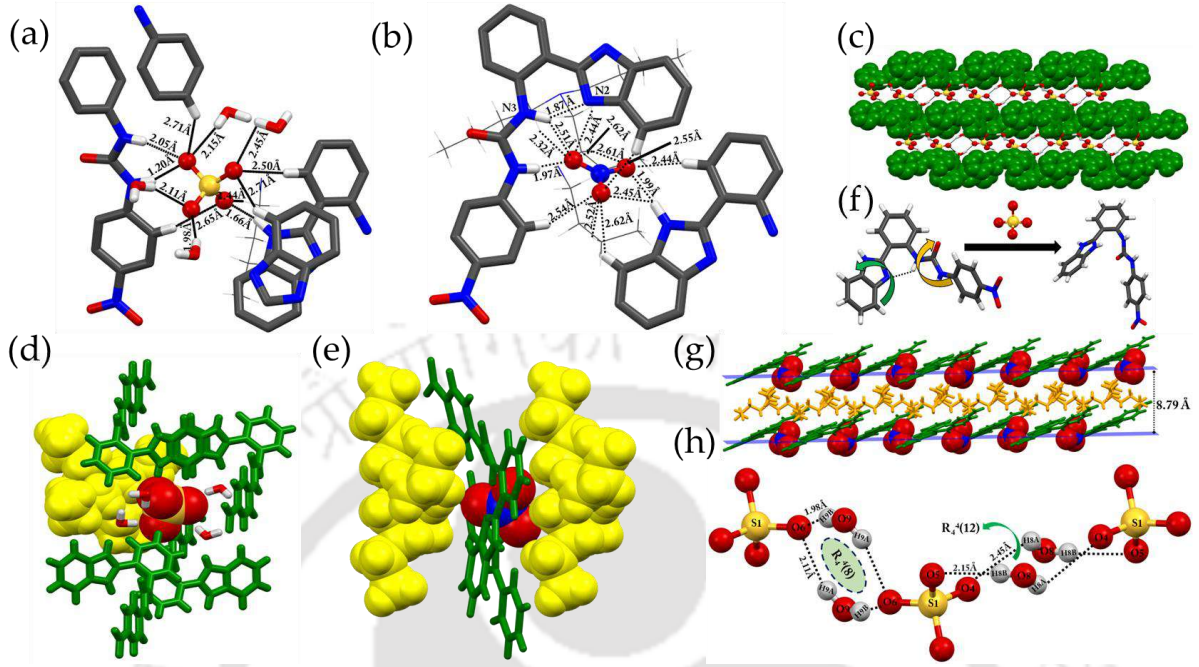

Figure 3B.5: Hydrogen-bonding interaction in (a) complex 1d and (b) complex 1e. (c) Packing arrangement of complex 1e. Encapsulation of (d) hydrated sulfate anion and (e) nitrate anion by receptor BPU-1. (f) Depicting conformational alteration of BPU-1 in the presence of SO_4^{2-} anions. (g) Layered arrangement in complex 1d. (h) Cyclic sulfate-water cluster $[SO_4(H_2O)_4]^{2-}$ running along the crystallographic b-axis.

On analyzing the ^{1}H NMR of the isolated crystal of complex 1e, it was observed that both the peaks representing NH_{urea} as well as $N–H_{benz}$ undergo severe broadening with a slight downfield shift of NH_b ($\Delta\delta NH_b$ = 0.11 ppm) and significant downfield shift of NH_a ($\Delta\delta NH_a$ = 0.91 ppm), suggesting strong hydrogen bonding between the receptor and the tetrahedral oxoanion. A significant upfield shift of the protons in the aromatic region can be attributed to the shielding effect due to SO_4^{2-} binding. (Figure A3B.10; Figure A2.35 of Chapter 2) In the FT-IR analysis of the isolated complex 1e, a broad peak at 3409 cm^{-1} was observed, indicating the presence of water molecules, (Figure A2.36 of Chapter 2) which was also quite evident in the crystal structure. Changes in the peak positioning for the characteristic peak for NH_{urea} (from 3287 cm^{-1} for the free receptor BPU-1 to 2962 cm^{-1} in complex 1e were also observed indicating the involvement of NH_{urea} in hydrogen-bonding interactions with SO_4^{2-} anions. (Figure A2.18, and Figure A2.36 of Chapter 2)

3B.3.3. Hirshfeld Surface Analyses

Various noncovalent interactions such as strong N–H···A (anion) and weaker interactions like C–H···Cl^-/Br^-, C–H···O, C–H···π, etc. dictate the characteristics associated with the surface of a molecule, and to establish the same, Hirshfeld surface (HS) analysis is performed. [3B.47] It also helps in visualizing structural modifications after anion complexation and comparing it with those of the free receptors. The strengths of the interactions either strong or weak can be visualized through HS, where the high-intense color and low-intense color signify strong and weak interactions, respectively. Quantification of the various noncovalent interactions in terms of "contact contribution" can also be done through the two-dimensional fingerprint plots (2D FPs) of HS analyses. [3B.48] The H–C, H–O, and H–X^- (halides) contact contributions in the free receptors as well as in their anion complexes (Table 3B.1). The bright red spots observed on the d_{norm} surfaces indicate the strong N–H···O/N–H···X^- interactions involving N–H_{urea}/N–H_{benz}, and the faded reddish spots are indicative of other important interactions such as C–H···O and C–H···π interactions. (Figure 3B.6a-c)

Table 3B.1: Contact contributions (%) from the d_{norm} surface area of dipodal segments in free receptors and the anion complex.

contacts	BPU-1.DMF	BPU-2	1(a)	1(b)	1(c)	1(d)	1(e)	2(a)	2(b)
H···X^-	-	-	10.6	10.8	16.0	-	-	7.4	8.1
H···O	20.0	5.2	5.8	11	11.1	24.2	31.2	2.2	2.1
H···C	21.6	18.4	19.8	18.5	11.0	14.5	11.1	17.3	17.1

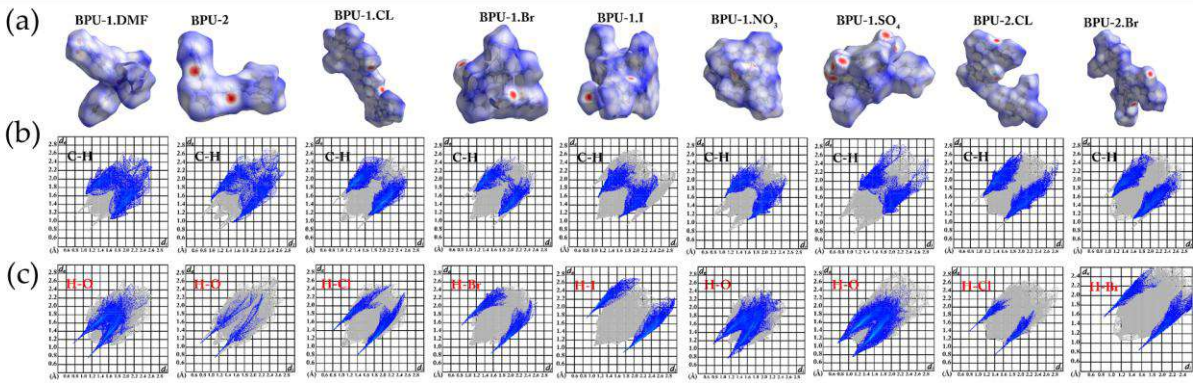

Figure 3B.6: HS analysis displaying (a) the d_{norm} surfaces of BPU-1.DMF, BPU-2, and the anionic complexes of both the receptors. (b) Corresponding 2D FPs with the C···H interactions involved in C–H···O or C–H···π contacts. (c) Corresponding 2D FPs with the H–O/H-X^- interactions highlighted in color involved in N–H···O/C–H···O/N–H···X^-/C–H···X^- close contacts.

The 2D FPs for the H···C close contacts show the highest contact contribution in the DMF-solvated BPU-1 receptor with a contact contribution of 21.6%. Complex 1e possesses the highest H···O (31.2%) contact contribution, which can be attributed to the presence of water molecules in that complex as well as the involvement of the oxygen atoms of SO_4^{2-} in hydrogen-bonding interactions. A quite significant H···O contact with a contribution of 24.2% has also been observed for complex 1d because of the involvement of oxygen atoms of the oxyanion NO_3^- in hydrogen-bonding interaction with its nearby $N–H_{urea}$/$N–H_{benz}$/$C–H_{phenyl}$. The bright red spots on the d_{norm} surface are observed to be localized mostly on the surfaces of $N–H_{urea}$, NH_{benz}, halides, oxygen atoms of the oxyanions, and water molecules (for complex 1e), which indicates strong interactions prevalent in those regions. All of the above observations in HS analyses corroborate well with the SC-XRD analysis.

3B.3.4. Solution-State Anion-Binding Study

Qualitative ^{1}H NMR study of both the receptors BPU-1 and BPU-2 in the solution phase has been performed for the anions of interest by adding aliquots them into the solution of the respective receptors in DMSO-d_6. Adding excess F^- (~20 equiv) anions into the DMSO-d_6 solution of both the receptors resulted in the disappearance of the NH_{benz} and NH_{urea} peaks, which might suggest the deprotonation or hydrogen bond-induced rapid dynamic effects which lead to significant –NH peak broadening. Parallelly, significant changes in the aromatic region protons were also observed for both receptors, which might be attributed to the different chemical environments experienced by those protons as a result of deprotonation. For both receptors, we could also detect a broad peak at around ~16 ppm, which can be attributed to the generation of HF_2^- species as a result of deprotonation. (Figure A3B.2)

For the BPU-1 receptor, a downfield shift was observed for NH_{benz} and both the urea protons NH_a and NH_b when an excess of Cl^- and Br^- (~20 equiv each) were added into the DMSO-d_6 solution of the BPU-1 receptor in 298 K. In the presence of an excess amount of Cl^-, the highest shift was observed for NH_{benz} ($\Delta\delta NH_{benz}$ = 0.56 ppm) with the concomitant broadening of the peak, followed by NH_a and NH_b ($\Delta\delta NH_a$ = 0.25 ppm and $\Delta\delta NH_b$ = 0.12 ppm). As compared to that of Cl^- anions, lower chemical shift values were observed for NH_{benz}, NH_a, and NH_b ($\Delta\delta NH_{benz}$ = 0.14 ppm, $\Delta\delta NH_a$ = 0.07 ppm, and $\Delta\delta NH_b$ = 0.06 ppm) in the case of Br^- anions, although the same chemical shift trend is followed. In the presence of I^- (~20 equiv), very negligible shift was observed ($\Delta\delta NH_{benz}$ = 0.003 ppm $\Delta\delta NH_a$ = 0.01 ppm and $\Delta\delta NH_b$ = 0.01 ppm), indicating negligible binding in the solution phase. For the oxoanions, the chemical shift

values were not that high, whereas for the NO_3^- anion, the changes in the chemical shift values for NH_{benz}, NH_a, and NH_b were observed to be 0.01 0.02, and 0.02, and 0.02 ppm, respectively. In the case of SO_4^{2-} anions, a significant downfield shift of the NH_a peak was observed, followed by a small shift of NH_b ($\Delta\delta NH_a$ = 0.93 ppm and $\Delta\delta NH_b$ = 0.08 ppm), and a slight upfield shift for the NH_{benz} peak was observed. (Figure 3B.7a)

The BPU-2 receptor molecule shows the same chemical shift trend as observed earlier in the case of receptor BPU-1 when an excess of anions were added (added ~20 equiv. each) to DMSO-d_6 at 298 K. Comparatively higher chemical shift values were observed for NH_{benz}, NH_a, and NH_b in the presence of Cl^- and Br^- anions. On adding an excess of Cl^- anions, downfield shifting of NH_{benz} occurs with concomitant broadening of the peak ($\Delta\delta NH_{benz}$ = 0.65 ppm), indicating strong hydrogen-bonding interaction involving the same. The urea hydrogen atom NHa undergoes larger downfield shift as compared to that of NH_b ($\Delta\delta NH_a$ = 0.52 ppm and $\Delta\delta NH_b$ = 0.15 ppm); such irregular peak shifting is due to the different chemical environments experienced by both hydrogen atoms (as evident from the crystal structures of both the receptors). For the Br^- anion, the peak shifts for both NH_{benz} and NH_a were observed to be smaller ($\Delta\delta NH_{benz}$ = 0.34 ppm and $\Delta\delta NH_a$ = 0.29 ppm) as compared to that of the Cl^- anion; however, the NH_b peak shift was comparable with that of the Cl^- anion ($\Delta\delta NH_b$ = 0.16 ppm). As observed earlier in the case of the BPU-1 receptor, for I^- anions, negligible chemical shift was observed for all the three hydrogen atoms ($\Delta\delta NH_{benz}$ = 0.01 ppm, $\Delta\delta NH_a$ = 0.01 ppm, and $\Delta\delta NH_b$ = 0.02 ppm). (Figure 3B.7b)

It is quite evident from this solution-phase study that both the receptor molecules BPU-1 and BPU-2 bind anions less strongly in the solution phase, which is also quite evident from the ^1H NMR titration experiment. (Section 2.4 of chapter 2; Table A3B.1)

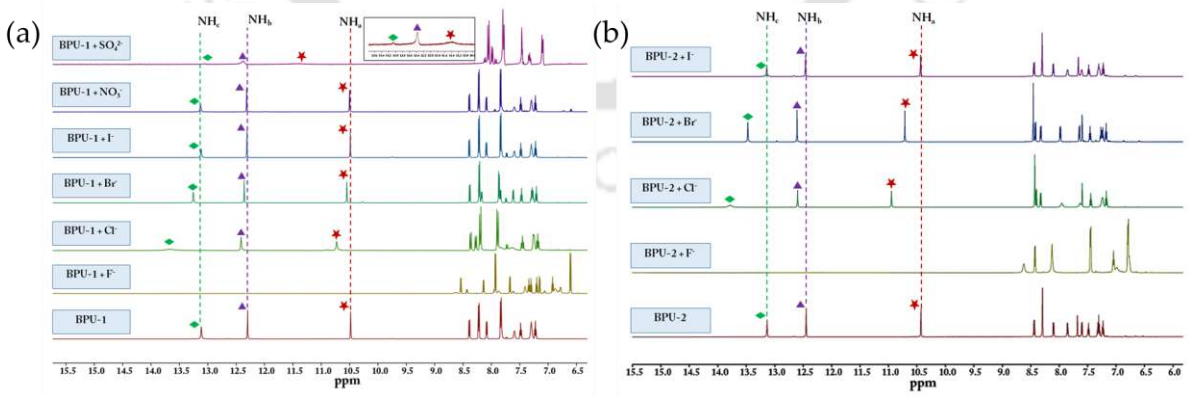

Figure 3B.7: Stacked ^1H NMR spectra of (a) receptor BPU-1 (DMSO-d_6, 298 K) in the presence of different anions, and (b) receptor BPU-2 (DMSO-d_6, 298 K) in the presence of different anions.

3B.3.5. Intramolecular Cyclization of BPU-1 and BPU-2

Serendipitous crystallization of BPU-1 and BPU-2 into benzimidazo[1,2-c]quinazolin-6-ones (BP-Cyc) occurred through intramolecular cyclization of BPU-1/BPU-2 while trying to crystallize them with F^-/HO^- anions (using TBAF/TBAOH) in acetonitrile medium, which was confirmed by SC-XRD analysis of BP-Cyc; however, the crystal structure of BP-Cyc is already reported (Figure A3B.15a-c). [3B.49] This result motivated us to conduct reactions of both BPU-1 and BPU-2 with TBAF/TBAOH using acetonitrile as a solvent, which yielded BP-Cyc as a product. Only room-temperature stirring was enough for BPU-1, while in the case of BPU-2, we had to reflux the whole reaction mixture to get the product BP-Cyc. To support this result, we have performed a UV–vis spectroscopic study of both receptors in acetonitrile by adding an excess of fluoride anions (~25 equiv), where a bathochromic shift of about 30 nm was observed for receptor BPU-1, which might indicate deprotonation, eventually leading to the formation of our desired cyclized product. (Figure 3B.8a) On the other hand, in the case of BPU-2, the changes were minimal, reflecting a slower reaction rate/requirement of extra activation energy of the same as compared to that of the receptor BPU-1. (Figure 3B.8b) Previously, many groups have reported numerous synthetic methods to prepare BP-Cyc and most of them suffer from some serious disadvantages such as the use of metals, low yield, and harsh as well as complicated reaction conditions/methods. So, our result might open a new avenue for the simplistic way of synthesizing heterocyclic compounds by using anions and completely prohibiting the use of any metals. To the best of our knowledge, this is the first ever we are reporting an anion-induced cyclization reaction for the synthesis of benzimidazo[1,2-c]quinazolin-6-ones using a urea-based compound as a starting material.

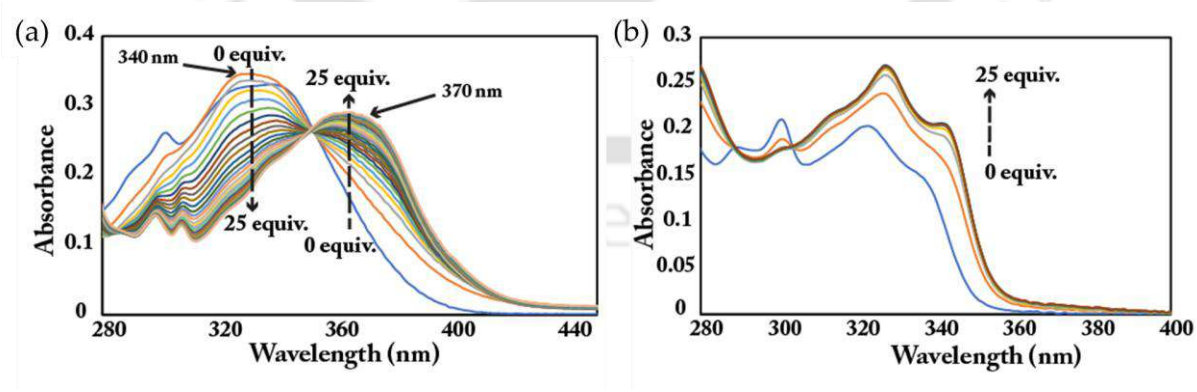

Figure 3B.8: (a) UV–vis spectrum in the presence of an excess of F^- in acetonitrile (a) for BPU-1 and (b) for BPU-2.

3B.3.6. Proposed Cyclization Mechanism

In the first step, F^-/HO^- mediated deprotonation occurs in the benzimidazole nitrogen atom, followed by nucleophilic attack by the deprotonated nitrogen atom at the urea C=O site, leading to the cyclic product BP-Cyc through elimination of amines [4-nitroaniline for BPU-1 and 3,5-Bis(trifluoromethyl) aniline for BPU-2]. (Scheme 3B.1) Trace of the leaving group, 4-nitroaniline along with n-tetrabutylammonium, has been detected for BPU-1 through ^{1}H NMR analysis of the filtrate. (Figure A3B.3) In the case of BPU-2, analysis of the filtrate was complicated through ^{1}H NMR because of the presence of multiple peaks, which might be because of the presence of unreacted substances in the filtrate.

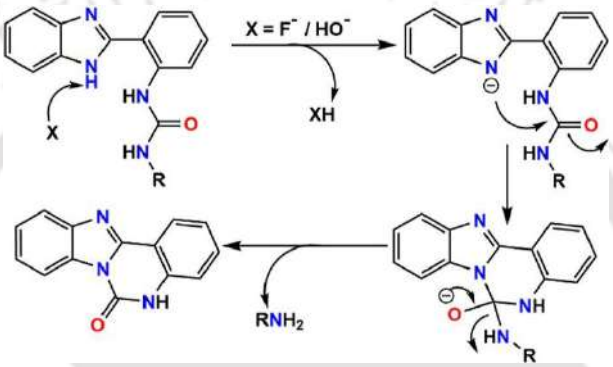

Scheme 3B.1: Plausible F^-/HO^- induced intramolecular cyclization mechanism.

3B.3.7. Selective UV–Vis and Fluorescence Response toward SO_4^{2-} and HSO_4^-

Anion-binding studies were performed for both the receptors, BPU-1 and BPU-2, in an aqueous medium for the biologically important anions, namely, F^-, Cl^-, Br^-, I^-, CN^-, AcO^-, ClO_4^-, HO^-, NO_3^-, HSO_4^-, and SO_4^{2-} using UV–vis and fluorescence spectroscopy. Both in UV–vis and fluorescence spectroscopy, receptor BPU-1 selectively responds in the presence of both SO_4^{2-} and HSO_4^- anions. (Figure 3B.9a,b) The free receptor BPU-1 shows two absorption bands at 300 and 340 nm in UV–vis; the band at the lower-wavelength region is presumably due to intramolecular π–π* transition, whereas the band at the higher wavelength region can be ascribed to intramolecular charge transfer (ICT) transition. On adding SO_4^{2-}/HSO_4^- to BPU-1, the band at 340 nm diminishes with a concomitant slight blueshift of the band at 300 nm. The reason for this might be attributed to the blocking of the ICT due to SO_4^{2-}/HSO_4^- binding through hydrogen-bonding interactions, which results in a slight blueshift of the band at 300 nm with simultaneous weakening of the absorption band at 340 nm. For BPU-2, some selectivity was observed for only HSO_4^- in the UV–vis spectra. The fluorescence response of both receptors BPU-1 and BPU-2 in the presence of different anions was also recorded, where selective quenching of the

fluorescence spectra for BPU-1 was observed in the presence of both SO_4^{2-} and HSO_4^-anions. For the BPU-2 receptor, no good selectivity was observed in the fluorimetric analysis. (Figure A3B.5a,b) Binding of SO_4^{2-}/HSO_4^- to the BPU-1 receptor through hydrogen-bonding interaction involving NH_{urea} and NH_{benz} as evident from ^{1}H NMR analysis/crystal structure of the [BPU-1.SO_4]$^{2-}$ complex facilitates photoinduced electron transfer from the electron-rich benzimidazole group to the electron-deficient nitro-phenyl ring, which leads to quenching of the fluorescence emission intensity. Limits of detection (LODs) for SO_4^{2-} and HSO_4^- anions were calculated to be 7.5 and 4.13 μM, respectively, following equation 1 (Chapter 2), far below the EPA (U.S. Environmental Protection Agency) permissible SO_4^{2-} limit in safe drinking water. (Figure A3B.4a,d) The binding constant values obtained from the Benesi–Hildebrand (B–H) plot (see Chapter 2) for SO_4^{2-} and HSO_4^- anions were found to be 3.45 × 10^8 M^{-1} and 15.51 × 10^8 M^{-1}, respectively. (Figure 3B.9c,d; Table 3B.2; Figure A3B.4b,e) The binding affinity of BPU-1 toward HSO_4^- is observed to be about 5 times higher than that of SO_4^{2-} anions along with a comparatively better LOD value. From Job's plot, the binding stoichiometry of 1:1 complex formation between BPU-1 and SO_4^{2-}/HSO_4^- was estimated. (Figure A3B.4c,f)

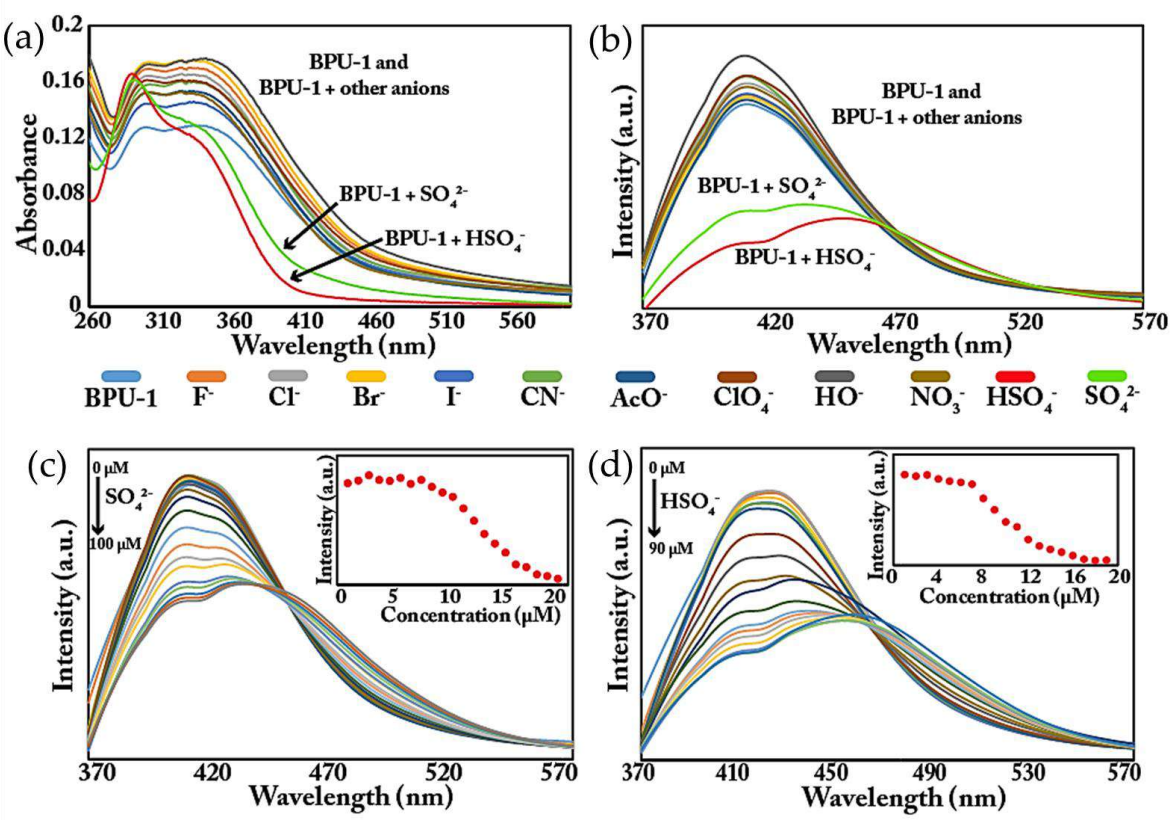

Figure 3B.9: (a) Depicting selective SO_4^{2-}/HSO_4^- sensing by BPU-1 in UV–vis spectroscopy. (b) Selective quenching of emission spectra of BPU-1 in the presence of SO_4^{2-}/HSO_4^- anions. (c, d) Fluorescence emission titration in 100% aqueous medium upon incremental addition of SO_4^{2-} and HSO_4^- to BPU-1.

Table 3B.2: Binding constant values obtained from fluorescence titration experiment conducted in water.

host	guest	binding Stoichiometry	binding Constant, K_a (M^{-1})
BPU-1	SO_4^{2-}	1:1	3.45×10^8
BPU-1	HSO_4^-	1:1	15.51×10^8

3B.4. Conclusions

In summary, two benzimidazole-based unsymmetrical dipodal monourea receptors, namely, BPU-1 and BPU-2 attached with two different π-acidic terminal substituents are synthesized. In both the receptors, monourea containing flexible arms preorganized to accommodate anions with varied geometries (spherical, trigonal planar, and tetrahedral) in the solid state. Receptor BPU-1 could entrap the hydrated sulfate anion inside its self-assembled cavity. Both receptors were cyclized to form benzimidazo[1,2-c] quinazolin-6-ones in the presence of F^-/HO^- (as their TBA salts). Receptor BPU-1 could also selectively sense SO_4^{2-}/HSO_4^- in aqueous medium among vast arrays of biologically relevant anions. Such concomitant SO_4^{2-} anion recognition in the solid state as well as its sensing in aqueous medium by a receptor are not very common in the literature. We have also evaluated and compared the binding constant values, LOD, and binding stoichiometry of both anions for receptor BPU-1.

References

[3B.1] L. K. Macreadie, A. M. Gilchrist, D. A. McNaughton, W. G. Ryder, M. Fares, and P. A. Gale, Chem, 2022, **8**, 46-118.

[3B.2] U. Manna, B. Portis, T. K. Egboluche, M. Nafis, and M. A. Hossain, Front. Chem., 2021, **8**, 575701.

[3B.3] P. D. Beer, P. A. Gale, and D. K. Smith, *Supramolecular Chemistry*; Oxford University Press: Oxford, U.K., 1999.

[3B.4] J. L. Sessler, P. A. Gale, W. S. Cho, *Anion Receptor Chemistry: Monographs in Supramolecular Chemistry*; RSC Publishing: Cambridge, UK, 2006.

[3B.5] C. J. Woods, S. Camiolo, M. E. Light, S. J. Coles, M. B. Hursthouse, M. A. King, P. A. Gale, J. W. Essex, *J. Am. Chem. Soc.*, 2002, **124**, 8644-8652.

[3B.6] C. A. Ilioudis, D. A. Tocher, and J. W. Steed, *J. Am. Chem. Soc.*, 2004, **126**, 12395-12402.

[3B.7] G. W. Bates, P. A. Gale, and M. E. Light, *Chem. Commun.*, 2007, 2121– 2123.

[3B.8] M. Cametti, and K. Rissanen, *Chem. Soc. Rev.*, 2013, **42**, 2016– 2038.

[3B.9] C. Caltagirone, and P. A. Gale, *Chem. Soc. Rev.*, 2009, **38**, 520– 563.

[3B.10] S. O. Kang, R. A. Begum, and K. Bowman-James, *Angew. Chem., Int. Ed.*, 2006, **45**, 7882-7894.

[3B.11] U. Manna, R. Chutia, and G. Das, *Cryst. Growth Des.*, 2016, **16**, 2893-2903.

[3B.12] J. Romański, and P. Piątek, *J. Org. Chem.*, 2013, **78**, 4341-4347.

[3B.13] J. W. Steed, and J. L. Atwood, Supramolecular Chemistry; Wiley: Chichester, U.K., 2009; p 226.

[3B.14] Y. Zhang, and P. S. Cremer, *Curr. Opin. Chem. Biol.*, 2006, **10**, 658-663.

[3B.15] A. I. Boldyrev, and J. Simons, *J. Phys. Chem.*, 1994, **98**, 2298-2300.

[3B.16] A. T. Blades, and P. Kebarle, *J. Am. Chem. Soc.*, 1994, **116**, 10761-10766.

[3B.17] X.-B. Wang, J. B. Nicholas, L.-S. Wang, *J. Chem. Phys.*, 2000, **113**, 10837-10840.

[3B.18] S.-Q. Chen, W. Zhao, and B. Wu, *Front. Chem.*, 2022, **10**, 905563.

[3B.19] K. H. Stern, and E. S. Amis, *Chem. Rev.*, 1959, **59** (1), 1-64.

[3B.20] D. W. Smith, *J. Chem. Educ.*, 1977, **54**, 540.

[3B.21] B. Gao, and Z.-f. Liu, *J. Chem. Phys.*, 2004, **121**, 8299-8306.

[3B.22] D. Markovich, *Physiol. Rev.*, 2001, **81**, 1499-1533.

[3B.23] J. W. Pflugrath, and F. A. Quiocho, *Nature*, 1985, **314**, 257-260.

[3B.24] J. W. Pflugrath, and F. A. Quiocho, *J. Mol. Biol.*, 1988, **200**, 163-180.

[3B.25] J. A. Lohrman, C.-L. Deng, T. A. Shear, L. N. Zakharov, M. M. Haley, and D. W. Johnson, Chem. Commun., 2019, 55, 1919-1922.

[3B.26] A. S. Singh, and S.-S. Sun, *J. Org. Chem.*, 2012, **77**, 1880-1890.

[3B.27] S. S. R. Namashivaya, A. S. Oshchepkov, H. Ding, S. Förster, V. N. Khrustalev, and E. A. Kataev, *Org. Lett.*, 2019, **21** (21), 8746-8750.

[3B.28] Y.-C. He, Y.-M. Yan, H.-B. Tong, Z.-X. Ren, J.-H. Wang, Y.-B. Zhang, J. B. Chao, and M.-L. Wang, *Chem. Commun.*, 2020, **56**, 9364-9367.

[3B.29] S. Kaur, V. W. Day, and K. Bowman-James, *Cryst. Growth Des.*, 2020, **20**, 4212-4216.

[3B.30] G. Zhao, S.-Q. Chen, W. Zhao, B. Li, W. Zhang, B. Zheng, X.-J. Yang, and B. Wu, *CCS Chem.*, 2022, **4**, 2498-2507.

[3B.31] M. Zaleskaya, M. Karbarz, M. Wilczek, Ł. Dobrzycki, and J. Romański, *Inorg. Chem.*, 2020, **59**, 13749-13759.

[3B.32] T. Fiehn, R. Goddard, R. W. Seidel, and S. Kubik, *Chem.—Eur. J.*, 2010, **16**, 7241-7255.

[3B.33] T. A. Shumilova, T. Rüffer, H. Lang, and E. A. Kataev, *Chem.—Eur. J.*, 2018, **24**, 1500-1504.

[3B.34] A. Das, B. Roy, B. Konwar, A. Ramesh, and G. Das, *Cryst. Growth Des.*, 2022, **22**, 1778-1791.

[3B.35] M. Basak, A. Das, and G. Das, *CrystEngComm*, 2021, **23**, 7771-7780.

[3B.36] A. Das, B. Nayak, and G. Das, *CrystEngComm*, 2020, **22**, 2197-2207.

[3B.37] U. Manna, S. Kayal, S. Samanta, and G. Das, *Dalton Trans.*, 2017, **46**, 10374-10386.

[3B.38] U. Manna, S. Kayal, B. Nayak, and G. Das, *Dalton Trans.*, 2017, **46**, 11956-11969.

[3B.39] P.-G. Li, C. Yan, S. Zhu, S.-H. Liu, and L.-H. Zou, *Org. Chem. Front.*, 2018, **5**, 3464– 3468.

[3B.40] L.-H. Zou, C. Yan, K. Shi, L. Su, S. Zhu, Z.-K. Jia, and Q. Wang, *Eur. J. Org Chem.*, 2019, **2019**, 7725-7729.

[3B.41] L. Chen, C. Li, X. Bi, H. Liu, and R. Qiao, *Adv. Synth. Catal.*, 2012, **354**, 1773-1779.

[3B.42] H.-B. Zhao, Z.-W. Hou, Z.-J. Liu, Z.-F. Zhou, J. Song, and H.-C. Xu, *Angew. Chem., Int. Ed.*, 2017, **56**, 587-590.

[3B.43] X. Zhao, and D.-Q. Shi, *J. Heterocycl. Chem.*, 2010, **47**, 524.

[3B.44] F. Wang, S. Sen, C. Chen, S. Bähring, C. Lei, Z. Duan, Z. Zhang, J. L. Sessler, and A. Jana, *J. Am. Chem. Soc.*, 2020, **142**, 1987-1994.

[3B.45] R. Custelcean, N. J. Williams, and C. A. Seipp, *Angew. Chem., Int. Ed.*, 2015, **54**, 10525-10529.

[3B.46] Y.-H. Luo, J.-W. Wang, Y.-J. Li, C. Chen, P.-J. An, S.-L. Wang, C.-Q. You, and B.-W. Sun, *CrystEngComm*, 2017, **19**, 3362-3369.

[3B.47] J. J. McKinnon, A. S. Mitchell, and M. A. Spackman, *Chem.─Eur. J.*, 1998, **4**, 2136-2141.

[3B.48] T. E. Clark, M. Makha, A. N. Sobolev, and C. L. Raston, *Cryst. Growth Des.*, 2008, **8**, 890-896.

[3B.49] P.-G. Li, C. Yan, S. Zhu, S.-H. Liu, and L.-H. Zou, *Chem. Front.*, 2018, **5**, 3464-3468.

Annexure 3B

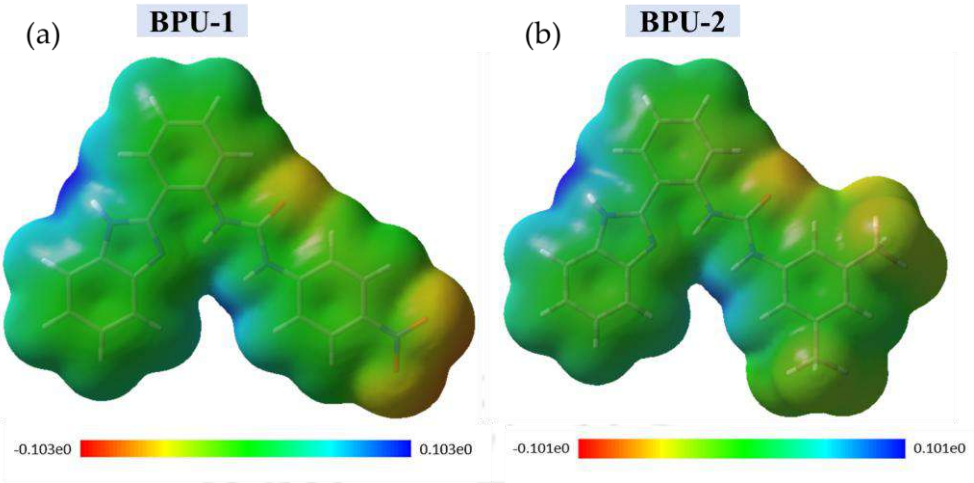

Figure A3B.1: Calculated electrostatic potential map (DFT, B3LYP/6-31+G(d)) depicting most probable anion binding sites.

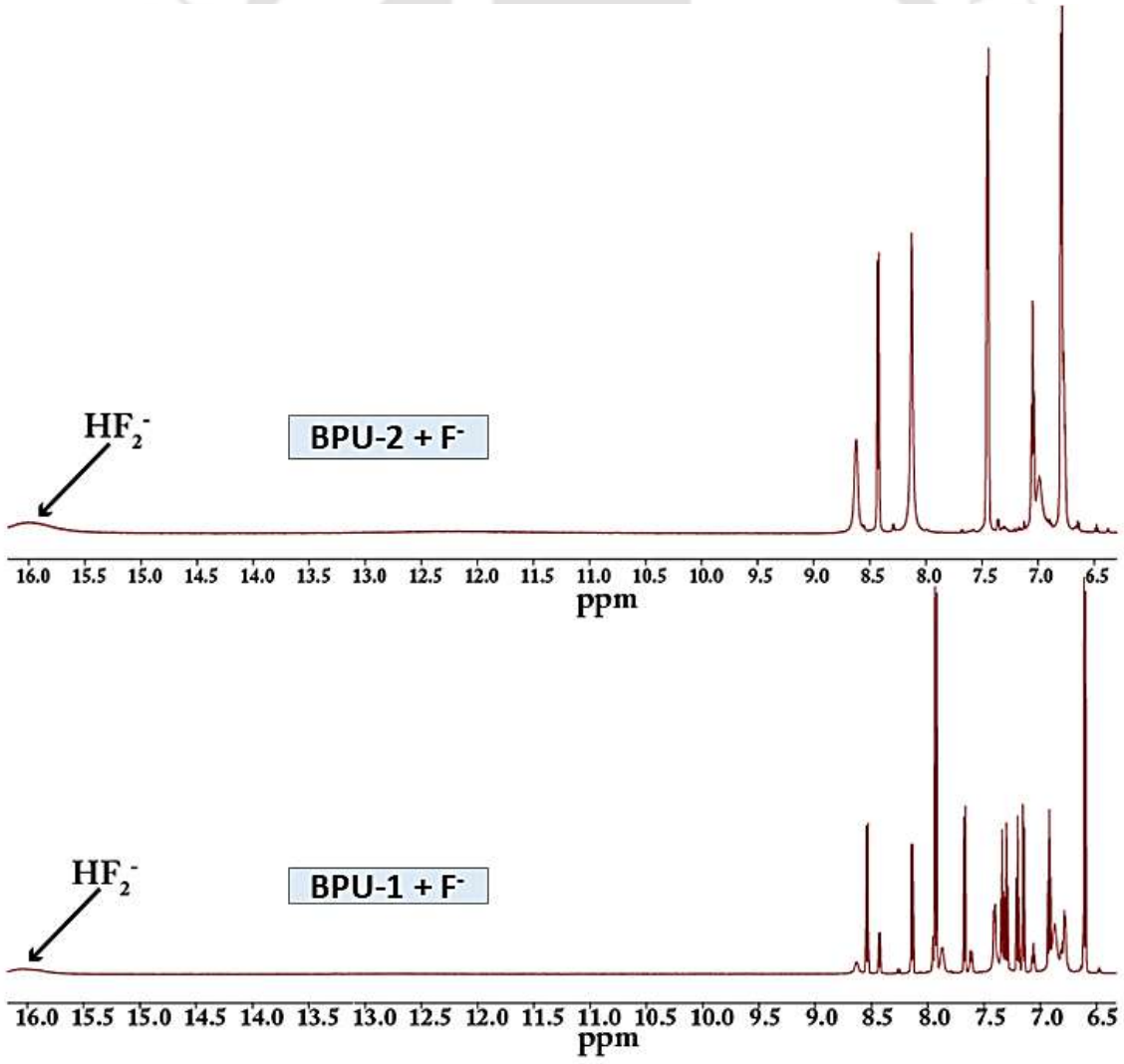

Figure A3B.2: ^{1}H NMR of BPU-1/BPU-2 in presence of excess F^{-} anion.

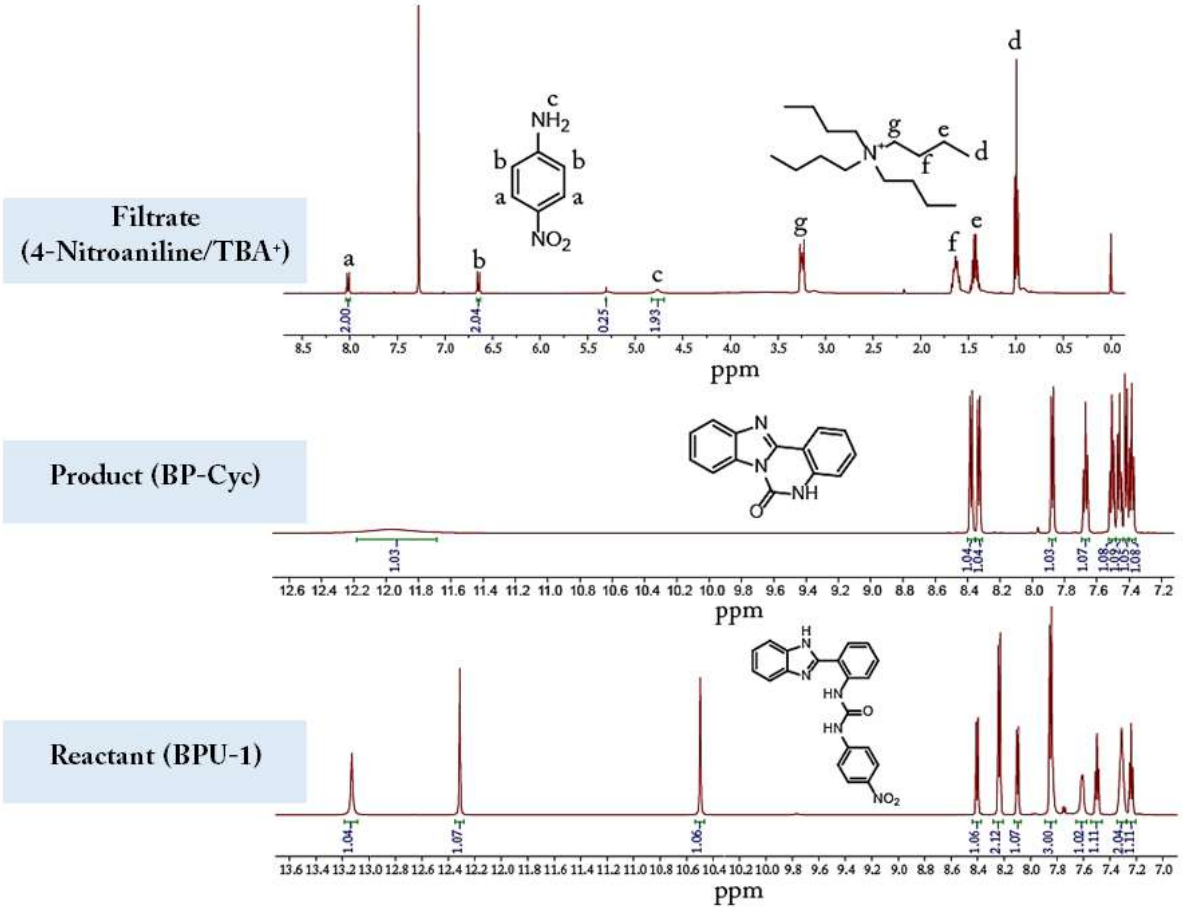

Figure A3B.3: Depicting stacked ^{1}H NMR spectra of the free receptor BPU-1 (in DMSO-d_6), cyclised product BP-Cyc (in DMSO-d_6) and the filtrate collected from the reaction of BPU-1 with TBAF in acetonitrile (in $CDCl_3$).

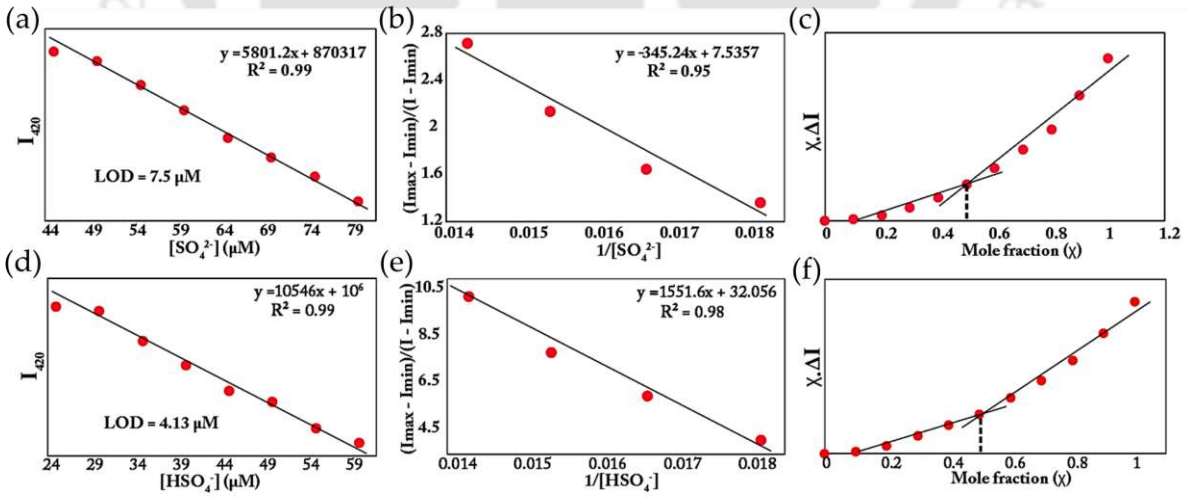

Figure A3B.4: (a) and (d) Fluorescence intensities at 420 nm versus SO_4^{2-} and HSO_4^- anion concentrations for lowest detection limits (LOD) calculation. (b) and (e) Benesi–Hildebrand plot for determination binding constant of BPU-1 with $SO_4^{2-}$and HSO_4^-anion. (c) and (f) Job's plot for BPU-1- SO_4^{2-} and BPU-1- HSO_4^-complexation from fluorescence emission spectrum.

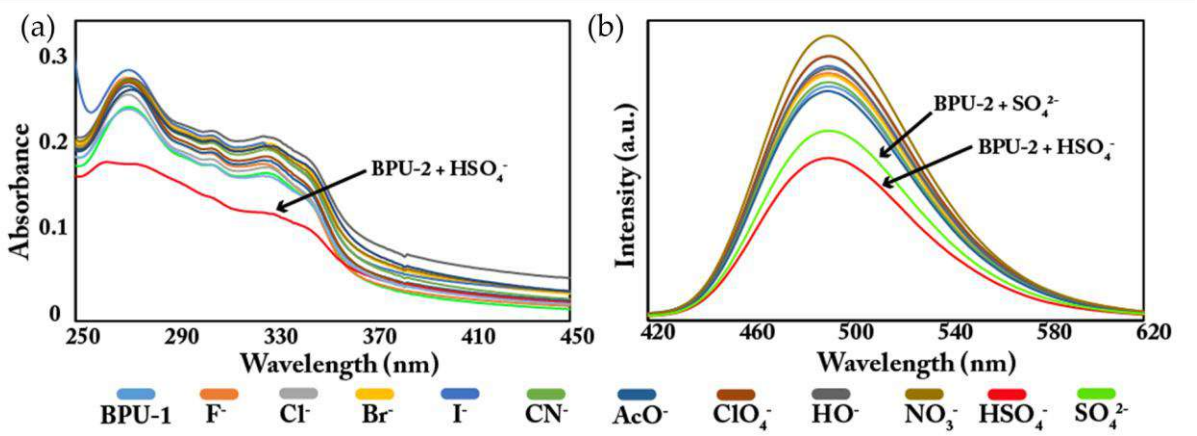

Figure A3B.5: (a) and (b) UV-vis and Fluorescence spectra of BPU-2 in presence of different anions in aqueous medium.

Table A3B.1: Binding stoichiometry and binding constant values obtained from ^{1}H NMR titration in DMSO-d_6.

Complex	Binding Stoichiometry	Binding Constant, K_a (M^{-1})	Error (%)
1a	1:1	7.04	± 3.4354
1b	1:1	0.92	± 2.0398
1d	1:1	0.53	± 1.0717
2a	1:1	7.31	± 5.1037
2b	1:1	1.32	± 1.5803

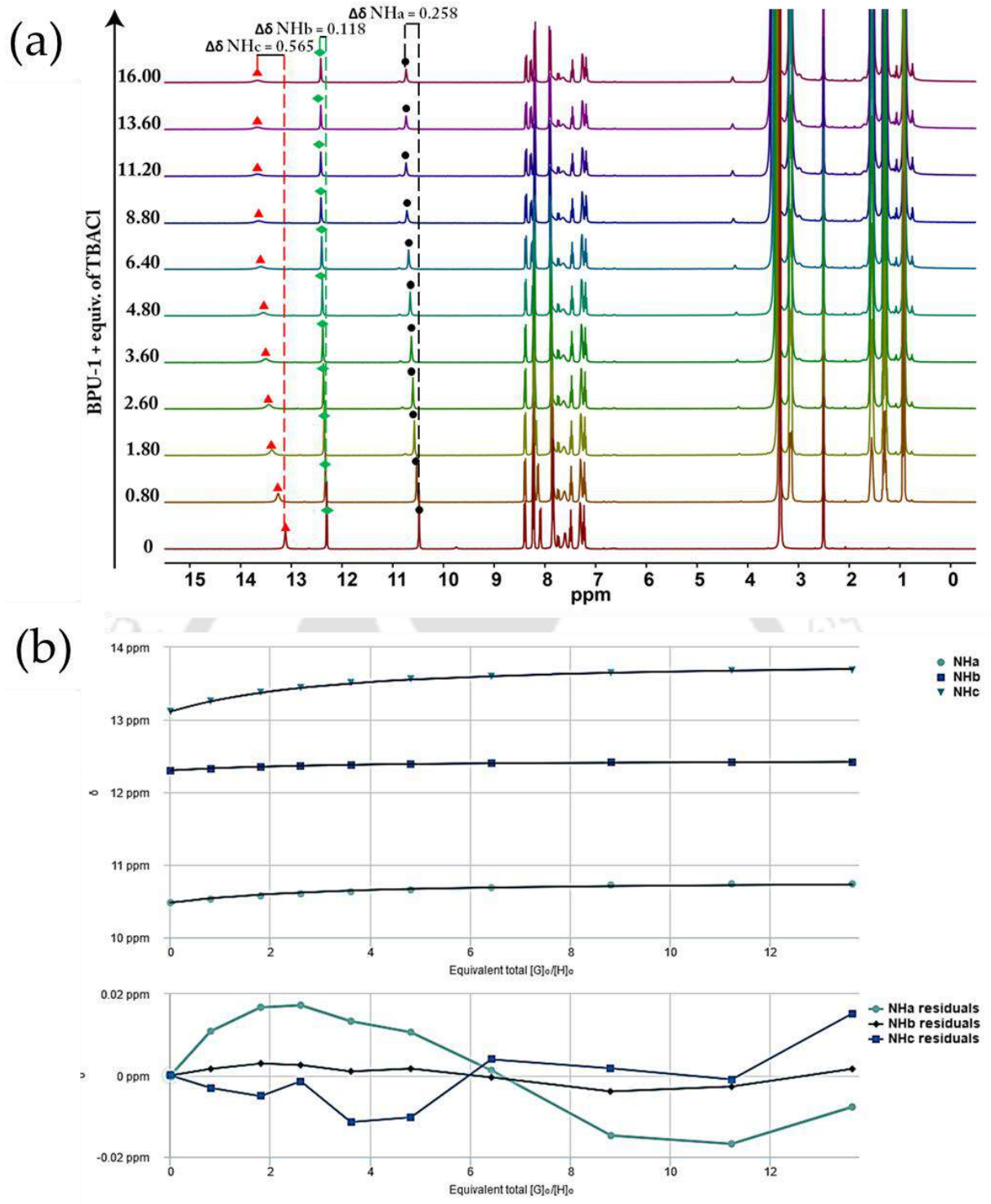

Figure A3B.6: a) ^{1}H-NMR titration spectra for receptor BPU-1 (50 mM) with the incremental addition of TBACl (1000 mM) in DMSO-d_6 solvent. The amounts of added TBACl are shown on the spectra. (b) The plot of chemical shift (δ) of NH_a, NH_b and NH_c protons vs. Equivalent total ($[G]_0/[H]_0$) added, fitted to 1:1 binding model of BindFit v0.5 program. Here 'H' represents Host and 'G' represents Guest (TBACl). (http://app.supramolecular.org/bindfit/view/6e469aa1-85dc-4805-9c1c-f4223f7e91bf)

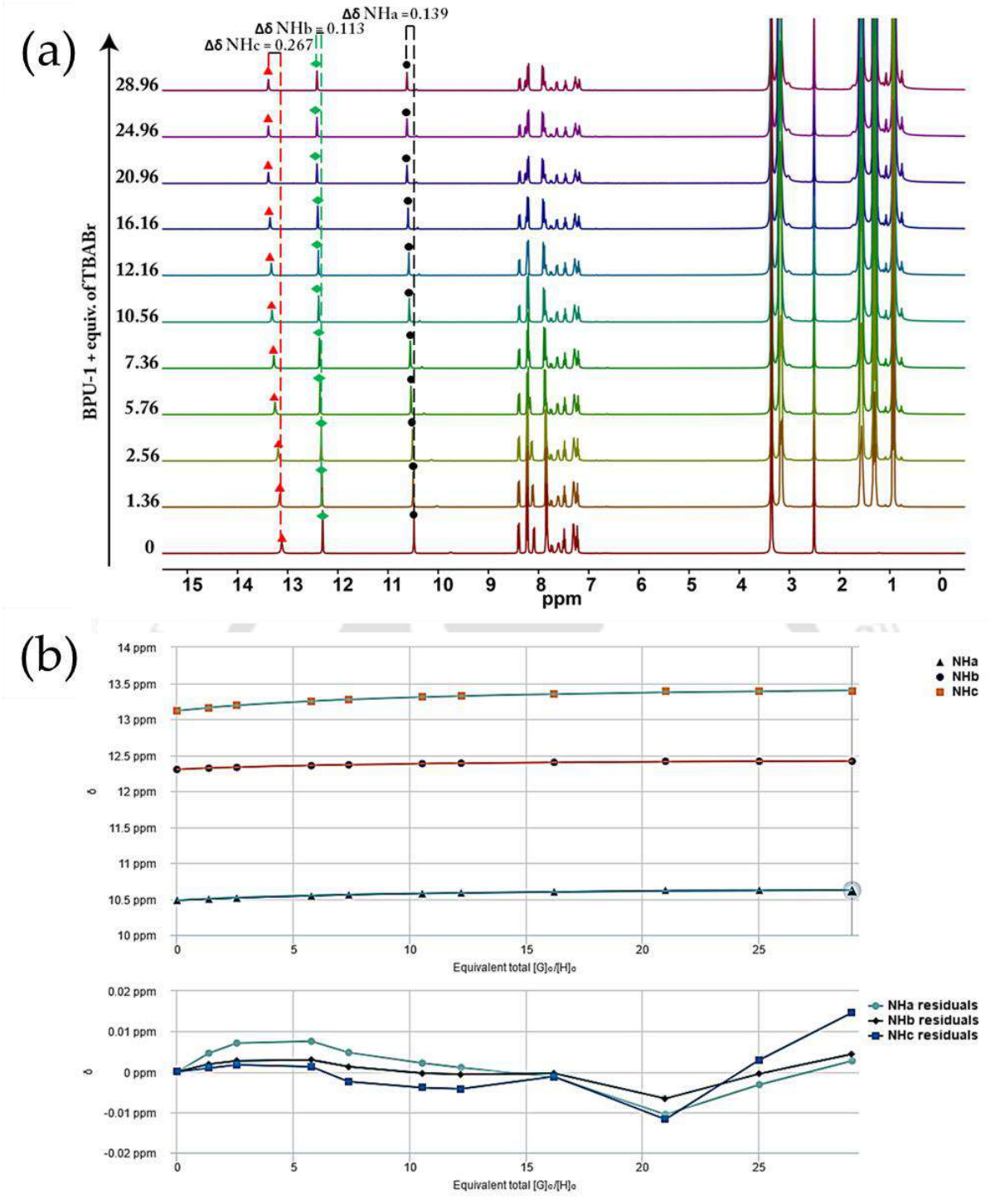

Figure A3B.7: (a) ^{1}H-NMR titration spectra for receptor BPU-1 (50 mM) with the incremental addition of TBABr (1000 mM) in DMSO-d_6 solvent. The amounts of added TBABr are shown on the spectra. (b) The plot of chemical shift (δ) of NH_a, NH_b and NH_c protons vs. Equivalent total ($[G]_0/[H]_0$) added, fitted to 1:1 binding model of BindFit v0.5 program. Here 'H' represents Host and 'G' represents Guest (TBABr). (http://app.supramolecular.org/bindfit/view/0b694dce-3b60-4338-b18a-329f2f67d213)

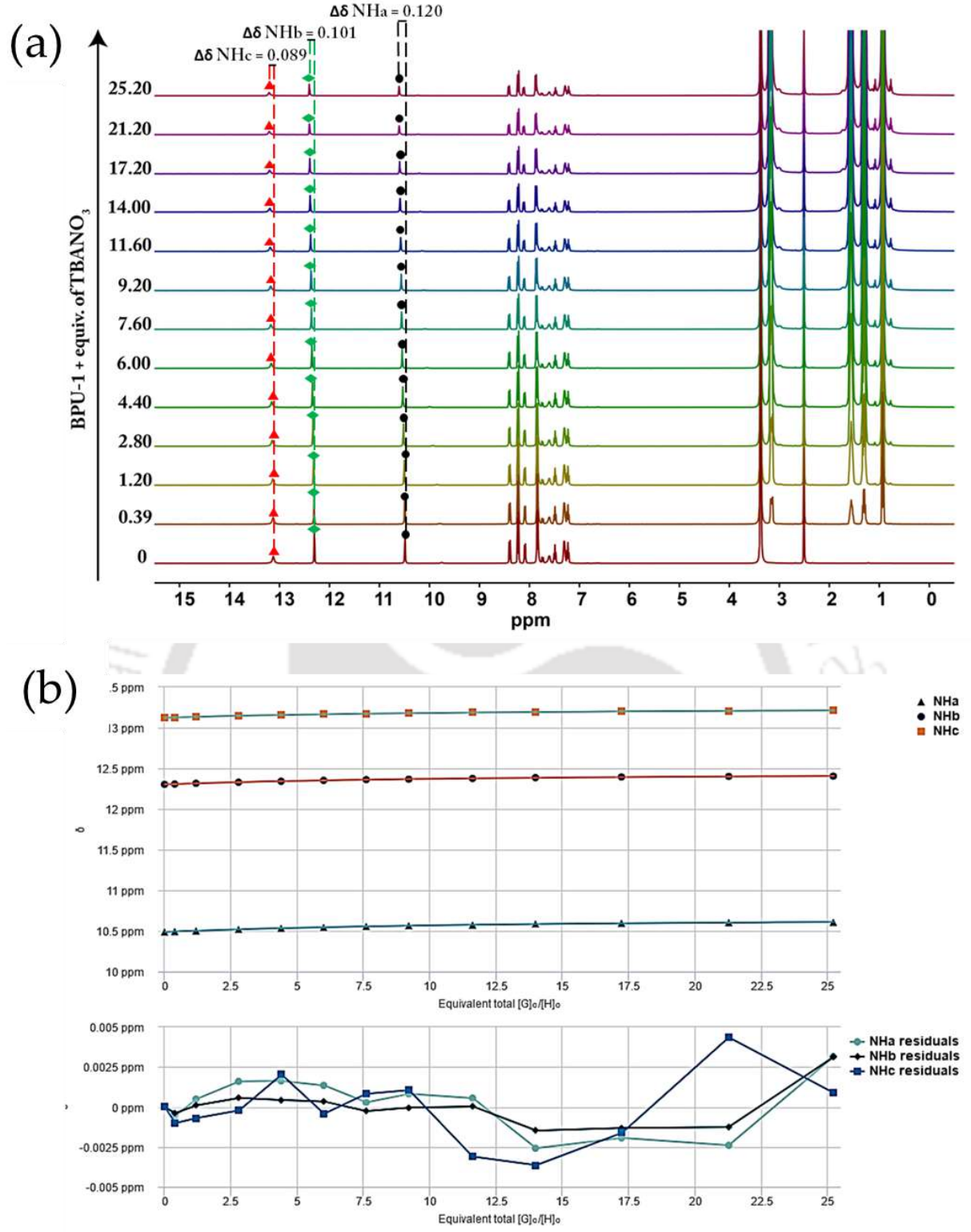

Figure A3B.8: (a) ^{1}H-NMR titration spectra for receptor BPU-1 (50 mM) with the incremental addition of $TBANO_3$ (1000 mM) in DMSO-d_6 solvent. The amounts of added $TBANO_3$ are shown on the spectra. (b) The plot of chemical shift (δ) of NH_a, NH_b and NH_c protons vs. Equivalent total ($[G]_0/[H]_0$) added, fitted to 1:1 binding model of BindFit v0.5 program. Here 'H' represents Host and 'G' represents Guest ($TBANO_3$). (http://app.supramolecular.org/bindfit/view/d657007e-e48e-406d-a3f2-9b05ee4da4aa)

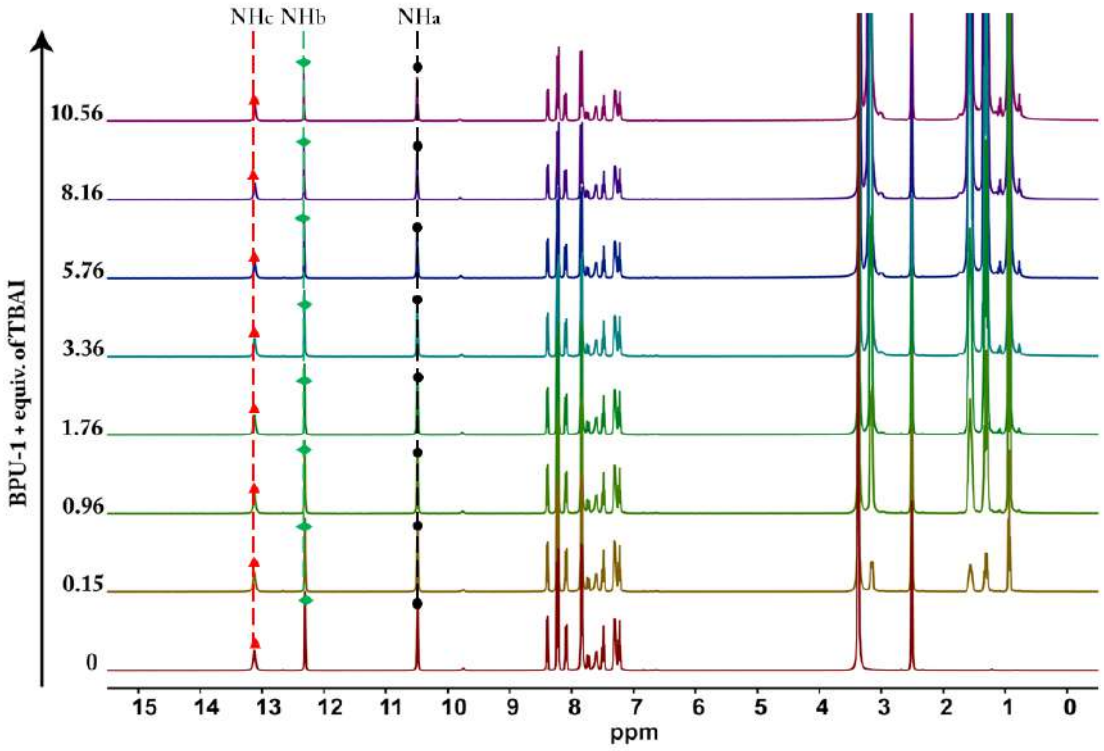

Figure A3B.9: ^{1}H-NMR titration spectra for receptor BPU-1 (50 mM) with the incremental addition of TBAI (1000 mM) in DMSO-d_6 solvent. The amounts of added TBAI are shown on the spectra.

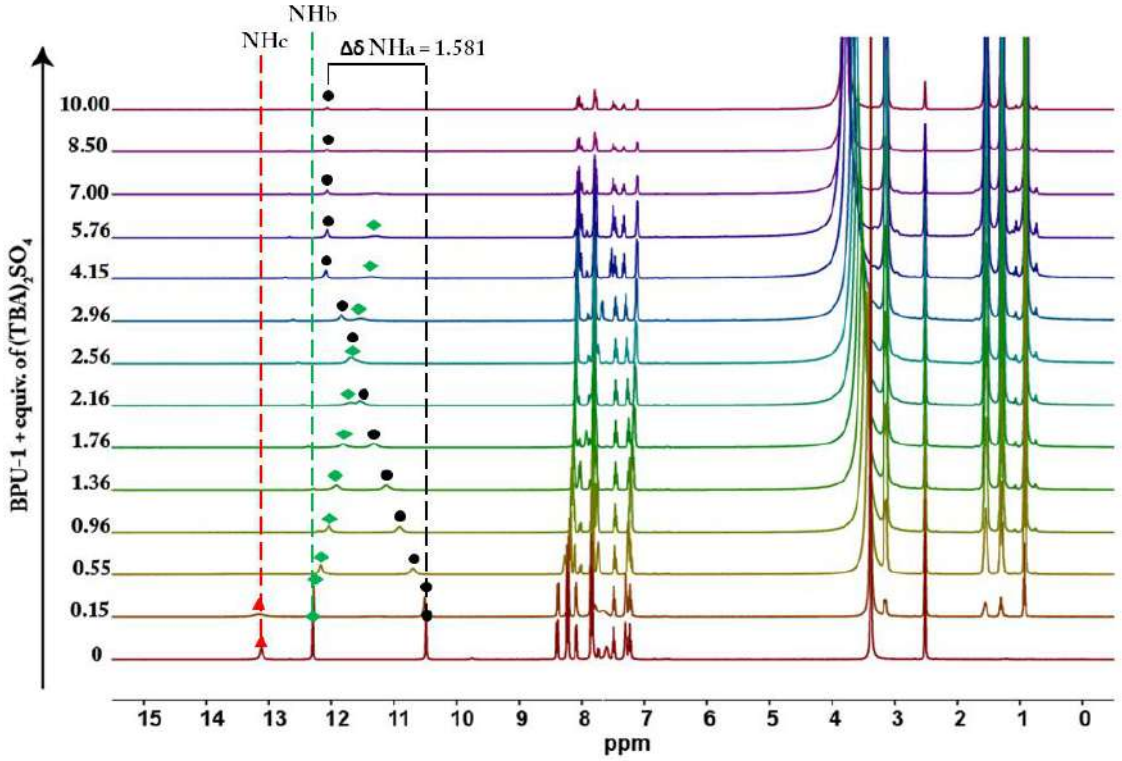

Figure A3B.10: ^{1}H-NMR titration spectra for receptor BPU-1 (50 mM) with the incremental addition of $(TBA)_2SO_4$ (1000 mM) in DMSO-d_6 solvent. The amounts of added $(TBA)_2SO_4$ are shown on the spectra.

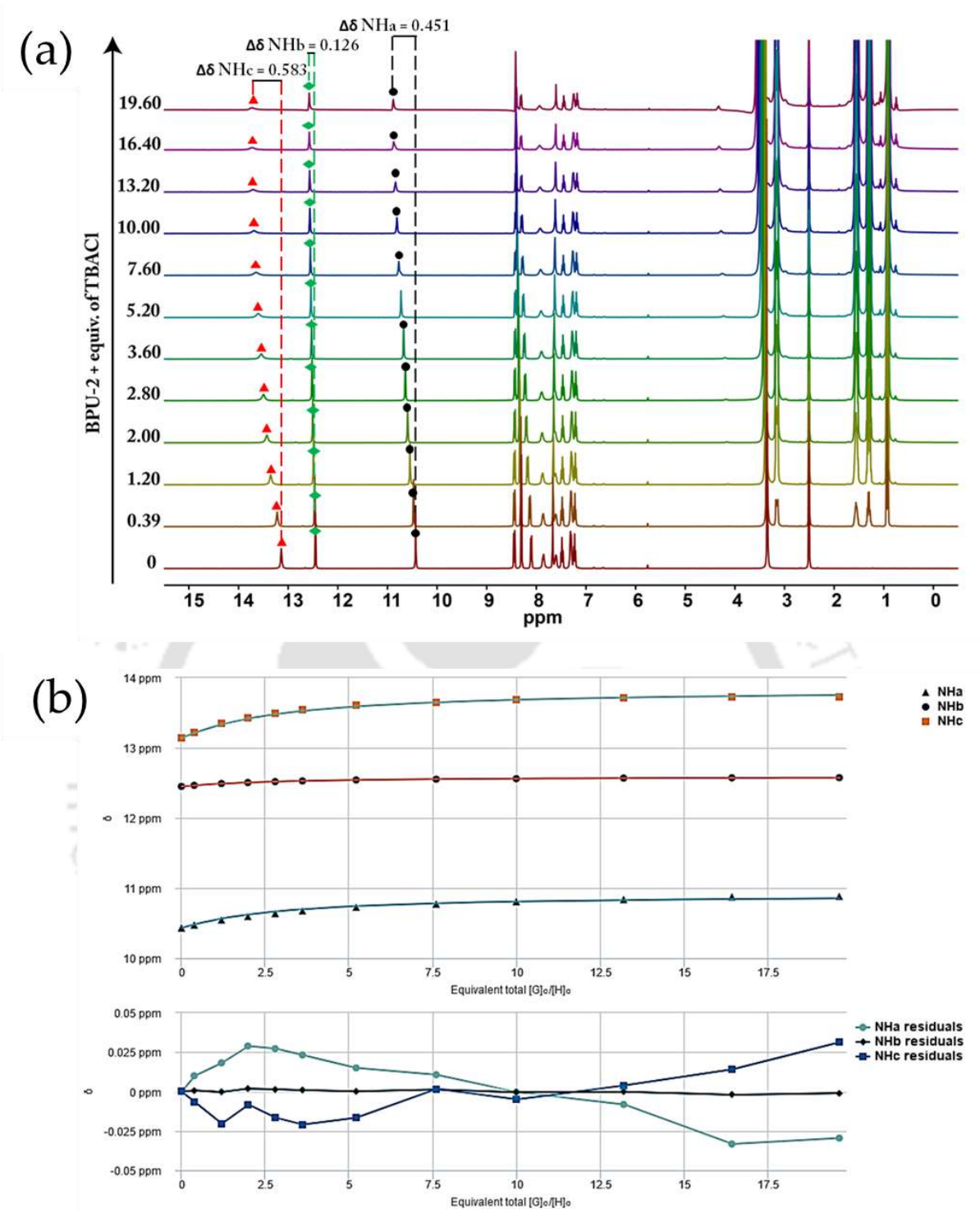

Figure A3B.11: (a) ^{1}H-NMR titration spectra for receptor BPU-2 (50 mM) with the incremental addition of TBACl (1000 mM) in DMSO-d_6 solvent. The amounts of added TBACl are shown on the spectra. (b) The plot of chemical shift (δ) of NH_a, NH_b and NH_c protons vs. Equivalent total ($[G]_0/[H]_0$) added, fitted to 1:1 binding model of BindFit v0.5 program. Here 'H' represents Host and 'G' represents Guest (TBACl).
(http://app.supramolecular.org/bindfit/view/3c15075b-cfde-4622-a30e-ce902d649eca)

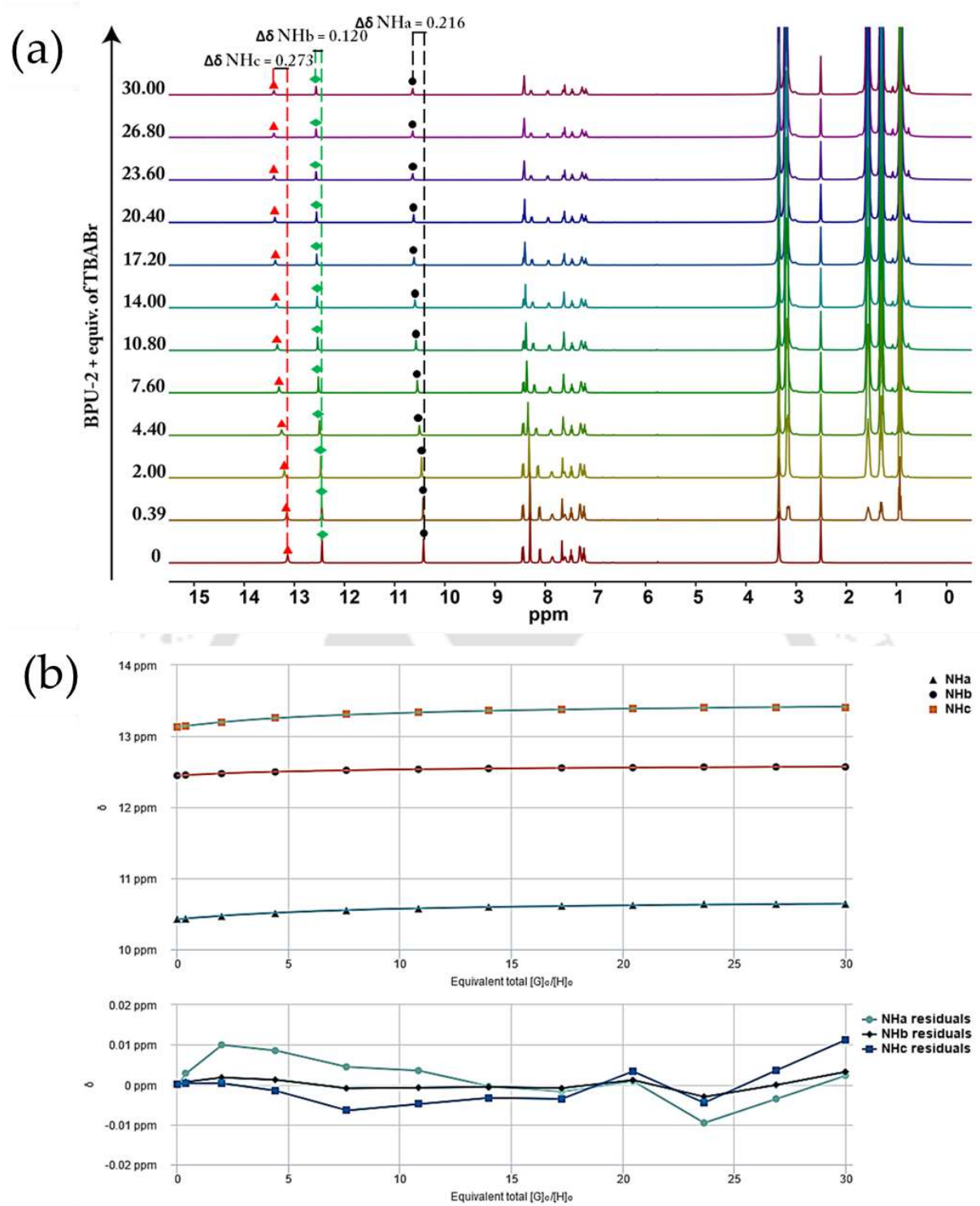

Figure A3B.12: (a) ^{1}H-NMR titration spectra for receptor BPU-2 (50 mM) with the incremental addition of TBABr (1000 mM) in DMSO-d_6 solvent. The amounts of added TBABr are shown on the spectra. (b) The plot of chemical shift (δ) of NH_a, NH_b and NH_c protons vs. Equivalent total ($[G]_0/[H]_0$) added, fitted to 1:1 binding model of BindFit v0.5 program. Here 'H' represents Host and 'G' represents Guest (TBABr). (http://app.supramolecular.org/bindfit/view/c3b34347-f8be-434e-a558-c64b08ba65bd)

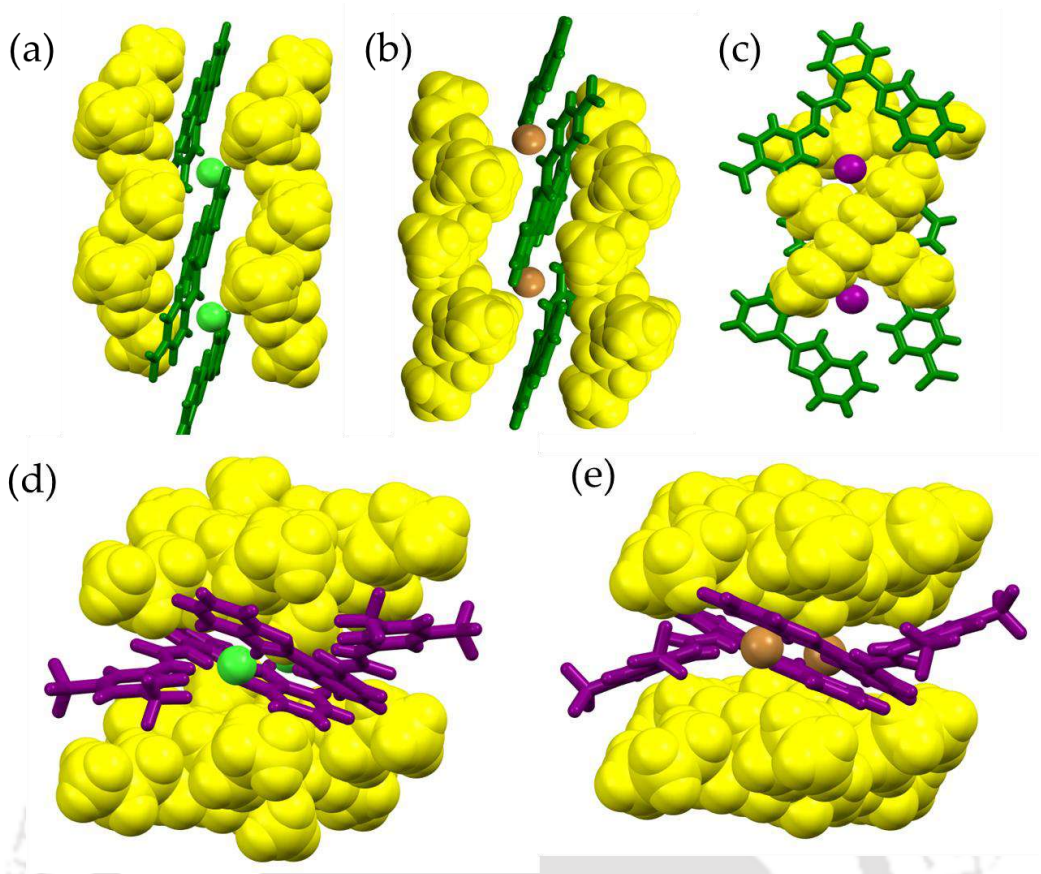

Figure A3B.13: (a), (b) & (c) Depicting encapsulation of Cl^-, Br^- and I^- anions by receptor BPU-1. (d) & (e) Encapsulation of Cl^- and Br^- by receptor BPU-2.

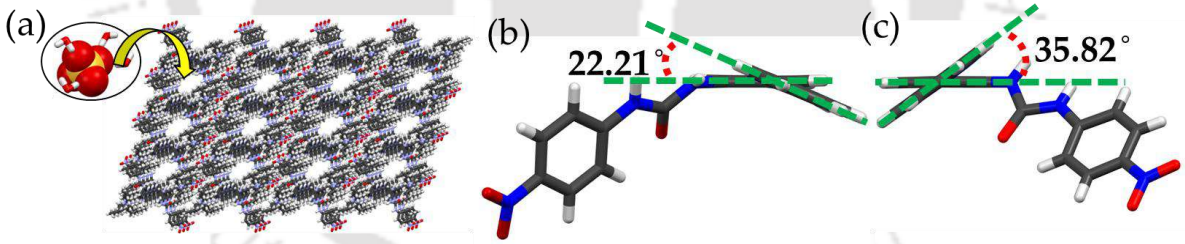

Figure A3B.14: (a) Depicting porous three-dimensional packing of the complex 1e. (b) Dihedral angle between the spacer phenyl ring and the benzimidazole ring of BPU-1.DMF. (c) Dihedral angle between the spacer phenyl ring and the benzimidazole ring of complex 1e.

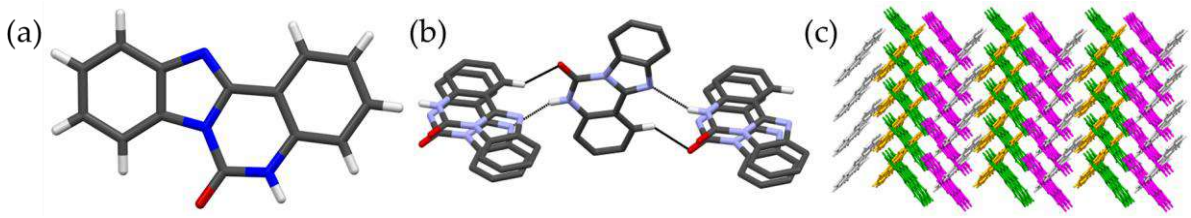

Figure A3B.15: (a) Crystal structure of BP-Cyc (already reported, DOI: 10.1039/c8qo01039k, CCDC No.: 1858811). (b) Intermolecular hydrogen-bonding interaction in BP-Cyc. (c) Symmetry operation view of BP-Cyc.

Table A3B.2.1: Crystallographic parameters and refinement data of anionic complex of BPU-1.

Parameters	1a	1b	1c	1d	1e
Formula	C_{36} H_{51} Cl N_6 O_3	C_{36} H_{51} Br N_6 O_3	C_{36} H_{51} I N_6 O_3	C_{36} H_{51} N_7 O_6	C_{36} H_{56} N_6 O_9 S
Fw	651.27	695.73	742.72	677.83	748.92
cryst syst	monoclinic	monoclinic	monoclinic	monoclinic	triclinic
space group	P 21/c	P 21/c	P 21/c	P 21/c	P -1
a (Å)	8.4951(11)	8.629(4)	10.2431(6)	8.808(3)	10.9597(13)
b (Å)	26.155(3)	25.728(11)	18.8471(10)	26.961(10)	11.9554(14)
c (Å)	16.640(2)	16.934(7)	19.6472(10)	15.403(6)	17.461(2)
α (deg)	90	90	90	90	90.263(3)
β (deg)	94.070(4)	91.993(13)	103.535(2)	93.569(10)	104.114(3)
γ (deg)	90	90	90	90	111.572(3)
V (Å^3)	3687.9(8)	3757(3)	3687.6(3)	3651(2)	2052.2(4)
Z	4	4	4	4	2
DC (g cm^{-3})	1.173	1.230	1.338	1.233	1.212
μ (Mo Kα) (mm^{-1})	0.145	1.135	0.910	0.085	0.136
F (000)	1400.0	1472.0	1544.0	1456.0	804.0
T (K)	297 K	296 K	297 K	138 K	295 K
θmax (deg)	24.709	24.999	24.999	24.998	23.248
total no. of rflns	97957	64193	85420	84317	43258
no. of indep rflns	6231	6595	6504	6412	5877
no. of obsd rflns	4190	4634	5148	5533	4849
no.of params refined	428	423	431	458	497
R1, I > 2σ(I)	0.0781(4190)	0.0569(4634)	0.0309(5148)	0.0389(5533)	0.0798(4849)
wR2, I > 2σ(I)	0.2898(6231)	0.1855(6595)	0.0889(6504)	0.1210(6412)	0.2420(5877)
GOF (F^2)	1.161	1.016	1.100	1.009	1.065
CCDC no.	2249703	2267434	2267435	2249708	2249710

Table A3B.2.2: Crystallographic parameters and refinement data of the receptors and anionic complex of BPU-2.

Parameters	BPU-1.DMF	BPU-2	2a	2b
formula	C_{23} H_{22} N_6 O_4	C_{22} H_{14} F_6 N_4 O	C_{38} H_{50} Cl F_6 N_5 O	C_{38} H_{50} Br F_6 N_5 O
fw	446.46	464.37	742.28	786.74
cryst syst	triclinic	orthorhombic	monoclinic	monoclinic
space group	P -1	P b c n	P 21/n	P 21/n
a (Å)	9.1317(13)	26.291(5)	8.455(2)	8.5817(4)
b (Å)	9.9054(15)	8.9895(18)	17.814(4)	18.2004(8)
c (Å)	12.6587(19)	16.892(4)	25.303(6)	25.6804(11)
α (deg)	104.002(4)	90	90	90
β (deg)	99.789(4)	90	94.265(7)	94.260(2)
γ (deg)	93.797(4)	90	90	90
V ($Å^3$)	1087.9(3)	3992.2(14)	3800.7(16)	3999.9(3)
Z	2	8	4	4
DC (g cm^{-3})	1.363	1.505	1.297	1.306
μ (Mo Kα) (mm^{-1})	0.097	0.137	0.167	1.091
F (000)	468.0	1888.0	1568.0	1640.0
T (K)	297 K	138 K	138 K	297 K
θmax (deg)	25.000	26.350	24.999	24.998
total no. of rflns	28589	93782	78515	80578
no. of indep rflns	3766	4029	6677	7043
no. of obsd rflns	3350	3641	5220	4387
no.of params refined	309	311	476	477
R1, I > 2σ(I)	0.0899(3350)	0.0539(3641)	0.0602(5220)	0.0560(4387)
wR2, I > 2σ(I)	0.2705(3766)	0.1325(4029)	0.1197(6677)	0.1675(7043)
GOF (F^2)	1.126	1.030	1.243	0.984
CCDC no.	2249705	2249712	2249713	2267436

Table A3B.3: Hydrogen bonding distances (Å) and Bond angles (°) in the neutral receptors and their anionic complexes.

Ligand/Complex	D–H···A	d(D···H)/Å	d(H···A)/Å	d(D···A)/Å	<D–H···A/°	Symmetry codes
BPU-1.DMF	N2-H2N···O4	0.86	2.08	2.8589 (4)	151	1-x, 1-y, 1-z
	N3-H3N···N4	0.82	2.14	2.7876 (4)	136	x, y, z
	N5-H5N···O3	0.78	2.11	2.8816 (4)	171	1-x, 1-y, -z
	C3-H3A···O3	0.93	2.28	2.8549 (4)	120	x, y, z
	C8-H8···O3	0.93	2.59	2.9114 (4)	101	x, y, z
1a	N2-H2N···CL1	0.84	2.38	3.1832 (4)	161	-1+x, 1/2-y, -1/2+z
	N3-H3N···N1	0.85	1.93	2.6529 (3)	142	x, y, z
	N4-H4N···CL1	0.86	2.40	3.2492 (4)	170	-1+x, y, z
	C9-H9···N2	0.93	2.59	2.9136 (4)	101	x, y, z
	C12-H12···O1	0.93	2.30	2.8523 (4)	117	x, y, z
	C16-H16···CL1	0.93	2.81	3.6198 (5)	146	-1+x, y, z
	C20-H20···O1	0.93	2.23	2.8251 (4)	121	x, y, z
1b	N1-H1N···Br1	0.77	2.59	3.3376 (15)	164	x, 1/2-y, -1/2+z
	N3-H3N···N2	0.86	2.04	2.6694 (12)	129	x, y, z
	N4-H4N···Br1	0.86	2.54	3.3906 (16)	171	x, y, z
	C00L-H00G···Br1	0.97	2.89	3.8459 (18)	169	1+x, y, z
	C11-H11···N1	0.93	2.58	2.9123 (13)	101	x, y, z
	C14-H14···O1	0.93	2.32	2.8611 (13)	117	x, y, z
	C18-H18···O1	0.93	2.24	2.8396 (13)	122	x, y, z
	C22-H22···Br1	0.93	2.92	3.7394 (17)	147	x, y, z
1c	N1-H1N···I1	0.79 (3)	2.87 (3)	3.639 (2)	165 (3)	2-x, ½+y, ½-z
	N3-H3N···N2	0.84 (3)	2.02 (3)	2.700 (3)	138 (2)	x, y, z
	N4-H4N···I1	0.75 (2)	3.04 (2)	3.756 (2)	161 (2)	x, y, z
	C9-H9···N1	0.93	2.55	2.889 (4)	102	x, y, z
	C12-H12···O1	0.93	2.25	2.831 (3)	120	x, y, z
	C20-H20···O1	0.93	2.34	2.838 (3)	113	x, y, z
	C25-H25A···O2	0.97	2.55	3.514 (3)	176	1-x, -y, -z
	C34-H34B···O1	0.97	2.50	3.380 (3)	150	1+x, y, z

Ligand/Complex	D–H···A	d(D···H)/Å	d(H···A)/Å	d(D···A)/Å	<D–H···A/°	Symmetry codes
1d	N1-H1N···O4	0.92	2.45	3.0980 (12)	127	x, 1/2-y, 1/2+z
	N1-H1N···O6	0.92	2.00	2.9012 (11)	167	x, 1/2-y, 1/2+z
	N3-H3N···O5	0.93	2.52	3.1202 (12)	123	x, y, z
	N3-H3N···N2	0.93	1.87	2.6628 (10)	142	x, y, z
	N4-H4N···O5	0.85	1.98	2.7868 (11)	159	x, y, z
	C4-H4A···O4	0.95	2.55	3.3959 (13)	148	x, y, z
	C9-H9···N1	0.95	2.57	2.9034 (11)	101	x, y, z
	C9-H9···O6	0.95	2.44	3.3818 (13)	170	x, 1/2-y, 1/2+z
	C12-H12···O1	0.95	2.31	2.8953 (11)	119	x, y, z
	C16-H16···O1	0.95	2.27	2.8671 (11)	120	x, y, z
	C20-H20···O4	0.95	2.55	3.4499 (13)	159	x, y, z
	C23-H23B···O4	0.99	2.53	3.2986 (13)	135	x, y, z
	C25-H25B···O5	0.99	2.44	3.3474 (13)	152	1+x, y, z
	C29-H29A···O5	0.99	2.33	3.2508 (13)	155	1+x, y, z
	C31-H31A···O2	0.99	2.58	3.3114 (13)	130	2-x, 1-y, -z
1e	N2-H2N···O5	0.86	2.00	2.8135 (3)	158	-1+x, y, z
	N3-H3N···O5	0.86	2.05	2.8277 (3)	150	-1+x, y, z
	N4-H4N···O9	0.85	1.90	2.7172 (3)	161	x, y, z
	N5-H5N···O7	0.95	1.67	2.6072 (3)	167	x, y, z
	O8-H8A···O4	1.00	2.45	2.9125 (3)	108	1-x, 1-y, 1-z
	O8-H8B···O5	0.84	2.14	2.9614 (4)	165	-1+x, y, z
	O9-H9A···O6	0.78	2.12	2.8509 (3)	158	-1+x, y, z
	O9-H9B···O6	0.90	1.98	2.8599 (3)	166	1-x, -y, 1-z
	C9-H9···O4	0.93	2.50	3.4279 (4)	177	x, y, z
	C20-H20···O3	0.93	2.28	2.8803 (3)	122	x, y, z
	C22-H22A···O3	0.97	2.59	3.5513 (4)	169	x, y, z
	C25-H25A···O8	0.97	2.56	3.3724 (4)	141	1+x, y, z
	C27-H27B···O8	0.97	2.51	3.4023 (4)	153	1+x, y, z
	C33-H33B···O7	0.97	2.44	3.3027 (4)	148	x, y, z

Ligand/Complex	D–H···A	d(D···H)/Å	d(H···A)/Å	d(D···A)/Å	<D–H···A/°	Symmetry codes
BPU-2	N1-H1N···O1	0.92	1.92	2.8300 (7)	171	-x, -y, -z
	N3-H3N···N2	0.89	2.12	2.8353 (7)	137	x, y, z
	N4-H4N···N2	0.91	2.04	2.9448 (7)	172	-x, y, 1/2-z
	C12-H12···O1	0.95	2.36	2.8576 (7)	112	x, y, z
	C16-H16···O1	0.95	2.27	2.8682 (7)	120	x, y, z
2a	N1-H1N···CL1	0.91	2.32	3.2115 (8)	169	3/2-x, 1/2+y, 1/2-z
	N3-H3N···N2	0.89	1.90	2.6792 (6)	145	x, y, z
	N4-H4N···CL1	0.92	2.33	3.2279 (8)	164	x, y, z
	C9-H9···N1	0.95	2.55	2.8845 (7)	101	x, y, z
	C11-H11···O1	0.95	2.56	3.4079 (8)	148	2-x, 1-y, 1-z
	C12-H12···O1	0.95	2.25	2.8141 (7)	118	x, y, z
	C16-H16···O1	0.95	2.34	2.7996 (7)	109	x, y, z
	C23-H23A···CL1	0.99	2.82	3.7130 (9)	150	-1+x, y, z
	C25-H25B···F3	0.99	2.49	3.3982 (8)	153	1-x, -y, 1-z
2b	N2-H2N···Br1	0.78 (4)	2.63 (4)	3.385 (4)	162 (4)	3/2-x, -1/2+y, ½-z
	N3-H3N···N1	0.78 (4)	2.01 (4)	2.683 (5)	144 (4)	x, y, z
	N4-H4N···Br1	0.85 (4)	2.57 (4)	3.403 (4)	167 (3)	x, y, z
	C9-H9···N2	0.93	2.56	2.899 (6)	102	x, y, z
	C12-H12···O1	0.93	2.27	2.807 (5)	116	x, y, z
	C20-H20···O1	0.93	2.33	2.802 (5)	111	x, y, z
	C29-H29B···Br1	0.97	2,92	3.826 (4)	156	x, y, z

Chapter 4A

Micellar Medium Assisted Recognition Guided Ultrafast Sensing of Cyanide in Water via Fluorogenic Nano-probes

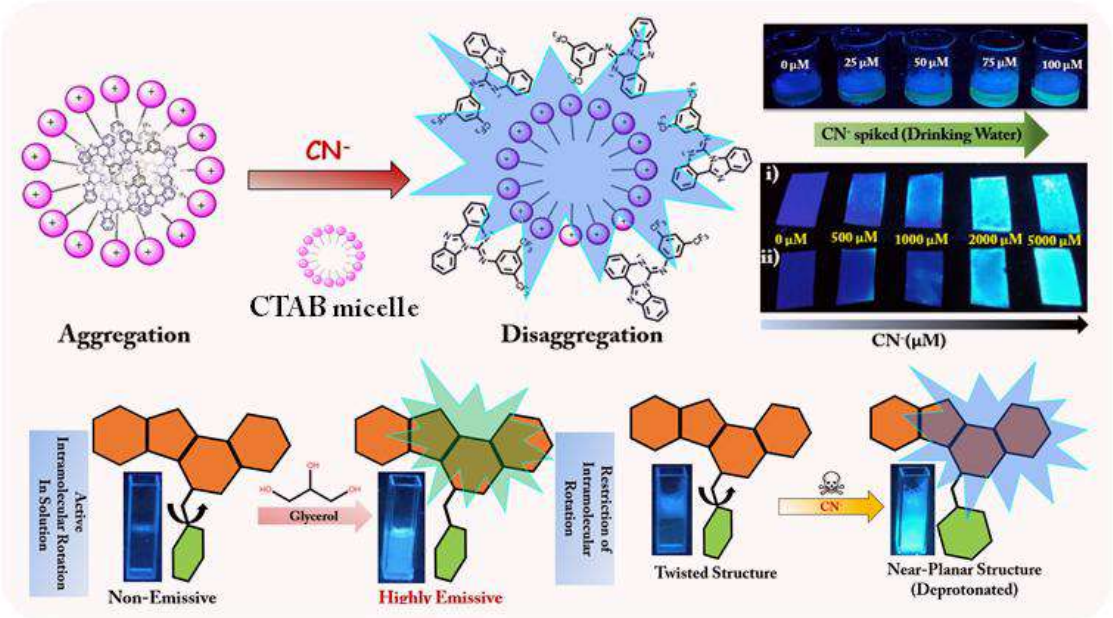

CHAPTER 4A

4A.1. Background and Focus of the Chapter

In recent times, development of selective and sensitive sensors for anions has received much attention owing to their vital role in environmental and biological applications. [4A.1-4A.9] Among various anions, cyanide (CN^-) is considered one of the most poisonous anions owing to its extreme toxicity towards human. [4A.10] Even at a very low concentration it causes serious health issues such as histotoxic anoxia, eventually leading to death. [4A.11, 4A.12] The long-term exposure to cyanide can cause severe health complications, including neurological damage, cardiovascular diseases, respiratory problems, and kidney damage.[4.13-4A.15] Despite such hazardous nature of CN^-, it still finds widespread use in various industries such as metal mining, jewellery manufacturing, electroplating, etc. [4A.16] Accidental leakage and inappropriate disposal of CN^- containing waste materials from various industries are potential threats to the environment. [4A.17] According to the World Health Organization (WHO), the maximum acceptable concentration of CN^- in drinking water is considered to be 1.9 μM. [4A.18] Therefore, there is growing interest in the development of highly selective as well as sensitive artificial chemosensors for CN^-, especially in aqueous medium. [4A.19-4A.21]

However, the detection of CN^- in an aqueous medium is challenging, yet very important from the biological point of view. Over the past decade, there has been a surplus of articles published on CN^- sensing in water by using different chromogenic and fluorogenic sensors. [4A.22-4A.25] Fluorescent chemosensors stand among different chemosensors as they offer specific advantages such as high sensitivity, remarkable selectivity, and accurate quantification. [4A.26-4A.29] The most commonly employed approaches for CN^- detection encompass the hydrogen bonding approach, chemodosimetric method, and deprotonation reaction-based sensing. [4A.30–4A.33] However, the high solvation energy of CN^- makes it difficult to achieve its effective or efficient sensing in aqueous medium. So, in terms of achieving superior sensitivity, selectivity, and applicability, there is still much room for improvement. Considering these, lately, researchers have started using surfactant molecules in the sensing process of different analytes, for the sake of achieving greater sensitivity as well as selectivity in an aqueous medium. [4A.34] Recently, Dey et al. have demonstrated how the use of surfactant molecules improves the overall selectivity and sensitivity of their sensory systems toward cyanide ions. [4A.35] A few years back, Yu et al. developed a highly sensitive as well as selective chemosensor for CN^- in aqueous medium with the assistance of cetyltrimethylammonium bromide (CTAB). [4A.36] With the

growing interest in the detection of toxic analytes in water with fluorescence detection methods, such as surfactant-assisted fluorescence detection method opens up a new avenue in the field of sensing toxic analytes.

In recent times the relatively simple yet fascinating concept that governs TICT has received plenty of attention [4A.37] since the ground-breaking review on TICT by Grabowski et al., [4A.38] as it opens up myriad possibilities for designing novel functional molecules. Modulating TICT could significantly alter the fluorescence behaviour of TICT compounds, which holds great promise for constructing fluorescent probes with excellent environmental sensitivity. [4A.39] The TICT relaxation pathways can be easily manipulated by substituents, local polarity, steric restrictions, etc., thus offering its applicability in various fields such as biomedical imaging and diagnostics, OLEDs, chemosensors, and photovoltaic devices. In spite of all such advantages, the TICT mechanism is seldom used to design fluorescent probes, the reason might be due to the difficulty in controlling the degree of electron transfer, and the alteration in molecular geometry. [4A.40-4A.42]

In our continuing effort to design various fluorescent probes for anion sensing in an aqueous medium, [4A.43-4A.50] in the present study, highly sensitive and selective sensing of CN^- in an aqueous medium by TICT active probes with the assistance of CTAB is demonstrated. The CN^- caused deprotonation inflicts significant changes in the pre-twisted geometries of the probes by restricting their intramolecular rotations. Such restriction in the intramolecular rotation is expected to prevent the generation of the TICT state, thus leading to significant spectral changes in both UV-vis and fluorimetric studies. CTAB improves the overall sensing process quite significantly in an aqueous medium by providing a viable environment for the same, thus bestowing our sensor system with a very low detection limit of 496.5 nM, and a very short sensing process within a few seconds. Moreover, the TICT probes preferentially self-assemble to form nano-aggregates in the solution state with the help of various non-covalent interactions, and such nano-aggregates disassemble in the presence of CN^- causing significant spectral changes in both UV-vis and fluorescence studies. We have presented the real-world applicability of our probes by demonstrating real-time monitoring of CN^- in drinking water under a UV-lamp, with the help of CTAB, which could be monitored in the solid state as well, by using cost effective paper strips coated with our probes. We have also demonstrated the tunability of sensitivity as well as selectivity of both the probes towards CN^- just by altering their substituents.

4A.2. Objective of the Chapter

Twisted benzimidazoquinazoline based fluorogenic probes (Benz-d-CF_3 and Benz-m-CF_3) with varying pi-acidic terminal substituents showed TICT (twisted intramolecular charge transfer)

behaviour. They formed self-assembled nano-aggregates in an aqueous CTAB medium, and only Benz-d-CF_3 displayed a selective fluorescence turn-on response toward CN^- in a 100% aqueous medium. However, the sensitivity and selectivity of fluorescence sensing towards CN^- enhanced exponentially in aqueous medium in the presence of CTAB. Probe Benz-d-CF_3 had a detection limit as low as 496.5 nM and a high-speed fluorescence response time, which promises its practical application for detecting CN^- in drinking water. The assistance of micelle systems facilitates a very fast, sensitive and selective detection of CN^- in water. The sensitivity as well as selectivity of the probes towards CN^- can just be fine-tuned by varying their terminal substituents. A detailed mechanistic insight of the role of the micelle system in such a sensing process has been investigated in this study. Moreover, this particular idea can also be expanded towards developing a portable device for the detection of CN^- in drinking water, which has been demonstrated in this particular study.

4A.3. Results and Discussion

4A.3.1. Design Rationale of Probes Benz-d-CF_3 and Benz-m-CF_3

Quinazoline-fused benzimidazole scaffolds with varying pi-acidic terminal substituents having donor–acceptor characteristics have been designed (namely, Benz-d-CF_3 and Benz-m-CF_3), where both donor and acceptor units are interconnected via imine linkage. The acceptor unit, that is the pi-acidic phenyl ring, is twistable around the single bond connected to the imine nitrogen atom, thus facilitating both the probes to behave as twisted-intramolecular-charge-transfer (TICT) molecules. (Scheme 4A.1) Apart from having such fascinating photophysical properties, the presence of a hydrogen bond donor site (N–H unit) provides us with an opportunity to further explore their anion recognition behaviour in terms of anion sensing and the effect of the terminal substituents in such sensing phenomena.

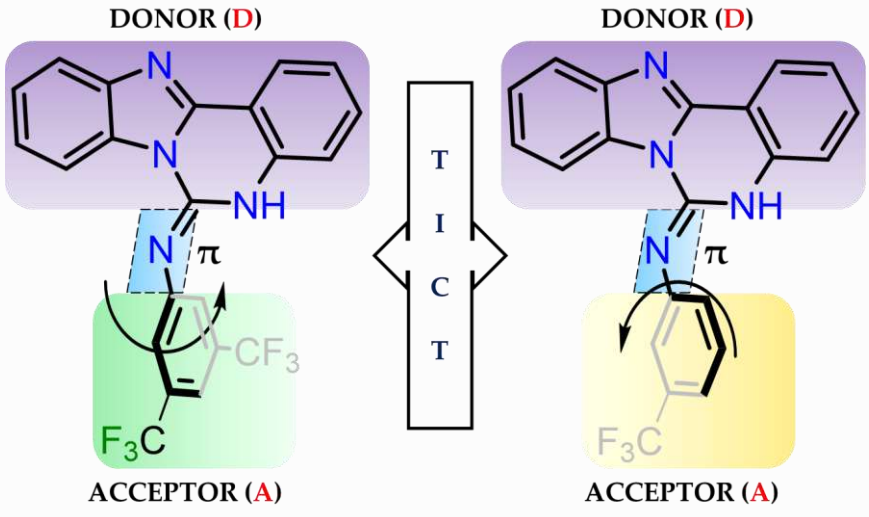

Scheme 4A.1: Design of probes Benz-d-CF_3 and Benz-m-CF_3.

4A.3.2. Solid-state Self-assembly

Solid-state structural investigation of both the probes Benz-d-CF_3 and Benz-m-CF_3 has been performed with the help of the SC-XRD (single crystal X-ray diffraction) study. Both the probes were successfully crystallized from a 1:1 solvent mixture of DMSO and ACN. We could isolate two crystals of Benz-d-CF_3, one with a water molecule (Benz-d-CF_3.H_2O) and the other with DMSO (Benz-d-CF_3.DMSO). (Figure 4A.1a,b) Both the derived structures were observed to be twisted at a certain angle, having dihedral angles of 62.66° and 63.14° respectively for Benz-d-CF_3.H_2O and Benz-d-CF_3.DMSO. (Figure A4A.32a,b) Different self-assembly patterns were observed for Benz-d-CF_3.H_2O and Benz-d-CF_3·DMSO. (Figure A4A.33a,b,d,e) Hydrogen bonding interaction as well as pi–pi interaction plays a major role in the self-assembly formation in both Benz-d-CF_3.H_2O and Benz-d-CF_3.DMSO. In Benz-d-CF_3.H_2O, the water molecules act as a bridging unit between two nearby Benz-d-CF_3 molecules with the help of hydrogen bonding interactions (O1···H3N = 1.97 Å, O1···H12 = 2.70 Å, H2O···N1 = 2.09 Å). Two of the nearby Benz-d-CF_3 molecules are observed to be arranged in an anti-parallel fashion, which forms pseudo-capsular cavities with the assistance of water molecules, and are held firmly via π···π interactions (π···π = 3.39 Å) between the two head groups (quinazoline-fused benzimidazole ring). Such pseudo-capsular cavities are interconnected via hydrogen bonding interactions (H20···N1 = 2.60 Å), thereby assisting the formation of self-assembled building blocks. Very similar head-to-head π···π interactions are also prevalent in Benz-d-CF_3.DMSO, where the distance between the two centroids of the head groups is observed to be 3.52 Å. Apart from π···π interactions, hydrogen bonding interaction plays a major role in dictating the self-assembly formation in Benz-d-CF_3·DMSO. Both π···π interactions and hydrogen bonding interactions (N1···H20 = 2.53 Å) allow two Benz-d-CF_3 molecules to form a kind of dimeric unit, where DMSO extends its arms as a bridging unit (O1···H3N = 2.04 Å, O1···H12 = 2.59 Å, F3···H23C = 2.55 Å) between two such nearby dimeric units, consequently forming a long self-assembled architecture. (Figure 4A.1d,e) Similarly, Benz-m-CF_3 was also crystallised in its twisted form (Figure 4A.1c) where the dihedral angle between the donor and the acceptor unit was observed to be 58.63°. (Figure A4A.32c) However, an altered self-assembly pattern has been observed in Benz-m-CF_3, where the adjacent molecules prefer to arrange in a head-to-tail fashion. (Figure A4A.33c,f) The head group is involved in a π···π interaction with the tail (pi acidic phenyl ring) counterpart of the adjacent molecule, where the distance between the two centroids is observed to be 3.48 Å. Here as well, hydrogen bonding interaction plays an indispensable part in the process of self-assembly formation. Unlike the other two aforementioned moieties, the –NH unit of the head group of Benz-m-CF_3 actively participates in intermolecular hydrogen bonding interaction with the nitrogen atom of the benzimidazole ring of the neighbouring molecule

(N1···H3N = 2.13 Å), thus enabling the formation of the self-assembled polymeric chain (Figure 4A.1f). (Table A4A.2, Table A4A.3)

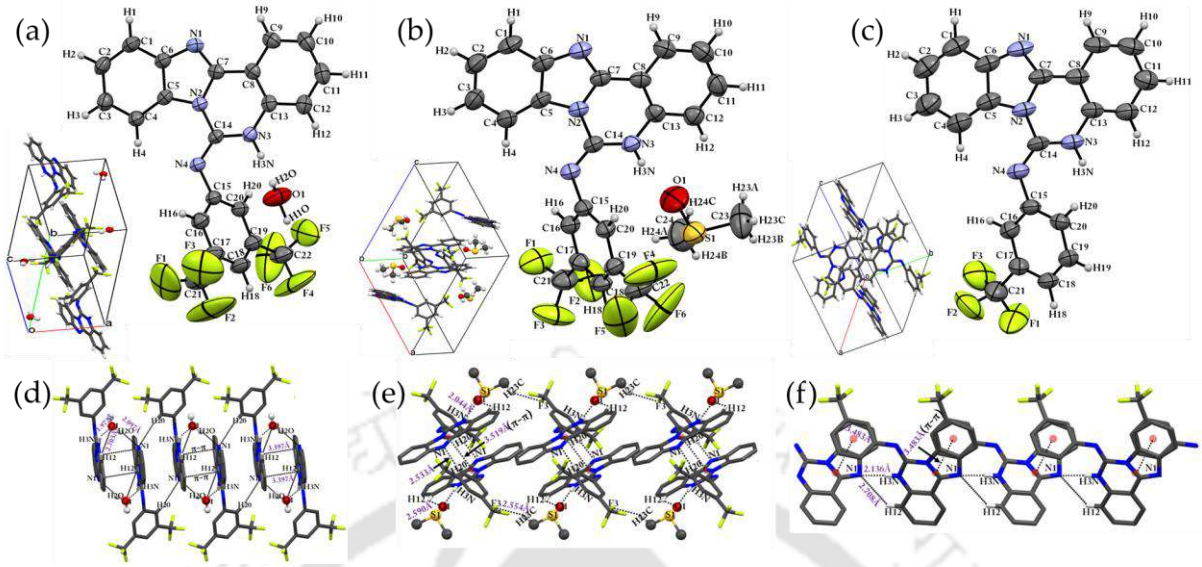

Figure 4A.1: (a)–(c) ORTEP diagram of Benz-d-CF_3·H_2O, Benz-d-CF_3·DMSO, and Benz-m-CF_3 respectively at the 50% probability level. Self-assembly formation in (d) Benz-d-CF_3·H_2O, (e) Benz-d-CF_3·DMSO and (f) Benz-m-CF_3 through various non-covalent interactions (non-interacting hydrogen atoms are omitted for clarity).

Two important points have to be noted from the solid-state structural analysis: firstly, the flexible dihedral angle between the donor and the acceptor units, which is quite noticeable in both the molecules, thus indicating their rotatability around their terminal pi-acidic phenyl rings, which makes both of them potential TICT active probes. Secondly, although the structures are observed to be twisted, all of them still are capable of forming pi–pi stacking interaction whether it is in a head-to-tail or tail-to-head fashion, indicating efficient solid-state self-assembly formation in their twisted conformations. Both these observations are significant, as they form the basis of our study in this article.

4A.3.3. UV-Vis-spectroscopy Study of Benz-d-CF_3 and Benz-m-CF_3

The UV-Vis spectra of both the probes, namely, Benz-d-CF_3 and Benz-m-CF_3, were recorded in almost 100% aqueous medium as well as in aqueous micellar medium (containing 0.2% DMSO). For both the probes, two distinct absorption peaks were observed at ~340 nm and ~355 nm in water, which might be attributable to π–π* and n–π* transitions respectively. (Figure A4A.9a,b) In aqueous CTAB medium (3 mM), the nature of the absorption peaks remains the same showing absorption peaks at ~335 nm and ~350 nm corresponding to π–π* and n–π* transitions respectively. (Figure A4A.9c,d) Both the probes did not show any distinct shift of the absorption peaks when combined with CN^- in aqueous medium. However, in an aqueous CTAB medium, for Benz-d-CF_3 the aforesaid two distinct peaks coalesce upon CN^- addition with a bathochromic

shift of the absorption peak giving rise to a new well-defined peak at ~360 nm having a higher absorption value along with a shoulder peak at ~400 nm indicating some sort of interaction of the probe with CN^-. (Figure A4A.9c) A somewhat similar behaviour was observed in the case of Benz-m-CF_3 as well in an aqueous CTAB medium, although the extent of coalescence of the absorption peaks at ~335 nm and ~350 nm was not that high, but the absorption peak was observed to be shifted upward along with the generation of a shoulder peak at ~400 nm. (Figure A4A.9d) Such distinct peak shifting towards the red region upon CN^- addition strongly suggests ICT (intramolecular charge transfer) phenomena.

4A.3.4. Fluorescence Spectroscopy Study and Investigating TICT

The fluorescence spectrum of both the probes Benz-d-CF_3 and Benz-m-CF_3 recorded in ~100% aqueous medium (contains 0.2% DMSO) revealed a very weak fluorescence emission at ~390 nm wavelength, which is ascribable to the locally excited (LE) state, (Figure A4A.10a,b) and the reason for such weak emission might be attributable to TICT phenomena. To affirm our TICT claim we conducted solvent polarity as well as viscosity-dependent fluorescence spectroscopic study for both the probes. As we increased the solvent polarity from hexane to acetonitrile bathochromic shift of the emission spectra of Benz-d-CF_3 was observed from 395 nm to 455 nm, (Figure A4A.13) which confirms the existence of intramolecular charge transfer property in the probe. To further realise whether the restriction of the intramolecular rotation of the probe had a direct impact on the emission intensity of the probe, we recorded the fluorescence spectra of Benz-d-CF_3 by varying solvent viscosity, which was done by varying water and glycerol ratios. Interestingly, it was observed that, as we increased the solvent viscosity from 0% glycerol to 100% glycerol, systematic enhancement of the fluorescence emission was observed with a ~50-fold enhancement in the emission intensity at 390 nm in 100% glycerol as compared to that of 100% water. (Figure 4A.2a) Such viscosity-dependent fluorescence change strongly validates the existence of TICT phenomena in the system. Similar experiments were also conducted for Benz-m-CF_3; although the probe was sensitive towards solvent polarity, it behaved non-uniformly. However, it showed viscosity-sensitive nature, where its emission intensity at 390 nm was enhanced regularly with an increase in the percentage of glycerol. We recorded ~70-fold enhancement in emission intensity in 100% glycerol as compared to that of 100% water, (Figure 4A.2b) which firmly validates the existence of TICT phenomena in Benz-m-CF_3. Such enhanced emission in a highly viscous medium (glycerol in this case) results from restriction in the intramolecular rotation of both probes, eventually obstructing TICT state formation. We also investigated the morphology of the probes in their restricted forms, and to do that, we performed FESEM imaging of both the probes in glycerol, which revealed a very similar morphology for

both probes, where the small rice grain-like particles were observed to form larger aggregates, completely distinctive from the glycerol alone. (Figure A4A.28a-c) We further performed a solid-state fluorescence spectroscopic study of the crystals of both probes, which unveiled a sharp fluorescence emission of the LE state at 390 nm, which is comparable to that of a glycerol medium. Such strong fluorescence enhancement of the LE state in its crystalline form is ascribable to the restriction of intramolecular rotation in the solid state. Hence, all the evidence obtained from both the solid and solution phase study strongly suggests that the reason for the weak fluorescence observed for both the probes in the solution state is due to TICT phenomena as induced by intramolecular rotation.

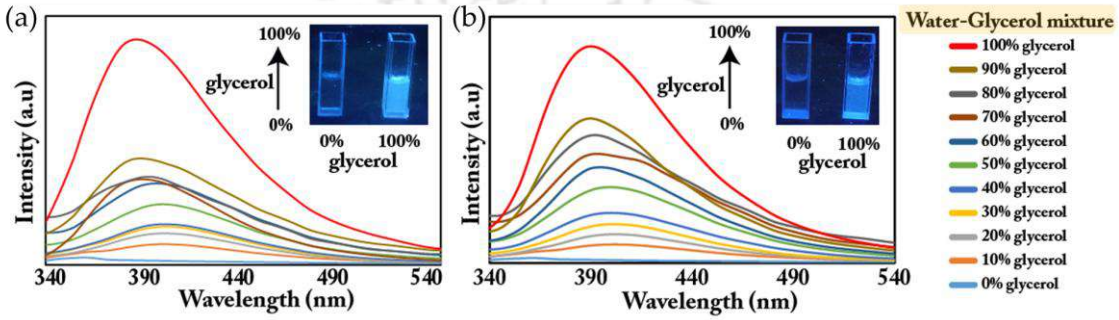

Figure 4A.2: Fluorescence spectra of (a) Benz-d-CF_3 and (b) Benz-m-CF_3 in a water–glycerol mixture of different ratios, depicting fluorescence changes with viscosity.

Besides the study conducted in an aqueous medium, we were also very keen on investigating the fluorescence behaviour of both probes in an aqueous micellar medium. While performing a fluorescence spectroscopic study in an aqueous medium containing CTAB, apart from having an emission peak at 390 nm for both the probes, additional new emission peaks at 460 nm (relatively strong) and 485 nm (relatively weak) were observed for Benz-d-CF_3 and Benz-m-CF_3, respectively. (Figure A4A.10c,d) Such an improved fluorescence response along with red-shifted emission indicates a lowering of conformation flexibility of the probes inside the micellar cavity, thus promoting the extent of intramolecular charge transfer. We made a conscious decision to choose a cationic surfactant, i.e. CTAB, as it is well known from the literature that the pK_a of the encapsulated organic dye molecules in a cationic surfactant diminishes, which is presumably due to charge pairing between the conjugate anion generated from the dye molecule and the positive head groups of CTAB, [4A.35, 4A.51] which will instinctively help in improving the sensitivity of the probes towards CN^-.

4A.3.5. Fluorescence Response to Cyanide in Water

Fluorescence response of both Benz-d-CF_3 and Benz-m-CF_3 was investigated in the presence of different anions encompassing F^-, Cl^-, Br^-, I^-, NO_3^-, SO_4^{2-}, HSO_4^-, $H_2PO_4^-$, ClO_4^-, CN^-, HO^-,

and CH_3COO^- (using their tetrabutyl ammonium salts), where probe Benz-d-CF_3 was found to be selectively responsive towards CN^- among all the other studied anions in water. Probe Benz-d-CF_3 could render a significant turn-on fluorescence response at 450 nm instigating ~3-fold enhancement in the emission intensity with a concomitant large redshift of ~60 nm (from 390 nm to 450 nm) in the presence of CN^-, whereas all the other anions remained silent to the fluorescence spectral changes when combined with Benz-d-CF_3. The bright blue fluorescence upon CN^- addition into the aqueous solution of Benz-d-CF_3 was conspicuous under a UV-lamp (at 365 nm); however, the other anions could not render any such distinct fluorescence emission. (Figure 4A.3a,b; Figure A4A.22) Interestingly, the fluorescence response was perceived only when instant fluorescence measurement of Benz-d-CF_3 was done with CN^-, which eventually falls very rapidly as time progresses, as evident from the time-dependent study of the probe with CN^- which is ascribable to rapid re-protonation followed by deprotonation. (Figure A4A.18) We further investigated the interference effect of other anions on the fluorescence enhancement of Benz-d-CF_3 by CN^-, where we did not observe any significant interference from the other anions in the enhanced fluorescence intensity induced by CN^-. (Figure 4A.3c) This observation indicates a high selectivity of Benz-d-CF_3 towards CN^- in water. Interestingly, Benz-m-CF_3 remained silent in both UV-vis and fluorescence measurements when combined with different anions. (Figure A4A.11a,-c) Such drastic change in sensing property upon removing one $-CF_3$ group is quite notable, as it allows us to modulate our probes according to our requirements. We also wondered whether the sensing could be performed by the probes in their restricted form or not, so we further investigated the CN^- sensing behaviour of both the probes in glycerol, where their rotations are expected to be restricted. We did not observe any spectral changes in the fluorescence spectral measurement when the probes were combined with CN^- in glycerol. (Figure A4A.20a,b) This observation made it clear that the probes were unable to sense CN^- in their restricted conformations.

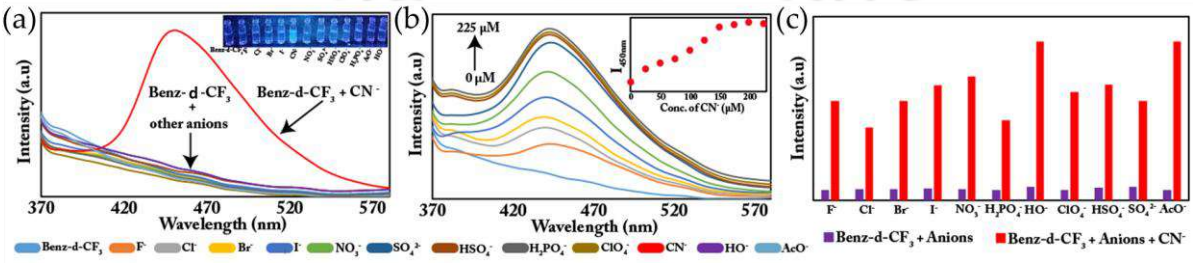

Figure 4A.3: (a) Fluorescence spectra of Benz-d-CF_3 (10 μM) in the presence of different anions (100 μM), (b) fluorescence titration of Benz-d-CF_3 (10 μM) with CN^-, and (c) emission intensity change by CN^- in the presence of other anions.

4A.3.6. Sensitive Fluorescence Detection of Cyanide with Micelles

We investigated the fluorescence response of both the probes, namely, Benz-d-CF_3 and Benz-m-CF_3, towards CN^- in an aqueous medium while using 3 mM CTAB, which is above its critical micellar concentration which is 1 mM. Formation of the CTAB micelle was confirmed through the DLS method and TEM. (Figure A4A.25, Figure A4A.29a,b) We expected an improved sensitivity vis-à-vis selectivity towards CN^- by the probe Benz-d-CF_3 in an aqueous micellar medium. Due to less hydration at the surfactant (CTAB in this case)–water interface as compared to that of the bulk water, the non-covalent interaction such as hydrogen bonding interaction and charge pairing with the target anions are expected to be improved. However, we did not expect selective CN^- sensing by the probe Benz-m-CF_3 at all in an aqueous CTAB medium, as that was the scenario in 100% water, and we were proved wrong. A very selective turn-on response towards CN^- (100 μM) was observed for Benz-d-CF_3 (10 μM) with ~9-fold enhancement of emission intensity at 460 nm. Benz-d-CF_3 was found to be non-responsive towards all the other remaining anions except for HO^-. (Figure 4A.4a) HO^- showed a similar emission enhancement at 460 nm with ~5-fold enhancement in the emission intensity as compared to that of the free Benz-d-CF_3. (Figure 4A.4b) However, Benz-m-CF_3 was found to be more selective towards CN^-, as it could selectively sense CN^- without showing any affinity towards the other studied anions. (Figure 4A.4d) A very similar red-shifted fluorescence enhancement was observed at 485 nm wavelength with ~8-fold enhancement in emission intensity for Benz-m-CF_3 as well, upon combination with CN^-. (Figure 4A.4e) The gradual red-shifted fluorescence enhancement in the presence of CN^- could be monitored through a fluorimetric titration experiment conducted with CN^- in an aqueous medium containing CTAB for both probes. (Figure 4A.4c,f) We further performed fluorescence microscopic imaging of both the probes Benz-d-CF3 and Benz-m-CF_3 in water containing CTAB (Figure 4A.9a(i),(ii); Figure 4A.9b(i),(ii)) which showed intense fluorescence in the presence of CN^- in all the channels, while minimal fluorescence intensity was observed for the free probes. This observation was in agreement with the solution-based CN^- sensing in an aqueous CTAB medium. We further studied the interference of other anions in CN^- sensing for both the probes, where we observed minimal interference from any of the competing anions, except for Bronsted acidic anions such as HSO_4^- and $H_2PO_4^-$, (Figure A4A.14a,b) which might be attributed to hydrogen bonding interaction of those anions with the deprotonated species, which inhibits the ICT process.

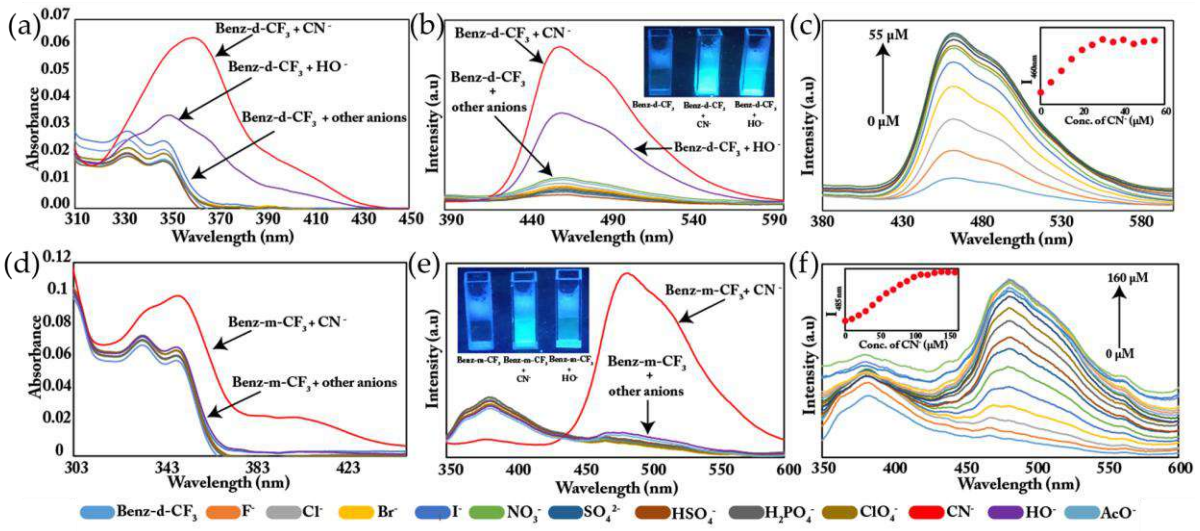

Figure 4A.4: UV-vis spectra of (a) Benz-d-CF_3 (10 μM) and (d) Benz-m-CF_3 (10 μM) in the presence of different anions (100 μM). Fluorescence spectra of (b) Benz-d-CF_3 (10 μM) and (e) Benz-m-CF_3 (10 μM) in the presence of different anions (100 μM). Fluorescence titration experiment of (c) Benz-d-CF_3 (10 μM) and (f) Benz-m-CF_3 (10 μM) with incremental addition of CN^-.

The binding stoichiometry of both Benz-d-CF_3 and Benz-m-CF_3 with CN^- was measured in aqueous solutions containing CTAB. From Job's plot analysis, we could observe a maximum at 0.5 mole fraction, which might indicate 1:1 binding stoichiometry of both the probes with CN^-. (Figure A4A.16; Figure A4A.17) We have also calculated the detection limit through the fluorescence titration experiment, where nanomolar level detection of CN^- was accomplished through Benz-d-CF_3 with a detection limit of 496.5 nM, whereas with the probe Benz-m-CF_3 the LOD was calculated to be 3.73 μM, (Figure A4A.23; Figure A4A.24) which compares well with previous reports. (Table A4A.4)

4A.3.7. Mechanistic Investigation of Cyanide Sensing

As evident from Job's plot, both the probes, namely, Benz-d-CF_3 and Benz-m-CF_3, were observed to be involved in 1:1 binding stoichiometry with CN^- in water as well as in aqueous CTAB medium. (Figure A4A.15-Figure A4A.17) While investigating the plausible mechanism of cyanide sensing, our next objective was to identify the primary interaction site of CN^- in Benz-d-CF_3 and Benz-m-CF_3. To do that, we performed ^1H NMR titration experiment of both the probes with CN^- in DMSO-d_6, where severe broadening of the peak corresponding to the –NH group was observed in the presence of CN^-, which eventually vanishes upon the addition of ~2 equiv. of CN^-, signifying the hydrogen bond induced rapid dynamic effect followed by deprotonation. (Figure 4A.8a,b) A completely new set of sharp peaks were observed after the addition of ~2 equiv. of CN^- in both cases, which are observed to be the same peaks obtained

from the isolated crystals of the deprotonated species (TBA^+ $[Benz\text{-}d\text{-}CF_3]^-$ and TBA^+ $[Benz\text{-}m\text{-}CF_3]^-$), (Figure A4A.7, Figure A4A.8) which has also been confirmed through mass spectrometry as well. (Figure A4A.3, Figure A4A.6) However, most of the aromatic peaks were observed to be shifted to the upfield region, which is attributable to the changes in the electronic environment in the aromatic ring due to CN^- caused deprotonation. The FT-IR study of the crystals of the deprotonated species showed a broadening of the initially observed sharp peak corresponding to the –NH group. Apart from that, the FT-IR peak corresponding to the C=N group was also observed to be shifted to the lower energy region owing to the changes in the electronics of the nearby –NH group due to CN^- caused deprotonation. (Figure A4A.2, Figure A4A.5) The long rod-shaped aggregated morphology of free Benz-d-CF_3 (drop cast using water as a solvent) was also observed to be completely disintegrated in the presence of CN^- as evident by FESEM. (Figure 4A.7a,d)

It is very interesting to note that, initially the structures of both the probes were rotatable around the pi acidic phenyl rings, as evident from the DFT study as well as SC-XRD structural analysis, (Figure A4A.30-Figure A4A.32) thus making both the probes favourable for TICT activity. As a result of TICT phenomena, both Benz-d-CF_3 and Benz-m-CF_3 were observed to be non-emissive. However, the addition of CN^- causes deprotonation in both probes, subsequently causing planarization of the deprotonated species, (Figure A4A.30; Figure A4A.34a,b) which eventually enhances the ICT process. Such enhanced ICT results in red-shifted enhanced fluorescence emission. (Figure 4A.3a) This proposed mechanism is further strengthened by the fact that the isolated crystals of the deprotonated species ($[Benz\text{-}d\text{-}CF_3]^-$ and $[Benz\text{-}m\text{-}CF_3]^-$), characterised through ^1H NMR, HRMS, and SC-XRD analysis, (Figure A4A.1-Figure A4A.6) display bright fluorescence under a UV-lamp at 365 nm, (Figure 4A.5a,b) and the crystal structures reveal that, the dihedral angle between the head and the tail part reduces significantly in the deprotonated structure as compared to that of the neutral probes (Figure A4A.32, Figure A4A.34a,b) (N.B.: due to very bad crystal quality, the crystallographic data obtained for $[Benz\text{-}d\text{-}CF_3]^-$ were very poor, so we did not incorporate those data in the main manuscript, instead it has been used as a supporting document to support our obtained results, CCDC: 2331471).

We could also crystallize the deprotonated species ($[Benz\text{-}m\text{-}CF_3]^-$) along with the neutral species [Benz-m-CF_3], which shows a remarkable difference in their dihedral angles, where the deprotonated species is observed to be more planar as compared to the neutral one. (Figure 4A.6a-c, Table A4A.3) On comparing solid-state fluorescence emission spectra of the crystals of the deprotonated species, $[Benz\text{-}d\text{-}CF_3]^-$ and $[Benz\text{-}m\text{-}CF_3]^-$, with the neutral free probes, a significant spectral shift of ~70 nm towards the red region was observed, which is quite similar to that of the solution state sensing study. (Figure 4A.5)

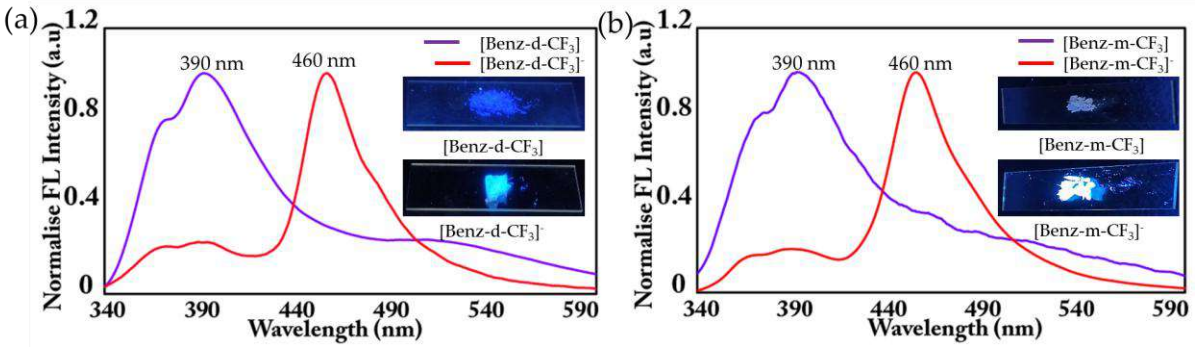

Figure 4A.5: Solid-state fluorescence spectra of (a) crystalline powder samples of Benz-d-CF_3 and [Benz-d-CF_3]$^-$ along with the photographs of their corresponding crystals under a UV-lamp (365 nm) [top right corner] and (b) crystalline powder samples of Benz-m-CF_3 and [Benz-m-CF_3]$^-$ along with the photographs of their corresponding crystals under a UV-lamp (365 nm) [top right corner].

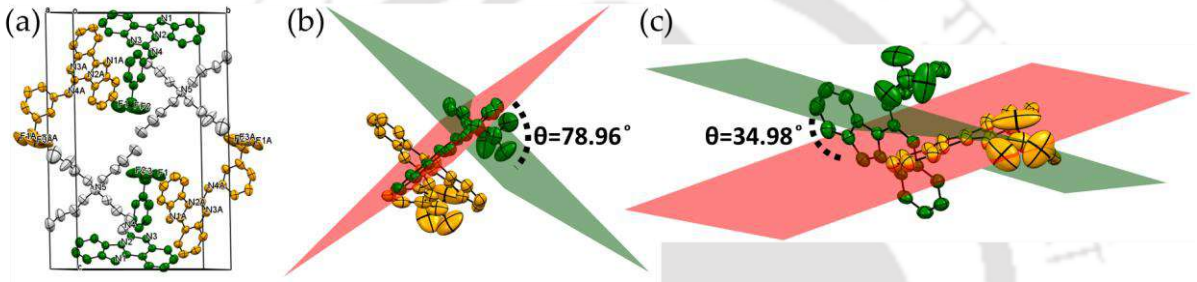

Figure 4A.6: (a) Crystal structures of [Benz-m-CF_3]. [Benz-m-CF_3]$^-$ TBA^+ inside a unit cell. The dihedral angle between the head and the tail counterpart of (b) neutral molecule, [Benz-m-CF_3], and (c) deprotonated species, [Benz-m-CF_3]$^-$.

We further conducted a pH dependent study of both Benz-d-CF_3 and Benz-m-CF_3, as well as both the probes combined with CN^- in five different pH, comprising highly acidic to highly basic pH (pH = 2.2, 5, 7.4, 9.12, and 11.8). The probe Benz-d-CF_3 did not show any spectral changes within the pH domain ranging from pH = 2.2 to pH = 9.12. However, when the pH was changed from pH = 9.12 to pH = 11.8, fluorescence enhancement at ~460 nm was observed which is similar to that of CN^- inflicted spectral change. This observation supports our proposed mechanism quite firmly. Moreover, we investigated the sensing ability of Benz-d-CF_3 in the same aforesaid pH range. It was observed that excluding pH = 2.2, as we increase the pH of the solution starting from pH = 5, the turn-on response towards CN^- at ~460 nm keeps on intensifying till it reaches the highest emission intensity at pH = 11.8. The fluorescence enhancement was observed to be ~25-fold higher at pH = 11.8 as compared to that observed at pH = 5, which is ascribable to the cumulative effects of both the basic medium and the CN^- itself. (Figure A4A.12a,b) Interestingly, Benz-m-CF_3 was found to be non-sensitive towards pH changes; however, a turn-on response at ~470 nm was observed at pH = 11.8, when combined

with CN^-. (Figure A4A.12c,d) One important takeaway from these pH-dependent studies is that the probe Benz-d-CF_3 is operatable even at physiological pH, at pH = 7.4, which is desirable for biological applications.

In an aqueous solution containing CTAB, the plausible mechanism has been illustrated in Scheme 4A.2. Both the probes Benz-d-CF_3 and Benz-m-CF_3 disperse readily in water with the assistance of CTAB, thus forming nano-aggregates with very little emission, which undergo disassembly or disaggregation when CN^- was added. It is quite clear that the overall particle size of the aggregates of Benz-d-CF_3 (Zaverage = 628.3 nm) and Benz-m-CF_3 ($Z_{average}$ = 556.9 nm) diminishes considerably (to $Z_{average}$ = 422.8 nm and $Z_{average}$ = 376.0 nm for Benz-d-CF_3 and Benz-m-CF_3 respectively) upon interaction with CN^- as evident from the DLS study. (Figure A4A.26, Figure A4A.27) Upon addition of CN^-, deprotonation takes place and subsequently leads to the formation of negatively charged species, thus causing disassembly of the nano-aggregates with concomitant planarization of the negative species with enhanced ICT characteristics. Such an enhanced ICT resulted in higher fluorescence emission with concurrent red shift of the emission peaks, which is well reflected in the UV-vis study as well, where significant bathochromic shifts were observed for both the receptors in the presence of CN^-. (Figure 4A.4a,b,d,e) The FESEM imaging study of both the probes also reveals the fact that, the initially existing aggregated morphology of both the probes disintegrates completely in the presence of CN^-. (Figure 4A.7b,c,e,f) We further observed that the fluorogenic response of the probe Benz-d-CF_3 upon the addition of TBAOH was very similar to that due to the addition of TBACN ions, (Figure 4A.4a,b) which firmly validates our proposed deprotonation mechanism.

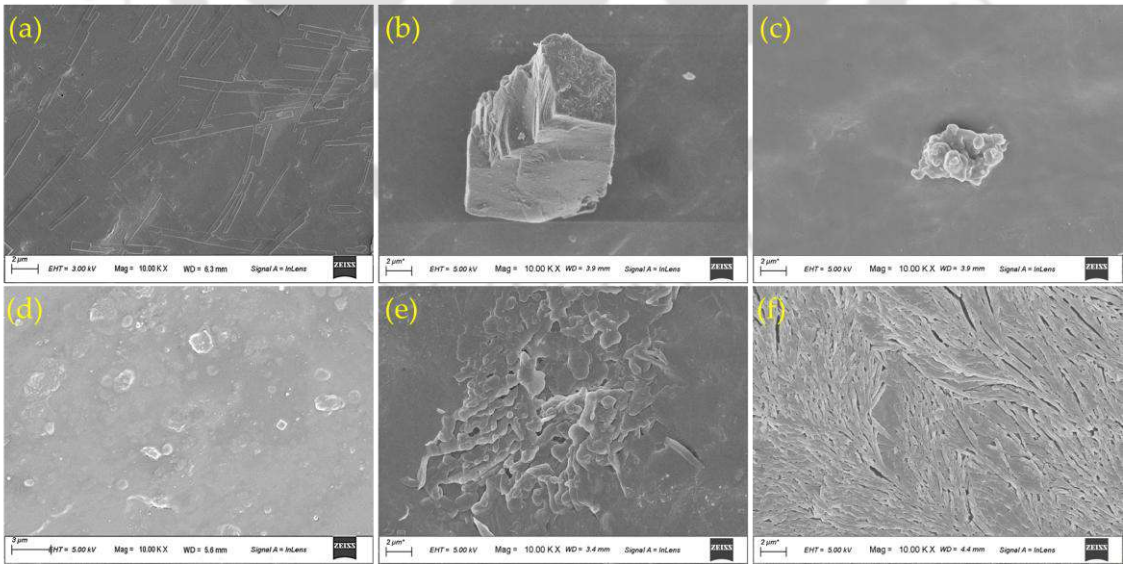

Figure 4A.7: FESEM image of (a) Benz-d-CF_3 (in water), (b) Benz-d-CF_3 (in CTAB), and (c) Benz-m-CF_3 (in CTAB) before CN^- addition. FESEM image of (d) Benz-d-CF_3 (in water), (e) Benz-d-CF_3 (in CTAB), and (f) Benz-m-CF_3 (in CTAB) after CN^- addition.

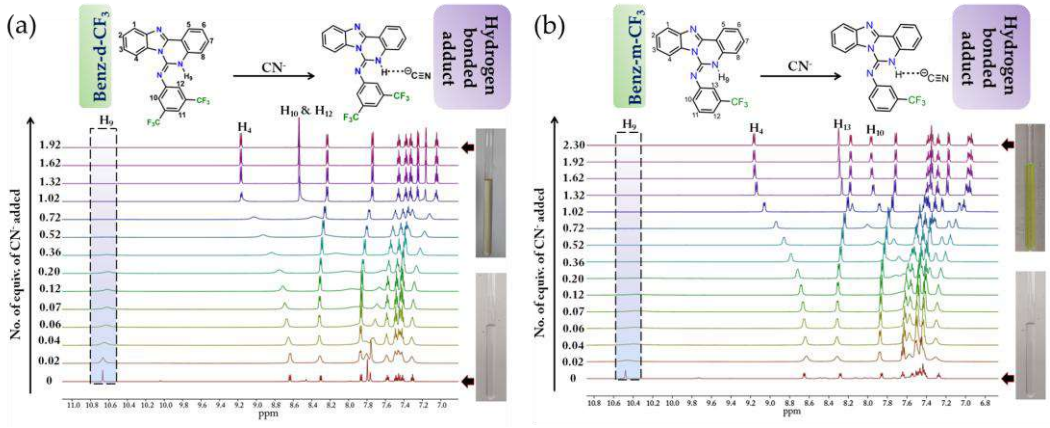

Figure 4A.8: ^{1}H-NMR titration spectra for probe (a) Benz-d-CF_3 (25 mM) and (b) Benz-m-CF_3 (25 mM) with the incremental addition of TBACN (250 mM) in DMSO-d_6 solvent. The amounts of added TBACN are shown on the spectra.

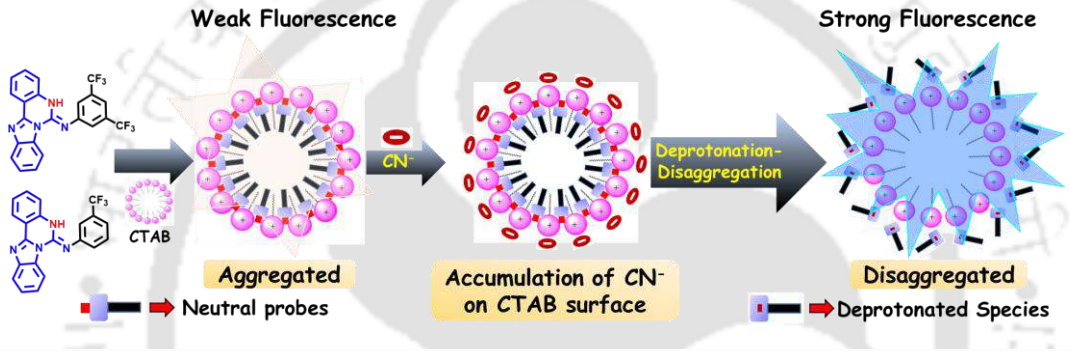

Scheme 4A.2: Schematic illustration of nano-aggregate formation in aqueous CTAB medium and disassembly of the aggregated form in the presence of CN^-.

4A.3.8. Comparative Study of CN^- Sensing in Water and CTAB

Two major factors play a very critical role in CN^- sensing in our study: firstly, substituents' effect, and secondly, choice of micellar medium. In water, the probe Benz-d-CF_3 was observed to be very highly selective towards CN^- among several other anions although the sensitivity remained an issue, whereas Benz-m-CF_3 having one less electron withdrawing substituent (–CF_3) was silent towards CN^-. However, in an aqueous medium containing CTAB (3 mM), we observed a completely different scenario, where both the probes Benz-d-CF_3 and Benz-m-CF_3 were very much responsive towards CN^-. However, the probe Benz-d-CF_3 was not only responsive towards CN^- but also towards HO^-. In contrast, Benz-m-CF_3 was found to be very highly selective towards CN^-, not showing any affinity towards HO^-. This result is quite interesting as it makes one thing very clear, that we can fine-tune the selectivity as well as sensitivity of our probes towards CN^- by just varying the pi acidic terminal substituents, that is the –CF_3 group. The time-dependent study of both the probes was conducted in the presence of CN^- in water as well as in aqueous CTAB keeping a time interval of one second.

It is interesting to observe that the fluorescence emission spectra fall rapidly within a few seconds in water, which is ascribable to faster re-protonation of the deprotonated species (caused by CN^-) in water as compared to that of CTAB. On the other hand, in CTAB, the fall in the emission is observed to be slower for both Benz-d-CF_3 and Benz-m-CF_3, which is attributable to the electrostatic interaction as well as the hydrophobic microenvironment facilitated by CTAB, which makes re-protonation much slower. Such very fast attainment of fluorescence emission maxima within a few seconds makes both probes fall into the category of ultrafast sensors. We further conducted a reversibility experiment of CN^- sensing, where we observed that both the probes were reversible as well as reusable in the solution state, which has been demonstrated by using the Cu^{2+} ion (using 50 mM $CuCl_2$ solution). (Figure A4A.19a,b)

4A.3.9. Detection of CN^- in Drinking Water

We investigated the real-world applicability of our designed probes towards CN^- sensing in both solid and solution states. Our prime objective was to detect CN^- in drinking water and to do that, we spiked different concentrations of CN^- (10 μM, 25 μM and 50 μM) in drinking water, and measured the recovery percent of the spiked CN^- using Benz-m-CF_3 with the assistance of CTAB (3 mM). The recovery percent of CN^- lies within the range of 90–98% suggesting very good practical applicability. (Table A4A.1) Moreover, we could visualise the changes in the emission intensity with varying spiked CN^- concentrations (spiked in drinking water) under a UV-lamp at 365 nm using the probe Benz-m-CF_3, where the emission intensifies as the spiked CN^- concentration increases. (Figure 4A.10c) We further performed a titration experiment of Benz-m-CF_3 with CN^- in drinking water to evaluate the LOD value, which was calculated to be 8.85 μM. (Figure 4A.10a,b) This result suggests that this method might be suitable for real-time monitoring of CN^- in drinking water under a UV-lamp as well as fluorimetrically. Benz-d-CF_3 could be employed for cyanide detection in various natural water sources such as lake water, tap water, drinking water, river water, and Milli-Q water. (Figure A4A.21) Moreover, we wondered whether the two probes would also be effective for CN^- detection in the solid state. To investigate the same, we prepared test strips of both the probes by immersing a few filter papers in the THF solution of Benz-d-CF_3 and Benz-m-CF_3 (25 mmol L^{-1} each) for 15 min and then dried them in air. Various concentrations of CN^- ions spiked in drinking water were applied onto the surface of the filter papers using capillary tubes; the cyan colour of the filter papers intensified with increasing concentrations of CN^- in both probes. (Figure 4A.10d) This result demonstrates a prototype device using Benz-d-CF_3 and Benz-m-CF_3 for real-world application. Furthermore, we prepared two paper strips by immersing filter papers in the THF solution of the two isolated deprotonated species TBA^+ $[Benz\text{-}d\text{-}CF_3]^-$ and TBA^+ $[Benz\text{-}m\text{-}CF_3]^-$ (5 mM each)

which were fluorescent. By using a cotton swab pre-immersed in an acid solution (aq. HCl, pH = 2) we could write on the paper strips, and this could be perceived under a UV lamp (365 nm), the reasons could be attributed to acid-caused protonation of the deprotonated species, and this might be useful in real-world as a security ink to transfer encrypted messages. (Figure 4A.10e,f)

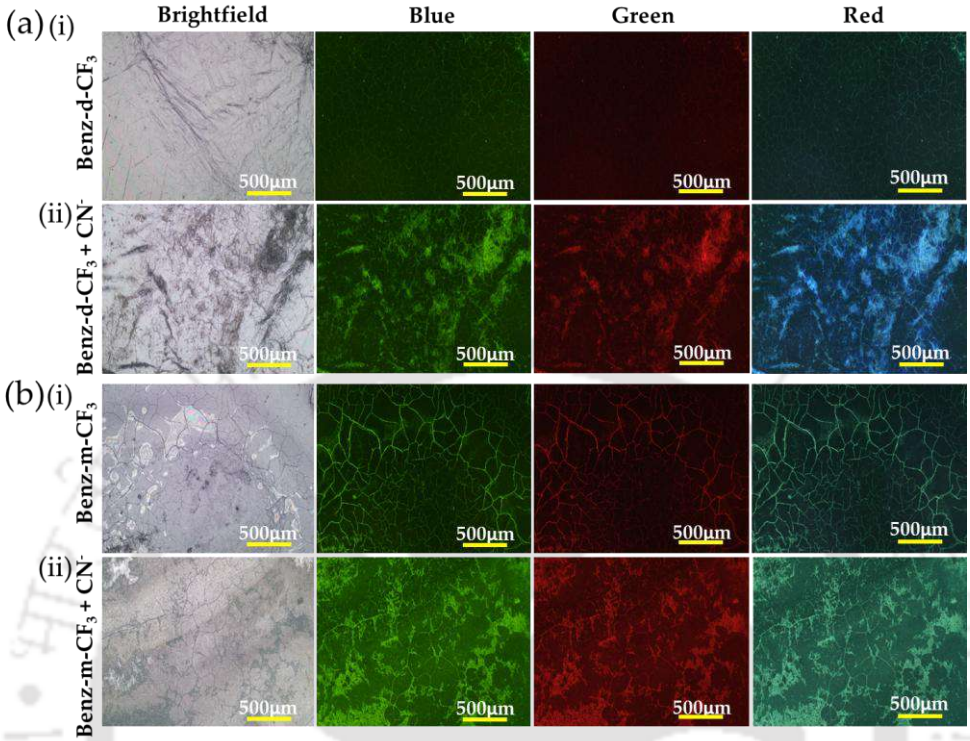

Figure 4A.9: Bright-field as well as fluorescence microscope images of (a) (i) Benz-d-CF_3, (ii) Benz-d-CF_3 + CN^-; and (b) (i) Benz-m-CF_3, (ii) Benz-m-CF_3 + CN^-.

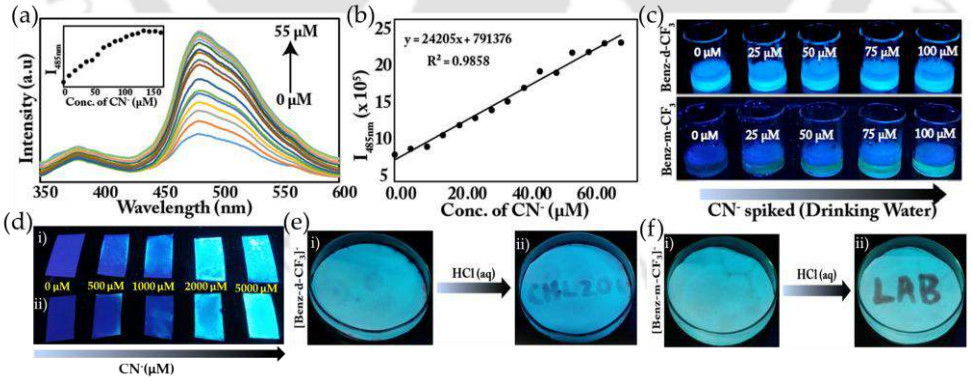

Figure 4A.10: (a) Fluorescence titration experiment of Benz-m-CF_3 (10 μM) with incremental addition of CN^- in drinking water (inset: plot of concentration of CN^- vs. fluorescence intensity at 485 nm). (b) Calibration curve plotted for Benz-m-CF_3 in different concentrations of CN^- in drinking water (recording emission intensities at 485 nm). (c) Drinking water spiked with different concentrations of CN^- monitored through changes in emission intensity upon addition of Benz-m-CF_3 (10 μM) (under a UV-lamp at 365 nm) (all the mentioned experimental measurements have been done with the assistance of CTAB (3 mM)). (d) CN^- sensing in the solid state by using paper strips loaded with (i) Benz-d-CF_3 and (ii) Benz-m-CF_3. (e) and (f) Applicability of the isolated deprotonated species (e) TBA^+ $[Benz\text{-}d\text{-}CF_3]^-$ and (f) TBA^+ $[Benz\text{-}m\text{-}CF_3]^-$ as a security ink.

4A.4. Conclusions

Two novel pre-twisted TICT active probes with varying pi-acidic terminal substituents displayed variable effects on their fluorescence response towards CN^- in the aqueous medium. In a 100% aqueous medium, Benz-d-CF_3 showed excellent selectivity towards CN^-, although the sensitivity was of concern. In contrast, Benz-m-CF_3 remained silent in fluorescence measurement when combined with CN^-. However, the selectivity as well as sensitivity towards CN^- in an aqueous medium enhanced quite significantly for both the probes with the assistance of CTAB, as it provides the viable hydrophobic environment and facilitates electrostatic interaction, bestowing our sensor system with a very low detection limit of 496.5 nM (Benz-d-CF_3) and a very short sensing process within a few seconds. It was observed that the degree of fluorescence response for CN^- ions depends majorly on two factors: the nature of the pi acidic terminal substituents and the nature of the surfactant used. We have presented the real-world applicability of our probes by demonstrating real-time monitoring of CN^- in drinking water under a UV lamp with the help of CTAB, which could be monitored in the solid state using cost-effective paper strips coated with our probes. To the best of our knowledge, this study reports for the first time that utilizing a TICT active probe in the micellar medium could help develop susceptible and selective cyanide sensors and a systematic study on substituent dependency of such a sensing process. Shortly, we intend to expand the study of our TICT probes toward biomedical applications by exploring their potential application as photothermal theranostics. Additionally, because of the viscosity-sensitive nature of both probes, they could also be employed for mitochondrial viscosity monitoring, which is very important from a biological point of view.

References

[4.1] M. Wenzel, J. R. Hiscock, and P. A. Gale, *Chem. Soc. Rev.*, 2012, **41**, 480-5202.

[4.2] F. Wang, L. Wang, X. Chen, and J. Yoon, *Chem. Soc. Rev.*, 2014, **43**, 4312-43243.

[4.3] A. Sebastian, and E. Prasad, *Langmuir*, 2020, **36** (35), 10537-10547.

[4.4] Z. Xu, X. Chen, H. N. Kim, and J. Yoon, *Chem. Soc. Rev.*, 2010, **39**, 127-137.

[4.5] Z. Xu, and L. Xu, *Chem. Commun.*, 2016, **52**, 1094-1119.

[4.6] P. A. Gale, and C. Caltagirone, *Coord. Chem. Rev.*, 2018, **354**, 2-27.

[4.7] X. Chen, S. W. Nam, G. H. Kim, N. Song, Y. Jeong, I. Shin, S. K. Kim, J. Kim, S. Park, and J. Yoon, *Chem. Commun.*, 2010, **46**, 8953-8955.

[4.8] O. A. Pegu, R. Moral, and G. Das, *Cryst. Growth Des.*, 2023, **23** (11), 8370-8380.

[4.9] R. Moral, O. A. Pegu, and G. Das, *New J. Chem.*, 2023, **47**, 19625-19632.

[4.10] J. M. Bak, M. Gupta, S. H. Jung, and H. Lee, *Polymer*, 2021, **213**, 123320.

[4.11] G. E. Isom, and J. L. Way, *J. Pharmacol. Exp. Ther.*, 1947, **189**, 235-243.

[4.12] A. Promchat, P. Rashatasakhon, and M. Sukwattanasinitt, *J. Hazard. Mater.*, 2017, **329**, 255-261.

[4.13] N. Kaur, G. Kaur, U. A. Fegade, A. Singh, S. K. Sahoo, A. S. Kuwar, and N. Singh, Trends Anal. Chem., 2017, 95, 86-109.

[4.14] V. Venkatesan, S. K. Ashok Kumar, and S. K. Sahoo, *Anal. Methods*, 2019, **11**, 1137-1143.

[4.15] T. Anand, A. K. Sk, and S. K. Sahoo, *ChemistrySelect*, 2017, **2**, 7570–7579.

[4.16] C. Young, L. Tidwell, and C. Anderson, *The Minerals, Metals, and Materials Society, Warrendale*, 2001.

[4.17] S. Suganya, E. Ravindran, M. K. Mahato, and E. Prasad, *Sens. Actuators B Chem.*, 2019, **291**, 426-432.

[4.18] H. G. Gorchev, and G. Ozolins, WHO Guidelines for Drinking-Water Quality, *WHO Chron.*, 2011, **38** (3), 104–108.

[4.19] Z. Xu, S. K. Kim, and J. Yoon, *Chem. Soc. Rev.*, 2010, **39**, 1457.

[4.20] D. G. Cho, and J. L. Sessler, *Chem. Soc. Rev.*, 2009, **38**, 1647-1662.

[4.21] C. Zhang, K. Ji, X. Wang, H. Wu, and C. Liu, *Chem. Commun.*, 2015, **51**, 8173-8176.

[4.22] L. Wang, L. Li, and D. Cao, *Sens. Actuators B Chem.*, 2016, **228**, 347-359.

[4.23] N. Kumari, S. Jha, and S. Bhattacharya, *J. Org. Chem.*, 2011, **76**, 8215-8222.

[4.24] A. M. Christianson, and F. P. Gabbaï, *Chem. Commun.*, 2017, **53**, 2471-2474.

[4.25] Q. Wu, S. Wang, E. Hao, and L. Jiao, *Spectrochim. Acta, Part A*, 2021, **247**, 119102.

[4.26] M. Gao, and B. Z. Tang, *ACS Sens.*, 2017, **2**, 1382-1399.

[4.27] F. Duarte, G. Dobrikov, A. Kurutos, H. M. Santos, J. Fernández-Lodeiro, J. L. Capelo-Martinez, E. Oliveira, and C. Lodeiro, *Dyes Pigm.*, 2023, **218**, 111428.

[4.28] B. Aydıner, *J. Photochem. Photobiol. A*, 2019, **382**, 111916.

[4.29] R. Moral, O. A. Pegu, and G. Das, *Dyes Pigm.*, 2023, **218**, 111502.

[4.30] J. Jo, A. Olasz, C. H. Chen, and D. Lee, *J. Am. Chem. Soc.*, 2013, **135** (9), 3620-3632.

[4.31] W. Saiyasombat, U. Eiamprasert, T. Chantarojsiri, K. Chainok and S. Kiatisevi, *Dyes Pigm.*, 2022, **206**, 110643.

[4.32] S. Li, F. Huo, K. Ma, Y. Zhang, and C. Yin, *New J. Chem.*, 2021, **45**, 1216.

[4.33] N. Saini, C. Wannasiri, S. Chanmungkalakul, N. Prigyai, V. Ervithayasuporn, and S. Kiatkamjornwong, J. *Photochem. Photobiol. A*, 2019, **385**, 112038.

[4.34] S. Oh, J. Jeon, J. Jeong, J. Park, E. T. Oh, H. J. Park, and K. H. Lee, *Anal. Chem.*, 2020, **92** (7), 4917-4925.

[4.35] R. S. Fernandes, J. Kumari, D. Sriram, and N. Dey, *ACS Appl. Bio Mater.*, 2023, **6**, 4158-4167.

[4.36] Y. Zhang, D. Li, Y. Li, and J. Yu, *Chem. Sci.*, 2014, **5**, 2710-2716.

[4.37] S. Sasaki, G. P. C. Drummen, and G. Konishi, *J. Mater. Chem. C*, 2016, **4**, 2731-2743.

[4.38] Z. R. Grabowski, K. Rotkiewicz, and W. Rettig, *Chem. Rev.*, 2003, **103** (10), 3899-4032.

[4.39] C. Wang, W. Chi, Q. Qiao, D. Tan, Z. Xu, and X. Liu, *Chem. Soc. Rev.*, 2021, **50**, 12656-12678.

[4.40] S. I. Reja, I. A. Khan, V. Bhalla, and M. Kumar, *Chem. Commun.*, 2016, **52**, 1182-1185.

[4.41] L. Zhu, J. Xu, Z. Sun, B. Fu, C. Qin, L. Zeng, and X. Hu, *Chem. Commun.*, 2015, **51**, 1154-1156.

[4.42] M. Ren, B. Deng, X. Kong, K. Zhou, K. Liu, G. Xu, and W. Lin, *Chem. Commun.*, 2016, **52**, 6415-6418.

[4.43] C. Kar, and G. Das, *J. Photochem. Photobiol. A*, 2013, **251**, 128-133.

[4.44] C. Kar, M. D. Adhikari, and G. Das, *Inorg. Chem.*, 2013, **52**, 743-752.

[4.45] C. Kar, S. Samanta, S. Mukherjee, B. K. Datta, A. Ramesh, and G. Das, *New J. Chem.*, 2014, **38**, 2660-2669.

[4.46] A. Gogoi, S. Samanta, and G. Das, *Sens. Actuators B Chem.*, 2014, **202**, 788-794.

[4.47] B. K. Datta, D. Thiyagarajan, R. Ramesh, and G. Das, *Dalton Trans.*, 2015, **44**, 13093-13099.

[4.48] A. Gogoi, S. Mukherjee, A. Ramesh, and G. Das, *Anal. Chem.*, 2015, **87**, 6974-6979.

[4.49] S. Samanta, P. Dey, R. Ramesh, and G. Das, *Chem. Commun.*, 2016, **52**, 10381-10384.

[4.50] A. Das, and G. Das, *J. Photochem. Photobiol. A*, 2022, **425**, 113669.

[4.51] V. Patel, N. Dharaiya, D. Ray, V. K. Aswal, and P. Bahadur, *Colloids Surf. A*, 2014, **455**, 67-75.

Annexure 4A

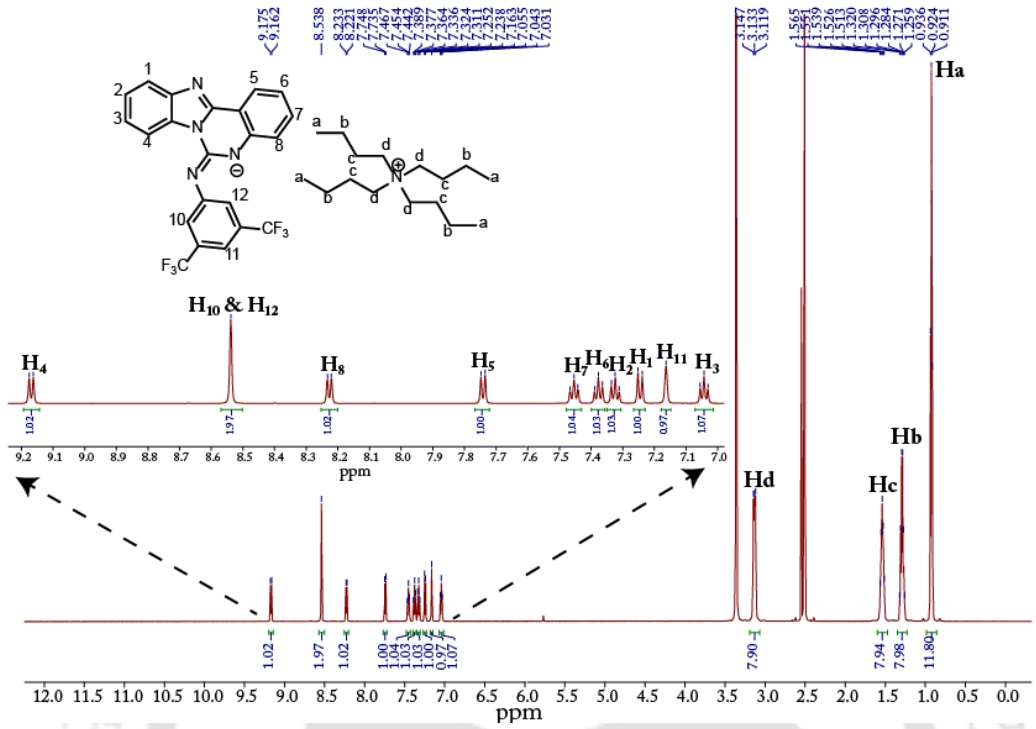

Figure A4A.1: ^{1}H NMR spectrum of crystals of TBA^{+} $[Benz\text{-}d\text{-}CF_3]^{-}$ in DMSO-d_6.

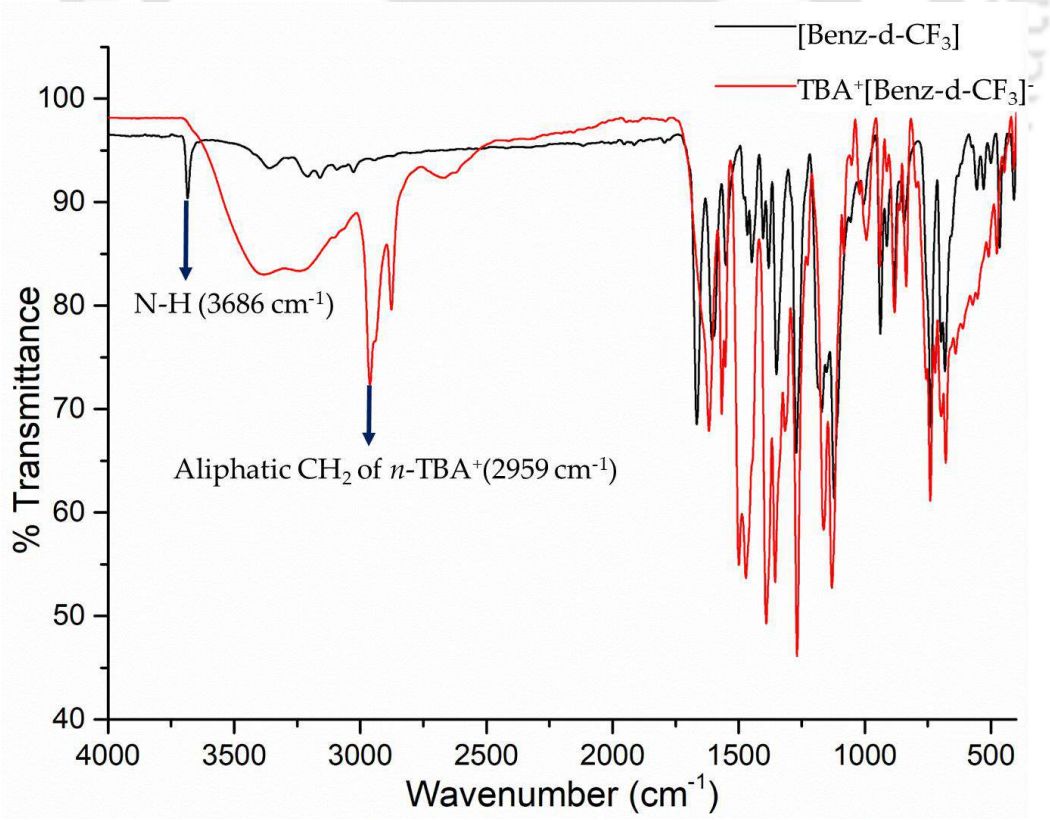

Figure A4A.2: Merged FTIR spectra of Benz-d-CF_3 and TBA^{+} $[Benz\text{-}d\text{-}CF_3]^{-}$.

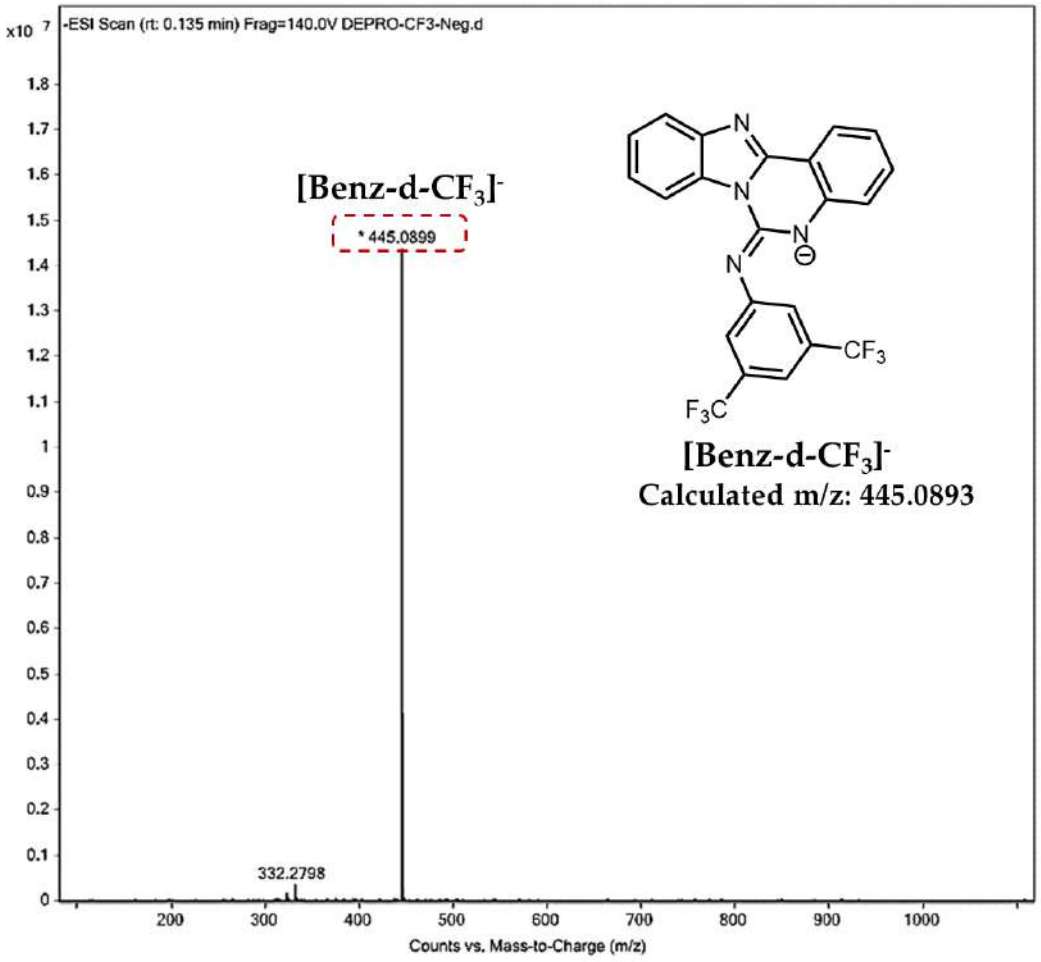

Figure A4A.3: HRMS of $[Benz\text{-}d\text{-}CF_3]^-$ (data collected in negative mode)

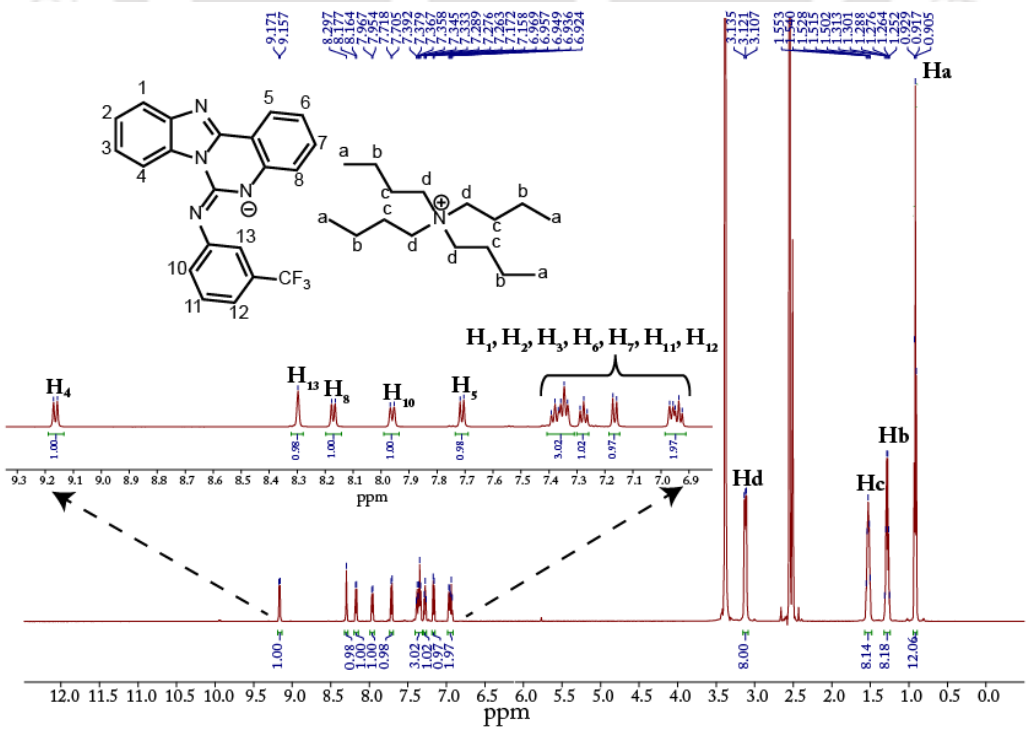

Figure A4A.4: ^1H NMR spectrum of crystals of TBA^+ $[Benz\text{-}m\text{-}CF_3]^-$ in DMSO-d_6.

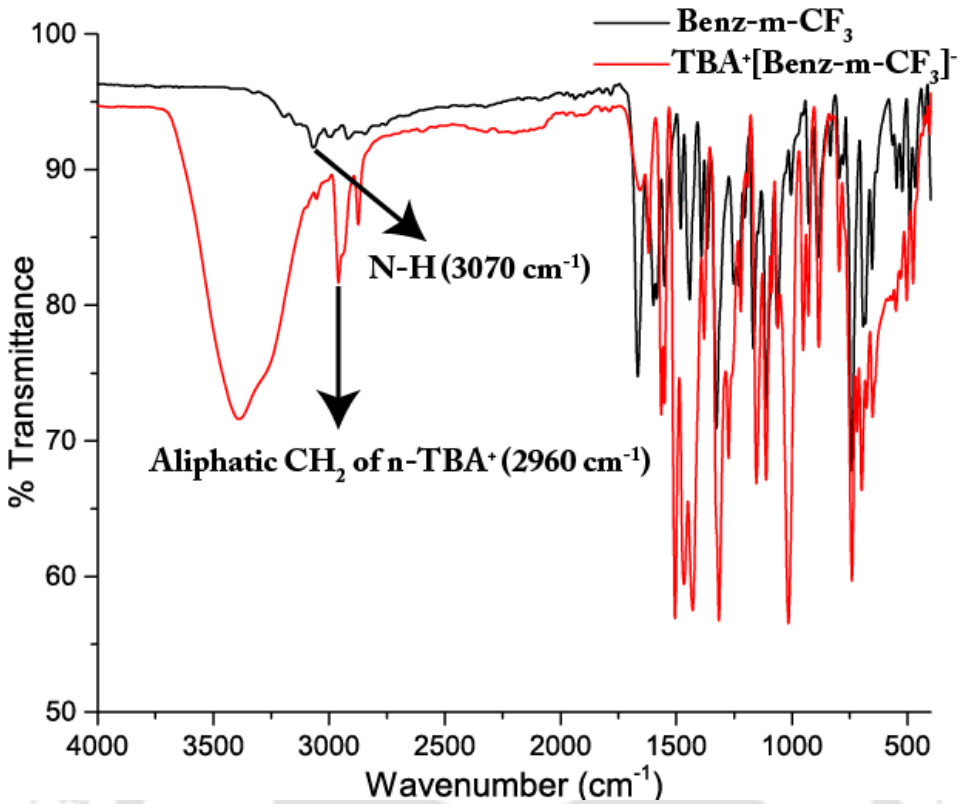

Figure A4A.5: Merged FTIR spectra of Benz-m-CF_3 and TBA^+ $[Benz\text{-}m\text{-}CF_3]^-$.

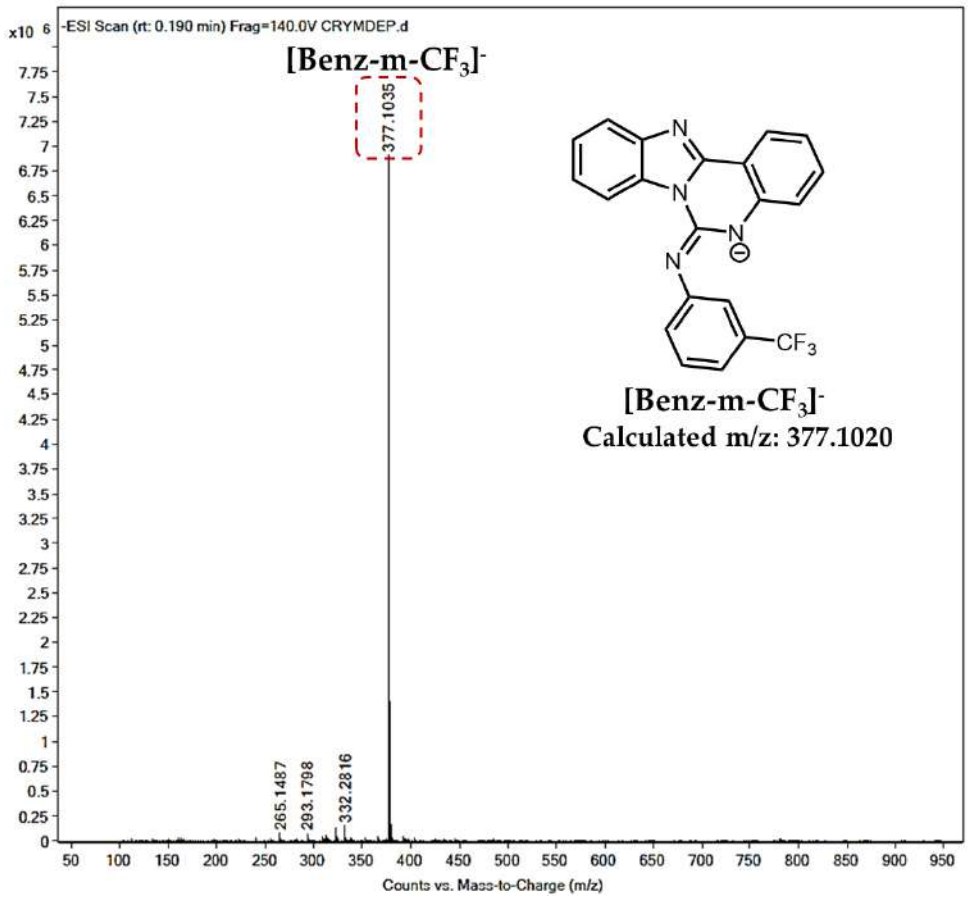

Figure A4A.6: HRMS of $[Benz\text{-}m\text{-}CF_3]^-$ (data collected in negative mode)

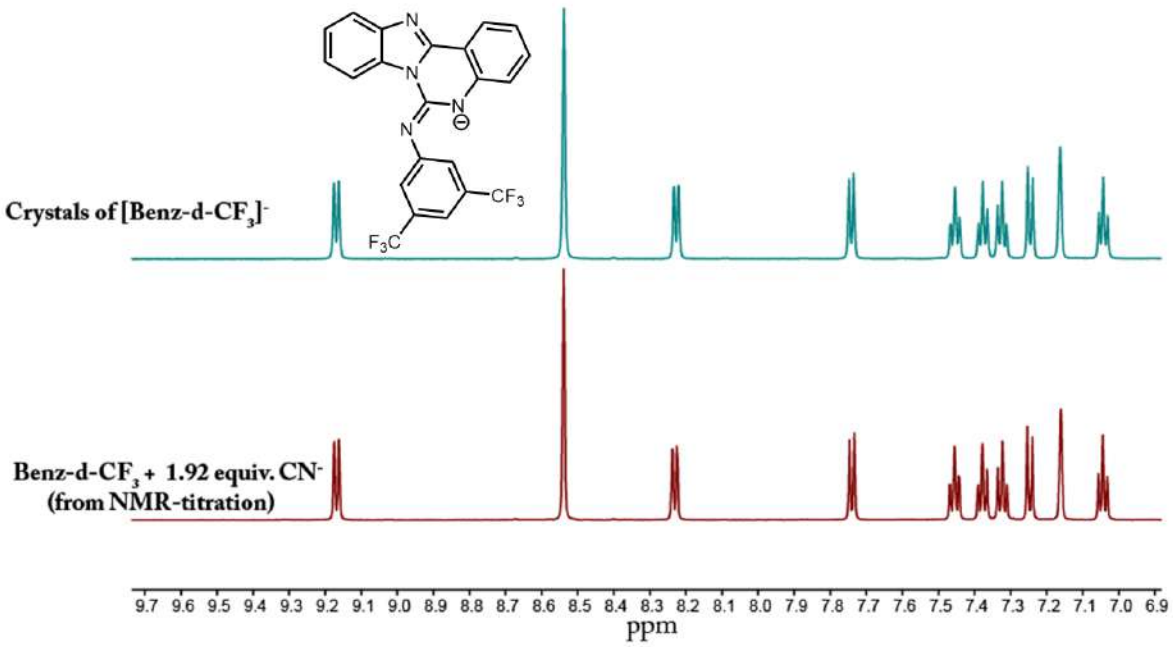

Figure A4A.7: Stacked ^{1}H NMR spectrum of crystals of TBA^{+} $[Benz\text{-}d\text{-}CF_3]^{-}$ and CN^{-} added Benz-d-CF_3 (obtained from NMR titration after adding 1.92 equiv. of CN^{-}) in DMSO-d_6.

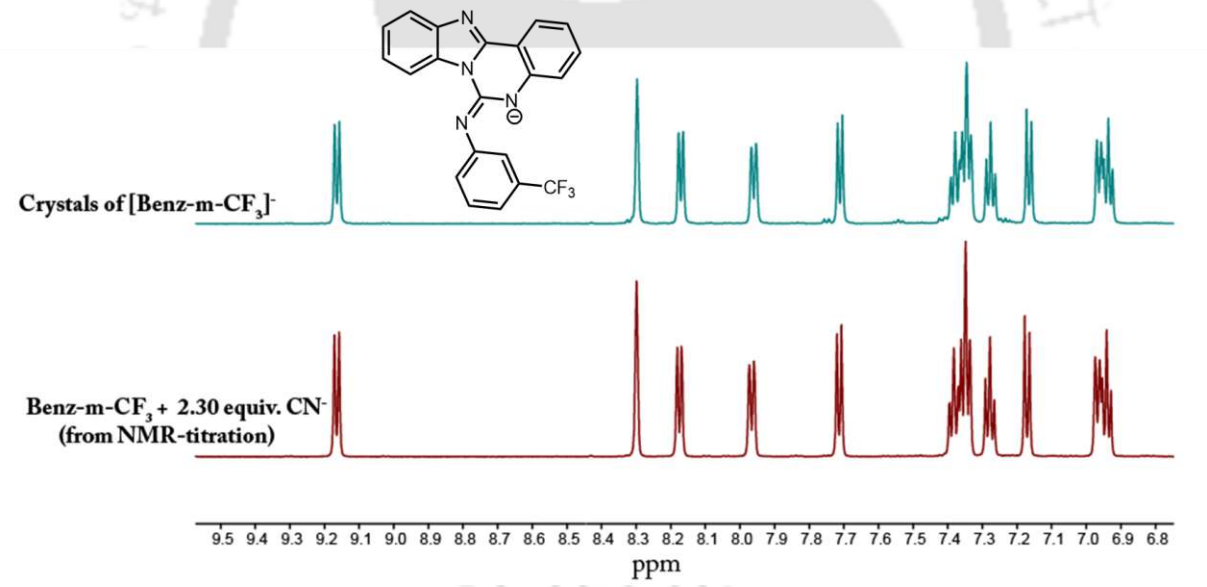

Figure A4A.8: Stacked ^{1}H NMR spectrum of crystals of TBA^{+} $[Benz\text{-}m\text{-}CF_3]^{-}$, and CN^{-} added Benz-m-CF_3 (obtained from NMR titration after adding ~2 equiv. of CN^{-}) in DMSO-d_6.

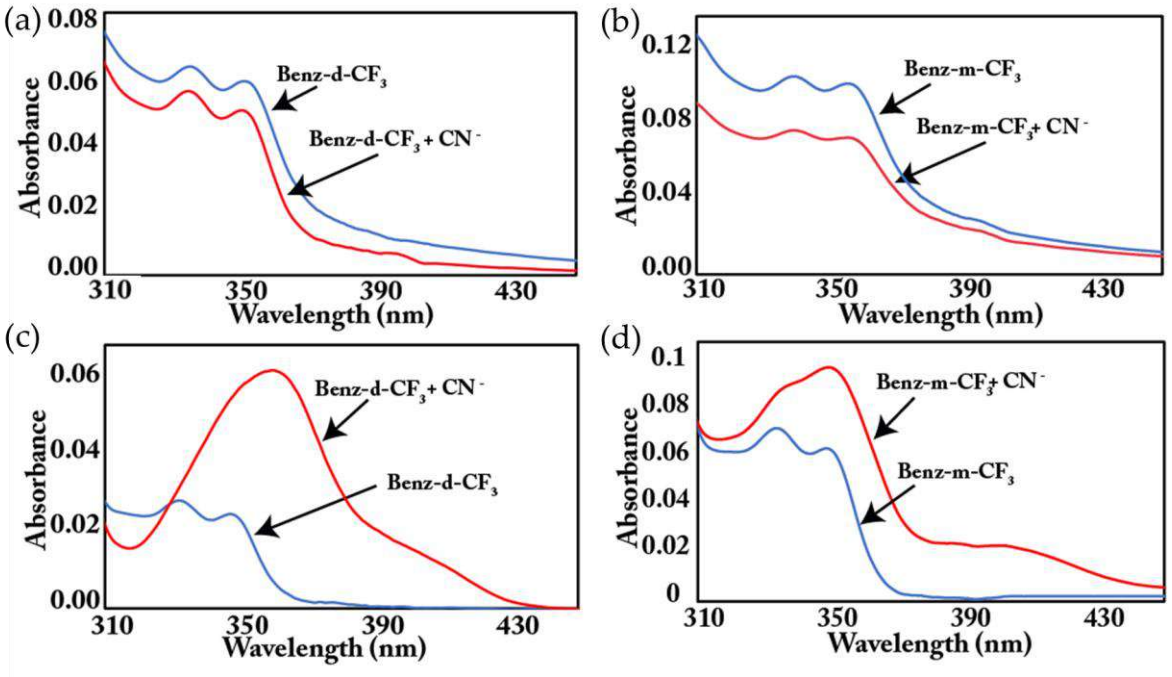

Figure A4A.9: UV-vis absorption spectra of (a) Benz-d-CF_3 and Benz-d-CF_3 + CN^-; (b) Benz-m-CF_3 and Benz-m-CF_3 + CN^- in water. UV-vis absorption spectra of (c) Benz-d-CF_3 and Benz- d-CF_3 + CN^-; (d) Benz-m-CF_3 and Benz-m-CF_3 + CN^- in aqueous CTAB medium (3 mM).

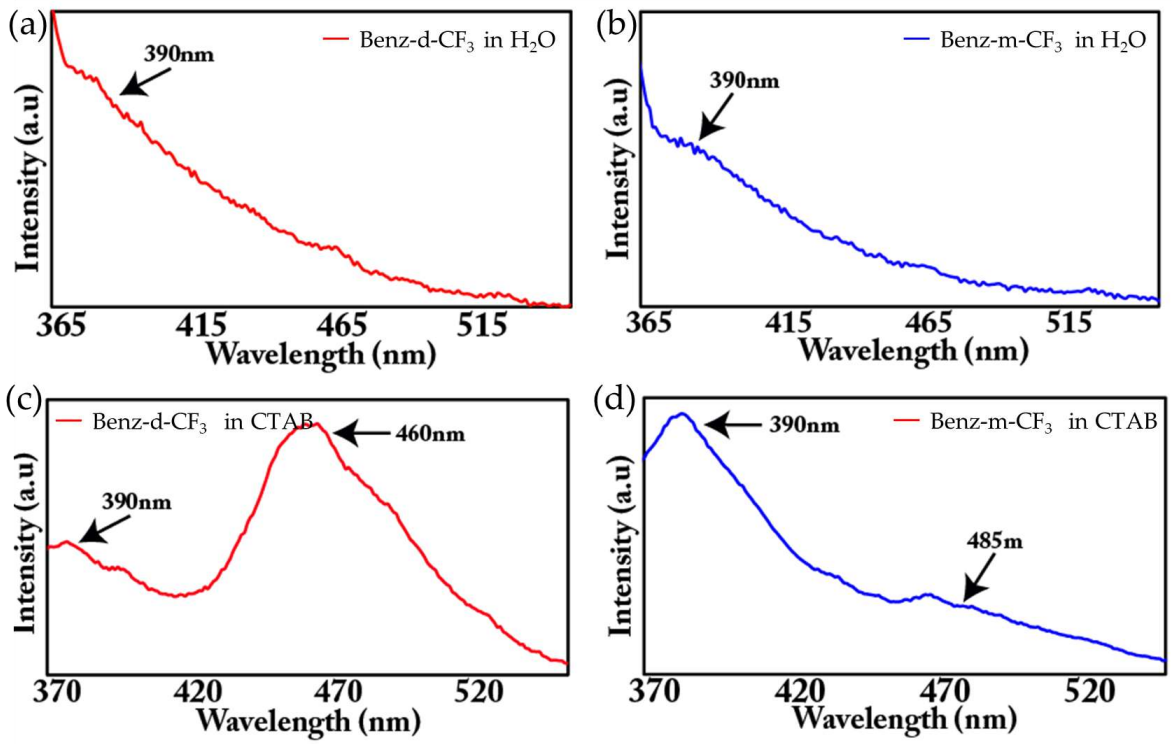

Figure A4A.10: Fluorescence emission spectra of (a) Benz-d-CF_3, and (b) Benz-m-CF_3 in water. Fluorescence emission spectra of (c) Benz-d-CF_3, and (d) Benz-m-CF_3 in aqueous CTAB medium (3 mM).

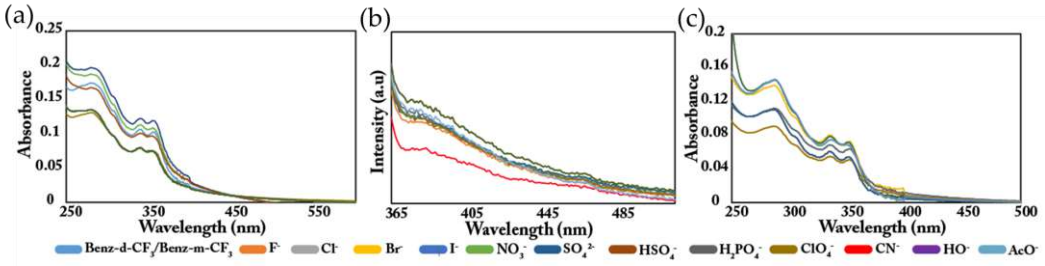

Figure A4A.11: Depicting UV-vis absorption spectrum of (a) Benz-m-CF_3, (c) Benz-d-CF_3 in presence of different anions in 100% aqueous medium. (b) Fluorescence emission spectrum of Benz-m-CF_3 in presence of different anions in 100% aqueous medium.

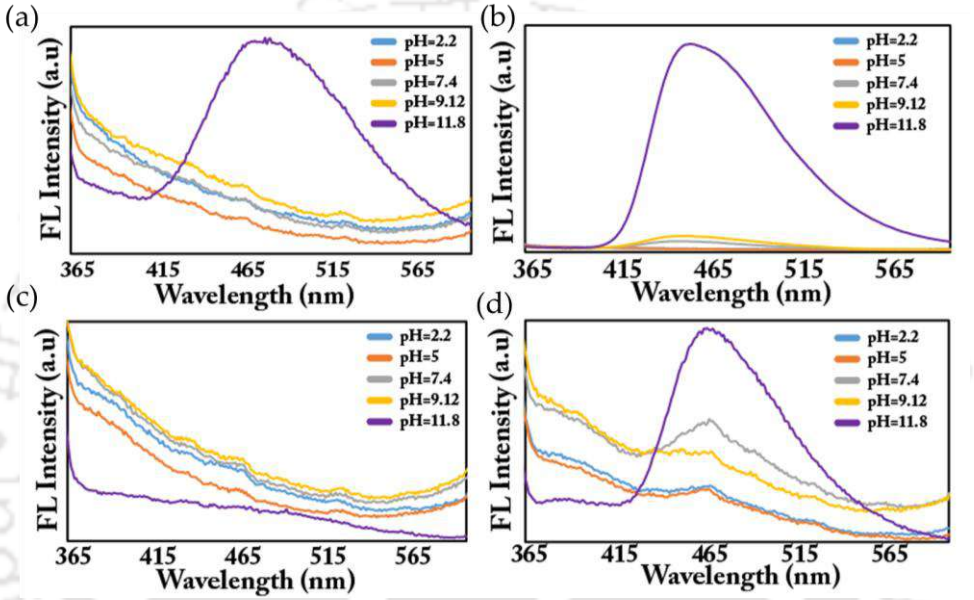

Figure A4A.12: Fluorescence emission spectra of (a) Benz-d-CF_3, (b) Benz-d-CF_3 + CN^-, (c) Benz-m-CF_3, and (d) Benz-m-CF_3 + CN^- in in different pH.

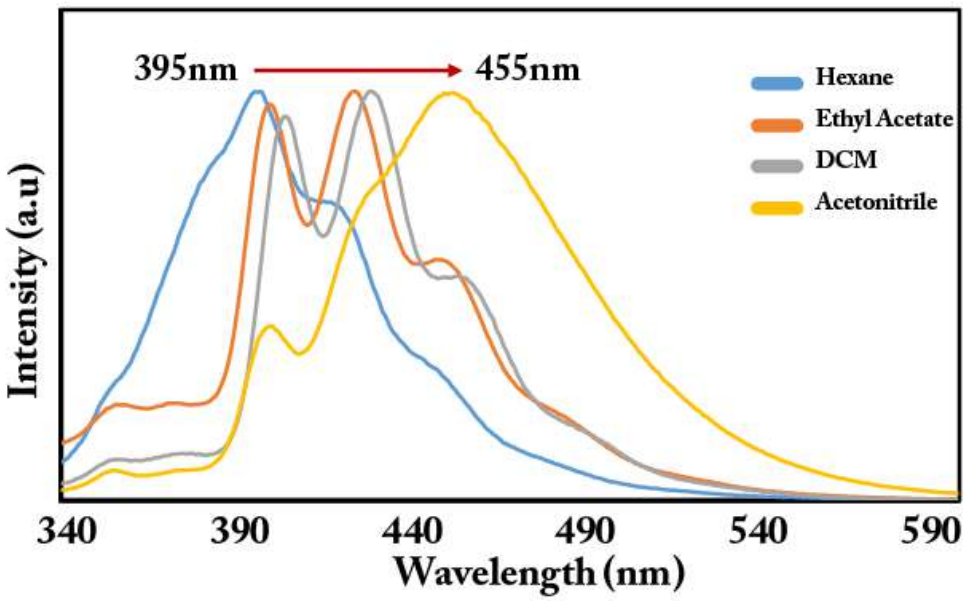

Figure A4A.13: Depicting solvatochromism in Benz-d-CF_3

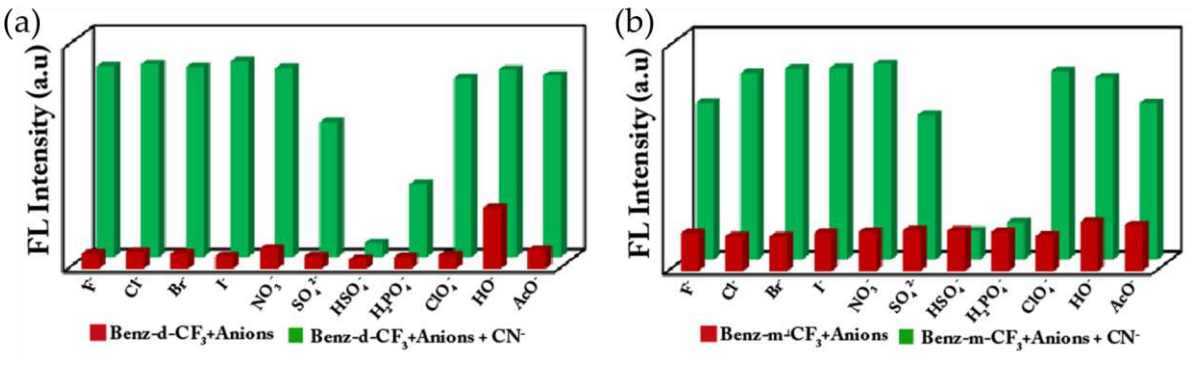

Figure A4A.14: Depict the interference study of receptor (a) Benz-d-CF_3, and (b) Benz-m-CF_3 (10 μM each) in the presence of various competitive anions (100 μM) in aqueous CTAB medium.

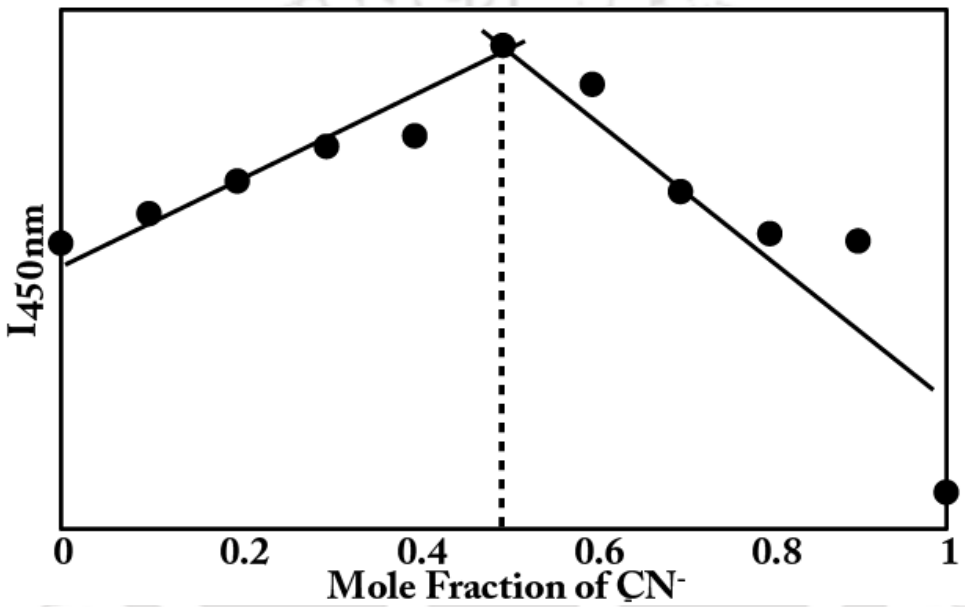

Figure A4A.15: Job's plot for Benz-d-CF_3 in presence of CN^- in water.

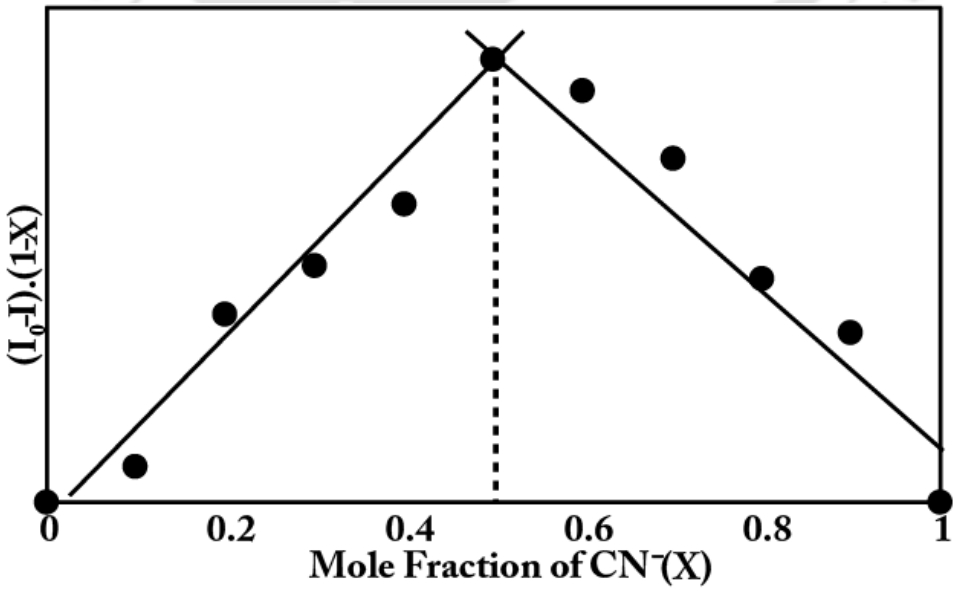

Figure A4A.16: Job's plot for Benz-d-CF_3 in presence of CN^- in aqueous CTAB medium.

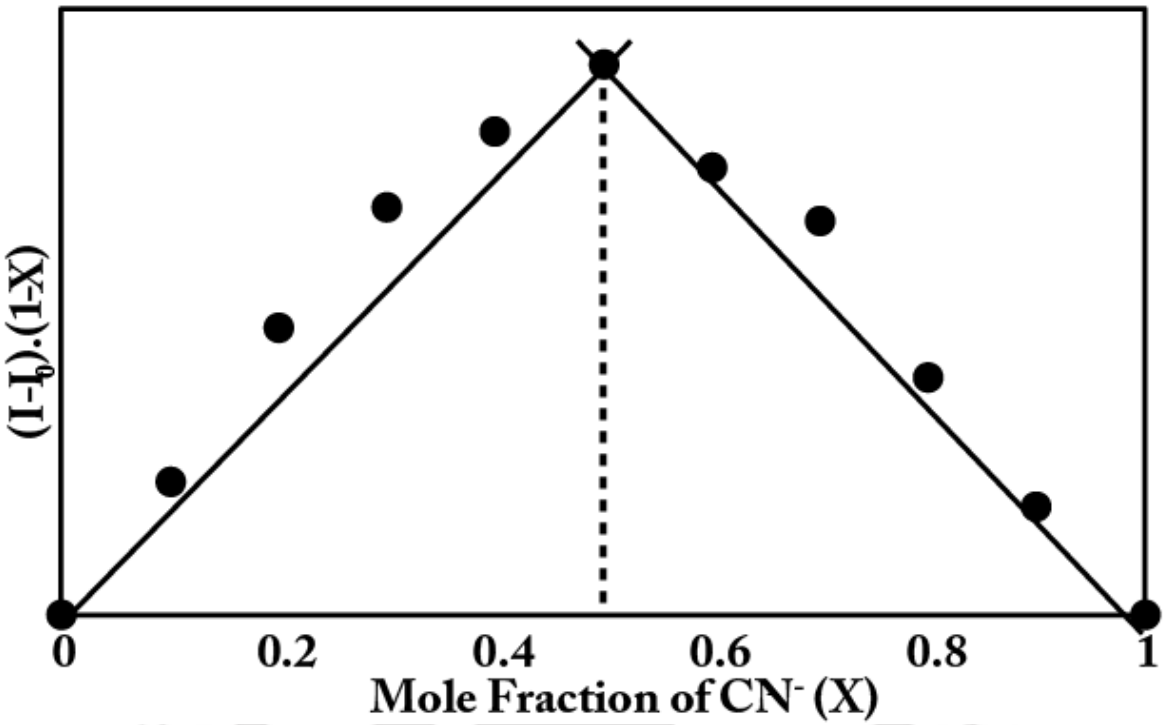

Figure A4A.17: Job's plot for Benz-m-CF_3 in presence of CN^- in aqueous CTAB medium.

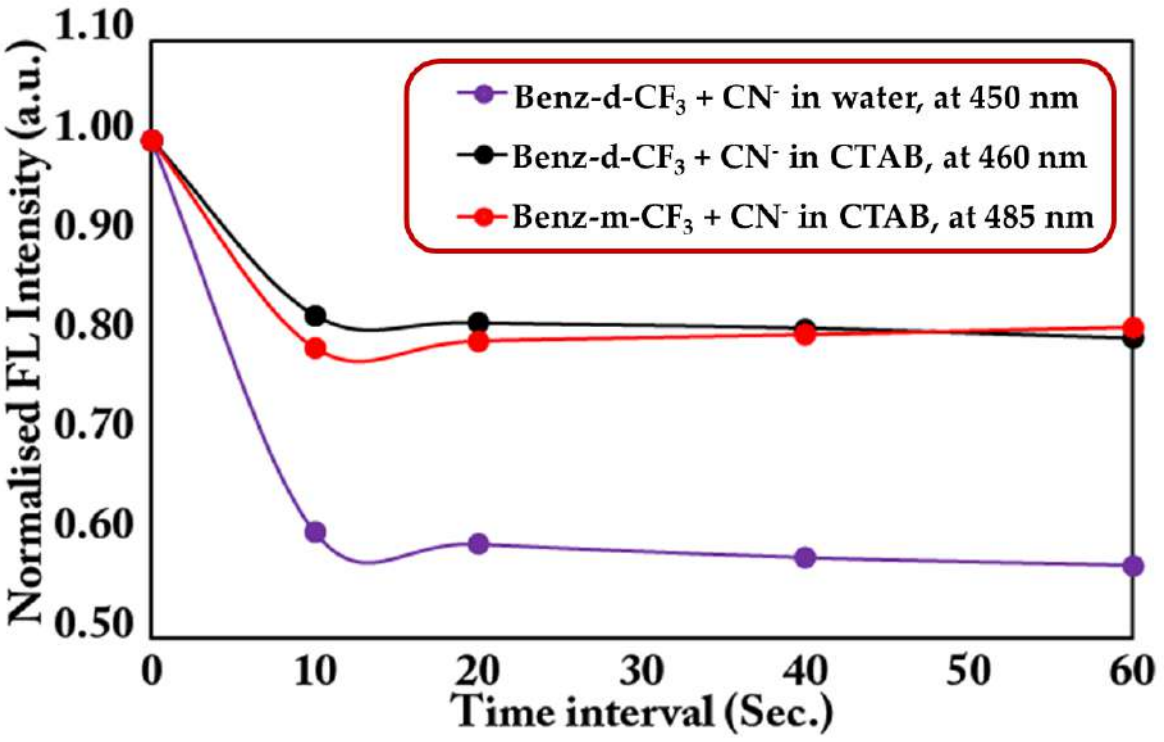

Figure A4A.18: Time dependent fluorescence emission study of Benz-d-CF_3, and Benz-m-CF_3 in water and aqueous CTAB medium.

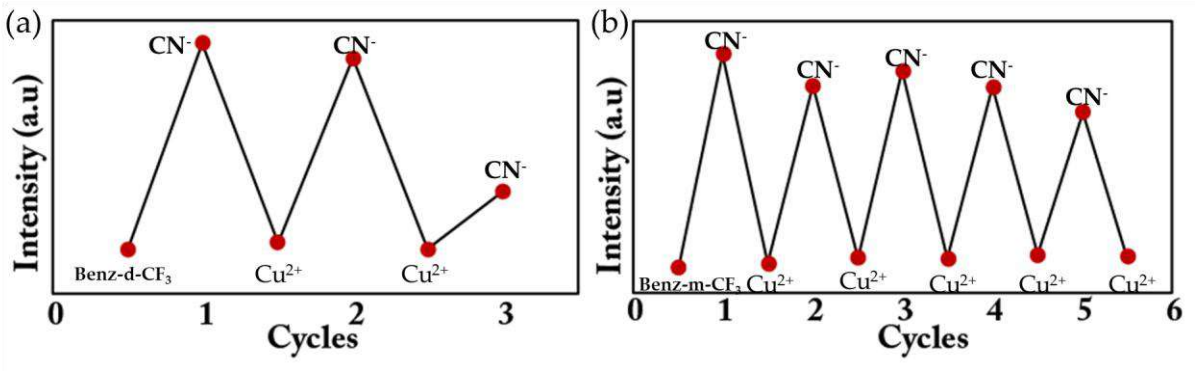

Figure A4A.19: (a, b) Depicting reversibility of CN^- sensing in aqueous CTAB medium with the help of Cu^{2+}.

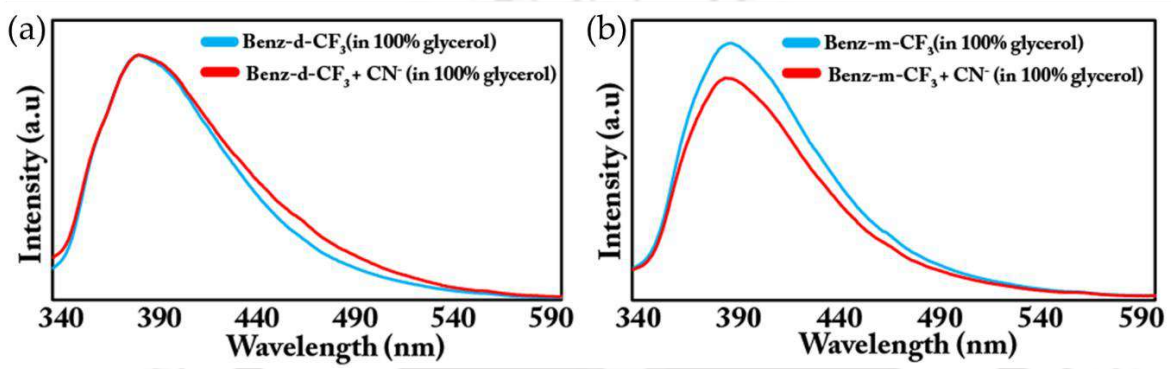

Figure A4A.20: Fluorescence spectra of (a) Benz-d-CF_3, and Benz-d-CF_3 + CN^-; (b) Benz-m-CF_3, and Benz-m-CF_3 + CN^- in 100% glycerol.

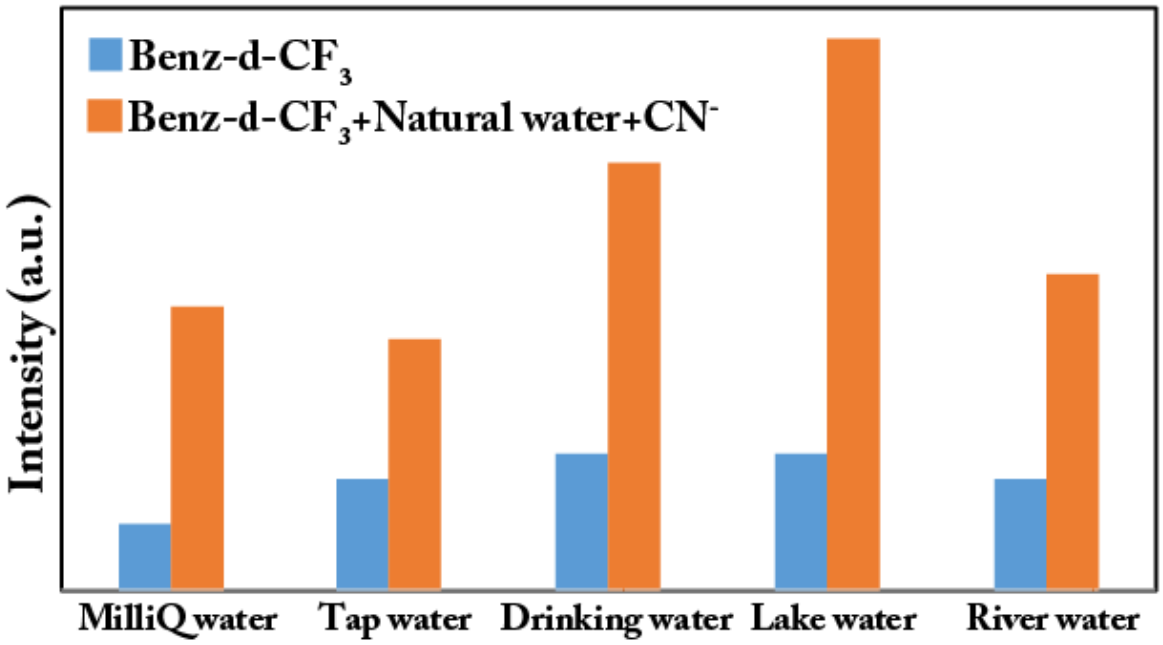

Figure A4A.21: Changes in emission intensity of Benz-d-CF_3 in the presence of CN- (100 μM) at 460 nm in natural sources of water.

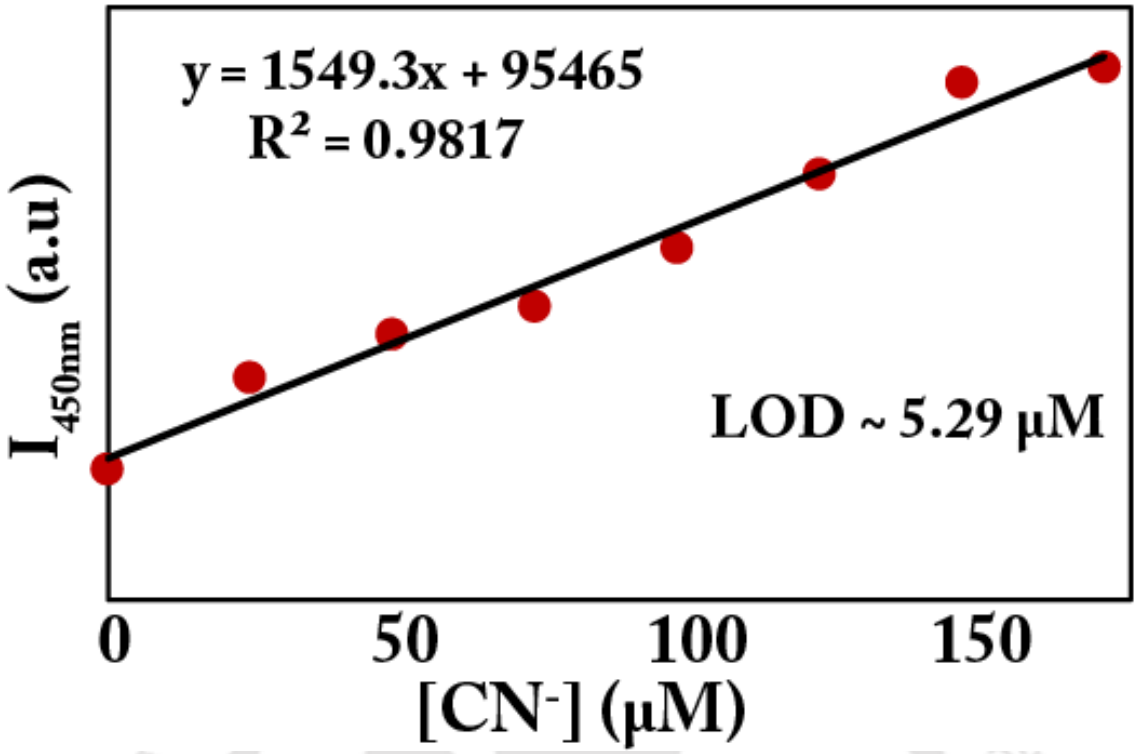

Figure A4A.22: Fluorescence intensity of Benz-d-CF_3 (at 450 nm) vs. concentration of CN^- plot for determination of detection limit in 100% aqueous medium.

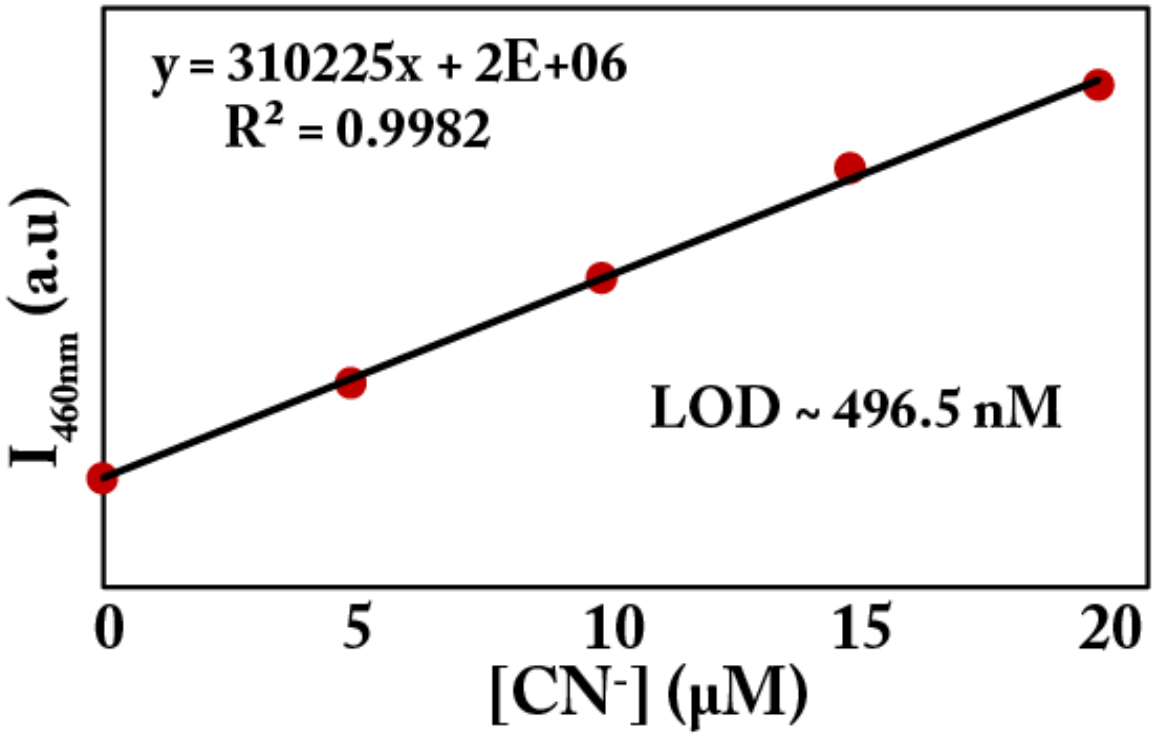

Figure A4A.23: Fluorescence intensity of Benz-d-CF_3 (at 460 nm) vs. concentration of CN^- plot for determination of detection limit in aqueous CTAB (3 mM) medium.

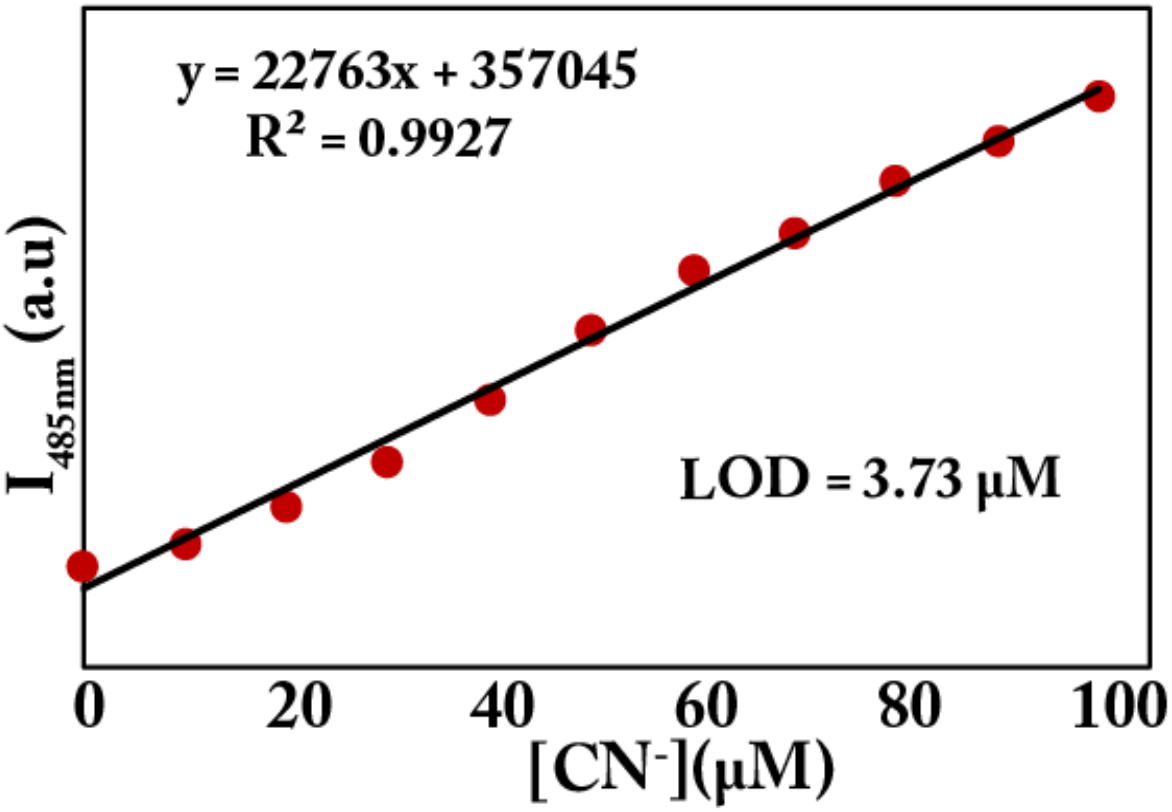

Figure A4A.24: Fluorescence intensity of Benz-m-CF_3 (at 485 nm) vs. concentration of CN^- plot for determination of detection limit in aqueous CTAB (3 mM) medium.

Table A4A.1: Detection of CN^- in Drinking water using Benz-m-CF_3 with the assistance of CTAB (3mM).

Spiked CN^- (µM)	Emission intensity at 485 nm	Emission intensity at 485 nm (from calibration curve)	Recovery (%)
65	2305932[a]	2372100	97.20
50	1815515[a]	1971670	92.08
25	12789675[a]	1359070	94.11
10	939525[a]	968060	97.05

[a]The emission intensities are the average of four independent emission spectra measurement.

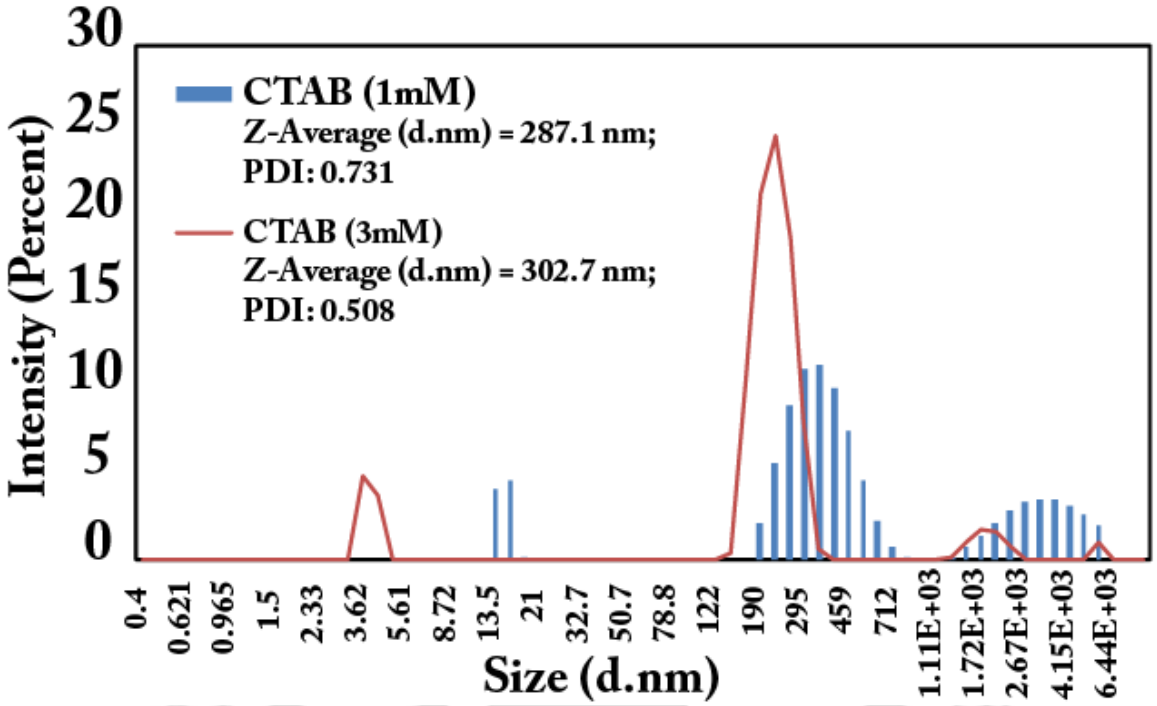

Figure A4A.25: Merged DLS-based particle size analysis of 1 mM and 3 mM aqueous CTAB solution.

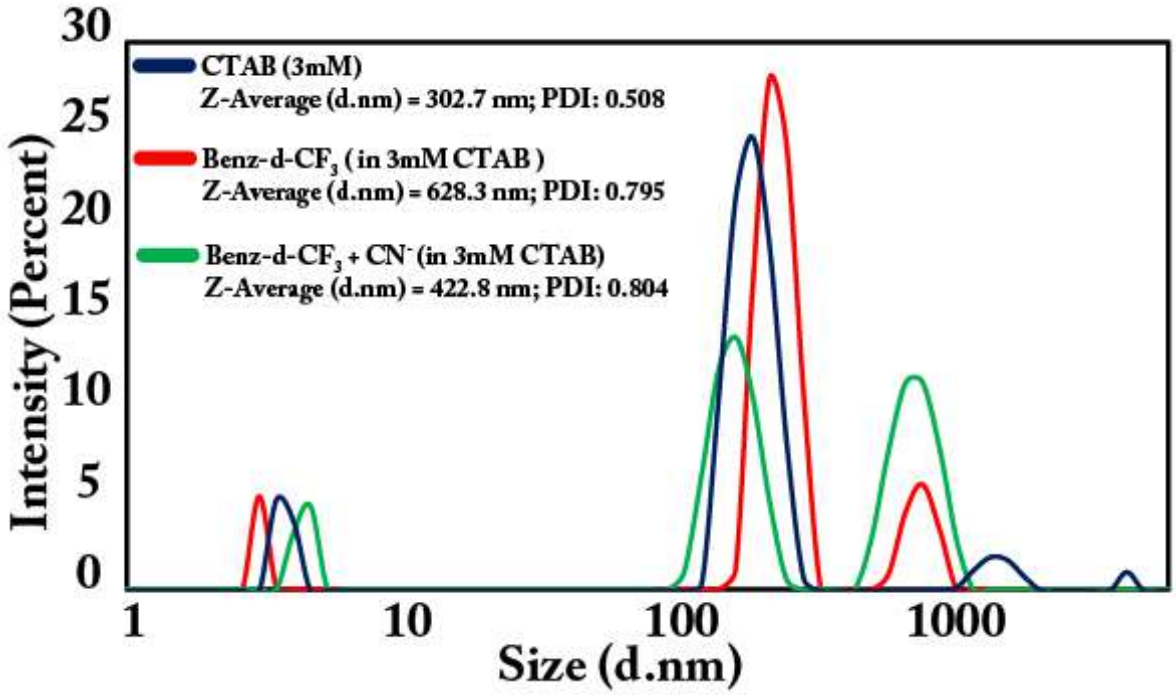

Figure A4A.26: DLS-based particle size analysis; change in particle size of Benz-d-CF_3 (10 μM) in aqueous CTAB solution (3 mM) upon interaction with 10 equivalents of CN^-, and comparison of particle size with aqueous CTAB only (3 mM).

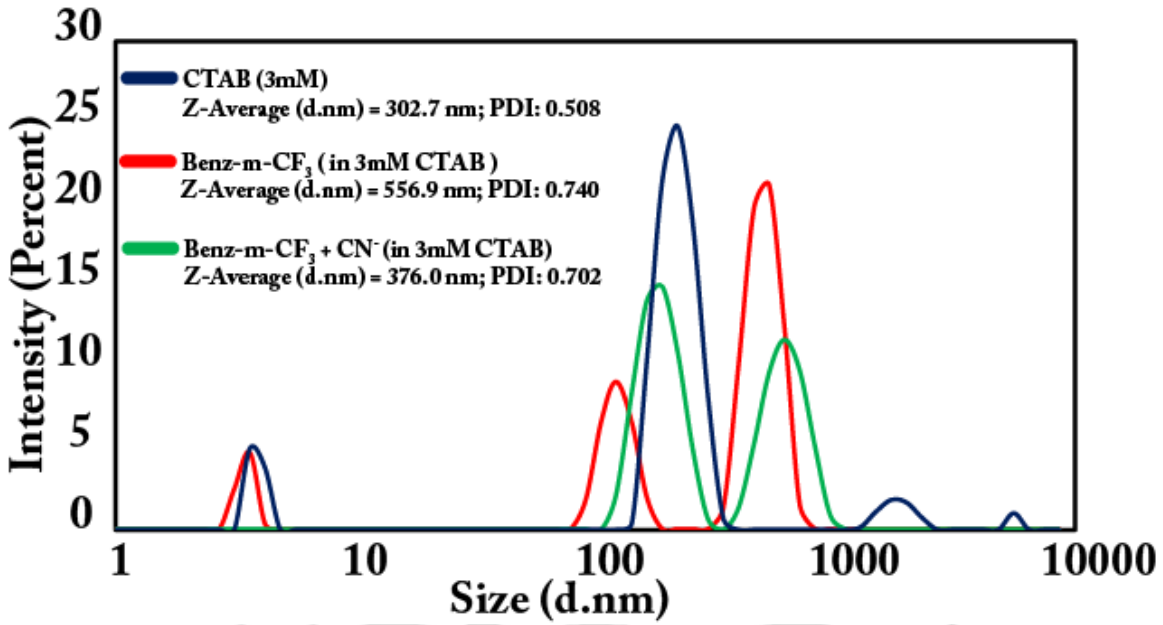

Figure A4A.27: DLS-based particle size analysis; change in particle size of Benz-m-CF_3 (10 μM) in aqueous CTAB solution (3 mM) upon interaction with 10 equivalents of CN^-, and comparison of particle size with aqueous CTAB only (3 mM).

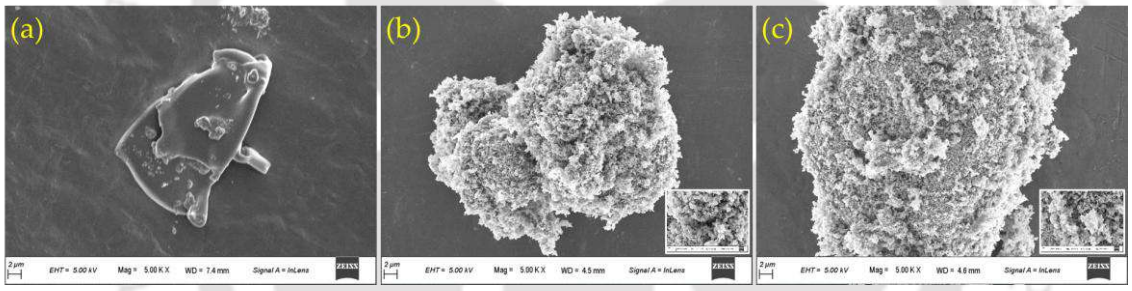

Figure A4A.28: FESEM images of (a) only Glycerol, (b) Glycerol + Benz-d-CF_3, and (c) Glycerol + Benz-m-CF_3.

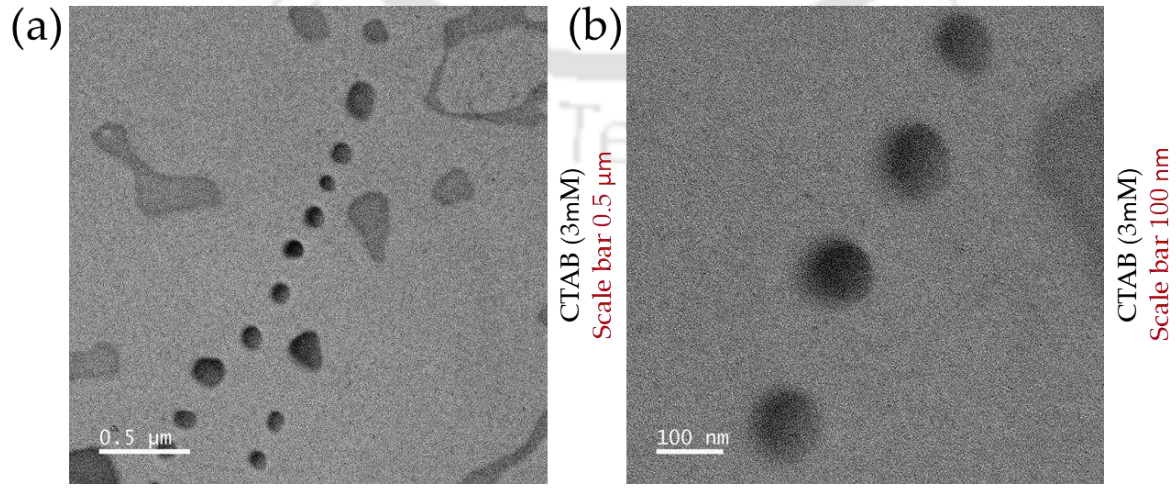

Figure A4A.29: (a) and (b) TEM images of micelle formation in aqueous CTAB (3 mM).

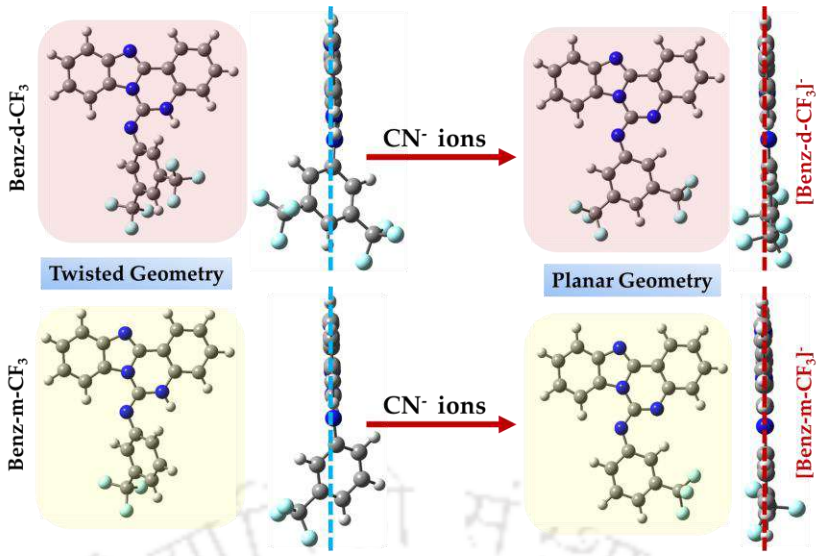

Figure A4A.30: Energy optimised structures of Benz-d-CF_3, [Benz-d-CF_3]$^-$, Benz-m-CF_3, and [Benz-m-CF_3]$^-$ in water using the B3LYP/6-31 G level of theory (CPCM model).

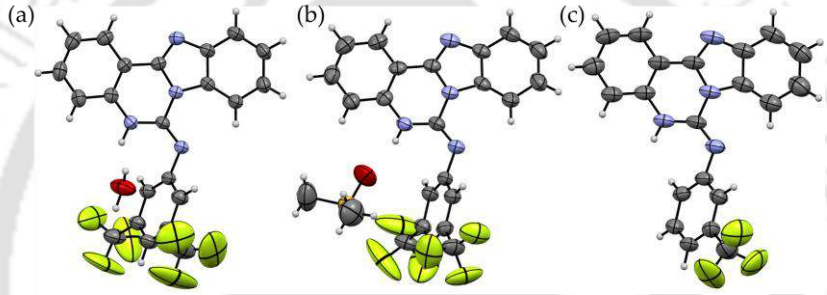

Figure A4A.31: ORTEP diagram of twisted (a) Benz-d-CF_3.H_2O, (b) Benz-d-CF_3.DMSO, and (c) Benz-m-CF_3 respectively at the 50% probability level.

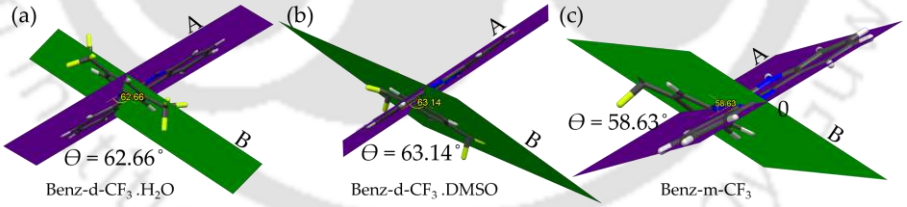

Figure A4A.32: Dihedral angle between the donor head and the acceptor tail of (a) Benz-d-CF_3.H_2O, (b) Benz-d-CF_3.DMSO, and (c) Benz-m-CF_3 as derived from SC-XRD study.

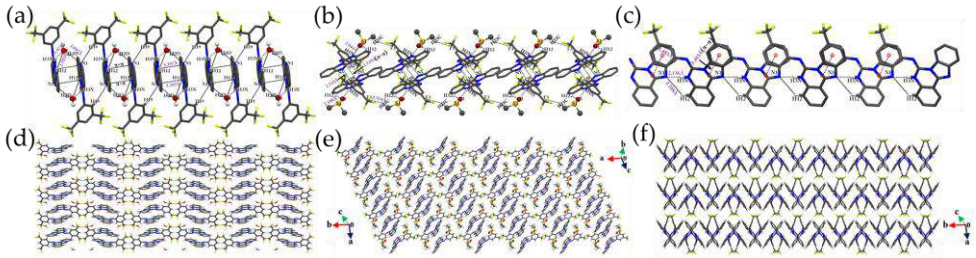

Figure A4A.33: Depicting non-covalent interaction mediated self-assembly of (a) Benz-d-CF_3.H_2O, (b) Benz-d-CF_3.DMSO, and (c) Benz-m-CF_3; (d), (e), and (f) depicting packing pattern of Benz-d-CF_3.H_2O, Benz-d-CF_3.DMSO, and Benz-m-CF_3 respectively.

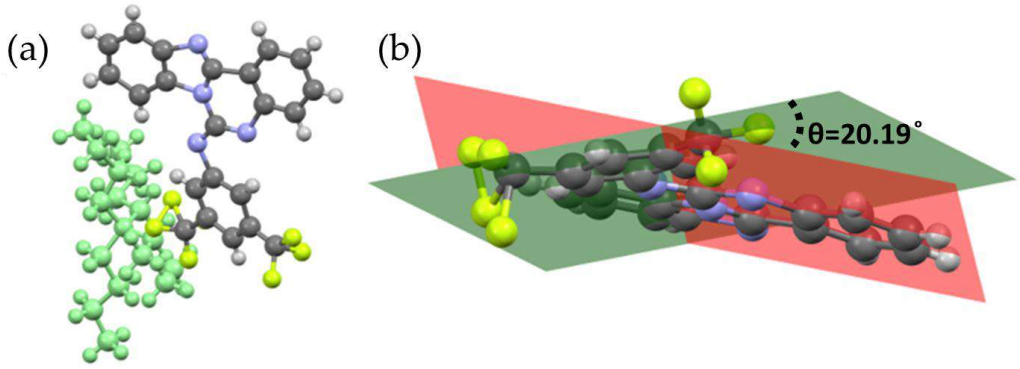

Figure A4A.34: (a) Depicting crystal structure of TBA+[Benz-d-CF_3]$^-$. b) Dihedral angle between the head and the tail part (CCDC no.: 2331471)

Table A4A.2: Hydrogen bonding distances (Å) and Bond angles (°) in the neural probes.

Ligand/ Complex	D-H···A	d(D···H)/Å	d(H···A)/Å	d(D···A)/Å	<D-H···A/°	Symmetry codes
Benz-d-CF_3.H_2O	O1-H10···F2	0.91 (9)	2.31 (8)	3.167 (5)	159 (7)	-1 + x, 1/2 – y, -1/2 + z
	O1-H20···N1	1.09 (6)	1.88 (6)	2.944 (4)	164 (5)	1 - x, -y, -z
	N3-H3N···O1	0.94 (4)	1.98 (4)	2.836 (4)	151 (3)	1 + x, y, z
	C4-H4···N4	0.93	2.50	2.998 (4)	114	x, y, z
	C19-H19···N1	0.93	2.60	3.523 (4)	169	1 - x, -y, -z
Benz-d-CF_3.DMSO	N3-H3N···O1	0.76 (6)	2.08 (5)	2.825 (8)	166 (6)	1 – x, -1/2 + y, 1/2 - z
	C4-H4···N4	0.93	2.52	2.998 (6)	112	x, y, z
	C16-H16···F1	0.93	2.42	2.738 (7)	100	x, y, z
	C20-H20···N1	0.93	2.53	3.438 (6)	164	1 – x, -y, -z
Benz-m-CF_3	N3-H3N···N1	0.89 (3)	2.14 (3)	2.988 (3)	161 (2)	x, 1/2 – y, 1/2 +z
	C4-H4···N4	0.93	2.50	2.984 (4)	113	x, y, z

Table A4A.3: Crystallographic parameters and refinement data of the probes.

Parameters	Benz-d-CF_3.DMSO	Benz-d-CF_3.H_2O	[Benz-m-CF_3]. [Benz-m-CF_3]$^-$. TBA^+
formula	$C_{24}H_{18}F_6N_4OS$	$C_{22}H_{14}F_6N_4O$	$C_{58}H_{61}F_6N_9$
fw	524.48	464.37	998.15
cryst syst	monoclinic	monoclinic	triclinic
space group	P 21/c	P 21/c	P -1
a (Å)	15.3037(6)	7.1823(6)	8.7718(6)
b (Å)	10.3312(4)	28.182(2)	13.5532(10)
c (Å)	16.3311(7)	10.1273(9)	22.6964(16)
α (deg)	90	90	90.310(2)
β (deg)	114.112(1)	91.871(2)	100.163(2)
γ (deg)	90	90	98.003(2)
V (Å^3)	2356.75(17)	2048.8(3)	2628.8(3)
Z	4	4	2
DC (g cm^{-3})	1.478	1.506	1.261
μ (Mo Kα) (mm^{-1})	0.210	0.133	0.091
F (000)	1072.0	944.0	1052.0
T (K)	297 K	295 K	297 K
θmax (deg)	25.000	24.998	24.996
total no. of rflns	52338	47401	62132
no. of indep rflns	4133	3575	9196
no. of obsd rflns	3104	3059	6809
no.of params refined	335	310	666
R1, I > 2σ(I)	0.0946(3104)	0.0813(3059)	0.0762(6809)
wR2, I > 2σ(I)	0.2520(4133)	0.2509(3575)	0.2363(9196)
GOF (F^2)	0.915	1.036	1.039
CCDC no.	2331451	2331449	2331466

Table A4A.4: A representative comparison table of the detection limits along with the receptor and solvent system used for the sensing of CN^-.

Sl. No.	References	Receptors	Solvent system	LOD
1.	**Present work**	Benzimidazoquinazoline-based fluorogenic probes	Aqueous medium and aqueous CTAB medium	0.496μM, and 3.73μM
2.	Journal of Molecular Liquids 336 (2021) 116861	Isophthaloyl dichloride/nitro-benzofurazan based fluorescent sensor	Aqueous medium	2.15μM
3.	Langmuir 2020, 36, 10537−10547	Copper based metallogel	Aqueous medium	1.09μM
4.	Chem. Commun., 2015, 51, 8173	1,8-naphthalimide based chemosensor (based on intramolecular $NH\cdots NH_2$ hydrogen bonding)	DMSO, DMSO/H_2O mixture (1 : 1, v/v), and pure 100% water	2.58μM(in DMSO), 7.98μM(in DMSO/H_2O), and 17.61μM(in pure 100% water)
5.	Chem. Sci., 2014, 5, 2710	Tetraphenylethene (TPE) derivatives containing dicyanovinyl groups	Aqueous CTAB medium	0.2μM
6.	Talanta 225 (2021) 122100	1,4-Dihydropyridines based	PBS water solution	0.274μM
7.	Analyst, 2017,142, 4825-4833	(2,4-di-tert-butyl-6-((2-hydroxyphenyl-imino)-methyl)phenol) containing two hydroxyl groups (Schiff base)	Aqueous CTAB medium	0.592μM
8.	Analyst, 2019,144, 2226-2230	1,4,5,8,9,12-Hexaazatriphenylene based fluorescent and colorimetric sensor	CH_3CN/H_2O 1 : 1 (v/v)	0.87μM
9.	J. Mater. Chem. B, 2019,7, 4620-4629	3-benzyl-2-(N-ethylcarbazole-3-vinyl)-benzothiazolium bromide	Neutral aqueous solution (HEPES buffer, pH 7.4)	0.339μM
10.	Sensors and Actuators B 228 (2016) 192–199	1,1-dimethyl-3-ethyl-2-(2-(N-ethyl-carbazol-3-yl)-vinyl)-1H-benzo[e]indolium iodide	DMSO	0.23μM

Chapter 4B

Highly Selective Anion Responsive Supramolecular Gel and Sequestration of Precious Metal Salt into its Nanoparticles

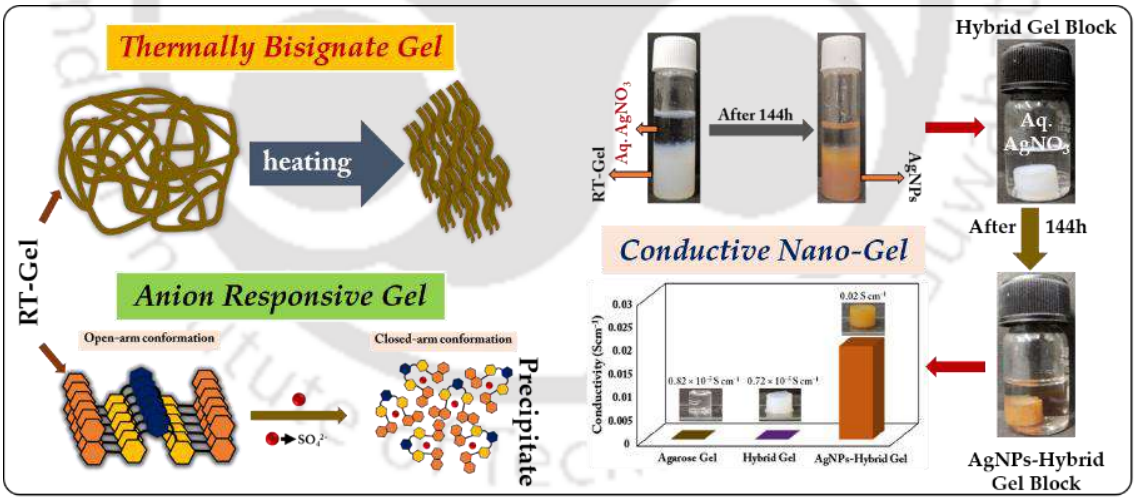

CHAPTER 4B

4B.1. Background and Focus of the Chapter

Supramolecular gels are colloidal, [4B.1] functional soft materials formed through the self-assembly of low-molecular-weight gelators (LMWGs) which transpires into long anisotropic structures that entangle and cross-link to form a nanoscale network capable of immobilizing the solvent, [4B.2] thus enabling translation of molecular scale information to materials performance. [4B.3] Supramolecular gel systems derived from LMWGs can be employed for some specific high-tech applications including the construction of stimuli-responsive materials, energy storage devices, environmental remediation, regenerative medicine, wound healing, etc. by optimizing the physical features and the chemical programming inherent within them. [4B.4, 4B.5]

Because of the innate weak nature and prevalence of reversible networks in LMWGs, as governed by various weak noncovalent interactions, these are known to be very good external stimuli-responsive (responsive toward pH, temperature, different analyte, etc.) in nature. [4B.6−8] Of various stimuli, anions are of great importance owing to the significant role played by them in both environments as well as in various biological processes. [4B.9, 4B.10] Over the years, designing of anion responsive supramolecular gels has become one of the most significant fields in soft materials as it integrates the ideas of the supramolecular self-assembly, stimuli-responsive function of nanomaterials, and smart designing of gelator molecules. [4B.11] Keeping all those things in mind, many researchers have embarked on their journey toward developing supramolecular gels capable of displaying anion-responsive behavior. [4B.12−4B.15, 4B.6] However, most of such outcomes are derived out of serendipity, [4B.15] since it is very difficult to draw a proper correlation between the structure and the property of the LMWGs, which leads to some serious problems, and one such issue is related to selectivity.

Apart from this, supramolecular gels are also known for their solvent compatibility nature and porous fibril network structure which facilitates rapid diffusion of small molecules within them, thus enabling their potential application in environmental remediation, nanoelectronics, and catalysis. [4B.1, 4B.16] The simultaneity of both softness and hardness in a supramolecular gel offers a platform to connect the hard world of electronics with the soft world of biology. In the pursuit of achieving this, much remarkable research has been done to develop conductive gel composites by adding conductive materials such as graphene, conductive polymers, carbon nanotubes, etc. into the gel matrix. [4B.17−4B.20] Another way of realizing this particular goal

is by incorporating metal nanoparticles inside the gel matrix, as the metal nanoparticles have the potential to conduct. In-situ reduction of metal salts to their nanoparticles [4B.21, 4B.22] inside the gel matrix is an efficient way of accomplishing the said task [4B.23, 4B.24] since gel nanofibers have the advantage of organizing the nanoparticles at the nanoscale level. [4B.24−4B.26] However, surprisingly, there have been only a few reports of supramolecular LMWGs being employed for generating such conductive nanocomposites by in situ reduction of the metal salts into nanoparticles. Smith et al. have done some significant research work toward this particular direction by demonstrating in situ generation of metal nanoparticles by using hydrogel based on d-sorbitol appended with acyl hydrazide, and their applicability in different fields such as catalysis and nanoelectronics. [4B.1, 4B.22] In a similar way Chen et al. went on to demonstrate in situ reduction of the Au nanoparticle, and its enhanced electrocatalytic performance on glucose owing to its good conductivity, using the d-sorbitol appended with an acyl hydrazide-based hydrogel. [4B.21] A few years back, Das et al. demonstrated in situ Pt nanoparticle generation inside a guanosine (G) based G-quadruplex hydrogel followed by utilization of the same for hydrogenation of aromatic nitro compounds in an aqueous medium. [4B.27] Coronado and his group have reported the in situ formation of gold nanoparticles inside poly(vinyl alcohol)–gallic acid hydrogels, [4B.28] and in a subsequent study they also demonstrated the synthesis of gold nanoparticles via controlled diffusion of gallic acid from poly(vinyl alcohol)–gallic acid hydrogels into an Au^{3+} solution. [4B.29] However, there is still much room for improvement in this particular area in terms of achieving greater efficiency, superior design of the LMWGs, and its real-world applicability, so it needs immediate attention to delve deeper into this, as it might unfold myriad possibilities with greater applicability soon.

In our continuing effort in the field of supramolecular self-assembly, and anion recognition chemistry, [4B.30−4B.38] herein we have tried to integrate the idea of self-assembly and anion recognition to develop anion-responsive supramolecular LMWGs. We also try to draw structure–function correlations to improve the selectivity-related issue of the receptor. Moreover, the effect of terminal substituent on gelation, vis a vis some fascinating properties of the resulting gel such as the “thermally bisignate” property have been investigated in detail in this article. We further delved into demonstrating the sequestration of precious metal ions from aqueous medium followed by in situ reduction into metal nanoparticles, and this particular idea has been translated toward the construction of a conductive hybrid gel nanocomposite. Such an idea perfectly demonstrates how the soft world of biology can be connected with the hard world of electronics via environmental remediation followed by the construction of conductive gel nanocomposite.

4B.2. Objective of the Chapter

Understanding the structure–function relationship is a significant challenge in designing supramolecular soft materials such as supramolecular gels. To address this challenge, herein, we have reported two urea-based dipodal ligands, PY-NAP, and PY-CF_3, with different terminal substituents influencing their gelation properties. The terminal substituents play a crucial role in the gelation abilities, which has been investigated thoroughly, and established rationally in this particular study. The gel formed from PY-NAP exhibited notably high thermal stability and displayed a unique "thermally bisignate" behavior. Both ligands contain urea and amide units, allowing them to encapsulate the SO_4^{2-} anion in their pincer cavities in the solid state. The solid-state anion recognition principle is used to construct a selective anion-responsive supramolecular gel. Additionally, the gel was used to sequester precious metal salts from aqueous solutions, achieving an uptake efficiency of over 90%, followed by in situ reduction to form nanoparticles. This concept was then applied to create a conductive supramolecular hybrid gel nanocomposite with significantly high conductivity, holding significant implications for industrial and environmental applications. This particular study upholds the concept of waste to wealth generation. Moreover, the idea proposed in this particular study has potential application in the field of soft electronics as well.

4B.3. Results and Discussion

4B.3.1. Design Rationale

Two pyridine-2,6-dicarboxamide-based urea-embedded ligands, namely, PY-NAP and PY-CF_3 with varying terminal substituents, have been designed to have a comparative study on their gelation ability. (Scheme 4B.1) The incorporation of urea and the amide units bear two significances in this particular study: a) both urea and the amide units act as a hydrogen bonding core, which facilitates self-assembly formation, and b) both of them can act as anion recognition sites. We have also varied the terminal substituents, where PY-NAP contains a planar electron-rich naphthyl moiety, and PY-CF_3 contains pi-acidic $-CF_3$ unit, where the F atoms are directed out of the plane. We hypothesized that such varied terminal substituents affect their gelation ability significantly. The idea of self-assembly and anion recognition has been unified to develop a selective anion-responsive supramolecular gel. Furthermore, the resulting gel has also been exploited for the sequestration of metal ions from an aqueous medium, followed by in situ reduction into nanoparticles, which is further explored to construct a conductive hybrid gel nanocomposite.

4B.3.2. Solid-state Self-assembly

Successful crystallization of PY-NAP and PY-CF_3 was achieved with DMSO. (Figure 4B.1a,b) However, it is important to note here that PY-CF_3 (as it took only 3–4 days to crystallize) was more prone to crystallization as compared to PY-NAP (required more than 20 days to crystallize), and in most cases, precipitation was observed for the latter in due course of its crystallization.

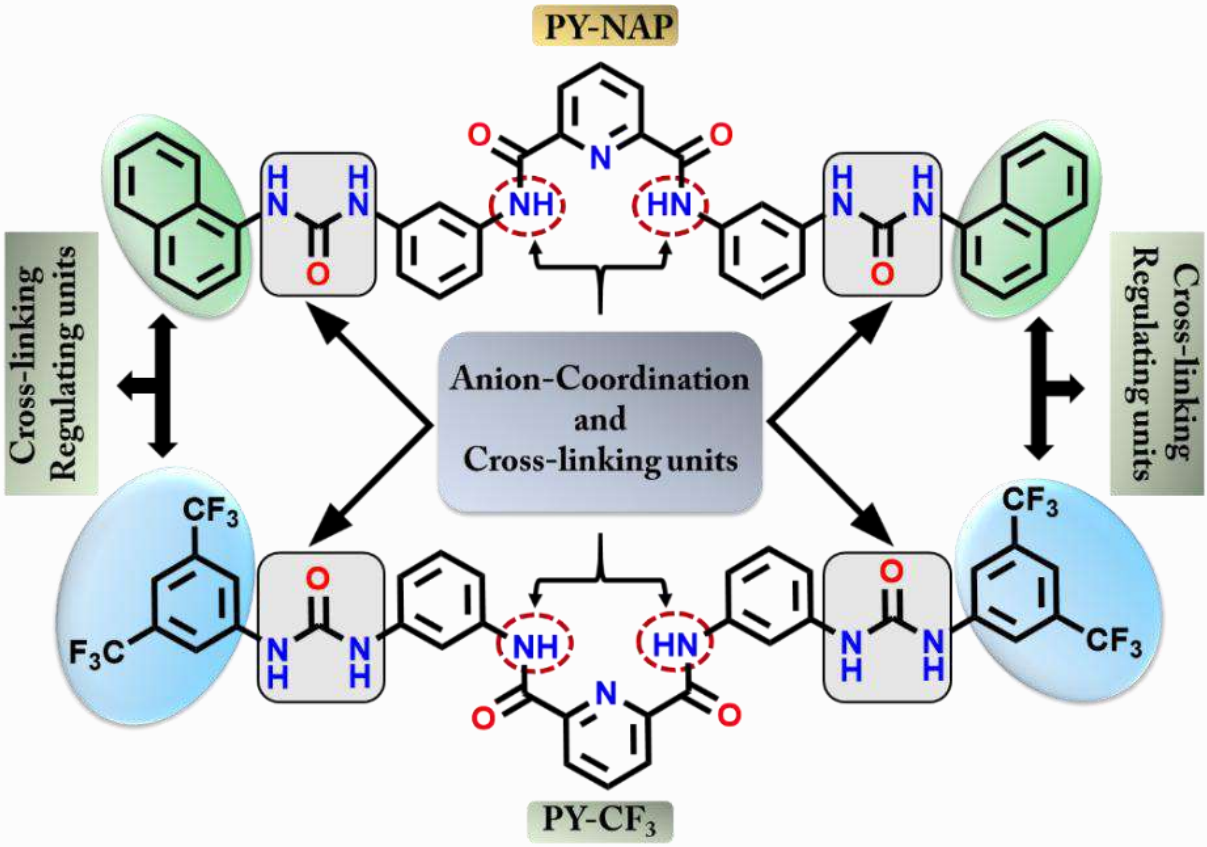

Scheme 4B.1: Design of ligands PY-NAP and PY-CF_3.

Crystal structure analysis of both PY-NAP.DMSO (the isolated crystal possesses some disorder) and PY-CF_3.DMSO revealed active participation of the urea -NH units in their self-assembly formation through strong hydrogen bonding interactions. PY-NAP.DMSO forms 1-D self-assembly with the assistance of DMSO involving strong hydrogen bonding interactions (O3···H3N = 2.01 Å, O3···H4N = 2.19 Å, O2···H23B = 2.37 Å, O4···H3NA = 2.20 Å, O4···H4NA = 2.30 Å, and O2A···H25B = 2.63 Å) when viewed along the crystallographic a-axis. (Figure 4B.1c(i)) Moreover, with π–π stacking interaction between the spacer pyridine, and the phenyl moieties (π_{py}–π_{ph} = 3.71 Å), accompanied by strong hydrogen bonding, and C–H···π interactions, the self-assembly extends toward crystallographic c-axis as well, with the assistance of DMSO (Figure 4B.1c(ii)). In the same way, DMSO also assists PY-CF_3 in its self-assembly formation (along the crystallographic b-axis) as observed earlier for PY-NAP (O3···H3N = 2.26

Å, O3···H4N = 2.06 Å, and O2···H21B = 2.48 Å). The terminal -CF_3 units facilitate the extension of both arms to form self-assembly in two opposite directions with the help of a hydrogen bonding interaction (F3···H15 = 2.66 Å). (Figure 4B.1d) It is important to note here that the π–π stacking interaction observed (π_{py}–π_{ph}) for PY-NAP was absent in PY-CF_3. Such ambiguity in intermolecular interactions results in differential self-assembly behavior, imparting different chemical properties in them, which forms the basis of our study. (Table A4B.2, Table A4B.3)

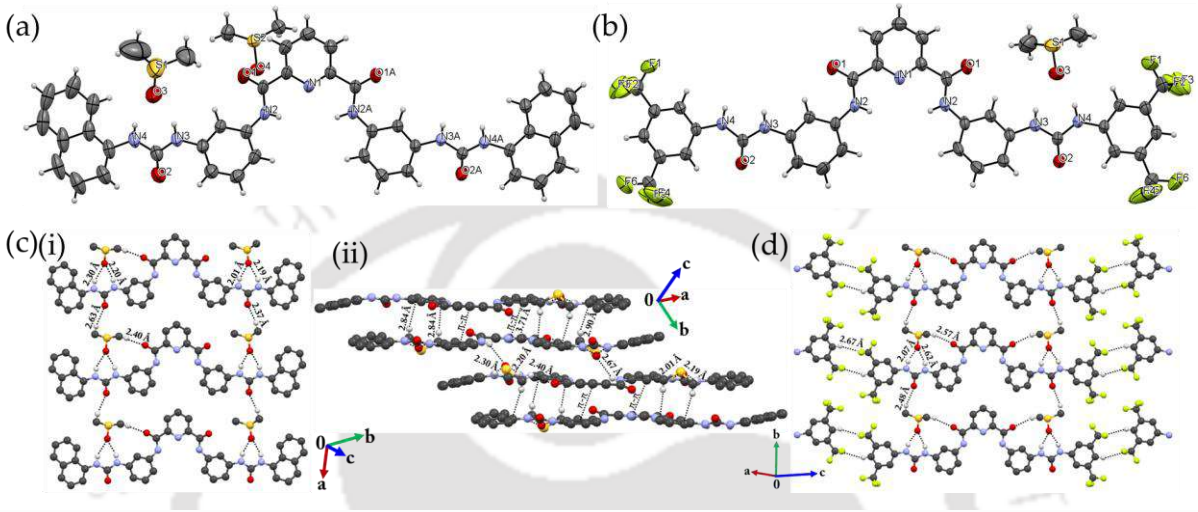

Figure 4B.1: Depicting ORTEP diagram of (a) PY-NAP.DMSO and (b) PY-CF_3.DMSO (at 50% probability level). (c) Self-assembled network formation in PY-NAP.DMSO (i) via hydrogen bonding interaction (viewed along the crystallographic a-axis), (ii) via π–π stacking interaction (viewed along the crystallographic c-axis). (d) Self-assembly formation in PY-CF_3.DMSO via hydrogen bonding interaction (viewed along the crystallographic b-axis).

4B.3.3. Dissecting the Effect of Terminal Substituents and Temperature on Gelation

Gelation ability of both PY-NAP and PY-CF_3 was investigated in different solvents, and mixed solvent systems. (Table A4B.1) We observed that only PY-NAP could form a gel upon the rapid addition of water in a DMSO: H_2O (3:2) mix solvent system at room temperature (RT-Gel). (Figure 4B.2a,b, Figure A4B.1a,b) Such gelation ability of PY-NAP can be attributed to its ability to form a hydrogen bonding network as facilitated by the presence of both hydrogen bond donors as well as acceptor sites such as urea and amide moieties and also its ability to undergo π–π stacking interactions as enabled by the planar naphthyl ring, which are well supported by the crystal structure analysis as discussed earlier. We reasoned that such a drastic change in the gelation ability between PY-NAP and PY-CF_3 is majorly due to the differential nature of the terminal substituents present in both of the ligands. A control gelation experiment was also performed for PY-NH_2 to further strengthen our claim. As evident from our study, PY-NH_2 does not form a gel in the aforementioned condition, which indeed infers the significant role played by the terminal substituent on gelation. (Figure A4B.1c)

We have performed both solid and solution state investigations to get insight into this behavioral anomaly toward gelation. We fortunately could crystallize both ligands with DMSO solvent. The commonality between both the ligands is that both of them could form two-dimensional (2-D) self-assembly with the help of hydrogen bonding interactions as assisted via DMSO. The major differentiating factor that greatly affects their gelation ability is expected to be their differential ability to undergo π–π stacking interactions.

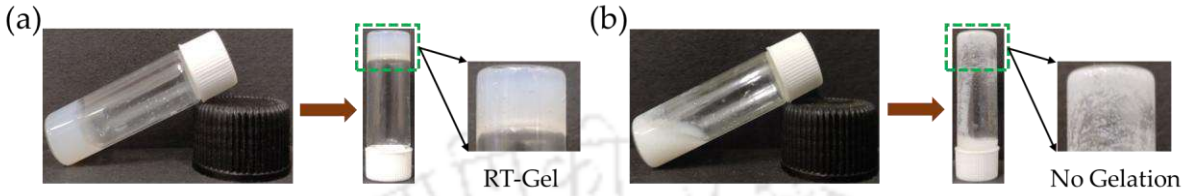

Figure 4B.2: Depicting (a) gel formation of PY-NAP (termed as RT-Gel), (b) no gelation in PY-CF_3 using a DMSO: H_2O (3:2) solvent system.

As evident from the crystal structure analysis, PY-NAP is observed to be involved in the π–π stacking interactions, thus facilitating the three-dimensional expansion of the self-assembled network. On the contrary, in PY-CF_3 no such π–π stacking interaction was apparent from the crystal structure analysis. This can be ascribed to the planarity of the naphthyl moiety present in the PY-NAP ligand, which facilitates a closer approach of the ligands unlike in the PY-CF_3, where in the bulky -CF_3 unit the fluoride atoms are directed out of the plane, which discourages such closer approaches of the ligands. PY-CF_3 was observed to be more prone to crystallization rather than gelation as compared to that of PY-NAP, which might be attributable to the existence of a stronger intermolecular hydrogen bonding interaction in PY-CF_3 due to the presence of two electron-withdrawing -CF_3 units. Apart from that, the presence of F atoms also enables further expansion of the hydrogen bonding network in 2-D space as discussed earlier. Here it is important to mention that we have used the crystallographic information on the molecules just to support our hypothesis, especially to showcase the plausible noncovalent interactions that are helping in cross-linking, and eventually leading to gelation, as crystal engineering is not the ultimate tool for the description of a gelation process. [4B.39]

Those observations are well supported by a solution state study, where ^{1}H NMR titration experiments were conducted for both ligands with the incremental addition of D_2O into the DMSO-d_6 solution of the respective ligands. As evident from the experiment, the peaks corresponding to the amide NH_a were observed to be downfield shifted, whereas upfield shifting of the urea $NH_{b,c}$ peaks was observed with incremental addition of D_2O, indicating an increase in hydrogen bonding interactions with enhanced aggregation. (Figure 4B.3a,b) If we observe, the peaks corresponding to the aromatic region protons are all observed to be upfield shifted as %

D_2O increases, which reveals the enhanced π–π stacking interaction because of aggregation. It is quite noticeable that all of the mentioned peaks, especially the peaks corresponding to the aromatic protons, were much more shifted in the case of PY-NAP as compared to that of PY-CF_3, (Figure 4B.3a,b) indicating the presence of extensive π–π stacking interactions in PY-NAP, which corroborates perfectly well with the crystallographic results. So, we reasoned that the presence of the planar naphthyl ring present in PY-NAP promotes stronger π–π stacking interactions, thus helping in the gelation process unlike in PY-CF_3. The gel formed by PY-NAP remained stable for more than a month.

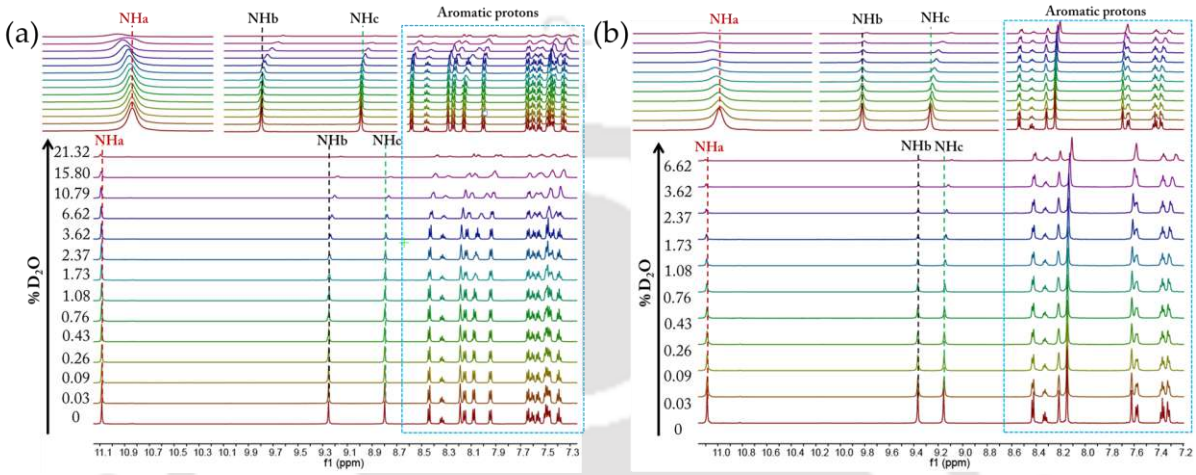

Figure 4B.3: Depicting ^1H NMR titration experiment of (a) PY-NAP (performed in DMSO-d_6, 298.15 K, 600Mz, 25 mM), and (b) PY-CF_3 (performed in DMSO-d_6, 298.15 K, 600 Mz, 25 mM) with increasing % of D_2O.

We further performed the effect of temperature on RT-Gel, and it is important to note that the RT-Gel was observed to remain intact inside a vial even after heating it at 100°C for about 20 min, (Figure 4B.4a(i),(ii)) and the resulting gel has been termed as H-Gel. As a result, the morphology of the resulting gel changes from a more contiguous fibrous network (in RT-Gel) to a more distinct worm-like structure (in H-Gel). (Figure 4B.5a,b) This resembles a complex system where a gel state can be tailored directly to form a different gel state by heating without the formation of a sol state, which is referred to as "thermally bisignate" gels. [4B.7] We reasoned that heating RT-Gel at 100 °C for a few minutes results in solvent exchange followed by a reorganization of hydrogen-bonded networks, which allows such temperature-induced gel-to-gel transition. [4B.7] It is also reflected very well in the rheology study of the respective gels, as discussed below. We further heated the RT-Gel above 100°C to have a better idea about its thermostability. Heating RT-Gel at 120°C for 15 min resulted in complete separation of the gel and the solvent (Figure 4B.4(ii),(iii)), and the resulting gel was observed to be mechanically more rigid as compared to that of the RT-Gel, as evident from its self-standing ability. (Figure 4B.4b) There are many reports available in the literature where the gels derived from LMWGs

undergo gel-to-sol transition at temperatures below 100°C, [4B.4, 4B.14, 4B.16, 4B.40−4B.43] and as per our knowledge, the reports on pure LMWGs (without incorporating any polymers) with such high thermal stability (stable above 100°C) are still scarce in the literature. Supramolecular gels derived from LMWGs are generally very weak, so in that scenario, our report possesses two very important features: (i) high thermal stability and (ii) enhanced mechanical strength at high temperature. Such temperature tunability of a supramolecular gel system provides a greater scope for exploring its applicability in the field of soft materials, which we are going to delve into soon.

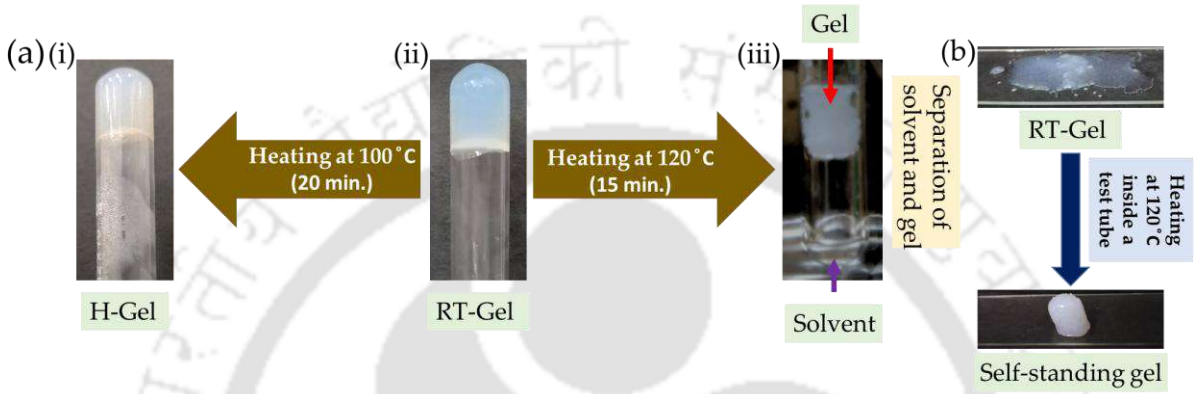

Figure 4B.4: Depicting gel-to-gel transition of RT-Gel on heating (a) (i) and (ii) at 100°C for 20 min; (a) (ii) and (iii) at 120°C for 15 min. (b) Depicting self-standing gel formed as a result of heating RT-Gel at 120°C for 15 min inside a test tube.

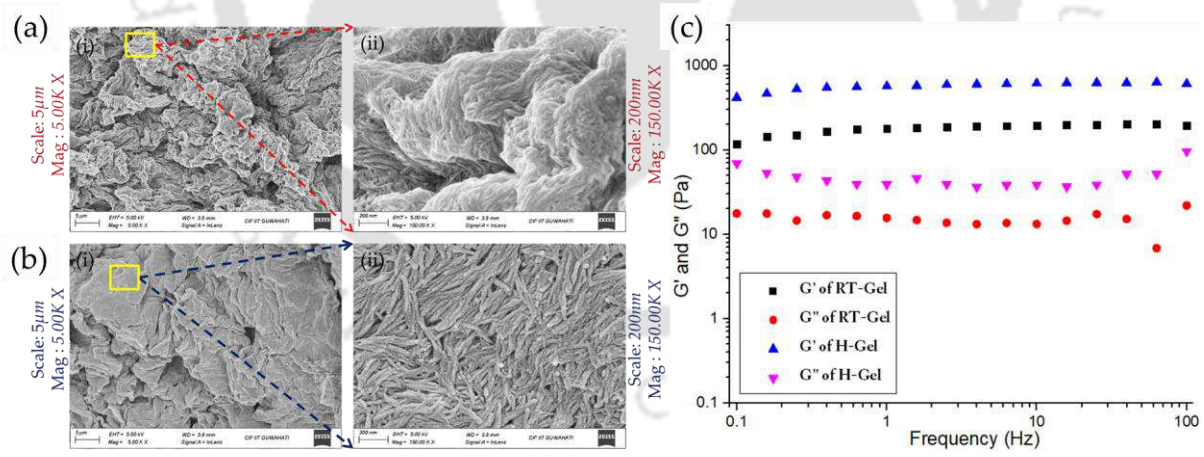

Figure 4B.5: Depicting FESEM image of the xerogel of (a) (i) and (ii) RT-Gel, (b) (i) and (ii) H-Gel. (c) Frequency-dependent rheological measurement of RT-Gel, and H-Gel with a shear strain of 0.1%.

Moreover, to investigate the viscoelastic nature and to have an idea about the mechanical strength of the obtained gels, rheological studies were performed. For all the gels namely, RT-Gel, and H-Gel, the gel–sol transitions were monitored over different shear strains with a fixed frequency at 1 Hz. As the storage modulus (G′) starts to decrease after a 1% shear strain, we decided on a shear strain of 0.1% to measure the frequency-dependent rheological behaviors of

the gels. (Figure A4B.2) The storage moduli (G′) and loss moduli (G″) were monitored as functions of frequency sweep for both gels at room temperature, and it was observed that G′ values are always above G″ over the entire range of frequencies tested, thus inferring the true gel nature of RT-Gel and H-Gel. Interestingly, the storage moduli (G′) value of H-Gel was well above the value obtained for RT-Gel indicating higher mechanical rigidity of the former as discussed above. (Figure 4B.5c)

4B.3.4. Recognition Guided Anion Responsive Gel

PY-NAP was observed to be prone to crystallization with sulfate (SO_4^{2-}) anions, where it could encapsulate a sulfate (SO_4^{2-}) anion inside its pincer cavity with the assistance of a water molecule, and tetrabutyl ammonium cation through a total of 13 strong hydrogen bonding interactions (average hydrogen bonding distance = 2.34 Å) (Figure 4B.6a,b) (the isolated crystal possesses some disorder). An SC-XRD study reveals that the bis-urea unit forms a strong hydrogen bonding interaction with the SO_4^{2-} anion, thus playing a major role in this encapsulation process. (Figure 4B.6b) Interestingly, direct involvement of the amide moiety was not observed in this encapsulation process. However, it captures a water molecule inside its pincer cavity, which eventually undergoes a hydrogen bonding interaction with the SO_4^{2-} anion. (Figure 4B.6b; Table A4B.2; Table A4B.3) It is also evident from the FTIR study of the crystals of the PY-NAP-Sulfate complex, where the peak corresponding to the urea -NH was observed to be broadened with concomitant peak shifting toward the lower energy region (from 3276 to 3200 cm^{-1}) signifying its involvement in hydrogen bonding interaction with SO_4^{2-} anions. (Figure A4B.4)

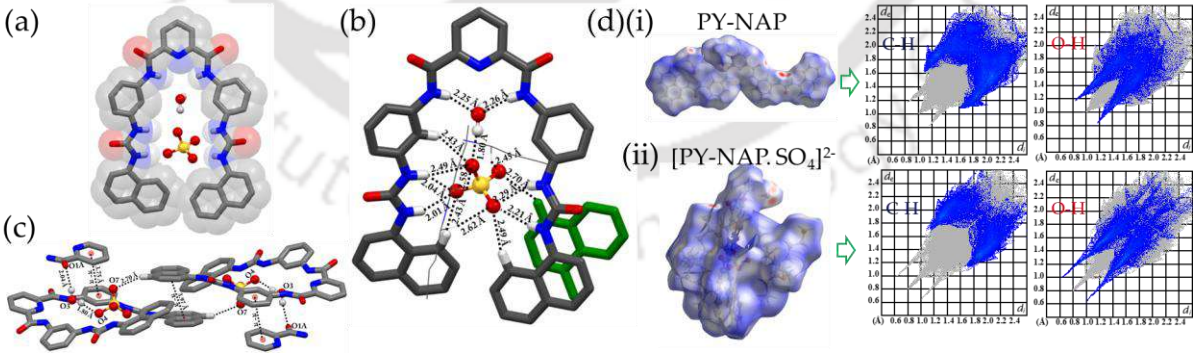

Figure 4B.6: Depicting (a) SO_4^{2-} anion encapsulation within the pincer-cavity of PY-NAP; (b) hydrogen bonding interactions involved in the SO_4^{2-} anion encapsulation process; (c) hydrogen bonding network formation in the PY-NAP.Sufate complex. (d) (i) and (ii) Hirshfeld surface analysis displaying the d_{norm} surfaces, and two-dimensional fingerprint plots (2D FPs) with the C–H, and H–O interactions.

^{1}H NMR study of the crystals of PY-NAP was performed. The sulfate complex reveals severe broadening of the peaks corresponding to -NH (urea/amide), indicating a hydrogen bonding

induced rapid dynamic effect, [4B.44] thus corroborating very well with the solid-state results. (Figure A4B.3) This SO_4^{2-} anion encapsulation results in a serious conformational alteration of PY-NAP, where its open arm conformation transformed into a closed arm conformation upon SO_4^{2-} anion binding, (Figure 4B.1a; Figure 4B.6a–c) thus inflicting significant structural change with concomitant alteration in the various intermolecular interaction eventually leading to disruption of a uniform self-assembly pattern existed earlier in PY-NAP. This can also be visualized through the changes in the various contact contributions such as H–C, and H–O contact contributions in PY-NAP as well as in its SO_4^{2-} anion complex, through Hirshfeld surface analyses. (Figure 4B.6d (i),(ii)) A significant reduction in the H···C contact contributions (which includes C–H···O or C–H···π contacts) was observed from 22.2% (in PY-NAP) to 13.1% (in the sulfate complex of PY-NAP), along with a slight reduction of the H–O contact contributions (from 13.7% to 12.2%), which signifies substantial disruption of various noncovalent interactions upon SO_4^{2-} anion coordination. (Table A4B.4) However, we also tried to crystallize different anions such as F^-, Cl^-, Br^-, I^-, NO_3^-, $H_2PO_4^-$, ClO_4^-, CN^-, HO^-, and CH_3COO^- with PY-NAP, but instead of crystallization, it resulted in precipitation.

Having witnessed the solid-state recognition of SO_4^{2-} by PY-NAP, we wondered if this idea could be translated toward the construction of an anion-responsive gel. As PY-NAP could undergo gelation (RT-Gel), we were very keen to investigate its anion-responsive behavior in the gel state. Subsequently, we started adding biologically relevant anions with varied dimensionality (2 equiv., and 5 equiv.) such as F^-, Cl^-, Br^-, I^-, NO_3^-, SO_4^{2-}, HSO_4^-, $H_2PO_4^-$, ClO_4^-, CN^-, HO^-, and CH_3COO^- on the top of the RT-Gel, and then all of them were kept under observation for 48 h, and pictures were taken after certain time intervals viz., 6, 24, and 48 h. After 48 h, the gel containing SO_4^{2-} collapsed completely to give a white-colored precipitate, when 5 equiv. of anions were added, while all the other gels containing different anions remained intact. (Figure 4B.7b(i)–(iii), Figure A4B.5) However, partial disruption of the RT-Gel was observed after 48 h for SO_4^{2-} when only 2 equiv. of anions were used. (Figure 4B.7a(i)–(iii)) Along with this, a partial disruption of the RT-Gel was observed in the presence of HSO_4^- (5 equiv.) as well after 48 h. (Figure A4B.5) The same experiment was performed using H-Gel too, where adding 5 equiv. of SO_4^{2-} resulted in only partial disruption of the gel matrix after 48 h, which is ascribable to the more rigid nature of H-Gel as compared to that of RT-Gel as evident from the rheology experiment.

We infer the mechanism behind such anion-responsive behavior is on account of the conformational alteration of PY-NAP, favoring or disfavoring intermolecular interactions as evidenced by the single crystal structure of PY-NAP.Sulfate complex. We reasoned that PY-NAP is expected to be in an open-arm conformation in the gel state, which is more favorable for

various intermolecular interactions to take place, thus favoring gelation. As soon as the SO_4^{2-} anion is added onto the RT-Gel, conformational alteration is expected to take place from open-arm to closed-arm conformation owing to SO_4^{2-} encapsulation by PY-NAP, which is evident from the crystal structures. The closed arm conformation is least favorable for the intermolecular interactions to take place as the −NH (urea/amide) units are involved in the hydrogen bonding interaction with SO_4^{2-}, consequently leading to the disruption of the gel state.

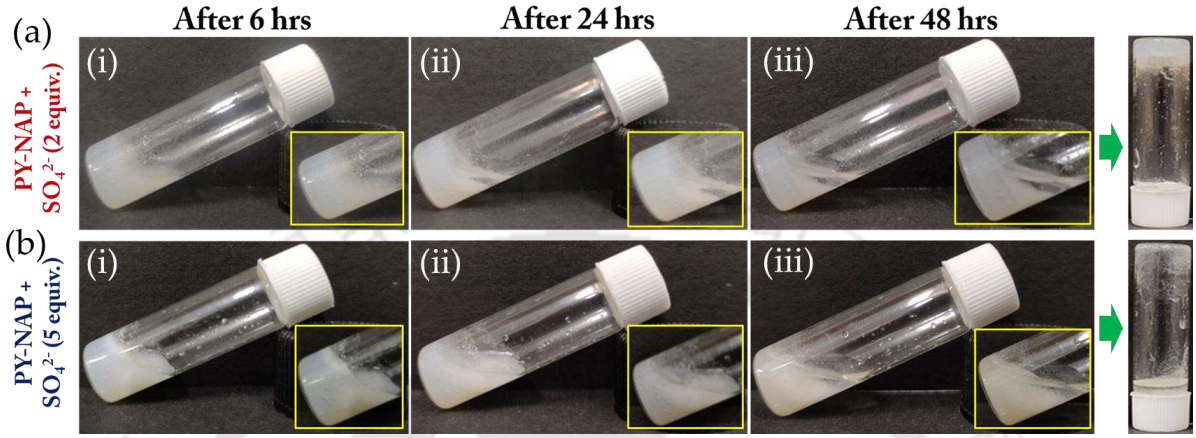

Figure 4B.7: Depicting gel to sol transition of RT-Gel in different time intervals on adding (a) (i–iii) 2 equiv., and (b) (i–iii) 5 equiv. of SO_4^{2-} anion.

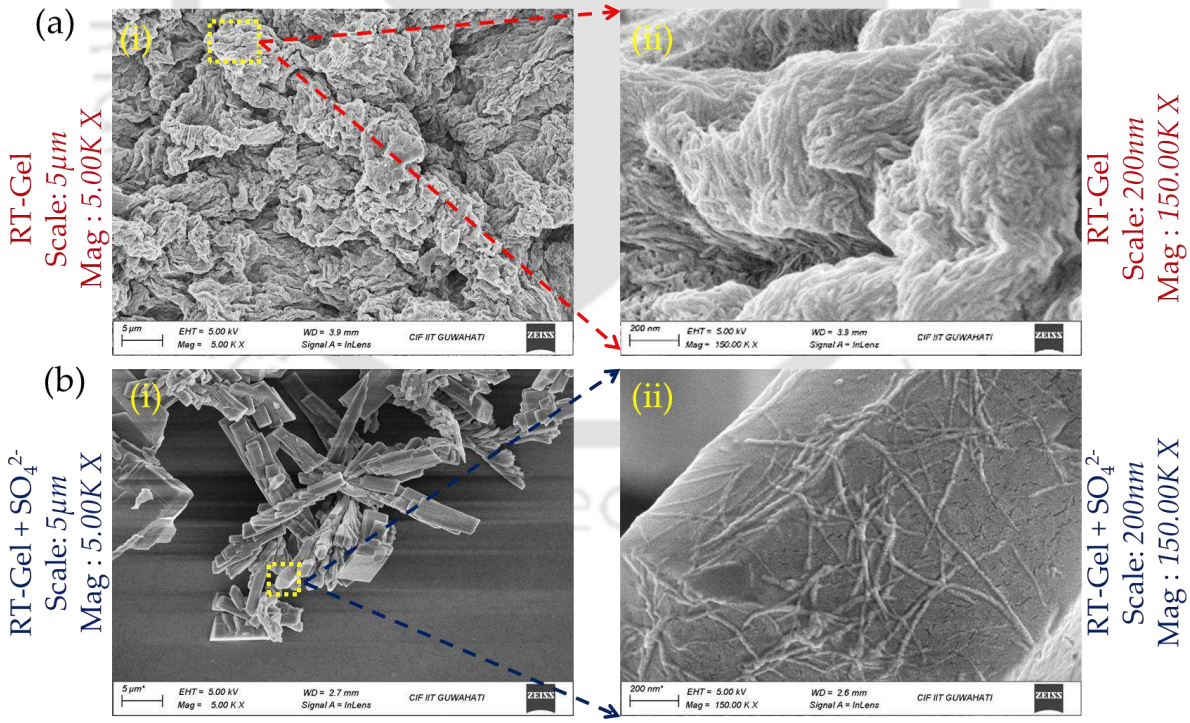

Figure 4B.8: FESEM imaging of (a) (i) and (ii) the xerogel of RT-Gel; (b) (i) and (ii) RT-Gel in the presence of SO_4^{2-} anion.

Such disruption of the gel state is accompanied by distinctive morphological alteration as evident from the FESEM (field emission scanning electron microscope) imaging where the fibrous network present in the RT-Gel disintegrates completely to give rod-shaped morphology with some remaining of the fibrous network on the surfaces of the rods upon SO_4^{2-} addition. (Figure 4B.8a(i),(ii); Figure 4B.8b(i),(ii)) On analyzing the precipitate obtained from the collapsed gel through ^1H NMR spectroscopy, severe broadening of the peak NH_a (corresponding to amide -NH) with concomitant downfield shifting was observed, and the peaks NH_b and NH_c (corresponding to urea -NH) were observed to vanish completely signifying strong sulfate binding through hydrogen bonding interactions. (Figure A4B.6) FTIR analysis of the precipitate also reveals the same story, where the peak corresponding to the urea/amide -NH at 3272 cm^{-1} undergoes severe broadening, thus supporting strong hydrogen bonding interaction of the SO_4^{2-} anion with PY-NAP involving urea/amide -NH units, inside RT-Gel. (Figure A4B.7)

4B.3.5. Sequestration and in-Situ Reduction of Precious Metal Salt

We demonstrated the sequestration of precious metal ions from water by showcasing the uptake of silver (Ag^+) ions from an aqueous medium by both RT-Gel and H-Gel. An aqueous solution of $AgNO_3$ (290 mM, 1500 µL) was added on the top of both the gels (1 wt %/vol) separately, and it was allowed to diffuse through them for 144 h. (Figure 4B.9a(i),(ii)) The supernatants were collected in certain time intervals such as 36, 72, 108, and 144 h, and analyzed through atomic absorption spectroscopy (AAS) to monitor the metal ion uptake. After 144 h, the % uptake was observed to be 90.49% for RT-Gel with Ag^+ ion loading of 6701.37 mg g^{-1} (metal: gelator) followed by H-Gel (85.19% uptake, and 6293.68 mgg^{-1} Ag^+ ion loading), which is far more superior than that of the earlier reports in the literature. (Figure 4B.9b,c; Figure A4B.9; Table A4B.5; Table A4B.6) [4B.36] Moreover, both the gels remained intact even after 144 h of metal ion uptake, (Figure 4B.9a(i),(ii)) which makes it very promising and advantageous as compared to earlier reports. Both the gels undergo a color change from white to yellow (in RT-Gel), and dark brown (in H-Gel) which are characteristics of the reduction of metals into metal NPs which are capped inside the gel fibers. The dark brown color in H-Gel might be attributable to the aggregation of AgNPs inside the gel matrix, which is comprehensible as in H-Gel the gel fibers were observed to be more distinct, thus leaving some room for the AgNPs to undergo aggregation. Such sequestration of metal ions from aqueous medium followed by spontaneous in situ reduction of metals into metal NPs inside supramolecular gel nanofibers without using any external reducing agents is very important yet scarce in the literature.

Different spectroscopic methods have been employed for a deeper understanding of the NPs residing inside the gel (AgNPs-RT-Gel) matrix. A UV–vis spectroscopic study in DMSO reveals

an absorption band at 460 nm (appears as a shoulder peak along with the characteristic peak of PY-NAP at 300 nm) corresponding to the surface plasmon resonance (SPR) band of AgNPs. (Figure A4B.8a,b) This particular SPR band shows the existence of spherical silver nanoparticles in the solution, [4B.45] which is also apparent from FESEM, and field emission transmission electron microscopy (FETEM) analysis. (Figure 4B.10a–f) The average diameter of AgNPs formed is observed to be 12 nm from FETEM analysis. Here it is important to note that the color of the AgNPs solution in DMSO turns dark brown from the initial yellow color after 10 min, which is attributable to nanoparticle aggregation. (Figure A4B.8c(i),(ii))

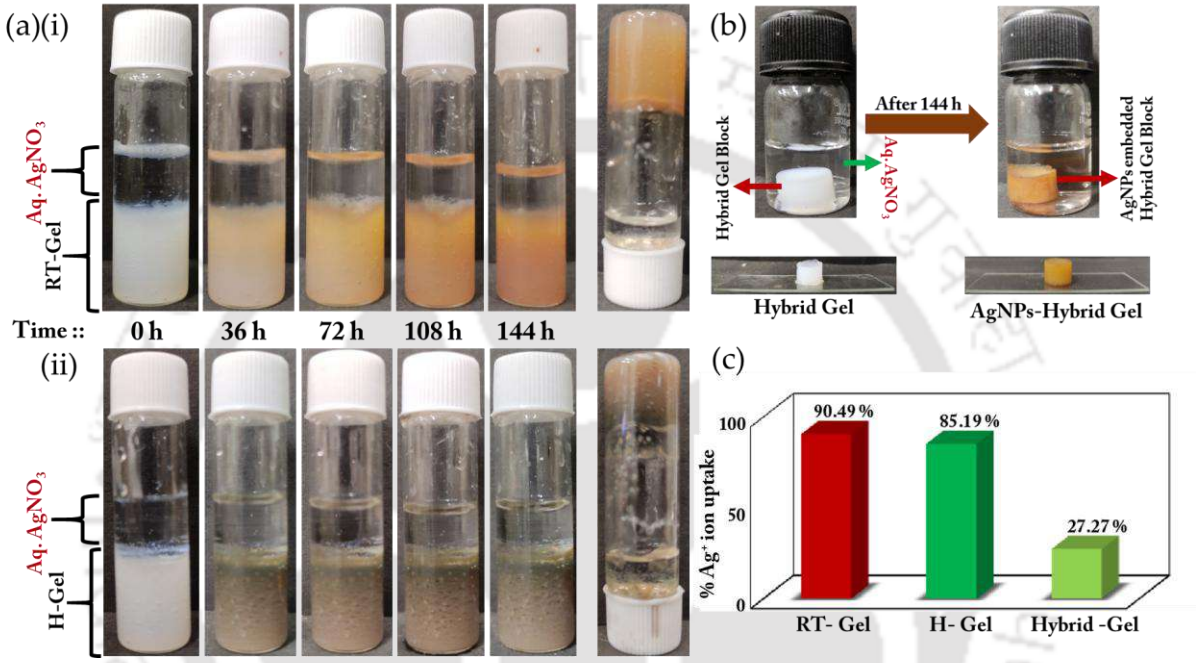

Figure 4B.9: (a) Depicting Ag^+ ion uptake from aqueous medium (Ag^+ salt used: 290 mM, 1500 µL) by using (i) RT-Gel, (ii) H-Gel. (b) Ag^+ ion uptake (Ag^+ salt used: 290 mM, 5 mL) by the hybrid gel block. (c) Bar diagram depicting Ag^+ ion uptake by different gels.

FESEM imaging and EDX analysis of the xerogel of AgNPs-RT-Gel reveals that most of the spherically shaped AgNPs are localized on the gel nanofibers. (Figure 4B.10d–f, Figure A4B.12) We reasoned that the interaction between the Ag^+ ion and the gel nanofibers leads to the formation of AgNPs, which are found to be localized on the gel nanofibers. This is also supported by the fact that the FTIR analysis of AgNPs-RT-Gel reveals broadening of most of the peaks; especially severe broadening of the peaks corresponding to -NH (urea/amide) was observed, thus inferring interaction of the gel nanofibers with the Ag^+ ion. (Figure A4B.11) Furthermore, we performed a ^1H NMR spectroscopic study of the AgNPs-RT-Gel composite, which reveals downfield shifting of the N–H peaks corresponding to the urea/amide units, and along with this, slight downfield shifting of some of the peaks in the aromatic region was also observed, thus supporting the interaction of the Ag^+ ion with RT-Gel nanofibers. (Figure

A4b.10) Such nanoparticle formation as a result of interaction between metal and the gel nanofibers has been reported earlier by Smith et al. [4B.1, 4B.24]

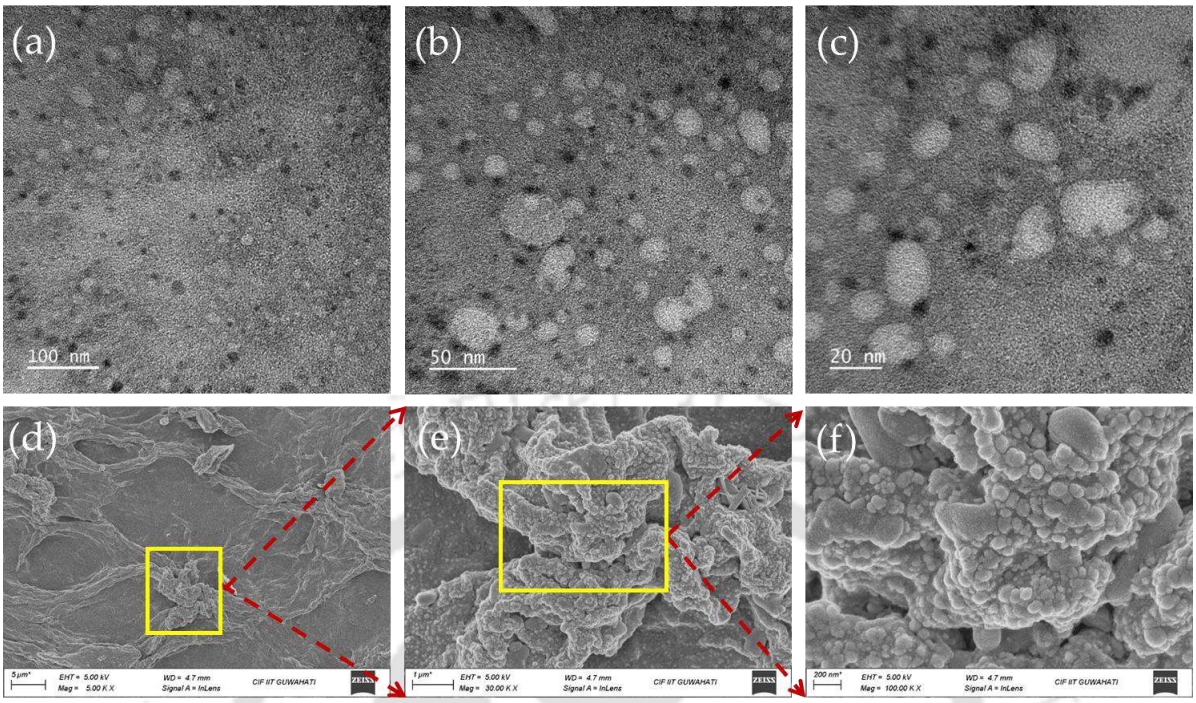

Figure 4B.10: (a–c) FETEM imaging of silver nanoparticles inside RT-Gel (drop-casted sample); (d–f) FESEM imaging of silver nanoparticles on the gel fibers of RT-Gel (xerogel sample).

4B.3.6. Conductive Hybrid Nano-Gel

We went on to demonstrate the electronic performance of the AgNPs-RT-Gel composite, which initially appeared impractical, as supramolecular self-assembled gels are known to be mechanically weak. To incorporate it with any electronic device, we needed a relatively strong gel. To achieve this, we decided to prepare a hybrid gel by mixing PY-NAP with an agarose polymer in DMSO: H_2O (3:2). The gel block was prepared in a cylindrical mold with a fixed dimension having length (l) = 0.7 cm and diameter (d) = 1.3 cm. (Figure A4B.13) FESEM imaging reveals the existence of a fibrous network inside the hybrid gel, which is very similar to that of RT-G. (Figure A4B.14) The hybrid gel block was suspended inside an aqueous solution of $AgNO_3$ (290 mM, 5 mL) and kept for 144 h. In situ, reduction occurs inside the hybrid gel block to yield NPs as evident from the color change from colorless to yellow. (Figure 4B.10b) FETEM, FESEM imaging, and EDX analysis indicated the formation of spherical AgNPs, (Figures A4B.15–Figures A4B.17) and the approximate diameter of the formed AgNPs was observed to be ~5 nm through FETEM. By using AAS, the Ag^+ ion uptake was calculated to be 27.27% after 144 h. (Figure 4B.10c)

To measure the conductivity of the AgNPs-Hybrid-Gel, the cylindrical gel block was placed in between two uniformly cut copper meshes connected with copper wires at the two ends, and both

the wires were connected to a source meter, (Figure A4B.18a,b) which gives a current (I) vs voltage (V) curve from which conductance is measured, and subsequently the conductivity was calculated. The conductivity of the AgNPs-Hybrid-Gel was calculated to be 0.02 S cm^{-1}, which is far superior to some of the earlier reports. [4B.24, 4B.46] For the sake of meaningful comparison, the conductivity of the agarose gel, and the hybrid gel were also measured, which were calculated to be 0.82 × 10^{-5} S cm^{-1} and 0.72 × 10^{-5} S cm^{-1} respectively. (Figure 4B.11b; Table A4B.7) Both the agarose gel and the hybrid gel were very poorly conducting with a very similar small conductivity value, whereas the conductivity of AgNP-Hybrid-Gel was enhanced exponentially (>2000 times better conductivity). Such a remarkable enhancement of conductivity in AgNPs-Hybrid-Gel prompted us to investigate its practical applicability in an electrical circuit. The electrical circuit consists of a battery, a switch, and a small LED bulb. The AgNPs-Hybrid-Gel block was incorporated into the circuit using copper mesh and a copper wire connected at two ends of the gel block. As soon as we switched on the circuit connected with the gel block, the LED bulb started glowing. (Figure 4B.11a(ii)) Such conductive nanocomposites have great potential in bridging the gap between the soft materials world and the world of the hard materials of electronics.

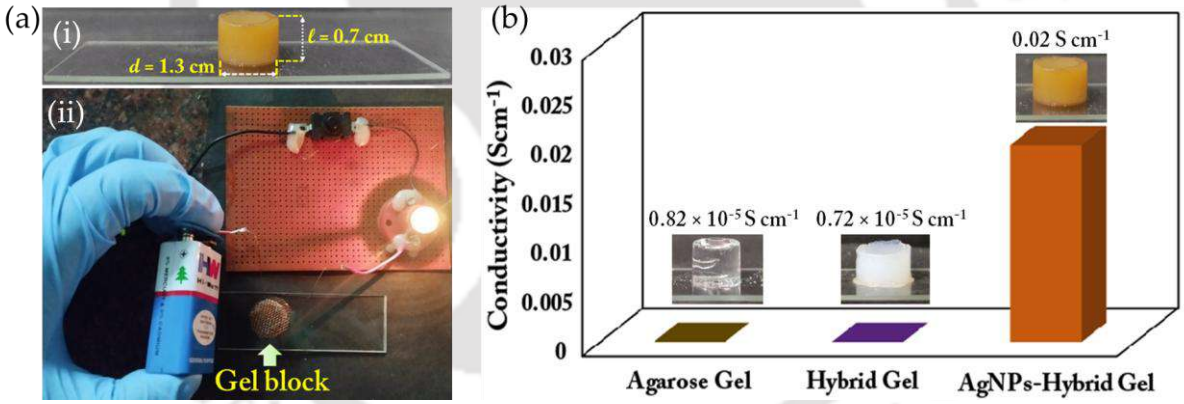

Figure 4B.11: (a) (i) Depicting dimensions of the AgNPs-Hybrid-Gel block, (ii) small circuit set up depicting the conductive nature of the AgNPs-Hybrid-Gel block by lighting up an LED bulb; (b) comparative bar diagram of conductivity measurement of different gel blocks.

4B.4. Conclusions

Our extensive gelation tests revealed that out of two pyridine-2,6-dicarboxamide-based urea-appended dipodal ligands, PY-NAP and PY-CF_3, only PY-NAP could form a gel in a mixed solvent system of DMSO and H_2O (3:2). The resulting gel exhibits high thermal stability and "thermally designate" characteristics. Additionally, we investigated the anion-responsive behavior of RT-Gel, finding that it selectively responds to the SO_4^{2-} anion. Moreover, we discovered that RT-Gel can effectively sequester precious metal ions, such as Ag^+, from aqueous

solutions, achieving a high uptake efficiency of approximately 90%. These metal ions undergo spontaneous reduction within the gel matrix, forming silver nanoparticles (AgNPs). Furthermore, we developed a hybrid gel composed of PY-NAP and agarose polymer to create a conductive nanostructured gel nanocomposite, demonstrating the concept of waste-to-wealth generation. Our future goal is to explore potential applications for this gel nanocomposite in various fields of soft electronics.

References

[4B.1] P. Slavík, D. W. Kurka, and D. K. Smith, *Chem. Sci.*, 2018, **9**, 8673-8681.

[4B.2] E. R. Draper, and D. J. Adams, *Chem.*, 2017, **3**, 390-410.

[4B.3] P. R. A. Chivers, and D. K. Smith, *Nat. Rev. Mater.*, 2019, 4, 463-478.

[4B.4] C. C. Piras, P. Slavik, and D. K. Smith, *Angew. Chem., Int. Ed.*, 2020, **59**, 853-859.

[4B.5] X. Du, J. Zhou, J. Shi, and B. Xu, *Chem. Rev.*, 2015, **115**, 13165-13307.

[4B.6] E. Saha, K. Karthick, S. Kundu, and J. Mitra, *ACS Sustain. Chem. Eng.*, 2019, **7**, 16094-16102.

[4B.7] S. Panja, and D. J. Adams, *Chem. Soc. Rev.*, 2021, **50**, 5165-5200.

[4B.8] S. Yamaguchi, S. Matsumoto, K. Ishizuka, Y. Iko, K. V. Tabata, H. F. Arata, H. Fujita, H. Noji, and I. Hamachi, *Chem.—Eur. J.*, 2008, **14**, 1891-1896.

[4B.9] N. Rahmati, F. E. Hoebeek, S. Peter, and C. I. De Zeeuw, *Front. Cell. Neurosci.*, 2018, **12**, 101.

[4B.10] WHO, Guidelines for Drinking-Water Quality, 4th ed.; World Health Organization, Geneva, 2017.

[4B.11] L. Li, R. Sun, R. Zheng, and Y. Huang, *Mater. Des.*, 2021, **205**, 109759.

[4B.12] S. Panja, S. Bhattacharya, and K. Ghosh, *Langmuir*, 2017, **33**, 8277-8288.

[4B.13] Y.-Y. Ren, Z. Xu, G. Li, J. Huang, X. Fan, and L. Xu, *Dalton Trans.*, 2017, **46**, 333-337.

[4B.14] Y. Feng, N. Jiang, D. Zhu, Z. Su, and M. R. Bryce, *J. Mater. Chem. C*, 2020, **8**, 11540-11545.

[4B.15] Q. Ma, M. Zhang, X. Xu, K. Meng, C. Yao, Y. Zhao, J. Sun, Y. Du, and D. Yang, *ACS Appl. Mater. Interfaces*, 2019, **11**, 47404-47412.

[4B.16] H.-L. Yang, X.-W. Sun, Y.-M. Zhang, Z.-H. Wang, W. Zhu, Y.-Q. Fan, T.-B. Wei, H. Yao, Q. Lin, *Soft Matter*, 2019, **15**, 9547-9552.

[4B.17] P. Li, Z. Jin, L. Peng, F. Zhao, D. Xiao, Y. Jin, and G. Yu, *Adv. Mater.*, 2018, **30**, 1800124.

[4B.18] Z. Deng, T. Hu, Q. Lei, J. He, P. X. Ma, and B. Guo, *ACS Appl. Mater. Interfaces*, 2019, **11**, 6796-6808.

[4B.19] W. Yang, B. Shao, T. Liu, Y. Zhang, R. Huang, F. Chen, and Q. Fu, *ACS Appl. Mater. Interfaces*, 2018, **10**, 8245-8257.

[4B.20] Y. Zhao, Y. Ohm, J. Liao, Y. Luo, H.-Y. Cheng, P. Won, P. Roberts, M. R. Carneiro, M. F. Islam, J. H. Ahn, L. M. Walker, and C. Majidi, *Nat. Electron.*, 2023, **6**, 206-215.

[4B.21] R. Jain, and G. Khandelwal, and S. Roy, *Langmuir*, 2019, **35** (17), 5878-5889.

[4B.22] S. Ye, W. Zhang, Z. Zhai, S. Shang, L. Huang, Z. Song, and J. Jiang, *Langmuir*, 2024, **40** (1), 647- 656.

[4B.23] J. Zhao, X. Hu, X. Huang, X. Jin, K. Koh, and H. Chen, *Colloids Surf. B*, 2019, **183**, 110404.

[4B.24] B. O. Okesola, S. K. Suravaram, A. Parkin, and D. K. Smith, *Angew. Chem., Int. Ed.*, 2016, **55**, 183-187.

[4B.25] E. Taboada, L. N. Feldborg, A. Perez del Pino, A. Roig, D. B. Amabilino, and J. Puigmarti-Luis, *Soft Matter*, 2011, **7**, 2755-2761.

[4B.26] M. Kimura, S. Kobayashi, T. Kuroda, K. Hanabusa, and H. Shirai, *Adv. Mater.*, 2004, **16**, 335-338.

[4B.27] T. Ghosh, A. Biswas, S. Bhowmik, and A. K. Das, *Chem. Asian J.*, 2021, **16**, 215-223.

[4B.28] S. D. Garcia Schejtman, P. A. Mercadal, M. L. Picchio, A. V. Veglia, and E. A. Coronado, *J. Phys. Chem. C*, 2022, **126** (23), 9979-9988.

[4B.29] S. D. Garcia Schejtman, P. A. Mercadal, M. L. Picchio, A. V. Veglia, and E. A. Coronado, *ACS Appl. Nano Mater.*, 2023, **6** (9), 7259-7268.

[4B.30] O. A. Pegu, R. Moral, and G. Das, *Cryst. Growth Des.*, 2023, **23**, 8370-8380.

[4B.31] O. A. Pegu, A. Das, and G. Das, *J. Mol. Struct.*, 2023, **1294**, 136427.

[4B.32] N. Borah, B. Nayak, A. Gogoi, and G. Das, *New J. Chem.*, 2019, **43**, 16497-16505.

[4B.33] U. Manna, S. Kayal, B. Nayak, and G. Das, *Dalton Trans.*, 2017, **46**, 11956-11969.

[4B.34] U. Manna, S. Kayal, S. Samanta, and G. Das, *Dalton Trans.*, 2017, **46**, 10374-10386.

[4B.35] O. A. Pegu, and G. Das, *J. Mater. Chem. C*, 2024, **12**, 6519-6527.

[4B.36] R. Moral, O. A. Pegu, and G. Das, *New J. Chem.*, 2023, **47**, 19625-19632.

[4B.37] R. Moral, O. A. Pegu, and G. Das, *Dyes Pigm.*, 2023, **218**, 111502.

[4B.38] S. De, O. A. Pegu, and G. Das, *Langmuir*, 2023, **39**, 2444-2449.

[4B.39] D. J. Adams, *J. Am. Chem. Soc.*, 2022, **144**, 11047-11053.

[4B.40] S. Panja, S. Bhattacharya, and K. Ghosh, *Mater. Chem. Front.*, 2018, **2**, 385-395.

[4B.41] X. Ma, Z. Zhang, H. Xie, Y. Ma, C. Liu, S. Liu, and M. Liu, *Chem. Commun.*, 2018, **54**, 13674-13677.

[4B.42] N. Malviya, M. Das, P. Mandal, and S. Mukhopadhyay, *Soft Matter*, 2017, **13**, 6243-6249.

[4B.43] Y. Liu, Y. Tan, Z. Liu, and G. Che, *Soft Matter*, 2021, **17**, 7227-7235.

[4B.44] S. K. Dey, B. Gil-Hernandez, V. V. Gobre, D. Woschko, S. S. Harmalkar, F. R. Gayen, B. Saha, R. L. Goswamee, and C. Janiak, *Dalton Trans.*, 2022, **51**, 15239-15245.

[4B.45] M. Vanaja, and G. Annadurai, *Appl. Nanosci*, 2013, **3**, 217-223.

[4B.46] K. Liu, X. Pan, L. Chen, L. Huang, Y. Ni, J. Liu, S. Cao, and H. Wang, *ACS Sustain. Chem. Eng.*, 2018, **6**, 6395-6403.

Annexure 4B

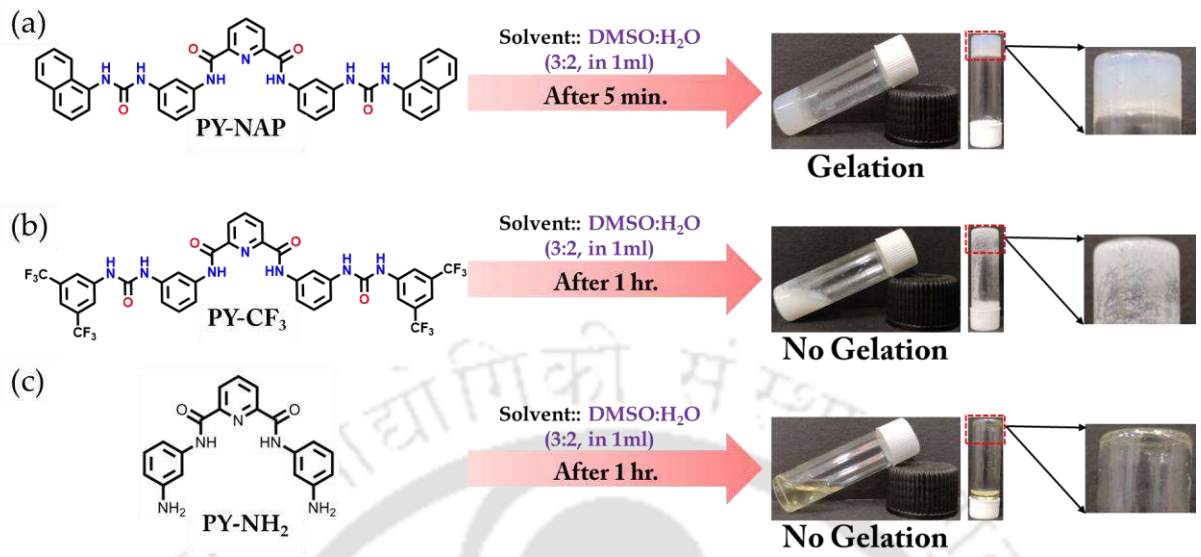

Figure A4B.1: Gelation study of (a) PY-NAP, (b) PY-CF_3, and (c) PY-NH_2.

Table A4B.1: Gelation study with different solvent/ solvent combinations in different conditions for PY-NAP.

Solvent	Condition	Gel/No Gelation	CGC
THF	Sonicate (RT)	Gel	10mg/ml
ACN	Sonicate (RT)	Gel	10mg/ml
DMSO: H2O (3:2)	Rapid addition of water (RT)/ Heating	Gel	8mg/ml
H_2O	Sonicate/Heating/Stirring	No Gelation	-
DMSO	Sonicate/Heating/Stirring	No Gelation	-
Ethanol	Sonicate/Heating/Stirring	No Gelation	-
Methanol	Sonicate/Heating/Stirring	No Gelation	-
Hexane	Sonicate/Heating/Stirring	No Gelation	-
Ethyl acetate	Sonicate/Heating/Stirring	No Gelation	-

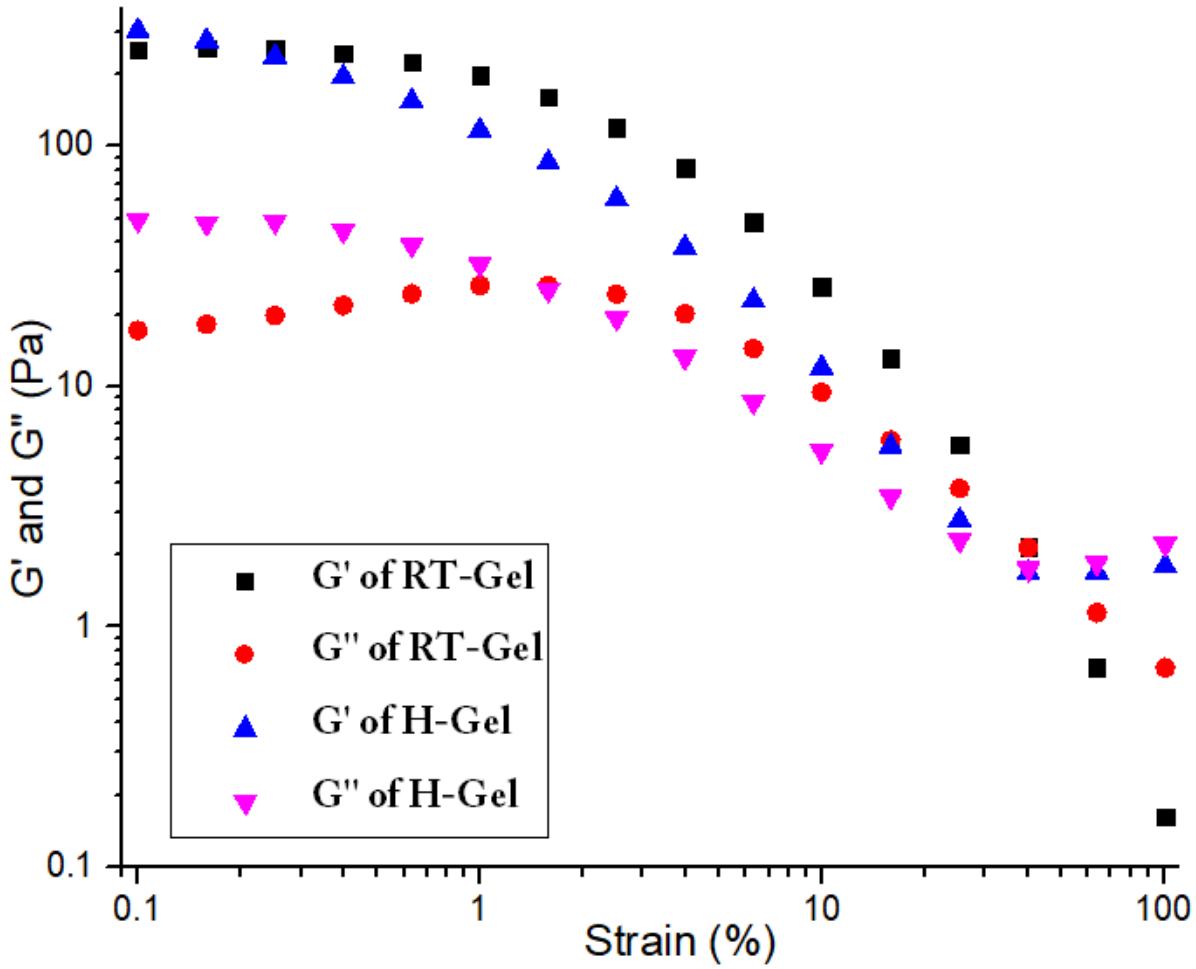

Figure A4B.2: Rheological analysis of dynamic strain sweep of the RT-Gel, and H-Gel.

Table A4B.2: Crystallographic parameters and refinement data of the probes, and anionic complex.

Parameters	PY-NAP.DMSO	PY-CF_3.DMSO	PY-NAP.Sulfate
Formula	$C_{45}H_{43}N_7O_6S_2$	$C_{41}H_{35}F_{12}N_7O_6S_2$	$C_{73}H_{105}N_9O_9S$
Fw	841.98	1013.88	1284.71
cryst syst	triclinic	monoclinic	triclinic
space group	P -1	P 2/c	P -1
a (Å)	9.689 (5)	12.7044 (12)	13.3781 (10)
b (Å)	13.112 (7)	9.7591 (9)	16.9674 (13)
c (Å)	16.678 (9)	17.9473 (17)	17.1930 (13)
α (deg)	90.543 (16)	90	95.456 (2)
β (deg)	98.953 (16)	97.929 (3)	109.314 (2)
γ (deg)	93.688 (15)	90	98.397 (2)

V (Å^3)	2088.1 (19)	2203.9 (4)	3600.3 (5)
Z	2	2	2
DC (g cm^{-3})	1.339	1.528	1.185
μ (Mo Kα) (mm^{-1})	0.186	0.228	0.106
F (000)	884.0	1036.0	1388.0
T (K)	295	299	295
θmax (deg)	24.999	25.000	25.000
total no. of rflns	34704	39746	81645
no. of indep rflns	7329	3882	12641
no. of obsd rflns	5342	2879	6800
no.of params refined	569	322	870
R1, I > 2σ(I)	0.0900 (5342)	0.0933 (2879)	0.0996 (6800)
wR2, I > 2σ(I)	0.2533 (7329)	0.1716 (3882)	0.3453 (12641)
GOF (F^2)	1.011	1.017	1.069
CCDC no.	2376906	2376907	2376908

Table A4B.3: Hydrogen bonding distances (Å) and Bond angles (°) of the crystals.

Ligand/Complex	D–H···A	d(D···H)/Å	d(H···A)/Å	d(D···A)/Å	<D–H···A/°	Symmetry codes
PY-NAP	N3A-H3NA···O4	0.82 (5)	2.20 (5)	2.978 (5)	159 (4)	1-x, -y, 1-z
	N4A-H4NA···O4	0.84 (5)	2.30 (5)	3.096 (5)	157 (4)	1-x, -y, 1-z
	N2-H2N···N1	0.77 (5)	2.27 (5)	2.705 (5)	117 (4)	x, y, z
	N2A-H2NA···N1	0.87 (5)	2.22 (5)	2.673 (5)	113 (4)	x, y, z
	N3-H3N···O3	0.82 (6)	2.01 (6)	2.792 (7)	158 (5)	1-x, 1-y, 1-z
	N4-H4N···O3	0.80 (5)	2.19 (5)	2.919 (7)	151 (5)	1-x, 1-y, 1-z
	C8-H8···O2	0.93	2.33	2.888 (7)	118	x, y, z
	C8A-H8A···O2A	0.93	2.33	2.865 (6)	116	x, y, z
	C10-H10···O1	0.93	2.33	2.911 (7)	120	x, y, z
	C10A-H10A···O1A	0.93	2.28	2.887 (6)	122	x, y, z
	C13-H13···O2	0.93	2.27	2.875 (6)	123	x, y, z
	C13A-H13A···O2A	0.93	2.28	2.837 (7)	118	x, y, z
	C18-H18···N4	0.93	2.54	2.850 (8)	100	x, y, z
	C18A-H18A···N4A	0.93	2.56	2.874 (6)	100	x, y, z
	C23-H23B···O2	0.96	2.37	3.256 (12)	152	-x, 1-y, 1-z
	C24-H24C···O1A	0.96	2.40	3.116 (6)	131	1-x, -y, 1-z
PY-CF$_3$	N2-H2N···N1	0.81 (5)	2.34 (5)	2.708 (5)	109 (4)	x, y, z
	N3-H3N···O3	0.80 (4)	2.25 (4)	2.984 (6)	152 (3)	x, y, z
	N4-H4N···O3	0.86 (5)	2.07 (5)	2.886 (6)	159 (5)	x, y, z
	C8-H8···O2	0.93	2.37	2.938 (7)	119	x, y, z
	C10-H10···O1	0.93	2.22	2.840 (6)	123	x, y, z

	C13-H13···O2	0.93	2.34	2.914 (6)	120	x, y, z
	C17-H17···F1	0.93	2.36	2.684 (7)	100	x, y, z
	C20-H20C···O1	0.96	2.57	3.429 (9)	148	x, y, z
	C21-H21B···O2	0.96	2.48	3.397 (8)	160	x, 1+y, z
PY-NAP. Sul	N2A-H2NA···N1	0.78 (5)	2.33 (5)	2.727 (7)	113 (4)	x, y, z
	N2A-H2NA···O3	0.78 (5)	2.26 (5)	2.979 (6)	154 (4)	1-x, 1-y, 1-z
	O3-H10···O1A	0.82 (8)	2.07 (7)	2.870 (6)	164 (7)	x, y, z
	N3A-H3NA···O5	0.75 (6)	2.30 (7)	3.000 (7)	157 (7)	x, y, z
	N2-H2N···N1	0.82 (5)	2.31 (5)	2.743 (7)	114 (5)	x, y, z
	N2-H2N···O3	0.82 (5)	2.23 (5)	3.016 (6)	160 (5)	1-x, 1-y, 1-z
	O3-H20···O4	0.85 (7)	1.78 (7)	2.622 (7)	171 (7)	1-x, 1-y, 1-z
	N4A-H4NA··O5·	0.77 (5)	2.23 (5)	2.956 (7)	158 (6)	x, y, z
	N3-H3N···O4	0.95 (5)	2.52 (5)	3.332 (8)	144 (5)	x, y, z
	N3-H3N···O6	0.95 (5)	2.05 (5)	2.921 (8)	152 (5)	x, y, z
	N4-H4N···O6	0.91 (5)	2.01 (5)	2.839 (7)	151 (5)	x, y, z
	C6-H6···O1		2.30	2.891 (8)	121	x, y, z
	C6A-H6A···O1A		2.30	2.890 (8)	121	x, y, z
	C8-H8···O2	0.93	2.23	2.813 (8)	120	x, y, z
	C8A-H8A···O2A	0.93	2.38	2.885 (8)	114	x, y, z
	C10-H10···O4	0.93	2.44	3.255 (7)	146	x, y, z
	C10-H10···O3	0.93	2.49	3.293 (6)	145	1-x, 1-y, 1-z
	C13-H13···O2	0.93	2.15	2.780 (9)	124	x, y, z
	C13A-H13A···O2A	0.93	2.22	2.839 (7)	123	x, y, z
	C18-H18···O6	0.93	2.43	3.340 (10)	164	x, y, z
	C18-H18···N4	0.93	2.56	2.874 (9)	100	x, y, z
	C18A-H18A···O5	0.93	2.49	3.387 (6)	163	x, y, z
	C18A-H18A···N4A	0.93	2.58	2.884 (8)	100	x, y, z
	C22-H22A···O7	0.97	2.46	3.286 (10)	143	1-x, 1-y, 1-z
	C46-H46B···O4	0.97	2.59	3.213 (9)	122	x, y, z
	C50-H50A···O2A	0.97	2.49	3.404 (9)	158	1-x, -y, 1-z

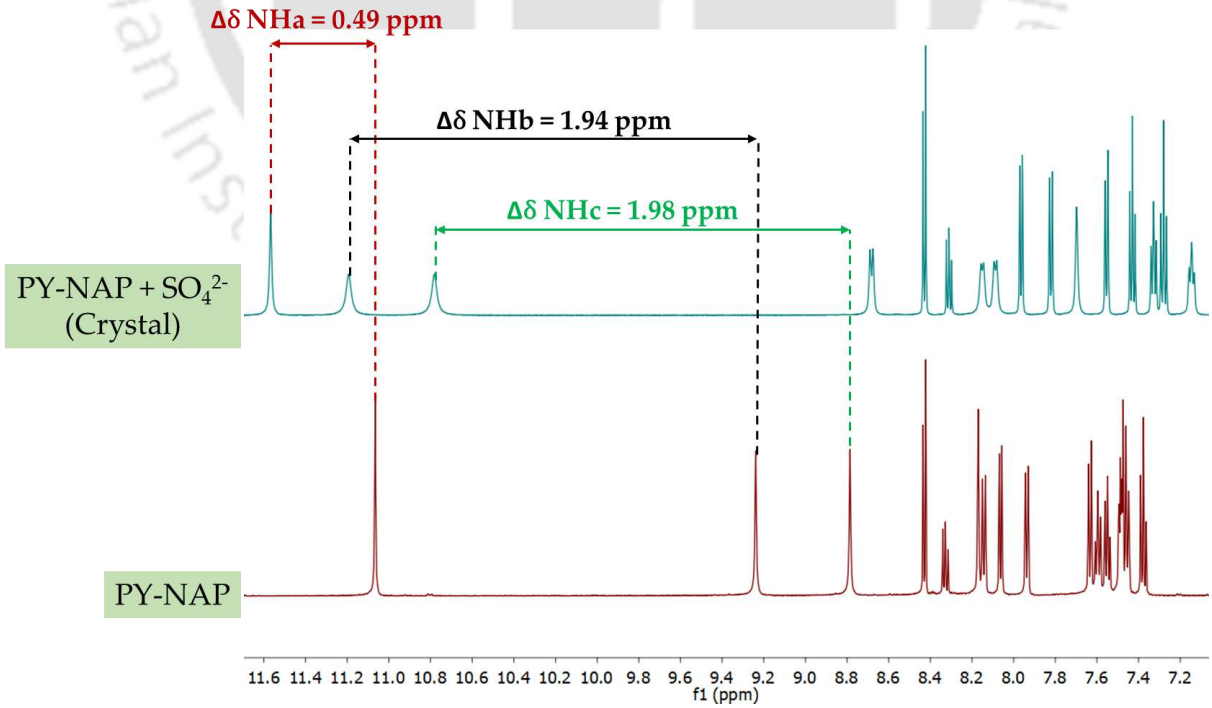

Figure A4B.3: Stacked ^{1}H NMR spectra of PY-NAP, and the crystals of PY-NAP.Sulfate complex (recorded in DMSO-d_6).

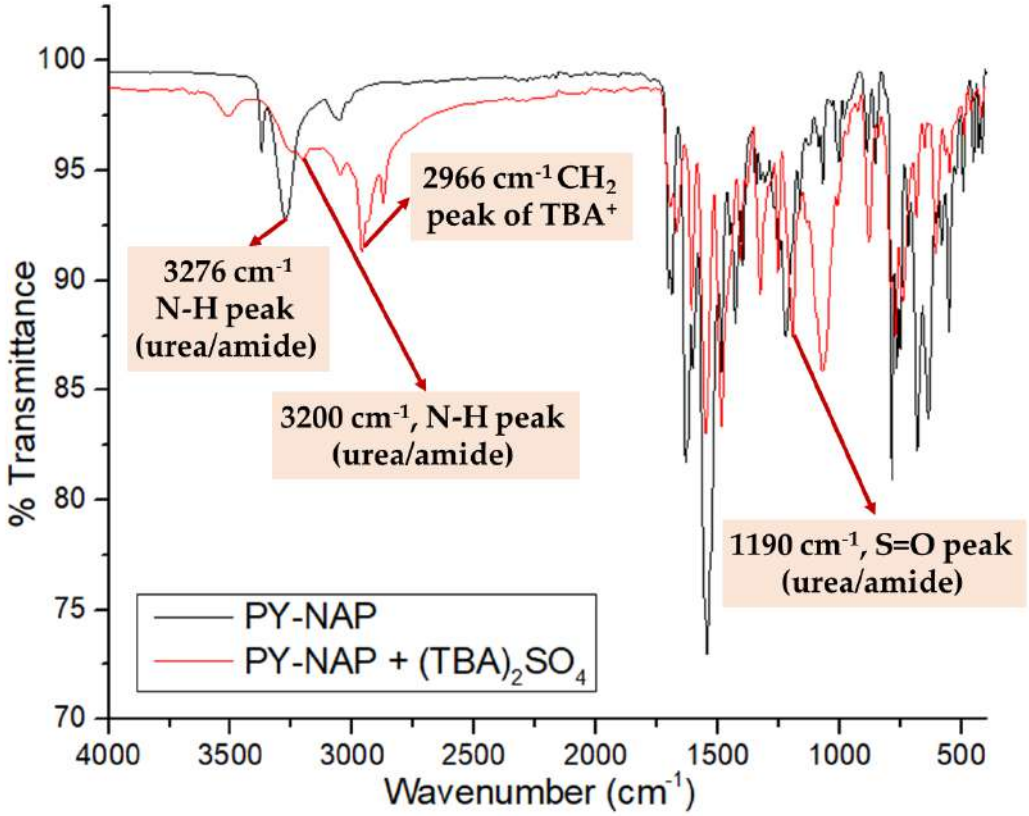

Figure A4B.4: Merged FTIR spectra of PY-NAP, and PY-NAP.Sulfate crystal.

Table A4B.4: Contact Contributions (%) from the d_{norm} Surface Area of PY-NAP and its sulfate Complex.

contacts	PY-NAP	$[PY\text{-}NAP.SO_4]^{2-}$
H···C	22.2	13.1
H···O	13.7	12.2

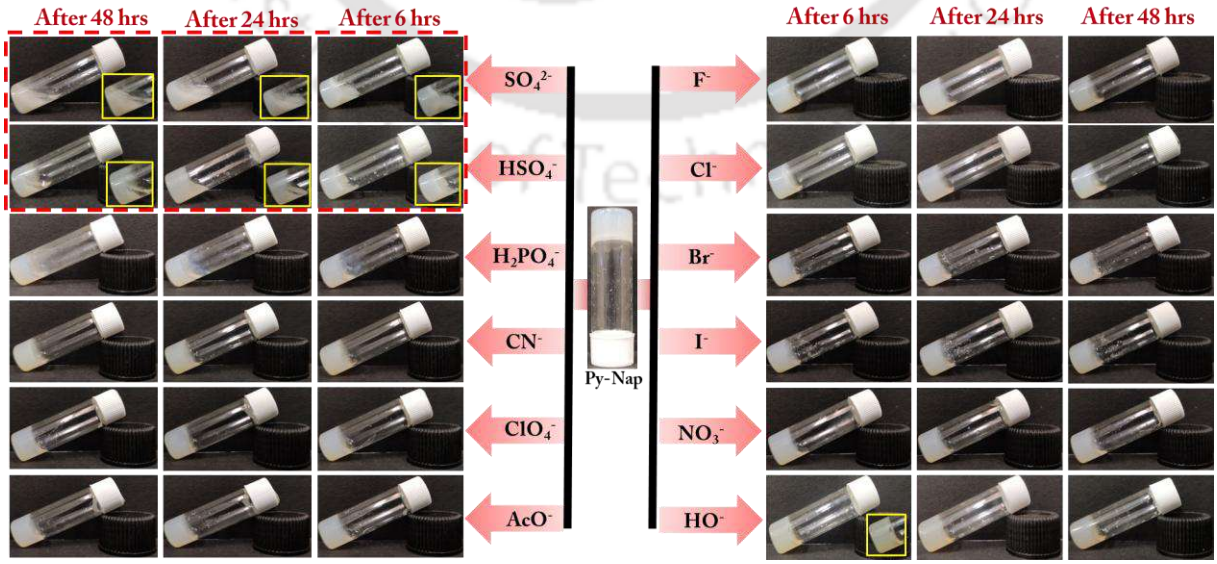

Figure A4B.5: Study for anion responsive behaviour of the RT-Gel.

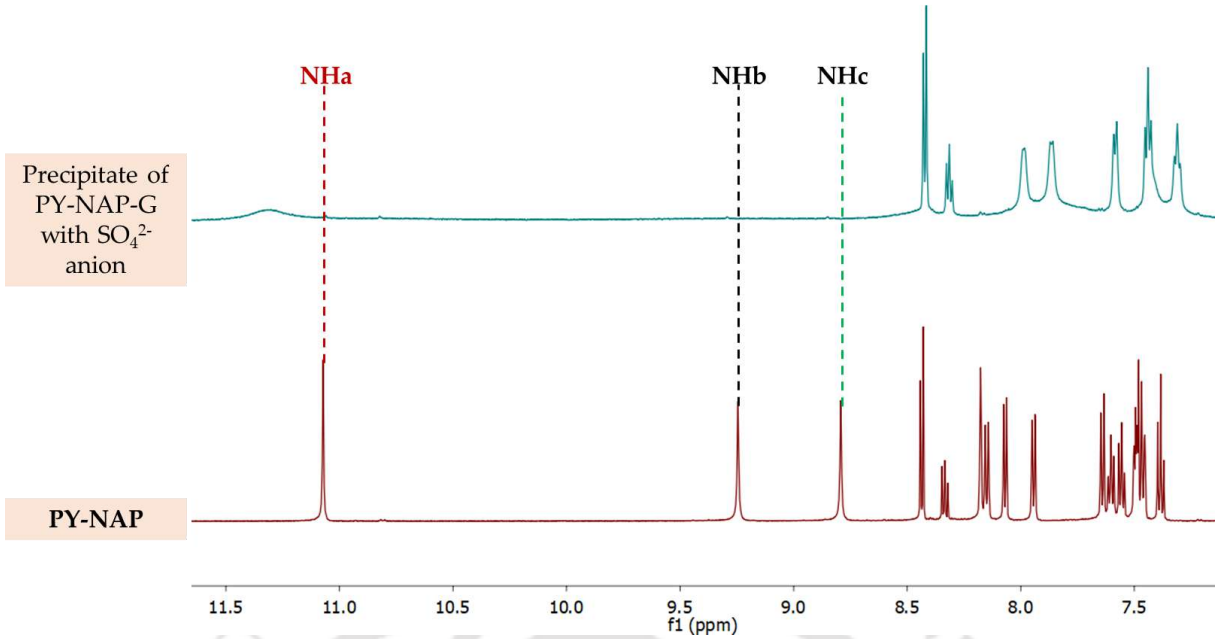

Figure A4B.6: Stacked ^{1}H NMR spectra of PY-NAP, and the precipitate of PY-NAP-G with SO_4^{2-} anion (recorded in DMSO-d_6).

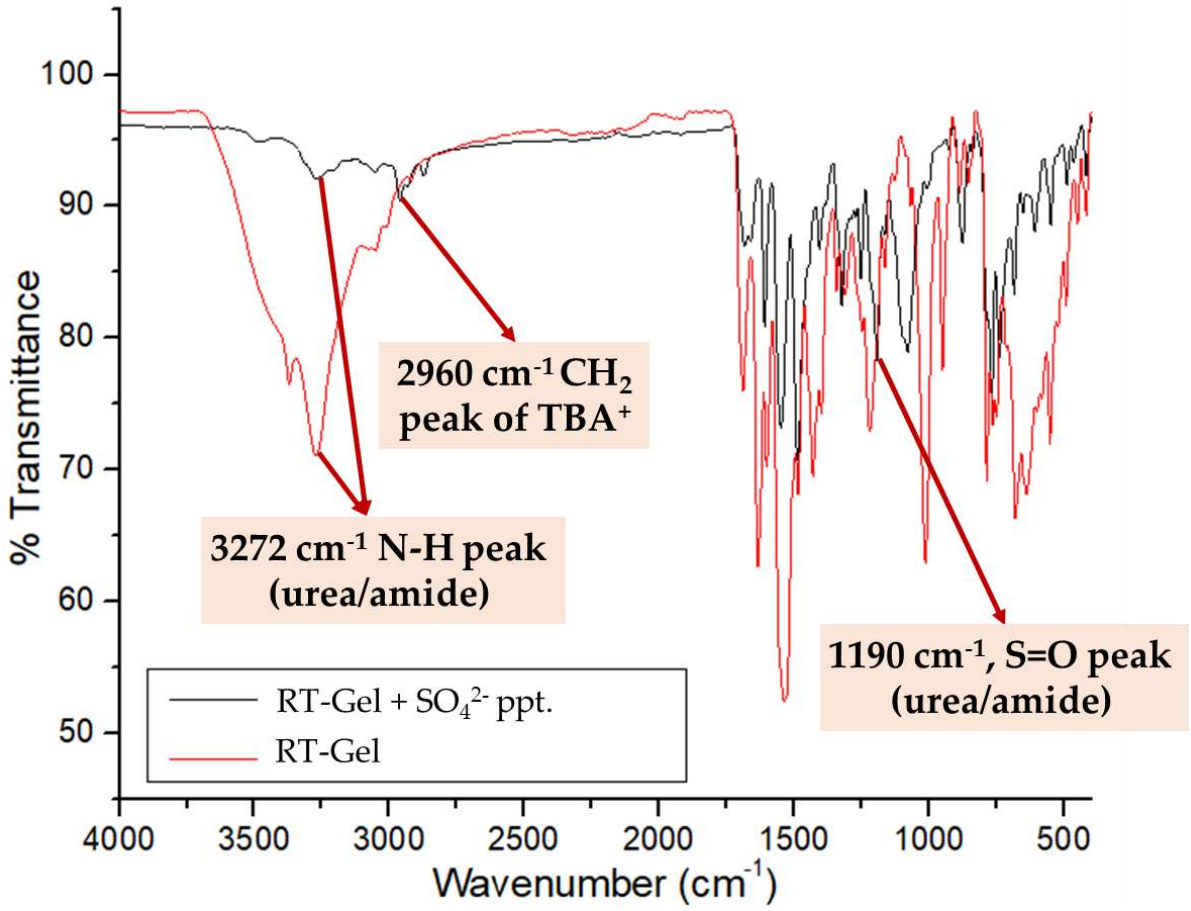

Figure A4B.7: Merged FTIR spectra of RT-Gel, and the obtained precipitate on combination of RT-Gel with SO_4^{2-} anion (RT-Gel + SO_4^{2-} ppt.)

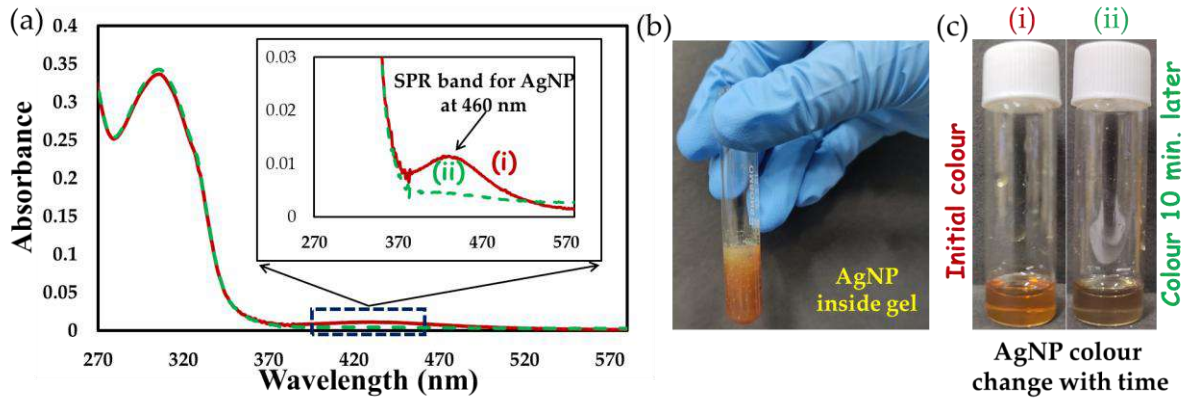

Figure A4B.8: (a) Depicting surface plasmon resonance (SPR) band of formed AgNPs in UV-vis spectroscopy; (b) AgNPs formed inside RT-Gel; (c) (i) & (ii) colour change of AgNPs with time.

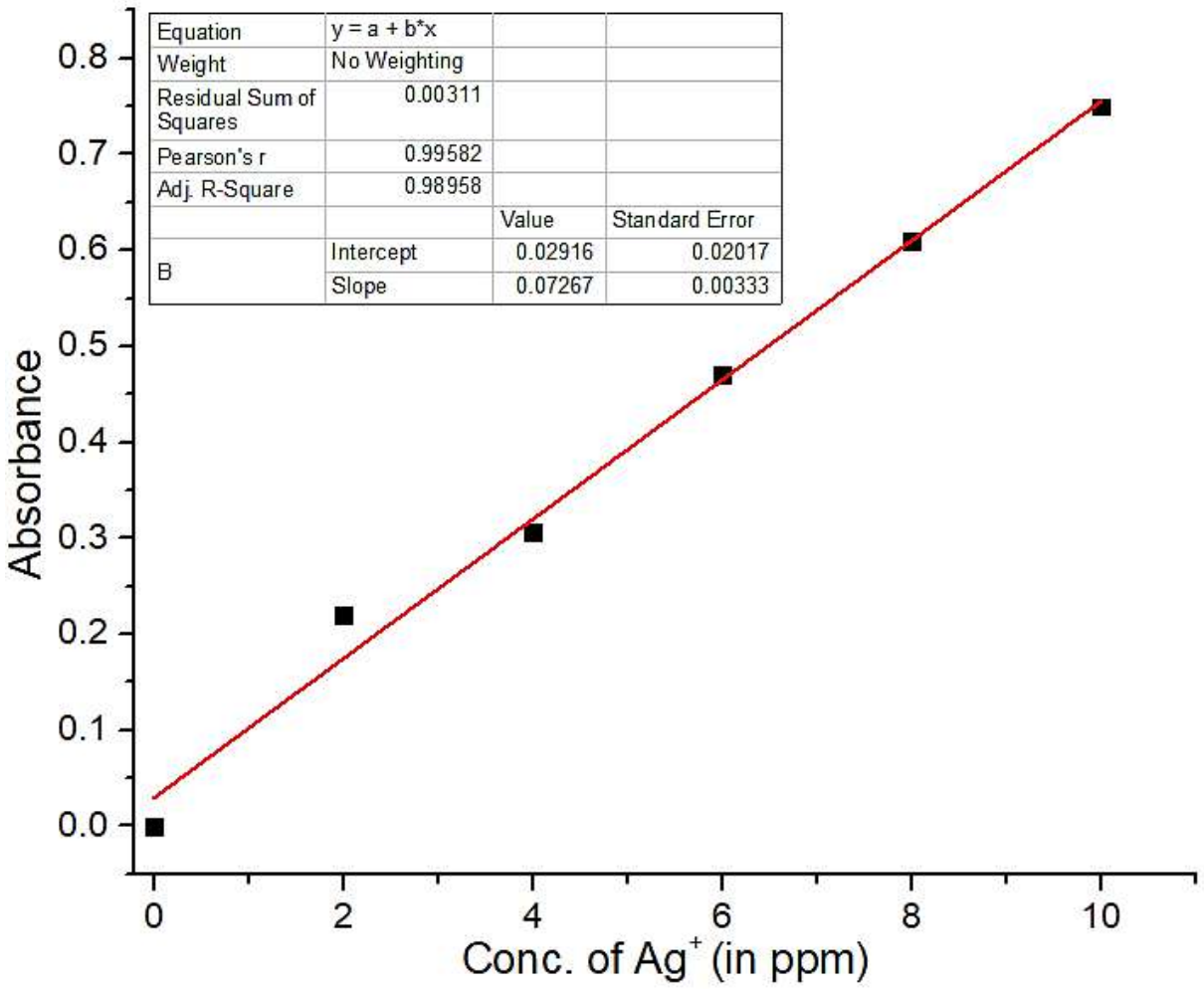

Figure A4B.9: Calibration curve for determination of Ag^{+} ion in aqueous medium by using atomic absorption spectroscopy (AAS).

Table A4B.5: Absorption measurement at different concentration of Ag^+ ion in different time intervals, and % uptake of Ag^+ ion calculation in **RT-Gel**, by using AAS. Here, $[C]_i$ = initial concentration, $[C]_f$ = final concentration.

Time (in hours)	Absorbance	Concentration of Ag^+ ion, $[Ag^+]$ (in mM)	Actual Concentration ($[Ag^+]$ × D.F.) in mM	% Uptake $([C]_i - [C]_f)/ [C]_i \times 100$
36	0.1387	0.006677	65.79	(290mM -27.57mM)/290mM × 100 = 90.49%
72	0.1315	0.006057	59.68	
108	0.1059	0.0038506	37.94	
144	0.0937	0.0027986	27.57	

** Here, $[C]_i$ = initial concentration, $[C]_f$ = final concentration. Dilution factor (D.F.) = 9852.55.

Table A4B.6: Absorption measurement at different concentration of Ag^+ ion in different time intervals, and % uptake of Ag^+ ion calculation in **H-Gel**, by using AAS.

Time (in hours)	Absorbance	Concentration of Ag^+ ion, $[Ag^+]$ (in mM)	Actual Concentration ($[Ag^+]$ × D.F.) in mM	% Uptake $([C]_i - [C]_f)/ [C]_i \times 100$
36	0.1914	0.01122	110.55	(290mM -42.95mM)/290mM × 100 = 85.19%
72	0.1620	0.008686	85.58	
108	0.1156	0.0046865	46.17	
144	0.1118	0.004359	42.95	

** Here, $[C]_i$ = initial concentration, $[C]_f$ = final concentration. Dilution factor (D.F.) = 9852.55.

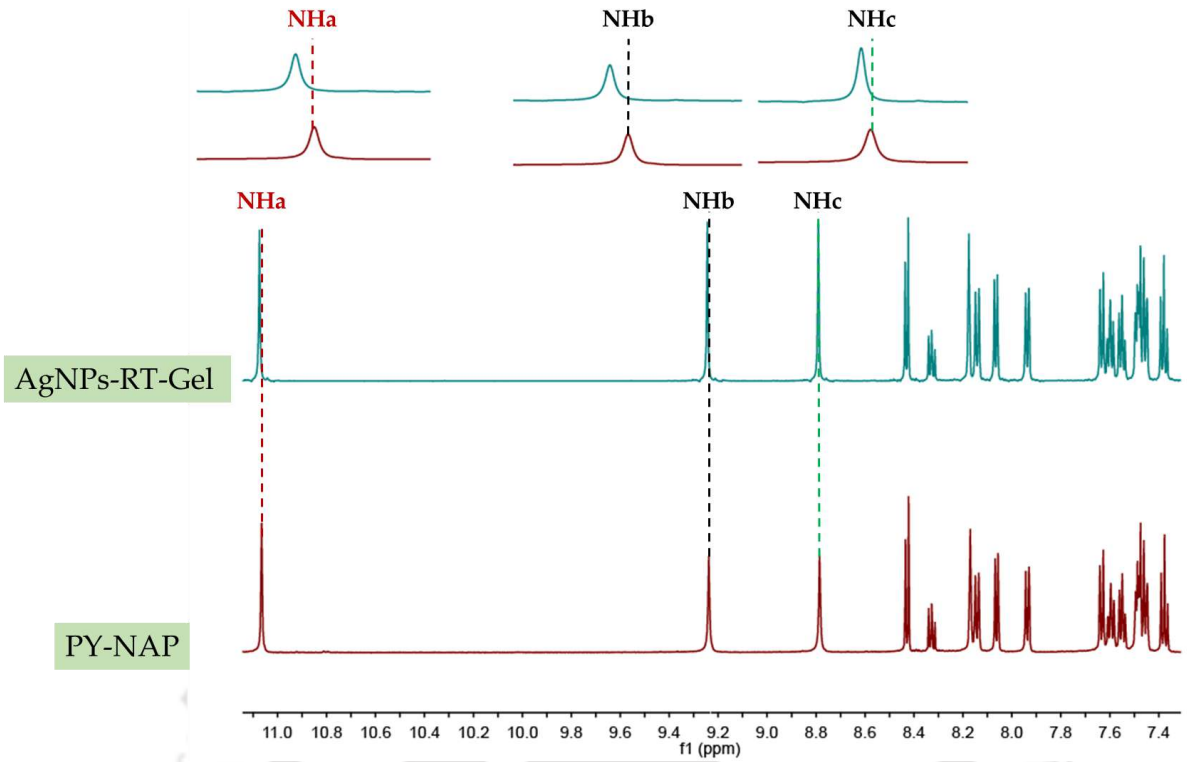

Figure A4B.10: Stacked ^{1}H NMR spectra of PY-NAP, and AgNPs-RT-Gel crystal (recorded in DMSO-d_6).

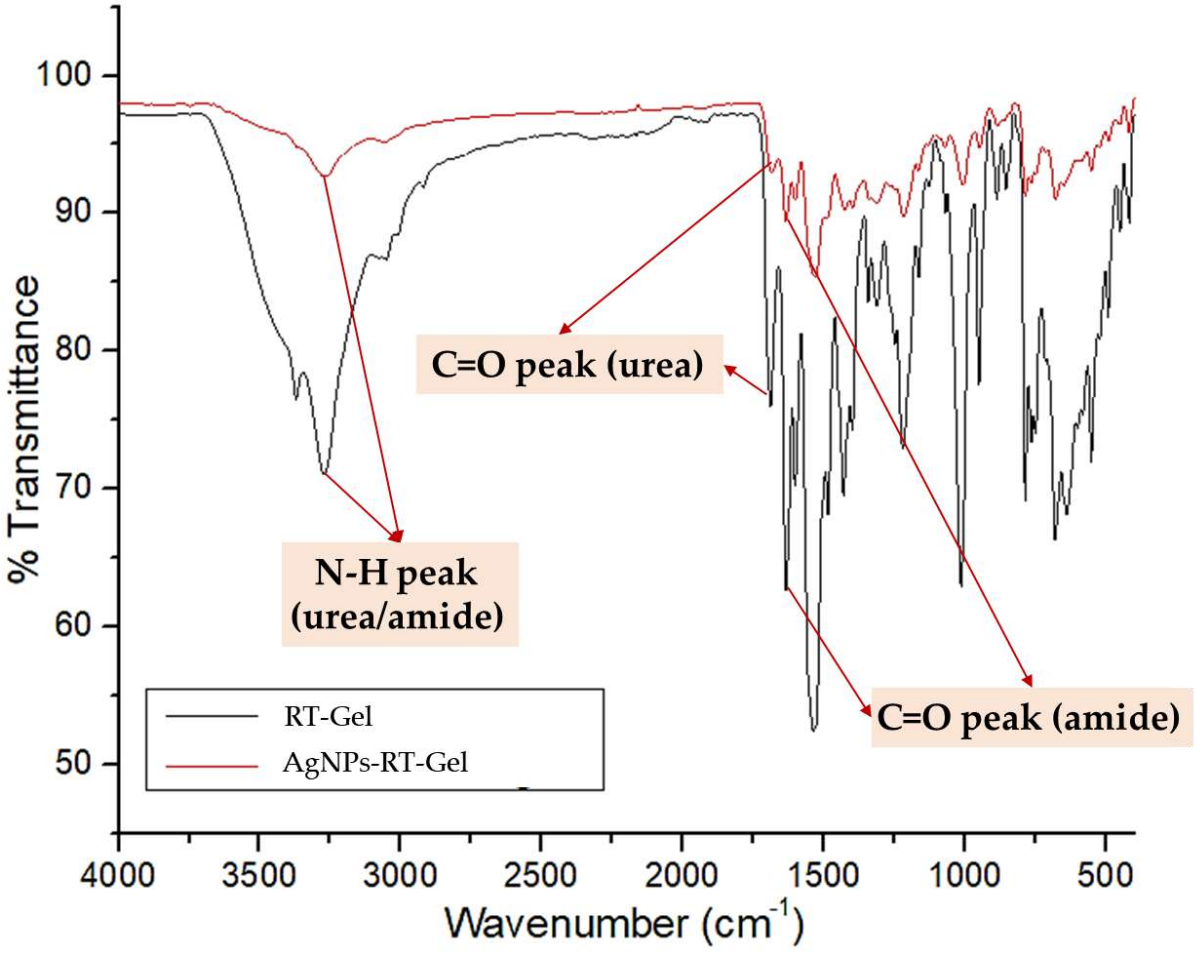

Figure A4B.11: Merged FTIR spectra of RT-Gel, and AgNPs-RT-Gel.

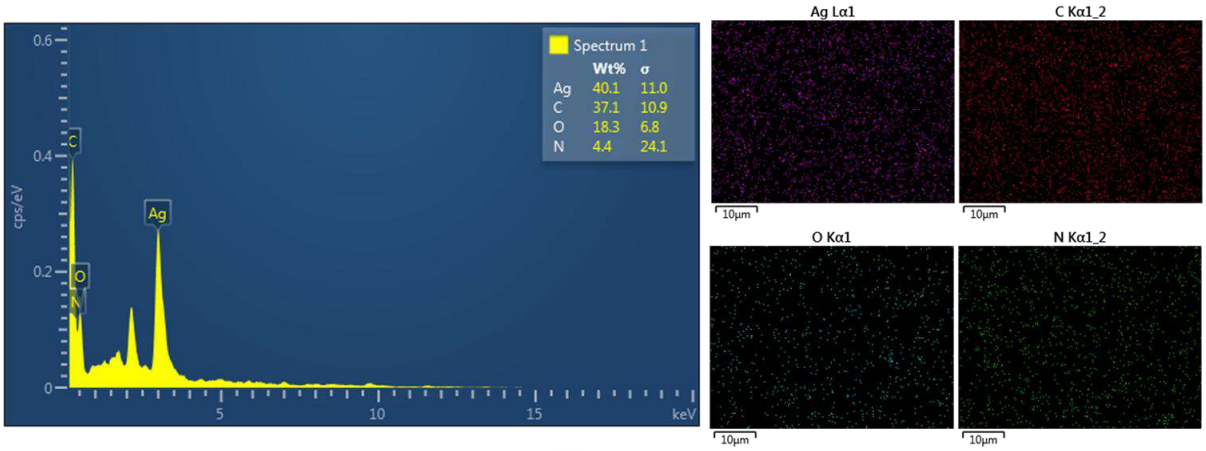

Figure A4B.12: Energy dispersive X-ray (EDX) spectrum and mapping analysis of the xerogel of AgNPs-RT-Gel. Ag: silver; C: carbon; O: oxygen; N: nitrogen

Figure A4B.13: Depicting different cylindrically moulded Gel blocks prepared in DMSO: H_2O (3:2).

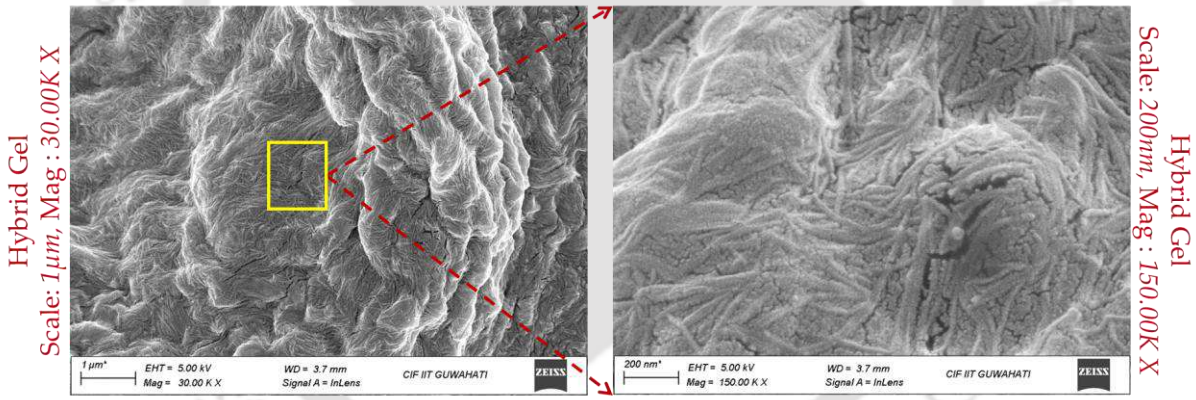

Figure A4B.14: FESEM imaging of the xerogel of Hybrid-Gel.

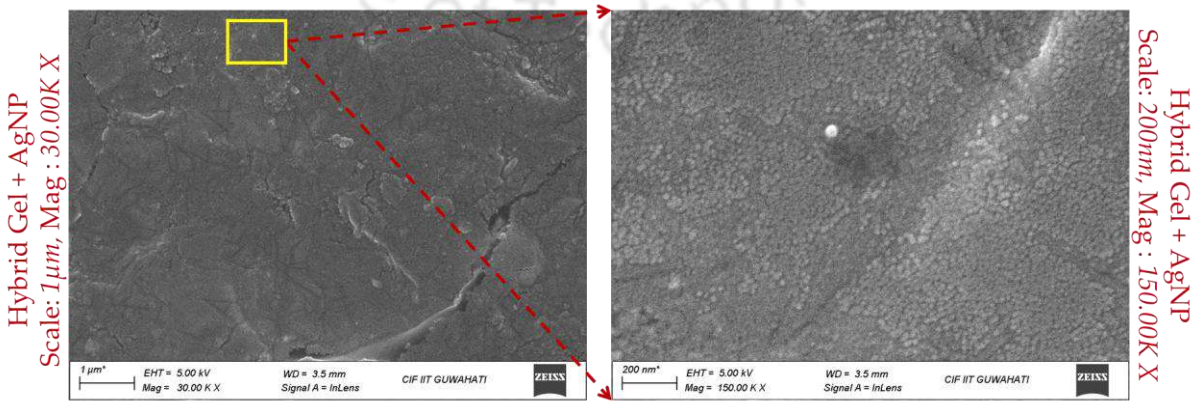

Figure A4B.15: FESEM imaging of the xerogel of AgNPs-Hybrid-Gel.

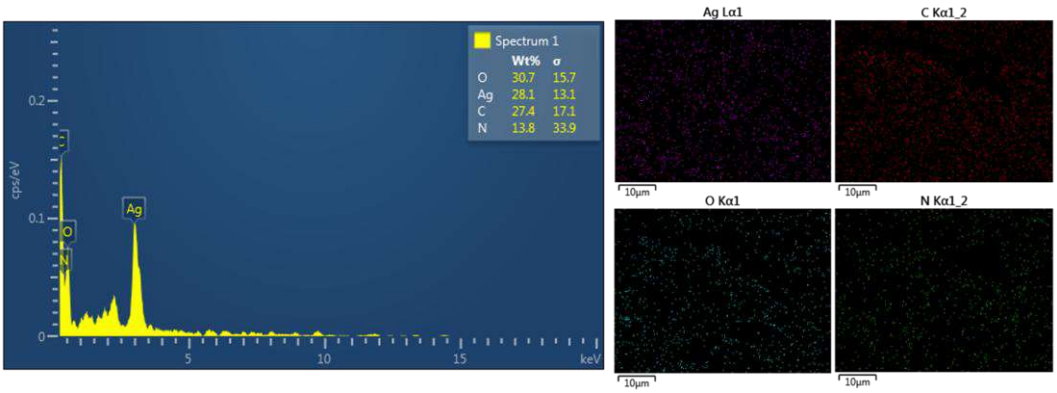

Figure A4B.16: Energy dispersive X-ray (EDX) spectrum and mapping analysis of AgNPs-Hybrid-Gel. Ag: silver; C: carbon; O: oxygen; N: nitrogen.

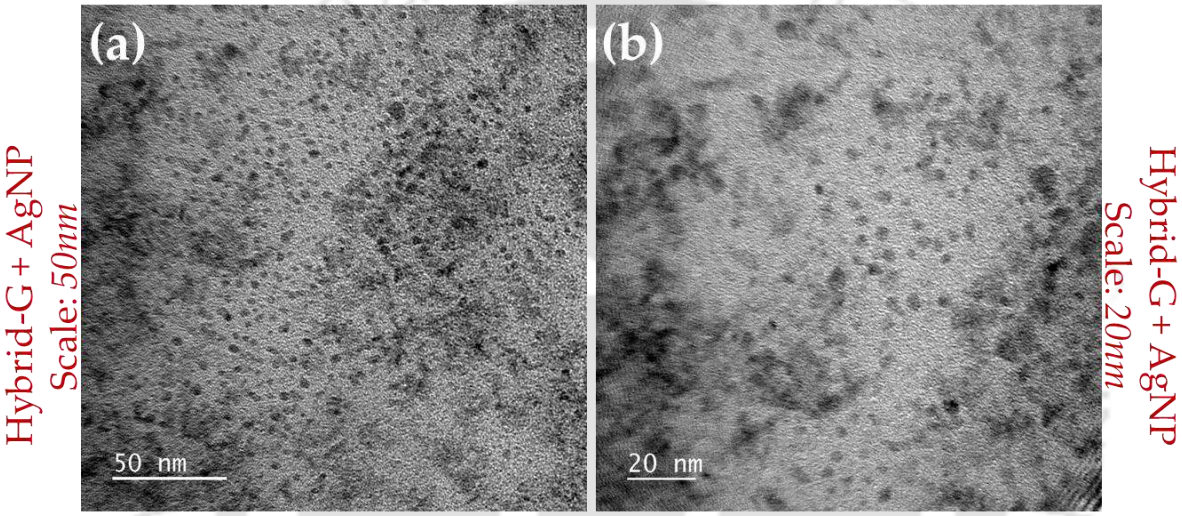

Figure A4B.17: (a), and (b) FETEM imaging of AgNPs-Hybrid-Gel (dropcasted sample) in two different scale bars.

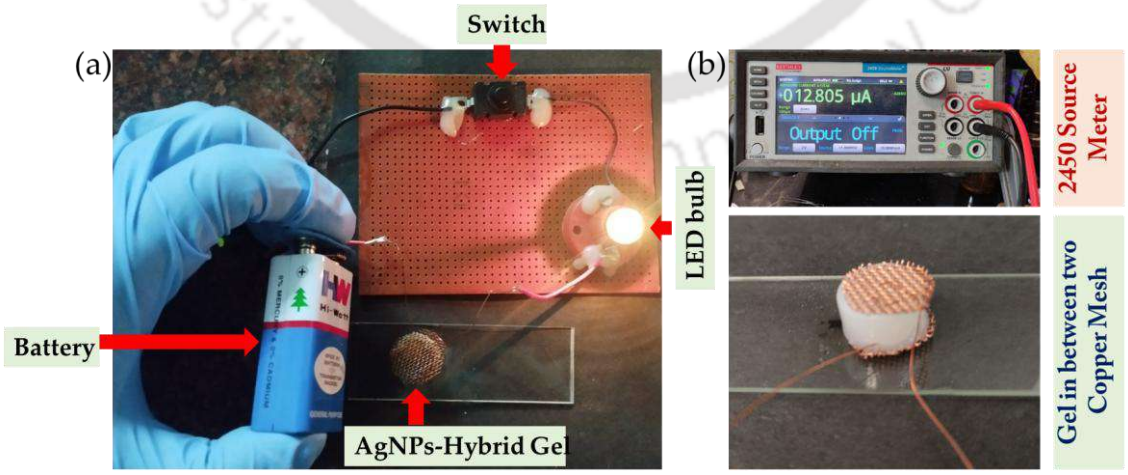

Figure A4B.18: (a) Circuit set up for demonstrating conductive property of AgNPs-Hybrid-Gel. (b) Depiction of conductivity measurement set up using source meter.

Table A4B.7: Conductivity measurement of different set of gels.

Gel	Conductance	Cell constant (l/a)	Conductivity (Conductance × l/a)
Agarose Gel	1.54×10^{-5} S	0.53 cm^{-1}	0.82×10^{-5} S cm^{-1}
Hybrid Gel	1.35×10^{-5} S	0.53 cm^{-1}	0.72×10^{-5} S cm^{-1}
AgNPs-Hybrid Gel	0.03216 S	0.53 cm^{-1}	0.02 S cm^{-1}

Chapter 5

Highly Selective Oil Gelation via PSOG: Recovery of Oil spill and Detection of Fuel-Adulteration

CHAPTER 5

5.1. Background and Focus of the Chapter

Within the realm of supramolecular chemistry, the nature-inspired supramolecular self-assembly process bears significant importance, where the entities with higher order complexities can be derived from the spontaneous association of more than one chemical species through various non-covalent interactions. [5.1-5.3] The concept of hierarchical supramolecular self-assembly can be employed for the construction of supramolecular soft materials, such as a supramolecular gel. Supramolecular gels derived from LMWG molecules are expected to be formed via three very crucial steps: a) formation of supramolecular polymers via one-dimensional self-assembly of LMWGs, b) hierarchical self-assembly of the supramolecular polymers to give mesoscopic fibers, and c) formation of a three-dimensional network through interwinding of these fibers with solvent molecules trapped inside the network. [5.4] Such gels find a myriad of applications in various fields, encompassing environmental remediation, [5.5,5.6] pharmaceuticals, [5.7] optoelectronic materials, [5.8] catalysis, [5.9, 5.10] batteries [5.11] etc.

Oil spills cause serious damage to the environmental well-being and impose devastating impacts on local economies, especially when they occur in ecologically sensitive areas such as mangroves, wetlands, etc. [5.12] Such oil spills might result from both anthropogenic and natural causes, which include oil drilling/shipping, volcanic eruption, etc. [5.13] One of the largest and catastrophic offshore oil spills is the Deepwater Horizon (DWH) oil spill of 210 million gallons, which occurred in April 2010, posing a threat to the entire Gulf and Atlantic coastline [5.14] in the Gulf of Mexico, costing British Petroleum (BP) more than $60 billion [5.15] for cleaning it up [5.16]. Various innovative technologies have been introduced for sustainable control of such oil spillage, which comprise methods like in situ burning, chemical methods such as the use of solidifiers and dispersants, bioremediation, carbon materials, etc. [5.17-5.21] Although the mentioned techniques solve the problem to some extent, but are still not devoid of some serious issues, such as requiring a much longer time, toxicity-related issues, low efficiency, and low selectivity. To tackle such problems, researchers have started thinking of sustainable alternatives, where the PSOGs have gained much attention recently owing to their simple design process, structural tunability, non-interference in the aquatic lives, etc.

PSOGs are capable of preferentially gelling one solvent among two immiscible solvents. [5.6, 5.22] These types of gelator molecules are very efficient in oil spill recovery from water, as they can selectively form gel with oil without interfering with the water medium. In 2016, Zeng et al.

reported very fast room temperature gelation of crude oil by chiral gelator molecules. [5.12] In the same year, Sureshan et al. demonstrated marine oil spill recovery using a sugar-based organogelator. [5.13] Chaudhuri et al., in 2018, demonstrated gelation of crude oil from water by using naphthalene diimide-based powder gelator. [5.23] Nandi et al. reported a phase-selective imine-based organogelator for oil spill recovery in 2019. [5.21] In 2020, Bagher et al. demonstrated phase-selective gelation of oil spills on water surfaces via xerogel derived from an oleylamide-based gelator molecule. [5.24]

In 2023, Baskoutas et al. reported fast and effective oil trapping from oil-contaminated soil/water bodies by employing oil gelators based on diisocyanates and alcohols. [5.25] Last year, Molla et al. demonstrated phase-selective gelation of diesel and petrol from water using an azobenzene-based organogelator. [5.26] In most of the discussed examples, the designed gelator molecules form gel in many different organic solvents in addition to oil samples, hence selectivity is compromised. Despite all such commendable advancements in this particular field, there has hardly been a discussion regarding selective gelation in spite of its great implications for the environment and economies. Specific oil samples can be targeted and congealed if a highly selective organogelator can be designed, thus making it an economically more viable approach.

Moreover, the concept of selective oil gelation can further be applied for the detection of fuel adulteration through gelation, thus helps in bypassing the use of sophisticated instrumentations. Fuel adulteration is a serious problem, especially in developing nations, where cheaper fuels like kerosene are mixed with diesel and petrol for economic benefits. Fuel adulteration as such is not viable both environmentally as well as economically. [5.27] So, keeping all those things in mind, many techniques have been devised for the effective detection of fuel adulterations, which include spectroscopic methods (such as fluorescence spectroscopy, FT-IR spectroscopy, etc.), hydrometer, microcontroller sensor, long-period fiber grating, chromatography, etc. [5.28-5.31] In 2019, Nandi et al. demonstrated the detection of adulteration in diesel and petrol by kerosene through fluorescence spectroscopic measurement of the produced gel in the adulterated fuels. [5.22] Very recently, Kota et al. reported an interesting technique that involves a device that can detect fuel adulteration based on the changes in mobility of fuel droplets on non-textured and non-polar solid surfaces. [5.31] However, the existing methods are not totally devoid of some major problems, such as the requirement of sophisticated instrumentation, complexities associated with the methods, etc. So, there is still room for improvement in some important areas in terms of reducing the complexities of the methods undertaken, making it more viable by avoiding the use of sophisticated instruments, and reducing the time taken for the detection and identification of the specific adulterants used.

In our continuous effort to design functional supramolecular LMWGs, [5.32, 5.33] herein we have designed an acylhydrazone-based phase-selective tripodal LMWG named THD, which could selectively congeal diesel and kerosene; none of the other tested organic solvents, as well as the oil samples, could render gel formation of THD. Here, we have focused on the selective gelation of oil as we believe that, with the rapid advancement of this particular field, the issue of selectivity is going to be very important for sustainable designing of LMWGs for oil spill recovery. This concept has the potential to effectively identify specific oil samples within a mixture of various oils or solvents in water. Doing so could help us eliminate the need for an additional separation strategy, streamlining the process and increasing efficiency. Moreover, for the first time, we have proposed an idea where the concept of selective oil gelation can be successfully applied for the detection of kerosene adulteration in petrol, which is much advantageous than many of the existing techniques, as it is much simpler, cost-effective, and capable of specifically detecting the presence of kerosene in petrol.

5.2. Objective of the Chapter

Highly selective oil gelation using phase-selective organogelators (PSOGs) is a largely unexplored and under-discussed topic that requires immediate attention due to its implications for the environment, health, and economies. One of the main reasons for the lack of reports on this critical concept is the unclear understanding of the structure-function relationship of the designed gelator molecules. We have rationally designed a phase-selective low molecular weight gelator (LMWG) molecule named, THD to address this challenge. This gelator can form gel in the presence of diesel and kerosene oil in a very highly selective manner, among a wide range of studied other organic solvents as well as oil samples. We applied this concept to perform oil spill recovery from aqueous environments, achieving a significantly high recovery percentage. Additionally, the concept of selective oil gelation has further been utilized to develop a novel and cost-effective method for detecting fuel adulteration, thus eliminating the need for sophisticated instrumental analysis.

5.3. Results and Discussion

5.3.1. Design Rationale of the Gelator

A tripodal arylhydrazone based PSOG namely, THD has been designed by integrating three key features: a) acylhydrazone unit acts as a hydrogen bond forming unit that helps in 1-D self-assembled network formation, b) the naphthyl moiety undergoes π-π staking interaction thus helps in cross-linking the hydrogen bonded assembly, and lastly, c) the long alkyl chain (dodecyl) undergoes van der Waals interaction. (Scheme 5.1a,b) Since the oil samples such as diesel, kerosene, petrol, etc., contain varying amounts of hydrocarbons with different carbon chain

lengths, aromatic/polyaromatic, etc. So, we hypothesize that the cumulative effect of all those non-covalent interactions would facilitate our designed LMWG, THD to undergo effective hierarchical self-assembly in the presence of certain oil samples, thus leading to gel formation. We further designed a control compound by reducing the alkyl chain length (named as THX), to see, there is any effect of the chain length on gelation, which would further help in the rational establishment of the gelation mechanism.

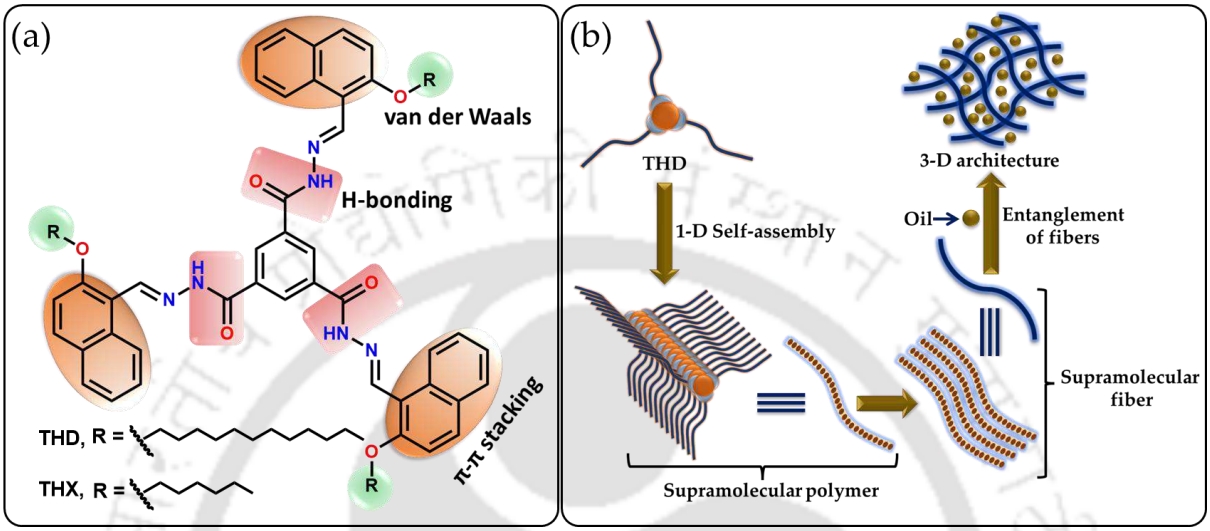

Scheme 5.1: (a) Design of the ligands THD and THX. (b) Representing the expected oil gelation pathway.

5.3.2. Investigation of Aggregation Property

To have an initial idea about the aggregation properties of THD and THX, we recorded UV–Vis spectra of both the molecules (10 μM each) in 100 % THF as well as in 100 % H_2O. In 100 % THF, both the molecules showed sharp absorption maxima (λ_{max}) at ~365 nm and a shoulder peak at ~380 nm, which might be attributable to π–π* and n–π* transitions, respectively, of the molecules. (Figure A5.1a,b) However, in 100 % H_2O, the λ_{max} value of both the molecules undergoes a significant bathochromic shift of ~15 nm (from ~365 nm in 100 % THF to ~380 nm in 100 % H_2O) with a severe broadening of the peaks and concomitant substantial upsurge of the baselines, thus inferring aggregation behaviour of both the molecules in 100 % H_2O. (Figure 5.1a,d) Such peak broadening, along with an upsurge in the baseline in 100 % H_2O, is expected to be due to Mie scattering. [5.34]

In a subsequent study, the aggregation properties of both THD and THX (10 μM each) were further investigated in a binary solvent system of THF: H_2O, by varying the % of H_2O through fluorescence spectroscopy. In pure THF, both THD and THX were observed to be weakly emissive. On increasing the % of H_2O (from 0 % to 100 %), the emission intensity enhances gradually and reaches a maximum at 100 % H_2O, accompanied by a significant bathochromic shift of ~55 nm from 420 nm (in 100 % THF) to 475 nm (in 100 % H_2O). In 100 % H_2O, the

enhancement of the emission intensity for THD and THX was recorded to be ~5 and ~2 times, respectively, as compared to that in 100 % THF. (Figure 5.1b,e,c,f) This result clearly validates the aggregation-induced emission (AIE) behaviour of both THD and THX. The observed highest emission in 100 % H_2O can be attributed to the aggregate formation of both molecules, resulting in restriction of intramolecular motion, thus blocking the non-radiative decay pathways and finally leading to enhanced emission. [5.35-5.37]

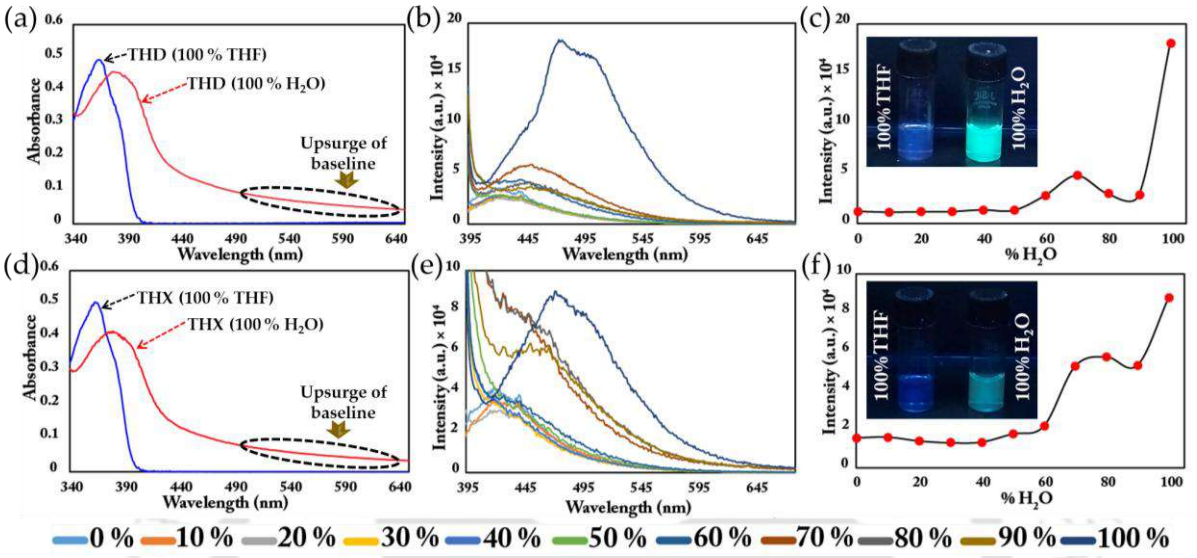

Figure 5.1: Depicting UV–Vis spectra of (a) THD, and d) THX in 100 % THF and 100 % H_2O. Representing AIE behaviour of (b) THD, and (e) THX through fluorescence emission measurement at different H_2O (%). Representing fluorescence emission intensity at 475 nm in different H_2O (%) portraying clear emission maxima in 100 % H_2O in (c) THD (inset: depicting fluorescence emission of THD in 100 % THF, and 100 % H_2O under 365 nm UV-lamp), and (f) THX (inset: depicting fluorescence emission of THX in 100 % THF, and 100 % H_2O under 365 nm UV-lamp).

Such aggregation formation is expected to be facilitated by various non-covalent interactions such as hydrogen bonding, as facilitated by the acylhydrazone unit, π-π stacking promoted by the naphthyl ring, and van der Waals interaction induced by the long alkyl chains. The aggregation behaviour of THD and THX was further visualized through FESEM imaging. For both THD and THX, we observed scattered or discrete particles in 0 % H_2O. (Figure 5.2a,e) To further visualize the progression of the aggregate formation process, we increased the water percentage to 30 %, where the particles became slightly more aggregated, (Figure 5.2b,f) and subsequently, the particles became even more aggregated when the water % was increased to 70 %. (Figure 5.2c,g) As evident from the FESEM imaging, the larger aggregates might have formed as a result of the accumulation of the smaller particles. Eventually, the aggregation reached its maximum in 100 % H_2O by forming a much larger aggregate, thus supporting our claim of the aggregate formation in H_2O. (Figure 5.2d,h)

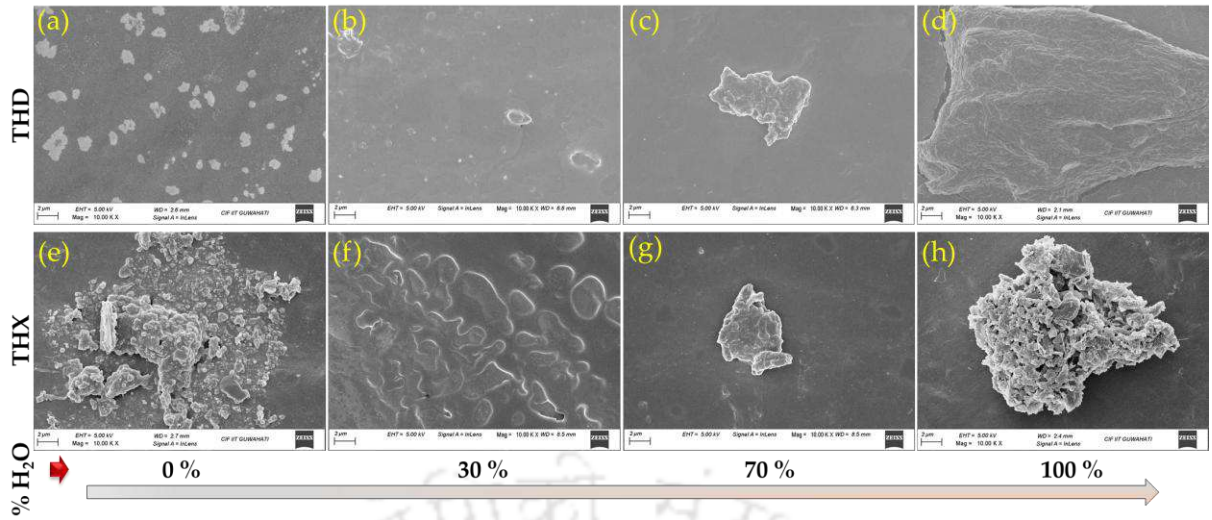

Figure 5.2: FESEM imaging of THD in (a) 0 % H_2O, (b) 30 % H_2O, (c) 70 % H_2O, (d) 100 % H_2O; and THX in (e) 0 % H_2O, (f) 30 % H_2O, (g) 70 % H_2O, (h) 100 % H_2O.

5.3.3. Selective Gelation of Oil

Gelation test of the compounds, THD, and THX was executed in a wide range of solvents, which have been listed in. (Table A5.1) Consequently, only THD was observed be form gel selectively in the presence of diesel (D-THD-G) and kerosene (K-THD-G) upon heating the diesel and kerosene solution of THD at 70 °C for 30 s, followed by resting the resulting semi-transparent solution for 5 min. (Figure 5.3b,d, Figure A5.2(i)-(iii)) The formation of the gels (D-THD-G) and K-THD-G) were confirmed through the inverted tube experiment, followed by rheology experiments. In the rheology experiment, firstly, we monitored the gel–sol transitions of both D-THD-G and K-THD-G over different shear strains with a fixed frequency at 1 Hz. (Figure A5.4a,b) After a 1 % shear strain, the storage modulus (G′) was observed to be declining; therefore, to measure frequency-dependent rheological behaviors of both gels, we decided on a shear strain of 0.15 %. From the frequency sweep experiment performed at room temperature, it was quite evident that the storage moduli (G′) are always above the loss moduli (G″) over the entire range of frequencies tested, thus referring true gel nature of both D-THD-G and K-THD-G. (Figure 5.3f) The critical gelation concentration (CGC) of THD in diesel and kerosene was calculated to be 1.5 mg/mL and 2 mg/mL, respectively, thus making THD a supergelator. [5.15, 5.33] Then, their respective T_{gel} were calculated, which were found to be 80 °C and 72 °C for D-THD-G and K-THD-G, respectively. We further investigated the morphology of THD (powder sample), and xerogels of D-THD-G and K-THD-G, which resulted in a long rod-shaped morphology for THD (powder sample), (Figure 5.3a) and dense fibrous morphology for both D-THD-G and K-THD-G (Figure 5.3c,e). The long rod-shaped morphology of THD (powder sample) might be attributable to the 1-D self-assembly architecture formation, whereas the dense fibrous morphology of D-

THD-G and K-THD-G correspondence to the entanglement of the 1-D fiber networks in the gel state (see section 2.9 of chapter 2 for the FESEM sample preparation methodology). The most intriguing part of this study is that none of the other organic solvents/oils studied could render gelation of THD, barring diesel, kerosene. Such very high selective oil gelling behaviour is scarce in the literature, as in many of the reports, the designed gelator molecules undergo gelation simultaneously in different oils as well as in different organic solvents. Surprisingly, the selectivity in oil-gelation has rarely been the prime focus of discussion despite its high practical implications. So, in view of that, our finding opens a new avenue towards designing LMWGs capable of selectively gelling some specific oil samples. However, the control compound, THX, could not form a gel in any of the studied oil samples as well as organic solvents; instead of gelation, precipitation or sol formation were observed, thus portraying the crucial role played by the long alkyl chain in such gelation process. (Figure A5.2(iv)-(vi))

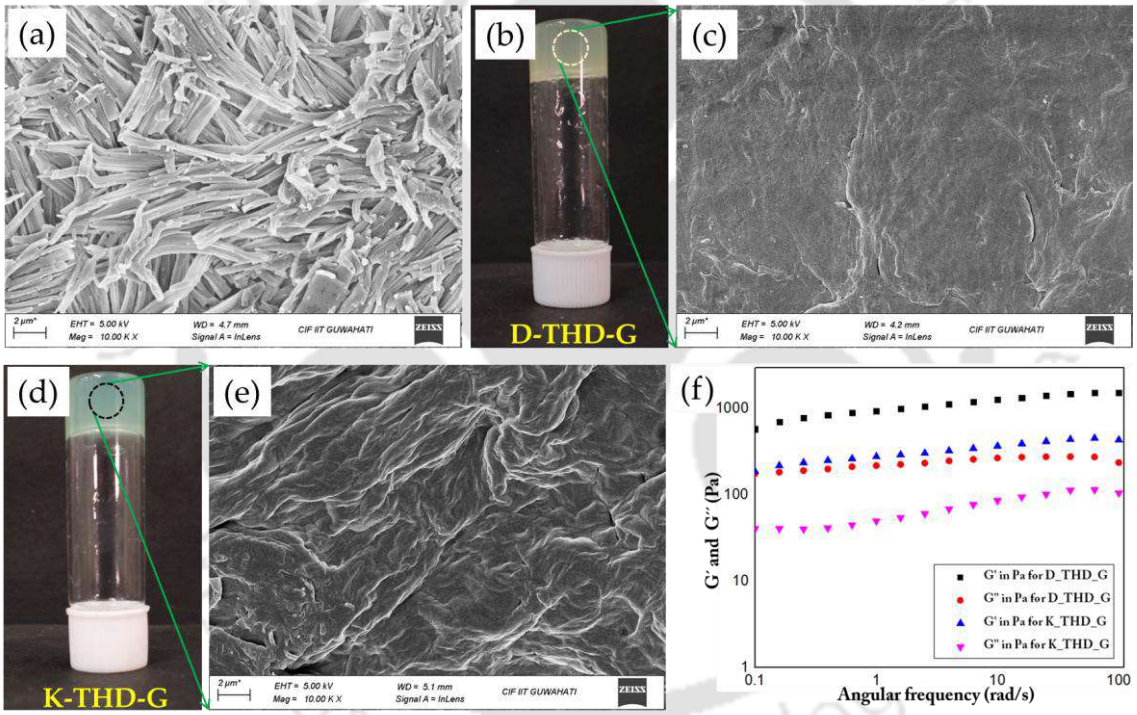

Figure 5.3: (a) FESEM imaging of powder sample of THD. Representing inverted tube experiment of the gel formed by THD with (b) diesel (D-THD-G), and (d) kerosene (K-THD-G). FESEM imaging of xerogel derived from (c) D-THD-G, and (e) K-THD-G. (f) Frequency-dependent rheological measurement of D-THD-G and K-THD-G.

5.3.4. Thixotropic and Thermoreversible Behaviour of the Oil-gel

Interestingly, both D-THD-G and K-THD-G were observed to possess thixotropic as well as thermoreversible properties. Initial assessment of the thixotropic behaviour was done via mechanical shaking of both the gels, which resulted in a gel-to-sol transformation, and resting them for 5 min. Reinstated the initial gel properties. (Figure 5.4a(i); Figure 5.4.b(i)) Rheological study was performed for the quantification of the thixotropic behaviour of both D-THD-G and K-

THD-G by applying and releasing a certain % strain cyclically. At first, both the gels were placed at a constant strain of 0.15 %, where G′ is higher than G″, inferring the presence of gel form. Subsequently, when the % strain is increased to 50 % and held for 25 s. resulted in a complete reversal of the G′ and G″, where the latter is higher than that of the former, indicating complete transformation of the gel to sol form. Upon releasing the % strain to 0.15 % and holding on for 50 s. resulted in higher G′ than G″ inferring restoration of the gel form. (Figure 5.4c,d) The said experiment was continued up to two cycles, and in each cycle, the restoration of the gel form was evident. Such gel restoration from its sol form advocates for the self-healing behaviour of the aforementioned gels. Apart from the thixotropic property, thermoreversible characteristics were also evident in both gels. D-THD-G and K-THD-G transformed into their corresponding sol form when heated above 80 °C and 72 °C, respectively. Upon cooling to room temperature, both the sol forms returned to their corresponding gel states, and the experiment can be continued for more than 10 cycles. (Figure 5.4a(ii); Figure 5.b(ii))

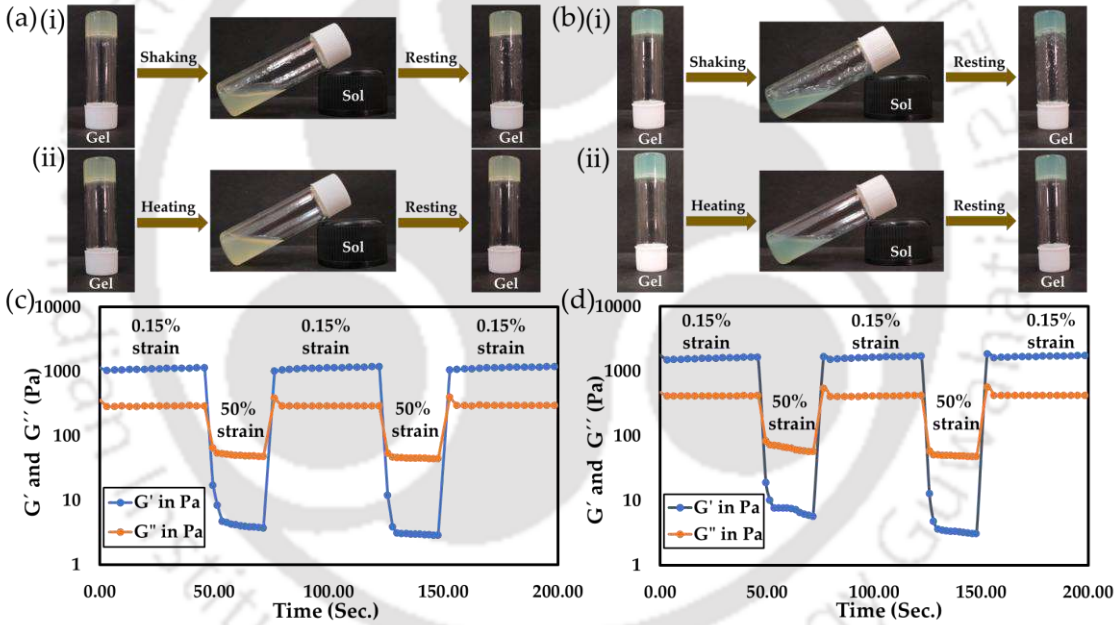

Figure 5.4: Representing the thixotropic behaviour of (a) i) D-THD-G, and (b) i) K-THD-G. Representing thermoreversible behaviour of (a) ii) D-THD-G, and (b) ii) K-THD-G. Representing thixotropic properties of (c) D-THD-G, and (d) K-THD-G through rheology experiments.

5.3.5. Mechanistic Insights into Highly Selective Oil-gelation

High selectivity of THD towards diesel and kerosene oil gelation is remarkable, and at the same time, it is quite surprising as well. We hypothesized that such selective oil gelation is due to the cumulative effect of hydrogen bonding, π-π stacking, and van der Waals interactions, and the extent of all those interactions varies significantly with different organic solvents/ oils. If we look inside the chemical composition of diesel and kerosene, we find that diesel and kerosene are mostly

composed of saturated hydrocarbons, where the carbon chain length varies from C8-C18 and C8-C40 for diesel and kerosene, respectively. [5.38] Additionally, both of them also contain a significant number of polyaromatic hydrocarbons, for instance naphthalene, as well as some other aromatic compounds such as alkylbenzenes [39,40]. Therefore, we envisaged that, the mentioned oils promote van der Waals and π-π stacking interactions thus helping in the entanglement of the 1-D self-assembly of THD to 3-D architectural arrangement ultimately leading to gelation, which is corroborated well by the morphological transformation of THD from its long rod-shaped morphology (in powder form) to dense fibrous network morphology in its gel states (in D-THD-G and K-THD-G). (Figure 5.3a,c,e) This is also strongly justified by the fact that, with petrol, THD could not form a gel. For instance, we also checked the gelation ability of THD in petrol at higher concentrations as well (15 mg/μL), where we could not perceive any kind of gelation. (Figure A5.3(i),(ii)) Petrol is mainly composed of hydrocarbons where the carbon chain length varies from C4-C12, and it contains a smaller number of polyaromatic compounds as compared to that of diesel and kerosene. [5.38, 5.40] As a result of the presence of lower alkyl chain length and a lesser number of polyaromatic compounds, the extent of non-covalent interactions such as van der Waals and π-π stacking interactions is not strongly prevalent in petrol, resulting in non-gelling behaviour of THD in petrol. The same reason is applicable to all the other studied organic solvents as well as oil samples.

To justify our proposed mechanism of the oil gelling behaviour of THD as well as the aggregation behaviour in the mentioned oil samples, firstly we performed UV–Vis spectroscopic study of THD (10 μM) in both diesel and kerosene, where the λ_{max} was observed at ~368 nm with a shoulder peak at ~385 nm, corresponding to π–π* and n–π* transitions respectively of THD. (Figure A5.5a,b) In a subsequent study, to understand the aggregation behaviour of THD in the mentioned oil samples, we performed concentration concentration-dependent study of THD in both diesel and kerosene. On increasing the concentration of THD in diesel from 5 μM to 40 μM slight bathochromic shift of the λ_{max} (from ~367 nm to ~370 nm) was observed, indicating some sort of aggregate formation in diesel. (Figure 5.5a) However, in kerosene oil, no such shifting was observed in the concentration-dependent study (Figure A5.5c) Furthermore, we performed a fluorescence spectroscopic study of THD in both oil samples. Upon excitation of THD (10 μM) at 390 nm, in diesel and kerosene, emission was observed at 420 nm in both the oil samples. However, at the same excitation wavelength, the emission of the gel derived from THD in diesel and kerosene oil (D-THD-G and K-THD-G) showed very large bathochromic shift of the emission of ~50 nm (from ~420 nm in the 10 mM solution to ~470 nm in the gel states) with concomitant annihilation of the emission intensity inferring aggregation caused quenching phenomena in the gel state. (Figure 5.5b, Figure A5.5d) To dive deeper into the molecular-level understanding of the various non-

covalent interactions facilitating those aggregations, we performed an FTIR study of the xerogels of D-THD-G and K-THD-G. On comparing the FTIR spectra of both the xerogels with the powder sample of THD, we observed significant spectral shifting of the peaks corresponding to –NH (acylhydrazone), (13 cm^{-1} and 10 cm^{-1} shifting corresponding to the xerogels of D-THD-G and K-THD-G respectively), and –C=O (carbonyl) (25 cm^{-1} and 27 cm^{-1} shifting corresponding to the xerogels of D-THD-G and K-THD-G respectively) towards higher wavenumber region, indicating active participation of both the groups in self-assembly formation through hydrogen bonding interaction. (Figure 5.5c) We further performed a concentration-dependent ^1H NMR study of THD in DMSO-d_6 for a better understanding of the involvement of different groups involved in non-covalent interactions, where, with an increase in the concentration of THD from 10 mM to 30 mM, slight downfield shifting of the peak corresponding to the –NH (acylhydrazone) (H_b) was observed, inferring its involvement in hydrogen bonding interaction. The peaks corresponding to the protons of the aromatic naphthyl moiety were observed to be little upfield shifted ($H_{d,e-i}$) with the increasing concentration of THD, indicating its involvement in π-π stacking interactions. Moreover, the peaks corresponding to the protons of the long aliphatic alkyl chain (H_{j-u}) were observed to be upfield shifted, stating involvement of van der Waals interaction in the self-assembly formation. (Figure 5.5d) Powder X-ray Diffraction (PXRD) analysis of the xerogels of D-THD-G and K-THD-G revealed a series of broad peaks at 2θ ranging from 22° to 60° (Figure A5.6 & Figure A5.7, see section 2.22 of chapter 2 for sample preparation method for PXRD). For both the xerogels, the peak at 22° with a d spacing of 4 Å suggests van der Waals interaction facilitated by the long alkyl chain, and the peak at 44° with a d spacing value of 2.08 Å corresponds to moderated hydrogen bonding interaction, which arises from the NH and C=O of the acyl hydrazide unit. We further observed two additional broad and weak peaks at 31.5° (d spacing value of 2.85 Å) and 60° (d spacing value of 1.54 Å) for the xerogel of D-THD-G, which corresponds to moderate and strong hydrogen bonding interactions, respectively, involved in the self-assembly process.

5.3.6. Phase Selective Gelation of Oil

Having witnessed the selective kerosene and diesel gelling ability of THD, we wondered whether it could gel oil spills in water in a phase-selective manner. To get an initial idea of the same, we performed a hydrophobicity test of THD, where uniformly cut filter paper was coated with THD, using THD solution prepared in DCM, and was dried for 1 h at room temperature. Water droplets were added onto the surface of the dried THD-coated filter paper via pipette, which resulted in a non-wettability of the same. Then we measured the contact angle of the water droplet placed on

the THD-coated filter paper, which was observed to be at an angle of 110°, indicating hydrophobic behaviour of THD. (Figure 5.6a(ii))

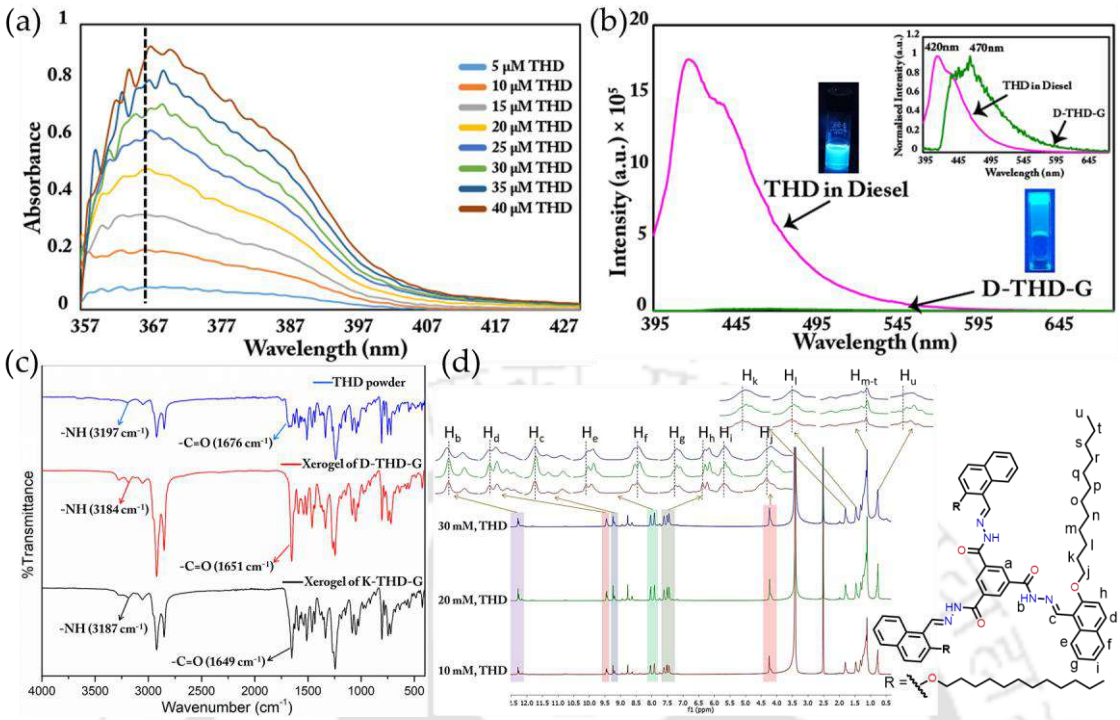

Figure 5.5: (a) Representing concentration-dependent UV–Vis spectroscopic study of THD in diesel. (b) Fluorescence spectra of THD in diesel (10 μM), and D-THD-G (inset: normalized fluorescence spectra of THD in diesel, and D-THD-G). (c) Stacked FT-IR spectra of THD powder, xerogel of D-THD-G, and xerogel of K-THD-G. (d) Concentration-dependent ^{1}H NMR study of THD.

A control experiment was also performed by using an uncoated filter paper, which could not hold water molecules, instead water spills as soon as it comes in contact with the filter paper. (Figure 5.6a(i)) This experiment showed the phase-selective nature of THD quite agreeably. Furthermore, we delved deeper into it and tested the phase-selective oil gelling ability of THD at oil oil-water interface. To do that, first we placed both oil (diesel) and water (1 mL each) inside a glass vial, where oil and water phases were completely separated, the top phase contains diesel, and the bottom phase consists of water. Then we added a powder sample of THD (10 mg) into the oil phase followed by heating at 70 °C for 30 s. and rested it for 5 min., as a result complete gelation of the oil phase was observed without interfering the water phase indicating phase selective oil gelling ability of THD as confirmed via inverted glass tube experiment, where the gel was able to hold the water phase quite comfortably (Figure A5.8(a),(b), see section 2.24 of chapter 2 for the methodology). In a subsequent study the similar experiment was performed in three different water samples which includes river water (collected from Brahmaputra river, near IIT Guwahati Campus, Assam, India), lake water (collected from the Serpentine lake, IIT Guwahati Campus Assam, India), and artificial sea water (prepared using the method of earlier literature report),

[5.41] which resulted in a phase selective oil gelling ability of THD. (Figure 5.6b(i)-(iii)) Furthermore, we performed the said experiment in water samples with a wide pH range (pH = 2, 7, and 12), and in all the cases the selective oil gelling ability of THD was apparent. (Figure 5.6c(i)-(iii)) The aforementioned experiments are testaments to the wide range of practical applicability of THD for oil-spill recovery.

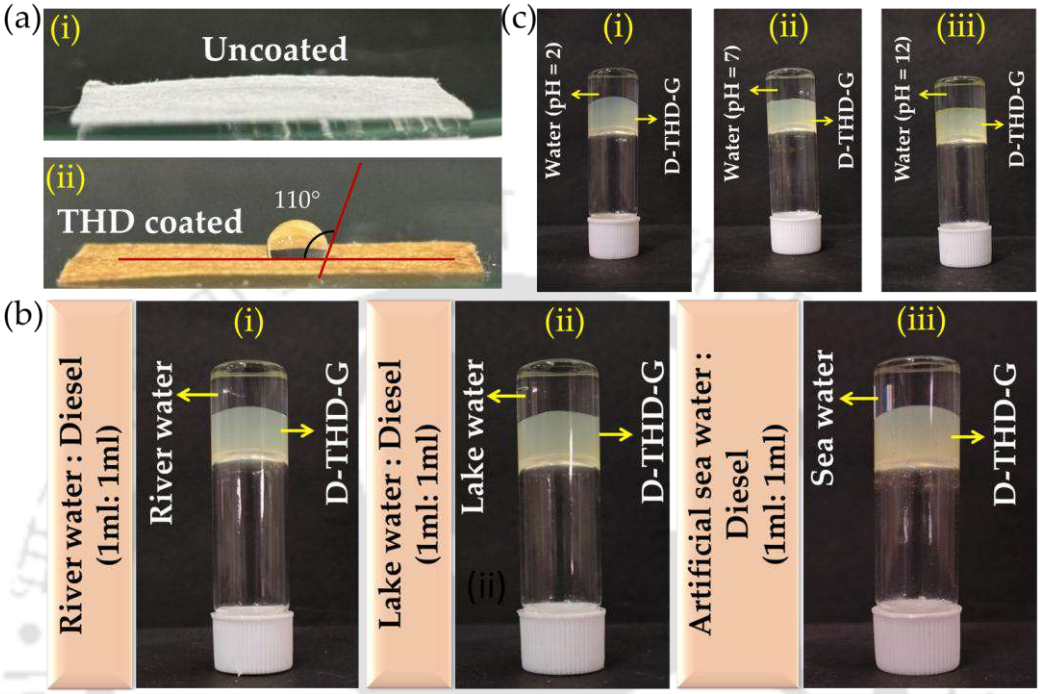

Figure 5.6: Representing phase selective behaviour of THD by placing a water droplet on the top of (a) (i) uncoated, and (ii) coated filter paper (coating was done with THD solution prepared in THF). (b) Depicting phase selective gelation of diesel oil by THD from (i) river water, (ii) lake water, and (iii) artificial sea water. (c) Demonstrating the phase selective diesel oil gelation from water having (i) pH = 2, (ii) pH = 7, and (iii) pH = 12.

5.3.7. Oil-spill Recovery from Water

As evident from the above discussion, THD can efficiently form gel selectively in the presence of diesel and kerosene in a phase-selective manner. So, we were very keen on applying the aforesaid idea in oil spill recovery from water. To do that, we mixed diesel (3 mL) and water (3 mL) inside a glass vial, and a phase separation was observed, where the oil phase occupies the upper phase and the water part remains at the bottom phase. Then, 15 mg of THD powder was added to the oil phase containing diesel, followed by heating at 70 °C, which resulted in the selective gelation of diesel after resting it for about ~5 min. The oil gel was scooped out in a round-bottom flask and subjected to vacuum distillation for the recovery of the oil sample. (Figure 5.7) The % recovery of diesel oil was calculated to be 83.33 % (2.5 mL), which is comparable with previous reports. The remaining 16.67 % diesel oil was expected to be lost during the distillation process.

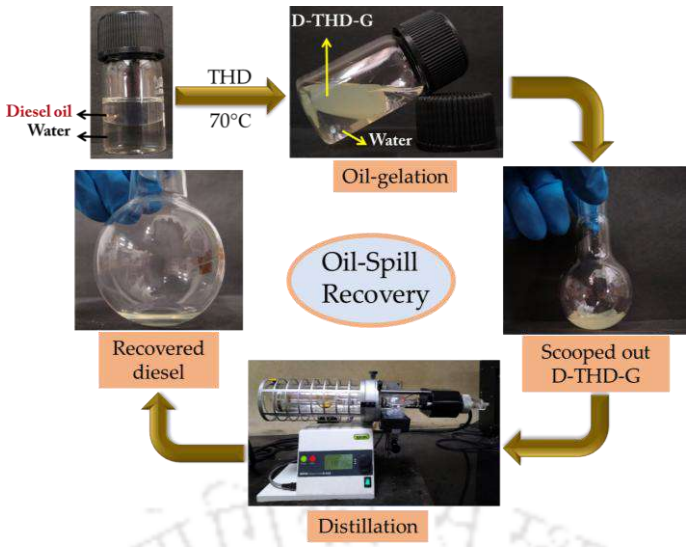

Figure 5.7: Representing the oil spill recovery process through phase selective oil gelation by THD from water (here demonstration has been done using diesel oil).

5.3.8. Detection of Kerosene Adulteration in Petrol via Selective Gelation

The illicit practice of fuel adulteration is quite common in developing nations, where often, low-cost fuels like kerosene are mixed with diesel or petrol for economic benefits, despite their several adverse impacts on the environment, economy, and health. Burning of adulterated fuels leads to the emission of large amounts of environmentally hazardous gases like CO_2, causing severe health concerns. Use of adulterated fuel in vehicles leads to engine failure and reduces the overall performance of the engine. Hence, the detection of fuel adulteration with precision is very important to negate all of its negative impacts. [5.42]

Owing to the selective gelation ability of THD with diesel and kerosene among different oil samples, and many other organic solvents, we were keen on using this particular concept of selective oil gelation towards the detection of kerosene adulteration in petrol. We expected that, presence of kerosene in petrol in certain percentages might induce gelation of THD. Therefore, we prepared samples of petrol adulterated with different percentages of kerosene oil with respect to the total volume of 500 µl (ranging from 0 % to 80 % kerosene in petrol). Afterward, we added 10 mg of THD powder to each sample, followed by sonication and heating (at 70 °C) till we got a clear solution. Subsequently, the heated samples were rested and checked for gelation at certain time intervals, and as a result, the formation of gel was observed in those adulterated solutions where the percentage of kerosene oil was 40 % or above. However, the time required for such gelation varies with the % of kerosene, which were observed to be ~48 h, ~24 h, ~12 h, ~12 h, and ~ 6 h respectively for 40 %, 50 %, 60 %, 70 % and 80 % kerosene adulterated solutions. (Figure 5.8a(i)-(iv), Figure 5.8b(v)-(ix), Table 5.1) As per our extensive literature survey, this is the first time we are reporting such a selective gelation method for the detection of oil adulteration.

In most of the earlier reports, the designed gelator molecules could form gel in many different oils, which were not selective towards any specific oil samples. For a gelator molecule to be used as a detection tool for such adulteration via gelation, it should discriminate between diesel, kerosene, and petrol in terms of gelation. So, considering all these, this particular experiment paves a novel, cost-effective way of detecting oil adulteration visually without the need for any sophisticated instrumental analysis. This experiment can further be expanded for the detection of diesel adulteration by kerosene as well, provided the designed rationale of the gelator molecule is improved to the extent that it forms a gel selectively in the presence of kerosene among different oil samples. (see section 2.25 of chapter 2 for detailed procedure)

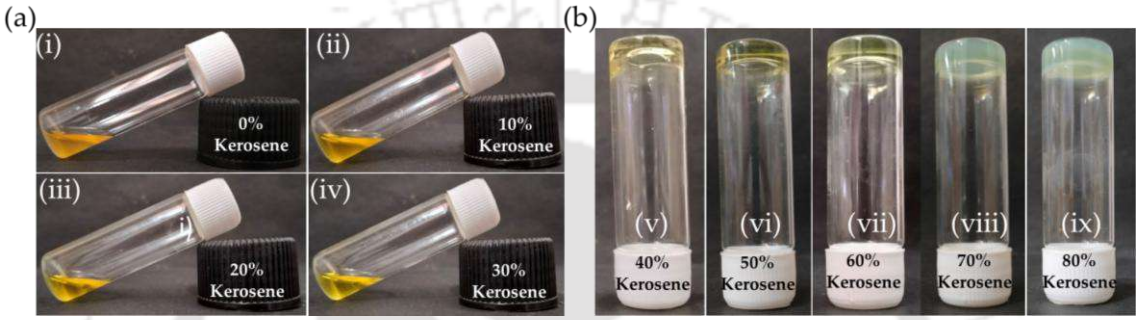

Figure 5.8: (a) (i)-(iv) Representing non-gelation of THD in 0 %–30 % kerosene adulterated petrol oil (after 48 h). (b) (v)-(ix) Depicting the detection of kerosene adulteration (40 %–80 %) in petrol oil by using THD via the gelation method.

Table 5.1: Details of the detection of different percentages of kerosene adulteration in petrol by using THD via gelation method.

Sl No.	*Kerosene (in µl)*	*Petrol (in µl)*	*% of Kerosene*	*Gel/Sol*	*Time required for gelation*
1	0	500	0%	Sol	–
2	50	450	10%	Sol	–
3	100	400	20%	Sol	–
4	150	350	30%	Sol	–
5	200	300	40%	Weak Gel	48h
6	250	250	50%	Gel	24h
7	300	200	60%	Gel	12h
8	350	150	70%	Gel	12h
9	400	100	80%	Gel	6h

5.4. Conclusions

In summary, we have successfully designed a tripodal acylhydrazone-based PSOG, namely, THD, which forms gel very selectively in the presence of diesel (D-THD-G) and kerosene (K-THD-G) in a phase-selective manner. This is a rare example of high selective gelation of oil samples by an organogelator, considering the earlier reports where, in most cases, the designed gelator molecules render gelation in many organic solvents in addition to different oil samples. Both D-THD-G and K-THD-G showed thixotropic as well as thermoreversible properties. The idea of phase-selective gelation has been further applied for oil spill recovery from water via THD, where the % recovery of diesel oil was observed to be as high as ~83.33 %. While the real-world application of PSOG presents particular challenges, our study aims to develop a PSOG with a highly selective oil-gelling capability specifically for oil spill recovery. This innovative approach may significantly enhance our ability to isolate specific oil samples from a complex mixture of different oils or solvents in water, paving the way for more effective environmental remediation solutions. We further went on to demonstrate a novel cost-effective way of detecting adulteration of petrol oil by kerosene oil by exploiting the idea of selective oil gelation of the PSOG, THD. We intend to further advance this particular idea shortly towards the detection of different fuel adulteration as well as to improve the overall sensitivity of the process, by improving the design rationale of the gelator molecules.

References

[5.1] J-. M. Lehn, Supramolecular Chemistry-Scope and Perspectives Molecules-Supramolecules-Molecular Devices, Nobel lecture, December 8, 1987

[5.2] G. M. Whitesides, and B. Grzybowski, *Science*, 2002, **295**, 2418-2421.

[5.3] J-. M. Lehn, Supramolecular Chemistry Concepts and Perspectives, ed. 1995.

[5.4] S. Kimura, K. Adachi, Y. Ishii, T. Komiyama, T. Saito, N. Nakayama, M. Yokoya, H. Takaya, S. Yagai, S. Kawai, T. Uchihashi, and M. Yamanaka, *Nat. Commun.*, 2025, **16**, 3758.

[5.5] B. O. Okesola, S. K. Suravaram, A. Parkin, and D. K. Smith, *Angew. Chem. Int. Ed.*, 2016, **55**, 183-187.

[5.6] B. O. Okesola, and D. K. Smith, *Chem. Soc. Rev.*, 2016, **45**, 4226-4251.

[5.7] E. Piantanida, G. Alonci, A. Bertucci, and L. D. Cola, *Acc. Chem. Res.*, 2019, **52**, 2101-2112.

[5.8] Z. Li, X. Ji, H. Xie, and B. Z. Tang, *Adv. Mater.*, 2021, **33**, 2100021.

[5.9] H. Wu, J. Zheng, A.- L. Kjøniksen, W. Wang, Y. Zhang, and J. Ma, *Adv. Mater.*, 2019, **31**, 1806204.

[5.10] P. Slavík, D. W. Kurka, and D. K. Smith, *Chem. Sci.*, 2018, **9**, 8673-8681.

[5.11] E. Lizundia, and D. Kundu, *Adv. Funct. Mater.*, 2021, **31**, 2005646.

[5.12] C. Ren, G. H. B. Ng, H. Wu, K. -H. Chan, J. Shen, C. Teh, J. Y. Ying, and H. Zeng, *Chem. Mater.*, 2016, **28**, 4001-4008.

[5.13] A. M. Vibhute, V. Muvvala, and K. M. Sureshan, *Angew. Chem. Int. Ed.*, 2016, **55**, 7782-7785.

[5.14] Z. Nixon, S. Zengel, M. Baker, M. Steinhoff, G. Fricano, S. Rouhani, and J. Michel, *Mar. Pollut. Bull.*, 2016, **107**, 170-178.

[5.15] S. B. Howes, K. Holmes, J. G. Morris, L. M. Grattan, and J. Behav. *Health Serv. Res.*, 2018, **46**, 294-305.

[5.16] O. Hettithanthri, T. B. T. Nguyen, T. Fiedler, C. Phan, M. Vithanage, S. Pallewatta, T. M. L. Nguyen, P. Q. A. Nguyen, and N. Bolan, *Asia-Pac. J. Chem. Eng.*, 2024, **19**, e3128.

[5.17] W. Wu, M. Du, H. Shi, Q. Zheng, and Z. Bai, *Sci. Total Environ.*, 2023, **856**, 159107.

[5.18] E. Nyankson, O. Olasehinde, V. T. John, and R. B. Gupta, *Ind. Eng. Chem. Res.*, 2015, **54**, 9328-9341.

[5.19] J. Aurell, and B. K. Gullett, *Environ. Sci. Technol.*, 2010, **44**, 9431-9437.

[5.20] R. M. Atlas, *Mar. Pollut. Bull.*, 1995, **31**, 178-182.

[5.21] H. Rezazad, S. Vahdati-Khajeh, and B. Eftekhari-Sis, *J. Porous Mater.*, 2020, **27**, 1439-1446.

[5.22] S. Mondal, P. Bairi, S. Das, and A. K. Nandi, *J. Mater. Chem. A*, 2019, **7**, 381-392.

[5.23] S. Datta, S. Samanta, and D. Chaudhuri, *J. Mater. Chem. A*, 2018, **6**, 2922-2926.

[5.24] B. Eftekhari-Sis, A. Bagheri, H. Y. Araghi, A. Akbaria, and M. F. Paige, *Soft Mater*, 2020, **18**, 55-66.

[5.25] Y. Saharan, J. Singh, R. Goyat, A. Umar, S. Akbar, A. A. Ibrahim, and S. Baskoutas, *J. Hazard. Mater.*, 2023, **442**, 129977.

[5.26] S. Sk, S. M. Ali, A. Aash, S. Kolay, A. Mondal, S. Mondal, A. H. Khan, N. Sepay, and M. R. Molla, *Chem. Eur. J.*, 2024, **30**, e202303369.

[5.27] B. P. Vempatapu, and P. K. Kanaujia, *TrAC*, 2017, **92**, 1-11.

[5.28] L. V. Bharath, and M. Himanth, *Int. J. Sci. Res. Publ.*, 2017, **7**, 447-451.

[5.29] L. S. G. Teixeira, F. S. Oliveira, H. C. dos Santos, P. W. L. Cordeiro, and S. Q. Almeida, *Fuel*, 2008, **87**, 346-352.

[5.30] N. K. L. Wiziack, A. Catini, M. Santonico, A. D'Amico, R. Paolesse, L. G. Paterno, F. J. Fonseca, and C. Di Natale, *Sens. Actuators B: Chem.*, 2009, **140**, 508-513.

[5.31] S. Movafaghi, S. Vallabhuneni, W. Wang, S. Jathar, and A. K. Kota, *Langmuir*, 2023, **39**, 9044-9050.

[5.32] O. A. Pegu, and G. Das, *Langmuir*, 2024, **40**, 24095-24105.

[5.33] R. Moral, and G. Das, *Soft Matter*, 2024, **20**, 7668-7677.

[5.34] R. Moral, O. A. Pegu, and G. Das, *Dyes Pigm.*, 2023, **218**, 111502.

[5.35] Z. Zhao, H. Zhang, J. W. Y. Lam, and B. Z. Tang, *Angew. Chem. Int. Ed.*, 2020, **59**, 9888-9907.

[5.36] J. Luo, Z. Xie, J. W. Y. Lam, L. Cheng, H. Chen, C. Qiu, H. S. Kwok, X. Zhan, Y. Liu, D. Zhu, and B. Z. Tang, *Chem. Commun.*, 2001, 1740-1741.

[5.37] W. -J. Wang, Z. -Y. Xin, X. Su, L. Hao, Z. Qiu, K. Li, Y. Luo, X. -M. Cai, J. Zhang, P. Alam, J. Feng, S. Wang, Z. Zhao, and B. Z. Tang, *ACS Nano*, 2025, **19**, 281-306.

[5.38] R. Haddad, T. Regiani, C. F. Klitzke, G. B. Sanvido, Y. E. Corilo, D. V. Augusti, V. M. D. Pasa, R. C. C. Pereira, W. Romão, B. G. Vaz, R. Augusti, and M. N. Eberlin, Energy Fuels, 2012, **26**, 3542-3547.

[5.39] J. O. Lalah, and P. N. Kaigwara, *Environ. Toxicol. Chem.*, 2005, **87**, 463-479.

[5.40] Y. Goto, K. Nakamuta, and H. Nakata, *Ecotoxicol. Environ. Saf.*, 2021, **224**, 112644.

[5.41] D. R. Kester, I. W. Duedall, D. N. Connors, and R. M. Pytkowicz, *Lim. Ocean.*, 1967, **12**, 176-179.

[5.42] L. Yang, Y. Shi, Z. Yi, X. Song, J. Lv, P. K. Chu, and C. Liu, *Anal. Methods*, 2022, **14**, 2153-2160.

Annexure 5

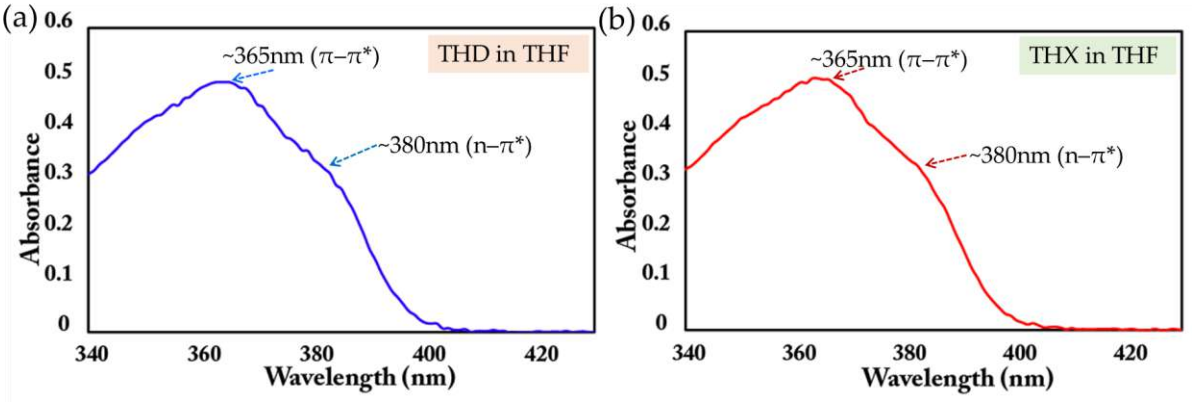

Figure A5.1: UV-Vis spectra of (a) THD, and (b) THX in THF.

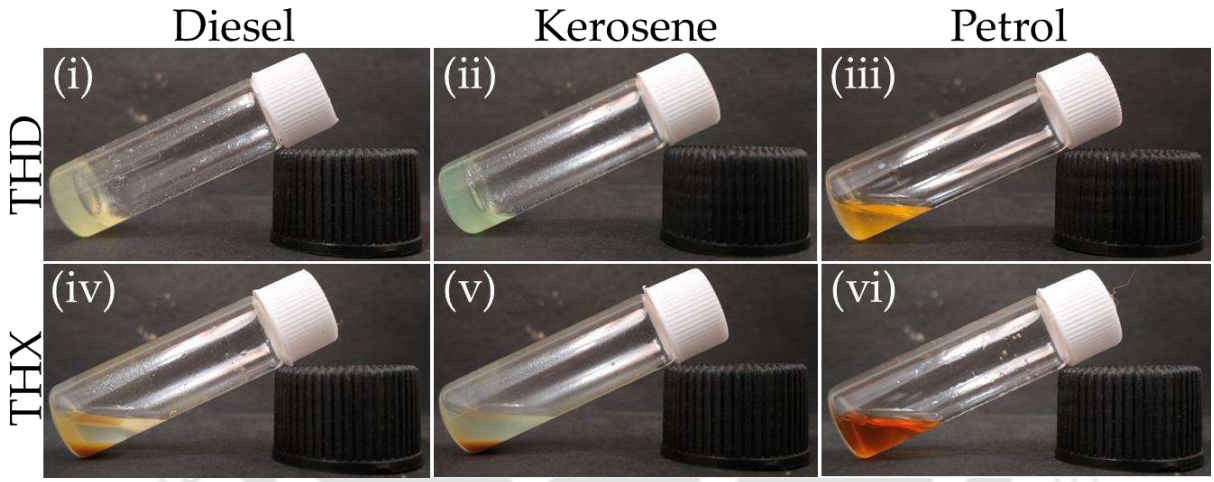

Figure A5.2: Gelation study of THD (i-iii), and THX (iv-vi) with diesel, kerosene, and petrol.

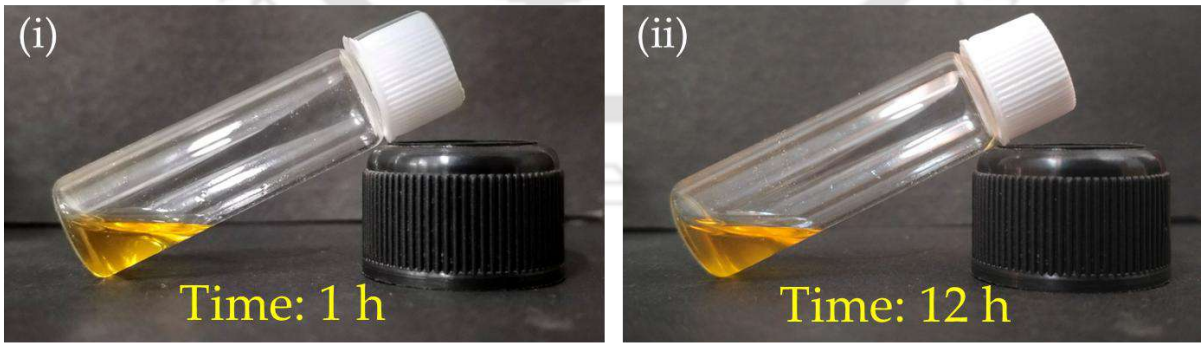

Figure A5.3: Gelation study of THD in petrol (15 mg/500 µL) in different time intervals [(i) & (ii)].

Table A5.1: Gelation study of THD with different solvents.

SL No.	*Solvents*	*Gel (G)*	*Sol (S)*	*Precipitate (P)*
1	Hexane	—	—	P
2	Toluene	—	S	—
3	DMSO	—	S	—
4	DCM	—	S	—
5	DMF	—	S	—
6	EtOH	—	—	P
7	Benzene	—	S	—
8	Ethyl acetate	—	—	P
9	THF	—	S	—
10	Ether	—	—	P
11	Kerosene oil	G	—	—
12	Diesel oil	G	—	—
13	Petrol oil	—	S	—
14	Crude Oil	—	S	—
15	Coconut oil	—	—	P
16	Mustard oil	—	—	P
17	Sesame Oil	—	—	P
18	Silicon oil	—	—	P
19	ACN	—	—	P
20	Acetone	—	—	P

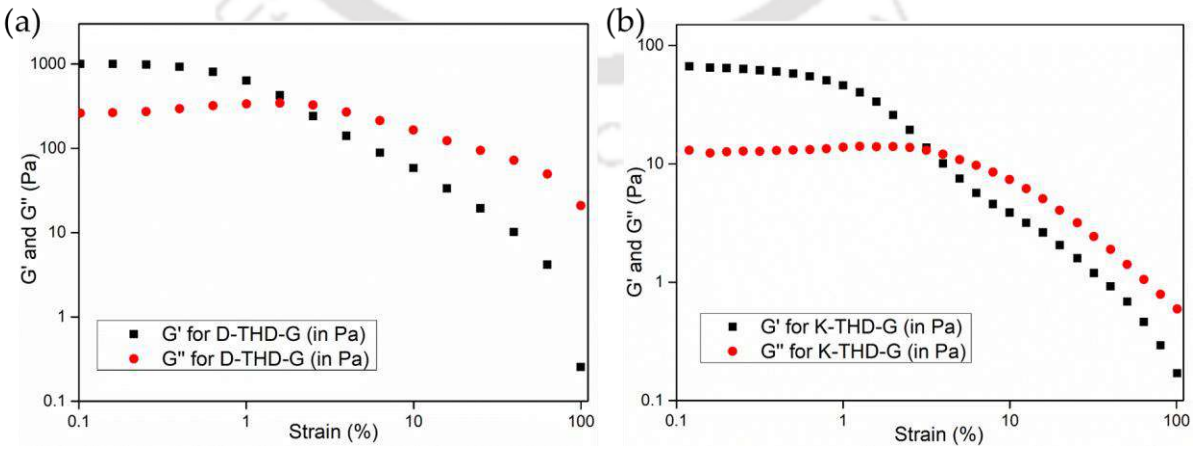

Figure A5.4: Rheological analysis of dynamic strain sweep of (a) D-THD-G, and (b) K-THD-G.

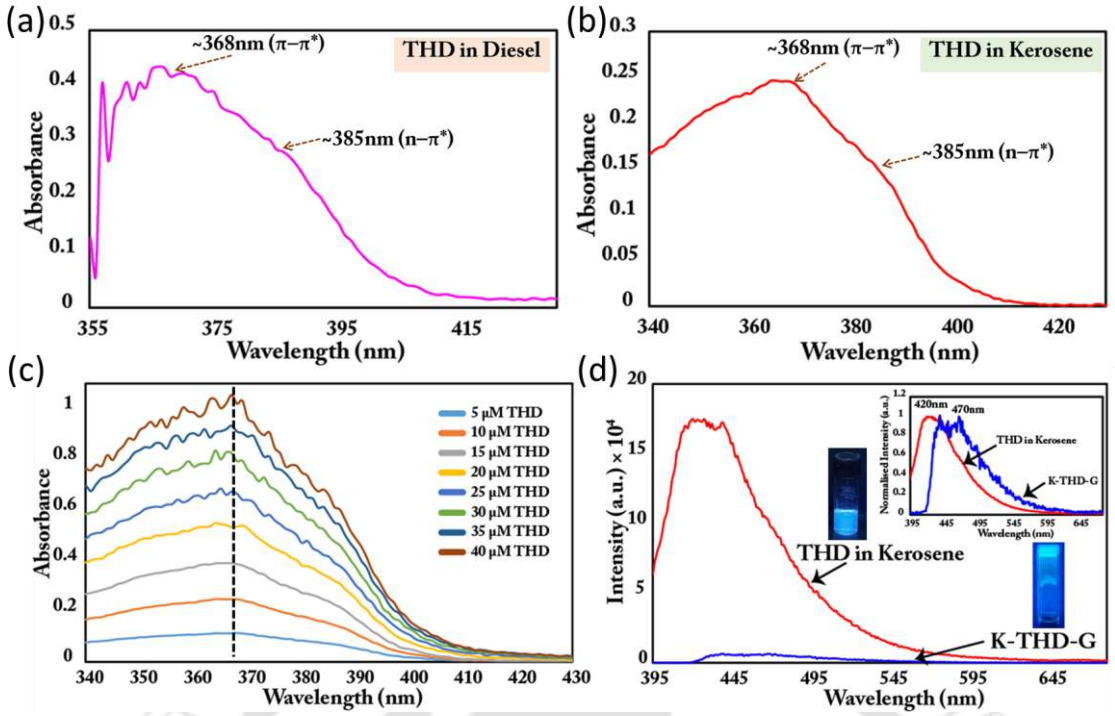

Figure A5.5: UV-Vis spectra of THD in (a) diesel, and (b) kerosene. (c) Concentration-dependent UV-Vis spectroscopic study of THD in kerosene; (d) Fluorescence spectra of THD in kerosene (10 μM), and K-THD-G (inset: normalized fluorescence spectra of THD in kerosene, and K-THD-G).

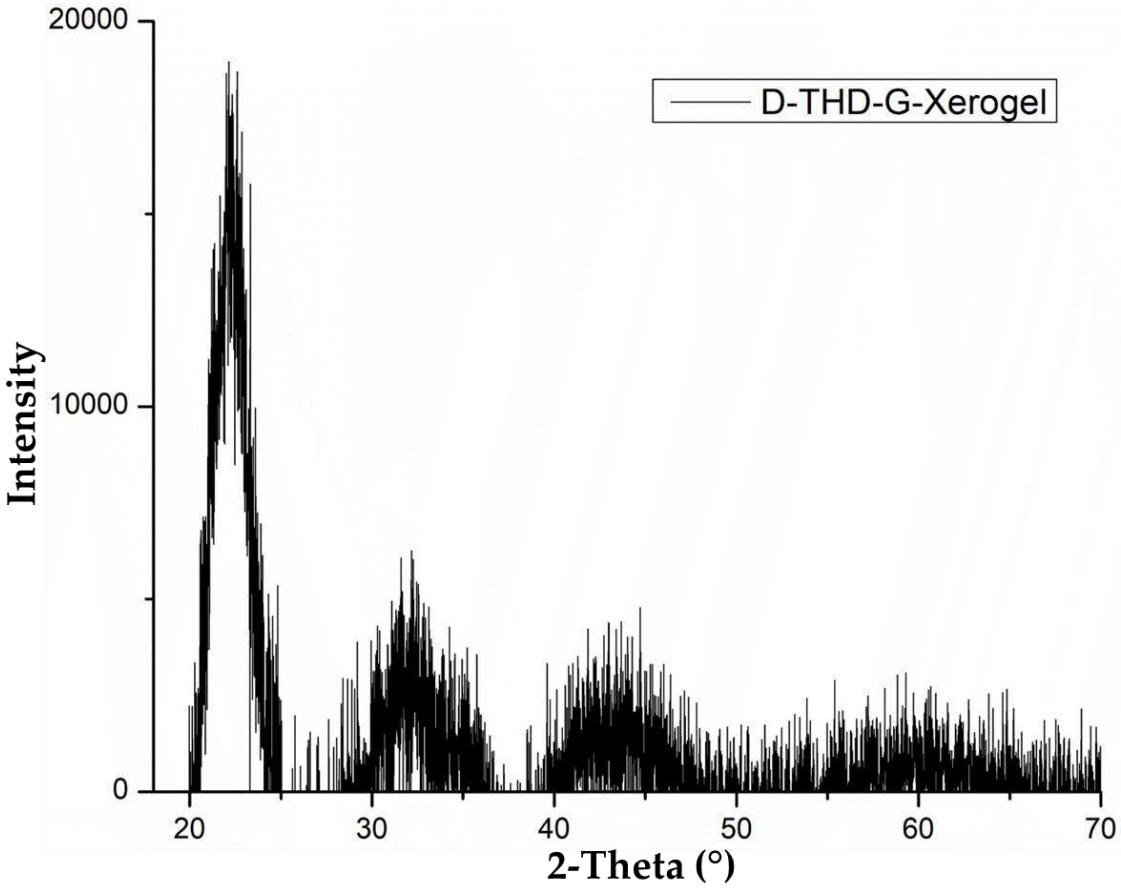

Figure A5.6: Powder X-ray Diffraction (PXRD) analysis of the xerogel derived from D-THD-G.

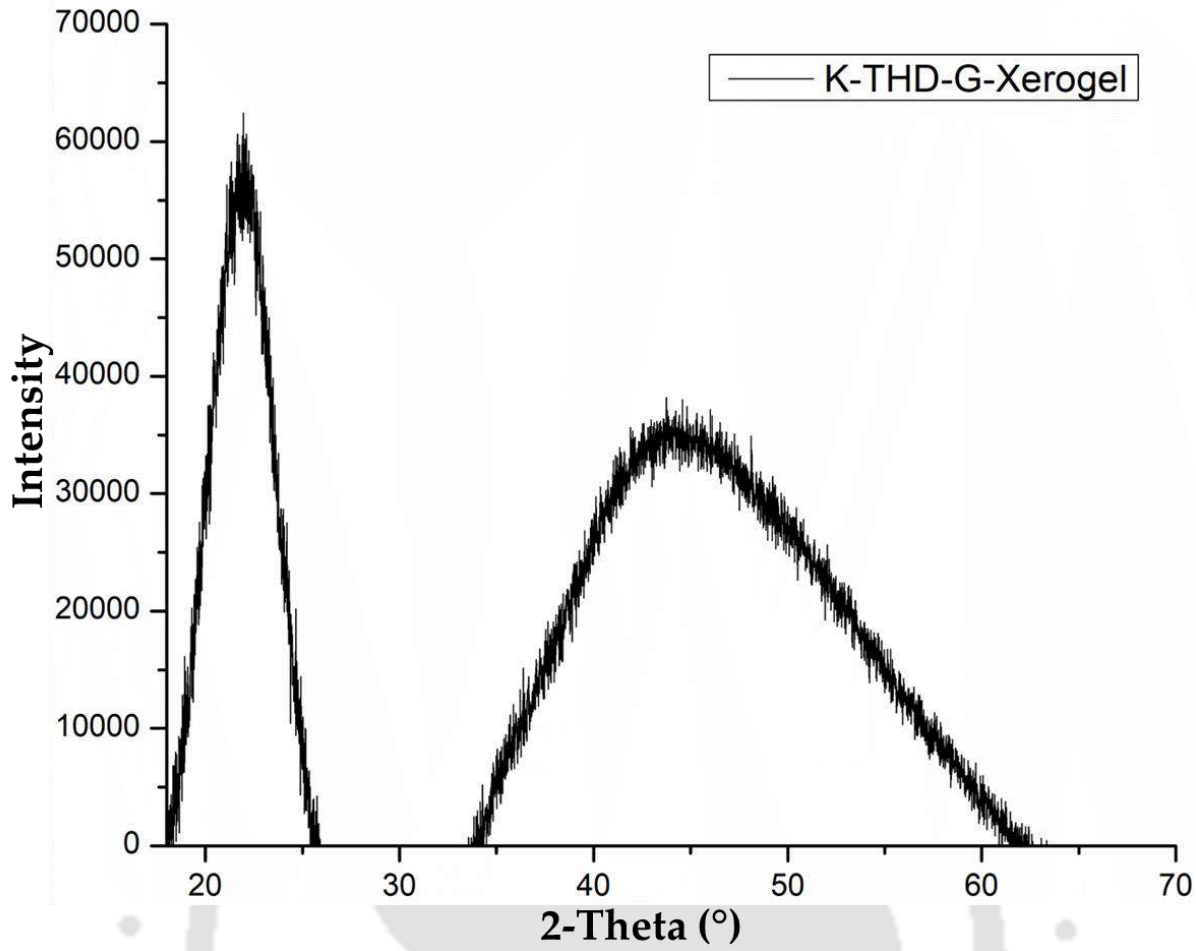

Figure A5.7: Powder X-ray Diffraction (PXRD) analysis of the xerogel derived from K-THD-G.

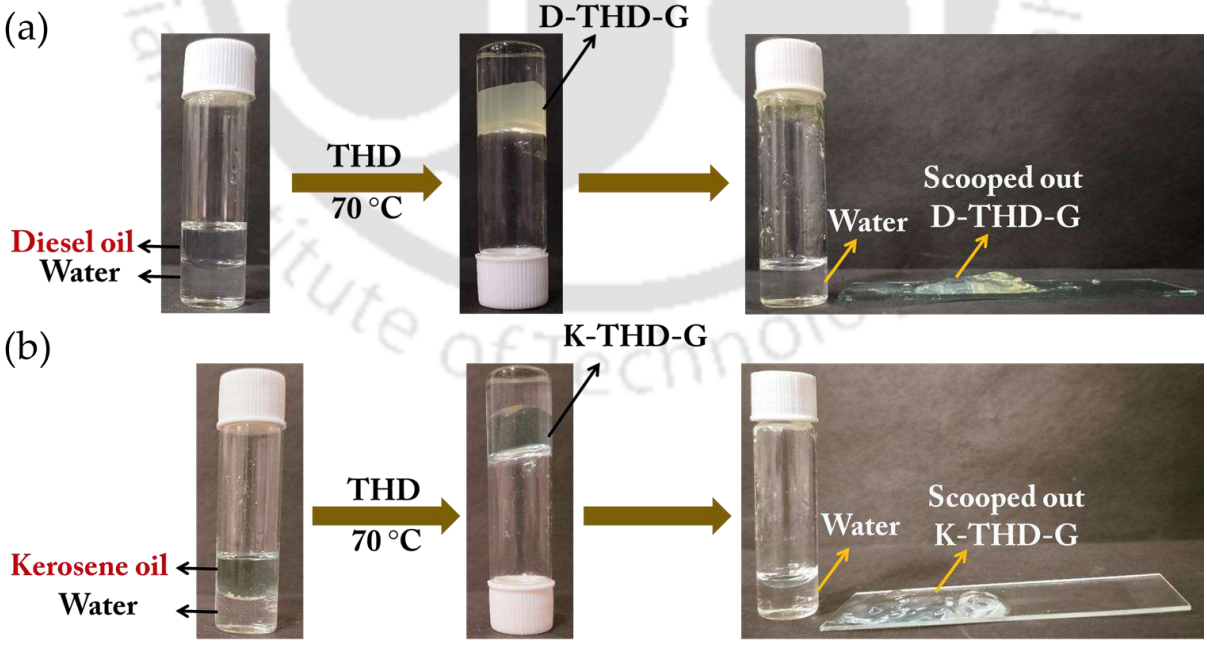

Figure A5.8: Depicting phase selective gelation of (a) diesel, and (b) kerosene oil by using THD.

Chapter 6

Regulating the Phase Transformation of a Kinetically Trapped Supramolecular Gel via Controlled Heating

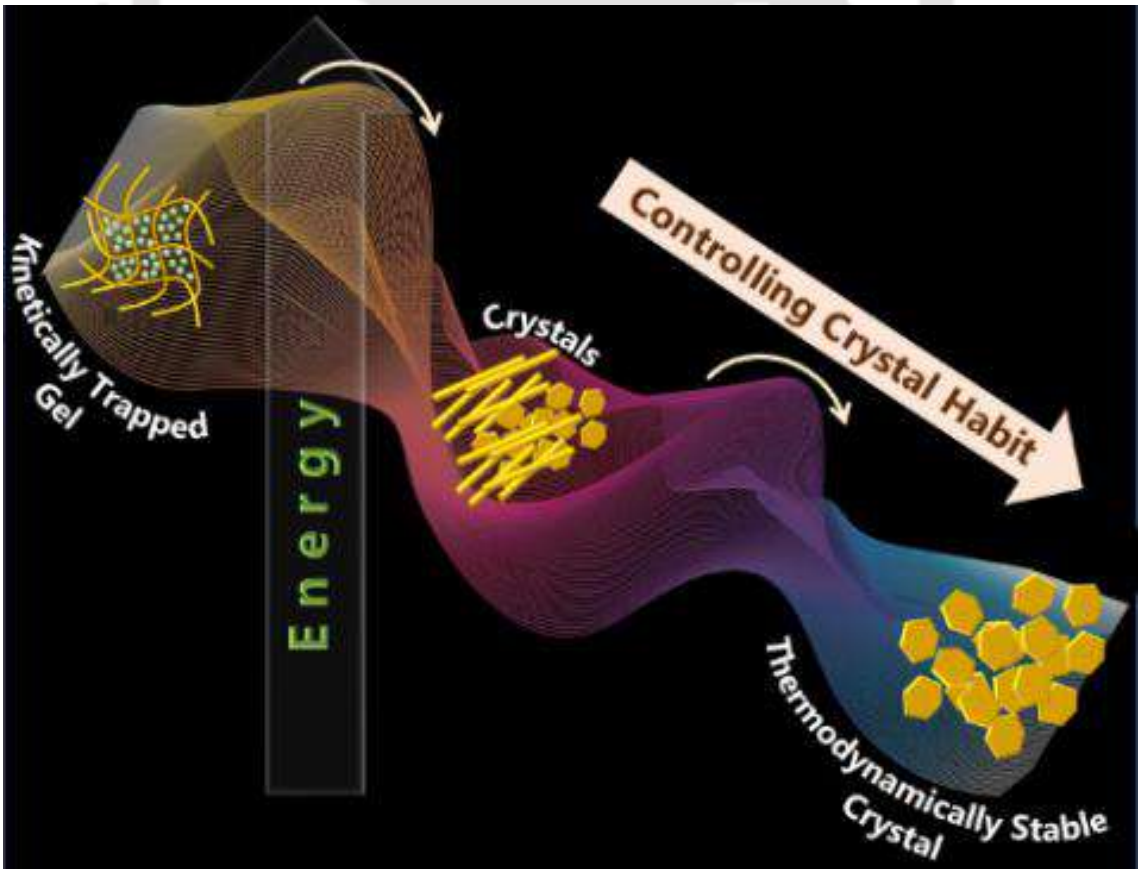

CHAPTER 6

6.1. Background and Focus of the Chapter

Hierarchical self-assembly of low-molecular-weight-gelator molecules results in the formation of supramolecular polymers, for instance supramolecular gel, which allows nanoscale engineering of functional materials with fascinating properties. [6.1-6.8] Transformation of the nano-assembly of supramolecular self-assembled systems like supramolecular gel often occurs in the presence of some external stimuli (such as light, heat, pH, sonication, etc.), and sometimes, such transformations occur spontaneously as well. [6.9-6.12] One such frequently observed transformation is the transition of a kinetically stable gel phase into a thermodynamically stable crystalline phase. [6.13-6.16] However, gel to crystal transformation often occurs serendipitously, thus resulting in crystals with varied habits, and sometimes polymorphs as well. Controlling the crystal shapes bears great importance in fields like the pharmaceutical industry and fine chemistry. [6.17] Crystal morphology greatly impacts its performance by influencing properties like bulk density, mechanical strength, sensitivity, wettability, drug dissolution, bioavailability, stability, etc. [6.18, 6.19] Moreover, it also impacts the downstream processing, including filtration and drying, during the drug manufacturing process as well. [6.20]

Proper understanding of the structure-function relationship of different aggregates or self-assembled systems is vital for the understanding of the functionalities of such aggregates, as well as the regulation of their properties. [6.21] Nature meticulously orchestrates different complex hierarchical assemblies with impeccable precision. [6.22] For instance, in nature, different amyloid fibrils resulting from the same protein might perform vital functions, or they might cause diseases like neurodegenerative disorders as well, based on their different assemblies. [6.23] Another example is the different assembly of the protein tubulin, where its microtubule assembly helps in cell division; on the contrary, its amorphous aggregates break down microtubule assembly, thus causing cell death. [6.24] So, nature has always given impetus to the chemists to construct artificial assemblies with similar precision over its shape, morphology, hierarchy, etc. To achieve such a goal, the understanding of the underlying mechanism of different self-assembled systems is of immense importance, especially to have control over the morphologies as well as properties of the resulting assemblies.

In 2016, Gazit et al. thoroughly demonstrated the spontaneous gel to multistage structural transition from spheres to ribbons, fibers, helices, nanotubes, and eventually to single crystals by using a minimal supramolecular model. [6.12] In another study, the same group explored the phase

transition of a pentapeptide gel to crystal and modulation of such transition by extrinsic factors, such as temperature, solvent composition, and mechanical perturbation. [6.12] Very recently, the Nanda group demonstrated modulation of the spontaneous self-assembly propensity of naphthalimide-(NMI)-conjugated dipeptide by changing the ratio of water, where at a lower water percentage, the self-assembly favors gelation, and at a higher water percentage, it leads to thermodynamically stable crystalline precipitate. [6.25] Adams et al., in 2021, demonstrated that the shape of the crystals resulting from gel to crystal transformation of a multicomponent gel could be controlled by using a magnetic field. [6.26] Furthermore, there is are surplus of reports on gel to crystal transformation of different supramolecular gel systems, encompassing both spontaneous and external stimuli facilitated transformation. [6.14, 6.27-6.29] However, very limited attempts have ever been made to strictly control the hierarchical self-assembly of supramolecular gel systems in such a way that the resulting single crystals during gel to crystal transition are of well-defined crystal habits. Such controlled transformation holds immense importance in very important fields such as drug designing in pharmaceutical industries, [6.17] microscopic crystal patterning for various materials applications, [6.30] etc., thus requiring a deeper understanding of the mechanistic insights of the complexities associated with such transformations.

In view of all those factors, in our study, we have adopted a minimalistic supramolecular model to demonstrate the heat-induced phase transformation of a supramolecular gel to single crystals with specific crystal habits instead of forming polymorphs or a mixture of differently shaped crystals. The hierarchical self-assembly of the resulting gel can be modulated via controlled heating, which leads to single crystals with well-defined crystal habits, and further demonstrates the complex pathways involved in such a transformation. (Scheme 6.1)

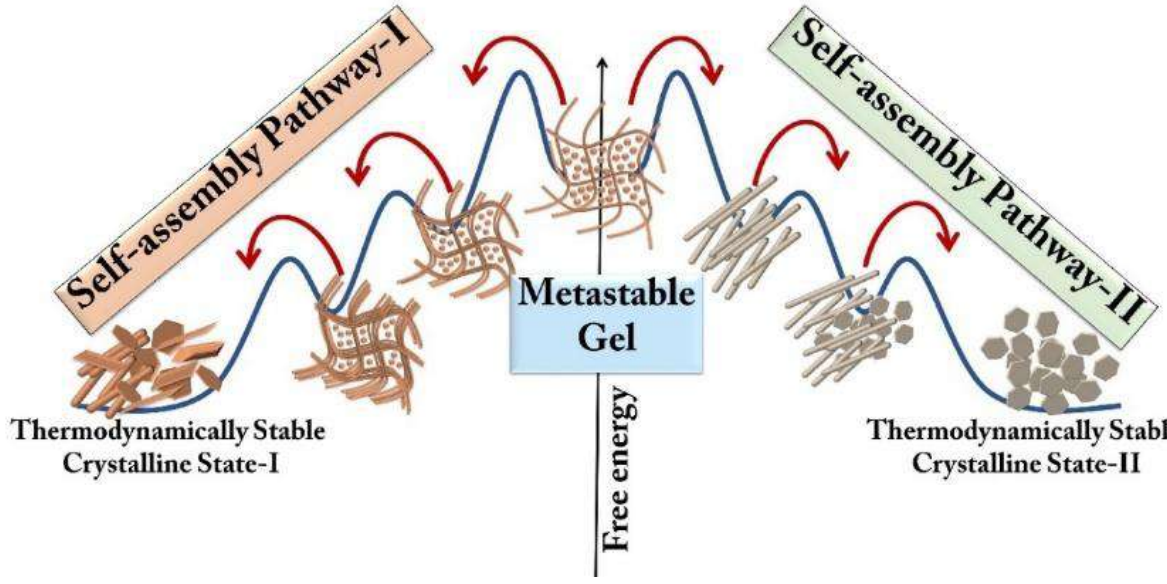

Scheme 6.1: Two different self-assembly pathways of the kinetically trapped gel, Py-M-G, driven by controlled heating.

6.2. Objective of the Chapter

Phase transformation of a gel to a crystal often occurs in an unanticipated way, and such transformations mostly result in crystals with varied habits. However, controlling crystal habits, especially confining the resulting crystals to a well-defined crystal habit during such a transformation, is quite difficult and therefore often overlooked. The reason is primarily due to the limited understanding of the complex pathways associated with such transformations. To address it, we have adopted a simplistic supramolecular model, Py-M, which forms a kinetically trapped or metastable gel in a mixed solvent system of DMSO and H_2O. We have demonstrated that the hierarchical self-assembly of the metastable gel can be well-regulated and directed towards a state of global minima to yield single crystals with well-defined crystal habits via controlled heating. The transformation proceeds through a novel and complex multistep phase transition pathway starting from nano-fiber to contiguous mesoscopic fiber, rod shape, and finally to hexagonally shaped single crystals. Such transformations have been thoroughly investigated and rationally established in this particular study.

6.3. Results and Discussion

6.3.1. Design Rationale

We have rationally designed a very simple amide and methyl ester unit appended low-molecular-weight gelator (LMWG) molecule, named Py-M, as a minimalistic supramolecular model for our study. (Scheme 6.2) Another molecule named Py-H was also designed as a control compound for our study, where the ester units of Py-M were replaced by four acylhydrazide units. (Scheme 6.2) The amide unit present in both molecules would facilitate hydrogen bonding interactions, and additionally, the ester unit present in Py-M would act as a hydrogen bond acceptor site. However, we expected that, in Py-H, the incorporation of the acylhydrazide unit would strengthen the extent of hydrogen bonding interactions as compared to that of Py-M. Moreover, the aromatic phenyl and pyridine rings present in both Py-M and Py-H might enable π-π stacking interactions as well, thereby contributing significantly to their self-assembly process.

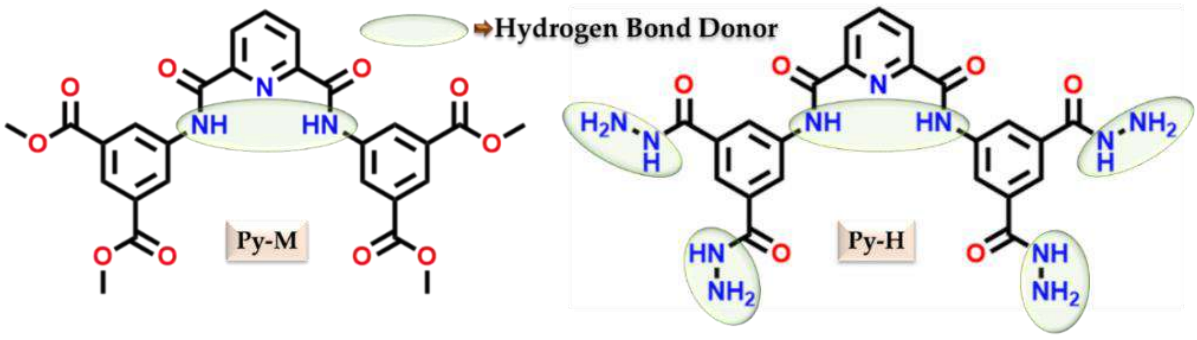

Scheme 6.2: Designing of LMWGs Py-M and Py-H.

6.3.2. Gelation Study and Mechanistic Insights

Gelation study of both Py-M and Py-H were conducted in a mixed solvent system of DMSO and H_2O in varied ratios (DMSO: H_2O ratio of 1:1, 1:4, 2:3, 3:2, 4:1). As a result, only Py-M was observed to be forming gel in all of the mentioned ratios barring DMSO: H_2O ratio of 1:4, where formation of gelatinous precipitate was evident. (Figure 6.1a, Figure A6.1a-e) Interestingly, despite having too many hydrogen bonding units in Py-H (more than that of Py-M), it could not form a gel in the abovementioned solvent combinations. (Figure A6.2a-e) However, for our subsequent studies, we decided to proceed with the gel derived from Py-M, named as Py-M-G, formed in the DMSO: H_2O ratio of 2:3, because of the higher water content. The critical gelation concentration (CGC) was calculated to be 0.6 % (w/v) in the DMSO: H_2O ratio of 2:3. (Figure A6.3a-d)

The gelation mechanism involved in the formation of Py-M-G was initially investigated through ^{1}H NMR experiment, where, on analyzing the ^{1}H NMR of the xerogel of Py-M-G (Py-M-G-Xero) (13.65 mM), we observed very slight upfield shifting of the amide -NH peak (NHc) by 0.006 ppm as compared to that of the crude product of Py-M (Py-M-Powder) (13.65 mM), indicating shielding of NH_c hydrogen, which might be due to the slight weakening of hydrogen bonding interaction in the xerogel state. (Figure 6.1b) The peaks corresponding to the aromatic hydrogen atoms (H_a, H_b, H_d, and H_e) were observed to be slightly upfield shifted, thus inferring the presence of π-π stacking interaction in the xerogel (Figure 6.1b). Moreover, the peak corresponding to the hydrogen atom of the methyl ester unit (H_f) experienced a slight upfield shift, which was indicative of a different packing arrangement in Py-M-G-Xero as compared to that of the Py-M-Powder (Figure 6.1b). For a deeper understanding of the role of the water molecule in the gelation process, we further recorded the ^{1}H NMR spectra by increasing the percentage of D_2O in the DMSO-d_6 solution of Py-M. As a result, we observed downfield shifting of the peak corresponding to the amide-NH unit with severe broadening, inferring a strong hydrogen bonding interaction between the amide -NH unit and water molecule. (Figure 6.1c) Most of the aromatic protons (such as H_a, H_b, and H_e) were observed to be downfield shifted except H_d, where upfield shifting was observed (with severe broadening), and the hydrogen atoms of the methyl unit, H_f were observed to be upfield shifted with severe broadening with an increase in the percentage of D_2O. (Figure 6.1c) Such an observation might be attributable to a change in the molecular packing of Py-M due to the alteration of various non-covalent interactions with an increase in the percentage of D_2O. FTIR-ATR study of Py-M-G-Xero revealed shifting of the peak corresponding to the two amide –NH units towards a higher energy region, from 3545 cm^{-1} and 3256 cm^{-1} in Py-M-Powder to 3555 cm^{-1} and 3345 cm^{-1} in Py-M-G-Xero, inferring weakening of the hydrogen bonding interaction in the xerogel state, which corresponded well with the ^{1}H NMR experiment of Py-M-G-Xero. (Figure

6.4b) However, PXRD analysis showed no peaks corresponding to hydrogen bonding and π-π stacking interactions, which might be due to the very weak nature of those interactions in the xerogel state. (Figure 6.4d) To dive deeper into the gelation mechanism, we additionally prepared a control compound by incorporating four acyl hydrazide units into Py-M (named as Py-H) by replacing the methyl ester units, as acyl hydrazide groups are known to promote the gelation process due to the presence of hydrogen bond donor as well as acceptor units in it. (Scheme 6.2) Gelation study of Py-H was also performed in DMSO: H_2O ratio of 1:1, 1:4, 2:3, 3:2, 4:1, using the same conditions as was done in the case of Py-M, and surprisingly, Py-H did not result in any kind of gel formation in the mentioned conditions. (Figure A6.2a-e) This particular study suggested the essence of a proper balance of various non-covalent interactions for the gelation to occur. The presence of excessive hydrogen bond-forming units in Py-H might have promoted precipitation rather than gelation.

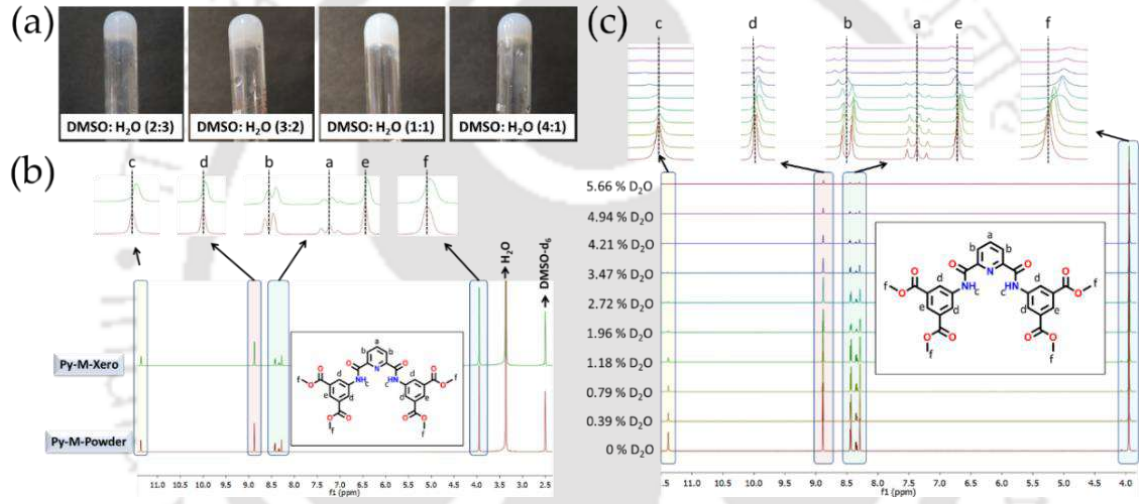

Figure 6.1: (a) Formation of gel by Py-M in DMSO: H_2O ratio of 2:3, 3:2, 1:1, and 4:1. (b) Stacked ^1H NMR spectra of Py-M-Powder and Py-M-Xero (13.65 mM each). (c) Stacked ^1H NMR spectra of Py-M with increasing D_2O (%).

6.3.3. Phase Transformation of Kinetically Trapped Gel

While trying to understand the effect of heating on Py-M-G, it resulted in some interesting transformations. The heating process was started slowly in an oil bath, and the first visual changes of Py-M-G were observed when the temperature reached ~120 °C, where the gel completely separated out from the solvent (the new gel has been named as Py-M-G-120). (Figure 6.2a,b) When the temperature was kept increasing, the gel completely converted into sol at ~150°C. (Figure 6.2c) Upon slow cooling, at the rate of ~1.5°C/min, the sol slowly converted into single crystals within 4-5 h (named as Crystal-I), instead of reverting back to its initial gel state. (Figure 6.2d) The resulting single crystals were observed to be of mixture of different shapes, (Figure 6.3a) and were analyzed through a single crystal X-ray diffraction (SC-XRD) study.

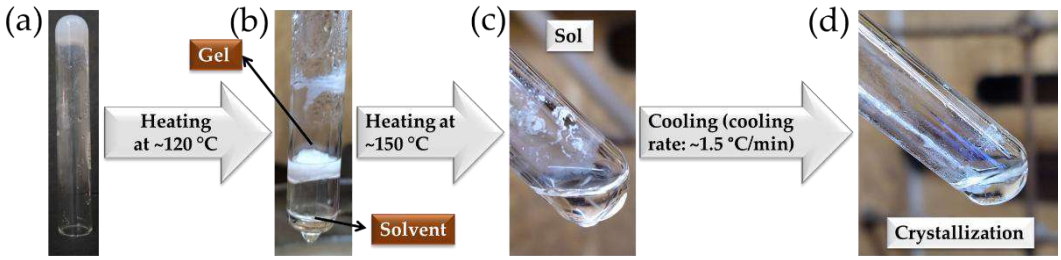

Figure 6.2: (a) Representing Py-M-G in a test tube. (b) Py-M-G-120 resulting from heating Py-M-G at ~120°C. (c) Sol formation as a result of heating Py-M-G at ~150°C. (d) Crystal-I obtained after cooling the sol.

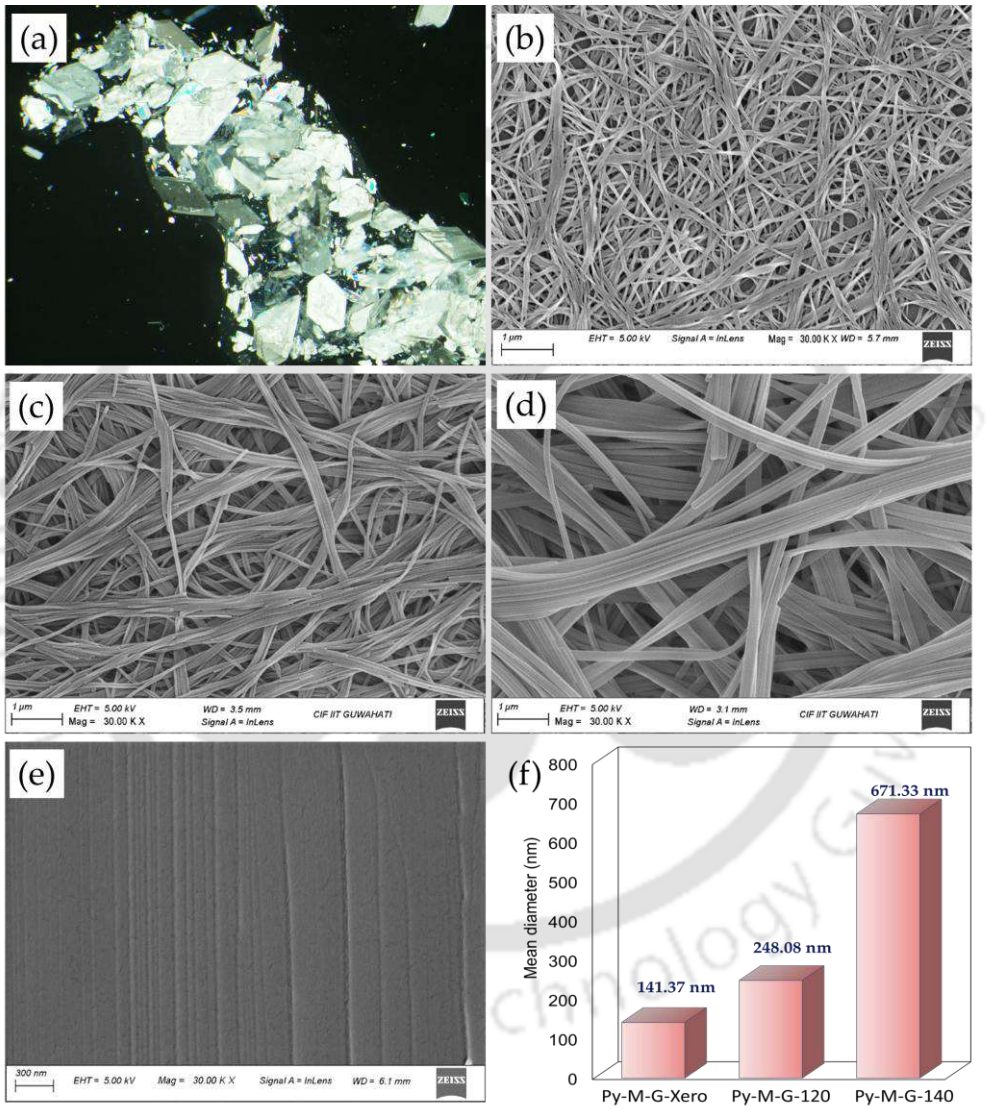

Figure 6.3: (a) Crystal-I with varied shapes. FESEM imaging of (b) Py-M-G-Xero, (c) Py-M-G-120, and (d) Py-M-G-140 resulting contiguous mesoscopic fibers with varied fiber diameter, and (e) Crystal-I. (f) Bar diagram depicting different fiber diameters in Py-M-G-Xero, Py-M-G-120, and Py-M-G-140.

To get microscopic level insights of such transformations, initially we performed FESEM imaging of Py-M-G at different temperatures or stages, such as at ~120°C (where the phase separation of the gel took place), ~140°C (just before the conversion of gel to sol), and lastly of the crystals.

FESEM imaging study revealed that, the initially present mesoscopic fibers with varied fiber diameter (formed from the hierarchical assembly of supramolecular polymers) in Py-M-G (mean diameter: 141.37 ± 31.12 nm) became thicker at ~120°C (mean diameter: 248.08 ± 72.06 nm), and slowly converted into a much thicker contiguous mesoscopic fiber at ~140 °C (mean diameter: 671.33 ± 192.6 nm). (Figure 6.3b-d,f; Figure A6.4a-c) Subsequently, the surface morphology of the resulting crystals became a ruled surface, which might have resulted from the accumulation of many contiguous gel nanofibers during the process of crystallization. (Figure 6.3e) Understanding of such a series of morphological changes during the process of gel to crystal transformation is very critical, as it allows regulation of the macroscopic properties of functional materials at its microscopic level. [6.31]

The gel-to-sol transformation was initially monitored through differential scanning calorimetry (DSC) measurement, which showed the first endothermic peak at ~90°C and a second endothermic peak at ~146°C, which were attributable to water vaporization and complete gel-to-sol transformation, respectively. (Figure 6.4a)

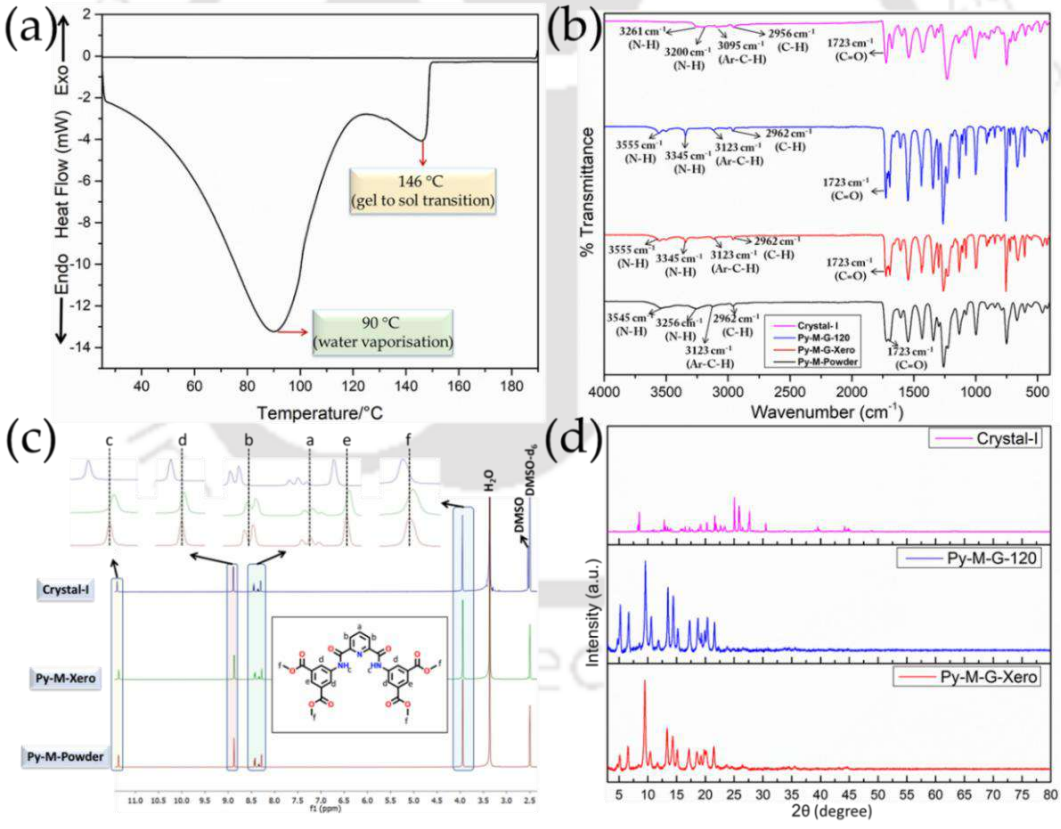

Figure 6.4: (a) Depicting the gel-to-sol transformation of Py-M-G via DSC measurement. (b) Stacked FTIR-ATR plot of Py-M-Powder, Py-M-G-Xero, Py-M-G-120, and Crystal-I. (c) Stacked ^{1}H NMR spectra of Py-M-Powder, Py-M-Xero, and Crystal-I. (d) Stacked PXRD patterns of Py-M-G-Xero, Py-M-G-120, and Crystal-I.

However, upon cooling, no exothermic peak corresponding to the crystallization was observed in the DSC measurement, which might be attributable to the long time required for the crystallization

process to occur. FTIR-ATR study of both Py-M-G-Xero and the xerogel derived from Py-M-G-120 resulted in shifting of the -NH peaks to 3555 cm^{-1} and 3345 cm^{-1} from 3545 cm^{-1} and 3256 cm^{-1} of Py-M-Powder. (Figure 6.4b) Such peak shifting to a higher energy region might be attributable to the weakening of the hydrogen bonding interaction in Py-M-G, which was the kinetically trapped or metastable state.

However, in Crystal-I, the peaks corresponding to both the -NH units shifted to a lower energy region, at 3261 cm^{-1}, and 3200 cm^{-1} as compared to that of Py-M-Powder, which was even lower than that of the Py-M-G-Xero, and Py-M-G-120. (Figure 6.4b) Additionally, the peaks corresponding to the two C-H units were also observed to be shifted to a lower energy region at 3095 cm^{-1} and 2956 cm^{-1}. (Figure 6.4b) Such significant peak shifting suggested strengthening of the hydrogen bonding interaction in Crystal-I, which was thermodynamically the most stable state. ^{1}H NMR spectroscopic study of Crystal-I (13.65 mM) revealed downfield shifting of the peak corresponding to -NH unit (H_c) by 0.029 ppm and 0.035 ppm as compared to that of the Py-M-Powder and Py-M-G-Xero, respectively, signifying the presence of extensive hydrogen bonding interaction in Crystal-I. (Figure 6.4c) This observation resonated very well with the previous observation made through the FTIR-ATR study. All the other peaks corresponding to the aromatic protons (H_d, H_b, H_a, and H_e) as well as the methyl hydrogen atoms (H_f) were also observed to be downfield shifted, thus inferring the existence of a different packing arrangement in Crystal-I as compared to that of Py-M-Powder and Py-M-G-Xero. (Figure 6.4c) PXRD analysis of the Py-M-G-Xero and Py-M-G-120 revealed a very similar kind of peaks. (Figure 6.4d) Surprisingly, no peaks corresponding to hydrogen bonding interactions were observed in PXRD analysis for both the mentioned samples. This result implied the involvement of very weak non-covalent interactions in the gelation process of Py-M, which resulted in metastable gel formation, Py-M-G. The PXRD pattern of the resulting crystal of Crystal-I showed a very close match with the simulated PXRD patterns generated using the crystallographic information file (CIF) of Crystal-I, thus indicating the phase purity of the bulk material. (Figure A6.5a) PXRD peak analysis of Crystal-I revealed sharp peaks at 25.04° (d spacing value of 3.55 Å) and 25.86° (d spacing value of 3.44 Å), which were attributable to π-π stacking interaction. (Figure 6.4d) The peaks at 27.66° (d spacing value of 3.22 Å) and 30.47° (d spacing value of 2.93 Å) could be ascribed to weak hydrogen bonding interactions. (Figure 6.4d) We further observed peaks at 39.54° (d spacing value of 2.27 Å), and 44.19° (d spacing value of 2.04 Å), (Figure 6.4d) which were representative of medium hydrogen bonding interactions. So, the non-covalent interactions such as hydrogen bonding and π-π stacking interactions fuelled the temperature-induced transformation of the kinetically trapped state of Py-M-G into the thermodynamically stable, Crystal-I state.

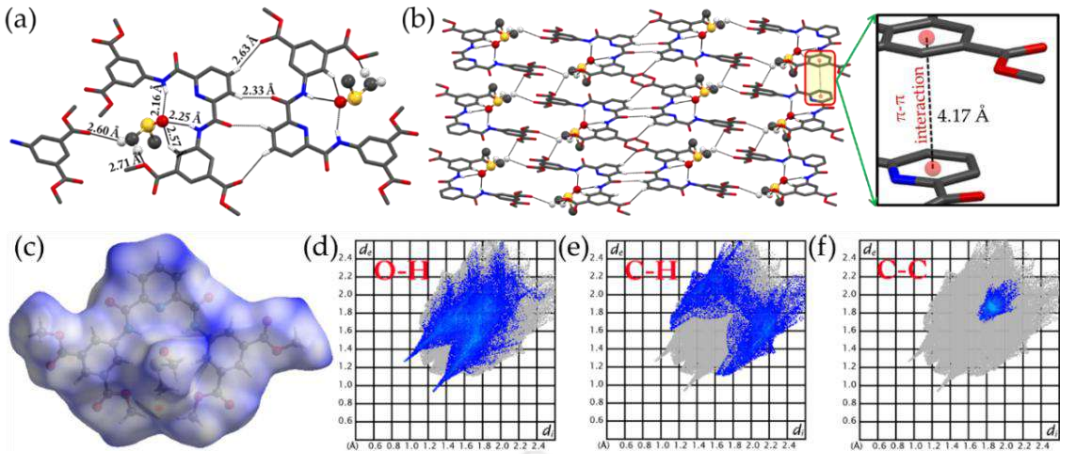

Figure 6.5: (a) Depicting intermolecular hydrogen bonding interactions between two nearby Py-M molecules, and (b) hydrogen bonding and π-π-stacking interactions facilitated self-assembly formation in Py-M (as established via SC-XRD study of Crystal-I). (c) HS analysis displaying the d_{norm} surfaces of Crystal-I. Representing 2D fingerprint plots (FPs) with d) O-H, (e) C-H, and (f) C-C contacts.

Crystal structure analysis of Crystal-I (Figure A6.6a-c) revealed that, Py-M formed dimeric assembly through four hydrogen bonding interactions (two H1···O2A = 2.63 Å, and two H2A···O1A = 2.33 Å), (Figure 6.5a) and the encapsulated DMSO molecule within the pseudo capsular cavity of Py-M, helped in connecting those dimers through hydrogen bonding interactions (H2N1···O6 = 2.16 Å, H2N2···O6 = 2.25 Å, H6A···O6 = 2.57 Å, O5A···H16C = 2.71 Å, and O4···H16B = 2.60 Å), thus helping in the formation of a one dimensional (1-D) polymeric chain. (Figure 6.5b, Figure A6.7a) Two such nearby 1-D polymeric chains are again interconnected via hydrogen bonding interactions, where the C-H unit of DMSO (H16B) and the oxygen atom of the ester (O3) unit played a crucial role (O3···H16B = 2.58 Å), thus helping in the expansion of the 1-D assembly to a 2-D network. (Figure 6.5b, Figure A6.7b) Moreover, π-π-stacking interaction between the phenyl ring and the pyridine unit (π_{phenyl}-$\pi_{pyridine}$ = 4.17 Å) of two nearby Py-M molecules also played a crucial role in connecting the two 1-D polymeric chains (Figure 6.5b) (all the hydrogen bonding distances (Å) and bond angles (º) have been furnished in Table A6.1). We further evaluated the various contact contributions from O-H (involving N–H···O/C–H···O contacts), C-H (involving C–H···O contacts), and C-C (involving contacts due to π-π-stacking interaction) contacts through Hirshfeld surface (HS) analysis, where, the contact contributions for the mentioned contacts were found to be 29.4 %, 16.4 %, and 4.3 % respectively. (Figure 6.5c-f; Table A6.2) So, from crystallographic structural analysis, we could conclude that the primary driving force for the crystallization of Py-M during gel to crystal transformation might be attributable to the extensive hydrogen-bonded self-assembled network formation, facilitated via the DMSO molecule, and to some extent π-π-stacking interaction as well.

However, we were also very keen on understanding whether the gel formed in different DMSO and H_2O ratios would also lead to similar kind of transformation or not. To verify it, we once again performed the heating experiment for all the gel samples obtained at DMSO and H_2O ratios of 1:1, 3:2, and 4:1. Consequently, in all the cases, crystallization was apparent, and the resulting crystals were a mixture of varied shapes, including rod, hexagonal, needle shapes, etc. (Figure A6.8a-d, Table A6.3). This particular experiment revealed that, although the shape of the resulting crystals varied with the varying DMSO and H_2O ratios, we could not control or restrict the resulting crystals to any specific habit.

6.3.4. Controlling the Crystal Habit

We further extended the experiment by smearing the Py-M-G on a glass plate, followed by instant heating at ~100 °C. (Figure 6.6a,b) The primary motive behind this experiment was to induce homogeneity in the heating process, unlike in the previous case, where the test tube, containing Py-M-G, was heated inside an oil bath.

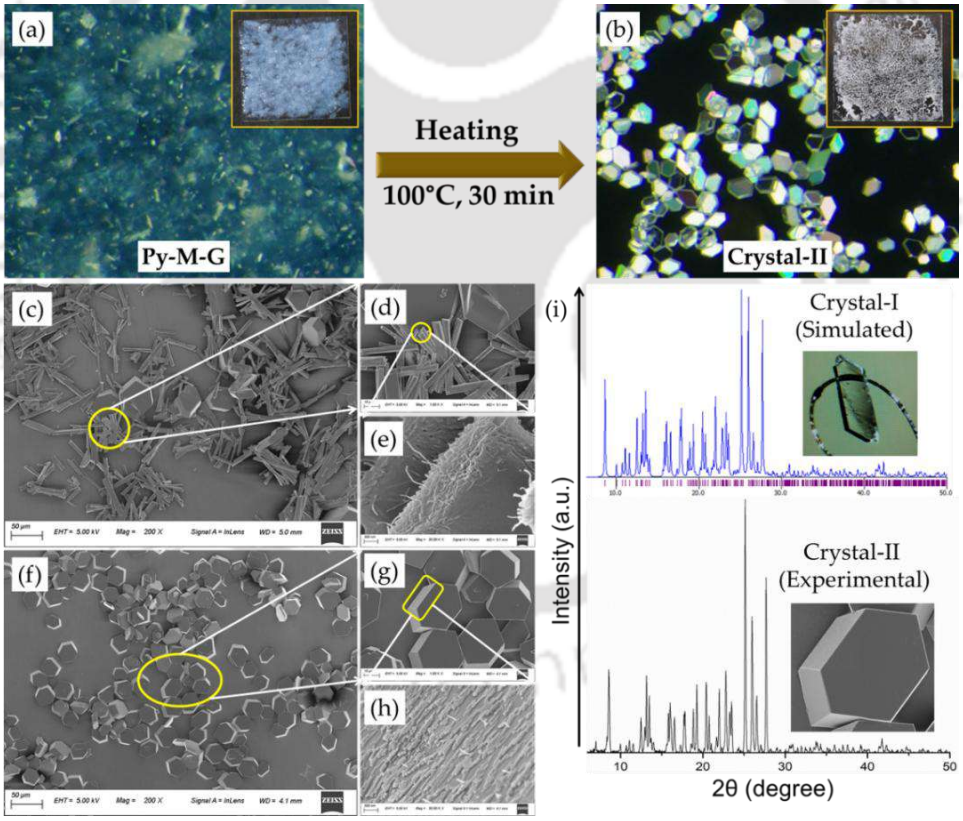

Figure 6.6: (a) Py-M-G under polarized optical microscopy (inset: photo of Py-M-G smeared on a glass plate) (b) Visualization of hexagonally shaped Crystal-II under a polarized optical microscope (inset: transformation of Py-M-G to Crystal-II on the surface of a glass plate after heating at 100 °C for 30 min). (c) (d), and (e) FESEM image depicting a mixture of hexagonally shaped and rod-shaped crystals generated after heating Py-M-G at 100 °C for 15 min. (f), (g), and (h) Hexagonal-shaped single crystals resulting from heating Py-M-G at 100 °C for 30 min, visualized through FESEM imaging. (i) Comparing the PXRD pattern of Crystal-II (Experimental) with the simulated PXRD pattern of Crystal-I (generated using the crystallographic information file in Mercury 4.2.0 software).

We expected that this changing condition would impact the gel-to-crystal transformation process, hence the habit of the resulting crystals. The smeared gel was visualized under a polarized optical microscope, revealing bright regions which might be attributable to the highly ordered internal structure and higher degree of molecular order in the gel. (Figure 6.6a) This observation is further supported by the presence of sharp peaks in the PXRD of Py-M-Xero as observed in the previous section, inferring the presence of a higher degree of crystallinity in the xerogel sample. (Figure 6.4d) After ~30 min of heating, we observed that the entire smeared gel got converted into single crystals of Py-M (named as Crystal-II) with well-defined hexagonal crystal habits on the surface of the glass plate, which could be visualized inside a polarized optical microscope. (Scheme 6.1; Figure 6.6b) The PXRD pattern of Crystal-II showed a very close match with the simulated PXRD pattern of Crystal-I, thus suggesting their similar crystalline phase. (Figure 6.6i; Figure A6.5b)

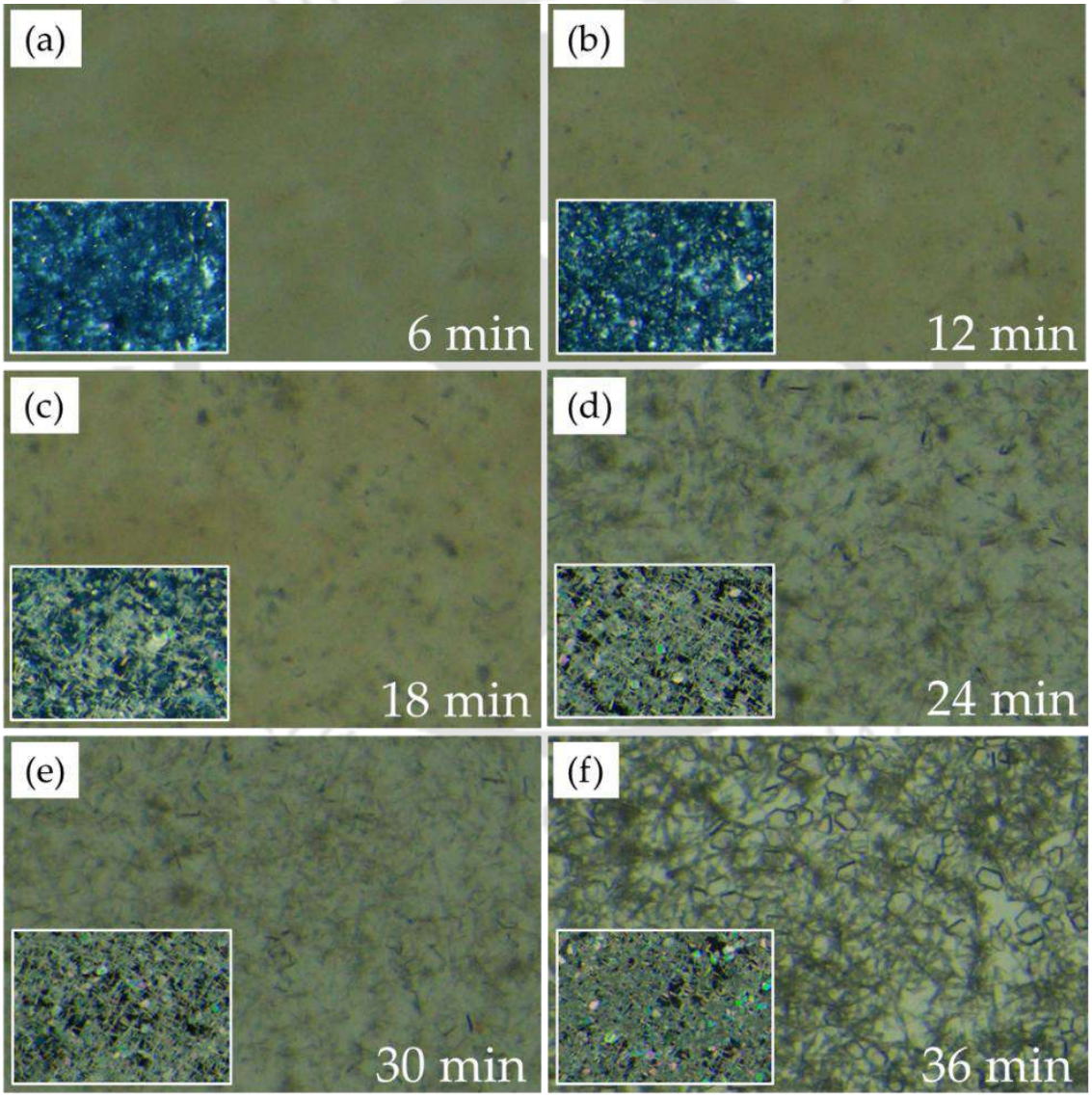

Figure 6.7: (a)-(f) Visualizing the transformation of Py-M-G to crystals at different time intervals under an optical microscope (inset: under polarized light).

The crystallization was observed in due course of heating only, without employing any kind of cooling process. Such heat-induced gel-to-crystal transformation was further visualized via FESEM imaging. As a result, after 15 min of heating, a mixture of rod-shaped and hexagonal-shaped crystals was evident from the FESEM imaging study. (Figure 6.6c-e) Close-up view of the rod-shaped crystals revealed densely packed and entangled gel nano-fibers, ready to expand in a particular direction. (Figure 6.6d,e) Upon heating the gel for 30 min, the gel nano-fibers further assembled in such a way that the shape of the resulting single crystals became hexagonal, and the whole surface of the glass plate was observed to be covered with single crystals having hexagonal crystal habits. (Figure 6.6f-h) The majority of the surface of the resulting hexagonal crystals was smooth, unlike the rod-shaped crystals; however, some rough surface with sparsely populated nano fibers was evident in one face of the crystal. (Figure 6.6g,h) We further wondered whether the varied ratios of DMSO and H_2O (2:3, 1:1, 4:1, 3:2) would have any impact on the final crystal habit formation in this particular study. However, interestingly, in all the cases, similar hexagonal-shaped crystals were evident upon 30 min of heating. (Figure A6.9a-d, Table A6.4) The result indicated that, unlike the earlier-mentioned case, here, in this process, the final crystal habit formed during the gel to crystal transformation was independent of the water or DMSO content.

We further monitored the gel-to-crystal transition under an optical microscope at different time frames. As a result, after up to 12 min of heating, no distinct changes were evident. (Figure 6.7a,b) However, very sharp, small rod-like crystals started growing within 18 min of heating. (Figure 6.7c) It slowly transformed into a little thicker rod-shaped crystal, along with the emergence of some small block-shaped crystals with no specific habits after 24 min of heating. (Figure 6.7d) After 30 min of heating, the crystals of both shapes became bigger in size with an increasing number of block-shaped crystals. (Figure 6.7e) The habit of the block-shaped crystals appeared to be more prominently hexagonal shaped with an increasing number of the same after 36 min of heating, and the hexagonal-shaped crystals became densely populated. (Figure 6.7f) As we disturbed the heating as well as the crystallization process at the cost of visualizing them inside an optical microscope, the appearance of the growth of crystals with different habits remained stagnant after 30 min of heating. Therefore, the complete conversion into hexagonally shaped crystals could not be visualized inside an optical microscope. Nevertheless, this observation helped us in understanding the complex pathways associated with the gel-to-crystal transformation process of the kinetically trapped gel, Py-M-G.

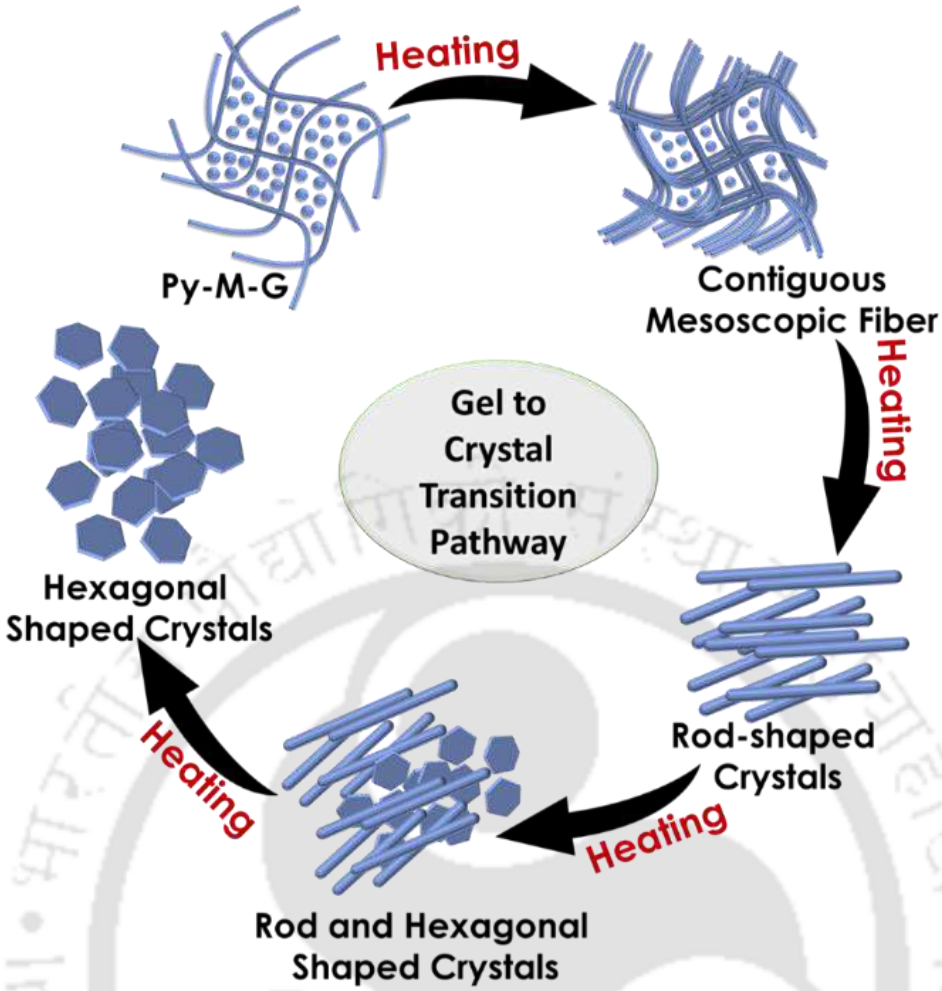

Figure 6.8: Schematic representation of the plausible pathways of the gel to crystal transition of Py-M-G achieved via controlled heating.

From all that experimental evidence, we could clearly say that, upon heating Py-M-G, it initially transformed into a contiguous fibrillar assembly, which slowly became a more complex assembly of mesoscopic entangled fibrils. The mesoscopic fibrils slowly expanded and self-assembled in a particular direction to give rise to rod-shaped crystals. Upon continuous heating, eventually the rod-shaped crystals transformed into the thermodynamically most stable hexagonal-shaped crystals. (Figure 6.8) It is interesting to note that, just by a simple alteration of the heating and sample preparation methodology, we could control the habits of the resulting single crystals during gel-to-crystal transition process. Most importantly, this particular process also allowed us to separate crystals of different shapes at different time frames. Such a transformation might be attributable to the important role played by the gel nano-fibers in maintaining the diffusion rate, upholding the nucleation rate uniformity during the event of heating in the smeared gel, and thus directing the hierarchical self-assembly towards a highly organized molecular level self-assembly pathway.

6.4. Conclusions

In summary, we have demonstrated the pathway complexity associated with the phase transformation (from a gel to a crystal) of a kinetically trapped supramolecular gel derived from an LMWG fabricated with a minimalistic design. We further established how such a transformation could be orchestrated to derive exclusively single crystals of a specific crystal habit via controlled heating and a different sample preparation methodology. Thus, different self-assembly pathways of our prepared gel were assessed and established carefully through different analytical tools. We believe that this particular study will be of immense importance, especially in fields like the pharmaceutical industry, where controlling crystal habit is of great importance. Besides, this study would also be beneficial for different materials applications involving crystal coating, crystal patterning, etc., as gel can be smeared on different surfaces, and single crystals with a specific habit can be generated in those surfaces. Moreover, the molecular-level understanding of such phase transformations opens up new possibilities in terms of developing novel functional materials, as the self-assembly process at the microscopic level can be controlled, which ultimately decides the fate of the macroscopic property of a material.

References

[6.1] N.-W. Wu, L.-J. Chen, C. Wang, Y.-Y. Ren, X. Li, L. Xu, and H. -B. Yang, *Chem. Commun.*, 2014, **50**, 4231-4233.

[6.2] E. R. Draper, and D. J. Adams, *Nat. Mater.*, 2024, **23**, 13-15.

[6.3] R. C.-Montoya, L. Á. d. Cienfuegos, J. A. Gavira, and J. W. Steed, *Chem. Soc. Rev.*, 2024, **53**, 10604-10619.

[6.4] D. J. Adams, *J. Am. Chem. Soc.*, 2022, **144** (25), 11047-11053.

[6.5] X. Liu, J. Fei, A. Wang, W. Cui, P. Zhu, and J. Li, *Angew. Chem. Int. Ed.*, 2017, **56** (10), 2660-2663.

[6.6] S. Kimura, K. Adachi, Y. Ishii, T. Komiyama, T. Saito, N. Nakayama, M. Yokoya, H. Takaya, S. Yagai, S. Kawai, T. Uchihashi, and M. Yamanaka, *Nat. Commun.*, 2025, **16**, 3758.

[6.7] D. K. Smith, *Soft Matter*, 2024, **20**, 10-70.

[6.8] D. K. Smith, *Angew. Chem. Int. Ed.*, 2025, **64** (24), e202502053.

[6.9] S. Panja, and D. J. Adams, *Chem. Soc. Rev.*, 2021, **50**, 5165-5200.

[6.10] C. D. Jones, and J. W. Steed, *Chem. Soc. Rev.*, 2016, **45**, 6546-6596.

[6.11] H. Wu, J. Zheng, A.-L. Kjøniksen, W. Wang, Y. Zhang, and J. Ma, *Adv. Mater.*, 2019, **31** (12), 1806204.

[6.12] G. Fichman, T. Guterman, J. Damron, L. Adler-Abramovich, J. Schmidt, E. Kesselman, L. J. W. Shimon, A. Ramamoorthy, Y. Talmon, and E. Gazit, *Sci. Adv.*, 2016, **2** (2), e1500827.

[6.13] E. R. Draper, K. L. Morris, M. A. Little, J. Raeburn, C. Colquhoun, E. R. Cross, T. O. McDonald, L. C. Serpell, and D. J. Adams, *CrystEngComm*, 2015, **17**, 8047-8057.

[6.14] D. Giuri, L. J. Marshall, C. Wilson, A. Seddon, and D. J. Adams, *Soft Matter*, 2021, **17**, 7221-7226.

[6.15] T. Yuan, Y. Xu, J. Fei, H. Xue, X. Li, C. Wang, G. Fytas, and J. Li, *Angew. Chem.*, 2019, **131** (32), 11189-11194.

[6.16] A. Vidyasagar, and K. M. Sureshan, *Angew. Chem. Int. Ed.*, 2015, **54** (41), 12078-12082.

[6.17] M. Salvalaglio, T. Vetter, F. Giberti, M. Mazzotti, and M. Parrinello, *J. Am. Chem. Soc.*, 2012, **134** (41), 17221-17233.

[6.18] Y. Zhao, G. Su, G. Liu, H. Wei, and L. Dang, *CrystEngComm*, 2021, **23**, 3524-3536.

[6.19] Y. Gao, W. Song, J. Yang, X. Ji, N. Wang, X. Huang, T. Wang, and H. Hao, *Crystals*, 2024, **14** (6), 484.

[6.20] E. Simone, A. R. Klapwijk, C. C. Wilson, and Z. K. Nagy, *Cryst. Growth Des.*, 2017, **17** (4), 1695-1706.

[6.21] A. Dawn, and H. Kumari, *Chem. Eur. J.*, 2018, **24** (4), 762- 776.

[6.22] S. Datta, H. Itabashi, T. Saito, and S. Yagai, *Nat. Chem.*, 2025, **17**, 477-492.

[6.23] E. Chuang, A. M. Hori, C. D. Hesketh, and J. Shorter, *J. Cell Sci.*, 2018, **131** (8), jcs189928.

[6.24] H. Wang, Z. Fenga, and Bing Xu, *Chem. Soc. Rev.*, 2017, **46**, 2421-2436.

[6.25] S. Kuila, S. Misra, T. Singha, A. Ghosh, P. Singh, R. Saha, D. Ganguly, P. Brandão, B. Satpati, and J. Nanda, *Small*, 2025, **21** (31), 2501718.

[6.26] D. Giuri, L. J. Marshall, B. Dietrich, D. McDowall, L. Thomson, J. Y. Newton, C. Wilson, R. Schweins, and D. J. Adams, *Chem. Sci.*, 2021, **12**, 9720-9725.

[6.27] E. C. Barker, A. D. Martin, C. J. Garvey, C. Y. Goh, F. Jones, M. Mocerino, B. W. Skelton, M. I. Ogden, and T. Becker, *Soft Matter*, 2017, **13**, 1006-1011.

[6.28] F. Cenciarelli, C. Tomasini, S. d'Agostino, and D. Giuri, *Cryst. Growth Des.*, 2024, **24** (22), 9331-9336.

[6.29] T. N. Das, G. Ghosh, R. Jena, S. Barman, F. A. Rahimi, A. Dey, S. R. V. Parambil, G. Fernández, and T. K. Maji, *Small*, 2025, **21** (47), e10082.

[6.30] S. A. McBride, S. Atis, A. A. Pahlavan, and K. K. Varanasi, *ACS Appl. Mater. Interfaces*, 2024, **16** (51) 70980-70990.

[6.31] A. R. Hirst, D. K. Smith, M. C. Feiters, H. P. M. Geurts, and A. C. Wright, J. Am. Chem. Soc., 2003, 125 (30), 9010-9011.

Annexure 6

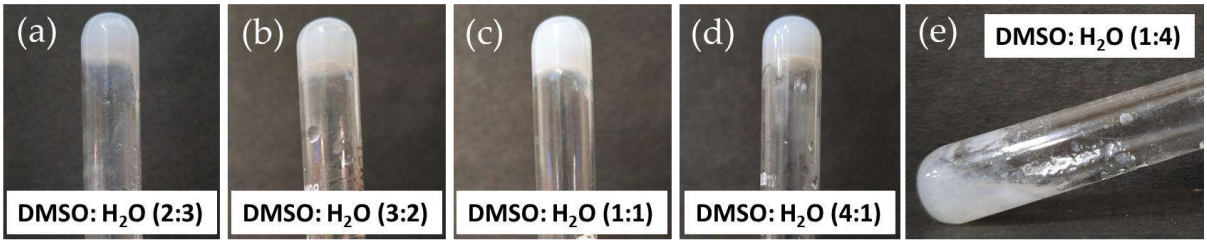

Figure A6.1: Formation of gel by Py-M in DMSO: H_2O ratio of (a) 2:3, (b) 3:2, (c) 1:1, (d) 4:1, (e) 1:4. (e) gelatinous precipitate formation by Py-M in DMSO: H_2O ratio of 1:4.

Figure A6.2: Gelation study of Py-H in DMSO: H_2O ratio of (a) 2:3, (b) 3:2, (c) 1:1, (d) 4:1, (e) 1:4, and (e) 1:4.

Figure A6.3: (a)-(d) Determination of critical gelation concentration (CGC) of Py-M in DMSO: H_2O ratio of 2:3.

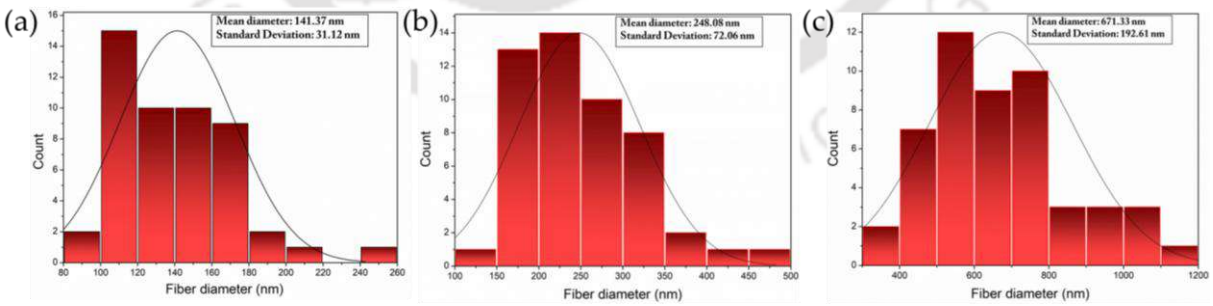

Figure A6.4: Histogram representing mean fiber diameter (in nm) of (a) Py-M-Xero, (b) Py-M-120, and (c) Py-M-140.

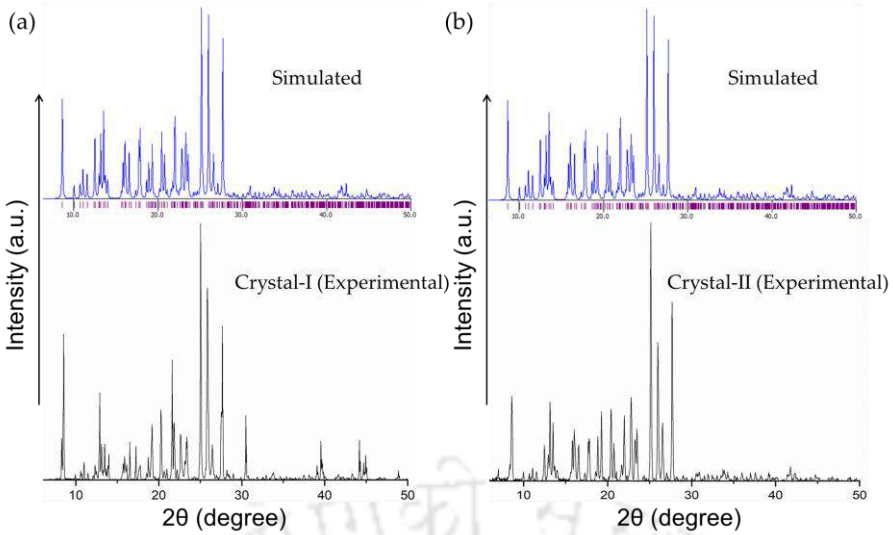

Figure A6.5: Comparing the PXRD pattern of (a) Crystal-I (Experimental), and (b) Crystal-II (Experimental) with the simulated PXRD pattern (generated using crystallographic information file in Mercury 4.2.0 software).

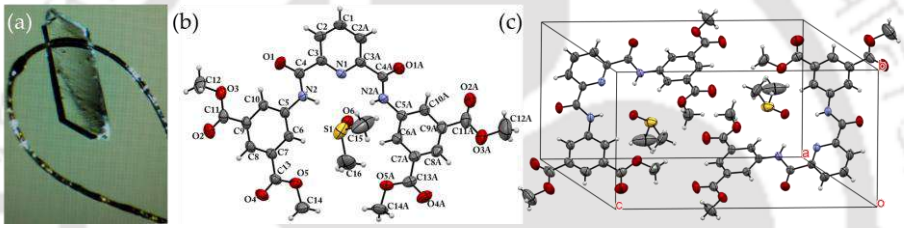

Figure A6.6: (a) Photograph of the mounted single crystal of Py-M. DMSO (Crystal-I). (b) Crystal structure of Crystal-I with atomic leveling. (c) Depicting the crystal packing of the Crystal-I.

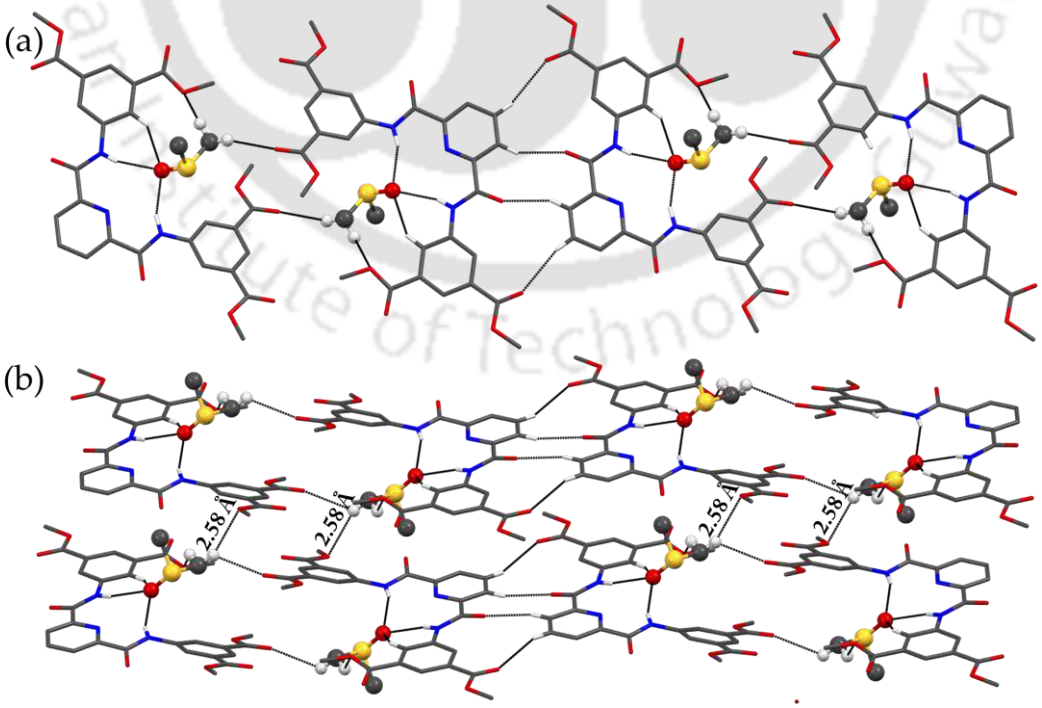

Figure A6.7: (a) Depicting 1-D polymeric chain formation in Crystal-I as facilitated via hydrogen bonding interaction. (b) Extension of 1-D self-assembly into 2-D self-assembly in Crystal-I.

Table A6.1: Hydrogen bonding distances (Å) and Bond angles (°) in Py-M. DMSO (Crystal-I) crystal.

Ligand/Complex	D–H···A	d(D···H)/Å	d(H···A)/Å	d(D···A)/Å	<D–H···A/°	Symmetry codes
Py-M. DMSO (Crystal-I)	N2-H2N1···O6	0.87 (4)	2.15 (4)	2.937 (5)	150 (4)	x, y, z
	N2-H2N1···N1	0.87 (4)	2.28 (4)	2.696 (5)	110 (3)	x, y, z
	N2A-H2N2···O6	0.78 (5)	2.25 (5)	3.014 (6)	164 (5)	x, y, z
	N2A-H2N2···N1	0.78 (5)	2.38 (5)	2.747 (5)	110 (5)	x, y, z
	C2A-H2A···O1A	0.93	2.33	3.193 (6)	154	-x, 1-y, -z
	C6-H6···O5	0.93	2.41	2.727 (5)	100	x, y, z
	C6A-H6A···O5A	0.93	2.41	2.729 (5)	100	x, y, z
	C6A-H6A···O6	0.93	2.57	3.325 (6)	138	x, y, z
	C10-H10···O1	0.93	2.37	2.859 (6)	113	x, y, z
	C10A-H10A···O1A	0.93	2.22	2.807 (6)	121	x, y, z
	C12A-H12D···O2A	0.96	2.08	2.553 (10)	108	x, y, z
	C14-H14A···O4	0.96	2.24	2.675 (7)	106	x, y, z
	C16-H16B···O3	0.96	2.58	3.459 (9)	152	x, 1+y, z
	C16-H16B···O4	0.96	2.60	3.177 (7)	119	1-x, 1-y, 1-z

Table A6.2: Depicting different contact contributions from the d_{norm} surface area of dipodal segments in Crystal-I.

Contacts	***Contact Contributions (%)***
C···C	4.3 %
C···H	16.4 %
O···H	29.4 %

Table A6.3: Depicting the effect of different DMSO-H_2O ratios on gelation and crystal shapes (gel inside test tube).

Py-M in different DMSO-H_2O ratios	***Gel/Sol/Precipitate***	***Heating Causes***	***Shape of Crystals***
1:1	Gel	Crystallization	Mixture of rod and needle shapes
2:3	Gel	Crystallization	Irregular block shape
3:2	Gel	Crystallization	Irregular block shape
4:1	Gel	Crystallization	Mixture of rod, needle, and irregular block shapes
1:4	Gelatinous precipitate	-	-

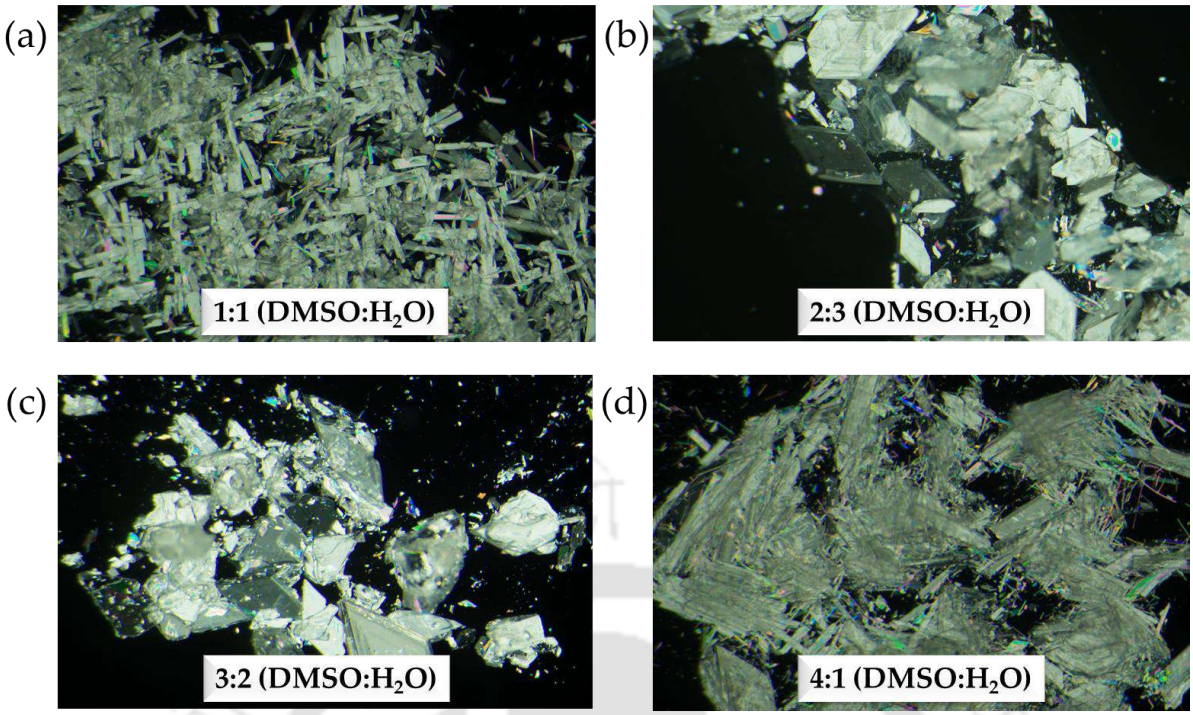

Figure A6.8: Visualizing crystals of Py-M derived from gel formed in DMSO: H_2O ratio of (a) 1:1, b) 2:3, (c) 3:2, and (d) 4:1 (Test tube experiment) under a polarized optical microscope.

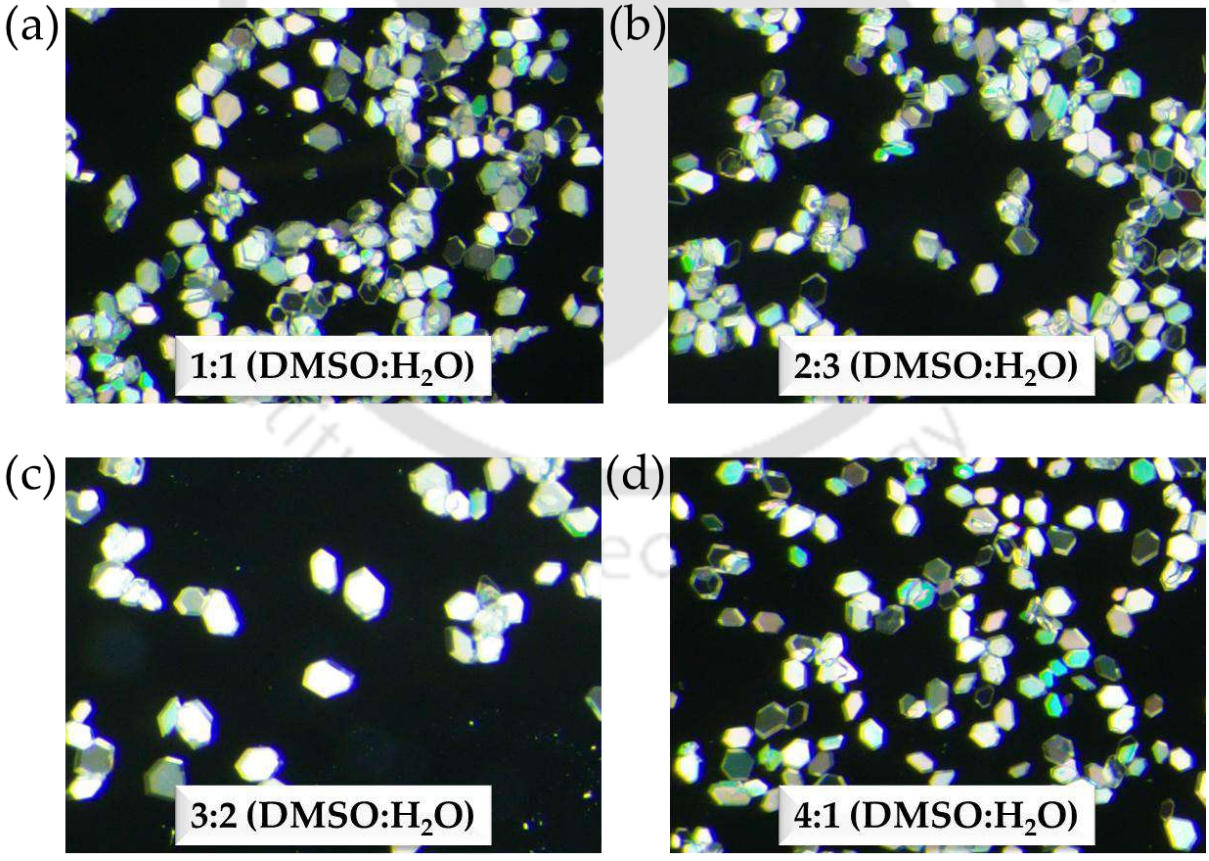

Figure A6.9: Visualizing crystals of Py-M derived from gel formed in DMSO: H_2O ratio of (a) 1:1, (b) 2:3, (c) 3:2, and (d) 4:1 (Glass plate experiment) under a polarized optical microscope.

Table A6.4: Depicting the effect of heating on crystal habits (heating the gel smeared on a glass plate)

Py-M in different DMSO-H_2O ratios	***Gel/Sol/Precipitate***	***Heating Causes (Heating at 100° C for 30 min)***	***Shape of Crystals***
1:1	Gel	Crystallization	Hexagonal
2:3	Gel	Crystallization	Hexagonal
3:2	Gel	Crystallization	Hexagonal
4:1	Gel	Crystallization	Hexagonal
1:4	Gelatinous precipitate	-	-

CONCLUSIONS & FUTURE PERSPECTIVES

In summary, this thesis presents some profound new ideas concerning utilization of artificial self-assembled systems for anion coordination and supramolecular gelation purposes. With respect to anion coordination, we have demonstrated in chapter 3A that, the anion recognition behavior of the artificial receptor systems can be well regulated via proper structural tuning of the receptor molecules. In this particular chapter we showed that, with increase in the π-acidic character of the terminal substituents of the symmetrical bis-urea based receptors, namely L_1, L_2, and L_3 containing electron deficient/π-acidic, -NO_2, -CF_3, and electron rich-hydrophobic naphthyl, respectively as their terminal substituents, their acetate anion recognition affinity increases in the solution phase, thus following the order: L_3 (11.65 M^{-1}) < L_1 (23.47 M^{-1}) < L_2 (40.38 M^{-1}). This observation was based on ^1H NMR titration experiment of all those three receptors with acetate anion conducted in DMSO-d_6 solvent. In a similar line, in chapter 3B, the design rationale of the receptor molecules was improvised and reported two unsymmetrical dipodal mono-urea based receptors containing only electron deficient/π-acidic terminal substituents. The receptors named BPU-1 (having -NO_2 as the terminal substituent), and BPU-2 (having two -CF_3 units as the terminal substituent) were further attached with a benzimidazole to the semi-rigid arm, which served two purposes, firstly it acts as a fluorophore signalling unit, and secondly, it also acts as anion recognition site as well. The combination of flexible mono-urea arm and the semi-rigid benzimidazole unit containing arm enabled recognition of anions with varied dimensionalities in the solid state. In the solid state, BPU-1 could capture all the halide anions (except F^- anion), and NO_3^- anion. BPU-1 further encapsulates SO_4^{2-} in its hydrated form as sulfate-water-sulfate cluster in the solid state. However, only Cl^- and Br^- anions were successfully crystallised with the receptor BPU-2. Interestingly, in presence of F^-/HO^- both BPU-1, and BPU-2 undergoes intramolecular cyclisation, thus yielding a heterocyclic compound, named as BP-Cyc. This observation paves a new way of synthesizing heterocyclic compound at ease. Moreover, the presence of the benzimidazole fluorophore unit further facilitated detection of SO_4^{2-}/HSO_4^- anions in water.

Subsequently, in chapter 4A, we intended to expanded the concept of anion recognition chemistry to sense/detect toxic analytes present in water. In that purpose, we developed two small molecule-based fluorogenic sensors, namely, Benz-d-CF_3 and Benz-m-CF_3 appended with only one anion binding site. We observed that, these sensors could be effectively utilized for the sensing of highly toxic CN^- anion present in drinking water with the help of CTAB. The LOD value was observed to be 496.5 nM for Benz-d-CF_3, which is far below the maximum acceptable concentration of CN^-

in drinking water (1.9 μM) as recommended by WHO. This sensing can also be visualized through naked eyes as well, under the UV-lamp of 365 nm. A simple device was also constructed for real world application, by using filter paper for the solid-state detection of CN^- present in drinking water. Afterward, we expanded our study towards development of small molecule based supramolecular soft materials, that is supramolecular gel in chapter 4B. In this chapter we developed LMWG, namely PY-NAP, appended with anion binding sites. The supramolecular gel derived from PY-NAP, named as RT-Gel, was observed to be selectively responsive towards SO_4^{2-} anion, and it showed thermally bisignate characteristics. RT-Gel could sequester Ag^+ from water with an uptake efficiency of ~90%, followed by spontaneous in situ reduction of Ag^+ to its nanoparticles inside the gel matrix of RT-Gel. This particular idea was further employed for the construction of conductive hybrid gel nanocomposite with the help of agarose polymer. This particular study upholds the very concept of waste to wealth generation.

In line with the previous chapter, in the nest chapter a PSOG, derived from a LMWG named THD was developed. Thus developed PSOG was observed to be capable of forming gel selectively in presence of diesel and kerosene oil among studied other different oil samples and organic solvents. This is for the first time we have introduced the idea of selectivity in oil gelation. Both the gel derived from diesel and kerosene were observed to be thixotropic as well as thermos-reversible in nature. The PSOG was further applied for the oil spill recovery from water, which showed more than 80 % diesel oil recovery percentage. The concept of selective oil gelation was further applied for the cost-effective visual detection of kerosene adulteration in petrol oil. This proposed idea circumvents the use of sophisticated instruments in fuel adulteration detection process.

Finally in the last chapter, we have demonstrated that, the phase transformation of a hierarchical nanofibrillar assembly of a kinetically trapped supramolecular gel could be well regulated via controlled heating. Initially, when the kinetically trapped gel, named Py-M-G (derived from Py-M), was heated at high temperature, single crystals with varied habits formed. Such a transformation could be directed to yield single crystals with well-defined crystal habits by implementing proper heating method.

Overall, this thesis emphasises on developing small molecule based self-assembled systems for different applications, particularly in recognition chemistry, sensing/detection of toxic chemicals, and water remediation. Due to their ease of preparation, highly structural tunability, and economic viability, such small molecule-based systems are becoming one of the most important systems to be studied for addressing different real-world challenges. We have demonstrated how the anion recognition behaviour could be fine-tuned by simple structural modification, and this could be helpful in designing receptor molecules to selectively target specific anions, especially toxic anions, and extract them from water. In addition, this particular study might be useful in biology

as well, in terms of anion transportation study. Furthermore, the concept of micelle assisted enhanced selectivity and sensitivity of a sensing process discussed in this thesis bears lots of potential for real-world application. Sequestration of metal salts from water employing a supramolecular gel system demonstrated in this thesis shows its potential in the field of water remediation. Subsequently, the oil spill remediation and detection of fuel contamination via a simple PSOG highlights the true potentials of small molecule based self-assembled systems. In pharmaceutical industries controlling of crystal habits is very important, in that context our study on controlled gel to single crystal transformation bears lots of significance. Based on all those studies and results enshrined in this thesis, the future goal is to carry forward this research journey with supramolecular self-assembled systems for advanced materials application that alleviate real world problems related to environment, health and economy.

Oiyao Appun Pegu
Research Scholar

CONTACT
Department of chemistry
IIT Guwahati, Assam-781039
Email: o.appun@iitg.ac.in /
oiyaoappunpegu@gmail.com
Phone no.: 6002831002

EDUCATION

INDIAN INSTITUTE OF TECHNOLOGY GUWAHATI, ASSAM, INDIA
Research scholar
Department of chemistry
(July 2021-current)
Thesis: *Anion Coordination and Gelation Study of Small Molecule based Self-assembled Systems: Recognition, Sensing and Water Remediation*
Supervisor: Prof. Gopal Das

INDIAN INSTITUTE OF TECHNOLOGY GUWAHATI, ASSAM, INDIA
Department of chemistry
MSc. in chemistry
(2016-2018)

JORHAT INSTITUTE OF SCIENCE AND TECHNOLOGY, ASSAM, INDIA
Department of chemistry
BSc. in chemistry
(2013-2016)

ISLAND ACADEMY JUNIOR COLLEGE, MAJULI, ASSAM, INDIA
Higher Secondary (2013)

JONAKI CHAMAHIYA ATI H.S. SCHOOL, MAJULI, ASSAM, INDIA
HSLC (2011)

PROFESSIONAL EXPERIENCE

- Served as a trained operator of single crystal x-ray diffractometer (SC-XRD) instrument at IIT Guwahati (2022-2026).

ACHIEVEMENTS

- Qualified JAM-2016.
- CSIR-UGC NET JRF June 2020 in CHEMICAL SCIENCES.

JOURNAL PUBLICATIONS

1. Effect of Terminal Substituents on Anion Recognition in Bis-Urea Receptors and Tetracycline Sensing in Water. **O A. Pegu**, A. Das, and G. Das, ***J. Mol. Struct.*, 2023, 1294, 136427**.
2. Anion Induced Intramolecular Cyclisation of Urea-Based Receptors: Entrapment of Cyclic $[SO_4(H_2O)_4^{2-}]_n$ Cluster and Encapsulation of Anions with varied Dimensionality, **O. A. Pegu**, R. Moral, and G. Das, ***Cryst. Growth Des.*, 2023, 23, 8370-8380**.
3. Twisted-Intramolecular-Charge-Transfer Based Fluorogenic Nano-Probe for Ultrafast Cyanide Sensing in Water and Micellar Medium. **O. A. Pegu**, and G. Das. ***J. Mater. Chem. C*, 2024, 12, 6519-6527**.
4. Thermally Bisignate Anion Responsive Supramolecular Gel and In Situ Generation of a Conductive Hybrid-Gel Nanocomposite. **O. A. Pegu**, and G. Das. ***Langmuir*, 2024, 40, 24095-24105**.
5. PSOG for selective thixotropic/thermo-reversible gelation in oil: Oil spill recovery and fuel-adulteration detection. **O. A. Pegu**, R. Moral, and G. Das, ***Chem. Eng. J.*, 2025 (Accepted)**.
6. Regulating the Phase Transformation of a Kinetically Trapped Hierarchical Nano-Fibrillar Assembly of Supramolecular Gel: Unveiling the Pathway Complexity. **O. A. Pegu**, and G. Das (Manuscript submitted).
7. Anion Coordination Chemistry: An Expedition Towards Designing of Functional Materials. **O. A. Pegu**, R. Moral, and G. Das, ***Chem. Asian J.*, 2025, 20, e202401236**.
8. Designing of self-assembled supramolecular frameworks for recognition of anion–water clusters: recent highlights. **O. A. Pegu**, and G. Das, ***CrystEngComm*, 2025, 27, 2964-2978**.
9. Metal-organic-framework-based functional materials for the removal of toxic anions from water: a recent perspective. **O. A. Pegu**, and G. Das, ***Polyhedron*, 2026, 284, 117887**.
10. Probing the aggregation potential and picric acid recognition aptitude by altering aromatic core substitution in a series of cinnamaldehyde-based receptors, R. Moral, **O. A. Pegu**, and G. Das. ***Dyes Pigm.*, 2023, 218, 111502**.
11. Terminal substituent induced differential aggregation and sensing properties: A case study of neutral benzimidazole based urea receptors, R. Moral, **O. A. Pegu**, and G. Das. ***New J. Chem., 2023, 47, 19625-9632***.
12. Carbazole derived amphiphile based AIEgen: Detection of Nitro-antibiotics and water repelling surface. S. De, **O. A. Pegu**, and G. Das. ***Langmuir*, 2023, 39, 2444-2449**.
13. Anion-driven supramolecular gel: naked-eye detection of picric acid, facilitating in situ formation of gel nanocomposites and enabling solid-state anion exchange. R. Moral, **O. A. Pegu**, and G. Das, ***Nanoscale*, 2025, 17, 26845-26854**.

CONFERENCES ATTENDED

1. Poster presentation in *North East Research Conclave (NERC 2022)*, IIT Guwahati, India May, 2022.
2. Attended *Frontiers in Chemical Sciences (FICS-2022)*, IIT Guwahati, India on December, 2022.
3. Poster presentation in *Modern Trends in Inorganic Chemistry (MTIC-2023)*, IISc Bangalore, India on December, 2023.

4. Poster presentation in *Frontiers in Chemical Sciences (FICS-2024)*, IIT Guwahati, India on December, 2024.
5. Poster presentation in *National Conference on Polymers and Advanced Functional Materials (NCPAFM-2024)*, IAAST, Guwahati, India on December, 2024. (**2nd Prize**)
6. Poster presented in the *36th CRSI National Symposium in Chemistry (CRSI-NSC-36) and CRSI–RSC Symposium*, Dibrugarh University, Dibrugarh, India, on February, 2026.

TEACHING EXPERIENCE

1. Teaching Assistantship at IIT Guwahati, Course: CH-515: Inorganic Chemistry Laboratory for M.Sc. students (July-Nov, 2022).
2. Teaching Assistantship at IIT Guwahati, Course: CH-314: Inorganic Chemistry Laboratory for B.Tech. students (July-Nov, 2023).
3. Teaching Assistantship at IIT Guwahati, Course: CH-515: Inorganic Chemistry Laboratory for M.Sc. students (July-Nov, 2024).
4. Co-guided a project of an M.Sc. final year student (2023).
5. Co-guided B. Tech. project of a final year student, Department of Chemical Science and Technology (CST) at IIT Guwahati (2025).
6. Co-guided internship project of two students (2026), NEP FYUG Program. (DBT sponsored Project).

PROJECT EXPERIENCE

1. Successfully completed the Summer Internship Programme held in Tocklai Tea Research Institute (TRI), Assam from 1st July,2015 to 15th July, 2015 under the guidance of Dr. I.K Phukan, Principal Scientist, Soil Department, TRI.
2. Successfully completed M. Sc. project entitled as *"Development of Curcumin Loaded Chitosan Stabilised Au-Nanoparticle Beads for Controlled Drug Delivery"* at IIT Guwahati, 2018, under the guidance of Prof. Lal Mohan Kundu, IIT Guwahati.

EXPERTISE

Instruments handled: Single crystal x-ray diffractometer (SC-XRD) (trained operator), Spectroscopic Techniques (UV-Vis, Fluorescence, and FTIR), Dynamic light scattering (DLS), and Fluorescence Microscopy.

Software handling: APEX 3/4/5 (for crystallography), Olex2 (for crystallography), Origin, Adobe Illustrator, MestreNova, ChemDraw, ImageJ, XPSPEAK41, etc.

I hereby declare that, all the aforementioned information is true to the best of my knowledge.

Oiyao Appun Pegu